

https://dspace.org/

Effect of microstructure on properties of selected Pt-based alloys

Shongwe, Mxolisi Brendon

2015-04-30
http://hdl.handle.net/10539/17582

Downloaded from a DSpace repository. https://dspace.org/

EFFECT OF MICROSTRUCTURE ON PROPERTIES OF SELECTED Pt-BASED ALLOYS

Mxolisi Brendon Shongwe

A thesis submitted to the Faculty of Engineering and the Built Environment, University of the Witwatersrand, in fulfilment of the requirements for the degree of Doctor of Philosophy in Engineering

JOHANNESBURG, JANUARY 2014

DECLARATION

I, Mxolisi Brendon Shongwe, declare that this thesis is my own work, except where otherwise acknowledged. It is submitted for the degree of Doctor of Philosophy in Engineering at the University of the Witwatersrand, Johannesburg. It is not been submitted previously at this, or any other university for any degree or examination.

SIGNATURE DATE

ABSTRACT

This study investigated the effect of microstructure on properties of selected Pt-based alloys. Six alloys of different compositions were analysed after heat treatment at 1500°C for 18 hours, followed by quenching in water; then annealed at 1100°C for 120 hours and air cooled, equivalent to a potential industrial specification. Microstructural characterisation utilised OM, SEM, AFM, TEM and EDX. Further characterisation was carried out using a nanoindentation hardness tester for nanohardness and elastic modulus measurements. The research focus was to characterize the different morphologies of γ′ ~Pt_3Al precipitates during a single heat treatment, and to understand the nano-mechanical properties of the γ′ precipitates and γ (Pt) matrix, taking their proportions into account.

In the present work, the samples were successfully etched, (which was not possible before) allowing optical microscopy and SEM to give much clearer microstructures than previously. The precipitate volume fractions were measured from SEM and AFM images, and agreed well. The γ′ volume fraction (expressed as percent) of nominal Pt_{78}:Al_{11}:Cr_6:Ru_5 (at.%) alloy was 51 ± 6% (SEM) and 57 ± 10% (AFM), while for nominal Pt_{85}:Al_7:Cr_5:Ru_3 (at.%) it was 45 ± 6% (SEM) and 48 ± 8% (AFM). A comparison of the γ′ volume fractions obtained from TEM showed that, compared to SEM, as the γ′ volume fraction observed with SEM increased, the γ′ volume fraction measured in TEM increased, although the TEM volume fraction results are believed to have considerable error due to TEM only revealing the microstructure of relatively small regions compared to SEM. Comparing with Pt-Al-Cr-Ni alternatives with γ′ volume fractions of 51-57%, the nominal Pt_{78}:Al_{11}:Cr_6:Ru_5 and nominal Pt_{85}:Al_7:Cr_5:Ru_3 (at.%) alloys have comparable γ′ volume fractions within, experimental error, and are considered as promising. From a microstructural viewpoint, these alloys were identified as the most promising.

TEM revealed that at the specific heat treatment there were multiple size ranges of γ′ precipitates. The ~Pt_3Al precipitate structure was found to be cubic $L1_2$, rather than tetragonal. The orientation relationship between the γ matrix and γ′ precipitates was found to be $[114]_M||[114]_P$; $[001]_M||[001]_P$; $[103]_M||[103]_P$.

The nano-mechanical properties of the γ matrix and γ′ precipitates of Pt-Al-Cr-Ru alloys were investigated for the first time. At 2.5mN, it was possible to measure mechanical properties inside the individual γ′ precipitates and γ matrix channels, and in all six alloys the

γ′ precipitates were the harder phase. The hardness of γ′, γ and the overall alloy was a function of the Pt content, and the hardness of the overall alloy was also a function of the Al content. The overall alloy hardness for nominal Pt_{85}:Al_7:Cr_5:Ru_3 (at.%) was 9.0 ± 0.3GPa and 9.2 ± 0.3GPa for nominal Pt_{78}:Al_{11}:Cr_6:Ru_5 (at.%).

The new findings on image analysis showed that the precipitate volume fractions of nominal Pt_{78}:Al_{11}:Cr_6:Ru_5, nominal Pt_{85}:Al_7:Cr_5:Ru_3 and nominal Pt_{78}:Al_{11}:Cr_8:Ru_3 (at.%) were comparable to commercial nickel-based superalloys (NBSAs). TEM has shown that the precipitate morphology was similar to that of NBSAs, while nanoindentation studies indicated that the Pt-Al-Cr-Ru alloys' overall, γ and γ phase nanohardnesses and elastic moduli were also similar to NBSAs. These results were encouraging, since the NBSAs already have commercial applications. Thus, more research efforts are encouraged on the Pt-Al-Cr-Ru alloys in order to further improve the properties of these alloys.

DEDICATION

I would like to dedicate this work to God and my parents: Edgar Shongwe and Anna Shongwe, for everything and being the best parents in the world, which God perfected before the foundations of the earth. I love you!! My sweetness, Tumisang Shongwe, thank you for being with me.

ACKNOWLEDGEMENTS

I would like to thank the following people and organisations, without which the work would not have been possible:

- My supervisors, Prof. L.A. Cornish and Prof. M.J. Witcomb for their continued support. Especially Prof. Cornish, for nurturing me till the end of this research work, I will remain grateful to you, for your effective supervision and understanding. Thank you!
- Prof. M.J. Witcomb, thank you for all the help with the preparation of the TEM samples and transmission electron microscopy, I do not see any other way I would have possibly prepared these samples successfully without your help.
- The Nelson Mandela Metropolitan University (NMMU), Department of Physics and Centre for HRTEM for use of the CSM nanohardness tester and the JEOL TEM 2100.
- William Goosen at NMMU is thanked with the help for the nanohardness tester operation.
- Dr Jaco Olivier at NMMU is thanked with the help for the TEM operation and assistance with the JEMS software.
- Thuto Makgato at the Microscopy and Microanalysis Unit at the University of the Witwatersrand for help with the AFM images and use of the WSxM software.
- Richard Couperthwaite for hours of invaluable work at the SEM at Mintek.
- Bernard Odera is thanked for the help and procedure used for electrolytic etching of the alloys at the School of Chemical and Metallurgical Engineering, University of the Witwatersrand.
- Edson Mahuma for manufacturing and sectioning of samples at Mintek.
- The financial assistance of the South African Department of Science and Technology (DST), National Research Foundation (NRF), through the DST-NRF Centre of Excellence in Strong Materials (CoE-SM), and the Mellon Foundation are gratefully acknowledged.
- The Microscopy and Microanalysis Unit at the University of the Witwatersrand.
- Mintek, for granting me this opportunity and for permission to publish the results.
- Finally, but not least, thanks to all my family and friends who helped me in many, treasured ways. I will never forget the love and support from every one of you.

TABLE OF CONTENTS

DECLARATION ..... **ii**
ABSTRACT ..... **iii**
DEDICATION ..... **v**
ACKNOWLEDGEMENTS ..... **vi**
TABLE OF CONTENTS ..... **vii**
LIST OF FIGURES ..... **xii**
LIST OF TABLES ..... **xxix**
CHAPTER ONE **1**
1. INTRODUCTION AND BACKGROUND **1**
1.1 Rationale of this Investigation **5**
1.2 Outline of the Thesis **7**
CHAPTER TWO **8**
2. LITERATURE SURVEY **8**
2.1 Introduction **8**
2.2 Development and History of Superalloys **8**
2.2.1 Microstructure 8
2.2.2 Mechanical Properties 9
2.2.3 Development of Processing 9
2.3 Nickel-based Superalloys **10**
2.3.1 Introduction 10
2.3.2. Single Crystal Alloys 10
2.3.3 Effect of Grain Boundaries on Mechanical Properties 15
2.3.4 Development of Different γ′ Morphologies and Sizes in NBSAs 15
2.3.5 Dislocation Networks in Ni-based Superalloys 18
2.3.6 Nanoindentation and Nanomechanical Properties of Ni-based Superalloys 23
2.4 Overview of the Search of a New Generation of Superalloys **32**
2.5 Platinum-based Superalloys **34**
2.5.1 Introduction 34
2.5.2 Binary Pt-Al Phase Diagram and the Pt_3Al Phases 36
2.5.2.1 Overview of the Pt-Al Phase Diagram 36
2.5.2.2 (Pt) Phase 39
2.5.2.3 Pt_3Al Phases 39
2.5.2.4 Recent Studies of the Pt-Al Phase Diagram at High Temperatures 42
2.5.3 Ternary Pt-based Superalloys 43
2.5.3.1 Preliminary Studies of Ternary Pt-based Alloys 44

2.5.3.2 Oxidation 48
2.5.4 Transmission Electron Microscopy Studies of Pt-based Superalloys 50
2.5.4.1 Microstructure and Crystal Structure of Pt_3Al in Binary Pt–Al Alloys 50
2.5.4.2 Microstructure and Deformation of Ternary Alloys 54
2.5.5 Development of Pt-Al-Cr-Ni Pt-based Superalloys 68
2.5.5.1 Quaternary Pt-Al-Cr-Ni alloys 68
2.5.5.2 Substitution of Ni in Pt-Al-Cr-Ni 71
2.5.5.3 TEM Investigations of the γ/γ′ Phase Boundary in Pt-Al-Cr-Ni Alloys 74
2.5.5.4 Microalloying of Pt-Al-Cr-Ni 75
2.5.6 Nanoindentation and Nanomechanical Properties of Pt-Based Superalloys 77
2.5.7 Quaternary Pt-Al-Cr-Ru Superalloys and their Derivations 79
2.5.7.1 Oxidation 81
2.5.7.2 Tensile Testing 82
2.5.7.3 Corrosion Testing of Pt-based Superalloys 85
2.5.7.4 Effect of Heat Treatment and Co Additions 87
2.5.7.5 Pt-Al-Cr-Ru and Higher Order Superalloys 89
2.6 Rationale for Further Research in Pt-Based superalloys 99
CHAPTER THREE 100
3. EXPERIMENTAL PROCEDURE 100
3.1 Sample Manufacture 100
3.2 Sample Annealing 100
3.3 Sample Preparation for SEM, AFM, TEM and Optical Microscopy (OM) 100
3.3.1 Sample Preparation for SEM, AFM and Optical Microscopy (OM) 100
3.3.1.1 Metallographic Sample Preparation 100
3.3.1.2 Electrolytic Etching of Samples 101
3.3.2 Sample preparation for TEM 101
3.4 X–ray diffraction (XRD) instruments 102
3.5 Optical Microscopy (OM) Instrument 103
3.6 SEM Instrument 103
3.7 SEM and OM investigation of previous Pt-based superalloys 103
3.8 Grid technique volume fraction measurements 103
3.9 Image analysis: Olympus stream software 104
3.10 AFM and WSxM Software for volume fraction analysis 104
3.11 TEM Instruments 105
3.12 Determination of the Structure of ~Pt_3Al and Orientation Relationship between the Matrix and Precipitates 106
3.12.1 Indexing of diffraction pattern using Java Electron Microscope Simulator (JEMS) software 106

3.13 Nanoindentation **107**
3.13.1 Nanoindentation Hardness Testing 107
3.13.2 Atomic Force Microscopy Imaging 108
3.13.3 Calculation of Nanohardness and Elastic Modulus 109
3.13.4 Indentation Procedure 109
3.13.5 Hertzian Fit Calculations 110
CHAPTER FOUR **112**
4. RESULTS **112**
4.1 X-ray diffraction (XRD) **112**
4.2 OM, SEM, AFM and Image Analysis Studies **117**
4.2.1 New observations in some Pt-Based Superalloys after Etching 117
4.2.1.1 Nominal Pt_{82}:Al_{12}:Cr_4:Ru_2 (at.%) 117
4.2.1.2 Nominal $Pt_{81.5}$:$Al_{11.5}$:$Cr_{4.5}$:$Ru_{2.5}$ (at.%) 118
4.2.1.3 Nominal Pt_{78}:$Al_{15.5}$:$Cr_{4.5}$:Ru_2 (at.%) 119
4.2.1.4 Nominal Pt_{80}:Al_{14}:Cr_3:Ru_3 (at.%) 121
4.2.1.5 Nominal Pt_{80}:Al_{11}:Cr_4:Ru_5 (at.%) 121
4.2.1.6 Nominal Pt_{78}:Al_{11}:Cr_3:Ru_8 (at.%) 123
4.2.1.7 Nominal Pt_{80}:Al_{11}:Cr_6:Ru_3 (at.%) 123
4.2.1.8 Nominal Pt_{78}:Al_{11}:Cr_6:Ru_5 (at.%) and Pt_{85}:Al_7:Cr_5:Ru_3 (at.%) 123
4.2.3 Image analysis 125
4.2.3.1 Olympus Software 125
4.2.3.2 AFM and WSxM 125
4.3 Transmission Electron Microscopy Studies **127**
4.3.1 TEM Microstructural Characterisation 127
4.3.1.1 Nominal Pt_{82}:Al_{12}:Cr_4:Ru_2 (at.%) 127
4.3.1.2 Nominal Pt_{85}:Al_7:Cr_5:Ru_3 (at.%) 130
4.3.1.3 Nominal Pt_{80}:Al_{11}:Cr_3:Ru_6 (at.%) 132
4.3.1.4 Nominal Pt_{80}:Al_{14}:Cr_3:Ru_3 (at.%) 136
4.3.1.5 Nominal Pt_{78}:Al_{11}:Cr_8:Ru_3 (at.%) 139
4.3.1.6 Nominal Pt_{78}:Al_{11}:Cr_6:Ru_5 (at.%) 141
4.3.2 TEM diffraction patterns and orientation relationship between the Matrix and Precipitate 143
4.4 Nanomechanical Properties Studies **148**
4.4.1 Effect of Indentation Depth on Nanohardness and Elastic Modulus 148
4.4.2 Nanohardness and Elastic Modulus: Matrix, Precipitates and Overall Alloy 157
CHAPTER FIVE **168**
5. DISCUSSION **168**
5.1 XRD, OM, SEM, AFM and IMAGE ANALYSIS STUDIES **168**
5.1.1 OM and SEM Microstructures and XRD 168
5.1.2 SEM and AFM Image Analysis 172

5.2 Transmission Electron Microscopy Studies **174**
5.2.1 TEM Microstructural Characterisation 174
5.2.1.1 Nominal Pt_{82}:Al_{12}:Cr_4:Ru_2 (at.%) 174
5.2.1.2 Nominal Pt_{85}:Al_7:Cr_5:Ru_3 (at.%) 176
5.2.1.3 Nominal Pt_{80}:Al_{11}:Cr_3:Ru_6 (at.%) 176
5.2.1.4 Nominal Pt_{80}:Al_{14}:Cr_3:Ru_3 (at.%) 178
5.2.1.5 Nominal Pt_{78}:Al_{11}:Cr_8:Ru_3 (at.%) 179
5.2.1.6 Nominal Pt_{78}:Al_{11}:Cr_6:Ru_5 (at.%) 179
5.2.1.7 Dislocations 180
5.2.2 TEM Diffraction Pattern and Orientation Relationship between Matrix and Precipitate 185
5.3 Comparison of γ´ Precipitate Volume Fraction by SEM, TEM, AFM and Commercial NBSAs **186**
5.4 Summary of γ´ Precipitate Formation Mechanisms **190**
5.5 Nanomechanical Properties Studies **193**
5.5.1 Effect of Indentation Depth on Nanohardness and Elastic Modulus 193
5.5.2 Hardness and Elastic Modulus: Matrix, Precipitates and Overall Alloy 195
CHAPTER SIX **218**
6. CONCLUSIONS AND RECOMMENDATIONS **218**
6.1 Conclusions **218**
6.2 Recommendations for Future Work: **220**
REFERENCES **222**
APPENDIX A **252**
Hertzian fitted results at loads of 2mN and 1mN compared with results at a load of 2.5mN **252**
APPENDIX B **253**
Nanohardnesses and elastic moduli for the γ phase calculated at final contact depth and maximum applied load of 5mN **253**
APPENDIX C **254**
ATTEMPT TO CAST SINGLE CRYSTALS **254**
CHAPTER ONE **254**
1. LITERATURE REVIEW **254**
1.1 Manufacture of Single Crystals **254**
1.2 Single Crystal Growth using the Bridgman Method **254**
1.3 Single Crystal Growth using the Czochralski Method **255**
CHAPTER TWO **256**
2. EXPERIMENTAL PROCEDURE **256**
2.1 Single Crystal Attempt: Sample Manufacture **256**

CHAPTER THREE **257**
3. RESULTS **257**
CHAPTER FOUR **258**
4. DISCUSSION **258**
CHAPTER FIVE **260**
5. CONCLUSION **260**
CHAPTER SIX **260**
6. REFERENCES **260**
APPENDIX D **263**
XRD Pattern of the Plasticine and the Methodology for Distinguishing between the two Forms of Pt_3Al and the Platinum-rich Solid Solution Phase **263**
APPENDIX E **265**
Hardness Testing and the Oliver-Pharr Approach **265**
APPENDIX F **269**
Conference Presentations **269**
Presentations **269**
Published Conference Abstracts and Papers **269**

LIST OF FIGURES

Figure 2.1. Two-phase γ - γ′ microstructure of fully annealed heat treated AM3, a first generation single crystal superalloy [1999Car1].....11
Figure 2.2. Microstructure of fully heat treated CMSX-4, a second generation single crystal superalloy [1993Har].....12
Figure 2.3. Microstructure of a third generation Rene N5 heat treated at 1025˚C for 16 hours showing a two-phase γ - γ′ microstructure [2003Yok]. 12
Figure 2.4. TMS-138 fourth generation single crystal superalloy, showing coarse and fine Ni_3Al cubic precipitates in a (Ni) matrix [2008Wu].....14
Figure 2.5. Heat treated fifth generation microstructures in (a) TMS-138A, and (b) TMS-196 [2008Yeh].....14
Figure 2.6. SEM-SE micrograph showing crack growth into grain E [1994Zha]. 15
Figure 2.7. Bright field TEM images, showing (a) Nimonic 115 with a well formed array of misfit dislocations in the γ/γ´ interface, and (b) Nimonic 80A with dislocations in the matrix and precipitate [1983Ric]. 20
Figure 2.8. Bright field TEM images showing (a) γ´ precipitates in a γ matrix after a two-step heat treatment, (b) γ´ precipitates in a γ matrix after heat treatment at 1240˚C for 80 minutes, and (c) dislocations at the γ/γ´ interfaces after after heat treatment at 1240˚C for 40 minutes [1998Gro]. 21
Figure 2.9. Morphology of γ´ phase and dislocation structure, showing (a) the base material with a γ´ volume fraction of 74% and dislocations are not observed, (b) HAZ closest to base material and the circled region shows the zig-zag nature of dislocation networks, (c) in the middle of the HAZ and the number of dislocations is increased, and (d) in the HAZ close to fusion line with complete dissolution of the γ´ phase and formation of dislocation network with zig-zag dislocations [2004Bar]. 22
Figure 2.10. Dislocation structure within the HAZ of the TSM 75 single crystal, close to the fusion line, (a) dislocation distribution along the γ/γ´ boundaries, both A (edge) and B (screw) type dislocation sets are visible, where A is zig-zag dislocations along the average direction [100] with Burgers vector parallel to b = [101]; (B) zig-zag dislocations along the average direction [010] with Burgers vector parallel to b = [011], (b) dislocation network in the γ matrix formed by screw-type dislocations, and

(c) dislocation network in the γ matrix formed by two edge-type dislocations [2004Bar]. 23
Figure 2.11. Typical load-displacement curves obtained for the γ′ and γ phases of CMSX-6 [1999Gök]. 25
Figure 2.12. Relationship between indentation depth and hardness for: (a) CMSX-6, and (b) Waspaloy [1999Gök]. 25
Figure 2.13. Relationship of the γ′ and γ moduli of elasticity with indentation depth for: (a) CMSX-6, and (b) Waspaloy [1999Gök]. 26
Figure 2.14. Hardness of Alloys R1 and R2 for different annealing times (10h and 120h) and possible indentation positions on γ′ and γ: (a) hardness as a function of indentation depth for γ′, (b,c) schematic diagrams showing possible positions of the final indentation on the γ′ and γ, and (d) hardness as a function of indentation depth for γ [2003Sch2]. 27
Figure 2.15. Reduced modulus of γ′ precipitates (prec) and γ matrix (matrix) as a function of indentation depth for Alloys R1 and R2 for different annealing times [2003Sch2]....28
Figure 2.16. Microstructures of different alloys with nanoindentations in the γ and γ′ phases, where the indentations were performed at the maximum applied load of 250 μN: (a) CMSX-6, (b) CMSX-4, and (c) CMSX-10 [2004Dur]. 29
Figure 2.17. Hardness and hardness ratio of γ′ and γ phases in CMSX-6, CMSX-4 and CMSX-10 [2004Dur]. 30
Figure 2.18. Modulus of elasticity of γ′/ γ phases in CMSX-6, CMSX-4 and CMSX-10 determined by the standard Oliver/Pharr method, where the cross on the lower curve indicates the modulus ratio determined by a Hertzian fit (Figure 2.19) [2004Dur]. 31
Figure 2.19. Load–displacement curves in CMSX-4 measured with a Berkovich-tip in γ matrix and γ′ precipitates, with the Hertzian fit [2004Dur]....31
Figure 2.20. Pt-Al phase diagram [1986McA]. 37
Figure 2.21. Pt-Al phase diagram showing the data from different sources [1986McA]....38
Figure 2.22. Partial Pt-Al phase diagram [1987Oya]. 38
Figure 2.23. Crystal structures of Pt_3Al viewed along the <001> direction: (a) High temperature $L1_2$ phase, b) intermediate temperature DO_c phase and, (c) low temperature DO'_c phase [1987Oya]....40
Figure 2.24. (a) DO'_c unit cell of the Pt_3Al tetragonal structure (low temperature), contains a distorted fct lattice, also shown in (b), where the Pt atoms (white) lie offset from the

centre of the faces and the Al atoms (black) sit at the corners of the cell. (In (b) for clarity, only the Pt atoms on the top and front faces are shown.) [1987Oya].....41
Figure 2.25. Composition dependence of the transformation temperatures of $\gamma' \rightarrow \gamma'_1$ and $\gamma'_1 \rightarrow \gamma'_2$ in Pt-Al alloys: circles were obtained by DTA and squares by dilatometry [1987Oya]. 42
Figure 2.26. Stress-rupture curves of PM2000 and Pt_{86}:Al_{10}:Z_4 alloys at 1300ºC in air [2002Süs1]. 46
Figure 2.27. Creep curves of PM2000 and Pt_{86}:Al_{10}:Z_4 alloys tested at 1300ºC and 30 MPa [2002Süs1].....47
Figure 2.28. Stress-rupture curves at 1300ºC of PM2000, Pt, ZGS platinum and Pt_{86}:Al_{10}:Cr_4 (at.%) compared with stress-rupture strength values, $R_{m/10h/1300ºC}$, of some conventional solid solution strengthened Pt-based alloys [2002Süs1].....48
Figure 2.29. Results of the isothermal oxidation tests conducted on Pt-Al-Z alloys at 1350ºC, showing the thickness changes with time over the first 1000 hours [2001Süs1]. 49
Figure 2.30. SEM-BSE images of alloys isothermally oxidised at 1350ºC for various times: (a) Pt_{86}:Al_{10}:Cr_4 (at.%) for 1000 hours, and (b) PM2000 for 10 hours, where (i) is transient oxidation, and (ii) is continuous oxidation [2001Süs1].....50
Figure 2.31. Bright field TEM image of a Pt_3Al precipitate in a Pt_{86}:Al_{14} (at.%) alloy, where P = stacked plates or laths, M = (Pt) solid solution matrix, and arrows indicate individual platelets inside the plate of stacked platelets in the region below [2007Dou]. 51
Figure 2.32. $Pt_{86}Al_{14}$ (at.%) TEM results: (a) SAD pattern corresponding to the matrix, B= [001], (b) SAD pattern corresponding to the precipitate, B= [110], (c) simulated matrix SAD pattern, B= [001], and (d) simulated precipitate SAD pattern, B= [110] [2007Dou]. 52
Figure 2.33. $Pt_{86}Al_{14}$ (at.%) TEM results: (a) unit cell of the DO'_c structure, B= [110], (b) unit cell of modified DO'_c unit cell, B= [110], (c) kinematically simulated SAD pattern of modified DO'_c unit cell, B= [110], and (d) experimental SAD pattern from a single broad plate, B= [110] [2007Dou]. 53
Figure 2.34. Typical TEM images of the ~Pt_3Al precipitates in Pt-Al-Z alloys (Z = Cr, Ir, Ru, Ta or Ti), with letters indicating the different size ranges (where P = primary; I or T = intermediate; S = secondary): (a) $L1_2$ precipitates stabilised by Cr, Ta and Ti additions. The inset shows the selected area diffraction (SAD) pattern, confirming

the $L1_2$ structure, and (b) DO'_c precipitates stabilised by Ir and Ru additions [2001Hil5, 2001Hil6, 2004Dou2, 2006Cor]. 54
Figure 2.35. Dark field TEM image of a typical Pt_{86}:Al_{10}:Ir_4 (at.%) alloy compressed at room temperature, with P denoting ogdoadically-diced precipitates, and C denoting secondary precipitates. (Inset shows a selected area electron diffraction pattern with reflection used to obtain the image circled.) [2004Dou2, 2006Cor]. 57
Figure 2.36. Bright field TEM image of $Pt_{86}Al_{10}Cr_4$ (at.%) deformed at room temperature showing small precipitates in the matrix with lobe contrast, box shows precipitates within the matrix and the circle shows finer precipitates [2004Dou2]. 58
Figure 2.37. Bright field TEM micrographs of the interfacial dislocation networks in $Pt_{86}Al_{10}Cr_4$ (at.%) deformed at 800°C under various diffraction conditions (scale bar = 200nm) [2004Dou2]. 59
Figure 2.38. Bright field TEM image of $Pt_{86}Al_{10}Cr_4$ (at.%) compressed at 1100˚C, showing a typical $L1_2$ precipitate (P), in a (Pt) solid solution matrix (M) [2004Dou2]..... 60
Figure 2.39. Bright field TEM micrographs of $Pt_{86}Al_{10}Cr_4$ (at.%) deformed at 1300°C showing γ/γ′ interface dislocations under different diffraction conditions (scale bar = 200nm) [2004Dou2]..... 61
Figure 2.40. Bright field TEM micrographs of room temperature compressed $Pt_{86}Al_{10}Ru_4$ (at.%) showing DO'_c precipitates: a) threading dislocations out of contrast and b) threading dislocations in contrast (scale bar = 300nm) [2004Dou2]. 61
Figure 2.41. Bright field TEM micrographs for $Pt_{86}Al_{10}Ru_4$ (at.%) taken from a tip of a precipitates' lobe showing evidence of part of a hexagonal interfacial dislocation network (scale bar = 50nm) [2004Dou2]. 62
Figure 2.42. Bright field TEM images of $Pt_{86}Al_{10}Ta_4$ (at.%) deformed at 1100˚C: (a) low magnification, and (b) high magnification, showing γ′ precipitates (P), in a (Pt) solid solution matrix (M) [2004Dou2]. 63
Figure 2.43. Bright field TEM image of $Pt_{86}Al_{10}Ta_4$ (at.%) deformed at 800˚C, showing γ′ precipitates (P) and larger secondary γ′ precipitates (A), in a (Pt) solid solution matrix (M) [2004Dou2]. 63
Figure 2.44. Bright field TEM image of $Pt_{86}Al_{10}Ti_4$ (at.%) deformed at 1100˚C, showing a typical $L1_2$ precipitate (P) in a (Pt) matrix (M) [2004Dou2]. 64
Figure 2.45. Bright field TEM image of $Pt_{86}Al_{10}Ti_4$ (at.%) deformed at 1100˚C, showing an isolated dislocation bowing out around precipitate [2004Dou2]. 64

Figure 2.46. Bright field TEM micrographs of $Pt_{86}Al_{10}Ti_4$ (at.%) deformed at 1100˚C, showing an interfacial dislocation network under various diffraction conditions (scale bar = 50nm) [2004Dou2]. 65
Figure 2.47. Bright field TEM micrographs of $Pt_{86}Al_{10}Ti_4$ (at.%) deformed at 1100˚C, showing a hexagonal dislocation network in the matrix/precipitate interface under various diffraction conditions (scale bar = 200nm) [2004Dou2]....65
Figure 2.48. Bright field TEM micrographs of $Pt_{86}Al_{10}Ti_4$ (at.%) deformed at 1100˚C, showing a hexagonal dislocation network in the matrix/precipitate interface under various diffraction conditions (scale bar = 100nm) [2004Dou2]....66
Figure 2.49. Bright field TEM micrographs of $Pt_{86}Al_{10}Ti_4$ (at.%) deformed at 1300˚C, showing coalesced cubic precipitates forming larger precipitates, as indicated in the rectangle [2004Dou2]. 67
Figure 2.50. TEM images of room temperature compressed $Pt_{86}Al_{10}Ir_4$ (at.%) alloys, a) dark field image showing the thin platelets within the broad plates in a γ′ precipitate, and b) bright field image of a precipitate showing the thin platelets [2004Dou2]. 67
Figure 2.51. SEM-SE images of alloys annealed for 12h at 1500°C and 120h at 1000°C in Ar, showing ~Pt_3Al (dark) in (Pt) (light) two-phase microstructures: (a) Pt_{79}:Al_{14}:Cr_3:Ni_4, (b) Pt_{77}:Al_{14}:Cr_3:Ni_6, and (c) Pt_{75}:Al_{14}:Cr_3:Ni_8 (at.%) [2005Wen1]....69
Figure 2.52. SEM-SE images of Pt-$Al_{12.5}$:Cr_3:Ni_6 (at.%) after homogenization for 12h at 1500°C with different cooling regimes: (a) water quenched, (b) air cooled, and (c) furnace cooled [2006Völ]. 70
Figure 2.53. High temperature compression strengths of Pt-based alloys homogenized at 800°C, 1000°C and 1200°C as a function of the γ′ volume fraction [2005Wen2]. 71
Figure 2.54. SEM-SE images of the γ-γ′ microstructures after heat treatment for 6h at 1500°C and 6h at 1510°C with air cooling: (a) Pt_{82}:A_{l7}:Cr_6:Nb_5, (b) Pt_{82}:Al_7:Cr_6:Ta_5, and (c) Pt_{82}:Al_7:Cr_6:Ti_5 (at.%) [2006Völ]....72
Figure 2.55. High-temperature compression strengths of polycrystalline Pt-Al-Cr-X alloys, Pt_{83}:Al_{12}:Cr_5 [2001Süs1] and the single-crystal Ni-based superalloy CMSX-4 [2006Völ]....73
Figure 2.56. SEM-SE images of the Pt_{82}:Al_7:Cr_6:Ta_5 (at.%) compression samples deformed at: (a) 800°C, (b) 1000°C, and (c) 1300°C [2006Völ]....73
Figure 2.57. Stress-rupture strength curves of different Pt-based alloys at 1300°C [2004Völ]....74

Figure 2.58. Many beam bright field TEM images of Pt_{79}:Al_{14}:Cr_3:Ni_4 (at.%) after homogenization for 12h at 1500°C and subsequent water quenching, then ageing for 120h at 1000°C and subsequent water quenching, showing hexagonal dislocation networks at γ/γ' phase boundaries: (a) $\vec{k}_0$ = [011], (b) $\vec{k}_0$ = [001], where $\vec{k}_0$ is the beam direction [2005Vor]. 75

Figure 2.59. Many beam bright field TEM images of Pt_{77}:Al_{14}:Cr_3:Ni_6 (at.%) after homogenization for 12h at 1500°C and ageing for 120h at 1000°C, both with subsequent water quenching, $\vec{k}_0$ = [001] [2005Vor]. 75

Figure 2.60. Compression creep curves of Pt_{77}:$Al_{12}Cr_6Ni_5$ (at.%): a) base alloy compared to alloys microalloyed with 0.3 and 0.7 at.% B at 1200°C, and b) alloys microalloyed with 0.3 and 0.7 at.% B, and with 2 at.% Re + 0.7 at.% B at 1300°C [2006Völ]. 76

Figure 2.61. AFM images of Pt_{75}:Al_{12}:Cr_6:Ni_5:Re_2 (at.%) with nanoindentations (black triangles) performed with a Berkovich tip at applied loads of: (a) 1.0mN, and (b) 10.0mN [2010Nik]. 78

Figure 2.62. Load-displacement curves for the matrix and primary precipitates at 0.5mN applied load [2010Nik]. 78

Figure 2.63. Properties of Pt_{75}:Al_{12}:Cr_6:Ni_5:Re_2 (at.%): (a) modulus of elasticity, and (b) nanohardness for different loading levels [2010Nik]. 78

Figure 2.64. SEM-BSE images of the two-phase Pt-based alloys: a) $Pt_{81.5}$:$Al_{11.5}$:$Cr_{4.5}$:$Ru_{2.5}$ (at.%) with primary ~Pt_3Al (dark contrast) in a fine matrix of (Pt) (light) and ~Pt_3Al, and b) Pt_{84}:Al_{11}:Cr_3:Ru_2 (at.%) with a fine matrix of (Pt) and ~Pt_3Al [2002Cor]. 79

Figure 2.65. SEM-SE image of Pt_{80}:Al_{14}:Cr_3:Ru_3 annealed at 1400ºC for 96 hours and water quenched, showing ~Pt_3Al (discrete, raised) in a (Pt) matrix [2003Ker1, 2003Ker2, 2003Ker3]. 81

Figure 2.66. SEM-BSE images of transverse sections of Pt_{80}:Al_{14}:Cr_3:Ru_3 (at.%) after exposure to air at 1350ºC for increasing time: (a) 1 hour, (b) 10 hours, and (c) 500 hours [2001Süs2]. 82

Figure 2.67. SEM-SE images of: (a) Pt_{84}:Al_{11}:Cr_3:Ru_2 (at.%) showing intergranular fracture, (b) Pt_{86}:Al_{10}:Cr_4 (at.%) showing cleavage fracture, and (c) Pt_{86}:Al_{10}:Ru_4 (at.%) showing localised dimples as a sign of ductility [2004Süs1]. 84

Figure 2.68. Corrosion of a coated CMSX-4 NBSA during exposure to Na_2SO_4 at 950ºC for the first 50 hours [2010Pot]. 86

Figure 2.69. Corrosion of five Pt-based alloys of different compositions for the first 50 hours [2010Pot].....86
Figure 2.70. SEM-SE image of a cross section of Pt-based superalloy RS-1, Pt_{86}:Al_{10}:Cr_4 (at.%), showing the thin protective scale [2006Mal].....88
Figure 2.71. Micrographs of hardness indentations of selected samples [2008Sho2].....91
Figure 2.72. SEM-BSE images of heat treated samples showing ~Pt_3Al precipitates (dark) in a (Pt) matrix (light): a) random precipitates, and b) aligned precipitates [2009Sho1].92
Figure 2.73. SEM-BSE images of heat treated Pt-based alloys, showing ~Pt_3Al precipitates (dark) in (Pt) matrices (light): (a) Pt_{78}:Al_{11}:Cr_3:Ru_8 (at.%) with rounded ~Pt_3Al, (b) Pt_{78}:Al_{11}:Cr_6:Ru_5 (at.%) with elongated ~Pt_3Al, and (c) Pt_{78}:Al_{11}:Cr_8:Ru_3 (at.%) with irregular ~Pt_3Al [2009Sho1].....93
Figure 2.74. Specific mass change with time of water-quenched and air-cooled nominal Pt_{84}:Al_{11}:Cr_3:Ru_2 (at.%) specimens after isothermal oxidation in air at different temperatures (water-quenched curves in red; air-cooled curves in blue) [2011Odu].....94
Figure 2.75. SEM-SE images of cross-sections of oxide scales showing: (a) water-quenched Pt_{84}:Al_{11}:Cr_3:Ru_2 (at.%) after 100h oxidation in air at 1350°C, and (b) air-cooled Pt_{84}:Al_{11}:Cr_3:Ru_2 (at.%) after 100h oxidation in air at 1250°C [2011Odu].....95
Figure 2.76. Mean stress in the scales of water-quenched and air-cooled Pt_{84}:Al_{11}:Cr_3:Ru_2 (at.%) calculated from the measured frequency shifts of the R2 luminescence line [2013Odu].....97
Figure 2.77. (a) SEM-BSE image of unetched, annealed $Pt_{64.7}$:$Al_{26.2}$:$V_{9.1}$ (at.%), showing medium contrast ~Pt_3Al, light ~Pt_5Al_3 and dark ~PtV [2011Ode], and (b) optical microscope image of etched, annealed $Pt_{64.7}$:$Al_{26.2}$:$V_{9.1}$ (at.%), showing light ~Pt_3Al, dark ~Pt_5Al_3 with needle-like precipitates [2012Ode].....98
Figure 3.1. (a) Gatan Precision Ion Polishing System (PIPS) used for TEM sample preparation, and (b) schematic representation of the sample holder [2007Rei].....102
Figure 3.2. CSM nanoindentation tester with AFM and optical microscope at NMMU.....108
Figure 3.3. Schematic diagram of the nano indenter head assembly [2006CSM].....108
Figure 3.4. Overall view of the Veeco Dimension^{TM} 3100 Atomic Force Microscope.....109
Figure 4.1. XRD pattern of nominal Pt_{82}:Al_{12}:Cr_4:Ru_2 (at.%) in the heat treated condition, showing all identified phases.....113
Figure 4.2. XRD pattern of nominal Pt_{85}:Al_7:Cr_5:Ru_3 (at.%) in the heat treated condition, showing all identified phases.....113

Figure 4.3. XRD pattern of nominal Pt_{80}:Al_{11}:Cr_3:Ru_6 (at.%) in the heat treated condition, showing all identified phases. 115
Figure 4.4. XRD pattern of nominal Pt_{80}:Al_{14}:Cr_3:Ru_3 (at.%) in the heat treated condition, showing all identified phases. 115
Figure 4.5. XRD pattern of nominal Pt_{78}:Al_{11}:Cr_8:Ru_3 (at.%) in the heat treated condition, showing all identified phases. 116
Figure 4.6. XRD pattern of nominal Pt_{78}:Al_{11}:Cr_6:Ru_5 (at.%) in the heat treated condition, showing all identified phases. 116
Figure 4.7. Annealed nominal Pt_{82}:Al_{12}:Cr_4:Ru_2 (at.%): (a) SEM-BSE image showing eutectoid (E) between dendrites (D), and irregular regions in the dendrites (I), (b) optical microscope image showing ~Pt_3Al precipitates in light (Pt) matrix in the dendrite (D), as well as a (Pt) + ~Pt_3Al eutectic (Eu), and (c) SEM-BSE image showing eutectic (Eu) between dendrites (D). 118
Figure 4.8. Annealed nominal $Pt_{81.5}$:$Al_{11.5}$:$Cr_{4.5}$:$Ru_{2.5}$ (at.%): (a) SEM-BSE image showing fine dark ~Pt_3Al precipitates in light (Pt) matrix and circular features (Arrows A), (b) optical microscope image showing fine dark ~Pt_3Al precipitates in light (Pt) matrix and grain boundaries, (c) coarsened eutectic/eutectoid ~Pt_3Al + (Pt) at the grain boundaries, and (d) and (e) SEM-BSE images of features indicated by Arrow B in (b) and (c), with laths (B) in (d), possibly a eutectoid (C) and (D) in (e)... 120
Figure 4.9. Annealed nominal Pt_{78}:$Al_{15.5}$:$Cr_{4.5}$:Ru_2 (at.%): (a) SEM-BSE image showing very fine dark ~Pt_3Al precipitates in light (Pt) matrix and precipitate-decorated grain boundary (indicated by arrow), and (b) optical microscope image showing different grains, and fine dark ~Pt_3Al precipitates in lighter (Pt) matrix. 121
Figure 4.10. SEM-BSE image of heat treated nominal Pt_{78}:$Al_{15.5}$:$Cr_{4.5}$:Ru_2 (at.%), showing dark ~Pt_3Al precipitates in light (Pt) matrix and precipitates on sub-grain boundaries. 122
Figure 4.11. SEM-BSE images of annealed nominal Pt_{80}:Al_{11}:Cr_4:Ru_5 (at.%) showing: (a) very fine dark ~Pt_3Al precipitates in light (Pt) matrix, and (b) optical microscope image showing differing contrasts due to different grain orientations, and porosity. ... 122
Figure 4.12. SEM-BSE image of heat treated nominal Pt_{78}:Al_{11}:Cr_3:Ru_8 (at.%) showing ~Pt_3Al precipitates in light (Pt) dendrite (D), and a coarsened (Pt) + ~Pt_3Al eutectic (E). 123

Figure 4.13. SEM-BSE images of annealed nominal Pt_{80}:Al_{11}:Cr_4:Ru_5 (at.%) showing: (a) dark ~Pt_3Al precipitates in light (Pt) matrix, and (b) porosity (black spots) and a pit from possible over-etching. 124
Figure 4.14. Annealed nominal Pt_{78}:Al_{11}:Cr_6:Ru_5 (at.%) and Pt_{85}:Al_7:Cr_5:Ru_3 (at.%): (a,b) SEM-BSE images showing fine dark ~Pt_3Al precipitates in light (Pt) matrix and decorated grain boundaries, and (c,d) optical microscope images showing fine dark ~Pt_3Al precipitates in light (Pt) matrix and grain boundaries.....124
Figure 4.15. Window for ~Pt_3Al volume fraction calculation from AFM images for nominal Pt_{80}:Al_{14}:Cr_3:Ru_3 (at.%) using the WSxM software flooding function: (a) AFM topographic image, and (b) AFM topographic image after flooding and identification of precipitates as “holes”. 127
Figure 4.16. Bright field TEM image of nominal Pt_{82}:Al_{12}:Cr_4:Ru_2 (at.%) after heat treatment, showing a high volume fraction of γ′ precipitates, which had a cubic, elongated and (A) “U morphology” in a γ matrix.....129
Figure 4.17. Bright field TEM image of nominal Pt_{82}:Al_{12}:Cr_4:Ru_2 (at.%) after heat treatment, showing coarsened γ′ precipitates and dislocations at the γ/γ′ interfaces, (B) isolated spherical γ′ precipitates, (C) tertiary γ′ precipitates, (D) irregular γ′ precipitates, and (E) γ matrix. 129
Figure 4.18. Bright field TEM image of nominal Pt_{82}:Al_{12}:Cr_4:Ru_2 (at.%) after heat treatment, showing (A) dislocations at the γ/ γ′ interface, and (B) dislocations in the γ matrix. 130
Figure 4.19. Bright field TEM image of nominal Pt_{85}:Al_7:Cr_5:Ru_3 (at.%) after heat treatment, showing homogenous distribution of mainly cubic shaped γ′ precipitates in a γ matrix. 131
Figure 4.20. Bright field TEM image of nominal Pt_{85}:Al_7:Cr_5:Ru_3 (at.%) after heat treatment, showing areas of different γ′ precipitate shapes, with (A) cubic and (B) fine rounded morphology in a γ matrix.....131
Figure 4.21. Bright field TEM image of nominal Pt_{85}:Al_7:Cr_5:Ru_3 (at.%) after heat treatment, showing (A) irregular, near-cubic shaped γ′ precipitates in a γ matrix, (B) tertiary precipitates, and (C) spherical γ′ precipitates.....132
Figure 4.22. Bright field TEM image of nominal Pt_{80}:Al_{11}:Cr_3:Ru_6 (at.%) after heat treatment, showing different morphologies, sizes of spherical and cuboid-like γ′ precipitates (A) in γ matrix. 133

Figure 4.23. Bright field TEM image of nominal Pt_{80}:Al_{11}:Cr_3:Ru_6 (at.%) after heat treatment, showing (A) dislocations at the γ/γ′ interfaces, the dotted line shows the region used to study the composition gradient reported in Figure 4.27, and (B) is a clear view of the matrix material between two precipitates. 134
Figure 4.24. Bright field TEM image of nominal Pt_{80}:Al_{11}:Cr_3:Ru_6 (at.%) after heat treatment showing: (A) coalesced γ′ precipitates, (B) cluster of secondary γ′, (C) curving γ′ interfaces, and (D) a fine tertiary precipitation of γ′ in a γ matrix. 134
Figure 4.25. Bright field TEM image of nominal Pt_{80}:Al_{11}:Cr_3:Ru_6 (at.%) after heat treatment, showing (A) network of dislocations at the γ/γ′ interfaces, (B) matrix dislocations pinned by the precipitates, and (C) a precipitate-free area. 135
Figure 4.26. Bright field TEM image of nominal Pt_{80}:Al_{11}:Cr_3:Ru_6 (at.%) after heat treatment showing a network of dislocations (A) at the γ/γ′ interface. 135
Figure 4.27. Composition gradient of Cr from centre of γ matrix to centre of γ′ precipitate in Pt_{80}:Al_{11}:Ru_6:Cr_3 (at.%), where the dotted line in Figure 4.23 is a typical region from the centre of the γ matrix channel to the centre of the γ′ precipitate. 136
Figure 4.28. Bright field TEM image of nominal Pt_{80}:Al_{14}:Cr_3:Ru_3 (at.%) after heat treatment showing: (A) large irregular γ′ precipitates, (B) spherical γ′ precipitates, (C) cubic γ′ precipitates in a γ matrix, and (D) coalesced γ′ precipitates connected by necks. 137
Figure 4.29. Bright field TEM image of nominal Pt_{80}:Al_{14}:Cr_3:Ru_3 (at.%) after heat treatment, showing cubic γ′ precipitates separated by varying widths of γ matrix.....137
Figure 4.30. Bright field TEM image of nominal Pt_{80}:Al_{14}:Cr_3:Ru_3 (at.%) after heat treatment, showing three different grains with different microstructures (Areas B, C and D).....138
Figure 4.31. Bright field TEM image of nominal Pt_{80}:Al_{14}:Cr_3:Ru_3 (at.%) after heat treatment, showing an isolated, rounded precipitate with an interface network of dislocations (A), and dislocations in the matrix (B). General spotty background is damage resulting from ion milling.....138
Figure 4.32. Bright field TEM image of nominal Pt_{80}:Al_{14}:Cr_3:Ru_3 (at.%) after heat treatment, showing an isolated, rounded precipitate with an interface network of dislocations (A), and dislocations in the matrix (B). General spotty background is damage resulting from ion milling.....139

Figure 4.33. Bright field TEM image of nominal Pt_{78}:Al_{11}:Cr_8:Ru_3 (at.%) after heat treatment, showing γ′ precipitates in a γ matrix, (A) rounded and (B) cubic γ′ with straight edges. 140
Figure 4.34. Bright field TEM image of nominal Pt_{78}:Al_{11}:Cr_8:Ru_3 (at.%) after heat treatment, showing an elongated morphology of γ′ precipitates in a γ matrix. 140
Figure 4.35. Bright field TEM image of nominal Pt_{78}:Al_{11}:Cr_6:Ru_5 (at.%) after heat treatment, showing cubic and (A) coalesced γ′ precipitates in a γ matrix. 141
Figure 4.36. Bright field TEM image of nominal Pt_{78}:Al_{11}:Cr_6:Ru_5 (at.%) after heat treatment, showing mainly cubic and irregular morphology (A) of γ′ precipitates in a γ matrix, dotted box indicates alignment of γ′ precipitates. 142
Figure 4.37. Bright field TEM image of nominal Pt_{78}:Al_{11}:Cr_6:Ru_5 (at.%) after heat treatment, showing a wider area of the thinned section, with a local homogenous distribution of γ′ precipitates in γ. 142
Figure 4.38. TEM diffraction pattern from nominal Pt_{78}:Al_{11}:Cr_6:Ru_5 (at.%) of: (a) γ matrix, and (b) γ′ precipitate. 143
Figure 4.39. JEMS simulated diffraction of the γ matrix corresponding to experimental diffraction in Figure 4.38(a) on the [114] zone axis. 144
Figure 4.40. JEMS simulated diffraction of the γ′ precipitate corresponding to experimental diffraction in Figure 4.38(b) on the [114] zone axis. 144
Figure 4.41. TEM diffraction patterns from nominal Pt_{78}:Al_{11}:Cr_6:Ru_5 (at.%) of: (a) γ matrix, and (b) γ′ precipitate. 145
Figure 4.42. JEMS simulated diffraction of the γ matrix corresponding to experimental diffraction in Figure 4.41(a) on the [001] zone axis. 145
Figure 4.43. JEMS simulated diffraction of the γ′ precipitate corresponding to experimental diffraction in Figure 4.41(b) on the [001] zone axis. 146
Figure 4.44. TEM diffraction patterns from nominal Pt_{78}:Al_{11}:Cr_6:Ru_5 (at.%) of: (a) γ matrix, and (b) γ′ precipitate. 146
Figure 4.45. JEMS simulated diffraction of the γ matrix corresponding to experimental diffraction in Figure 4.44(a) on the [103] zone axis. 147
Figure 4.46. JEMS simulated diffraction of the γ′ precipitate corresponding to experimental diffraction in Figure 4.44(b) on the [103] zone axis. 148
Figure 4.47. Example of a typical load-displacement curve (P-h curve) obtained during nanoindentation of Pt_{85}:Al_7:Ru_3:Cr_5 (at.%) in γ phase at 2.5mN load, showing no pop-in effect. 149

Figure 4.48. Example of a typical load-displacement curve (P-h curve) obtained during nanoindentation of Pt_{85}:Al_7:Cr_5:Ru_3 (at.%) in γ phase at 2.0mN load, showing a pop-in event and fitted Hertzian contact curve, with the final indentation depth re-defined, as h_{fi}.....150
Figure 4.49. Nanohardness as a function of indentation depth for the γ′ precipitates in Pt_{78}:Al_{11}:Cr_6:Ru_5 (at.%).....151
Figure 4.50. Nanohardness as a function of indentation depth for the γ matrix in Pt_{78}:Al_{11}:Cr_6:Ru_5 (at.%).....151
Figure 4.51. Nanohardness as a function of indentation depth for γ′ precipitates in Pt_{80}:Al_{14}:Cr_3:Ru_3 (at.%). 152
Figure 4.52. Nanohardness as a function of indentation depth for γ matrix in Pt_{80}:Al_{14}:Cr_3:Ru_3 (at.%).....152
Figure 4.53. Load-displacement curves for the γ matrix and the γ′ precipitates in Pt_{78}:Al_{11}:Cr_6:Ru_5 (at.%) at a maximum applied load of 2.5mN, showing the final contact depth. 153
Figure 4.54. Elastic modulus as a function of indentation depth for Pt_{78}:Al_{11}:Cr_6:Ru_5 (at.%).....154
Figure 4.55. Elastic modulus as a function of indentation depth for Pt_{80}:Al_{14}:Cr_3:Ru_3 (at.%).....154
Figure 4.56. Alloy overall nanohardness as a function of the indentation depth for Pt_{78}:Al_{11}:Cr_6:Ru_5 (at.%). 155
Figure 4.57. Alloy overall nanohardness as a function of the indentation depth for Pt_{80}:Al_{14}:Cr_3:Ru_3 (at.%). 155
Figure 4.58. Alloy overall elastic modulus as a function of the indentation depth for Pt_{78}:Al_{11}:Cr_6:Ru_5 (at.%).....156
Figure 4.59. Alloy overall elastic modulus as a function of the indentation depth for Pt_{80}:Al_{14}:Cr_3:Ru_3 (at.%).....156
Figure 4.60. AFM images of Pt_{80}:Al_{14}:Cr_3:Ru_3 (at.%), showing ~Pt_3Al precipitates (dark) in a (Pt) matrix (light) with indentations (black triangles) performed with a Berkovich tip at an applied load of 2.5mN, and an example of an indentation in ~Pt_3Al is marked A: (a) height difference, and (b) contrast difference. 157
Figure 4.61. AFM images of Pt_{80}:Al_{11}:Cr_3:Ru_6 (at.%), showing ~Pt_3Al precipitates (dark) in a (Pt) matrix (light) with nanoindentations (black triangles) performed with a

Berkovich tip at an applied load of 2.5mN, and an example of an indentation in ~Pt_3Al is marked A: (a) height difference, and (b) contrast difference. 158
Figure 4.62. AFM images of Pt_{80}:Al_{14}:Cr_3:Ru_3 (at.%), showing ~Pt_3Al precipitates (dark) in a (Pt) matrix (light) with nanoindentations for the alloy hardness, performed with a Berkovich tip at an applied load of 10mN: (a) height difference, and (b) contrast difference, where circles (similar in size to the indentations) indicate regions that are almost precipitate-free.....160
Figure 4.63. AFM images of Pt_{82}:Al_{12}:Cr_4:Ru_2 (at.%), showing ~Pt_3Al precipitates (dark) in a (Pt) matrix (light) with nanoindentations for the alloy hardness, performed with a Berkovich tip at applied loads of 10 and 20mN, revealing material pile-up: (a) height difference, and (b) contrast difference.....160
Figure 4.64. (a) Nanohardness of Pt-based alloys at different loads, and (b) Nanohardness of Pt-based alloys at loads of 10 and 100mN to show clearly the error bars, where A1 = Pt_{82}:Al_{12}:Cr_4:Ru_2, A2 = Pt_{85}:Al_7:Cr_5:Ru_3, A3 = Pt_{80}:Al_{11}:Cr_3:Ru_6, A4 = Pt_{80}:Al_{14}:Cr_3:Ru_3, A5 = Pt_{78}:Al_{11}:Cr_8:Ru_3, and A6 = Pt_{78}:Al_{11}:Cr_6:Ru_5 (at.%).....163
Figure 4.65. Effect of γ′ volume fraction on nanohardness of Pt-based alloys at a maximum load of 100mN. 164
Figure 4.66. Effect of γ′ volume fraction on elastic moduli at a maximum load of 100mN for Pt-based alloys.....164
Figure 4.67. AFM images of Pt_{80}:Al_{11}:Cr_3:Ru_6 (at.%), showing ~Pt_3Al precipitates (dark) in a (Pt) matrix (light) with nanoindentations for the alloy hardness, performed with a Berkovich tip at an applied load of 20mN: (a) height difference, and (b) contrast difference. 165
Figure 5.1. SEM-BSE images of annealed nominal Pt_{78}:Al_{11}:Cr_3:Ru_8 (at.%) showing ~Pt_3Al precipitates in light (Pt) matrix [2008Sho1, 2009Sho1]: (a) before etching, and (b) after etching, now showing a eutectic as well. 170
Figure 5.2. Schematic illustration of the formation of γ′ platelets: (a) alignment of γ′ particles to minimise misfit stresses, followed by coalescence to reduce interface area, widening some matrix corridors, facilitating dislocation movement, (b) continued coalescence and formation of dislocation networks, and (c) final coalescence and complete loss of coherence [1997Dur]. 172
Figure 5.3. Relationship between overall Pt content (at.%) and precipitate volume fraction (measured from SEM images), showing a strong correlation with the γ′ volume fraction decreasing with increasing Pt content. 174

Figure 5.4. Bright field TEM images showing similar misfit dislocations in the γ/γ′ interfaces of Pt-Al-Cr-Ru and NBSAs: (a) Pt_{82}:Al_{12}:Cr_4:Ru_2 (at.%), (b) Pt_{80}:Al_{14}:Cr_3:Ru_3 (at.%), (c) Nimonic 115 [1983Ric], and (d) Nimonic 80A [1983Ric]. 182

Figure 5.5. Bright field TEM images showing similar misfit dislocations in the γ/γ′ interfaces of Pt-Al-Cr-Ru and some ternary alloys: nominal (a) Pt_{86}:Al_{10}:Ti_4 (at.%) [2001Hil5], (b) Pt_{86}:Al_{10}:Cr_4 (at.%) [2001Hil5], (c) Pt_{80}:Al_{11}:Cr_3:Ru_6 (at.%) and (d) Pt_{80}:Al_{14}:Cr_3:Ru_3 (at.%). 184

Figure 5.6. Comparison of precipitate volume fractions from TEM, SEM and AFM, showing consistently higher TEM γ′ volume fractions, with similar fractions for SEM and AFM: A1 = Pt_{82}:Al_{12}:Cr_4:Ru_2, A2 = Pt_{85}:Al_7:Cr_5:Ru_3, A3 = Pt_{80}:Al_{11}:Cr_3:Ru_6, A4 = Pt_{80}:Al_{14}:Cr_3:Ru_3, A5 = Pt_{78}:Al_{11}:Cr_8:Ru_3 and A6 = Pt_{78}:Al_{11}:Cr_6:Ru_5 (at.%)..... 187

Figure 5.7. Comparison of γ′ volume fractions as measured by SEM and TEM, showing that SEM γ′ volume fraction is proportional to TEM γ′ volume fraction. 188

Figure 5.8. Schematic diagram of the successive shape changes encountered during the structural evolution of a freely growing precipitate [1997Dur]..... 192

Figure 5.9. Schematic diagram showing possible positions of the final indentation and effect of the precipitate size on the hardness: (a) precipitate too narrow for indentor and load, (b) precipitate is too shallow for indentor and load, and (c) precipitate much too shallow for indentor and load [1956Mot]. 194

Figure 5.10. Elastic modulus as a function of indentation depth for fine γ′ precipitates and narrow regions of the γ matrix of Pt-based alloys, showing no effect of indentation depth on the matrix, and for precipitates, a slight decrease with increasing elastic modulus. 195

Figure 5.11. Comparison of nanohardnesses of γ′ precipitates and γ matrix at maximum load of 2.5mN and final indentation depth, showing a higher γ′ phase hardness than the matrix for all six alloys: A1 = Pt_{82}:Al_{12}:Cr_4:Ru_2, A2 = Pt_{85}:Al_7:Cr_5:Ru_3, A3 = Pt_{80}:Al_{11}:Cr_3:Ru_6, A4 = Pt_{80}:Al_{14}:Cr_3:Ru_3, A5 = Pt_{78}:Al_{11}:Cr_8:Ru_3, and A6 = Pt_{78}:Al_{11}:Cr_6:Ru_5 (at.%)..... 196

Figure 5.12. Relationship between nanohardness and measured Pt content for γ′, where each datum point represents the average Pt composition for each sample, showing a decrease in nanohardness with increasing Pt content γ′, but with large scatter..... 197

Figure 5.13. Relationship between nanohardness and measured Pt content for γ, where each datum point represents the average Pt composition for each sample, showing a decrease in nanohardness with increasing Pt content for γ, but with large scatter. 197
Figure 5.14. Relationship between alloy overall nanohardness and overall measured Pt content, where each datum point represents the average Pt composition for each sample, showing a high hardness at lower Pt contents (<~83 at.%) and lower hardness above ~83 at.% with a slight decrease at the highest Pt content.....198
Figure 5.15. Relationship between nanohardness and measured Al content for γ′, where each datum point represents the average Al composition for each sample. 198
Figure 5.16. Relationship between nanohardness and measured Al content for γ, where each datum point represents the average Al composition for each sample. 199
Figure 5.17. Relationship between alloy overall nanohardness and measured Al content, where each datum point represents the average Al composition for each sample, showing a low hardness at lower Al contents (<~9 at.%) and higher hardness above ~9 at.% Al content. 199
Figure 5.18. Nanohardness of coarse and fine γ′, showing smaller precipitates with lower nanohardnesses and large standard deviations compared to the larger precipitates, where A1 = Pt_{82}:Al_{12}:Cr_4:Ru_2, A2 = Pt_{85}:Al_7:Cr_5:Ru_3, A3 = Pt_{80}:Al_{11}:Cr_3:Ru_6, A4 = Pt_{80}:Al_{14}:Cr_3:Ru_3, A5 = Pt_{78}:Al_{11}:Cr_8:Ru_3, and A6 = Pt_{78}:Al_{11}:Cr_6:Ru_5 (at.%).....200
Figure 5.19. Nanohardness of broad and narrow γ channels, showing similar hardness of the γ phase for broad and narrow γ regions, where A1 = Pt_{82}:Al_{12}:Cr_4:Ru_2, A2 = Pt_{85}:Al_7:Cr_5:Ru_3, A3 = Pt_{80}:Al_{11}:Cr_3:Ru_6, A4 = Pt_{80}:Al_{14}:Cr_3:Ru_3, A5 = Pt_{78}:Al_{11}:Cr_8:Ru_3, and A6 = Pt_{78}:Al_{11}:Cr_6:Ru_5 (at.%). 201
Figure 5.20. Nanohardnesses of γ′ and γ for different alloys [2003Wöl, 2004Dur], showing higher nanohardnesses for Pt-Al-Cr-Ru alloys than the CMSX alloys and comparable hardnesses to B1, where B1 = Pt_{75}:Al_{12}:Cr_6:Ni_5:Re_2 [2010Nik], A1 = Pt_{82}:Al_{12}:Cr_4:Ru_2, A2 = Pt_{85}:Al_7:Cr_5:Ru_3, A3 = Pt_{80}:Al_{11}:Cr_3:Ru_6, A4 = Pt_{80}:Al_{14}:Cr_3:Ru_3, A5 = Pt_{78}:Al_{11}:Cr_8:Ru_3, and A6 = Pt_{78}:Al_{11}:Cr_6:Ru_5 (at.%).....202
Figure 5.21. Nanohardness of Pt-Al-Cr-Ru alloys compared with Pt_{75}:Al_{12}:Cr_6:Ni_5:Re_2 (at.%) [2010Nik] and PWA1484 [2003Wöl] for different loading levels, showing similar γ′ precipitate nanohardnesses for all alloys, and a spread in γ matrix and overall alloy nanohardnesses. 203
Figure 5.22. Comparison of elastic modulus for γ′ and γ at maximum load of 2.5mN and final indentation depth, showing no significant difference in the modulus of

elasticity between precipitates in the different Pt-Al-Cr-Ru alloys, and ~10% higher γ′ modulus than γ, where A1 = Pt_{82}:Al_{12}:Cr_4:Ru_2, A2 = Pt_{85}:Al_7:Cr_5:Ru_3, A3 = Pt_{80}:Al_{11}:Cr_3:Ru_6, A4 = Pt_{80}:Al_{14}:Cr_3:Ru_3, A5 = Pt_{78}:Al_{11}:Cr_8:Ru_3, and A6 = Pt_{78}:Al_{11}:Cr_6:Ru_5 (at.%).....204

Figure 5.23. Elastic modulus of γ′ and γ for different alloys [2004Dur], showing similar moduli, except for B1 and CMSX-6, with a lower γ elastic modulus and slightly higher γ′ elastic moduli than for the other alloys, where B1 = Pt_{75}:Al_{12}:Cr_6:Ni_5:Re_2 [2010Nik], A3 = Pt_{80}:Al_{11}:Cr_3:Ru_6, A4 = Pt_{80}:Al_{14}:Cr_3:Ru_3, and A6 = Pt_{78}:Al_{11}:Cr_6:Ru_5 (at.%).....204

Figure 5.24. Comparison of the overall elastic modulus of Pt-Al-Cr-Ru alloys (A2 = Pt_{85}:Al_7:Cr_5:Ru_3, A6 = Pt_{78}:Al_{11}:Cr_6:Ru_5 (at.%)) with Ni-based superalloys [2003Wöl, 2008Saw, 2010Kob] and B1 = Pt_{75}:Al_{12}:Cr_6:Ni_5:Re_2 (at.%) [2010Nik], showing that within experimental error, the modulus of elasticity of A2 and A6 were equivalent to the NBSAs and Pt_{75}:Al_{12}:Cr_6:Ni_5:Re_2 (at.%) [2010Nik].....205

Figure 5.25. Overall alloy nanohardnesses and γ′ volume fractions as a function of the differences between γ and γ′ nanohardnesses, showing the γ′ volume fraction decreasing with increasing differences between γ and γ′ nanohardnesses, with the exception of one point (Arrow), and no clear trend between the overall alloy nanohardness and differences in hardness of the γ and γ′. 206

Figure 5.26. Overall alloy nanohardnesses as a function of the γ′ volume fractions, showing lower overall alloy nanohardness at low precipitate volume fractions (< ~35%) and higher above ~44% precipitate volume fraction.....207

Figure 5.27. Comparison of Pt-Al-Cr-Ru overall alloy nanohardnesses with commercial alloys [2003Wöl, 2011Oh, 2012Her] and Pt_{75}:Al_{12}:Cr_6:Ni_5:Re_2 (at.%) [2010Nik], showing the nanohardness increasing with increasing volume fraction for the different alloys. 208

Figure 5.28. Comparison of Pt-Al-Cr-Ru overall alloy elastic modulus with commercial alloys [2003Wöl, 2008Saw, 2010Kob] and Pt_{75}:Al_{12}:Cr_6:Ni_5:Re_2 (at.%) [2010Nik], showing that within experimental error, the elastic modulus of Pt_{85}:Al_7:Cr_5:Ru_3 and Pt_{78}:Al_{11}:Cr_6:Ru_5 (at.%) were similar to the other alloys. 208

Figure 5.29. Relationship between alloy nanohardness and interaction of overall Pt content, overall Al content and γ′ volume fraction, showing a strong correlation with the alloys' nanohardnesses increasing with increasing x variables. 214

Figure 5.30. Relationship between γ′ volume fraction and overall Pt content, showing a strong correlation with the γ′ volume fraction decreasing with increasing overall Pt content. 214
Figure 5.31. Relationship between alloy nanohardness and γ′ volume fraction, showing a strong correlation with the alloys' nanohardnesses increasing with increasing γ′ volume fraction. 215
Figure 5.32. Relationship between γ′ nanohardness and interaction of γ′ Pt content, γ′ Al content and γ′ volume fraction, showing no correlation of the y value and x variables. 216
Figure 5.33. Relationship between γ′ nanohardness and interaction of γ′ Pt content and γ′ Al content, showing a weak correlation with the γ′ nanohardness increasing with increasing γ′ Pt content and γ′ Al content. 216
Figure 5.34. Relationship between γ nanohardness and interaction of γ Pt content, γ Al content and γ′ volume fraction showing a medium correlation with the γ nanohardness increasing with increasing γ Pt content, γ Al content and γ′ volume fraction. 217

LIST OF TABLES

Table 2.1. Nominal compositions (wt%) of single crystal superalloys, balance Ni [1996Eri]. .11
Table 2.2. Crystal structure data for Pt_3Al variants [1961Sta, 1962Bro, 1975Cha, 1987Oya].....41
Table 2.3. Compositions and lattice parameters for Pt_3Al variants [1961Sta, 1962Bro, 1975Cha, 1987Oya]. 41
Table 2.4. Comparative lattice misfits of selected Pt_{86}:Al_{10}:Z_4 alloys comprising (Pt) matrix and ~Pt_3Al precipitates (ppt) [2001Hil6, 2004Dou2].....55
Table 2.5. TEM EDX analyses (at.%) of $Pt_{86}Al_{10}Cr_4$ (at.%) matrix and precipitate compositions [2004Dou2].....58
Table 2.6. TEM EDX analyses (at.%) of $Pt_{86}Al_{10}Ru_4$ (at.%) matrix and precipitate compositions [2004Dou2].....60
Table 2.7. Lattice misfits at room temperature after heat treatment and water quench, determined by XRD [2006Vor]. 69
Table 2.8. Vickers hardness, using a 10 kg load, of two-phase quaternary alloys after annealing at 1350ºC for 96 hours [2002Cor]. 80
Table 2.9. Tensile test results for Pt-based alloys at room temperature [2004Süs1].....83
Table 2.10. Hardness, ultimate tensile strength and elongation for platinum-based alloys, pure platinum and selected high-temperature alloys [2004Süs2]. 84
Table 2.11. Corrosion of selected Pt-based superalloys and CMSX-4, after immersion in Na_2SO_4 at 950ºC for 564 hours [2010Pot]. 85
Table 2.12. Summary of microstructure, hardness and slip modes for heat treated Pt-based alloys [2009Sho1].....90
Table 3.1. Pt-based samples manufactured in the current investigation.....100
Table 3.2. Pt-based samples previously studied [2009Sho1], indicating samples for which different microstructural observations were made after electrolytic etching.....104
Table 4.1. Differences in the angular positions of the XRD peaks for pure DO'_c - Pt_3Al phase from the ICDD database [2003Xpe], where Y = match and N = no match. 114
Table 4.2. EDX analyses (at.%) of etched nominal Pt_{82}:Al_{12}:Cr_4:Ru_2 (at.%) in the heat treated condition (Figure 4.7(a) and (c)).....117
Table 4.3. EDX analyses (at.%) of etched nominal $Pt_{81.5}$:$Al_{11.5}$:$Cr_{4.5}$:$Ru_{2.5}$ (at.%) in the heat treated condition for the different features in Figure 4.8. 119

Table 4.4. EDX analyses (at.%) of etched nominal Pt_{78}:$Al_{15.5}$:$Cr_{4.5}$:Ru_2 (at.%) in the heat treated condition. 119
Table 4.5. EDX analyses (at.%) of etched nominal Pt_{80}:Al_{14}:Cr_3:Ru_3 (at.%) in the heat treated condition. 121
Table 4.6. EDX analyses (at.%) of etched nominal Pt_{80}:Al_{11}:Cr_4:Ru_5 (at.%) in the heat treated condition. 122
Table 4.7. EDX analyses (at.%) of etched nominal Pt_{78}:Al_{11}:Cr_3:Ru_8 (at.%) in the heat treated condition. 123
Table 4.8. Approximate ~Pt_3Al volume fractions using the Olympus stream image analysis software on SEM-BSE images. 126
Table 4.9. Approximate ~Pt_3Al volume fractions analysed with WSxM software on AFM images. 126
Table 4.10. EDX analyses (at.%) of nominal Pt_{82}:Al_{12}:Cr_4:Ru_2 (at.%) in the heat treated condition for Figure 4.17. 129
Table 4.11. EDX analyses (at.%) of nominal Pt_{85}:Al_7:Cr_5:Ru_3 (at.%) in the heat treated condition for Figure 4.18. 130
Table 4.12. EDX analyses (at.%) of nominal Pt_{80}:Al_{11}:Cr_3:Ru_6 (at.%) in the heat treated condition for Figure 4.24. 133
Table 4.13. EDX analyses (at.%) of nominal Pt_{80}:Al_{11}:Cr_3:Ru_6 (at.%) in the heat treated condition for Figure 4.23, measured across a precipitate/matrix interface. 134
Table 4.14. EDX analyses (at.%) of overall compositions of areas C and D in Figure 4.30 for nominal Pt_{80}:Al_{14}:Cr_3:Ru_3 (at.%) in the heat treated condition. 137
Table 4.15. EDX analyses (at.%) of nominal Pt_{78}:Al_{11}:Cr_8:Ru_3 (at.%) in the heat treated condition. 140
Table 4.16. Nanohardnesses and elastic moduli calculated at final contact depth and maximum applied load 2.5mN for the different heat treated alloys. 158
Table 4.17. Nanohardnesses and elastic moduli for the γ phase calculated at final contact depth and maximum applied load of 5mN for the different heat treated alloys. 159
Table 4.18. Nanohardnesses for heat treated Pt-based samples at maximum loads of 10mN, 20mN and 100mN. 161
Table 4.19. Alloy elastic moduli for heat treated Pt-based samples at maximum loads of 10mN, 20mN and 100mN. 161
Table 4.20. Nanohardnesses and elastic moduli of Pt-based alloys at subgrain boundaries for a maximum applied load of 20mN. 162

Table 4.21. EDX analyses (at.%) and nanohardnesses of γ′ measured at 2.5mN on heat treated samples. 165
Table 4.22. EDX analyses (at.%) and nanohardnesses of γ matrix measured at 2.5mN on heat treated samples. 166
Table 4.23. EDX analyses (at.%) and nanohardnesses of heat treated alloys measured at 100.0mN 166
Table 4.24. Nanohardnesses of larger and smaller γ′ precipitates measured at 2.5mN on heat treated samples. 166
Table 4.25. Nanohardnesses of broad and narrow γ matrix channels measured at 2.5mN on heat treated samples. 167
Table 5.1. Examination of Pt-Al-Cr-Ru alloys XRD spectra using the methodology of Biggs [2004Big2]. 169
Table 5.2. Approximate ~Pt_3Al volume fractions from previous work [2009Sho1], compared to re-measured previous samples (after repolishing and etching) and newly-prepared etched alloys. 173
Table 5.3. Matrix and precipitates' orientation relationship in Pt_{86}:Al_{10}:Z_4 (Z = Cr, Ta, Ti, Ir and Ru) (at.%) alloys [2004Dou2] and Pt-Al-Cr-Ru Alloys 186
Table 5.4. Summary of γ′ volume fractions of commercial NBSAs. 189
Table 5.5. Regression output for dependant variable (γ′ volume fraction), and independent variables (Al and Pt contents), with no interaction term. 211
Table 5.6. Regression output for dependant variable (γ′ volume fraction), and independent variables (Al and Pt contents), with an interaction term. 212
Table 5.7. Regression output for dependant variable (alloy nanohardness), and independent variables (Al and Pt contents), with an interaction term. 212

CHAPTER ONE

1. INTRODUCTION AND BACKGROUND

The term “superalloy” applies to a group of alloys that have been developed for optimal performance at high temperatures. As such, these alloys have been designed to maximize corrosion and creep resistance. A large variety of superalloys has been established to date, although the group finds its roots in research on steels during the First World War [1997Dur]. At that time, researchers both in France and the USA filed the first patents for complex Fe-based alloys for land-based gas turbine engines and jet engines.

Superalloys emerged in the 1940s as the optimal material for the demanding environment in the hot section of gas turbine engines. In the decades following, researchers aggressively pursued improvements in high temperature mechanical properties and stability, bringing about a diverse variety of superalloys generally categorized by their base material, for example, Fe-based, Ni-based and Co-based alloys [1972Sim, 1987Sim, 2006Ree]. Driven by the demands of World War II applications, the United States of America and the United Kingdom were the principle players in superalloy development. By the 1970s and 1980s, Ni-based superalloys became prominent as corrosion-resistant, high-strength, high temperature alloys, with numerous variations commercially available. Ni-based superalloys have excellent mechanical properties due to precipitation strengthening. The microstructure comprises many small, strained-coherent, particles of the γ' phase based on Ni_3Al, in a softer matrix of the γ phase, the solid solution (Ni) of nickel [1987Sim]. The strengthening originates from dislocations being slowed down as they negotiate the small ordered γ' particles. In addition to advances based on alloy chemistry, researchers also explored production techniques to optimize the microstructure and properties of these superalloys [1987Sim, 2006Ree]. Beyond traditional cast and wrought methods, superalloys can be produced as directionally-solidified metals, single crystal products, or by powder metallurgy. Each processing technique caters to a specific application and presents unique advantages and challenges. In addition to aircraft, marine, and industrial gas turbines, superalloys see service in space vehicles, rocket engines, nuclear reactors, submarines, steam power plants, and petrochemical equipment [1987Sim, 2006Ree]. About 15-20% of the alloys have been developed for utilization in corrosion-resistant applications [1987Sim, 1997Dur, 2006Ree].

A combination of increasing refractory alloying additions and advances in processing has resulted in substantial increases in the maximum temperature capability of superalloys over the past few decades [2000Tan]. For example, considering a creep-rupture life of 1000h at a stress of 137 MPa, single-crystal superalloys have a temperature capability of approximately 1100˚C [2004Wal], whereas conventionally cast equiaxed alloys developed in the 1970s had a temperature capability of 900–950˚C [2000Tan]. The temperature capabilities have reached 85–90% of the melting point, and even higher [2004Wal]. However, the melting temperatures and oxidation resistances of these alloys ultimately limit the maximum temperature attainable [1987Sim, 1999Cle, 2006Ree]. The demand for materials capable of attaining even higher operating temperatures is increasing, since increased operating temperatures imply: greater thrust-to-mass ratios, improved fuel efficiency, reduction of noise levels and reduced pollution [1987Sim, 2003Yok, 2006Ree].

The search for improved superalloys continues with possibly more resources and techniques than that for any other alloy system [1996Yam, 2000Wol, 2003Sch1]. Although nickel-based superalloys will probably continue to form the basis of jet engines for many years to come, there is an argument for examining a completely new system with the potential for operation in the ultra-high temperature regime [1996Yam, 2000Wol, 2003Sch1]. Higher melting point alloys have the additional advantage of microstructural stability and hence improved creep resistance, since the diffusion rates of high melting point elements are generally extremely slow [1974Avn].

To meet the demands of increased strength and particularly thermal fatigue resistance for turbine blades and vanes, material scientists developed methods of directional solidification whereby all the grains are aligned along the length of the component, thus eliminating weakening transverse grain boundaries [1972Sim, 2006Ree]. In the past forty years, material scientists have developed advanced methods to produce single crystal components.

Degradation by high-temperature oxidation, hot corrosion, and erosion are the main failure modes of components in the hot sections of gas turbines, boilers, industrial waste incinerators, metallurgical furnaces and petrochemical installations [1995Esm, 2010Kam]. Superalloys have been developed for high temperature applications, but they are not able to meet the requirements of both the high-temperature strength and the high-temperature erosion–corrosion resistance simultaneously [2010Kam]. The turbine engines are exposed to high temperatures and harsh environments and therefore tend to suffer from significant

material degradation during service [1995Esm]. Numerous Ni-, Co-, and Fe-based superalloys are used in gas turbine engine applications [2010Kam]. Fuel oils and fossil fuels used in energy generation systems contain complex mixtures of molten sodium sulphate (Na_2SO_4) and vanadium pentoxide (V_2O_5). The Na_2SO_4 can be ingested in the turbine intake air or it can be produced by the reaction between sodium chloride (NaCl) ingested with the intake air and sulphur impurities in the fuel. Vanadium is present in the fuel in the form of vanadium porphyrin ($C_{24}H_{18}N_4VO$), which transforms during combustion into V_2O_5. The V_2O_5 and Na_2SO_4 form low melting point inorganic compounds, which undergo a eutectic reaction below 600°C. When the temperature exceeds the melting point of the deposits, these compounds start slowly depositing on the turbine blades, and consequently the corrosion rate rapidly increases due to faster transport phenomena in liquid phase [2010Kam]. Hence, for efficient functioning of gas turbine components, it is essential to develop superalloys with high-temperature strength as well as good hot corrosion resistance [1999Gur, 2010Kam].

Alloys based on intermetallic compounds such as NiAl, TiAl and RuAl have received considerable attention in the past 30 years, because the ordered structure of intermetallic compounds imparts good high temperature strength [1986Gia, 1990Fle, 1991Fle, 1997Wil]. However, most intermetallic compounds are inherently brittle at room temperature, and the development of useful alloys is limited by this brittleness [1986Gia, 1993Fle, 1997Wil, 1997Yam1]. Refractory metals such as Mo, Ta and W have also been considered, but their alloys have limited high temperature oxidation resistance, and also limited creep resistance, because of their more open body-centred cubic (bcc) crystal structure [1987Sim, 2006Ree]. Ceramics and composite materials have also been the focus of considerable research, but their poor room-temperature toughness, low resistance to thermal shock and poor oxidation resistance remain problematic [1981Gan, 1986Hil, 1993Raj].

Mo–Si–B alloys have attracted attention as alternatives to Ni-based superalloys for gas turbine blades due to their high melting point and excellent oxidation resistance, as well as good mechanical properties at a higher service temperature than that of Ni-based superalloys. The Mo–Si–B alloys consisting of α-Mo (solid solution) and two intermetallic phases of Mo_3Si (A15) and Mo_5SiB_2 (T2) have excellent properties at both high temperature and room temperature [1997Ber1, 1997Ber2], although the intermetallic compounds are brittle, whereas α-Mo is relatively ductile. Therefore, to develop Mo–Si–B alloys with both superior mechanical properties and oxidation resistance, it is necessary to control their microstructures,

ensuring that intermetallic phases are distributed within a continuous ductile phase matrix of αMo [2014Hwa].

An alternative approach is the development of alloys based on the platinum group metals (PGMs) [1996Yam]. The PGMs (Ru, Ir, Rh, Os, Pd and Pt) generally have high melting temperatures, and superior environmental resistance to the refractory alloys. Additionally, certain PGMs such as Rh, Pd, Ir and Pt have face-centred cubic (fcc) crystal structures, to potentially allow analogous alloys to the nickel-based superalloys to be developed. Scientists at the National Institute for Materials Science (NIMS, formerly NRIM) in Japan have achieved promising results for Ir- and Rh-based alloys [1981Liu, 1993Gyu, 1994Har, 1996Yam, 1997Yam1, 1997Yam2, 1998Yam]. Alloys with strengths of up to 200 MPa at 1800°C have been produced.

Experimental Pt-based alloys have been studied at Mintek and the University of the Witwatersrand. It was found that successful Ni-based superalloy analogues could be manufactured with alloys of the approximate composition Pt_{82}:Al_{14}:X_4 (at.%) where X was Cr, Ti and Ru [2001Hil1, 2001Hil2]. The best properties were exhibited by the Pt-Al-Cr and Pt-Al-Ru alloys, although the precipitate volume fraction was not as high as in the Ni-based superalloys [2009Cor1, 2009Cor2]. A quaternary alloy was targeted from a combination of these alloys to have both alloys' properties and increase the ~Pt_3Al volume fraction [2001Hil2, 2007Cor]. Chromium stabilized the cubic $L1_2$ ~Pt_3Al precipitate, and Ru gave solid-solution strengthening to the (Pt) matrix. Experimentation gave Pt_{84}:Al_{11}:Cr_3:Ru_2 (at.%) as the best composition with a reasonable proportion of precipitates and good properties, including hardness. The volume fraction of ~Pt_3Al was estimated, using image analysis, to be approximately 25 – 30%. The highest hardness was found in the alloy without primary ~Pt_3Al. There was no clear relationship between the hardness and the composition.

On the basis of hardness and microstructure, a later study identified a new optimum alloy composition [2008Sho1, 2008Sho2, 2008Sho3, 2009Sho1, 2009Sho2]: Pt_{78}:Al_{11}:Cr_6:Ru_5 (at.%). However, characterisation of the samples was not easy and needed further work [2009Sho2], such as suitable etching and TEM studies. The eutectic formation of Pt + ~Pt_3Al could not be suppressed, and so the alloys still showed brittle failure along the interdendric regions, where the eutectic formed [2008Süs1]. Süss *et al*. [2006Süs, 2008Süs1] varied the cooling rates for Pt-Al-Cr-Ru and Pt-Al-Cr-Ru-Co alloys by furnace cooling, air cooling and water quenching of the heat treated 1200°C to 1400°C samples. Water quenching the Pt-Al-

Cr-Ru alloys from either 1350°C or 1400°C was found to yield low ~Pt_3Al precipitate volume fractions. However, Süss *et al.* [2008Süs1] recognised that it was possible that some the precipitates may have been too small to be observed, and that if this was the case, TEM should be employed.

1.1 Rationale of this Investigation

Research work on Pt-based alloys for high temperature applications in aggressive environments has progressed well [2007Cor]. The first tensile tests of the alloys worldwide were undertaken at ambient temperature. The results were very encouraging, since they were comparable to those of other high temperature alloys [2004Süs1, 2004Süs2]. TEM studies have shown that between 810°C and 870°C, some precipitate dissolution occurs [2007Cor, 2004Dou1]. The results suggested that further additions to stabilize the small precipitates would be beneficial above 1300°C, because changes to the microstructure were observed at this temperature [2004Dou1, 2004Dou2, 2007Cor, 2007Dou]. Work at the Fachhochschule Jena and the University of Bayreuth started from a promising Pt-Al-Cr alloy [2002Süs1], and investigated the influence of additions of further elements on mechanical strength and microstructure. Niobium, Ta and Ti were found to increase strength when added as a partial substitute for Al, although there was higher susceptibility to internal oxidation [2005Hül, 2005Vor, 2005Wen1, 2005Wen2]. After ageing, finely dispersed precipitates in the matrix were observed. Minor additions of B greatly increased creep resistance and rupture time, due to strengthening of the grain boundaries [2006Völ]. Rhenium was found to slow down precipitate growth and to further increase creep strength.

Hill *et al*. [2001Hil3] expected that increasing research efforts in this area by thorough characterization of the platinum alloys would assist future development for current and future application needs. The current PhD work continued from where the MSc work stopped [2009Sho1], in which nominal Pt_{78}:Al_{11}:Cr_6:Ru_5 (at.%) was found to be the promising alloy from both microstructure and economical considerations [2009Sho1]. Using the optimum composition from the MSc [2009Sho1], new samples were made to study the effect of the microstructure on the properties of selected Pt-based superalloys, which was the purpose of the PhD work. To achieve this purpose, the original objective of the PhD was two-fold: to

grow single crystals of Pt-based superalloys, and compare the microstructure and properties with conventionally-produced (polycrystalline) material; and to undertake transmission electron microscopy (TEM) studies, atomic force microscopy (AFM), carry out better etching on these materials, as well as produce a range of polycrystalline alloys of different compositions. However, since the crystal grower took longer than expected to become fully operational, the project focus was changed, although the work done on the single crystal grower is reported in Appendix C. The new objective was to study the effect of the microstructure on the properties of selected Pt-based superalloys.

The strength of the Pt-based alloys depends primarily on the ordered strengthening precipitates dispersed in the γ matrix. The properties depend on the microstructure of the alloy, which is directly influenced by the composition and heat treatments [1987Sim, 2006Ree]. Thus, an in-depth TEM study was important in understanding the properties of these alloys. The contributions of the TEM studies were to firstly show the effect of the heat treatment compared to the as-cast samples on the morphology and distribution of γ′ precipitates, as well as the variation in the partitioning of different alloying elements in the γ matrix and γ′ precipitates. Secondly, the objectives included achieving an understanding of the formation of different morphologies of γ′ precipitates that occur during heat treatment by comparing with NBSAs. Thirdly, TEM work was to be used to assist in determination of the precipitate volume fraction, to allow for the comparison of different alloys.

There are at least two ~Pt_3Al allotropes [1986McA, 1987Oya], and the high temperature cubic structure has better properties than the lower temperature tetragonal form, and as such it needs to be stabilised. Thus, the fourth contribution of the TEM studies was to undertake diffraction pattern analyses to determine the ~Pt_3Al structure and the orientation relationship between the γ matrix and γ′ precipitates.

Since the Pt-based superalloys are intended for applications similar to NBSAs, a comparison of the nanomechanical properties of the Pt-based alloys to the NBSAs was considered important. Thus, the mechanical properties of the individual phases (the precipitates and matrix) were studied by means of nanoindentation using AFM, to measure the hardness and modulus of elasticity of the ~Pt_3Al precipitates and (Pt) matrix. It is desirable to maximise the hardness of the Pt-based alloys without compromising properties such as high temperature

strength, and to attain hardnesses at least as high as for the NBSAs. This can be achieved by optimizing the microstructure to give high volume fractions of the small precipitates.

The volume fraction of the γ′ precipitates is such an important aspect with regard to the properties of these alloys, that the volume fractions of the γ′ precipitates were measured using SEM images after successful electrolytic etching, and the results were compared with both the AFM and TEM measurements.

1.2 Outline of the Thesis

Chapter Two presents a short literature review with regard to Ni-based superalloys relevant to this work and also previous work that has been done on the Pt-based superalloys. A review on the instrumentation and methods used in the current work is presented in the experimental procedure, the third chapter. The fourth chapter is dedicated to the results obtained, starting with XRD, followed by OM, SEM, AFM and image analysis studies, TEM studies, and finally, nanomechanical properties. The fifth chapter is a discussion of the results, while conclusions and recommendations for future work are presented in Chapter Six. Appendices A and B present more results from nanoindentation studies. Appendix C documents work undertaken on the single crystal grower. Appendix D shows the XRD pattern of the plasticine and the methodology for distinguishing between the two forms of Pt_3Al and the platinum-rich solid solution phase. Appendix E gives a summary of the Oliver-Pharr method used in this work and explains the phenomenon of the pop-in event, and also the method of calculations. The papers published and presentations made during the course of this investigation are shown or listed in Appendix F.

CHAPTER TWO

2. LITERATURE SURVEY

2.1 Introduction

Superalloys based on platinum-group metals are being developed for high-temperature applications [2000Wol]. These Pt-based alloys have two-phase microstructures comprising either ordered precipitates in a matrix, analogous to the nickel-based superalloys [2000Hil1, 2002Hil, 2009Cor1, 2009Cor2, 2009Dou] or a fine dispersion of oxide particles in a matrix, analogous to oxide-dispersion-strengthened nickel-based alloys [2001Fis1].

The aim of this literature survey is to provide a review on the development stages and progress made in the development of platinum group metal (PGM) superalloys for high temperature use, as well as their properties and morphology, with more attention given to the Pt-Al-Cr-Ru superalloys. The review will first highlight the history of superalloys, nickel-based single crystal superalloys, earlier work done on the development of a new generation of materials to succeed the nickel-based superalloys, ending with the latest work done on Pt-based alloys through collaborative studies undertaken by Mintek, the University of the Witwatersrand, University of Bayreuth and the Fachhochschule Jena-University of Applied Sciences, and NIMS.

2.2 Development and History of Superalloys

2.2.1 Microstructure

In the 1950s, adding strengthening elements increased the NBSAs' strength, but then led to significant problems created by embrittling phases [1987Sim, 2006Ree]. The 1950s also saw the generation of very complex grain boundaries, with carbides enclosed in γ', creating a dispersion-strengthened layer bonding the grain boundaries. By 1970, the effects of hafnium had been discovered, and the γ'-enclosed carbide structure was not essential. Directional solidification (DS) processing created aligned grains, hence aligned grain boundaries, and even aligned strengthening filaments (such as TaC) were documented. In the 1980s, aligned homogeneous single crystal (SC) structures improved the properties. Through heat treatment,

transverse plates of γ′ were created in single crystals, which gave still further strengthening [1987Sim, 2006Ree].

2.2.2 Mechanical Properties

The prime reason for the existence of superalloys is their outstanding strength over the temperature ranges at which gas turbine components operate [1970Ver, 1979Nor]. Their close packed fcc lattice has the capability to maintain relatively high and reliable tensile, rupture, creep, and thermomechanical fatigue properties at temperatures that are much higher than for equivalent bcc systems [1970Nor]. Contributing factors are the high modulus of the fcc lattice, high density of slip systems, and its low diffusivity for secondary elements. The broad solubility ranges of secondary elements in the fcc matrix enables precipitation of intermetallic compounds (such as γ′ and γ′′) for strength. Strengthening effects also can be obtained by solid-solution strengthening, carbide precipitation, grain boundary control, and single crystal generation [1970Nor, 1972Sim, 1987Sim, 2006Ree]. Solid solution strengthening is obtained from the broad solubility ranges and a sloping solidus is also needed.

2.2.3 Development of Processing

The material and casting improvements that have taken place during the last 50 years have enabled superalloys to be used first as equiaxed castings in the 1940s, then as directionally solidified (DS) materials during the 1960s, and finally as single crystals (SC) in the 1970s. The advancement in each casting technique resulted in higher application temperatures [1970Pie, 1972Sim, 1970Ver, 2006Ree]. There are two primary reasons that explain why DS superalloys are superior to conventionally cast superalloys. Alignment, or elimination in the case of SC superalloys, of the grain boundaries normal to the stress axis enhances elevated temperature ductility by eliminating the grain boundaries as failure initiation sites. The second reason is that the DS process provides the preferred <001> orientation, which has a low modulus, parallel to the solidification direction. This results in a significant enhancement in thermal fatigue resistance, which is important for components used at elevated temperatures [1970Ver]. Ver Snyder *et al.* [1970Ver] were the first to demonstrate for superalloys that by aligning the grain boundaries parallel to the principal stress axis, the stresses acting at elevated

temperatures on the weak grain boundaries could be minimized, thus delaying failure and initiation and enhancing creep rupture life.

2.3 Nickel-based Superalloys

2.3.1 Introduction

Nickel-based alloys are the most complex and widely-used superalloys for high temperature applications when significant resistance to spontaneous deformation under sustained load, as well as resistance to oxidation (as in the case of gas turbine engines) is required [1987Sim, 2006Ree]. The combination of high-temperature strength and oxidation resistance renders them highly successful in service as structural high-temperature materials. These alloys contain up to 14 elemental alloying constituents, as well as additions of trace elements [1992Bro]. The chemical compositions of these alloys are selected to produce the desired structure and properties for a specific application [1987Sim, 1990Lee, 2006Ree]. From 1940 to 1965, the properties given the most attention for applications such as aircraft engine blades were high-temperature tensile strength, creep rupture strength to 5000 hours, and oxidation resistance [1987Sim, 1990Lee, 2006Ree].

2.3.2. Single Crystal Alloys

The single-crystal (SC) superalloys are often classified into first to fifth generation alloys. The second and third generations have improved creep properties and increased volume fraction of the precipitates compared to the first generation and contain about 3 wt% and 6 wt% rhenium respectively (Table 2.1), while the first generation had no rhenium [1990Lee, 1999Car1]. Figures 2.1 to 2.3 [1999Car1, 1993Har, 2003Yok] show typical microstructures of the first, second and third generation superalloys and their similarities. The main feature of the AM3 first generation microstructure is the homogeneous distribution of γ' micro-precipitates in the γ matrix (Figure 2.1) [1999Car1]. The second generation microstructure (Figure 2.2) is characterised by remnants of the dendritic growth. The second and perhaps the most important feature is the rough edges of the γ' precipitates. Porosity is the third important microstructural feature of the CMSX-4 second generation NBSA, and this affected the fatigue properties, causing fatigue crack initiation [1993Har]. The third generation

microstructure (Figure 2.3) is characterised by elongated γ′ precipitates and looks similar to the AM3 first generation SC superalloy [1999Car1, 2003Yok].

Table 2.1. Nominal compositions (wt%) of single crystal superalloys, balance Ni [1996Eri].

	Cr	Co	Mo	W	Ta	V	Nb	Al	Ti	Hf	Re
1st Generation											
PWA1480	10	5	0	4	12			5	1.5	0	
Rene N4	9	8	2	6	4		0.5	3.7	4.2	0	
SRR99	8	5	0	10	3			5.5	2.2	0	
RR2000	10	15	3	0	0	1		5.5	4	0	
AM1	8	6	2	6	9			5.2	1.2	0	
AM3	8	6	2	5	4			6	2	0	
CMSX2	8	5	0.6	8	6			5.6	1	0	
CMSX3	8	5	0.6	8	6			5.6	1	0.1	
CMSX6	10	5	3	0	2			4.8	4.7	0.1	
AF56	12	8	2	4	5			3.4	4.2	0	
										0	
2nd Generation											
CMSX4	7	9	0.6	6	7			5.6	1	0.1	3
PWA1484	5	10	2	6	9			5.6	0	0.1	3
SC180	5	10	2	5	9			5.2	1	0.1	3
MC2	8	5	2	8	6			5	1.5	0	0
Rene N5	7	8	2	5	7			6.2	0	0.2	3
										0	
3rd Generation											
CMSX10	2	3	0.4	5	8			5.7	0.2	0.03	6
Rene N6	4.2	12.5	1.4	6	7.2		0.1	5.75	0	0.15	5.4
TMS75	3	12	2	6	6			6	0	0.1	5
TMS113	2.89	11.93	1.99	5.96	5.96			6.56	0	0.1	5.96
	Cr	Co	Mo	W	Ta	V	Nb	Al	Ti	Hf	Re

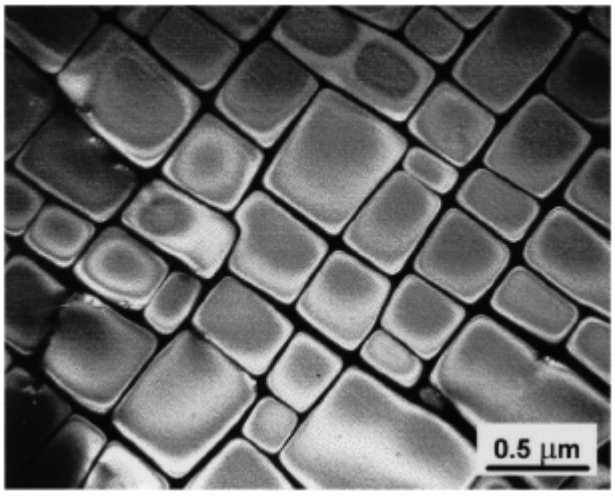


Figure 2.1. Two-phase γ - γ′ microstructure of fully annealed heat treated AM3, a first generation single crystal superalloy [1999Car1].

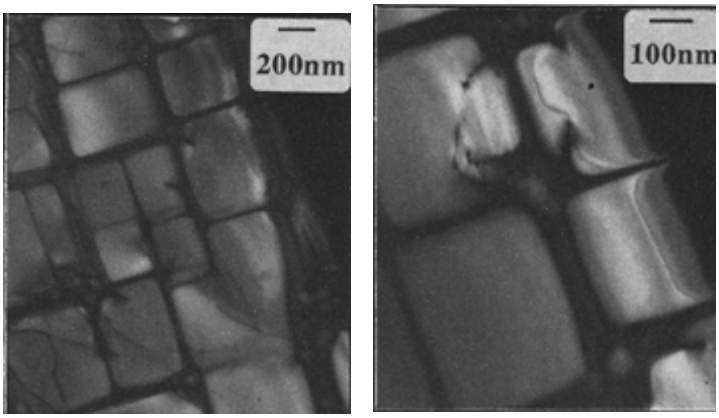


Figure 2.2. Microstructure of fully heat treated CMSX-4, a second generation single crystal superalloy [1993Har].

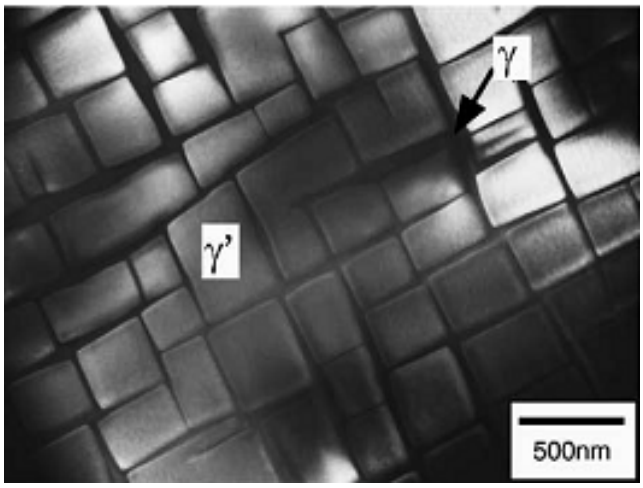


Figure 2.3. Microstructure of a third generation Rene N5 heat treated at 1025˚C for 16 hours showing a two-phase γ - γ′ microstructure [2003Yok].

The single crystal NBSAs contain a high volume fraction of strengthening LI_2 ordered Ni_3Al-based γ′ phase particles homogeneously distributed in the γ matrix as near cubic precipitates. Most NBSAs contain 10-20 wt% Cr, up to 8 wt% Al and Ti, 5-10 wt% Co, and small amounts of B, Zr and C (Table 2.1). Other common additions are Mo, W, Ta, Hf and Nb [1995Eri, 1996Eri, 1999Car2]. In broad terms, the elemental additions in Ni-based superalloys can be categorized as being [1987Sim, 2006Ree]:

i) γ-formers (elements that tend to partition to the γ matrix)

ii) γ′-formers (elements that partition to the γ′ precipitate)

iii) Carbide formers, and

iv) Elements that segregate to the grain boundaries.

Elements which are considered γ-formers are Group V, VI, and VII elements such as Co, Cr, Mo, W, and Fe [1986Gia, 1995Eri, 1996Eri]. The atomic diameters of these alloys are only 3-13% different from Ni (the primary matrix element). The γ′-formers come from Group III, IV, and V elements and include Al, Ti, Nb, Ta and Hf. The atomic diameters of these elements differ from Ni by 6-18%. The main carbide formers are Cr, Mo, W, Nb, Ta and Ti. The elements B, C and Zr form grain boundary precipitates, which, when present as discrete particles, are believed to pin grain boundaries and thereby inhibit grain boundary sliding. They have also been reported [1986Gia, 1995Eri, 1996Eri] to significantly improve creep life, rupture strength, and tensile ductility at elevated temperatures. Their atomic diameters are 21-27% different from Ni [1986Gia, 1995Eri, 1996Eri].

Rhenium is a very expensive addition, but leads to an improvement in the creep strength and fatigue resistance. It is argued that some of the enhanced resistance to creep comes from the promotion of rafting by rhenium, which partitions into the γ phase and makes the lattice misfit more negative [1996Eri]. Rafting is a phenomenon that occurs under the combined influence of stress and temperature, where the initial γ′ phase separated by channels of γ matrix transforms into plates or coalesces to form layers [1997Nab]. Atomic resolution experiments have shown that the Re occurs as clusters in the γ phase [1997Nab]. It is also claimed that rhenium reduces the overall diffusion rate in NBSAs [1996Eri]. The properties of superalloys deteriorate if topologically close-packed phases (TCP) precipitate. In these phases, some of the atoms are arranged as in nickel, where the close-packed planes are stacked in the fcc sequence ABCABC. The addition of rhenium promotes TCP formation, so alloys containing these solutes must have reduced Cr, Co, W or Mo concentrations to compensate. It is generally not practical to remove all these elements, but the chromium concentration in the new generation superalloys is much reduced, to about 2.5 wt% Cr. Chromium does protect against oxidation, but oxidation can also be prevented by coating the blades [1970Ver, 1995Eri, 1996Eri, 1999Car2].

The fourth-generation nickel-based single-crystal superalloys contain large amounts of refractory metals for strengthening and platinum group metals for the prevention of TCP precipitates, and they show excellent high-temperature strength [2008Wu]. However, these alloying elements decrease the high-temperature oxidation resistance. The alloys contain 2 wt% Ru, which improves the stability of the microstructure. The addition of ruthenium also results in excellent high temperature strength compared to the previous generation of

superalloys [2006Kaw, 2008Wu]. Figure 2.4 [2008Wu] shows the microstructure of a fourth generation superalloy, TMS-138, with fine ~Ni_3Al precipitates between the coarser precipitates which did not occur in the prior generations.

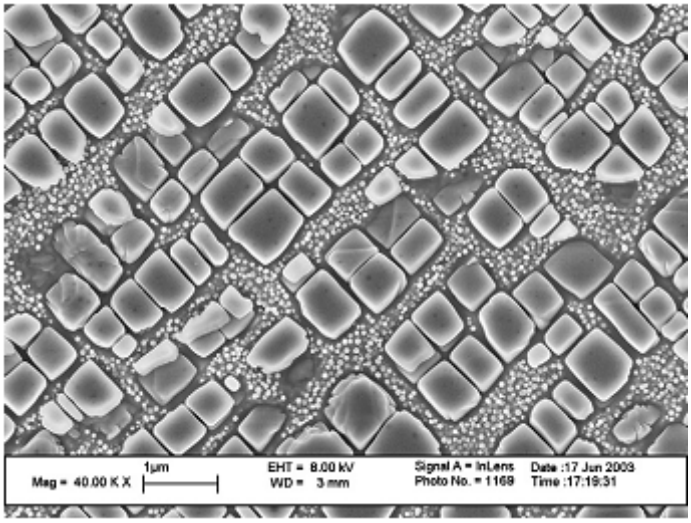


Figure 2.4. TMS-138 fourth generation single crystal superalloy, showing coarse and fine Ni_3Al cubic precipitates in a (Ni) matrix [2008Wu].

The latest, fifth generation superalloys TMS-138A and TMS-196 are advanced nickel-based single crystal superalloys containing 5 wt% Ru and 4.6 wt% Cr. They exhibit not only good microstructural stability, but also excellent resistance against creep, thermo-mechanical fatigue and oxidation. The microstructure (Figure 2.5 [2008Yeh]) is similar to those of the third generation superalloys [2006NIM].

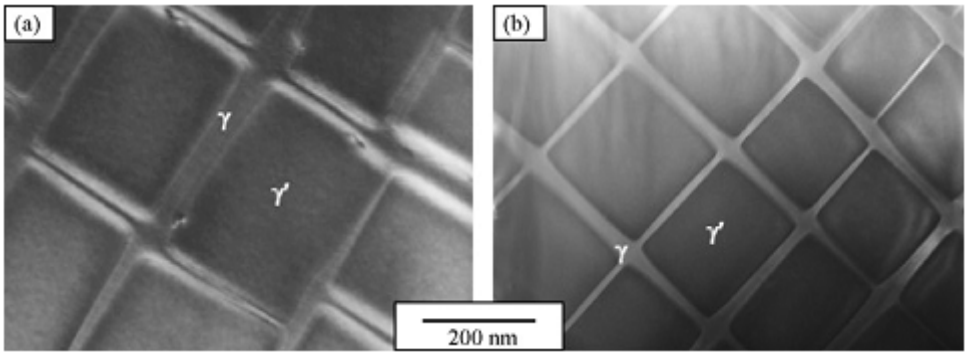


Figure 2.5. Heat treated fifth generation microstructures in (a) TMS-138A, and (b) TMS-196 [2008Yeh].

2.3.3 Effect of Grain Boundaries on Mechanical Properties

Crack formation during directional solidification (DS) of Ni-based superalloys in investment casting is a well-known problem [1999Boy]. Cracking occurs at the columnar grain boundaries in the last stages of the DS process, and is also known as hot tearing, hot cracking, or solidification cracking. It has been well established that the DS versions of particularly high chromium superalloys, such as IN792, suffer significantly from this problem [1999Boy].

Zhang and Singer [2002Zha1] examined the effects of grain boundary misorientation on the castability of IN792 and CM247 by casting single-crystal (SC) and bi-crystal specimens. Crack-free specimens were obtained in castings with grain boundary misorientation angles of less than ~12º. Severe cracking occurred if the grain boundary angle was greater than 25º. The amounts of eutectic melt and foreign element segregation were also larger at the grain boundaries. The greater susceptibility of the grain boundary to hot tearing was almost certainly caused by a reduced strength compared to that of the grain interior. Grain boundary weaknesses of nickel-based superalloys have also been observed during service in the hot turbine engine sections and also during welding [1999Boy, 1994Zha]. Figure 2.6 [1994Zha] shows a crack in a turbine engine superalloy initiated along the grain boundaries.

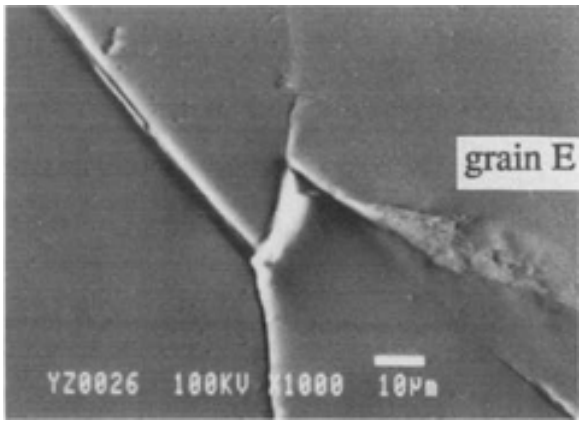


Figure 2.6. SEM-SE micrograph showing crack growth into grain E [1994Zha].

2.3.4 Development of Different γ' Morphologies and Sizes in NBSAs

This section of the literature review gives a brief summary on the mechanisms responsible for the development of different γ' Ni_3Al precipitate morphologies in NBSAs. These are considered important to explain the precipitate morphologies and overall microstructure

observed.

In this work, the Pt-based alloys being developed are NBSAs analogues. Little work has been undertaken in order to understand the mechanisms involved in the development of different γ′ morphologies. Thus, in this section, the mechanisms involved in the development of different γ′ morphologies in NBSAs which are useful to explain the observations made of the Pt-based superalloys microstructure will be considered.

The distribution, size and morphology of γ′ precipitates in NBSAs depends significantly on the processing route and the heat treatments involved [2001Bab, 2003Sub, 2003Wen]. The rate of cooling and the grain size effect the serrations at the grain boundaries during cooling, which affects the mechanical properties. Thus, the study of the cooling rate on the microstructural evolution is extremely important. Serrations are developed by applying a heat treatment below the solvus temperature of the γ′ phase. The presence of homogeneously distributed serrations along the grain boundary can improve the crack growth resistance in superalloys. The variation in microstructure due to different cooling rates has been studied [2006Wen1, 2007Sar, 2007Sei1, 2007Sei2]. Formation of a monomodal distribution of precipitates has been observed at high cooling rates after solutionizing the material in the single γ phase field [2009Hwa]. These precipitates possessed relatively high nucleation rates to give a high precipitation density, which has been observed by different characterization techniques [2003Sub, 2005Sar, 2007Sei1, 2007Sei2, 2009Hwa]. Due to the limited growth of these precipitates, they maintain close to spherical morphologies [2009Hwa].

Even though there has been extensive research on the morphology of NBSA precipitates using energy filtered transmission electron microscopy (EFTEM) and routine TEM [1996Haz, 1997Tor, 2007Sei2, 2008Elb], less work has been carried out on the mechanisms that lead to the formation of these precipitates. With the development of atom probe tomography, the compositional partitioning between the ordered γ′ precipitates and disordered γ matrix, leading to the different precipitate size distributions has been studied [2008Tia]. The effect of cooling rate on the size distribution of the γ′ precipitates and subsequent properties is of particular interest, since the volume fraction, size, morphology and distribution can be controlled [1997Tor, 2008Tia]. Jackson *et al*. [1999Jac] and Babu *et al.* [2001Bab] studied the effects of cooling rate on the microstructure and chemical partitioning of various elements between γ and γ′. With increasing cooling rate, the morphology of the γ′ precipitates changed from cuboid to irregular. Water quenched samples

produced γ′ precipitates close to spherical morphology, whereas slow cooled samples showed a bimodal distribution of precipitates and larger precipitates exhibiting a cuboid to irregular morphology. The overall size of the larger precipitates decreased with increased cooling rate. There was negligible change in partitioning of elements for larger precipitates with changes in cooling rate, whereas changes in Al concentration were found for smaller precipitates.

Grosdidier [1998Gro] analyzed the effect of cooling rate on the γ-γ′ transformation and γ′ morphology for two NBSAs, AM1 and CMSX-2, and found that the γ′ morphology changed from spherical to irregular with decreased cooling rate. Mackay *et al*. [1988Mac] studied a Ni-Al-Mo-Ta alloy and reported that forced air cooling resulted in the formation of coarser precipitates than oil quenching. All these studies [1997Tor, 1998Gro, 2001Bab, 2008Tia] showed that with decreasing cooling rate, the size distribution of γ′ particles changed from unimodal to bimodal or multimodal. This indicates that the mechanism of precipitate formation also varies with changing cooling rate.

The formation of multiple size ranges of γ′ precipitates during slow cooling, due to multiple nucleation events, is obviously a complex process with an interplay of multiple factors. However, a clear understanding of the interplay of the factors has been lacking [1998Gros].

Hwang *et al.* [2009Hwa] studied the compositional variations between different generations (i.e. primary, secondary and tertiary precipitates) of γ′ precipitates using atom probe tomography and found that the compositions of different size ranges of precipitates were different. In addition, the composition of the γ matrix was found to be different near the primary and secondary γ′ precipitates. They [2009Hwa] found that the interface widths between precipitate and matrix for primary and secondary precipitates were different, and the interface width was greater for the secondary than the primary precipitates. Thus, partitioning between the different generations of γ′ and matrix was also found to be different. Formation of bimodal microstructures has been reported many times [2008Elb, 2009Bou, 2010Elb], although little emphasis has been given to explaining the formation of different generations of γ′ obtained experimentally [2008Elb, 2009Bou, 2010Elb]. Wen *et al.* [2003Wen] simulated the microstructure evolution in superalloys for continuous cooling conditions, and demonstrated that at intermediate cooling rates, the first nucleation burst was stopped by both the closeness of the precipitates and the competition in diffusion direction around the precipitates. However, with decreasing temperature during continuous cooling, supersaturation increased and at a high undercooling, a second burst of nucleation occurred.

Consequently, a bimodal microstructure was obtained as a result of two successive nucleation events.

The change in morphology during coarsening of γ′ has been of considerable interest. The effect of misfit on the change in morphology of γ′ is important in superalloys. Ricks *et al.* [1983Ric] showed that with increasing ageing time, the shape of γ′ precipitates changed from spherical to an array of cubes. Initially, when the γ′ nucleates, it develops a spherical morphology to minimize the interfacial energy (which is dependent on surface area), since the contribution due to strain energy resulting from lattice misfit is low (dependent on volume). During growth, the contribution of strain energy increases, and the precipitates attain a cuboid morphology. However, further growth of the precipitates leads to increased strain energy and the system tries to minimize the free energy by splitting the γ′ precipitates. This is because the decrease in strain energy is more than the increase in interfacial energy [1983Ric]. The splitting phenomenon was observed earlier by Westbrook [1958Wes], where larger cubes split into about one tenth of their size to form smaller cubes.

Doi *et al*. [1984Doi] created a theoretical model which agreed with their experimental investigations and also those of Ricks *et al.* [1983Ric], where strain resulting from lattice misfit caused splitting of γ′ precipitates. The model also suggested that for very low lattice misfits, the precipitates would not split, but above a certain lattice misfit, the precipitates could split to form parallel platelets. Theoretical analysis of the effect of strain on morphology during coarsening suggested that strain induces splitting of γ′ precipitates, although the model assumed that the elastic constant of matrix and precipitate were the same and that the interfaces were coherent [1988Kac]. The model was found to be valid for low γ′ volume fraction alloys, and matched well with the experimental investigations of Doi *et al*. [1984Doi] and Miyazaki *et al*. [1982Miy]. The γ′ splitting phenomenon was also investigated by Hazotte *et al*. [1996Haz] using finite element modelling and it showed that the splitting of coherent γ′ precipitates occurred due to the effect of strain energy.

2.3.5 Dislocation Networks in Ni-based Superalloys

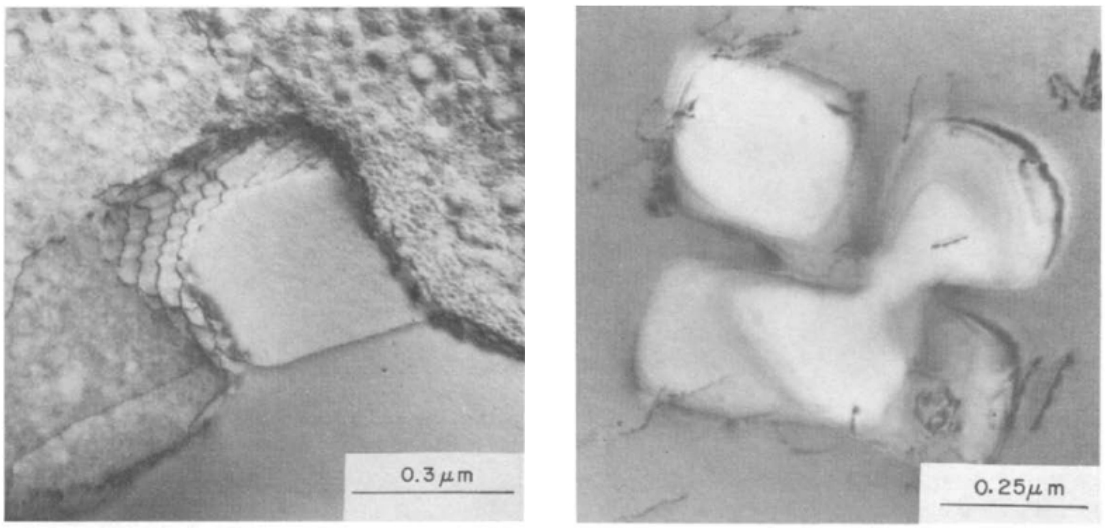
This section gives a summary of studies done on dislocation networks in NBSAs with particular attention given to alloys that were not subjected to any externally applied load, but heat only. This is to make a better comparison with the current alloys in this work because they were only heat treated.

It is well known that NBSAs are strengthened by a fine dispersion of γ′ precipitates [1987Sim, 2006Ree]. The dislocation networks at the γ/γ′ phase interface can effectively strengthen the interface and enhance the creep resistance. Creep, tensile or fatigue loading of superalloys at temperatures above 870°C produce dislocation networks at the γ/γ′ interfaces [1968Wea]. These networks act in some part to relieve elastic strains at the interfaces induced by lattice mismatch and the externally applied loads. Externally applied loads accelerate the formation of interfacial dislocation networks [1968Wea, 1975Las, 1984Fre]. Dislocations networks are often evenly mixed (edge and screw) in character [1984Fre] or edge [1975Las, 1977Car, 1980Pea].

The development of γ′ precipitates in NBSAs Nimonic 80A and Nimonic 115 was investigated by Ricks *et al.* [1983Ric]. Each alloy was treated at 1200°C for 30 minutes, followed by a furnace cooling (1°C/s) to approximately 20°C below the γ′ solvus temperature determined during that investigation. Ageing was then carried at this temperature for up to 24h. Thin foil specimens for transmission electron microscopy were prepared from discs 3mm in diameter, punched from thin slices of the material and ground to 0.1mm. These discs were then thinned to perforation in a Fischione twin-jet electro-polisher using an electrolyte consisting of 10% perchloric acid in glacial acetic acid at 5°C and a voltage of 35V. All electron microscopy was performed on a Philips EM400 TEM/STEM. Different γ′ morphologies and dislocations were observed in the two alloys (Figure 2.7) [1983Ric], and the morphology was a function of both misfit and particle size. To explain the formation of the dislocations, they [1983Ric] proposed that during heat treatment the thermal expansion coefficients of the γ and γ′phases were dissimilar, thus altering the effective misfit experienced by the growing γ′ at the heat treatment temperature. Since γ′ is ordered, the thermal expansion of this phase would probably be less than for the γ matrix, and this would tend to increase mismatch with increasing temperature.

A TEM study of the dislocations present in NBSA AM1 after exposure to different heat treatments was undertaken by Grosdidier *et al*. [1998Gro]. The starting microstructure was from a two-step ageing treatment, 16h at 1050°C then air cooling, followed by 24h at 850°C then air cooling. This gave a microstructure with about 70% volume γ′ precipitates in the γ matrix, Figure 2.8(a) [1998Gro]. The two halves of the alloy were then subjected to another heat treatment at 1240°C for 80 minutes, followed by air cooling for one half, and the other

half at 1260°C for 40 minutes followed by air cooling. No dislocations were observed after 80 minutes at 1240°C (Figure 2.8(b)) compared to 40 minutes at 1260°C (Figure 2.8(a)).



(a) **(b)**

Figure 2.7. Bright field TEM images, showing (a) Nimonic 115 with a well formed array of misfit dislocations in the γ/γ´ interface, and (b) Nimonic 80A with dislocations in the matrix and precipitate [1983Ric].

After 40 minutes at 1260°C, the alloy had interfacial dislocation networks at the γ/γ´ interface (Arrow N on Figure 2.8(c)). The precipitates had lost their cubic shape for a more rounded one. To explain the relationship between heat treatment temperature and dislocation formation, Grosdidier *et al*. [1998Gro] suggested that at high temperature, the motion of dislocations is enhanced, and coherency can be lost early enough to prevent plate formation. With the loss of coherency, the precipitates also lost their cubic shape for a more rounded one. Under thermal treatments, loss of coherency occurs by the migration, trapping and rearrangement of dislocations moving from carbides [1975Car] or from sub-boundaries [1975Car, 1977Car]. Since the loss of coherency requires the motion of dislocations, it preferentially happens at high temperature and/or for fairly long ageing treatments. This process can be enhanced with applied stress [1987Nat, 1996Ver]. The interfacial dislocation networks were also explained by lattice mismatch strains during high temperature, since there was no applied stress or load [1998Gro].

The structure of the heat affected zone (HAZ) formed during spot welding of a TSM 75 nickel-based single crystal has been analysed by Barabash *et al.* [2004Bar]. The dislocation structure was studied using polychromatic microbeam synchrotron diffraction, together with electron microscopy. The welding experiments were carried out on the end of a single crystal

rod that was 60mm long and 13mm in diameter. The initial single crystal had a dendritic microstructure as a result of its original casting. The welding arc was on for 17s and then it was switched off immediately so that the samples were rapidly cooled.

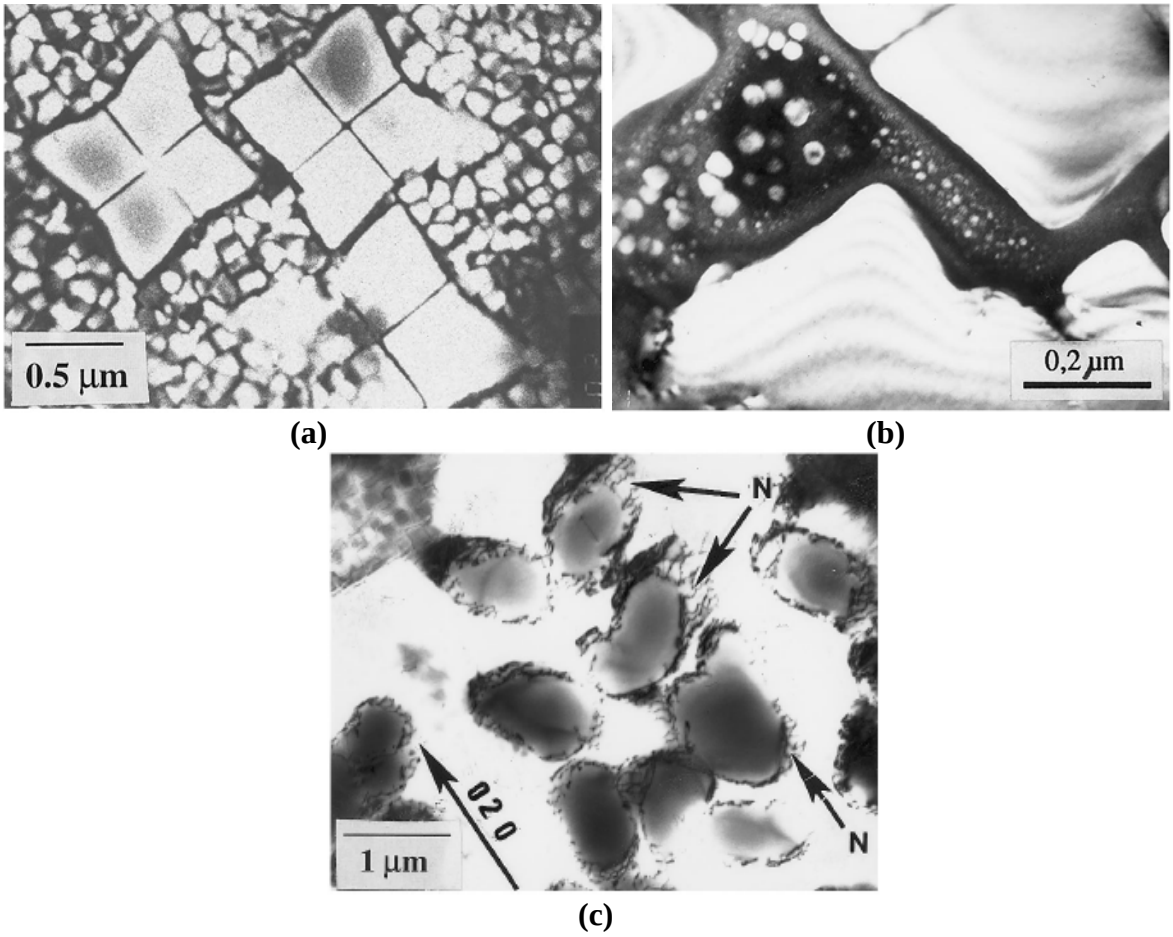


Figure 2.8. Bright field TEM images showing (a) γ′ precipitates in a γ matrix after a two-step heat treatment, (b) γ′ precipitates in a γ matrix after heat treatment at 1240˚C for 80 minutes, and (c) dislocations at the γ/γ′ interfaces after after heat treatment at 1240˚C for 40 minutes [1998Gro].

The microstructure of the single crystal base material, far from the HAZ is shown in Figure 2.9(a) [2004Bar], and is typical of NBSAs after thermal treatment. It had cuboid particles of γ′ evenly distributed in the γ matrix. The average size of the particles was 650nm and their volume fraction was 74%. The microstructure of the HAZ (Figure 2.9(b)) differed from the base material structure (Figure 2.9(a)). Only approximate positions of the regions in the HAZ were specified since their exact position relative to the fusion line could not be determined in the TEM samples. Material closer to the fusion line experienced higher temperatures during welding, promoting more dissolution of large primary γ′ phase particles in Figure 2.9(c) than

Figure 2.9(a). The bimodal nature of γ′ particles observed in Figure 2.9(b) was interpreted as follows [2004Bar]. During heating to high temperatures, the primary γ′ particles dissolved, which led to increased activity of dislocations along the {111} planes in the γ′ phase as the sample cooled from high temperature. These mobile dislocations interacted with each other to form a stack of dislocations. With further cooling, the second wave of γ′ precipitates formed, which led to the bimodal distribution of γ′ in the final microstructure interspersed with dislocation networks. Close to the fusion line, γ′ phase particles dissolved completely, leaving only small secondary γ′ phase particles (Figure 2.9(d)). In the regions more distant from the fusion line, but still within the HAZ, the volume fraction of large particles was ~66% by volume (Figure 2.9(b)). The dislocation structure in the HAZ also changed significantly. In the base material, dislocations were absent (Figure 2.9(a)), while dislocations were present in the HAZ. Their density was minimal far from the fusion line and increased closer to it (Figures 2.9(b), 2.10(b), and 2.10(c)), reaching a maximum next to the fusion line (Figure 2.9(d)). The maximum number of dislocations was observed in the matrix of the single crystal between the large γ′ phase particles and near the γ/γ′ interface boundary (Figure 2.10(a)).

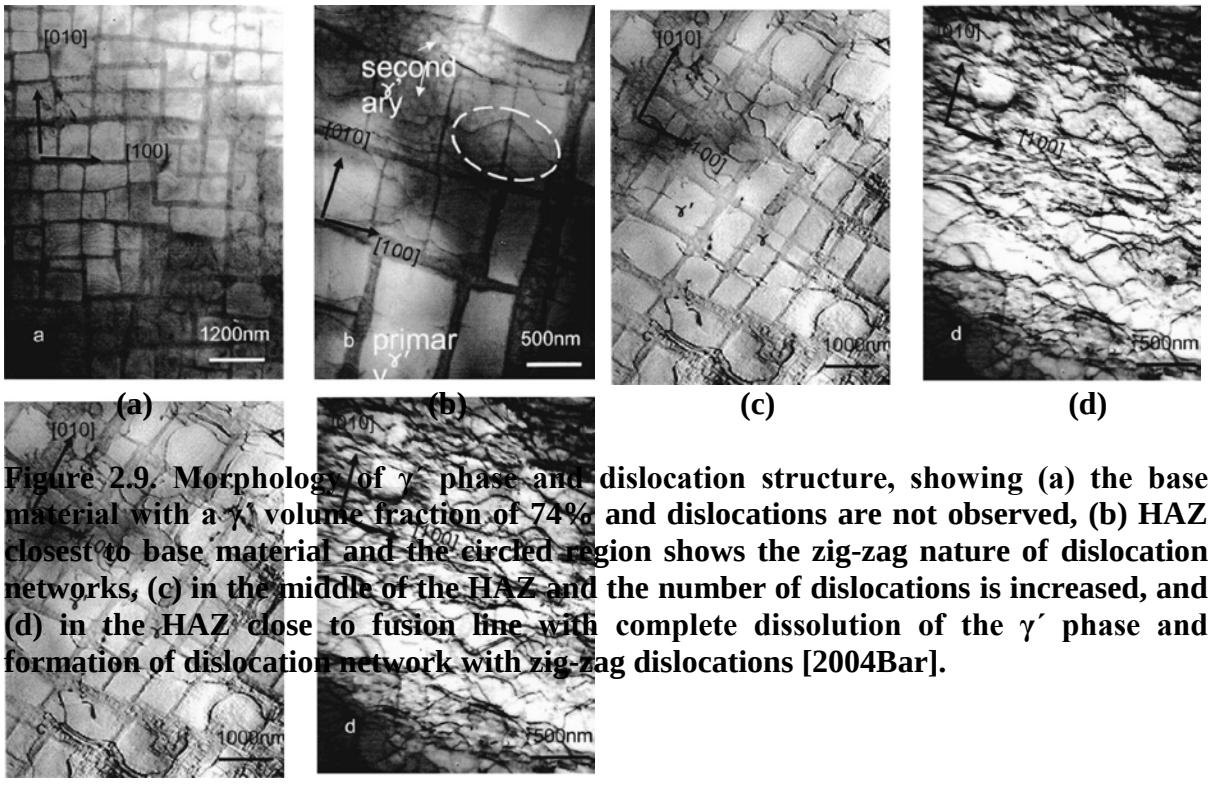


Figure 2.9. Morphology of γ′ phase and dislocation structure, showing (a) the base material with a γ′ volume fraction of 74% and dislocations are not observed, (b) HAZ closest to base material and the circled region shows the zig-zag nature of dislocation networks, (c) in the middle of the HAZ and the number of dislocations is increased, and (d) in the HAZ close to fusion line with complete dissolution of the γ′ phase and formation of dislocation network with zig-zag dislocations [2004Bar].

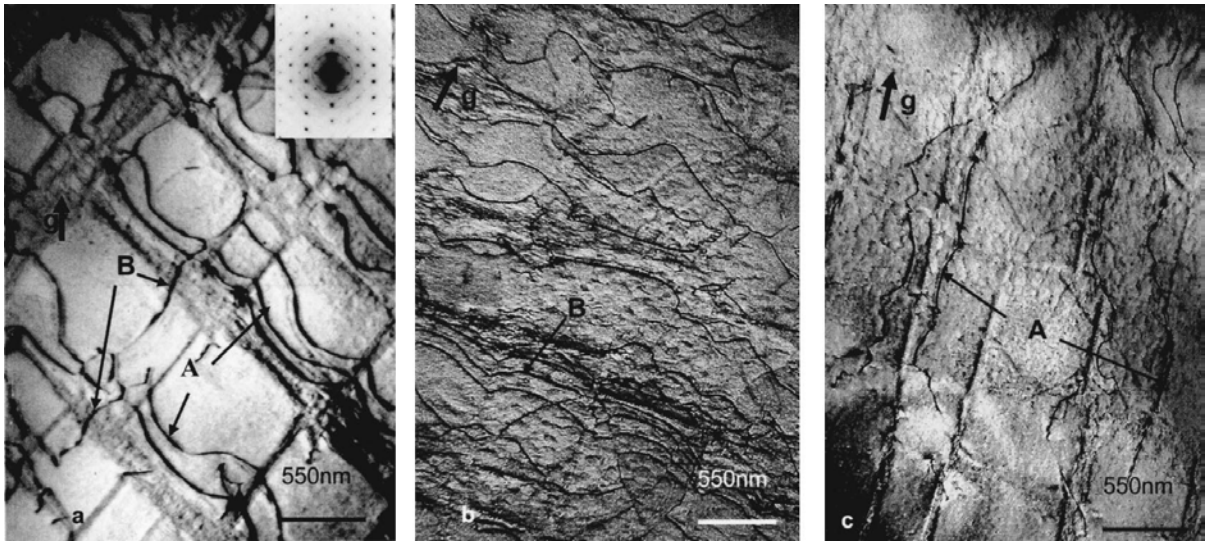


Figure 2.10. Dislocation structure within the HAZ of the TSM 75 single crystal, close to the fusion line, (a) dislocation distribution along the γ/γ´ boundaries, both A (edge) and B (screw) type dislocation sets are visible, where A is zig-zag dislocations along the average direction [100] with Burgers vector parallel to b = [101]; (B) zig-zag dislocations along the average direction [010] with Burgers vector parallel to b = [011], (b) dislocation network in the γ matrix formed by screw-type dislocations, and (c) dislocation network in the γ matrix formed by two edge-type dislocations [2004Bar].

2.3.6 Nanoindentation and Nanomechanical Properties of Ni-based Superalloys

This section of the literature review summarises work that has been done on nanoindentation of Ni-based superalloys and the technique used which is relevant to the current research work.

For an improved insight into the mechanical behaviour of materials with a structure below the micrometre scale, the knowledge of local mechanical properties is an important step forward. Since it is difficult to machine tensile samples of a small size from macroscopic samples, other methods have been considered [1956Mot, 1984Bla]. One such technique is nanoindentation. A commercially-available solution for implementing these experiments is to mount a nanoindentation device on the scanner head of an atomic force microscope (AFM), where imaging and indenting are performed by the same tip. This technique has been already applied to several materials [1992Oli, 1999Gök, 2004Dur]. Its application is especially promising for precipitate-hardened materials with a precipitate diameter/width below 1µm, e.g. for Ni-based alloys [1999Gök, 2004Dur].

For the first time, Göken and Kempf [1999Gök] determined the hardness and elastic modulus separately for the γ matrix and γ′ precipitates directly on the superalloys CMSX-6 and Waspalloy. All specimens were prepared by standard metallographic preparation techniques. First, they were ground on SiC papers and polished with a diamond paste. After that, electropolishing was done in a solution of acetic acid and ammonium sulphide, and γ was etched more. Very small height differences (nanometres) between the phases in combination with very smooth specimen surfaces were responsible for the high contrast achieved in the AFM images. Low roughness values were obtained after electropolishing, but since electropolishing etched the matrix phase more strongly than the γ′-phase, the roughness of both phases were also different [1999Gök].

The nanoindentation measurements were performed with an add-on force transducer from Hysitron Inc. coupled with a Berkovich tip. This transducer, mounted on a conventional AFM, controlled the z-movement of the tip and measured the indentation force [1999Gök]. Load-displacement curves were evaluated using the method of Oliver and Pharr [1992Oli] and the hardness, *H*, was determined from the actual contact area. The modulus of elasticity, *E*, was calculated from a reduced modulus, which was determined from the elastic contact stiffness. Extensive nanoindentation tests were performed to study the different mechanical properties of the γ′ and γ phases. The precipitate hardness was found to be higher than the matrix, and both decreased with increasing indentation depth. Figure 2.11 [1999Gök] shows the corresponding load-displacement plots for the indentations in the precipitates and matrix, and Figure 2.12 [1999Gök] shows the depth dependence of hardness for CMSX-6 and Waspaloy measured by nanoindentation tests on the γ′ and γ phases. The modulus of elasticity for CMSX-6 and Waspaloy for both phases differed only slightly (Figure 2.13) [1999Gök]. No systematic change of the modulus was observed with decreasing indentation depth [1999Gök].

The effect of the annealing time and therefore the size of the precipitates on Ni-based superalloys was investigated by Schöberl *et al.* [2003Sch2]. Two ternary NBSAs (single crystal) with differing chemical compositions were used. From the known equilibrium phase diagram of these alloys [1984Mir], the two alloys, R1 and R2, were chosen to lie on the same tie-line (9.6 wt% Al, 0.9 wt% Mo, Ni balance for R1, and 6.6 wt% Al, 1.9 wt% Mo, Ni balance for R2). The materials were in the form of rods with the <100> direction parallel to the length of the rods. The alloys were first homogenized in high-purity argon for 48h at

1310°C, which was above the solvus temperatures for both alloys (1300°C for R1 and 1020°C for R2), followed by water-quenching. Discs were cut perpendicular to the rod axis and annealed under flowing argon at 950°C, which was below the solvus temperatures for both alloys [1984Mir]. After annealing for 10, 40 and 120h, the specimens were removed from the furnace and air-cooled to room temperature. They were then ground and polished with 1µm diamond paste to a mirror finish.

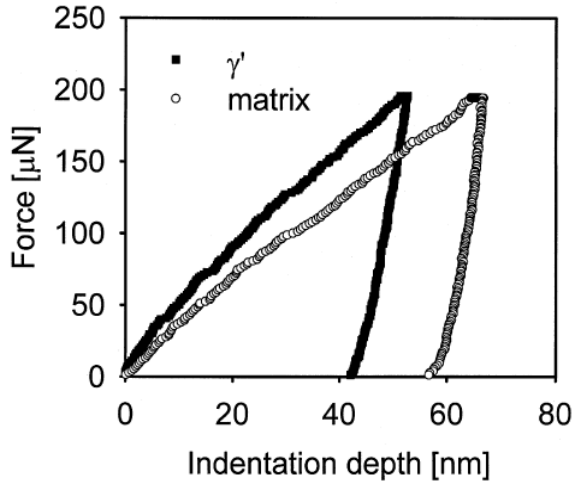


Figure 2.11. Typical load-displacement curves obtained for the γ´ and γ phases of CMSX-6 [1999Gök].

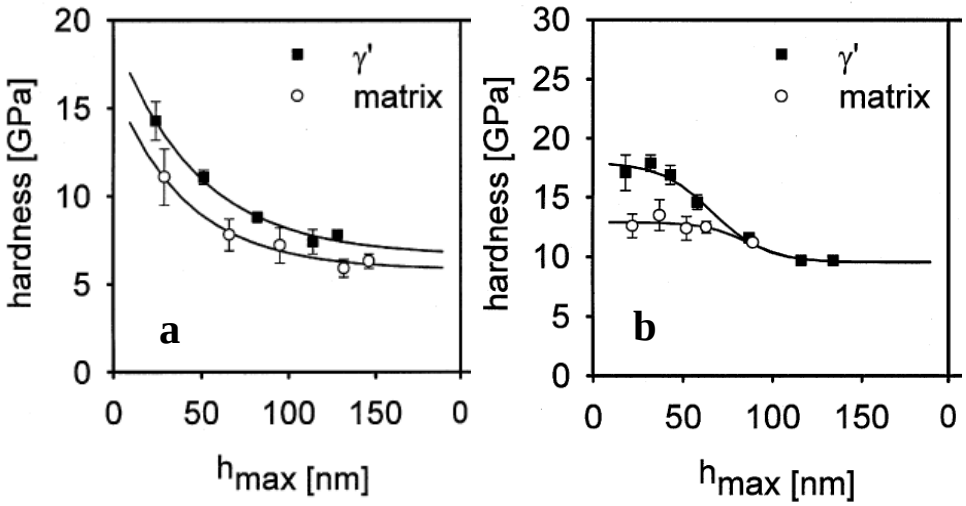


Figure 2.12. Relationship between indentation depth and hardness for: (a) CMSX-6, and (b) Waspaloy [1999Gök].

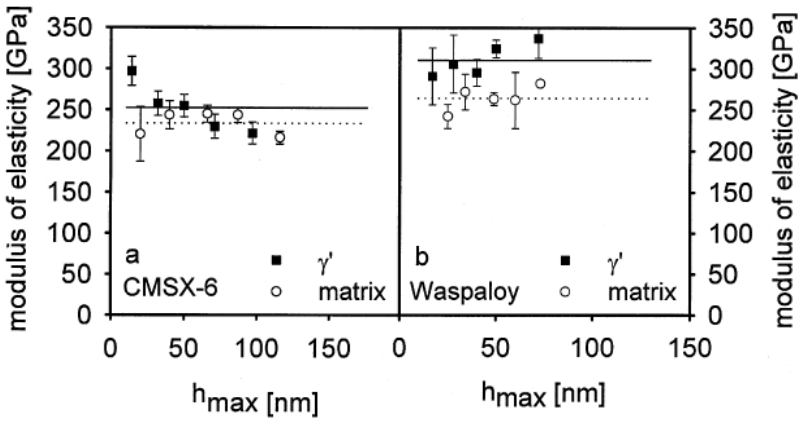


Figure 2.13. Relationship of the γ´ and γ moduli of elasticity with indentation depth for: (a) CMSX-6, and (b) Waspaloy [1999Gök].

The nanohardness results are given in Figure 2.14 [2003Sch2] for the γ´ precipitates and γ matrix. Each datum point represents the average values of indentation depth, *h*, and hardness, *H*, from 15 indentations with the same maximum load. Generally, the hardness was higher (up to 45%) for the γ´ precipitate regions (Figure 2.14(a)) than the γ matrix (Figure 2.14(d)) and decreased with increasing indentation depth in both phases. In the precipitates, the hardness values coincided, within experimental error, for both alloys and showed no dependence on annealing time, composition and precipitate size. Only on sample R2 after 10 hours anneal at the largest indentation depth of ~85nm (marked by an arrow) was a deviation found, the hardness being slightly lower than that of the other three samples. This was explained by the precipitates being too small in R2-10h, and at the largest indentation depth, the indentation was below the precipitate region, and so was influenced by the surrounding matrix (Figure 2.14(b) [2003Sch2]).

The depth dependence of the γ hardness is shown in Figure 2.14(d) [2003Sch2]. The γ hardness showed a strong dependence on alloy composition and annealing time for R1. For the precipitate-rich R1 (Figure 2.14(d)), hardness was usually higher by ~1GPa for shorter annealing times (10h) compared to longer annealing times (120h) (Figure 2.14(a)) [2003Sch2]. The main reason for this behaviour was the high concentration of γ´ precipitates, together with secondary precipitates that were present in R1-10h compared to R1-120h. Thus, the matrix channels in R1-10h were too narrow for measurement and the indentations were also on very fine secondary precipitates, resulting in a higher hardness (Figure 2.14(c)) [2003Sch2]. For the matrix-rich R2 alloy, there was no significant dependence of hardness on annealing time. However, the R2 matrix hardness at 120h was higher than the R1 matrix hardness at 120h.

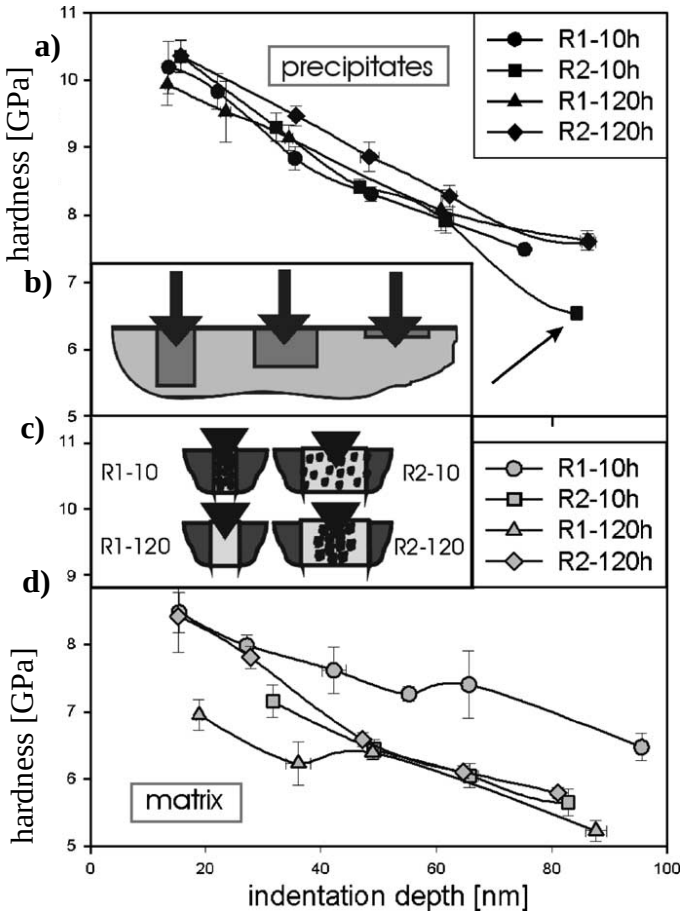


Figure 2.14. Hardness of Alloys R1 and R2 for different annealing times (10h and 120h) and possible indentation positions on γ´ and γ: (a) hardness as a function of indentation depth for γ´, (b,c) schematic diagrams showing possible positions of the final indentation on the γ´ and γ, and (d) hardness as a function of indentation depth for γ [2003Sch2].

The elastic modulus as a function of indentation depth is shown Figure 2.15 [2003Sch2] in terms of the reduced modulus E_r, which were derived from the Oliver–Pharr method [1992Oli]. E_r was slightly lower than the true modulus of the sample under consideration, since the stiffness of the diamond tip affects the mechanical properties, and the higher stiffness of the diamond tip than the sample adds (to a moderate extent) to the total compliance of the whole mechanical contact. The true modulus of the sample takes into consideration that the stiffness of the diamond tip is much higher than that of the sample, and so the tip could indent the sample much deeper, while in the reduced elastic modulus, this effect is not taken into account. The relationship between reduced modulus, elastic modulus and the Poisson's ratios of the tip and the sample material has been given severally [1992Oli, 1999Gök]. Within experimental error, the reduced modulus of γ´ was between 142 and 158GPa and did not depend on the indentation depth, annealing time and alloy composition. The average values for the matrix were slightly lower, by 4–10GPa.

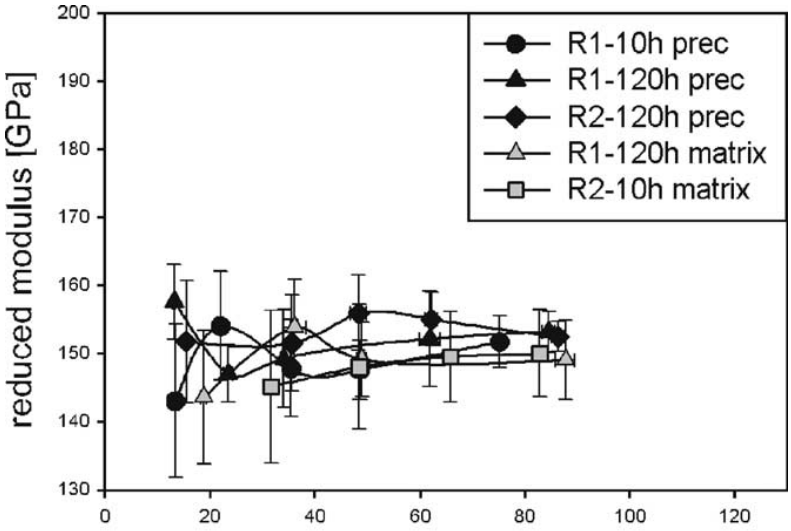


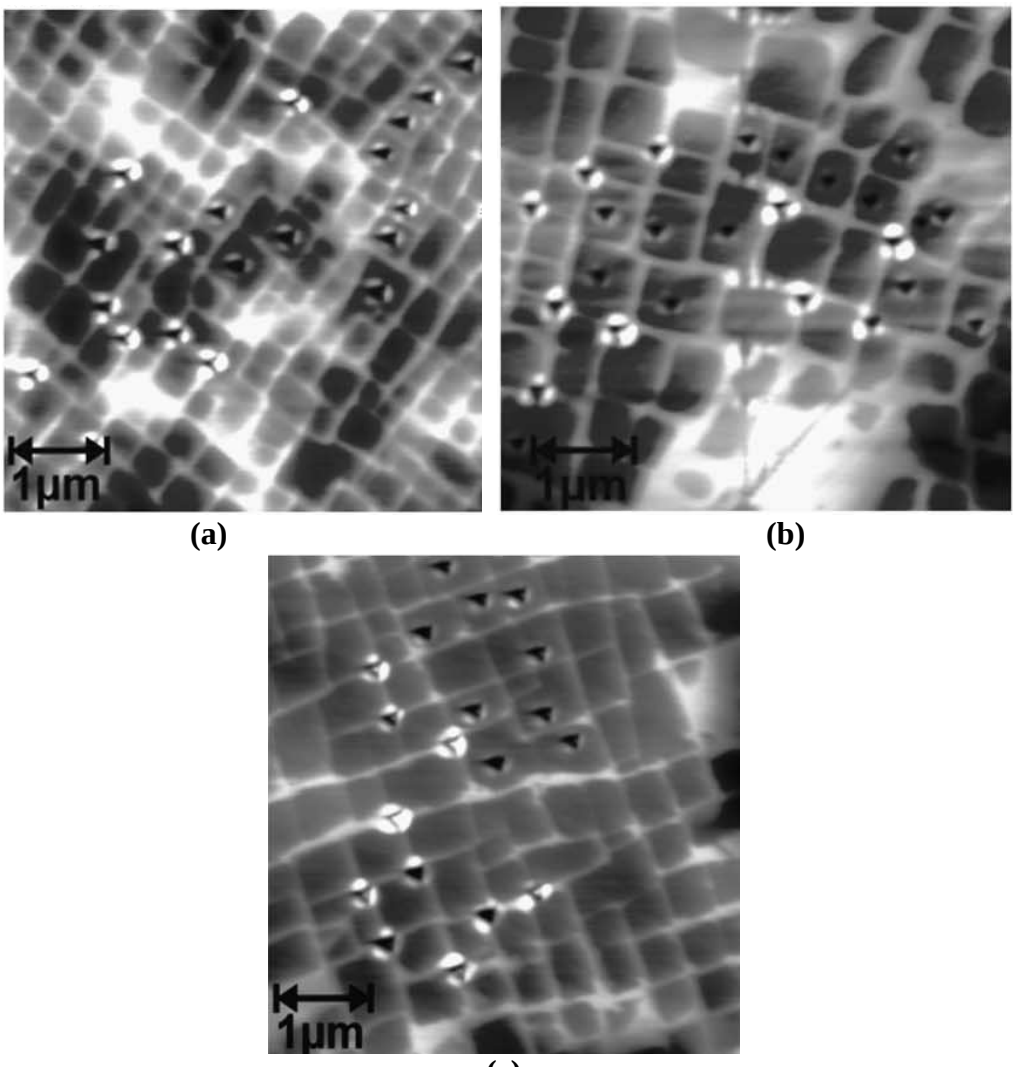
Figure 2.15. Reduced modulus of γ´ precipitates (prec) and γ matrix (matrix) as a function of indentation depth for Alloys R1 and R2 for different annealing times [2003Sch2].

Nanoindentation experiments were carried out by Wöllmer *et al.* [2003Wöl] to determine the nanohardness of small precipitates in a single crystal NBSA, PWA 1484, at a load of 0.5mN. An AFM combined with a nanoindentation system from Hysitron Inc. was used. Indenting and imaging was carried out by a Berkovich shaped diamond tip. The load-displacement curves were evaluated with the Oliver and Pharr method. The nanohardness of the PWA 1484 was measured as 11.9GPa for the γ´ precipitates, and 9.8GPa for the matrix, similar to the values for the R1 and R2 alloys studied by Schultz *et al.* [2003Sch2].

Durst and Göken [2004Dur] investigated three commercial single crystal NBSAs, CMSX-6, CMSX-4 and CMSX-10, which contained varying amounts of rhenium and tungsten. The micro-mechanical properties, such as hardness and modulus of elasticity of the individual phases, were tested in a nanoindentation AFM and the influence of the Re concentration on the hardness and modulus of elasticity was investigated. Standard metallographic preparation techniques for AFM studies often make use of electrolytic polishing to prepare a smooth surface with a small height difference between different phases in alloys [1999Gök, 2001Dur]. In this study, a different, well-known chemical-mechanical polishing with a nanodispersed SiO_2 suspension was used [2004Dur]. The local roughness after electrolytical polishing was found to be in the same range as after chemical-mechanical polishing with a nanodispersed SiO_2 suspension. Figure 2.16 [2004Dur] shows AFM images of CMSX-6,

CMSX-4 and CMSX-10 with nanoindentations performed using a Berkovich tip on the γ and γ´ phases.

The microstructure of CMSX-10 showed relatively small precipitates and a γ channel thickness of about 100nm [2004Dur]. In CMSX-4, the precipitates were larger, and the matrix channel width was slightly wider than for CMSX-10. CMSX-6 had smaller precipitates and a channel width of about 160nm. At a maximum applied indentation load (P_{max}) of 250μN, a maximum indentation depth of ~50nm in the precipitates, and ~80nm in the matrix was reached. The mechanical properties were calculated from the load–displacement curves recorded during indentation [1990Jos, 1992Oli, 2004Dur].



(a) **(b)**

(c)

Figure 2.16. Microstructures of different alloys with nanoindentations in the γ and γ´ phases, where the indentations were performed at the maximum applied load of 250 μN: (a) CMSX-6, (b) CMSX-4, and (c) CMSX-10 [2004Dur].

Figure 2.17 shows the hardness of the γ and γ´ phases of the investigated alloys [2004Dur]. Each datum point was an average of at least 10 indentations in each phase. The difference in the mechanical properties of both phases was more pronounced than in the work of Göken *et al*. [1999Gök], especially for the hardness of the matrix. CMSX-10 had the highest matrix hardness, followed by CMSX-4 and CMSX-6. The hardness difference was even more evident in the γ´/γ hardness ratio, since the γ´ precipitates had nearly the same hardness. In order to understand the difference in the matrix hardness, phase size effects and the chemical composition were investigated. The thicknesses of the matrix channels in CMSX-10 and CMSX-4 were fairly similar, thus the influence of the surrounding γ´ phase on the matrix hardness was thought to be about the same in CMSX-10 and CMSX-4 alloys. It was therefore concluded that the measured hardness increase of the three alloys (CMSX-4, CMSX-6 and CMSX-10) was due to the chemical composition differences, i.e. the higher content of refractory elements (Figure 2.17) [2004Dur].

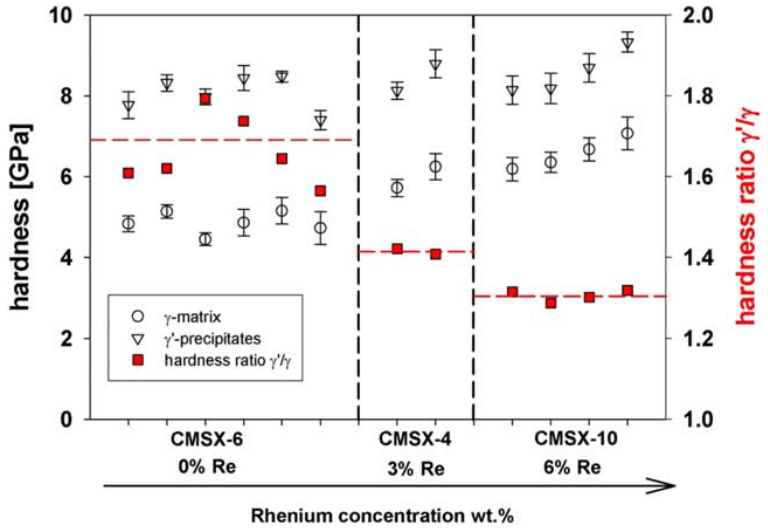


Figure 2.17. Hardness and hardness ratio of γ´ and γ phases in CMSX-6, CMSX-4 and CMSX-10 [2004Dur].

Durst *et al*. [2004Dur] concluded that the hardness could be measured as a function of the chemical composition in phases as small as 100nm. The hardness ratio of γ´/γ ranged from 1.31 for CMSX-10 to 1.41 for CMSX-4 and 1.67 for CMSX-6. The modulus of elasticity increased with the concentration of refractory elements (Figure 2.18) [2004Dur]. The analysis of the load–displacement curves gave a ratio of $E_{\gamma'}/E_{\gamma}$ as 1.10 for CMSX-10, 1.12 for CMSX-4, and 1.19 for CMSX-6. CMSX-10 exhibited a slightly higher matrix modulus, whereas the matrix modulus was smaller for CMSX-6 [2004Dur]. The cross in Figure 2.18 indicates the

modulus ratio determined by a Hertzian fit, due to a discontinuity (pop-in effect) found in the load-displacement curve during loading (Figure 2.19) [2004Dur]. This pop-in effect is related to the nucleation of dislocations on carefully prepared smooth sample surfaces [1992Pag]. The load-displacement curve shows the different elastic properties of the two phases, with the γ´ showing a lower indentation depth than γ [2004Dur].

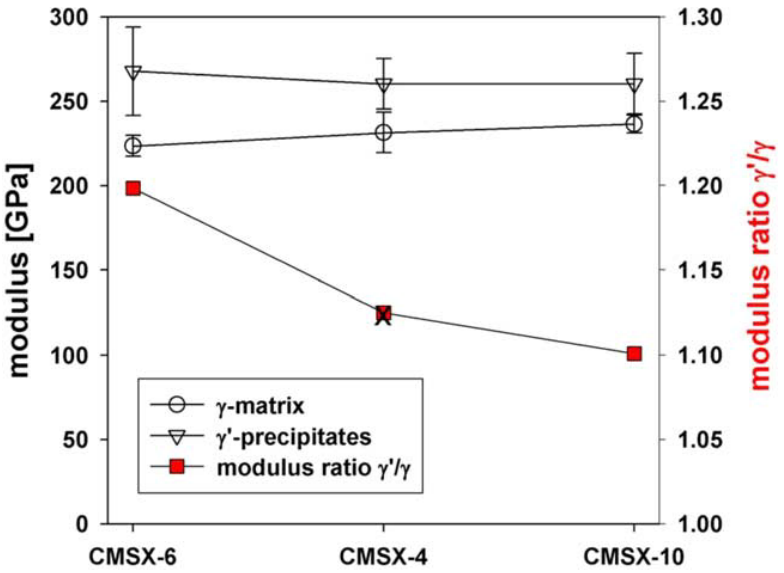


Figure 2.18. Modulus of elasticity of γ´/ γ phases in CMSX-6, CMSX-4 and CMSX-10 determined by the standard Oliver/Pharr method, where the cross on the lower curve indicates the modulus ratio determined by a Hertzian fit (Figure 2.19) [2004Dur].

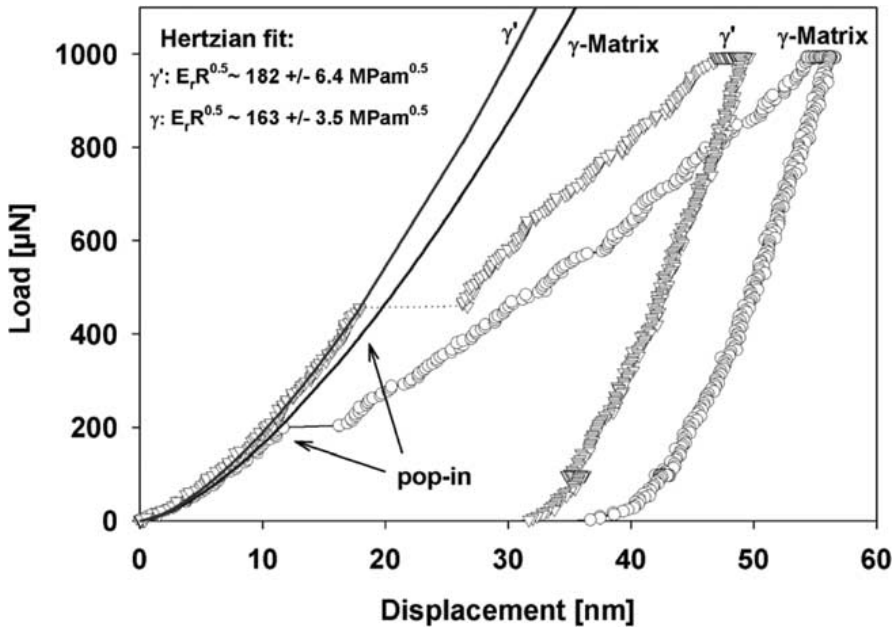


Figure 2.19. Load–displacement curves in CMSX-4 measured with a Berkovich-tip in γ matrix and γ´ precipitates, with the Hertzian fit [2004Dur].

2.4 Overview of the Search of a New Generation of Superalloys

The attributes that make intermetallic compounds desirable materials for high-temperature structural applications have been widely reported [1995Wes, 1996Yam, 1997Dur, 1997Wil, 2000Fai1, 2000Fai2]. These attributes are good diffusional creep resistance, high-temperature strength, high melting points, good oxidation resistance and low densities for performance in service regimes in which the nickel-based superalloys cannot operate. Unfortunately, the low tolerance of intermetallic compounds to defects makes them unsuitable for application in critical components. Engineering design and alloy development therefore have to address the competing requirements for high-temperature strength and ambient-temperature toughness. This has led to the interest in multi-phase systems which bring together these apparently contradictory attributes. Three such approaches have been under investigation [2000Wol]:

(1) Analogous γ/γ' systems with much higher melting points, based on $L1_2$ precipitates in a fcc matrix.

(2) Analogous precipitation-strengthened systems based on a bcc structure contained within a ductile bcc matrix (or β/β').

(3) *In situ* composite microstructures, which exploit 'ductile phase toughening'.

In the first instance, the success of the Ni-based superalloys has led to succeeding generations of high-temperature alloys that make use of the principles of a high volume fraction of finely-dispersed, coherent precipitates within a ductile matrix [1987Sim, 2006Ree]. Analogous γ/γ' systems with much higher melting points, based on $L1_2$ precipitates (ordered fcc) in a fcc matrix (the matrix usually has the higher melting point) are limited in number. Some of the platinum group metals are almost unique among the high-melting point metals in that they have fcc structures. Moreover, they have good environmental resistance that enables them to be considered for high-temperature use. Systems based on iridium, rhodium and platinum have attracted attention that has led to the suggestion that they form a class of alloys to be named 'refractory alloys' by Yamabe-Mitarai *et al.* [1997Yam1]. (This terminology is something of a misnomer since refractory metals are normally associated with strong affinities for oxygen, whereas most of the platinum metals are relatively noble in this respect [2000Wol].) The general accepted definition of refractory metals is metals that are resistant to heat and wear and belong to Groups IV, V, VI and VII [1981Oto].

Secondly, analogous precipitation-strengthened systems have similarly been proposed for the bcc metals, in this case with an ordered bcc structure contained within a ductile bcc matrix (or β/β'). Among the most oxidation-resistant materials are ferritic alloys based on iron-chromium-aluminium (Fe-Cr-Al), typically with compositions around 20 wt% Cr and 5 wt% Al (balance Fe) which are necessary for the formation of Al_2O_3 and Cr_2O_3. Various attempts at alloying have been made to induce the precipitation of coherent precipitates in these systems, and one study examined alloying with ruthenium to enhance not only the strength, but also the oxidation and corrosion resistance of these alloys [1999Ngw].

Thirdly, there are the so-called *in-situ* composite microstructures, which exploit 'ductile phase toughening'. Methods to produce ductile phase toughening stem from the recognition that 'ductile' secondary phases contribute not only towards deflecting crack propagation in the usual way, but also to strengthening (by acting as obstacles to dislocation motion at the phase interfaces). In particular, eutectic systems lend themselves to exploitation of inherently compatible phases in a finely divided mixture, and are natural candidates for structural intermetallic composites. Some eutectic systems, based on Ru-Nb, Ru-Al-Ni, Ir-Nb [1996Wol], Ru-Al and Ir-Al, Ru-Al-Ir [1999Hil] have been examined. The systems are unusual because although the ductilities of elemental Ru and Ir are low, some of the phases are ductile [2000Wol].

Other potential alloys systems for high temperature applications include Mo-Si-B alloys and ceramics. High melting-point (>2000ºC) materials, based on refractory metals such as molybdenum, represent a higher-temperature alternative, but suffer from oxidation and creep. In this regard, molybdenum silicides and borosilicides have shown promise in improving the oxidation and creep resistance [1996Mey1, 1996Mey2, 1999Akin], leading to the development of two specific Mo–Si–B alloy systems by Meyer and co-workers [1996Mey1, 1996Mey2, 1999Akin, 1999Mey] and Berczik [1997Ber1, 1997Ber2]. However, the silicide intermetallic compounds are hard and brittle, providing little fracture resistance for most structural applications without significant additional toughening. Alloys with the α-Mo particles surrounded by the Mo_3Si and Mo_5SiB_2 (T2) intermetallic phases, showed small improvements in toughness. One promising approach would be to design Mo–Si–B alloys where the intermetallic phases are completely surrounded by a continuous α-Mo matrix; higher toughness would be expected since incipient cracks would be forced to interact with the locally tougher α-Mo. A powder processing route was developed to produce such alloys

[2002Sch]. Studies have been undertaken [2014Hwa] to further improve the properties (e.g. toughness and oxidation) of Mo-Si-B alloys using mechano-chemical processes to control the microstructure [2014Hwa]. To produce nano-sized Mo (<200nm), the process used starting powders of MoO_3, Si_3N_4 and BN, ball-milling for mechanical mixing and refinement, with continuous heat treatment under a hydrogen atmosphere. Finally, intermetallic powders of Mo_5SiB_2, Mo_3Si and small amounts of α-Mo were manufactured with particle sizes up to 3μm.

Other systems that possess potential for high temperature applications are ceramics. Many monolithic ceramic materials have good strength and excellent oxidation resistance [2003Zha], but are prone to brittleness. Their inherent brittleness poses a significant challenge in withstanding the rigors of assembly and the impact damage caused by foreign objects that may pass through the engines in operation, and other high temperature applications that involve moving parts [2003Zha].

2.5 Platinum-based Superalloys

2.5.1 Introduction

Since many engineering processes are run at high temperatures (e.g. glass industry) or in aggressive chemical environments, there is a need for materials that can withstand extreme thermal, mechanical and chemical conditions in these applications, such as aircraft gas turbine engines [1988Wha]. Platinum-based alloys are recognized for their high melting points, thermal stability and thermal shock resistance, as well as good corrosion and oxidation resistance, e.g. nozzles to bring satellites into orbit from the carrier rocket or for nozzles to make trajectory correction [1988Wha]. Another important field of application for platinum alloys as structural materials lies in the glass industry [1988Wha]. High melting glasses and high-quality glass fibres require the use of platinum-tank furnaces, stirrers and feeders. For these applications, the good electrical and thermal conductivity of Pt are utilised. In terms of mechanical properties, Pt-based alloys are fcc and so combine high ductility with high creep strength. This combination of properties has led Pt-based alloys to be widely used in the chemical, space technology and glass industries [1988Wha, 1990Lup, 2001Fis1].

A promising approach for a strong Pt-based alloy is to mimic the microstructure of Ni-based superalloys. Hill and co-workers [2001Hil1, 2002Hil] conducted an extensive assessment of systems with Pt as major constituent based on these criteria: high temperature phase stability, high melting point, oxidation and hot corrosion resistance, and (if possible) low density. Alloys based on Pt-Al turned out to have the highest potential, not only because of possible precipitation strengthening through Pt_3Al, but also due to high oxidation resistance. However, in the Pt-Al system, the cubic $L1_2$ Pt_3Al phase that exists at high temperatures transforms to a tetragonal structure at lower temperatures [1986McA, 1986Mis]. Since such good properties exist with the $\gamma + \gamma'$ structure in Ni-based superalloys, alloying with additional elements was envisaged to stabilize the high temperature $L1_2$ structure of Pt_3Al [2001Hil1, 2002Hil, 2005Wen1]. Appropriate alloying and heat treatment of a so called "Pt-based superalloy" led to a fine distribution of a γ' phase with the $L1_2$ structure coherently embedded in the Pt-rich fcc γ matrix [2004Vor, 2005Hül, 2006Cor, 2009Cor1, 2009Cor2, 2009Sho1].

The University Bayreuth and the Fachhochschule Jena-University of Applied Sciences in Germany were already researching NBSAs in the 1990s [1994Gla, 2002Gla, 2004Vor]. However, the basis for their development programme on precipitation hardened Pt alloys was the ternary Pt-Al-X alloys being investigated in South Africa [2002Süs2]. The Pt_{86}:Al_{10}:Cr_4 (at.%) composition, with good properties, was the foundation for further work [2004Vor, 2005Wen1]. Nickel was added to a Pt-Al-Cr alloy in varying amounts [2005Hül], since nickel has a good solid-solution strengthening effect on the (Pt) matrix [2002Zha2], and also to decrease the Pt content, and thus the density and price of the Pt-based alloys. A very promising microstructure was found in the alloy Pt_{79}:Al_{11}:Cr_3:Ni_7 (at.%): a homogeneous distribution of $L1_2$ ordered ~Pt_3Al precipitates with widths of 200-500nm and volume fraction of 23%. Ageing for 120h at 1000°C gave a lattice misfit of about -0.1%, which is in the same range as commercial Ni-based superalloys. Based on these results, Pt-Al-Cr-Ni alloys with an increased Al content [2005Wen1], near the solubility limit of ~15 at.% Al [1987Oya], were made to increase the γ' volume fraction. Despite heat treatments being undertaken in flowing argon, there was 6 ppm by volume of residual oxygen, which was sufficient to form an oxide layer 10μm thick on the sample surfaces. Very fine γ' precipitates formed throughout the alloys from the supersaturated matrix during quenching after ageing, although much coarser γ' precipitates were found at a depth of 100μm beneath the surface oxide layer [2005Wen1]. Alloying the Pt-Al system with both Cr and Ni consistently

stabilised the $L1_2$ high temperature allotrope of Pt_3Al at room temperature. In alloys with less than 6 at.% nickel, precipitates lost coherency after ageing, resulting in spherical particles. Pt_{80}:Al_{11}:Cr_3:Ni_6 (at.%) had the highest γ′ volume fraction (~23%) after ageing, and well-aligned cuboid precipitates with 0.2–0.5μm widths and a misfit of -0.1%. The shape of γ′ was due to a decreasing absolute misfit with increasing Ni content. Ageing at 1100°C produced coarse γ′ particles and reduced the γ′ volume fraction.

2.5.2 Binary Pt-Al Phase Diagram and the Pt_3Al Phases

This section of the literature review gives an overview of structures in the Pt-based alloys: fcc for (Pt) and also the three different structures of Pt_3Al, namely cubic and two tetragonal Pt_3Al phases. This is necessary to understand the alloys.

2.5.2.1 Overview of the Pt-Al Phase Diagram

There are currently two conflicting phase diagrams: McAlister and Kahan [1986McA] (Figures 2.20 and 2.21) and Oya *et al.* [1987Oya] (Figure 2.22). The major differences, which are crucial in the development of Pt-based alloys using the ~Pt_3Al precipitates in a platinum solid solution, are the phase transformation temperature for cubic to tetragonal ~Pt_3Al, and the number and types of the ~Pt_3Al phases. The slope of the γ solvus is also important, because a more sloping solvus allows for more precipitation. The γ solvus is not very sloping in the phase diagram of McAlister and Kahan [1986McA], whereas it has a more beneficial slope in that due to Oya *et al.* [1987Oya].

McAlister and Kahan [1986McA] assessed the Pt-Al phase diagram given in Figure 2.20 from the thermal analysis data of Huch and Klemm [1964Huc], Darling *et al.* [1970Dar], Guex and Feschotte [1976Gue] and Schubert [1978Sch]. They reported a displacive transformation of the high-temperature cubic Pt_3Al γ′ to a tetragonal low temperature variant γ'_2 at 1280°C as shown in Figure 2.20 [1986McA]. However, Oya *et al.* [1987Oya] reported the transformation of cubic Pt_3Al to tetragonal Pt_3Al ($\gamma' \rightarrow \gamma'_2$) at 340°C, and an additional transformation $\gamma'_1 \rightarrow \gamma'_2$ ($DO_c \rightarrow DO'_c$) at 127°C as shown in Figure 2.22 [1987Oya].

Figure 2.21 [1986McA] shows that the binary Pt-Al phase diagram derived by McAlister and Kahan which agrees with data from other sources. Darling *et al.* [1970Dar] employed microprobe analyses, metallographic methods and X-ray lattice parameter measurements to determine the solvus of (Pt) over a wide range of temperatures. All data points of the liquidus and solidus of the terminal (Pt) solid solution were consistent with Huch and Klemm's results [1964Huc]. The results of Darling *et al.* [1970Dar] of the solvus of (Pt) were also consistent with the X-ray parameter studies of Schubert [1978Sch] and Schaller [1979Sch].

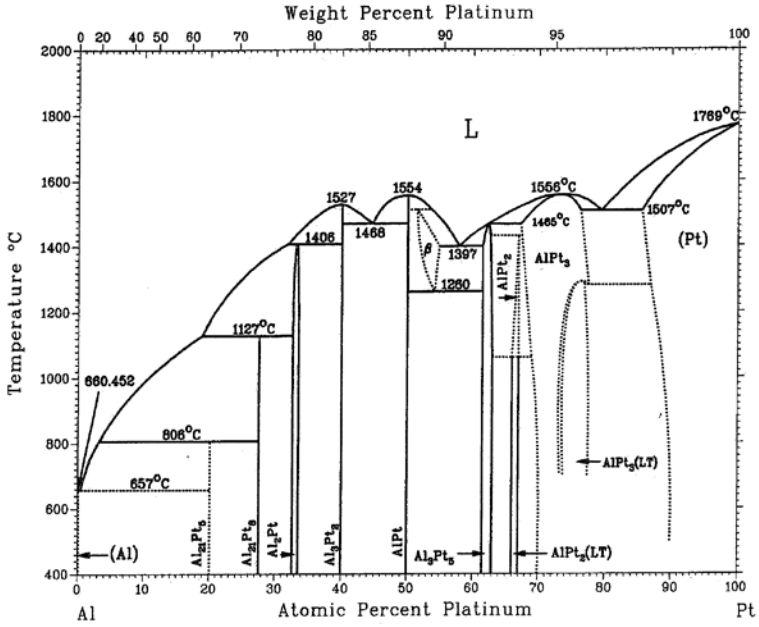


Figure 2.20. Pt-Al phase diagram [1986McA].

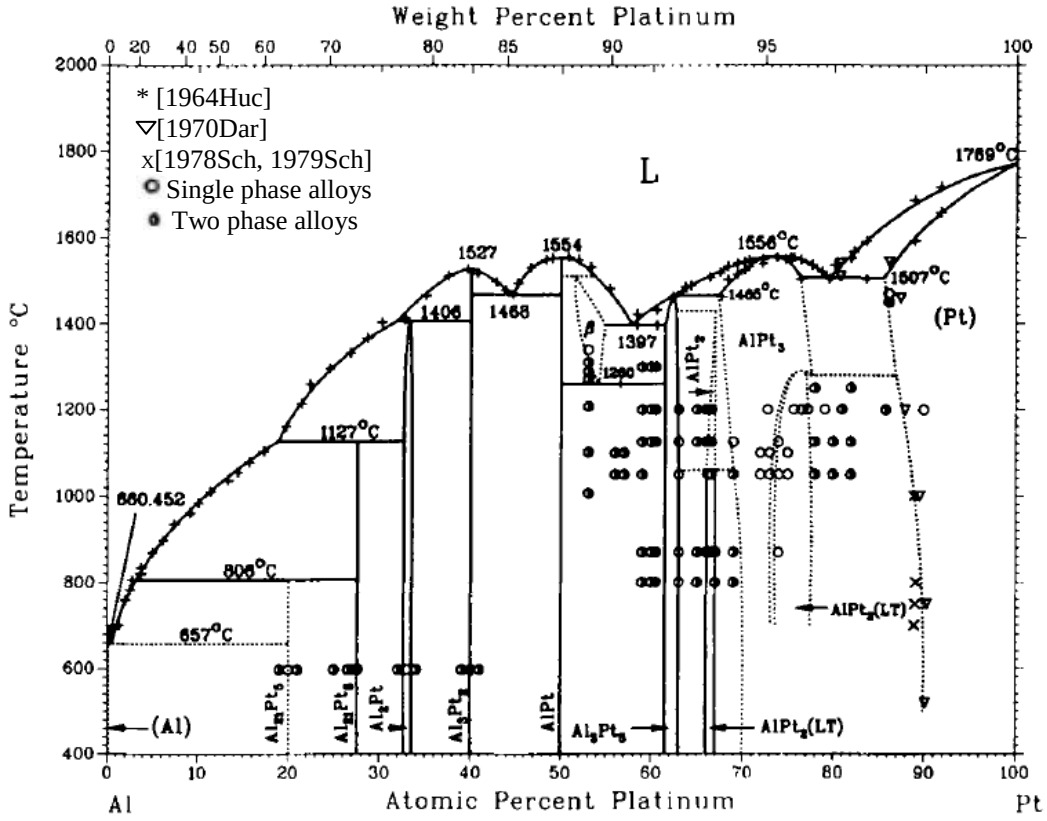


Figure 2.21. Pt-Al phase diagram showing the data from different sources [1986McA].

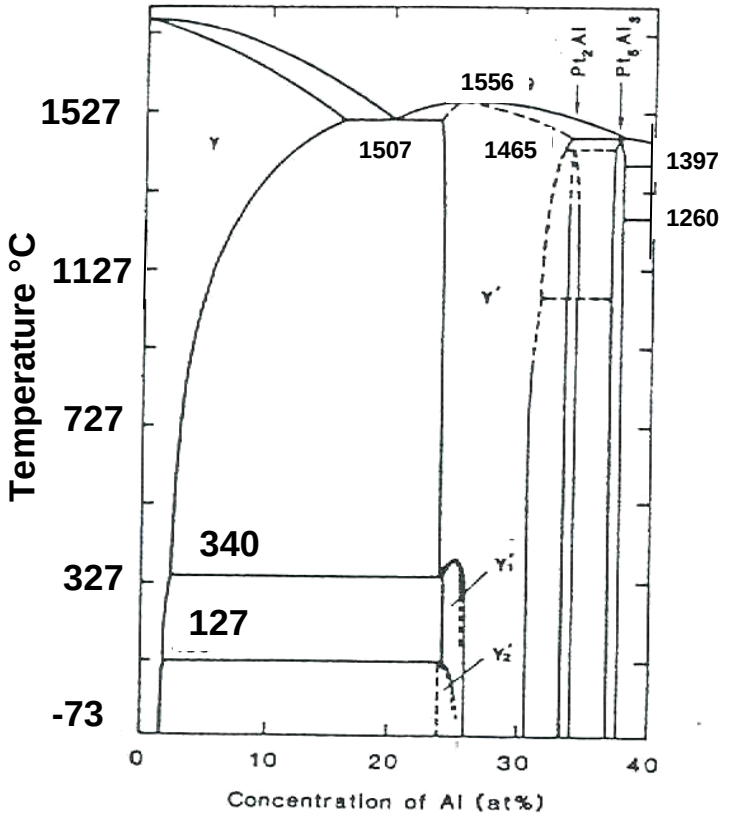


Figure 2.22. Partial Pt-Al phase diagram [1987Oya].

2.5.2.2 (Pt) Phase

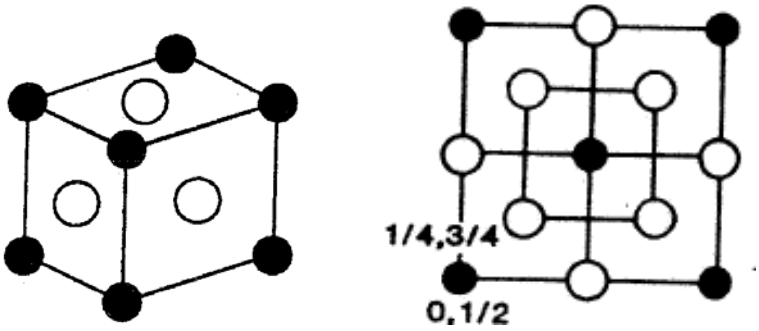
The (Pt) phase has been reported by McAlister and Kahan [1986McA] to have the simple disordered fcc structure. In (Pt), any given lattice point is occupied indifferently by either A (Pt) or B atoms that could be a solute (e.g. B = Cr or Ru) [1986McA].

2.5.2.3 Pt_3Al Phases

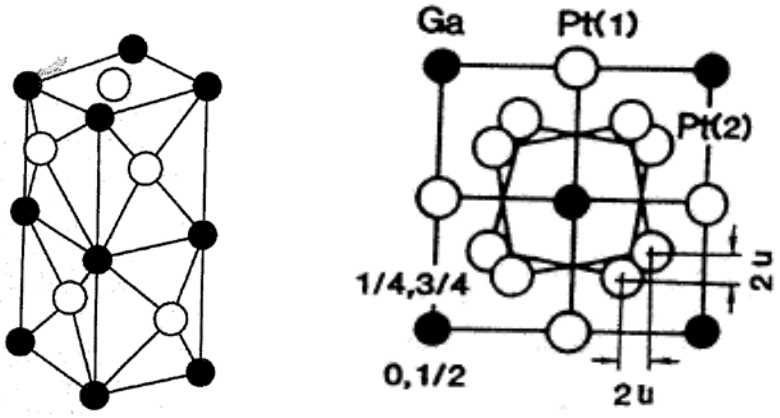
In the two conflicting phase diagrams of McAlister and Kahan [1986McA] (Figure 2.20) and Oya *et al.* [1987Oya] (Figure 2.22)), the major differences are the phase transformation temperatures for cubic to tetragonal Pt_3Al, the number and types of the Pt_3Al phases, and the shape of the γ solvus. McAlister and Kahan [1986McA] reported one transformation for the Pt_3Al phase: a high-temperature cubic Pt_3Al (γ′) to a tetragonal low-temperature variant (γ′$_1$) at 1280°C. However, Oya *et al.* [1987Oya] reported the transformation of cubic Pt_3Al to tetragonal Pt_3Al, γ′ → γ′$_1$ at 340°C, and an additional transformation γ′$_1$ → γ′$_2$ (DO_c → DO'_c) at 127°C. Figure 2.23 [1987Oya] shows the phase structures from the consecutive transformations γ′ → γ′$_1$ → γ′$_2$ ($L1_2$ → DO_c → DO'_c).

The high temperature cubic $L1_2$ Pt_3Al form has an ordered fcc structure of $AuCu_3$ type (a = 0.3876nm), with a space group of *Pm*3*m* (Table 2.2) [1962Bro, 1964Huc]. This cubic Pt_3Al phase has a solubility range of 67.3 at.% Pt to 77.7 at.% Pt [1962Bro, 1964Huc]. The $L1_2$ phase melts congruently at 1556°C [1964Huc, 1976Geu], and forms a eutectic at 1507°C with (Pt) [1986McA, 1987Oya].

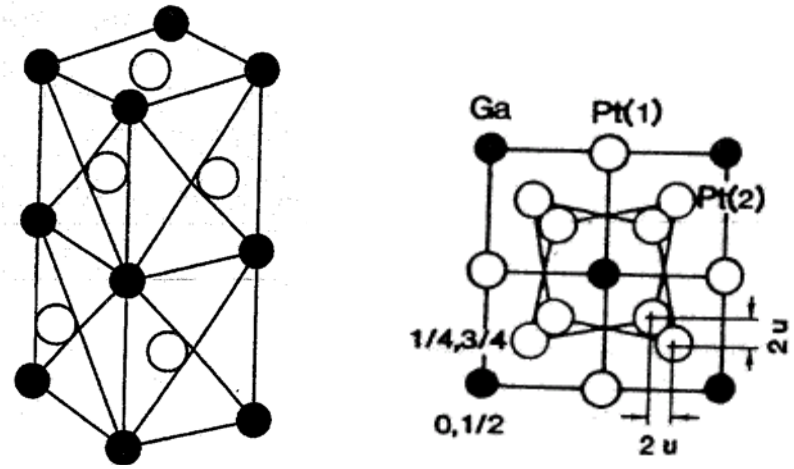
The lower temperature tetragonal Pt_3Al phase was reported to have a DO_c lattice (a = 0.5459nm, c = 0.7806nm), with a distorted fct structure the DO_c lattice (Figure 2.24), and a solubility range of 74 at.% Pt to 78 at.% Pt [1986McA]. A space group of *P*4*/mbm*, based on Pt_3Ga, was reported, although there is a resemblance to the space group of the I_4/mcm and prototype Ir_3Si, and the Pt_3Ga lattice was reported to be a more primitive lattice [1962Bro, 1975Cha, 1986McA]. Crystal structure and lattice parameter data for these phase interpretations from the different authors [1961Sta, 1962Bro, 1975Cha, 1987Oya] are summarised in Tables 2.2 and 2.3.



a) High temperature phase ($L1_2$ type).

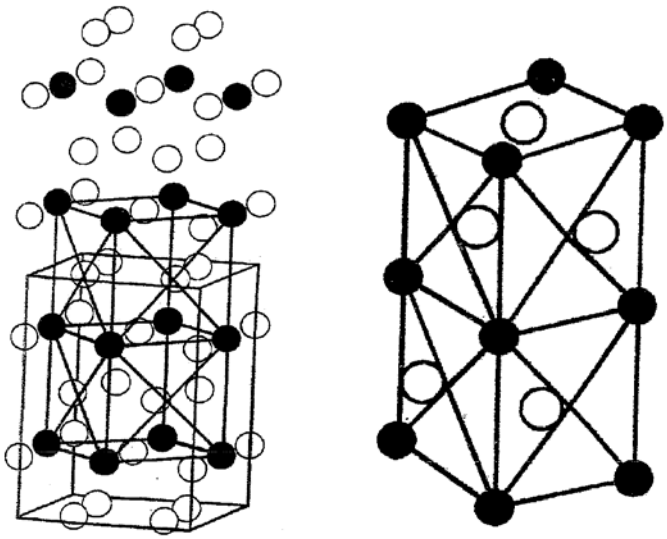


b) Intermediate temperature phase (DO_c type).



c) Lowest temperature phase (DO'_c type).

Figure 2.23. Crystal structures of Pt_3Al viewed along the <001> direction: (a) High temperature $L1_2$ phase, b) intermediate temperature DO_c phase and, (c) low temperature DO'_c phase [1987Oya].



(a) **(b)**

Figure 2.24. (a) DO'_c unit cell of the Pt_3Al tetragonal structure (low temperature), contains a distorted fct lattice, also shown in (b), where the Pt atoms (white) lie offset from the centre of the faces and the Al atoms (black) sit at the corners of the cell. (In (b) for clarity, only the Pt atoms on the top and front faces are shown.) [1987Oya].

Table 2.2. Crystal structure data for Pt_3Al variants [1961Sta, 1962Bro, 1975Cha, 1987Oya].

Unit cell geometry	Pearson symbol	Space group	Strukturbericht designation	Prototype	Reference
Cubic	*cP*4	*Pm*3*m*	$L1_2$	$AuCu_3$	[1962Bro]
Tetragonal	*tP*4	*P*4/*mmm*	$L6_0$	$CuTi_3$	[1961Sta]
Tetragonal	*TI*16	*I*4/*mcm*	DO_c, DO'_c	SiU_3	[1987Oya]
Tetragonal	*tP*16	*P*4/*mbm*	None	$Pt_3Ga(r)$	[1975Cha]

Table 2.3. Compositions and lattice parameters for Pt_3Al variants [1961Sta, 1962Bro, 1975Cha, 1987Oya].

Unit cell Geometry	Space Group	Composition (at.% Pt)	Lattice parameters (Å)		Reference
			a	***c***	
Cubic	*Pm*3*m*	72.8	3.876	-	[1962Bro]
Tetragonal	*P*4/*mmm*	Not available	3.83	3.89	[1961Sta]
Tetragonal	*I*4/*mcm*	~75	5.471	7.775	[1987Oya]
Tetragonal	*P*4/*mbm*	74	5.459	7.806	[1975Cha]

The DTA results of Oya *et al.* [1987Oya] showed that the γ'_1 intermediate phase is stable over a narrow composition range ($10<x<25$ at.% Al) and over a small temperature interval ($400°C<T<600°C$) as shown in Figure 2.25 [1987Oya].

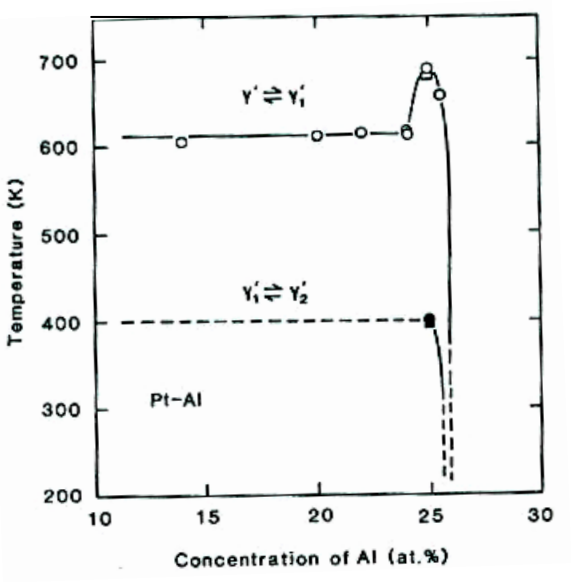


Figure 2.25. Composition dependence of the transformation temperatures of $\gamma' \rightarrow \gamma'_1$ and $\gamma'_1 \rightarrow \gamma'_2$ in Pt-Al alloys: circles were obtained by DTA and squares by dilatometry [1987Oya].

2.5.2.4 Recent Studies of the Pt-Al Phase Diagram at High Temperatures

A study of all relevant phases in the Pt-Al phase diagram was undertaken by Tshawe *et al.* [2006Tsh, 2008Tsh, 2008Cor] to clarify the phase boundaries of the phases: (Pt), Pt_3Al (all temperature versions), Pt_2Al (both phases), β and Pt_5Al_3, by use of high resolution SEM and XRD. The results of the Pt-rich side were found to be generally consistent with the Pt-Al phase diagram of McAlister and Kahan [1986McA], and disagreed with the phase diagram Oya *et al.* [1987Oya]. However, the work of Douglas *et al.* [2009Dou], identified the formation of the middle tetragonal Pt_3Al phase (DO_c) and agreed with the findings of Oya *et al.* [1987], as did Biggs [2001Big2]. However, the conditions for its formation have not been fully explained, and may depend on impurities [2009Dou] since separate research groups, using differently sourced platinum have given different, but reproducible results [2011Cor]. The samples of Tshawe *et al.* [2008Tsh] had the tetragonal Pt_3Al phase (by a solid phase transformation) at higher temperatures than recorded in the phase diagram of Oya *et al.* [1987Oya], since Oya *et al.* [1987Oya] reported the tetragonal Pt_3Al phase to be below 340°C, although the quenching rates of Oya *et al.* [1987Oya] might not have been enough to retain the higher temperature structure.

Furthermore, Tshawe *et al.* [2006Tsh, 2008Tsh, 2008Cor] found that samples at 72 at.% Pt and in the region 75 to 81.5 at.% Pt consisted of (Pt) and two of the three forms of the ~Pt_3Al

phase, cubic ($L1_2$) and tetragonal (DO'_c), therefore a displacive or martensite-type transformation had occurred. The (Pt) phase boundary, which was drawn from the 67 at.% Pt as-cast and 1100°C annealed samples, narrowed as the temperature decreased, thus the (Pt) phase field width decreased as temperature decreased, which agreed with Huch and Klemm [1964Huc], Darling *et al.* [1970Dar] and Guex and Feschotte [1976Gue]. The ~Pt_3Al phase fields, which were drawn from the samples annealed at 1400°C, 1300°C and 1100°C, became narrower as temperature decreased, thus increasing the two-phase ((Pt) and ~Pt_3Al) field widths and decreasing the tetragonal ~Pt_3Al phase field width [2006Tsh, 2008Tsh, 2008Cor].

Tshawe *et al.* [2006Tsh, 2008Tsh, 2008Cor] confirmed a displacive transformation from high temperature Pt_2Al to low temperature Pt_2Al. The XRD results showed the presence of both ~PtAl and Pt_5Al_3 phases in the as-cast 53.5 at.% Pt sample. These phases confirmed the existence of the β-phase, because they are the eutectoid decomposition products of the β-phase [1986McA], but the β-phase itself was not observed in the as-cast sample, as it had already decomposed [2008Tsh]. Similar results were observed in the as-cast 51 at.% Pt sample, and indicated that the β-phase decomposed. The existence of the β-phase was also found by Prins *et al*. [2005Pri] in the as-cast sample Pt_{33}:Al_{28}:Ru_{39} (at.%). The Pt_6Al_{21} phase was identified instead of Pt_5Al_{21}, and was deduced to be a different interpretation of the same phase, although the former had been described as a metastable phase [2008Tsh, 2008Cor].

2.5.3 Ternary Pt-based Superalloys

Platinum-based alloys have already been successfully applied in the aerospace [1990Lup, 1982Ham] and glass industries [1973Sel, 1981Roe, 1988Wha]. For these applications, exceptional chemical stability, oxidation resistance, high melting points, good ductility, thermal-shock resistance, and good electrical or thermal conductivity counterbalance the exceptionally high price of platinum. Pure platinum has low mechanical strength; therefore, platinum is usually alloyed with up to ~20 wt% rhodium or up to about ~30 wt% iridium. [1990Lup, 1999Fis, 2001Mer]. Platinum alloys with more than 20 wt% rhodium or iridium are generally very difficult to process, and alloys with iridium contents of more than 20 wt% tend to embrittle when exposed at intermediate temperatures. The solid-solution alloys have good ductility at high temperatures and can be welded to themselves or similar alloys. Pure platinum and solid-solution platinum-rhodium alloys are virtually oxidation resistant, even at temperatures above 1000ºC. Platinum-iridium alloys show small weight losses after long

exposure to high temperatures due to evaporation of iridium. Oxide-dispersion-strengthened (ODS) platinum-based alloys [1988Wha, 1990Lup, 1990Tho, 2001Fis2] are used for the most demanding applications, at temperatures of up to 95% of the melting temperature of the platinum matrix.

Following the success of the two-phase structures in iridium- and rhodium-based refractory superalloys [1996Yam, 1997Yam1, 1997Yam2, 1997Yam3, 1998Yam], a two-phase microstructure in platinum-based alloys was attempted [2000Wol]. Since platinum has the same structure as nickel and a similar chemistry, a Pt-based superalloy analogous to NBSAs was considered possible, but with a higher melting point (1769ºC for platinum, compared with 1455ºC for nickel) and much improved oxidation resistance.

2.5.3.1 Preliminary Studies of Ternary Pt-based Alloys

A platinum-based solid solution was selected for the matrix phase. An ordered fcc precipitate was preferred for the main precipitate because it could provide the same good properties as the NBSAs [2001Hil1]. A literature survey was conducted of the Pt binary systems based on these criteria: high phase stability, high melting point, oxidation resistance, hot corrosion resistance, high thermal conductivity, low thermal expansion, and (if possible) low density. The selected candidate alloying elements were Al, Nb, Ta, and Ti [2001Hil1]. A literature survey of Rh, Ni, and Ru was also conducted for the solid-solution strengthener. Ternary systems from these elements were examined experimentally, and if intermetallic phases other than the $L1_2$ phase formed between the two elemental additions in the targeted range, the system was excluded from further study. The first systems evaluated were Pt-Al-Ni, Pt-Al-Ru, Pt-Al-Cr, Pt-Al-Ti, Pt-Al-Re, Pt-Ti-Ru, Pt-Ti-Re, Pt-Ta-Ru, Pt-Ta-Re, and Pt-Nb-Ru. Alloys were manufactured with compositions to contain a reasonable proportion of the targeted precipitate in the matrix [2001Hil1].

The selected ternary alloys were annealed at 1350ºC, characterised in terms of microstructure (phase distribution and morphology), phase relationships, and subjected to stepped isothermal oxidation tests and hardness testing. Characterisation included scanning electron microscopy and X-ray diffraction. Large losses of niobium showed that Pt-Nb-Ru was insufficiently stable, and the lath-like structure of the second Nb-based phase indicated that it was likely to

be incoherent with the matrix, as would be expected from the Pt_3Nb crystal structure. It was realised that rhenium additions must be limited to ~3 at.% in order to avoid precipitation of the Re-rich needle-like phase. Two-phase microstructures, leading to a considerable precipitation-strengthening effect were achieved in Pt-Al-Z and Pt-Ti-Z systems, where Z = Ni, Re and Ru [2000Hil1, 2001Hil1]. Alloys in these systems showed promising mechanical properties at room temperature, with hardnesses higher than $400HV_1$ and high resistance to crack initiation and propagation. Aluminium was added in order to develop an oxidation-resistant alloy [2001Hil1]; this was supported by the findings of Felten *et al.* [1976Fel] on a study of Pt-Al system, which showed that as little as 2 wt% of Al in Pt is sufficient to establish a thin protective oxide coating at temperatures up 1450°C.

Extensive work was done on the phase relations and room temperature mechanical properties of the Pt-Al-Z alloys, with Z = Cr, Mo, Ni, Re, Ru, Ta, Ti and W, after annealing the alloys at 1350ºC for 96 hours [2001Hil1, 2002Hil]. Microstructures similar to Ni- and Co-based superalloys were achieved in the Pt-based alloys Pt_{86}:Al_{10}:Z_4 (at.%) (Z = Cr, Ru and Ti), which consisted of cuboid ~Pt_3Al precipitates in a (Pt) matrix. From the preliminary assessment of the mechanical properties of the Pt-Al-Cr and Pt-Al-Ru alloys using room-temperature hardness tests, these alloys displayed good resistance to cracking at room temperature. More extensive work was carried out on the phase relations, and Cr was found to stabilise the cubic form of the ~Pt_3Al phase, whereas Ru acted as a solid solution strengthener [2001Big1, 2001Big2, 2001Hil2]. Other alloying additions are known to stabilise the high-temperature cubic form: Ta, Ti [2001Hil6, 2005Hül] and Co, Hf, Fe, Mn, Zr [2005Hül, 2005Wen1]. It was found that ternary alloying elements, and in particular Cr and Ru, conferred additional benefits. The lowest misfit between the (Pt) and ~Pt_3Al phases was found between 3–5 at.% Ru at over 20 at.% Al [2001Big2]. The lowest misfit between (Pt) and cubic ~Pt_3Al was 0.3%, and between (Pt) and tetragonal ~Pt_3Al was 0.2%. The tungsten-containing alloys also had the tetragonal Pt_3Al structure (lower temperature DO'_c form of Pt_3Al), as did Ni-containing alloys [1995Wes]. Coarse microstructures were produced in molybdenum-containing alloys and Mo substituted for Pt in ~Pt_3Al. All the Cr-, Ta- and Ti-containing alloys had favourable microstructures [2001Big1, 2001Big2].

The next stage was to study the effects of various ternary substitutional alloying additions on the high-temperature compressive strengths of Pt-Al-Z alloys (where Z = Cr, Re, Ru, Ta and

Ti) [2001Hil2, 2001Hil3, 2001Hil4, 2002Hil]. It was found that the Pt-Al-Z alloys had higher strengths above 1150ºC than the commercial NBSA MAR-M247 [2002Hil]. However, further work was necessary to determine the effects of the ternary alloying additions on the high temperature mechanical properties of Pt-Al-Z alloys, because differences between the microstructures and Pt:Al:Z ratios of the alloys tested made it difficult to isolate the influences of the ternary additions and high-temperature compressive strength does not equate to creep strength [2001Hil4, 2002Hil]. An investigation was therefore carried out on the effects of alloying additions on the creep properties of Pt-Al-Z alloys at 1300ºC [2002Süs1]. The ternary elements (Z = Cr, Ir, Ru, Ta and Ti) were selected to improve the high-temperature mechanical properties and phase stability of the alloys, in accordance with the earlier findings [2001Big1, 2001Hil2, 2001Hil4, 2002Hil]. The Pt:Al:Z ratios of the alloys tested were standardised to eliminate the effects of differing Al contents. PM2000, a dispersion strengthened alloy, was used as a benchmark, and is an iron-chromium-aluminium alloy with a fine dispersion of yttrium oxide (Y_2O_3) particles in a ferritic matrix. It is a high temperature alloy, with fine precipitates, and so was considered good for comparison [2011Cor]. Figure 2.26 [2002Süs1] shows the stress-rupture curves of all the alloys tested. PM2000 had the highest strength, but the shallow slope of the stress-rupture curve indicated high stress sensitivity and brittle creep behaviour. In practice, this meant that PM2000 structures are more likely to fail in the presence of stress concentrations or short overloads during usage [2002Süs1].

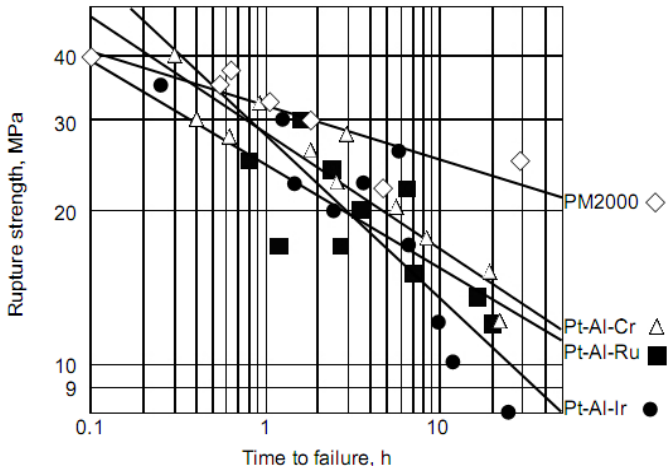


Figure 2.26. Stress-rupture curves of PM2000 and Pt_{86}:Al_{10}:Z_4 alloys at 1300ºC in air [2002Süs1].

The Pt_{86}:Al_{10}:Cr_4 (at.%) alloy possessed the highest strength of the investigated Pt-based alloys [2002Süs1]. Figure 2.27 [2002Süs1] shows selected creep curves at 30 MPa for the

four alloys. No primary creep stage could be observed for any of the three Pt-based alloys within the measurement error of the creep test facility. After secondary creep, the Pt-based alloys experienced substantial tertiary creep leading to fracture strain values between 10% and 50% at 1300ºC. For PM2000, it was not possible to resolve the different stages of the creep curves because of very low creep rates, together with fracture strains below 1% [2002Süs1]. The stress-rupture curves of PM2000 and the most promising Pt-based alloy, Pt_{86}:Al_{10}:Cr_4 (at.%), are shown in Figure 2.28 [2002Süs1]. Also shown is the 10 hour stress-rupture strength values at 1300ºC of several conventional solid-solution strengthened Pt-based alloys [2000Lup], as well as those of pure Pt and zirconia grain stabilised (ZGS) platinum [1994Bar], an oxide dispersion strengthened Pt alloy from Johnson Matthey Noble Metals.

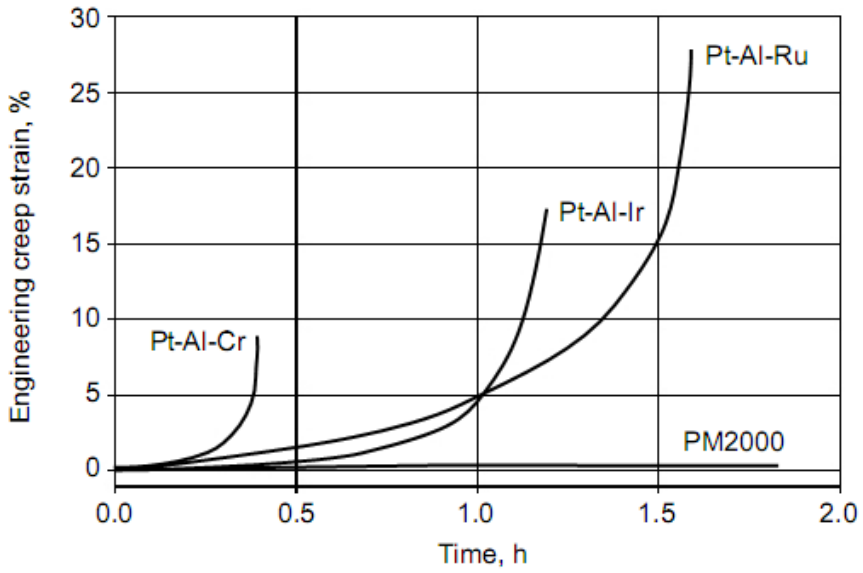


Figure 2.27. Creep curves of PM2000 and Pt_{86}:Al_{10}:Z_4 alloys tested at 1300ºC and 30 MPa [2002Süs1].

Strengthening was achieved by precipitation of γ′ particles, and gave considerably increased stress-rupture strength, $R_{m/10h/1300ºC}$ (where m denotes maximum), by a factor of 8 from 2.2 MPa for the pure Pt matrix to 17MPa for Pt_{86}:Al_{10}:Cr_4 (at.%) [2002Süs1]. The strength of the Pt_{86}:Al_{10}:Cr_4 (at.%) alloy was also higher than the solution strengthened Pt-based alloys, Pt-10 wt% Rh and Pt-20 wt% Rh. Alloying with 30 wt% Rh would be necessary to reach the strength of the alloy Pt_{86}:Al_{10}:Cr_4 (at.%), and the exceptionally volatile price of Rh and enormous machining problems limit the practical use of Pt-30 wt% Rh [1999Fis, 2006Völ, 2009Cor1]. The creep strengths of the Pt-based alloys at 1300ºC were higher than those of the Ni- and Co-based superalloys, whose precipitates dissolved at this high-temperature regime,

resulting in loss of strength. The creep strength of the Pt_{86}:Al_{10}:Z_4 (at.%) system was comparable to the mechanically alloyed ferritic oxide dispersion strengthened alloys [2002Süs1].

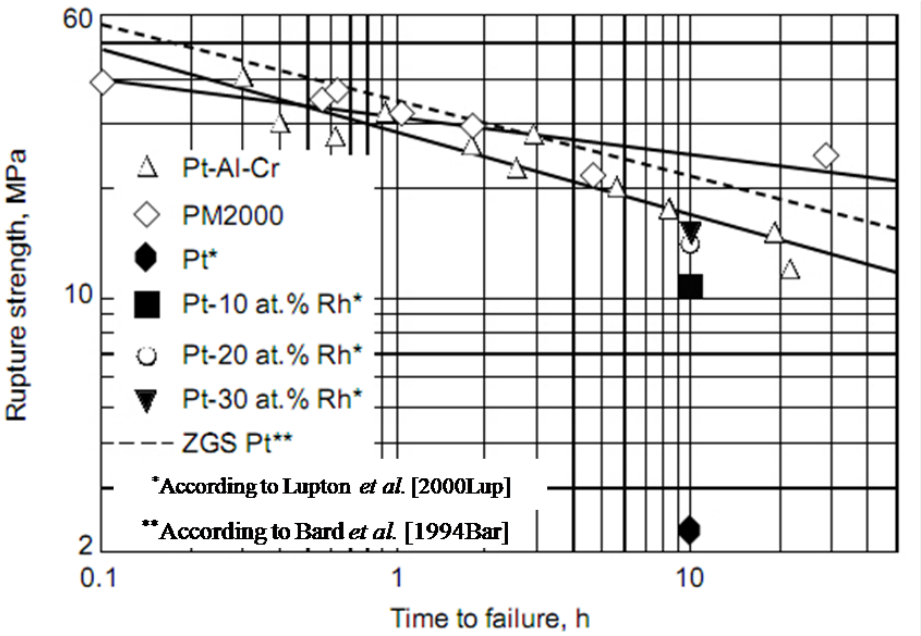


Figure 2.28. Stress-rupture curves at 1300ºC of PM2000, Pt, ZGS platinum and Pt_{86}:Al_{10}:Cr_4 (at.%) compared with stress-rupture strength values, $R_{m/10h/1300ºC}$, of some conventional solid solution strengthened Pt-based alloys [2002Süs1].

2.5.3.2 Oxidation

Although some alloys (Pt_{86}:Al_{10}:Cr_4, Pt_{86}:Al_{10}:Ti_4 and Pt_{86}:Al_{10}:Ru_4 (at.%)) with potential for high-temperature applications had already been identified [2001Hil3], more information was needed on the high-temperature properties, since they were being targeted for this niche. Additionally, the oxidation resistance was ascertained by a stepped thermo-gravimetric testing regime in a Setaram TG-DTA 92 analyser, with halts of 10,000s (2.8h) at 900ºC, 1100ºC, 1300ºC and 1400ºC. There was internal grain boundary oxidation in the Pt-Ti-Ru alloys, and extensive internal oxidation in the Pt-Nb-Ru and Pt-Ta-Re alloys. The alloys containing Al exhibited considerably better oxidation resistance than the other alloys; this was attributed to the formation of a protective Al oxide scale. Internal oxidation was observed in alloys containing Ti instead of Al, and this was presumed to be the cause of their inferior properties. Aluminium was regarded as the essential addition in order to develop an oxidation-resistant alloy [2001Hil1], confirming Felton's work [1976Fel], therefore further work focused on Pt-Al-Z alloys only.

The high-temperature oxidation behaviour of Pt-Al-Z alloys (Z = Cr, Ir, Re, Ru, Ta and Ti) was studied by isothermal oxidation tests at 1200ºC, 1280ºC and 1350ºC for at least 1000 hours [2000Hil1, 2001Süs1]. Figure 2.29 [2001Süs1] shows the increase in the thickness of the continuous layers with time for the different alloys tested.

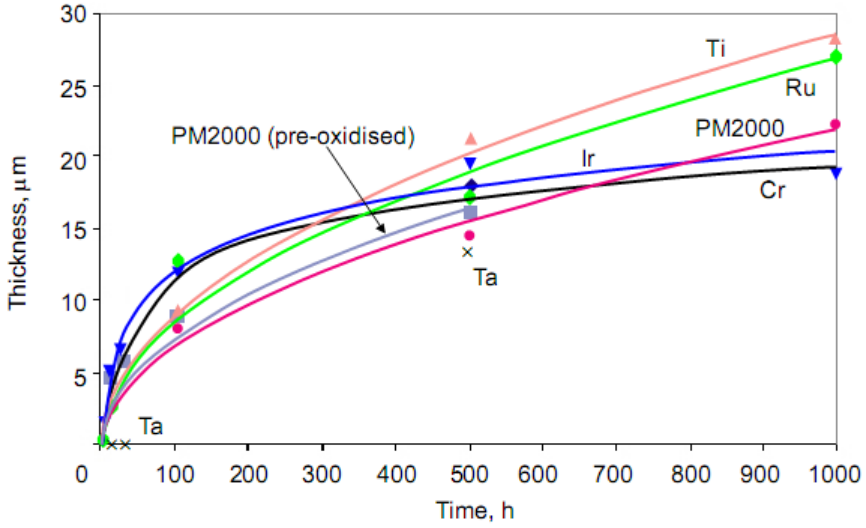


Figure 2.29. Results of the isothermal oxidation tests conducted on Pt-Al-Z alloys at 1350ºC, showing the thickness changes with time over the first 1000 hours [2001Süs1].

The Pt_{86}:Al_{10}:Ti_4 and Pt_{86}:Al_{10}:Ru_4 (at.%) alloys showed similar parabolic oxidation behaviour to the benchmark [2001Süs1]. The Pt_{86}:Al_{10}:Ir_4 and Pt_{86}:Al_{10}:Cr_4 (at.%) alloys showed parabolic behaviour during the early stages of oxidation (with high initial oxidation rates), after which their continuous oxide layers grew at a logarithmic rate, giving these two alloys the thinnest continuous oxide layers after 800 hours exposure. After a transient period, during which discontinuous alumina particles precipitated in the (Pt) matrix (Figure 2.30(a) 2001Süs1), an external alumina film formed. This was formed because oxygen diffused through the scale more quickly than Al diffused in the alloy [2001Süs1]. Only when a critical volume of oxides was reached, did transition from internal oxidation to external scale formation occur [1987Woo]. The continuous film appeared to provide protection for the alloy, since no internal oxidation occurred during long-term exposure (Figure 2.30(a) [2001Süs1]). However, the alloys were still outperformed by the PM2000, which formed a perfectly continuous oxide layer (Figure 2.30(b) [2001Süs1]. Further work was required in order to accelerate the formation of the continuous layer of the Pt-based alloys. It was deduced that this could be achieved by increasing the Al content [2001Süs1].

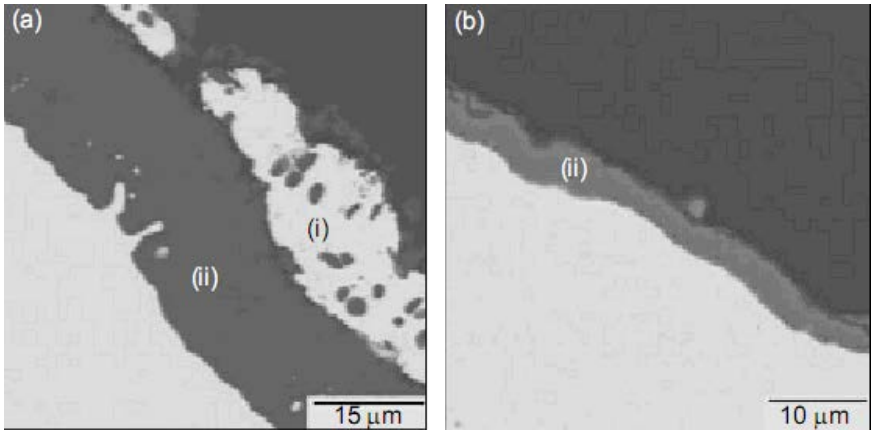


Figure 2.30. SEM-BSE images of alloys isothermally oxidised at 1350ºC for various times: (a) Pt_{86}:Al_{10}:Cr_4 (at.%) for 1000 hours, and (b) PM2000 for 10 hours, where (i) is transient oxidation, and (ii) is continuous oxidation [2001Süs1].

2.5.4 Transmission Electron Microscopy Studies of Pt-based Superalloys

2.5.4.1 Microstructure and Crystal Structure of Pt_3Al in Binary Pt–Al Alloys

In order to maintain the analogous γ/γ′ microstructure in the Pt–Al alloys over the whole operating temperature regime (room temperature to above 1100°C), the $L1_2$ structure of the precipitates must be prevented from transforming to the tetragonal structure upon cooling. Some success has been achieved in stabilising the high temperature $L1_2$ form by ternary alloying of Pt and Al with Cr [2001Hil1, 2001Hil2, 2005Hül, 2005Wen1]. However, the precipitates are distorted tetragonally in the simple binary Pt–Al alloy. Douglas *et al.* [2004Dou2, 2007Dou] carried out a detailed TEM study of the microstructure and crystal structure of the tetragonally distorted Pt_3Al precipitates in a binary Pt–Al alloy.

The chosen sample composition was within the Pt solid solution and Pt_3Al two-phase field of the Pt–Al phase diagram [2004Dou, 2007Dou]. The alloy was heat treated for 96h at 1350°C, followed by furnace cooling. A Philips CM20 TEM operating at 200kV was used for conventional transmission electron microscopy. High-resolution imaging was performed on a JEOL 4000EX HRTEM operated at 400kV. The atomic structure of the tetragonal (DO'_c) phase of Pt_3Al was constructed by using the atomic positions determined by Bronger *et al.* (1997Bro) for the space group *P*4/*mbm*. The unit cells were constructed using the JEMS software package from P.A. Stadelmann, CIME EPFL, Lausanne, Switzerland, which was also used to simulate the diffraction patterns. The unit cell construction was repeated using

the MacTempas software package from Total Resolution LLC, Berkeley, U.S.A., which gave the same results, and high resolution images were also simulated [2004Dou2, 2007Dou, 2009Dou].

Figure 2.31 [2007Dou] is a bright-field TEM image of a typical Pt_3Al precipitate in the Pt_{86}:Al_{14} (at.%) alloy, containing a number of stacked plates or laths (P) (which are characteristic of alloys in which a martensitic transformation has occurred) in a (Pt) solid solution matrix (M) [2007Dou, 2009Dou].

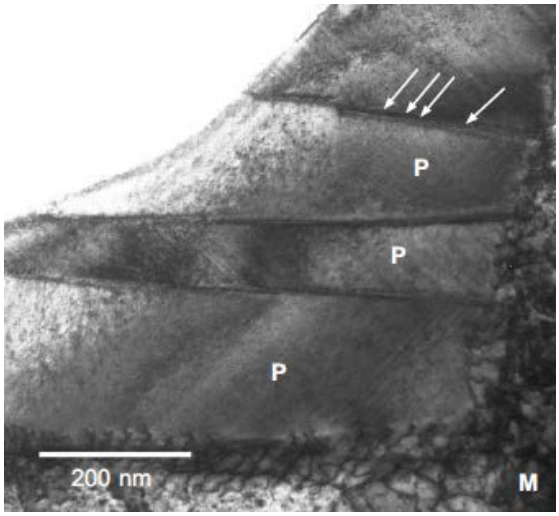


Figure 2.31. Bright field TEM image of a Pt_3Al precipitate in a Pt_{86}:Al_{14} (at.%) alloy, where P = stacked plates or laths, M = (Pt) solid solution matrix, and arrows indicate individual platelets inside the plate of stacked platelets in the region below [2007Dou].

Selected area diffraction (SAD) patterns for the matrix and the precipitate are shown in Figure 2.32 [2004Dou2, 2007Dou]. The selected area aperture was positioned to include two adjacent plates in the precipitate. The SAD pattern of the matrix was simulated along the [001] beam direction based on an fcc unit cell. This simulation is shown in Figure 2.32(c) [2007Dou]. The SAD pattern of the precipitate was simulated along the [110] beam direction, based on the DO'_c (Pt_3Ga) unit cell, and is shown in Figure 2.32(d) [2007Dou]. The matrix diffraction pattern, which is supposed to be from a disordered fcc phase, had faint extra spots in addition to the fundamental reflections expected for the fcc structure. There was a high density of small precipitates throughout the matrix, which made it impossible to isolate the information contributed to the diffraction pattern by the matrix by using the selected area aperture. The matrix diffraction pattern was thus a composite of the diffraction patterns from the matrix and the precipitates. The experimental γ' precipitate diffraction pattern contained fine structure in the form of additional extra spots (indicated by arrows in Figure 2.32(b))

[2004Dou2, 2007Dou] that were found neither in the experimental matrix nor in the simulated DO′$_c$ diffraction pattern. The primary spots in the experimental SAD pattern of the γ′ phase (Figure 2.32(b)) [2004Dou], e.g. $2\bar{2}0$, $2\bar{2}4$ and 004, match the high intensity reflections of the simulated diffraction pattern based on the DO′$_c$ structure (Figure 2.32(d)) [2004Dou2, 2007Dou].

Comparison of the experimental primary spots in the [110] selected area diffraction (SAD) with the simulated DO′$_c$ diffraction pattern revealed some differences [2007Dou, 2009Dou]. There were no experimental <001> and <003> reflections, and there were extra experimental spots with reciprocal lattice vectors ± $^1/_3$[002] and ± $^2/_3$[002].

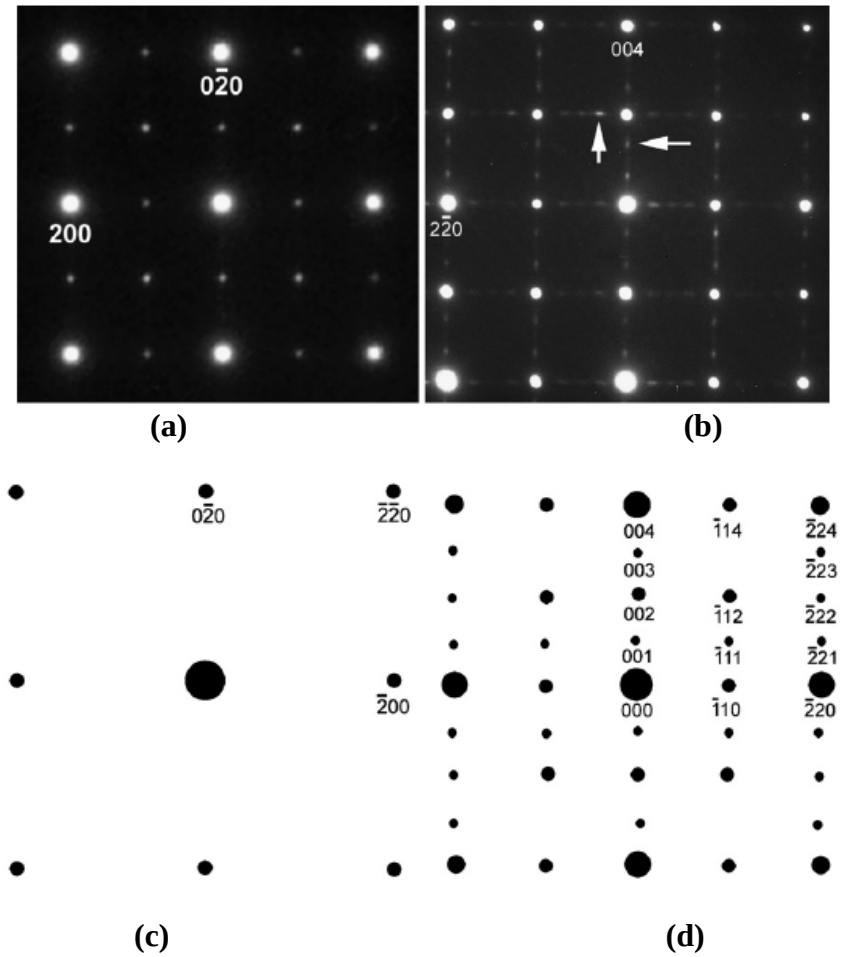


Figure 2.32. $Pt_{86}Al_{14}$ (at.%) TEM results: (a) SAD pattern corresponding to the matrix, B= [001], (b) SAD pattern corresponding to the precipitate, B= [110], (c) simulated matrix SAD pattern, B= [001], and (d) simulated precipitate SAD pattern, B= [110] [2007Dou].

The reflections at ± $^1/_3$[002] indicated that the precipitate phase had a tetragonal unit cell with a *c*-axis 1½ times that of the DO′$_c$ unit cell. Various modelling attempts were tried for the

DO'_c structure, and only one modification was successful [2007Dou, 2009Dou]. The atomic configuration of the DO'_c structure, projected along the [110] direction, is shown in Figure 2.33(a) [2007Dou, 2009Dou]. The simulated diffraction pattern using this unit cell is shown in Figure 2.33(d) [2007Dou, 2009Dou]. A modified tetragonal Pt_3Al unit cell, with the *c* axis equal to 1½ times that of the DO'_c structure, is shown in Figure 2.33(b) [2007Dou, 2009Dou]. The modified unit cell was constructed by repeating half of the DO'_c structure, as shown in the dashed rectangles in Figure 2.33(a) and (b) [2007Dou, 2009Dou]. The simulated SAD pattern, based on the modified unit cell, is shown in Figure 2.33(c) [2007Dou, 2009Dou]. A selected area diffraction pattern of a single broad precipitate plate is shown in Figure 2.33(d) [2007Dou, 2009Dou]. The simulated SAD pattern based on the modified DO'_c unit cell agreed well with the experimental diffraction pattern.

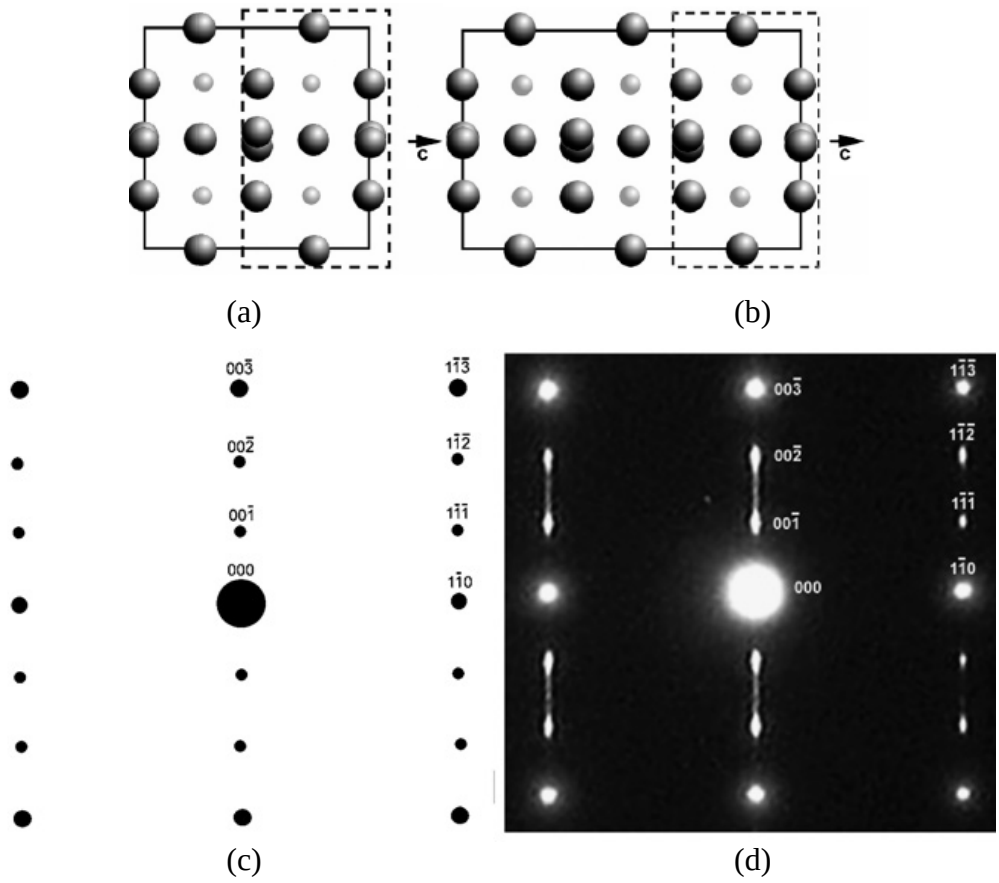


Figure 2.33. $Pt_{86}Al_{14}$ (at.%) TEM results: (a) unit cell of the DO'_c structure, B= [110], (b) unit cell of modified DO'_c unit cell, B= [110], (c) kinematically simulated SAD pattern of modified DO'_c unit cell, B= [110], and (d) experimental SAD pattern from a single broad plate, B= [110] [2007Dou].

2.5.4.2 Microstructure and Deformation of Ternary Alloys

After Pt-Al was identified as the basis for the alloys [2001Hil1], ternary additions were made to stabilize the high temperature $L1_2$ cubic form of ~Pt_3Al. Without these additions, a martensitic transformation occurred in ~Pt_3Al forming DO'_c twin-like bands [2003Big, 2004Cor]. TEM was then used to study the precipitate structures of the Pt-Al-Z alloys (where Z = Cr, Ir, Ru, Ta or Ti) [2001Hil2, 2001Hil4, 2001Hil6, 2009Cor1] at different testing temperatures [2004Dou1, 2004Dou2].

The samples had only a small amount of deformation [2001Hil6]. The precipitates showed at least a bimodal distribution, which could even be interpreted as a trimodal distribution (Figure 2.34(a) [2001Hil5, 2001Hil6, 2006Cor]). The elements Cr, Ta and Ti partitioned to ~Pt_3Al and stabilised the cubic $L1_2$ structure, giving cuboid precipitates, with no discernable inner structure (Figure 2.34(a)) [2001Hil5, 2001Hil6, 2004Dou2, 2006Cor]. Conversely, Ir and Ru partitioned to the matrix, and the precipitates transformed to the DO'_c structure (Figure 2.34(b)) [2001Hil5, 2001Hil6, 2004Dou2, 2006Cor], with alternating contrast bands. These were acknowledged as being due to the twinning of the stacked plates and the modified DO'_c structure [2007Dou], although the transformation had already been recognised as displacive [1986McA, 1987Oya].

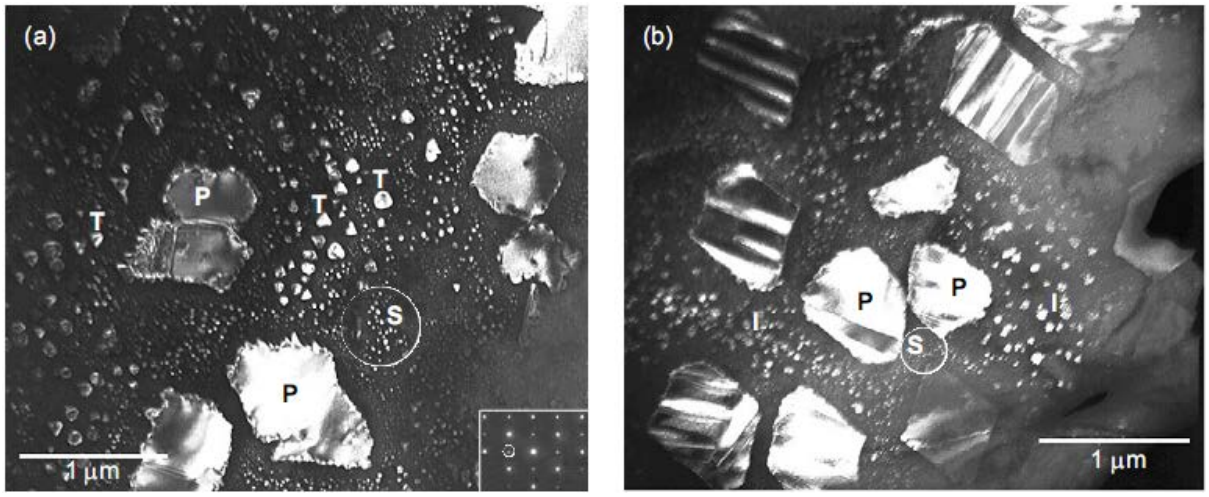


Figure 2.34. Typical TEM images of the ~Pt_3Al precipitates in Pt-Al-Z alloys (Z = Cr, Ir, Ru, Ta or Ti), with letters indicating the different size ranges (where P = primary; I or T = intermediate; S = secondary): (a) $L1_2$ precipitates stabilised by Cr, Ta and Ti additions. The inset shows the selected area diffraction (SAD) pattern, confirming the $L1_2$ structure, and (b) DO'_c precipitates stabilised by Ir and Ru additions [2001Hil5, 2001Hil6, 2004Dou2, 2006Cor].

The lattice misfits between the matrix and precipitate phases were also measured at room temperature and at 800ºC by X-ray diffraction (XRD) on a JEOL JDX-3500 diffractometer, with a copper source [2001Hil6]. The (220) peak was used to derive the (Pt) lattice parameters, (112) was used for tetragonal DO'_c ~ Pt_3Al, and (211) was used for cubic $L1_2$ ~Pt_3Al. Lattice misfits, δ, were then calculated from these measurements, using Equation 2.1 [1987Sim, 2006Ree]:

$$\delta = 2((a_{ppt} - a_{matrix}))/(a_{ppt} + a_{matrix})) \qquad \text{Equation 2.1}$$

where a_{ppt} denotes the lattice parameter for the ~Pt_3Al precipitate phase and a_{matrix} denotes the lattice parameter for the (Pt) matrix phase. The results are presented in Table 2.4 [2001Hil6, 2004Dou2]. There was little difference between the misfits at different temperatures, and they were all negative. With the exception of the Ru alloy, all the other alloys showed an increased misfit at the higher temperature. The misfits were lower for the $L1_2$ phases (Cr, Ta and Ti alloys) than for the lower temperature DO′c structure (Ir and Ru alloys).

Table 2.4. Comparative lattice misfits of selected Pt_{86}:Al_{10}:Z_4 alloys comprising (Pt) matrix and ~Pt_3Al precipitates (ppt) [2001Hil6, 2004Dou2].

Alloy	Pt_3Al type	Room temperature			800ºC		
		a_{matrix} (nm)	a_{ppt} (nm)	Lattice misfit (δ)	a_{matrix} (nm)	a_{ppt} (nm)	Lattice misfit (δ)
Pt_{86}:Al_{10}:Cr_4	$L1_2$	3.9022	3.8741	-0.0072	3.9390	3.9103	-0.0073
Pt_{86}:Al_{10}:Ir_4	DO'_c	3.8983	3.8507	-0.0123	3.9246	3.8747	-0.0128
Pt_{86}:Al_{10}:Ru_4	DO'_c	3.9001	3.8530	-0.0121	3.9349	3.8967	-0.0098
Pt_{86}:Al_{10}:Ta_4	$L1_2$	3.8941	3.8682	-0.0067	3.9246	3.8961	-0.0073
Pt_{86}:Al_{10}:Ti_4	$L1_2$	3.8921	3.8642	-0.0072	3.9246	3.8961	-0.0073

Since the interaction of dislocations with precipitates is important for determining the mechanical properties, these interactions were studied using TEM, and the different effects of the ternary additions on the ~Pt_3Al precipitates were compared. New samples were made to study the dislocation content and precipitation characteristics. The samples had been compressed at different temperatures (21ºC, 800ºC, 1000ºC and 1300ºC) for Pt_{86}:Al_{10}:Z_4 (at.%) alloys where Z = Cr, Ir, Ru, Ta and Ti [2004Dou1, 2004Dou2]. Lattice parameters of the (Pt) matrix phase in Pt-Al-Z (Z = Cr, Ru and Ti) alloys were derived from selected area

electron diffraction (SAD), and all the patterns were of a <112> zone type. The results were slightly different from those of Hill *et al.* [2001Hil6]; this was attributed to calibration differences in the camera length of the two microscopes. Unlike NBSAs which have precipitates with {100} interfaces, the interfaces of the Pt-based alloys were not necessarily {100}, and this made the dislocations more complex, as did the different lower temperature non-cubic structure [1987Sim]. However, the dislocations were analysed to have a Burgers vector of ± ½<110>, similar to those found in NBSAs.

The density of the small precipitates decreased with increasing compression temperature, while the dislocation density in the matrix increased, but the changes were not large in either [2009Dou]. There were paired dislocations in all the large precipitates, and these were interpreted to be misfit dislocations because there were different types of dislocations at different parts of the precipitate, and networks around the edges. With increasing temperature, the structure of the dislocation system remained the same, and no other slip systems were activated [2009Dou]. Cornish *et al.* [2006Cor] found that in Pt-Al-Cr the precipitates were not cuboid, but octahedral in nature. In Pt-Al-Ru, the morphology of the precipitates differed markedly from those of the Pt-Al-Cr sample. They were ogdoadically-diced [1957Wes] (otherwise described as cruciform or maltese cross-shaped) as shown in Figure 2.35 [2004Dou2, 2006Cor], generally consisting of four interconnected lobes and similar to those in the Pt-Al-Ir sample [2004Dou2, 2006Cor]. The precipitates showed twinned regions, indicating that a martensitic transformation had occurred. Their edges were curved, suggesting low surface energy for their boundaries, but became more straight at higher compression temperatures. The twin bands also became better developed at higher temperatures, with dislocations found in alternating twin bands. The dislocations occurred in pairs, indicative of superlattice dislocations, which were expected in the ordered structure of these precipitates, just as in the γ' phase of NBSAs. The long dislocations shared the same Burger's vector as those in the Pt-Al-Cr system [2004Dou2, 2006Cor].

In Pt_{86}:Al_{10}:Cr_4 (at.%) (Figure 2.36) [2004Dou2] after being compressed at room temperature, the matrix surrounding the precipitate appeared to be largely devoid of dislocations, although this region contained features that indicated strain contrast as seen in the black circle and white box in Figure 2.36. The strain contrast lobes in the circle are visible in Figure 2.36(a) to (c), invisible in Figure 2.36(d) to (g), and show sharp dislocations in Figure 2.36(h). It was concluded that these features may be due to ion milling damage from

the TEM sample preparation process. The features within the white box were visible under all the diffraction conditions in Figure 2.36, and were thought to be small γ′ precipitates, which could account for the low matrix dislocation density, since they would have had a significant hardening effect on the matrix. The finer precipitates were found to serve as a barrier to the motion of matrix dislocations, as indicated at the red arrows in Figure 2.36 [2004Dou2]. The Pt_{86}:Al_{10}:Cr_4 (at.%) matrix and precipitate orientation relationships derived from the SAD pattern was: $(110)_M||(110)_P$; $<002>_M||<002>_P$; $<\bar{2}20>_M||<\bar{2}20>_P$. The TEM EDX analyses of Pt_{86}:Al_{10}:Cr_4 (at.%) for both matrix and precipitate compositions are shown in Table 2.5 [2004Dou2]. Figure 2.37 shows bright field TEM micrographs of the interfacial dislocation networks in Pt_{86}:Al_{10}:Cr_4 (at.%) deformed at 800°C under various diffraction conditions. The dislocations seen in Figure 2.37 were observed in regions of the sample where there were no fine precipitates (but larger precipitates) and wide matrix channels; the dislocations were confined within the precipitates, since the wide matrix channels did not provide resistance to dislocation motion during deformation.

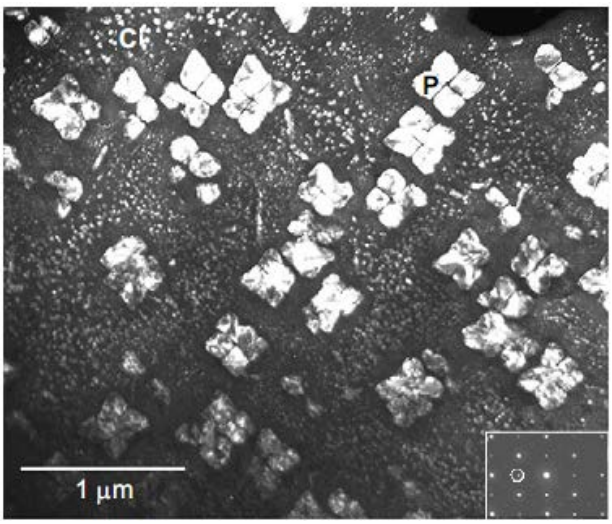


Figure 2.35. Dark field TEM image of a typical Pt_{86}:Al_{10}:Ir_4 (at.%) alloy compressed at room temperature, with P denoting ogdoadically-diced precipitates, and C denoting secondary precipitates. (Inset shows a selected area electron diffraction pattern with reflection used to obtain the image circled.) [2004Dou2, 2006Cor].

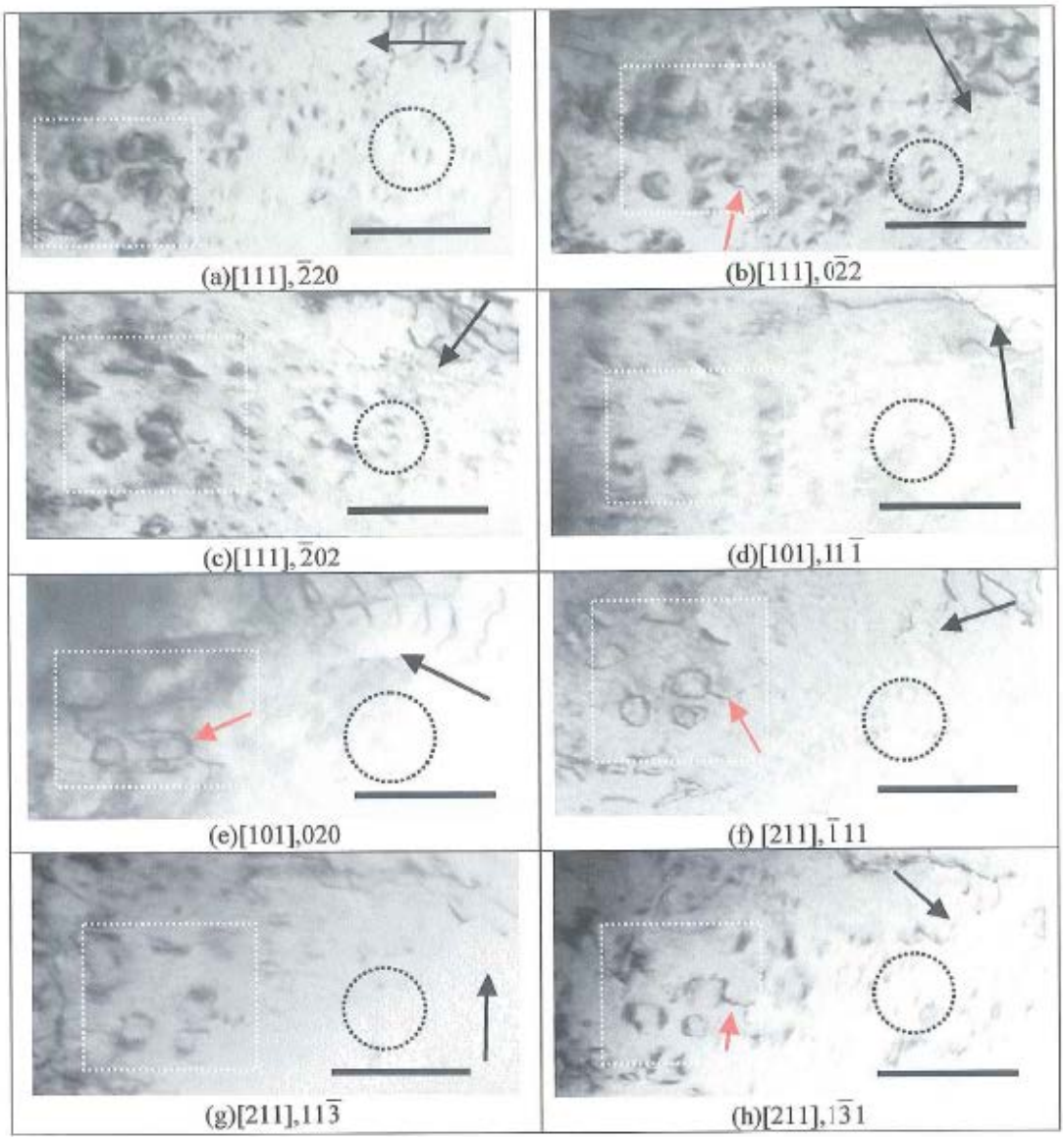


Figure 2.36. Bright field TEM image of $Pt_{86}Al_{10}Cr_4$ (at.%) deformed at room temperature showing small precipitates in the matrix with lobe contrast, box shows precipitates within the matrix and the circle shows finer precipitates [2004Dou2].

Table 2.5. TEM EDX analyses (at.%) of $Pt_{86}Al_{10}Cr_4$ (at.%) matrix and precipitate compositions [2004Dou2].

Element	Matrix (at.%)	Precipitate (at.%)
Pt	86 ± 2	78 ± 2
Al	10 ± 2	20 ± 2
Cr	4 ± 2	2 ± 2

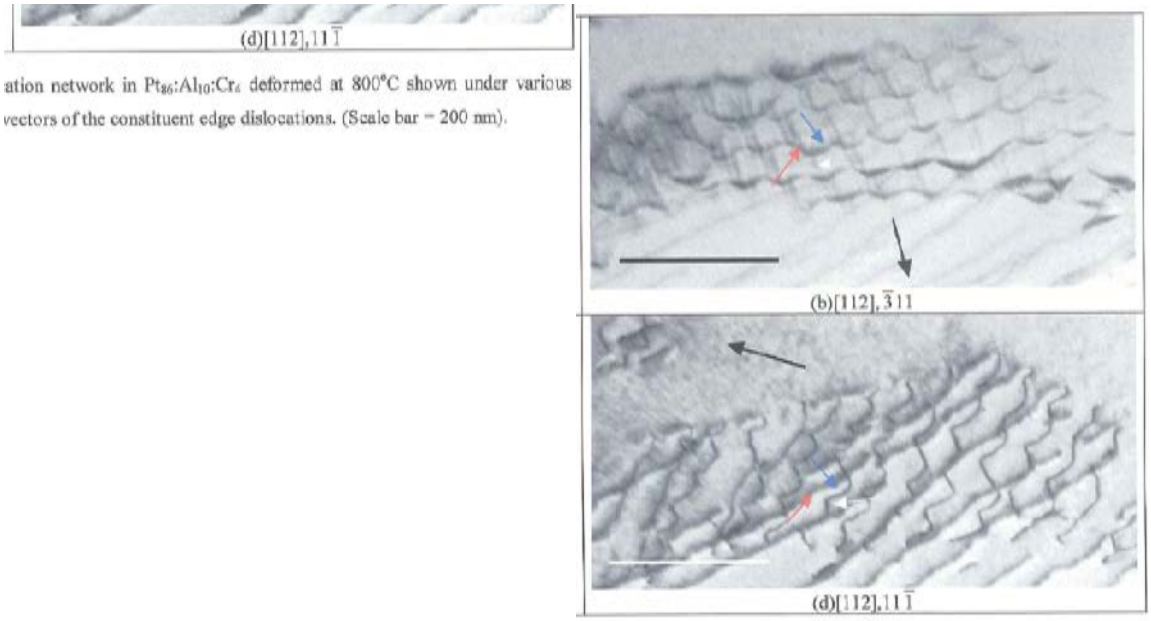


Figure 2.37. Bright field TEM micrographs of the interfacial dislocation networks in $Pt_{86}Al_{10}Cr_4$ (at.%) deformed at 800°C under various diffraction conditions (scale bar = 200nm) [2004Dou2].

The Pt_{86}:Al_{10}:Cr_4 (at.%) sample after deformation at 1100˚C (Figure 2.38) [2004Dou2] showed different features from those of the sample deformed at room temperature in Figure 2.36 [2004Dou2]. The microstructure consisted of large, irregular γ′ precipitates (P), and smaller, almost cubic precipitates (F) embedded in the fcc (γ) matrix. Small features exhibiting strain contrast were observed (circle). Once again, the strain contrast was attributed to ion milling damage. Some isolated dislocations (d) were observed in the matrix. The precipitates contained a high density of threading dislocations (D). The threading dislocations exhibited double contrast, probably because the specimen was not tilted to an exact two-beam condition. The γ/γ′ interfacial dislocation networks could also be seen (box). Figure 2.39 shows bright field micrographs of Pt_{86}:Al_{10}:Cr_4 (at.%) deformed at 1300°C with γ/γ′ interface dislocations under different diffraction conditions [2004Dou2].

The $Pt_{86}Al_{10}Ru_4$ (at.%) matrix and precipitate orientation relationships derived from the SAD pattern were: $(001)_M||(100)_P$; $[110]_M||[100]_P$. The TEM EDX analyses of $Pt_{86}Al_{10}Ru_4$ (at.%) for both matrix and precipitate compositions are shown in Table 2.6 [2004Dou2]. The precipitate structures of the alloys with Ti, Ta and Cr was $L1_2$, while the alloys with Ir and Ru were the modified DO'_c. The DO'_c precipitates (P) are shown under different diffraction conditions, in the bright field images, Figure 2.40 [2004Dou2]. These precipitates contain alternating broad plates, as shown by the red and blue arrows. The plate indicated by the red

arrow appears darker than that indicated by the blue arrow under the same diffraction conditions. This fact implies that there is a difference in orientation, and hence diffraction conditions, between the plates [2004Dou2]. There were dislocation tangles, as shown by the dashed arrows in Figure 2.40(a), which appear to be associated with the γ/γ′ interfaces. The threading dislocations are invisible in Figure 2.40(a) and visible in Figure 2.40(b), while the "interface" dislocations show the reverse contrast behaviour [2004Dou2]. Figure 2.41 [2004Dou2] shows a precipitate under different diffraction conditions. The region within the blue dotted circle in Figure 2.41(a) and (b) contains the dislocations making up the interfacial network. Figure 2.41(c) is a composite of Figure 2.41(a) and (b) showing the hexagonal nature of the network. The individual segments are shown schematically in different coloured lines in Figure 2.41(d). The interface was curved, which caused the dislocation network to be distorted [2004Dou2].

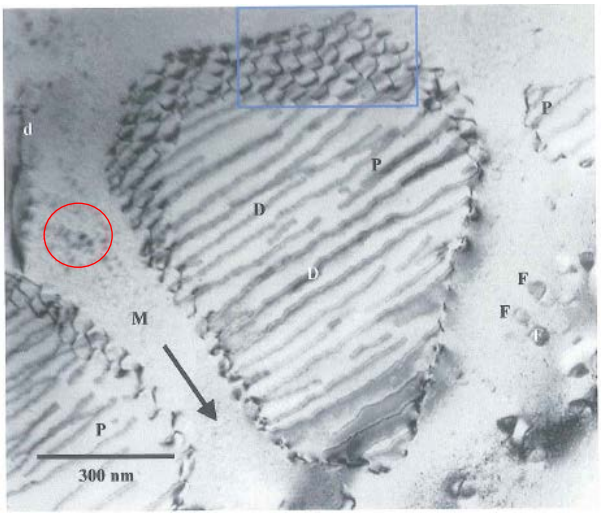


Figure 2.38. Bright field TEM image of $Pt_{86}Al_{10}Cr_4$ (at.%) compressed at 1100˚C, showing a typical $L1_2$ precipitate (P), in a (Pt) solid solution matrix (M) [2004Dou2].

Table 2.6. TEM EDX analyses (at.%) of $Pt_{86}Al_{10}Ru_4$ (at.%) matrix and precipitate compositions [2004Dou2].

Element	Matrix (at.%)	Precipitate (at.%)
Pt	88 ± 2	79 ± 2
Al	10 ± 2	20 ± 3
Ru	2 ± 2	1 ± 1

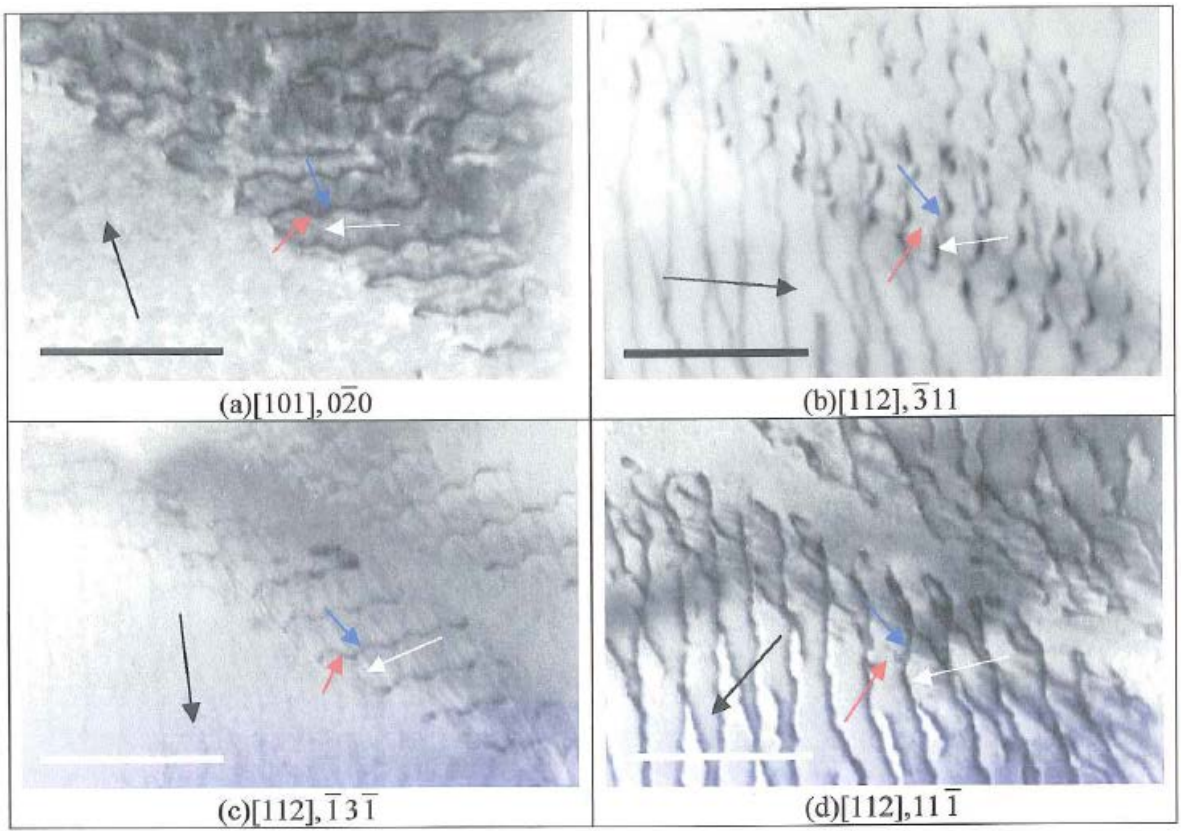


Figure 2.39. Bright field TEM micrographs of $Pt_{86}Al_{10}Cr_4$ (at.%) deformed at 1300°C showing γ/γ′ interface dislocations under different diffraction conditions (scale bar = 200nm) [2004Dou2].

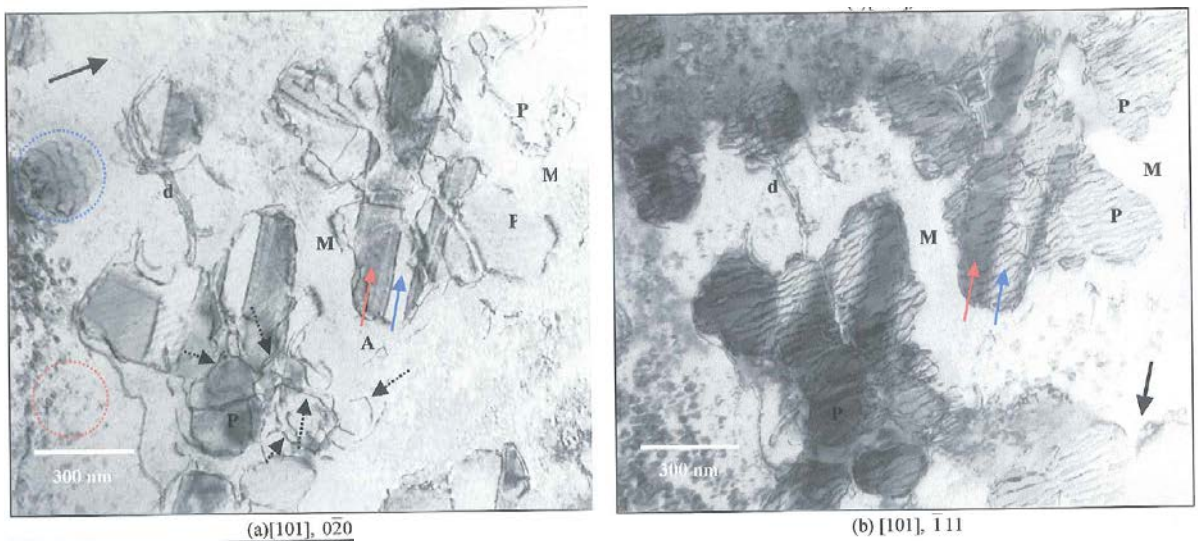


Figure 2.40. Bright field TEM micrographs of room temperature compressed $Pt_{86}Al_{10}Ru_4$ (at.%) showing DO'_c precipitates: a) threading dislocations out of contrast and b) threading dislocations in contrast (scale bar = 300nm) [2004Dou2].

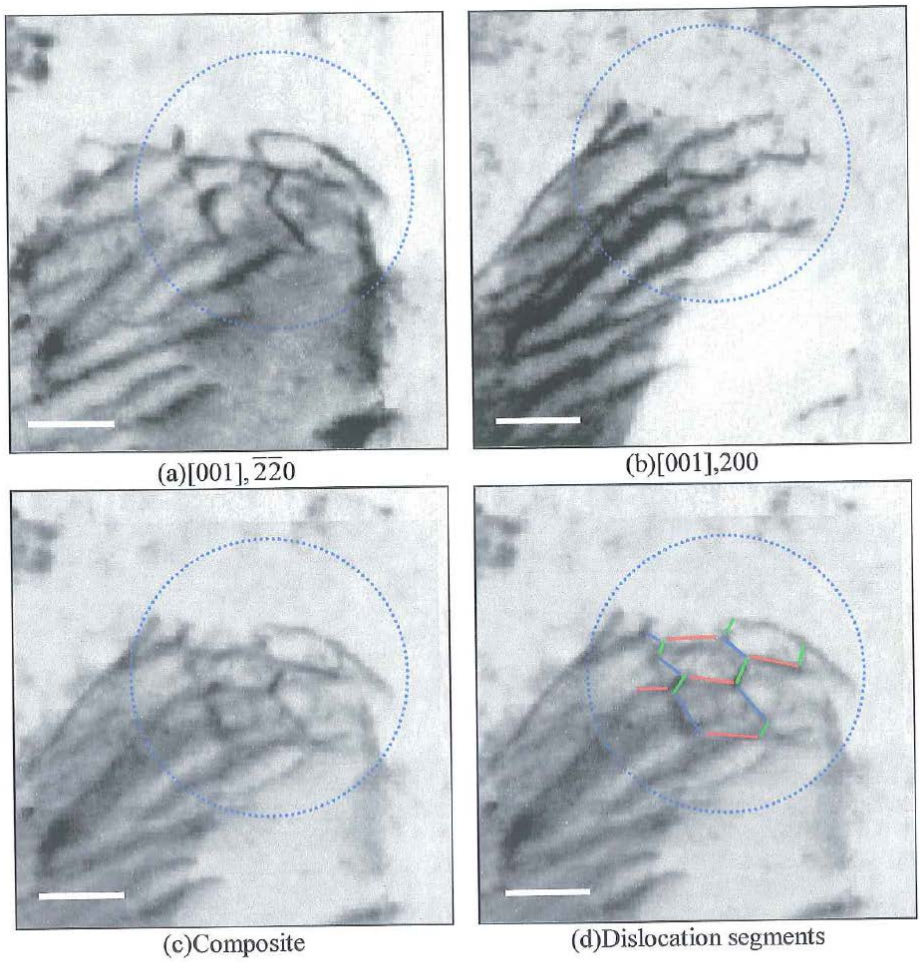


Figure 2.41. Bright field TEM micrographs for $Pt_{86}Al_{10}Ru_4$ (at.%) taken from a tip of a precipitates' lobe showing evidence of part of a hexagonal interfacial dislocation network (scale bar = 50nm) [2004Dou2].

Low and high magnification images of $Pt_{86}Al_{10}Ta_4$ (at.%) (Figure 2.42) [2004Dou2] after deformation at 1100˚C show the morphology and dislocation distribution in the γ′ precipitates (P). The matrix (M) did not contain any small precipitates unlike $Pt_{86}Al_{10}Cr_4$ (at.%) deformed at room temperature (Figure 2.36 [2004Dou2]). Isolated dislocations (D) occurred in the matrix, but their density was much lower than the precipitates. The γ/γ′ interfaces contained dislocation networks, as seen in the box. The same alloy deformed at a low temperature (800˚C) showed distorted γ/γ′ interface dislocations (Figure 2.43, box) [2004Dou2], different from those in Figure 2.42 [2004Dou2] as they were slightly elongated. The matrix (M) had small $L1_2$ precipitates (B), in addition to the larger secondary γ′ precipitates (A). The matrix and precipitate orientation relationships derived from the SAD pattern was: $<11\bar{1}>_M||<11\bar{1}>_P$; $<2\bar{2}0>_M||<2\bar{2}0>_P$; $(112)_M||(112)_P$.

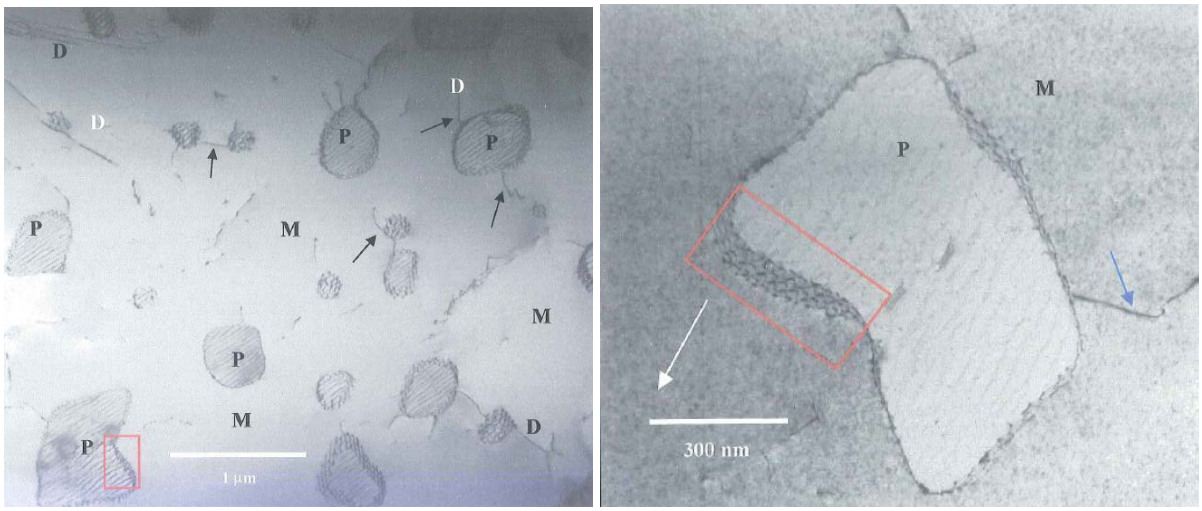


Figure 2.42. Bright field TEM images of $Pt_{86}Al_{10}Ta_4$ (at.%) deformed at 1100˚C: (a) low magnification, and (b) high magnification, showing γ′ precipitates (P), in a (Pt) solid solution matrix (M) [2004Dou2].

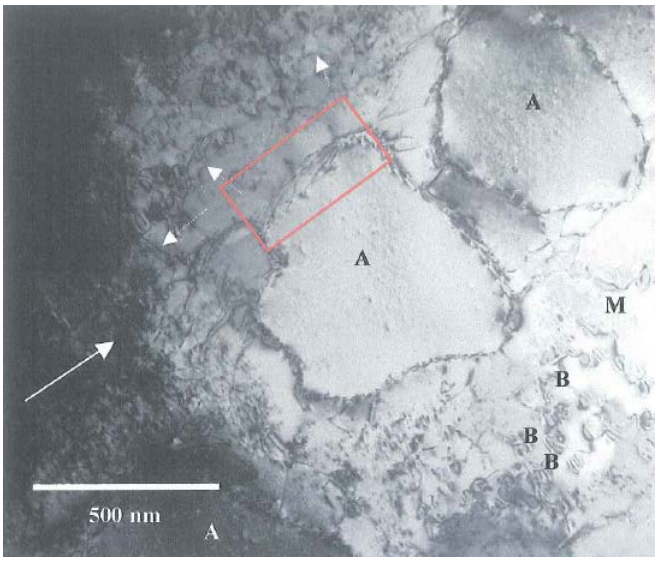


Figure 2.43. Bright field TEM image of $Pt_{86}Al_{10}Ta_4$ (at.%) deformed at 800˚C, showing γ′ precipitates (P) and larger secondary γ′ precipitates (A), in a (Pt) solid solution matrix (M) [2004Dou2].

A TEM image of $Pt_{86}Al_{10}Ti_4$ (at.%) after deformation at 1100˚C is shown in Figure 2.44 [2004Dou2]. The precipitates contained no threading dislocations, even when imaged under a variety of diffraction conditions [2004Dou2], and only a few isolated dislocations (D) were present in matrix. The matrix dislocation (arrow) did not appear to penetrate the large γ′ precipitate, as seen in the highlighted box in Figure 2.45 [2004Dou2]. The matrix dislocation interacted with the dislocations in the interfacial network, causing this matrix dislocation to be embedded into the interface and not enter the precipitate. The matrix and precipitate orientation relationships derived from the SAD pattern were: $<101>_M||<101>_P$;

$<111>_M||<111>_P$; $(001)_M||(001)_P$. Interfacial dislocation networks can be been in Figure 2.46 taken under different diffraction conditions. Figure 2.47 shows the hexagonal nature of the networks after deformation [2004Dou2]. Another hexagonal dislocation network is shown in greater detail, under different diffraction conditions, in Figure 2.48 [2004Dou2]. The microstructure of $Pt_{86}Al_{10}Ti_4$ (at.%) deformed at 1300°C is shown in Figure 2.49 [2004Dou2]. The microstructure consists of $L1_2$ precipitates within a fcc matrix (M). The precipitates have a trimodal size distribution, with large (> 1µm) precipitates (P), cubic precipitates (C, ~100nm) and small (S, < 20nm) precipitates. The cubic precipitates can coalesce to form larger precipitates, as indicated in the rectangle in Figure 2.49.

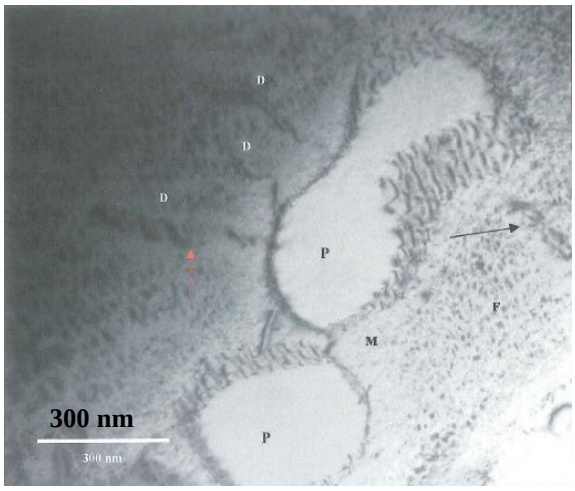


Figure 2.44. Bright field TEM image of $Pt_{86}Al_{10}Ti_4$ (at.%) deformed at 1100˚C, showing a typical $L1_2$ precipitate (P) in a (Pt) matrix (M) [2004Dou2].

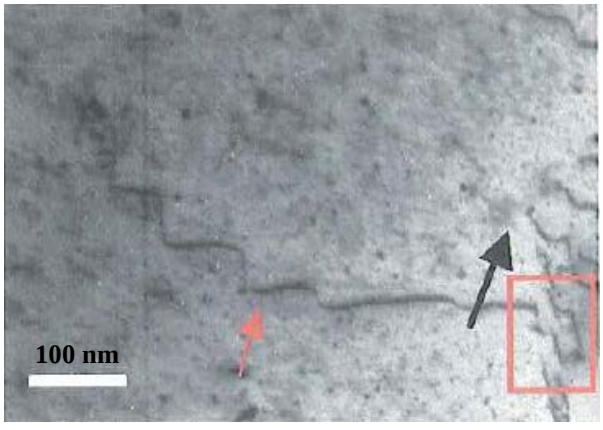


Figure 2.45. Bright field TEM image of $Pt_{86}Al_{10}Ti_4$ (at.%) deformed at 1100˚C, showing an isolated dislocation bowing out around precipitate [2004Dou2].

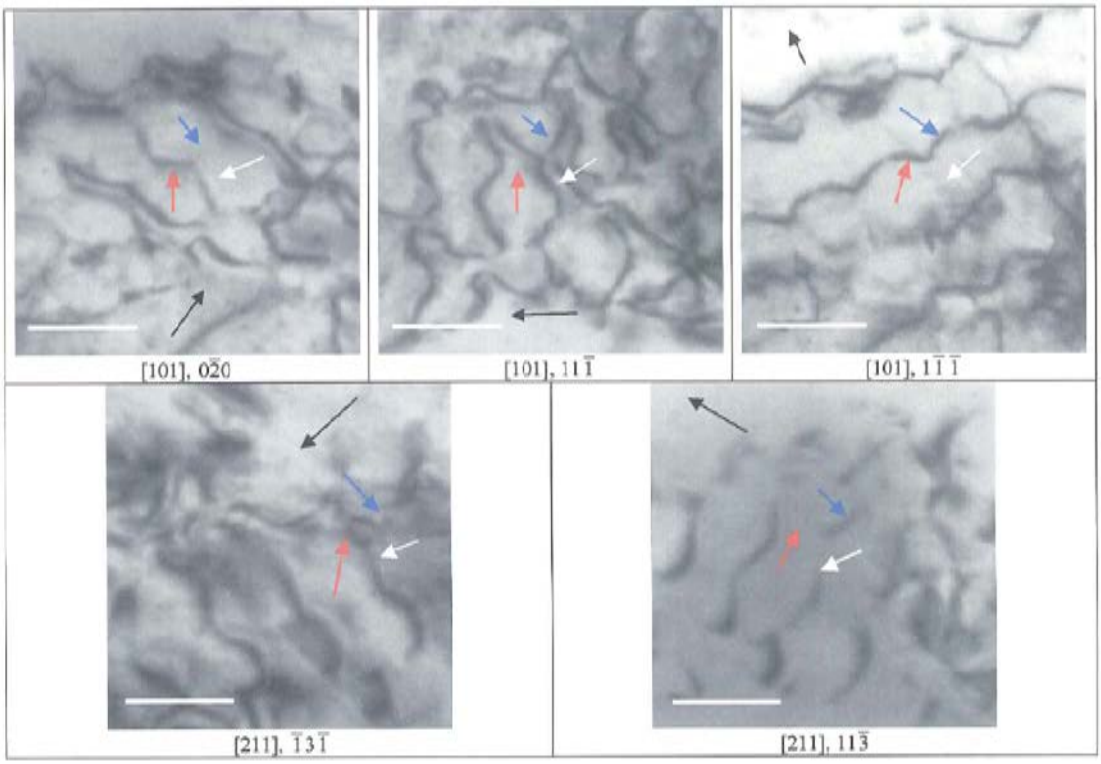


Figure 2.46. Bright field TEM micrographs of $Pt_{86}Al_{10}Ti_4$ (at.%) deformed at 1100˚C, showing an interfacial dislocation network under various diffraction conditions (scale bar = 50nm) [2004Dou2].

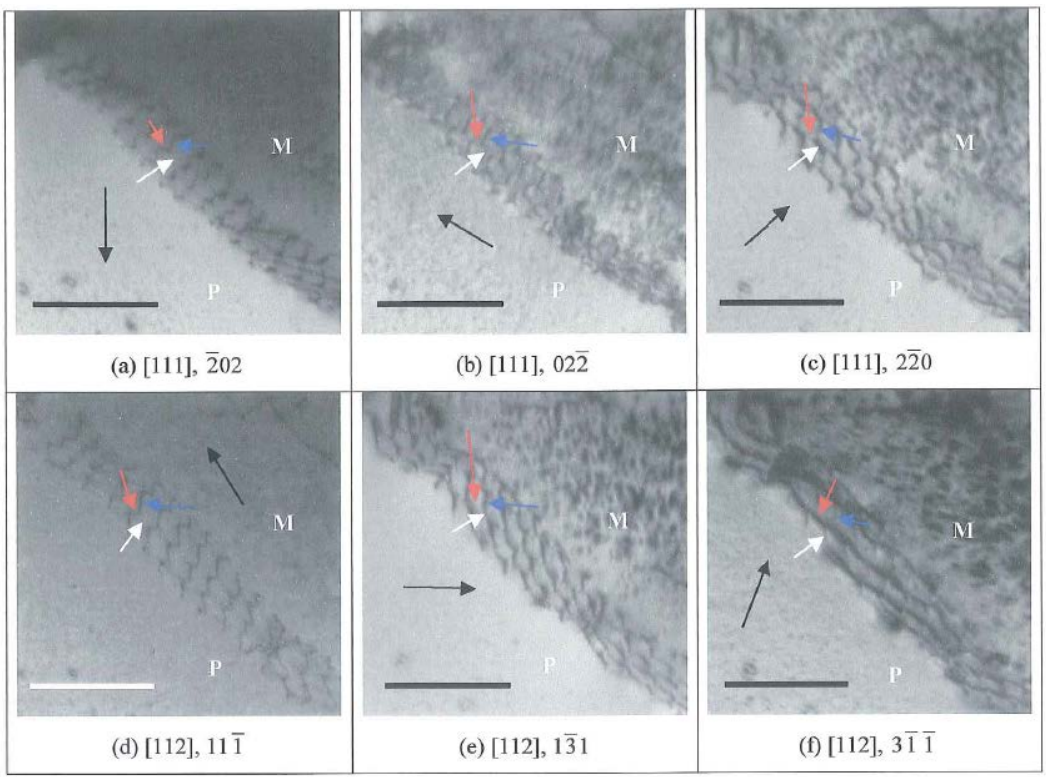


Figure 2.47. Bright field TEM micrographs of $Pt_{86}Al_{10}Ti_4$ (at.%) deformed at 1100˚C, showing a hexagonal dislocation network in the matrix/precipitate interface under various diffraction conditions (scale bar = 200nm) [2004Dou2].

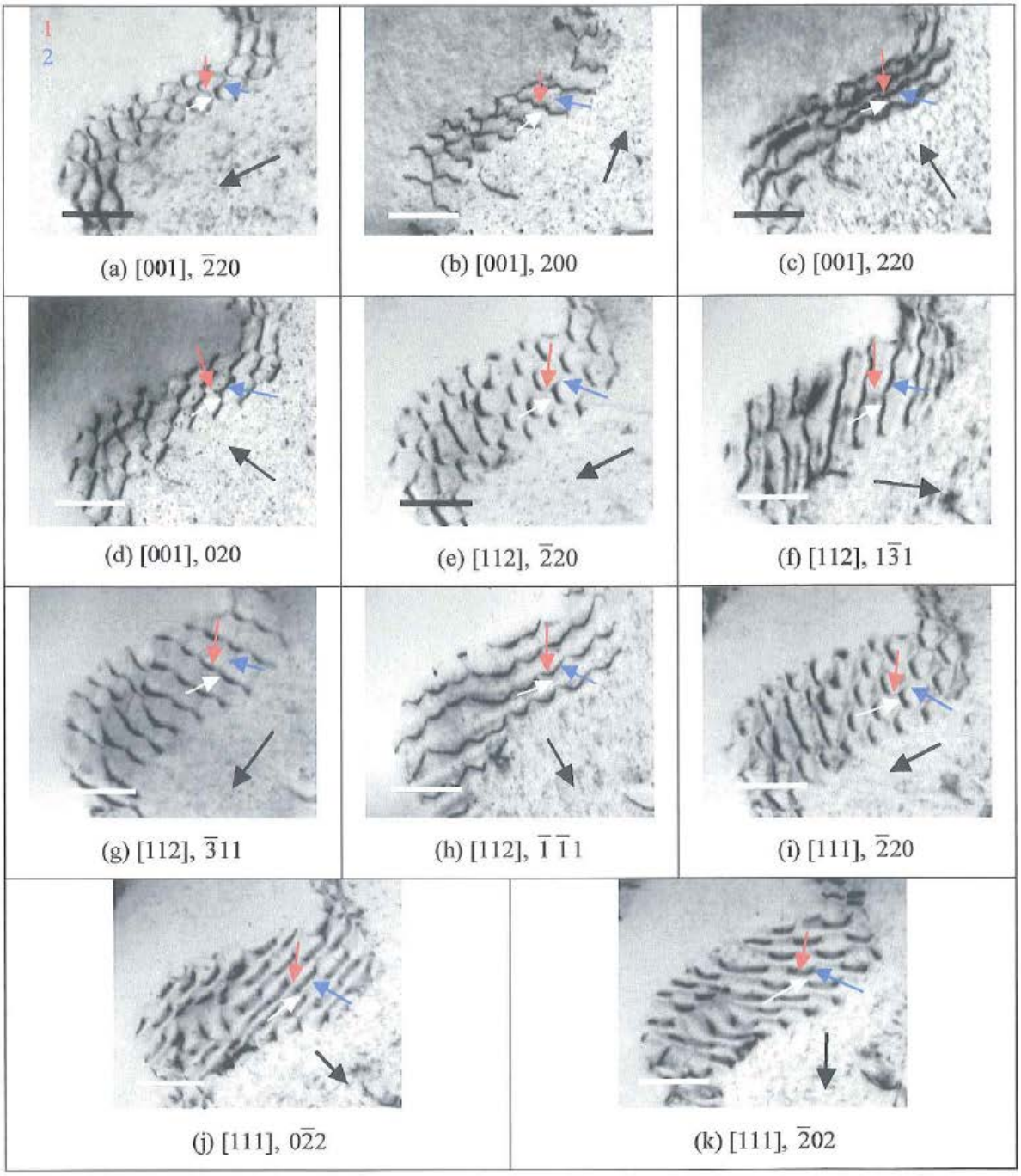


Figure 2.48. Bright field TEM micrographs of $Pt_{86}Al_{10}Ti_4$ (at.%) deformed at 1100˚C, showing a hexagonal dislocation network in the matrix/precipitate interface under various diffraction conditions (scale bar = 100nm) [2004Dou2].

In the Pt_{86}:Al_{10}:Ir_4 (at.%) alloy, the matrix and precipitate orientation relationships derived from the SAD pattern were: $(001)_M \| (100)_P$; $[110]_M \| [100]_P$. The γ′ precipitates contained a fine structure in the form of thin platelets within the broad plates, as shown in Figure 2.50 [2004Dou2]. Figure 2.50(a) is a dark field image of the same precipitate taken with a superlattice spot in order to show the thin platelets more clearly. These fine platelets are

indicative of a modification of the DO'_c crystal structure, and have also been observed in the γ' phase in $Pt_{86}Al_{10}Ru_4$ (at.%).

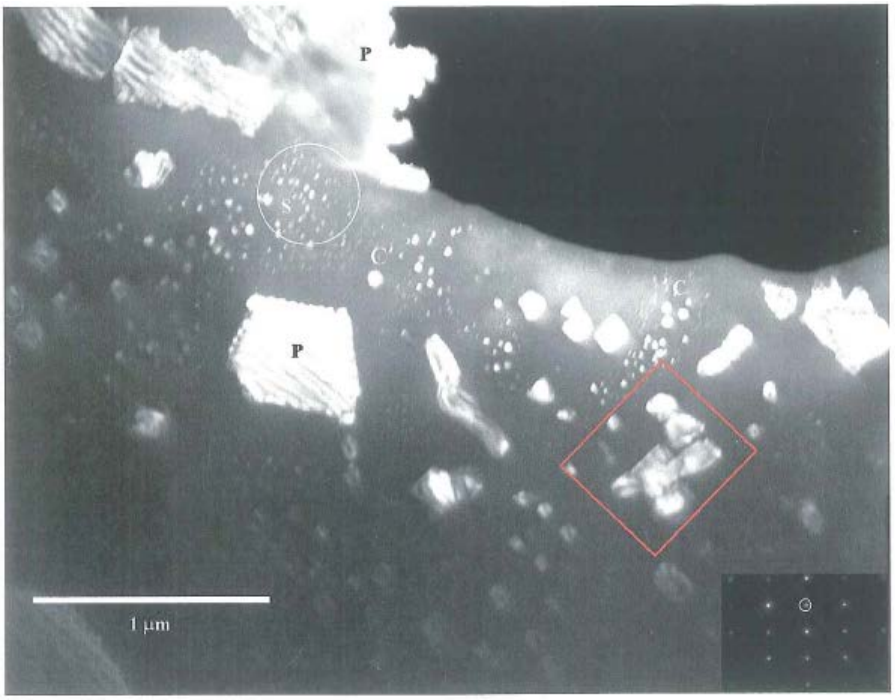


Figure 2.49. Bright field TEM micrographs of $Pt_{86}Al_{10}Ti_4$ (at.%) deformed at 1300˚C, showing coalesced cubic precipitates forming larger precipitates, as indicated in the rectangle [2004Dou2].

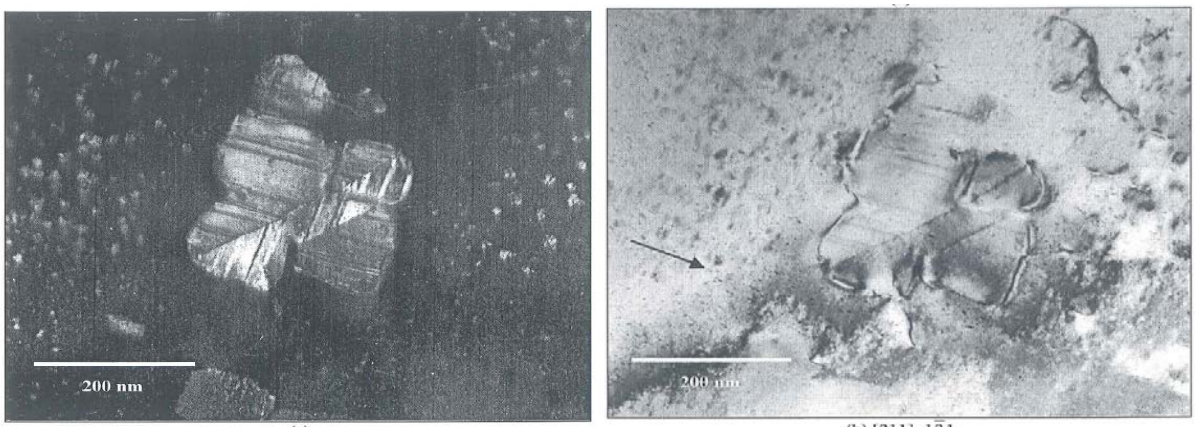


Figure 2.50. TEM images of room temperature compressed $Pt_{86}Al_{10}Ir_4$ (at.%) alloys, a) dark field image showing the thin platelets within the broad plates in a γ' precipitate, and b) bright field image of a precipitate showing the thin platelets [2004Dou2].

2.5.5 Development of Pt-Al-Cr-Ni Pt-based Superalloys

2.5.5.1 Quaternary Pt-Al-Cr-Ni alloys

Since nickel has a good solid-solution strengthening effect on the (Pt) matrix [2002Zha2], it was added to a Pt-Al-Cr alloy in varying amounts [2005Hül]. Nominal compositions of the alloys had a Pt:Al:Cr at.% ratio of about 86:11:3, in keeping with preceding results on the alloy Pt_{86}:Al_{10}:Cr_4 (at.%) [2002Süs1]. $Pt_{86\text{-}76}$:Al_{11}:Cr_3:$Ni_{0–10}$ (at.%) alloys with up to 10 at.% Ni were arc-melted under argon to make button ingots of about 4 g. Each sample was turned and remelted 2 times to promote homogeneity. Metallographic preparation was carried out by embedding the samples in phenolic resin with a carbon filler, then grinding, followed by polishing with diamond paste down to 1μm particle size. The samples were electrolytically etched for 20 seconds with 5V direct current in 5 % aqueous solution of potassium cyanide (KCN). Alloying the Pt-Al system with both Cr and Ni consistently stabilized the $L1_2$ high temperature form of Pt_3Al at room temperature [2005Hül]. The $Pt_{86\text{-}76}$:Al_{11}:Cr_3:$Ni_{0–10}$ (at.%) alloys were all single-phase after solution heat treatment at 1450°C. Ageing at 1000°C produced microstructures similar to Ni-based superalloys. Precipitates in alloys with less than 6 at.% Ni appeared to lose coherency after ageing [2005Hül]. The Pt_{80}:Al_{11}:Cr_3:Ni_6 (at.%) alloy after ageing not only had the highest γ′ volume fraction, ~23%, but also had well-aligned cuboid precipitates, with 0.2–0.5μm widths and a misfit of -0.1%, similar to Ni-based superalloys. Spherical particles were observed in alloys with more than 6 at.% Ni. These changes of γ′ morphologies were correlated to decreasing values of the misfits with increasing Ni concentration, so that positive values gave round ~Pt_3Al precipitates, values of ~-0.002 gave a cuboid morphology, and values of ~-0.005 gave an irregular morphology [2006Vor]. Ageing at 1100°C led to coarse γ′ particles and reduced γ′ volume fractions. However, volume fractions decreased less with temperature in alloys containing Ni than in those without Ni.

Alloys in the range Pt-$Al_{12–15}$:Cr_3:$Ni_{4–8}$ (at.%) were chosen near the solubility limit of about 15 at.% Al in order to achieve high γ′ volume fractions [2005Hül, 2005Wen1]. Alloys with up to 13 at.% Al were successfully homogenized in the single phase γ region at 1500°C, and still higher Al contents formed a eutectic, even after heat treating at 1530°C. Ageing alloys with up to 13 at.% Al for 120h at 1000°C led to homogeneous distributions of ~Pt_3Al particles. Alloy Pt_{79}:Al_{14}:Cr_3:Ni_6 (at.%) showed cubic ~Pt_3Al particles with 520μm average widths (Figure 2.51(b) [2005Wen1]), a microstructure very close to that of Ni-based superalloys.

The absolute lattice misfit between γ and γ′ decreased with increasing Ni content. Once again, the slightly negative misfits found at room temperature, together with cubic or spherical particles (Table 2.7 [2006Vor]), signified coherency between γ and γ′ in alloys with more than 5 at.% Ni (Figure 2.51(b and c) [2005Wen1]). A lack of coherency was apparent in the alloy with Ni below 5 at.% and high negative misfit of about -0.5 % (Figure 2.51(a) [2005Wen1]). By raising the concentration of the major γ′-forming element, Al, up to 13 at.%, the γ′ volume fraction was increased to 30% [2005Wen1].

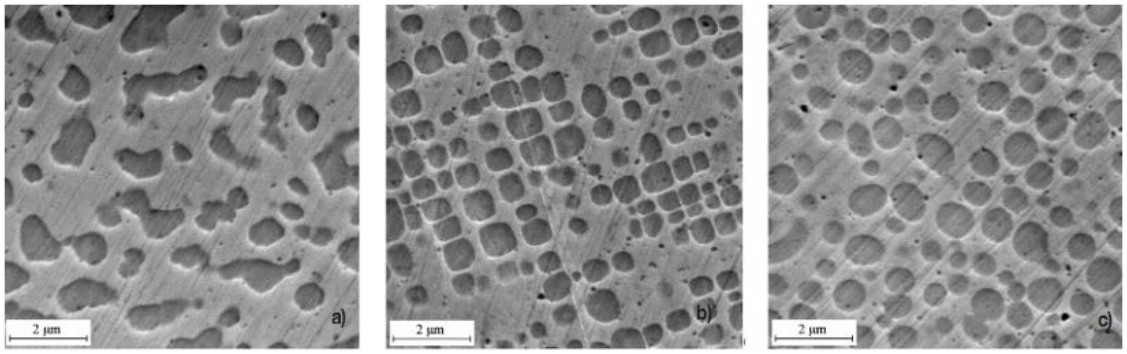


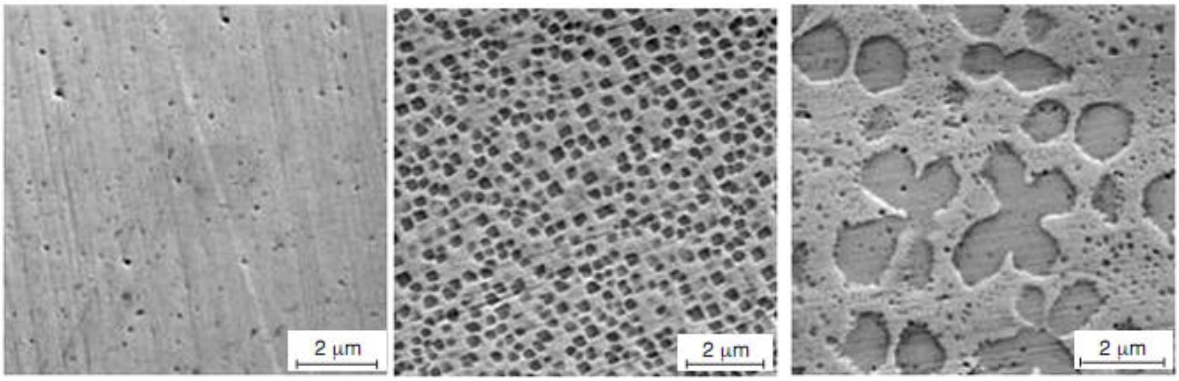
Figure 2.51. SEM-SE images of alloys annealed for 12h at 1500°C and 120h at 1000°C in Ar, showing ~Pt_3Al (dark) in (Pt) (light) two-phase microstructures: (a) Pt_{79}:Al_{14}:Cr_3:Ni_4, (b) Pt_{77}:Al_{14}:Cr_3:Ni_6, and (c) Pt_{75}:Al_{14}:Cr_3:Ni_8 (at.%) [2005Wen1].

Table 2.7. Lattice misfits at room temperature after heat treatment and water quench, determined by XRD [2006Vor].

Nominal Composition (at.%)	Heat Treatment	Misfit (%)	γ′ Shape
Pt_{77}:Al_{14}:Cr_3:Ni_6	12h at 1530°C	-0.3	Cubes, partly aligned
Pt_{79}:Al_{14}:Cr_3:Ni_4	12h at 1530°C, 120h at 1000°C	-0.5	Irregular, coarsened
Pt_{77}:Al_{14}:Cr_3:Ni_6	12h at 1530°C, 120h at 1000°C	-0.1	Cubes, aligned
Pt_{75}:Al_{14}:Cr_3:Ni_8	12h at 1530°C, 120h at 1000°C	0.0	Spherical

In another alloy series, the composition range was Pt-$Al_{12.5}$:$Cr_{0–6}$:Ni_6 (at.%) to ensure coherency between γ and γ′. Dendritic as-cast structures of Pt-$Al_{12.5}$:Cr_3:Ni_6 (at.%), Pt-Al_{12}:Ni_6 (at.%) and Pt-Al_{12}:Cr_6:Ni_6 (at.%) were homogenized by heat treatment at 1500-1510°C [2005Hül, 2005Vor, 2005Wen1]. Different cooling regimes were tried. Formation of ~Pt_3Al precipitates was almost completely suppressed in Pt-$Al_{12.5}$:Cr_3:Ni_6 (at.%) after homogenization for 12h at 1500°C and subsequent water quenching (Figure 2.52(a) [2006Völ]), demonstrating that all the ~Pt_3Al could be taken into solid solution at 1500°C. Air cooling led to homogeneous distributions of ~Pt_3Al particles with 200nm average widths

and a volume fraction of about 30% (Figure 2.52(b) [2006Völ]). Furnace cooling from 1500°C produced a bimodal particle distribution with a coarse particle fraction (Figure 2.52(c) [2006Völ]), and a γ′ volume fraction of 34%. Increasing the Cr content to 6 at.% led to γ′ average sizes of 500nm and a volume fraction of 50% in Pt-Al_{12}:Cr_6:Ni_6 (at.%) after homogenization for 6h at 1500°C, then 6h at 1510°C in Ar, followed by air cooling. For these Pt-based superalloys, controlled air cooling after solution heat treatment was sufficient to achieve the targeted microstructure, similar to Ni-based superalloys.



a) **b)** **c)**

Figure 2.52. SEM-SE images of Pt-$Al_{12.5}$:Cr_3:Ni_6 (at.%) after homogenization for 12h at 1500°C with different cooling regimes: (a) water quenched, (b) air cooled, and (c) furnace cooled [2006Völ].

Pt–Al–Cr–Ni alloys with different γ′ volume fractions were investigated by Wenderoth *et al.* [2005Wen2] in terms of microstructure and compression strength at high temperature. Compositions on the γ/γ′ tie-line of Pt_{77}:Al_{12}:Cr_6:Ni_5 (at.%) heat treated at 1200°C were chosen in order to obtain alloys with γ′ volume fractions of ~0%, ~25%, ~50%, ~75% and ~100%. The investigated alloy compositions were (A) Pt_{78}:Al_8:Cr_7:Ni_7, (B) Pt_{78}:Al_{11}:Cr_6:Ni_5, (C) Pt_{77}:Al_{13}:Cr_6:Ni_4, (D) Pt_{76}:Al_{14}:Cr_6:Ni_4 and (E) Pt_{75}:Al_{15}:Cr_5:Ni_5 (at.%). Alloy samples for mechanical tests and SEM investigations were homogenized for 6h at 1500°C and 6h at 1510°C with subsequent air cooling. A number of samples were aged for 72h at 1200°C with subsequent water quenching and without prior homogenization to provoke the growth of large γ′ particles and single-phase γ regions for electron probe microanalysis (EPMA). The samples for SEM and EPMA were ground, polished and electrolytically etched with 5 % aqueous solution of potassium cyanide (KCN). From the homogenization heat treated button ingots, cylindrical compression test samples of 4mm diameter and 4mm length were cut by electron discharge machining (EDM) and all sides were ground to 600 mesh finish. High temperature compression tests with a strain rate of $10^5 s^{-1}$ were conducted under a 10^{-3}Pa

vacuum. After ageing at 1200°C without prior homogenization, the γ′ volume fractions were determined by image analysis [2005Wen1]. The γ′ particles were marked manually in several digital SEM micrographs for each alloy. The digital SEM micrographs were successively converted into binary images by means of the standard software Photoshop (Adobe Systems Inc.). The γ′ area fraction was given by the number of pixels belonging to γ′ divided by the number of pixels in the entire micrograph. The standard deviations of the area fractions were below ±2% in each case [2005Wen1, 2005Wen2]. The γ′ volume fractions of the alloys after ageing were A: 2±2%, B: 29±2%, C: 52±2%, D: 77±2% and E: 94±2% [2005Wen2]. Compression tests of the alloys after homogenization heat treatment (Figure 2.53 [2005Wen2]) showed that Alloy A had the lowest strength at all investigated temperatures. Alloy C had the highest strength at 800°C, but at 1000°C and 1200°C the highest strength was observed for Alloy E (Figure 2.53 [2005Wen2]).

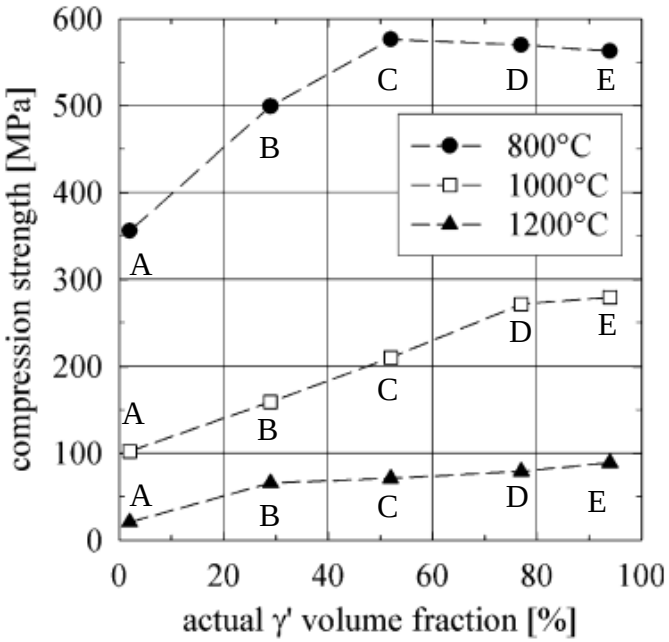


Figure 2.53. High temperature compression strengths of Pt-based alloys homogenized at 800°C, 1000°C and 1200°C as a function of the γ′ volume fraction [2005Wen2].

2.5.5.2 Substitution of Ni in Pt-Al-Cr-Ni

In a trial-and-error approach, the high melting elements Nb, Ta and Ti were chosen [2005Hül, 2005Vor, 2005Wen1] to substitute nickel. By XRD analysis, the fcc γ matrix and the $L1_2$-ordered γ′ ~Pt_3Al phases were identified in Pt_{82}:Al_7:Cr_6:Nb_5, Pt-Al_7:Cr_6:Ta_5 and Pt_{82}:Al_7:Cr_6:Ti_5 (at.%). The lattice misfit ratios were ~-3 x 10^{-3} in all alloys. After

homogenization, the alloys showed bimodal size distributions of the γ′ particles (Figure 2.54 [2006Völ]). Besides coarse and irregularly shaped particles with a volume fraction between 10 and 20%, small cuboids of up to 300µm in size were observed. After subsequent ageing for 264h at 1200°C with water quenching, measurement of the compositions revealed Nb and Ta to be almost evenly distributed within the γ matrix and γ′ precipitates, whereas Ti partitioned to the γ′ phase. The γ′ volume fractions after ageing were 34% in Pt_{82}:Al_7:Cr_6:Nb_5, 33% in Pt_{82}:Al_7:Cr_6:Ta_5 and 35% in Pt_{82}:Al_7:Cr_6:Ti_5 (at.%) [2006Völ].

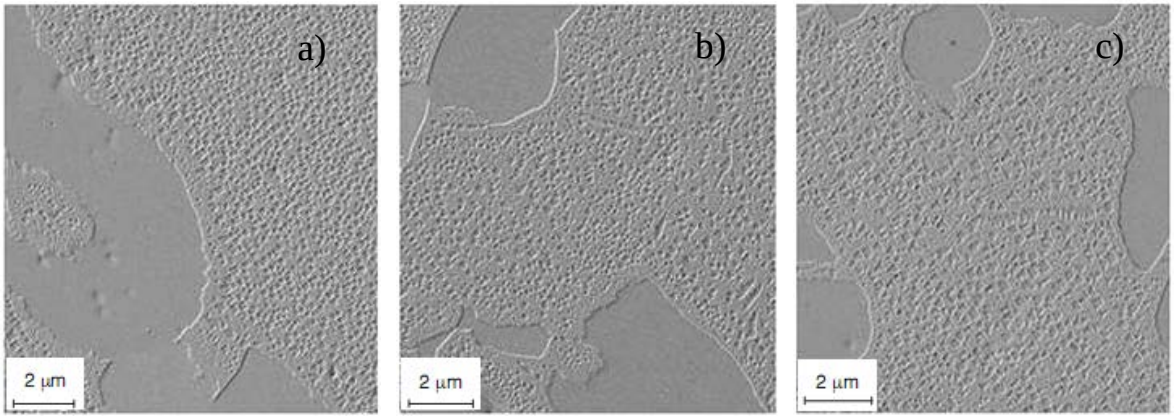


Figure 2.54. SEM-SE images of the γ-γ′ microstructures after heat treatment for 6h at 1500°C and 6h at 1510°C with air cooling: (a) Pt_{82}:A_{l7}:Cr_6:Nb_5, (b) Pt_{82}:Al_7:Cr_6:Ta_5, and (c) Pt_{82}:Al_7:Cr_6:Ti_5 (at.%) [2006Völ].

Compression strengths of polycrystalline Pt_{82}:Al_7:Cr_6:Nb_5, Pt_{82}:Al_7:Cr_6:Ta_5 and Pt_{82}:Al_7:Cr_6:Ti_5 (at.%) [2005Hül, 2005Vor, 2005Wen1, 2006Völ] were higher than the recorded 190MPa at 1000°C of Pt_{83}:Al_{12}:Cr_5 (Figure 2.55 [2006Völ]). At 800°C, Pt_{82}:Al_7:Cr_6:Ta_5 (at.%) was the strongest, whereas at higher temperatures, Pt_{82}:Al_7:Cr_6:Nb_5 (at.%) showed the highest strength. Above 1200°C, Pt_{82}:Al_7:Cr_6:Nb_5 and Pt_{82}:Al_7:Cr_6:Ta_5 (at.%) outperformed the CMSX-4 single-crystal Ni-based superalloy. The deformed samples experienced rupture on the outside surface, which was also observed in the case of the Nb- and the Ti-containing Pt-based alloys (Figure 2.56 [2006Völ]). Due to the ongoing dissolution of the γ′ phase at about 1250°C in NBSAs [1998Gro], the Pt-based superalloys are being developed for applications up to 1300°C [2000Wol]. Stress-rupture curves at 1300°C were determined for Pt 10%Rh, Pt 10%Rh DPH and Pt_{82}:Al_{12}:Cr_6:Ni_5 (at.%) (Figure 2.57 [2006Völ]), and the latter had the highest stress rupture strength.

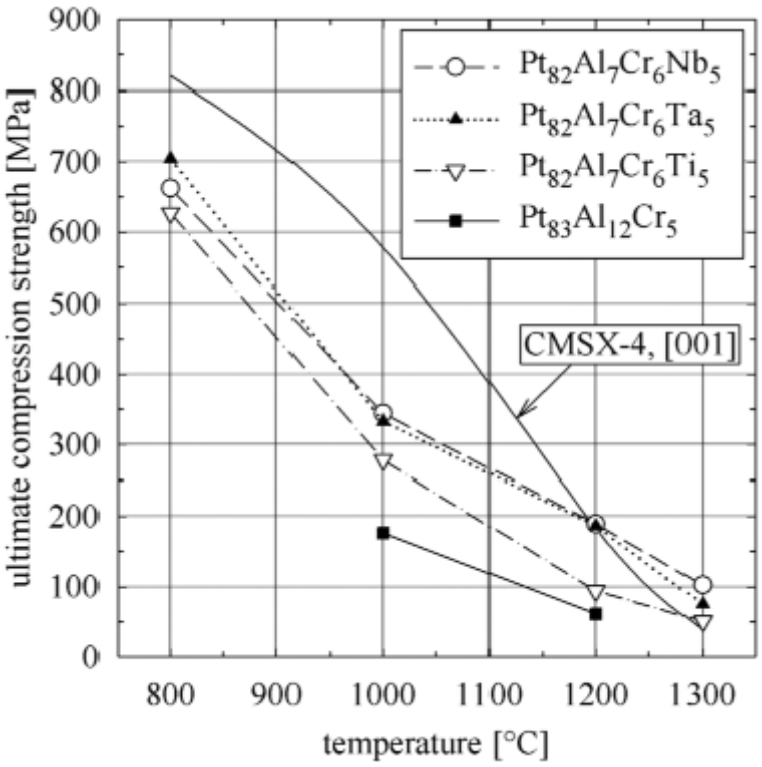


Figure 2.55. High-temperature compression strengths of polycrystalline Pt-Al-Cr-X alloys, Pt_{83}:Al_{12}:Cr_5 [2001Süs1] and the single-crystal Ni-based superalloy CMSX-4 [2006Völ].

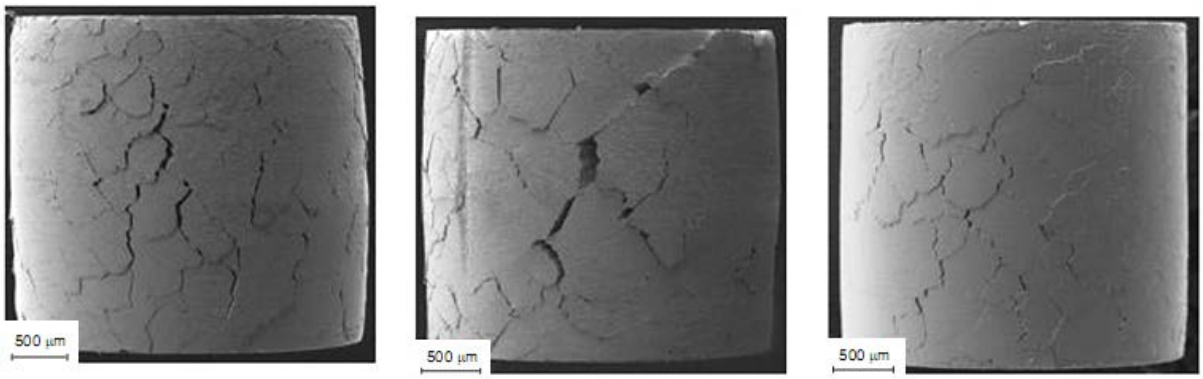


Figure 2.56. SEM-SE images of the Pt_{82}:Al_7:Cr_6:Ta_5 (at.%) compression samples deformed at: (a) 800°C, (b) 1000°C, and (c) 1300°C [2006Völ].

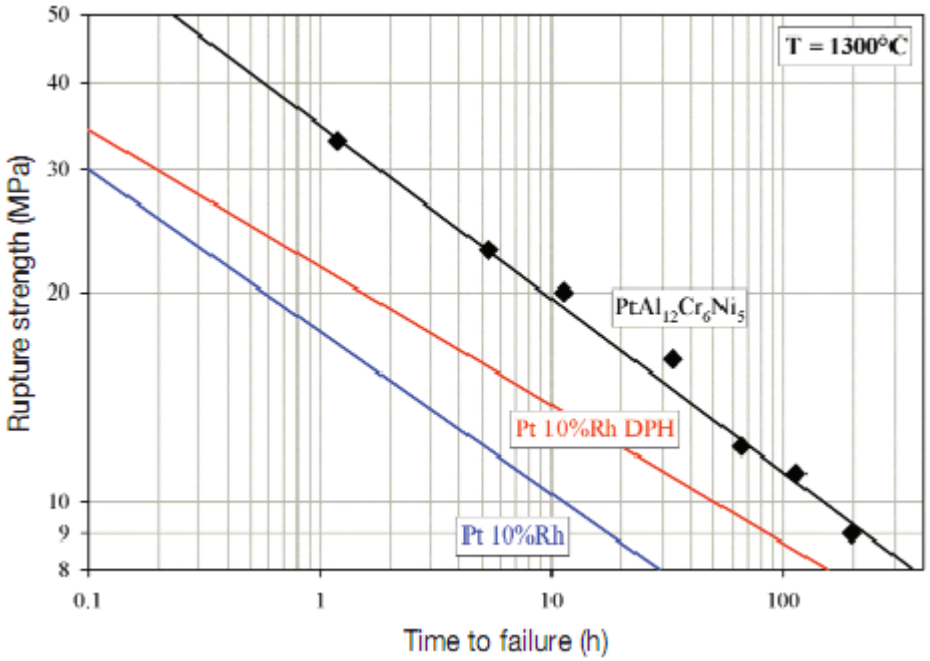
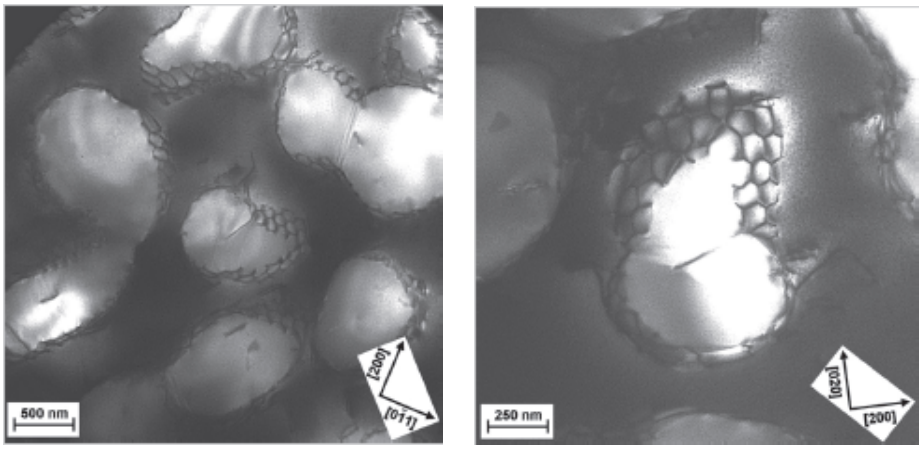


Figure 2.57. Stress-rupture strength curves of different Pt-based alloys at 1300°C [2004Völ].

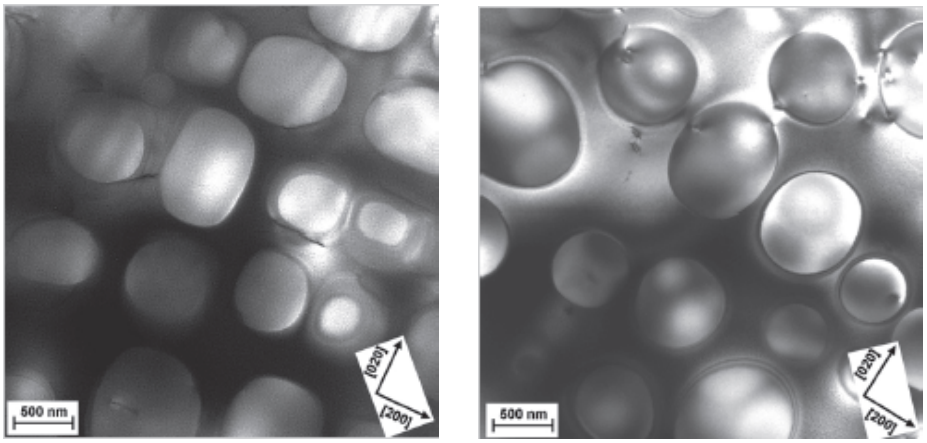
2.5.5.3 TEM Investigations of the γ/γ′ Phase Boundary in Pt-Al-Cr-Ni Alloys

In the TEM investigations by Vorberg and co-workers [2005Vor, 2005Wen2], dense dislocation networks were found in a Pt_{79}:Al_{14}:Cr_3:Ni_4 (at.%) alloy after homogenization for 12h at 1500°C and ageing for 120h at 1000°C. An alloy with higher nickel content (Pt_{75}:Al_{14}:Cr_3:Ni_8 (at.%)) showed low overall dislocation densities and the γ/γ′ phase boundaries were almost free of dislocations. The loss of coherency between the γ and γ′ phases in the alloy with low nickel content was explained by high lattice misfit [2005Vor, 2005Wen2]. Nickel was added in the alloys to act as a solid-solution strengthener, and for adjustment of the lattice misfit [2000Zha, 2005Wen1]. Transmission electron microscopy bright field images of alloy Pt_{79}:Al_{14}:Cr_3:Ni_4 (at.%) (with the lowest nickel content) are shown in Figure 2.58 [2005Vor, 2005Wen2]. The precipitates had irregular shapes with rounded edges. Dense hexagonal dislocation networks were found at the γ/γ′ interfaces, whereas the γ matrix was almost free of dislocations. Near-cubic precipitates, analogous to those in nickel-based superalloys, were observed in Pt_{77}:Al_{14}:Cr_3:Ni_6 (at.%) (Figure 2.59(a) [2005Vor]). Spherical γ′ particles with an average diameter of 750nm were observed in Pt_{77}:Al_{14}:Cr_3:Ni_6 (at.%) (Figure 2.59(b) [2005Vor]). The γ/γ′ phase boundaries, as well as the matrix, were free of dislocations [2005Vor].



(a) **(b)**

Figure 2.58. Many beam bright field TEM images of Pt_{79}:Al_{14}:Cr_3:Ni_4 (at.%) after homogenization for 12h at 1500°C and subsequent water quenching, then ageing for 120h at 1000°C and subsequent water quenching, showing hexagonal dislocation networks at γ/γ' phase boundaries: (a) $\vec{k}_0$ = [011], (b) $\vec{k}_0$ = [001], where $\vec{k}_0$ is the beam direction [2005Vor].



(a) **(b)**

Figure 2.59. Many beam bright field TEM images of Pt_{77}:Al_{14}:Cr_3:Ni_6 (at.%) after homogenization for 12h at 1500°C and ageing for 120h at 1000°C, both with subsequent water quenching, $\vec{k}_0$ = [001] [2005Vor].

2.5.5.4 Microalloying of Pt-Al-Cr-Ni

Boron and rhenium were added to the Pt_{77}:Al_{12}:Cr_6:Ni_5 (at.%) alloy in varying amounts [2006Völ]. Boron was chosen since its small size can often enable it to segregate to grain boundaries and it can therefore influence grain boundary adhesion, while Re is very beneficial for the creep strength of Ni-based superalloys [2004Dur, 2006Völ]. Compression creep tests at 1200°C revealed that minor B additions increased both creep strength and

ductility considerably (Figure 2.60(a) [2006Völ]). Additions of 0.3 at.% B, together with 2 at.% Re, further increased creep strength (Figure 2.60(b)) [2006Völ].

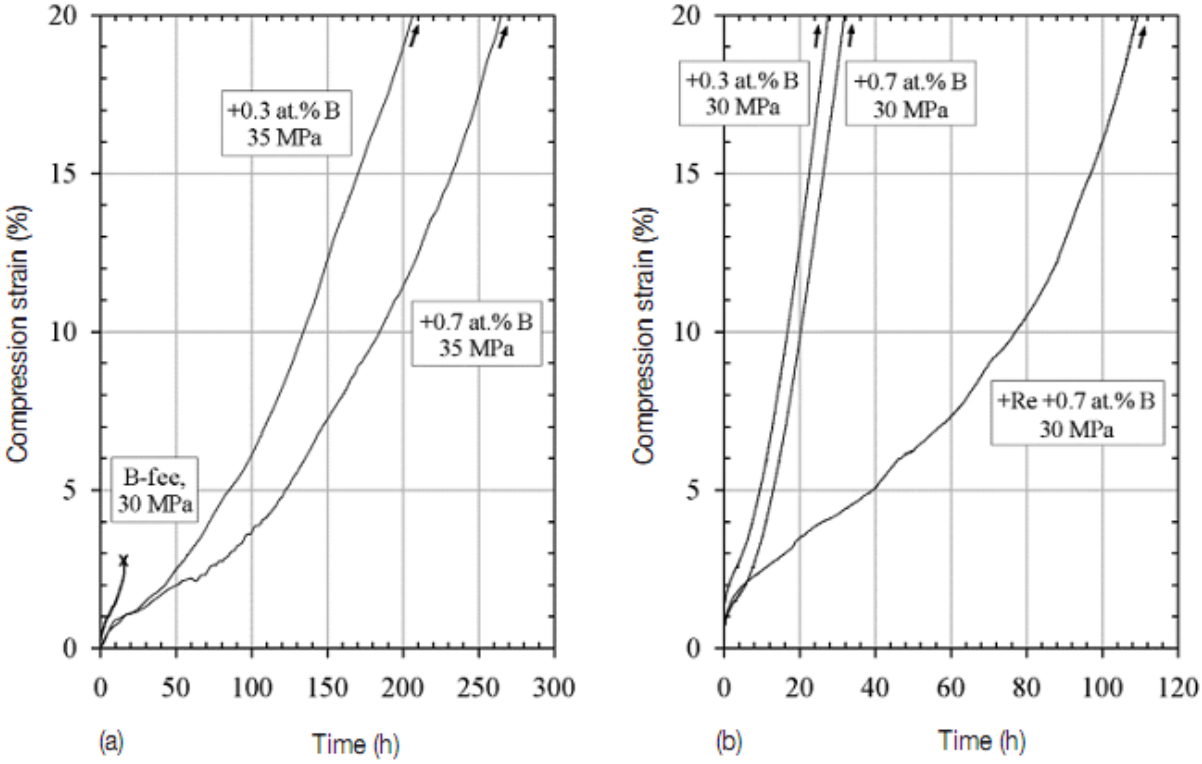


Figure 2.60. Compression creep curves of Pt_{77}:$Al_{12}Cr_6Ni_5$ (at.%): a) base alloy compared to alloys microalloyed with 0.3 and 0.7 at.% B at 1200°C, and b) alloys microalloyed with 0.3 and 0.7 at.% B, and with 2 at.% Re + 0.7 at.% B at 1300°C [2006Völ].

Further work has been done by Wenderoth and co-workers [2007Wen] on Pt-Al-Cr-Ni alloys with additions of 2 at.% Mo, Re, Ru and W. After the homogenisation heat treatment and air cooling, all alloys showed a bimodal distribution of γ′ precipitates. Molybdenum, Re, and W additions increased strength above 1000°C, whereas Ru had no beneficial effect. Tungsten increased the γ′ volume fraction most effectively. However, the oxidation resistance was worsened considerably by W additions, and Re-containing alloys showed the best resistance against γ′ growth and coarsening during long-term ageing [2007Wen].

2.5.6 Nanoindentation and Nanomechanical Properties of Pt-Based Superalloys

This section reviews work that has been done on nanoindentation of Pt-based superalloys relevant to this research work.

The local nanomechanical properties of γ matrix and γ′ precipitates in a Pt_{75}:Al_{12}:Cr_6:Ni_5:Re_2 (at.%) alloy were investigated by Nikulina *et al*. [2010Nik] by nanoindentation. The alloy was prepared from pure elements (99.9 wt%) by arc-melting under an argon atmosphere. In order to avoid melting of the residual eutectic in the interdendritic regions after non-equilibrium solidification, the button ingots were solid solution heat treated in air in two steps. The first annealing for 6h at 1500°C, below the equilibrium eutectic temperature of 1507°C in the Pt-Al binary [1986McA], was immediately followed by a second homogenization annealing for 6h at 1510°C, and after each heat treatment the sample was water quenched. Subsequently, samples were aged for 120h at 1200°C and then air cooled. Any further sample preparation for nanoindentation was not stated. Nanoindentations were performed using a Hysitron triboscope on a DI multimode AFM and a 3-sided diamond Berkovich type indenter. For indentation, a trapezoidal load profile was used with a holding time of 20s at maximum load levels of 0.5, 1.0, 5.0 and 10.0mN. The small load levels (i.e. 0.5 and 1.0mN) were used for probing the properties of the individual phases, and large loads for testing the properties of the alloy. At least five individual indentations were averaged for determining the nanohardness and modulus of elasticity of the matrix and precipitates.

Figure 2.61 [2010Nik] shows AFM images of the residual indentations at 1.0 and 10.0mN maximum load levels. Figure 2.62 [2010Nik] shows a typical load-displacement curve of the matrix and primary precipitates at a 0.5mN load. At the same applied load, a smaller indentation depth was found for the γ′ precipitates, indicating a higher hardness compared to the matrix. At a load of 1mN, the nanohardness of Pt_{75}:Al_{12}:Cr_6:Ni_5:Re_2 (at.%) was 11.5GPa for the γ′ precipitates and 7.5GPa for the matrix. From the load-displacement curves, the modulus of elasticity and the nanohardness were evaluated using the Oliver-Pharr method [1992Oli, 2002Pha] (Figure 2.63), which is described in Appendix E. For indentation loads of 0.5mN and 1mN, nearly the same nanohardness was found, indicating that even at 1mN, the particle properties were tested. However, at larger loads (e.g. 5mN), the nanohardness values converged to the alloy's hardness. The nanohardness and modulus of elasticity for γ′ and γ were comparable to the values of NBSAs PWA 184 [2003Wöl] and CMSX-4 [2004Dur].

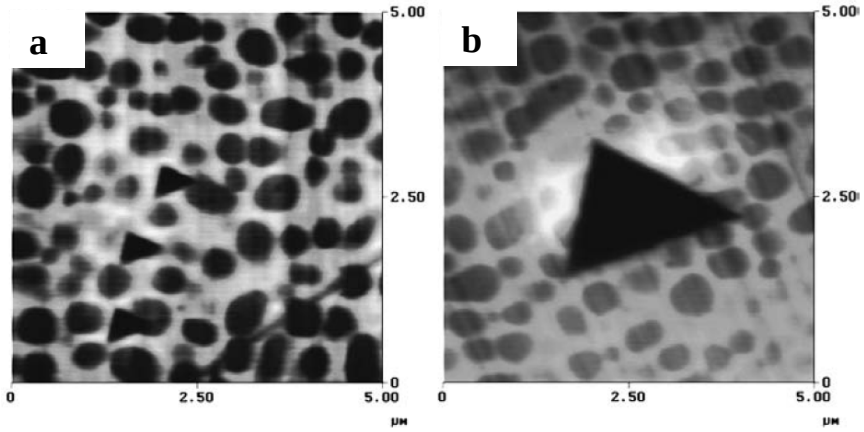


Figure 2.61. AFM images of Pt_{75}:Al_{12}:Cr_6:Ni_5:Re_2 (at.%) with nanoindentations (black triangles) performed with a Berkovich tip at applied loads of: (a) 1.0mN, and (b) 10.0mN [2010Nik].

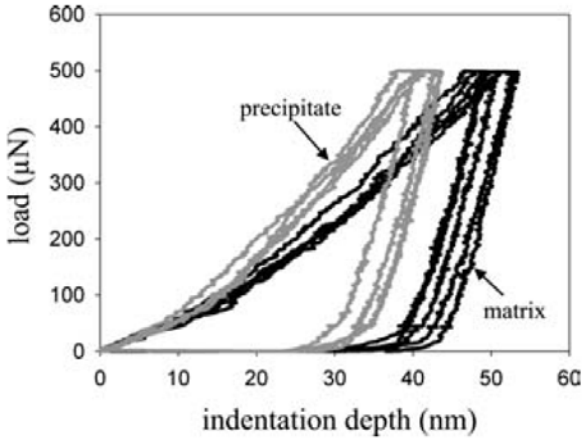
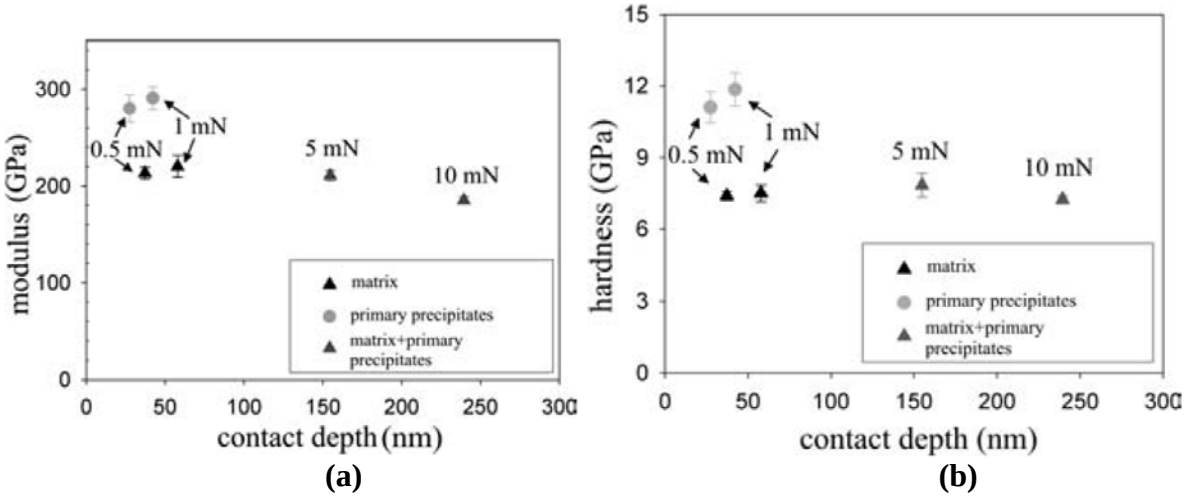


Figure 2.62. Load-displacement curves for the matrix and primary precipitates at 0.5mN applied load [2010Nik].



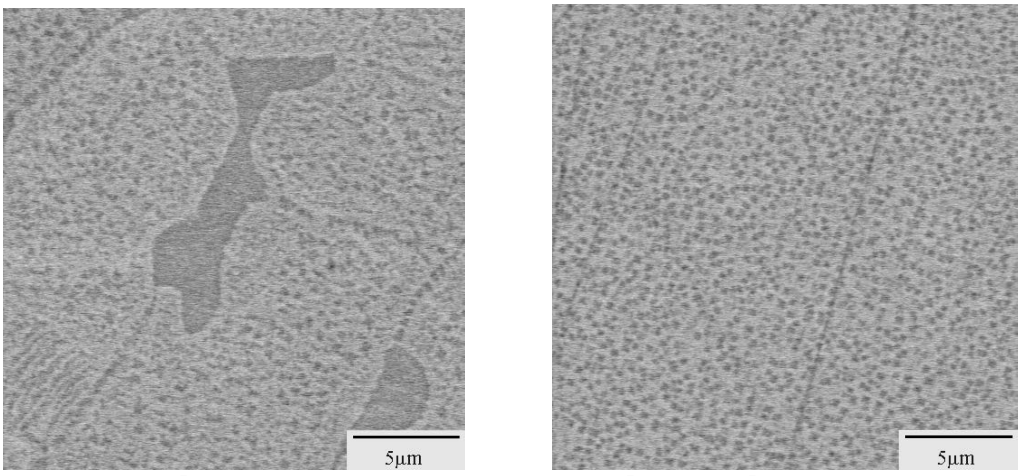
(a) **(b)**

Figure 2.63. Properties of Pt_{75}:Al_{12}:Cr_6:Ni_5:Re_2 (at.%): (a) modulus of elasticity, and (b) nanohardness for different loading levels [2010Nik].

2.5.7 Quaternary Pt-Al-Cr-Ru Superalloys and their Derivations

This section gives more attention to work done on Pt-Al-Cr-Ru alloys, how the ternary alloys compare with the quaternary alloys, quinary alloys, and the recent work which was focused on the optimisation and heat treatments of Pt-Al-Cr-Ru. A sub-section is also devoted to the corrosion behaviour of selected Pt-based alloys (ternary and quaternary) compared with those of coated and uncoated CMSX-4 NBSAs.

The composition of the Pt-Al-Cr-Ru quaternary alloy needed to be optimised so that a higher proportion of the ~Pt_3Al second phase was achieved, to enhance the strength of the alloy's. Several alloys were therefore manufactured with this objective [2002Cor], and the compositions were selected based on the results of the ternary Pt-Al-Cr and Pt-Al-Ru systems [2001Süs1]. The alloys were prepared by arc-melting the pure elements together and turning the buttons several times to achieve the highest possible homogeneity, followed by heat treatment at 1350ºC for 96h. Hardnesses of the alloys were measured using a Vickers hardness tester with a 10 kg load. Some of the alloys were single-phase, and these showed cracking around the indentations [2002Cor]. Two alloys, Pt_{78}:$Al_{15.5}$:$Cr_{4.5}$:Ru_2 and $Pt_{81.5}$:$Al_{11.5}$:$Cr_{4.5}$:$Ru_{2.5}$ (at.%), had large areas of ~Pt_3Al, together with a fine mixture of (Pt) and ~Pt_3Al (Figure 2.64(a) [2002Cor]). Another alloy, Pt_{84}:Al_{11}:Cr_3:Ru_2 (at.%), was composed entirely of a fine two-phase mixture, which was the desired microstructure (Figure 2.64(b) [2002Cor]).



a) $Pt_{81.5}$:$Al_{11.5}$:$Cr_{4.5}$:$Ru_{2.5}$ (at.%) **b) Pt_{84}:Al_{11}:Cr_3:Ru_2 (at.%)**

Figure 2.64. SEM-BSE images of the two-phase Pt-based alloys: a) $Pt_{81.5}$:$Al_{11.5}$:$Cr_{4.5}$:$Ru_{2.5}$ (at.%) with primary ~Pt_3Al (dark contrast) in a fine matrix of (Pt) (light) and ~Pt_3Al, and b) Pt_{84}:Al_{11}:Cr_3:Ru_2 (at.%) with a fine matrix of (Pt) and ~Pt_3Al [2002Cor].

The volume fraction of ~Pt_3Al was estimated, using image analysis, to be approximately 25% to 30% [2002Cor, 2009Cor2]. More alloys were produced in an attempt to increase the volume fraction of the ~Pt_3Al precipitates. After heat treatment (again, 96 hours at 1350ºC in air), some oxidation took place, and, due to the small sample size (and large surface area), losses of aluminium also occurred. No improvement in the microstructure was observed. The hardnesses of the alloys were measured and the results are given in Table 2.8 [2002Cor]. The alloys were reasonably ductile, with no cracking around the indentations, unlike some of the earlier single-phase quaternary alloys [2002Cor]. In an attempt to improve the microstructure, a second heat treatment was conducted for 96 hours at 1350ºC, after which the alloy $Pt_{81.5}$:$Al_{11.5}$:$Cr_{4.5}$:$Ru_{2.5}$ (at.%) showed a clear, fine two-phase microstructure, possibly due to the change in its overall composition. There was no primary ~Pt_3Al (so the overall composition is that of the two-phase mixture: 85.2 ± 0.3 at.% Pt, 7.1 ± 0.8 at.% Al, 3.1 ± 0.8 at.% Ru and 4.6 ± 0.1 at.% Cr). The loss of Al was concerning, especially after such a short anneal, but that was the only alloy to suffer such a large change. After the second heat treatment, the precipitates in Pt_{84}:Al_{11}:Cr_3:Ru_2 (at.%) were approximately twice the size of the precipitates in Pt_{85}:Al_7:Cr_5:Ru_3 (a.t%) and more well-defined than those of Pt_{85}:Al_7:Cr_5:Ru_3 (at.%) [2002Cor].

Table 2.8. Vickers hardness, using a 10 kg load, of two-phase quaternary alloys after annealing at 1350ºC for 96 hours [2002Cor].

Nominal alloy composition (at.%)	Hardness after first anneal (HV_{10})	Hardness after second anneal (HV_{10})
Pt_{85}:Al_{11}:Cr_2:Ru_2	430 ± 5	403 ± 20
Pt_{84}:$Al_{11.5}$:$Cr_{2.5}$:Ru_2	425 ± 21	403 ± 14
Pt_{83}:Al_{11}:$Cr_{3.5}$:$Ru_{2.5}$	421 ± 12	405 ± 8
$Pt_{80.5}$:$Al1_{2.5}$:$Cr_{4.5}$:$Ru_{2.5}$	419 ± 22	414 ± 9
$Pt_{81.5}$:$Al_{11.5}$:$Cr_{4.5}$:$Ru_{2.5}$	423 ± 10	396 ± 6
$Pt_{79.5}$:$Al_{10.5}$:$Cr_{5.5}$:$Ru_{4.5}$	417 ± 8	415 ± 10

The Vickers hardnesses of the Pt:Al:Cr:Ru alloys within the composition ranges selected were relatively independent of both alloy content and the number of annealing stages, and fell within the range HV_{10} ~400 to ~430 [2002Cor]. Hardnesses were slightly lower after the second anneal (Table 2.8 [2002Cor]). The volume fraction of ~Pt_3Al was estimated, using image analysis, to be approximately 25% to 30%. The highest hardness was found in the alloy without primary ~Pt_3Al. In the second batch of quaternary alloys, there was no clear

relationship between the hardness and the composition or microstructure. The decrease in hardness after the second heat treatment was likely to be due to the changes in composition due to oxidation [2002Cor]. The best alloy at this stage was Pt_{84}:Al_{11}:Ru_2:Cr_3 (at.%), which had the required fine two-phase structure, with no primary ~Pt_3Al and reasonable hardness.

Similar alloys annealed at 1300ºC for 96 hours and quenched in water gave better all-round results for Pt_{80}:Al_{14}:Ru_3:Cr_3 than Pt_{86}:Al_{10}:Cr_4 (at.%) because there was more of the ~Pt_3Al phase, although it was more coarse, as shown in Figure 2.65 [2003Ker1, 2003Ker2, 2003Ker3]. The high-temperature compressive strength of Pt_{84}:Al_{11}:Cr_3:Ru_2 (at.%) was significantly higher than that of Pt_{86}:Al_{10}:Cr_4 (at.%) [2003Ker1, 2003Ker3].

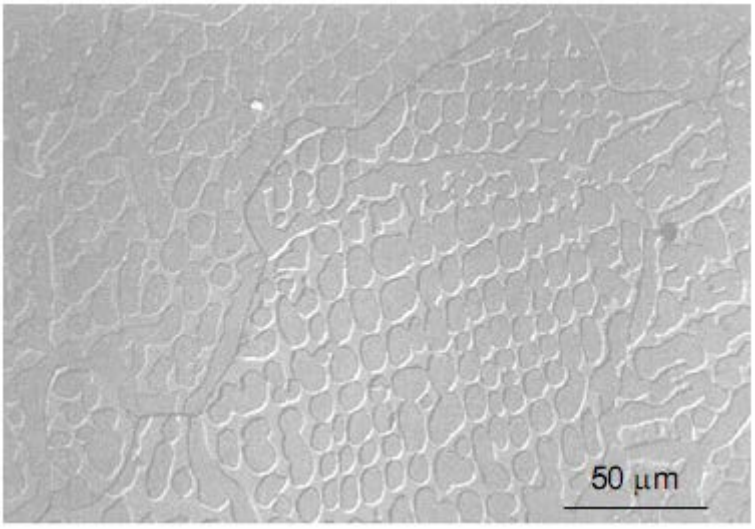


Figure 2.65. SEM-SE image of Pt_{80}:Al_{14}:Cr_3:Ru_3 annealed at 1400ºC for 96 hours and water quenched, showing ~Pt_3Al (discrete, raised) in a (Pt) matrix [2003Ker1, 2003Ker2, 2003Ker3].

2.5.7.1 Oxidation

Since Pt_{86}:Al_{10}:Cr_4 (at.%) was very promising with regard to high-temperature strength and oxidation resistance, it was decided to test a quaternary alloy (Pt_{80}:Al_{14}:Cr_3:Ru_3 (at.%)) to verify that the good oxidation resistance was retained [2001Hil3, 2001Süs1]. More Al was added in an effort to accelerate the protective oxide scale formation [2001Hil4, 2001Süs2]. After one hour at 1350ºC, a thin continuous oxide layer had formed. After 10 hours exposure (Figure 2.66 [2001Süs2]), the scale was already about three times as thick as that observed on Pt_{86}:Al_{10}:Cr_4 (at.%) after the same time period [2001Süs2]. No zone of discontinuous oxides, nor any other internal oxidation, was observed, as had been seen in some of the earlier ternary

alloys, Pt:Al:X where X = Re, Ta and Ti [2000Hil1, 2001Süs1]. The increased Al content of the alloys clearly accelerated the formation of a continuous layer, and prevented mass loss due to volatilisation. Although this showed good properties for the short test period, in the long term, the oxidation of the alloy might be too severe. The alloy should ideally form a continuous oxide layer quickly, but then behave logarithmically with regard to mass increase [2001Hil4, 2001Süs2].

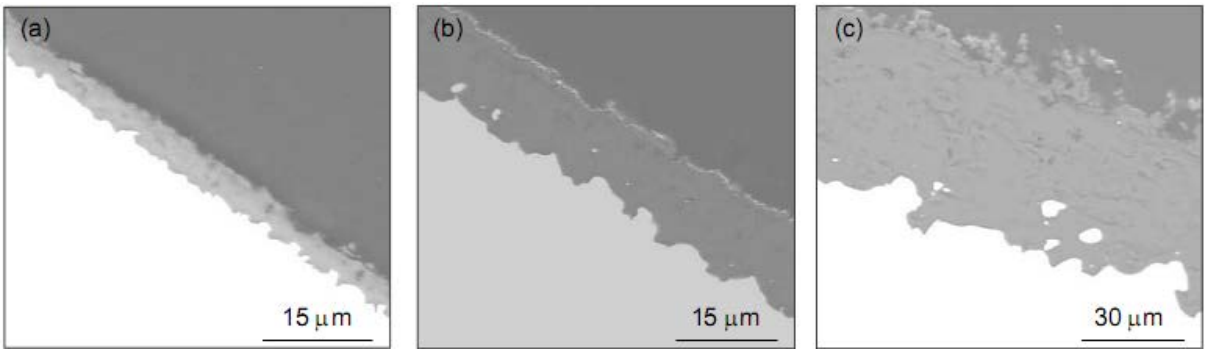


Figure 2.66. SEM-BSE images of transverse sections of Pt_{80}:Al_{14}:Cr_3:Ru_3 (at.%) after exposure to air at 1350ºC for increasing time: (a) 1 hour, (b) 10 hours, and (c) 500 hours [2001Süs2].

2.5.7.2 Tensile Testing

The room temperature tensile properties of the best ternary alloys were evaluated and compared with that of the quaternary alloy [2004Süs1]. The specimens were prepared from 50g ingots, manufactured by arc-melting, aged in air in a muffle furnace at 1250ºC for 100 hours, then quenched in water. This treatment produced a homogeneous two-phase microstructure, without primary ~Pt_3Al. Flat mini-tensile specimens were machined from each ingot by wire spark erosion. Tensile tests were performed at a cross-head speed of $5mm.min^{-1}$. Samples were prepared metallographically, and then Vickers hardness tests (20 kg load) were carried out. The average hardnesses, maximum ultimate tensile strength and estimated elongations are given in Table 2.9 [2004Süs1]. The results were spread out, inconsistent and unexpected, since it was anticipated that Ru, being a better solid solution strengthener in these alloys than Cr [2001Hil6], would produce Ru-containing alloys with a higher ultimate tensile strength. Characterisation was then undertaken to explain this discrepancy.

Table 2.9. Tensile test results for Pt-based alloys at room temperature [2004Süs1].

Alloy composition (at.%)	Hardness (HV_{10})	Maximum ultimate tensile strength achieved (MPa)	Elongation (%)
Pt_{86}:Al_{10}:Cr_4	317 ± 13	836	~4
Pt_{86}:Al_{10}:Ru_4	278 ± 14	814	~9
Pt_{84}:Al_{11}:Cr_3:Ru_2	361 ± 10	722	~1

One half of the sample was used and analysed with a SEM in backscattered electron imaging mode (BSE), as well as using energy dispersive X-ray spectrometry (EDX) [2004Süs2]. No significant differences between the targeted and actual compositions were found, although the Pt_{86}:Al_{10}:Cr_4 alloy was contaminated with ~ 0.2 at.% Ru and the Pt_{86}:Al_{10}:Ru_4 with ~ 0.2 at.% Cr [2004Süs1]. This contamination was thought to have arisen from minor sputtering during melting in the button arc furnace as the samples were part of the same batch. The fracture surfaces of the other half of each sample were also examined using SEM in secondary electron (SE) mode. TEM specimens were made and examined in a Philips CM200 [2004Süs]. XRD analyses were also conducted on polished samples using molybdenum K_α radiation.

The microstructures characterised by SEM, XRD and TEM analyses indicated that all samples contained both (Pt) and ~Pt_3Al precipitates [2004Süs1]. The volume fraction of the precipitates varied between the compositions. Pt_{86}:Al_{10}:Cr_4 (at.%) was harder and also had a higher ultimate tensile strength than Pt_{86}:Al_{10}:Ru_4 (at.%), because there was a very low volume fraction (~5%) of ~Pt_3Al precipitates in the alloy with Ru. Thus, it was deduced that Pt_{86}:Al_{10}:Ru_4 (at.%) had been annealed above its solvus, which was thought to be between 1250ºC and 1300ºC, to dissolve the precipitates. Thus, the higher ductility of this alloy was due to its nearly single-phase Pt solid solution without the strengthening precipitates. Having a significant volume fraction of ~Pt_3Al, Pt_{84}:Al_{11}:Cr_3:Ru_2 (at.%) was the hardest alloy, although it had the lowest ultimate tensile strength. The fracture surfaces (Figure 2.67 [2004Süs1]) showed that only Pt_{84}:Al_{11}:Cr_3:Ru_2 (at.%) failed intergranularly, with the ternary alloys failing mainly by intragranular cleavage with some localised dimpling. Thus, it is likely that the lower ultimate tensile strength was related to the intergranular failure mode, which also correlated to its lower elongation.

The results for the Pt-based alloys are summarised in Table 2.10 [2004Süs2], together with values for pure Pt and selected high-temperature alloys. The values of hardness and ultimate tensile strength for the Pt-based alloys were higher than those of pure Pt. Compared to other high-temperature alloys, such as the ferritic oxide dispersion strengthened (ODS) alloy PM2000 [2003Pro], γ-titanium-aluminium [2002Pat] and CMSX-4 [2001Mac], it was clearly demonstrated that these Pt-based alloys were within the range of the high-temperature alloys in terms of ultimate tensile strength at room temperature. The findings were encouraging since the samples had not been optimised in terms of either heat treatment or microstructure (they had just been homogenised). Creep testing of the Pt_{84}:Al_{11}:Cr_3:Ru_2 (at.%) alloy was undertaken, and the results were worse than Pt_{86}:Al_{10}:Cr_4 (at.%) [2004Süs1]. This was deduced to arise from a different atmosphere being used, since the initial tests were done under argon, and in air for Pt_{84}:Al_{11}:Cr_3:Ru_2 (at.%). The results of Pt_{84}:Al_{11}:Cr_3:Ru_2 (at.%) were slightly worse than a commercial Pt alloy strengthened by dispersion hardening (DPH).

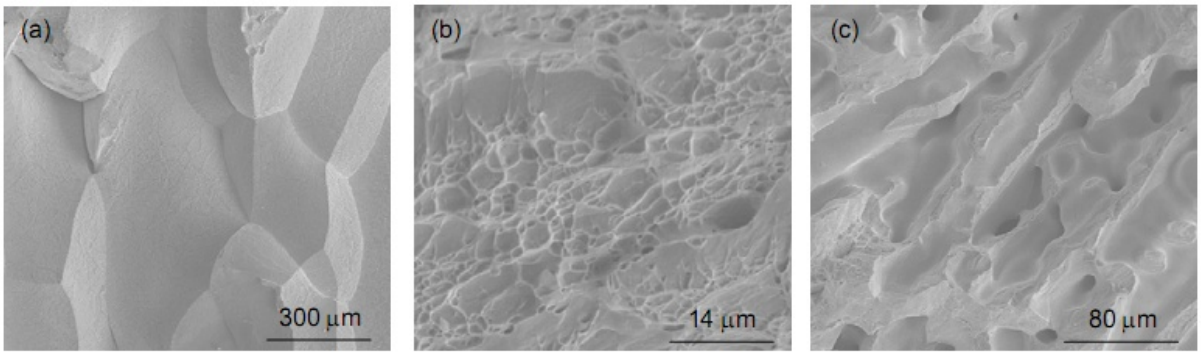


Figure 2.67. SEM-SE images of: (a) Pt_{84}:Al_{11}:Cr_3:Ru_2 (at.%) showing intergranular fracture, (b) Pt_{86}:Al_{10}:Cr_4 (at.%) showing cleavage fracture, and (c) Pt_{86}:Al_{10}:Ru_4 (at.%) showing localised dimples as a sign of ductility [2004Süs1].

Table 2.10. Hardness, ultimate tensile strength and elongation for platinum-based alloys, pure platinum and selected high-temperature alloys [2004Süs2].

Alloy or metal	Hardness range (HV_{10})	Ultimate tensile strength at room temperature (MPa)	Elongation (%)	References
Pt-based alloys	300–350	~800	-	[2001Süs1, 2004Süs2]
Pure Pt (“soft state” - not hardened)	~40	~140	-	[URLPGM]
Ferritic ODS alloy PM2000	-	720	14	[2003Pro]
γ-TiAl	-	950	~1	[2002Pat]
CMSX-4	-	870	-	[2001Mac]

2.5.7.3 Corrosion Testing of Pt-based Superalloys

The high-temperature corrosion behaviour of Pt-based superalloys has been studied by Maledi *et al.* [2006Mal, 2010Pot] by performing a crucible test at 950ºC to increase the corrosion kinetics. This temperature was selected because it is within the temperature range at which hot corrosion has the greatest effect [1993Yos, 2001Put, 2002Pra]. The samples consisted of five Pt-based superalloys containing Pt and Al with Cr, Co and/or Ru, and two samples of a single-crystal CMSX-4 NBSA of composition $Ni_{66.5}$:$Cr_{6.5}$:Co_{11}:$Mo_{0.3}$:$W_{1.7}$:$Ta_{1.8}$:$Al_{11.3}$:$Ti_{0.9}$ (at.%), Table 2.11. Starting weights were approximately 2 g. A thin Pt aluminide coating (Pt_2Al – Pt_{67}:Al_{33} (at.%)) of approximately 1.25μm thickness had been deposited on one of the CMSX-4 samples, while the other was uncoated [2010Pot].

Table 2.11. Corrosion of selected Pt-based superalloys and CMSX-4, after immersion in Na_2SO_4 at 950ºC for 564 hours [2010Pot].

Alloy name	Nominal composition (at.%)	Cumulative weight gain during corrosion, ($mg.cm^{-2}$)
RS-1	Pt_{86}:Al_{10}:Cr_4	0.00004
RS-2	Pt_{86}:Al_{10}:Ru_4	0.00008
RS-2	Pt_{84}:Al_{11}:Cr_3:Ru_2	0.0001
P420	Pt_{79}:Al_{15}:Co_6	0.0001
P421	Pt_{73}:Al_{15}:Co_{12}	0.004
CMSX-4 (uncoated)	$Ni_{66.5}$:$Cr_{6.5}$:Co_{11}:$Mo_{0.3}$:$W_{1.7}$:$Ta_{1.8}$:$Al_{11.3}$:$Ti_{0.9}$	0.470
CMSX-4 (coated)	$Ni_{66.5}$:$Cr_{6.5}$:Co_{11}:$Mo_{0.3}$:$W_{1.7}$:$Ta_{1.8}$:$Al_{11.3}$:$Ti_{0.9}$	0.038

All samples were covered in analytical anhydrous Na_2SO_4 salt, which acted as the corrosive electrolyte, in a 20ml high alumina crucible that was placed inside a furnace with a static dry air environment [2006Mal, 2010Pot]. The test was performed for an initial 60 cycles of 1h of heating and 20 minutes of cooling to room temperature, followed by up to 11 subsequent long cycles of 72h, giving a maximum total of 852h of heating. Samples were washed free of salt residues and weighed at the end of each long cycle and fresh salt was provided for every cycle [2010Pot]. Table 2.11 [2006Mal, 2010Pot] shows the cumulative weight gains during the first 60 cycles of 1h, plus a further 7 cycles of 72h (564h in total). Weight changes for the first 50h are shown in Figures 2.68 and 2.69 [2006Mal, 2010Pot].

The mass gain measurements on samples that had been immersed in Na_2SO_4 at 950ºC for 852h indicated that there was very little change for the Pt-based alloys, this being due to the formation of a protective scale on their surface [2010Pot]. In the case of the uncoated NBSA, there was an initial mass gain from the formation of oxides, with further reactions, the formation of non-protective oxides resulted in catastrophic corrosion which led to large mass changes. Testing of the uncoated NBSA was discontinued after 564h as the sample was degrading exponentially. The coated NBSA had better resistance than the uncoated one, up to the first testing stage after 564h, but even this eventually also degraded before the final testing time of 852h was reached and its further testing was therefore also discontinued. The findings of Maledi *et al*. [2006Mal, 2010Pot] demonstrated that the Pt-based alloys have good hot corrosion resistance in the presence of molten sodium sulphate salt (Figures 2.68 and 2.69 [2010Pot]), outperforming the coated and uncoated NBSA [2006Mal]. Figure 2.69 shows the different samples and the corresponding weight changes with time with the legend corresponding to Table 2.11.

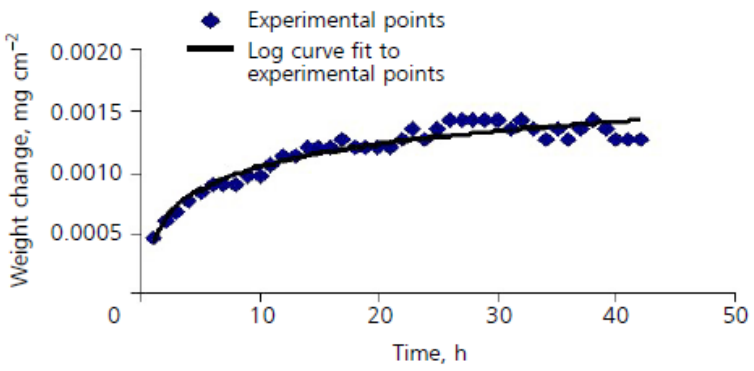


Figure 2.68. Corrosion of a coated CMSX-4 NBSA during exposure to Na_2SO_4 at 950ºC for the first 50 hours [2010Pot].

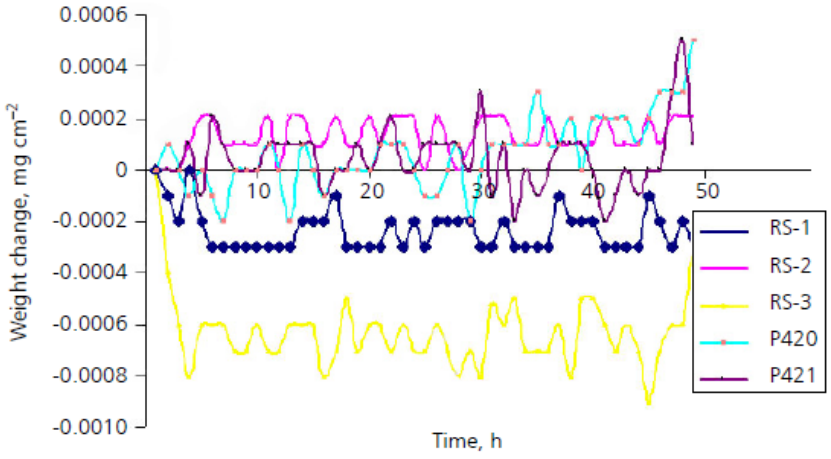


Figure 2.69. Corrosion of five Pt-based alloys of different compositions for the first 50 hours [2010Pot].

XRD analysis of the corrosion products on the NBSA samples showed a mixture of compounds based mainly on Na and Ni [2010Pot]. Conversely for the Pt-based superalloys, XRD analysis showed mainly alumina (Al_2O_3), which is the oxide coating usually present under atmospheric conditions. This was a good indication that the Pt-based alloy substrate was supporting the protective Al_2O_3 layer well. The corrosion morphologies of the Pt-based alloys were much better than those of CMSX-4. Under the SEM, Pt_{86}:Al_{10}:Cr_4 (at.%) had the best appearance, while Pt_{84}:Al_{11}:Cr_3:Ru_2 and Pt_{86}:Al_{10}:Ru_4 (at.%) were slightly pitted, with the latter showing more pits. Pt_{79}:Al_{15}:Co_6 (at.%) was good in some places, with losses in other places. Maledi *et al.* [2006Mal, 2010Pot] found that in all cases, the pits were very small, and could be considered negligible when compared with the damage to the NBSA samples under the same experimental conditions. With the naked eye, no change in appearance could be seen for the Pt-based alloy samples [2006Mal].

The samples' cross-sections were studied by SEM, which confirmed that both the coated and uncoated CSMX-4 samples had suffered a greater degree of attack than the Pt-based superalloys [2010Pot]. Both NBSA samples suffered from acidic fluxing, forming voluminous non-protective oxide scales. The corroded morphologies of Pt_{73}:Al_{15}:Co_{12} and Pt_{79}:Al_{15}:Co_6 (at.%) had a disintegrated scale layer, indicating that the scale was not protective in this environment. The scale morphologies of Pt_{86}:Al_{10}:Cr_4, Pt_{86}:Al_{10}:Ru_4 and Pt_{84}:Al_{11}:Cr_3:Ru_2 (at.%) were similar, the Pt_{86}:Al_{10}:Cr_4 (at.%) being shown in Figure 2.70 [2006Mal]. The NBSAs showed the lowest resistance and disintegrated in a short time, suffering internal sulphidation, and forming Cr and Ni sulphide corrosion compounds. Raman spectra indicated that sulphate salts, with possible traces of nitrates, formed on the surfaces of the Pt-based superalloys [2006Mal, 2010Pot]. This study [2006Mal, 2010Pot] showed that the Pt-based superalloys displayed a high potential for successful application as high-temperature corrosion resistant materials, particularly for applications such as gas turbines for the aerospace industry and possibly also for other high-temperature processes.

2.5.7.4 Effect of Heat Treatment and Co Additions

Süss *et al.* [2006Süs] studied the effects of heat treatment temperatures and different cooling rates on the microstructure of the quaternary alloy Pt_{86}:Al_{11}:Cr_3:Ru_2 (at.%) as well as the quinary alloy Pt_{79}:Al_{11}:Cr_3:Ru_2:Co_5 (at.%). The objective was also to determine the effect of

Co additions. The samples were melted in a button arc furnace, sectioned and heat treated in a muffle furnace for 96h. Since the best ternary microstructures had been obtained by annealing either at 1350ºC [2004Cor] or 1400ºC [2003Ker1, 2003Ker2] and quenching, both alloys were then heat treated at 1350°C and 1400°C for 96h, and cooled via three different methods: in the furnace (slow), in air when removed from the furnace (intermediate), and in water (fast). The samples were then prepared metallographically and OPS-polished and examined using a FEI Nova NanoSEM with EDX. XRD was also carried out and confirmed the presence of γ and γ′ phases in all alloys for all conditions.



Figure 2.70. SEM-SE image of a cross section of Pt-based superalloy RS-1, Pt_{86}:Al_{10}:Cr_4 (at.%), showing the thin protective scale [2006Mal].

For Pt_{79}:Al_{11}:Cr_3:Ru_2:Co_5 (at.%), Süss *et al.* [2006Süs] found that air-cooling after annealing at 1400°C gave ~25% volume fraction of precipitates with a size less than 100nm. This agreed with the results from Bayreuth and Jena Universities [2004Vor]. A volume fraction of about 20% for 100-200nm precipitates was also obtained by furnace cooling from 1350°C [2006Süs]. For the quaternary alloy as well, volume fractions of ~20% of 100-200nm particles were obtained after annealing and furnace or air cooling from 1350°C [2006Süs]. Furnace cooling from both temperatures promoted the formation of ogdoadically-diced precipitates ("Maltese crosses") [1958Wes] in both alloys, which are associated with unsuitable heat treatment and sub-optimal properties for NBSAs [1987Sim, 2006Ree]. Water quenching the Pt-based alloys from either 1350°C or 1400°C yielded low volume fractions (~15%), although some precipitates were likely too small to be observed. Thus, TEM was considered necessary for viewing the precipitates. XRD confirmed the presence of (Pt) and ~Pt_3Al, without stating whether the latter was $L1_2$ or DO'_c [2006Süs].

2.5.7.5 Pt-Al-Cr-Ru and Higher Order Superalloys

This section summarizes work on the Pt-Al-Cr-Ru Pt-based superalloys carried out at the University of the Witwatersrand by Shongwe [2009Sho1], Odusote [2011Odu, 2012Odu1, 2012Odu2, 2013Odu, 2014Odu], and Odera et al. [2012Ode]. The work by Shongwe [2009Sho1] focused on the optimisation of compositions and heat treatment of Pt-Al-Cr-Ru superalloys, while that of Odusote [2011Odu, 2012Odu1, 2012Odu2, 2013Odu, 2014Odu] was on the high temperature oxidation of Pt-based alloys and for Odera et al. [2012Ode] on the electrolytic etching of platinum-aluminium based alloys which was part of his PhD work on the addition of vanadium and niobium to platinum-based alloys [2013Ode, 2014Ode].

As a starting point in the optimisation of compositions and heat treatment of Pt-Al-Cr-Ru superalloys, six alloys of different compositions (Table 2.12) [2009Sho1] were selected using the optimum composition Pt_{84}:Al_{11}:Ru_2:Cr_3 (at.%) [2007Cor]. These alloys were analysed in both the as-cast and heat treated conditions. The heat treatment comprised two stages, first at 1500°C for 18h and quenched in water, followed by 1100°C for 120h and then air cooled. Microstructural characterisation was carried out in an FEI Nova NanoSEM in BSE mode, also using EDX, and XRD. The as-cast alloys had (Pt) dendrites with a eutectic/eutectoid of (Pt) + ~Pt_3Al, and tetragonal ~Pt_3Al precipitated in the dendrites. All heat treated alloys had precipitates of tetragonal ~Pt_3Al in a (Pt) matrix [2008Sho1, 2008Sho2, 2008Sho3]. Since the contrast of the phases was not sufficient for image analysis, five SEM micrographs of each sample with the same magnification (12000X) were printed and a grid (with 25 nodes) of 25 by 25mm was placed on the micrographs. The precipitate volume fractions were then derived from counting the precipitates that were on the nodes of grid placements. The volume fraction of the precipitates varied, and the maximum proportion was ~30%. To increase the volume fraction, more samples were made with 11 at.% Al (Table 2.12 [2009Sho1]). Also, the higher Al content was to ensure better oxidation resistance [2000Hil1] and to reduce the Pt content. All of the 78 at.% Pt alloys had more ~Pt_3Al precipitates than the 80 at.% Pt alloys, as expected. The microstructure was similar to the earlier samples and Pt_{78}:Al_{11}:Cr_6:Ru_5 (at.%) had the highest precipitate volume fraction.

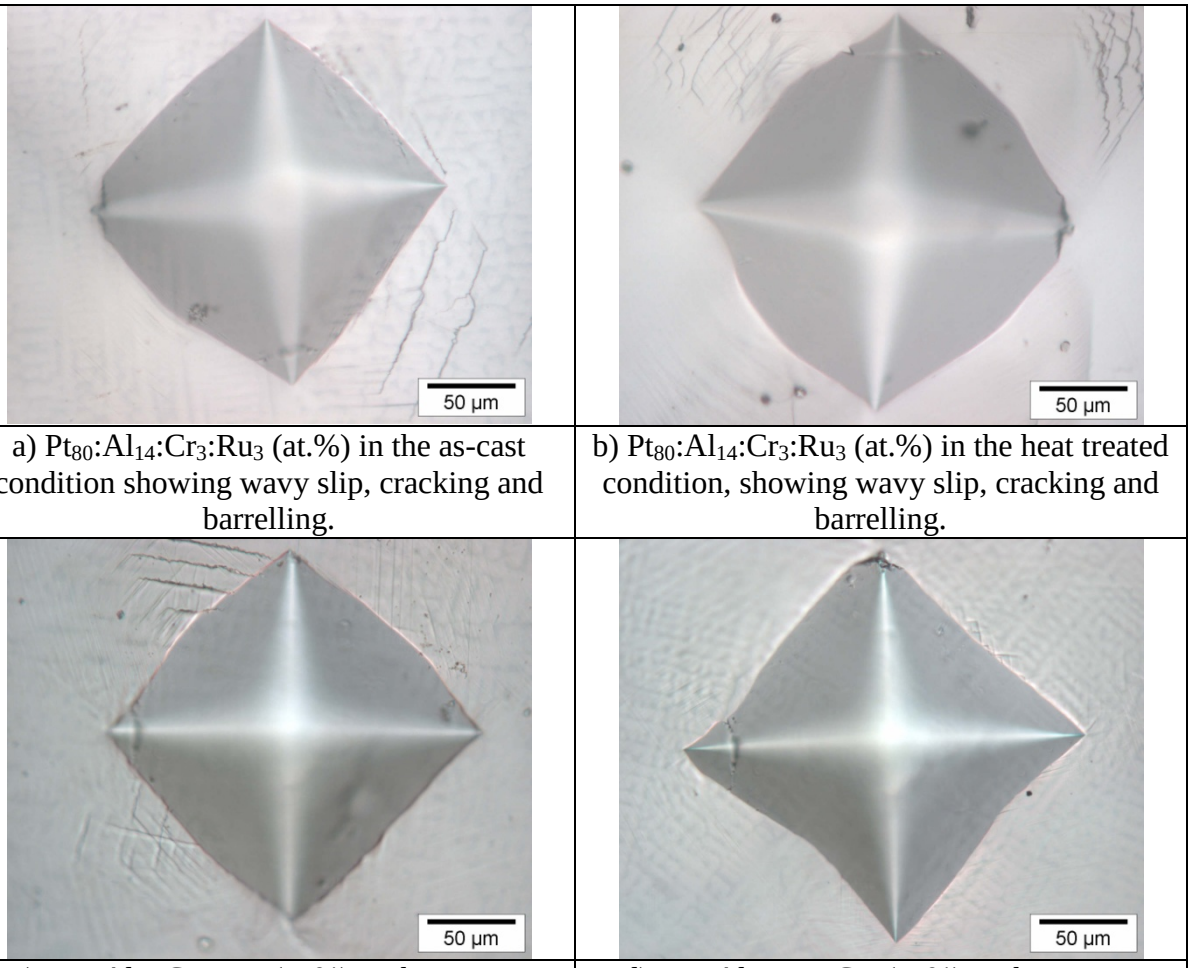
The hardness of the alloys was also studied in the as-cast and heat treated conditions [2009Sho1]. The hardnesses quoted are the average of at least five indentations on different areas (Table 2.12 [2009Sho1]). Cracking and slip modes around the hardness indentations

were studied to evaluate the toughness. Examples of the indentations of one alloy (Pt_{80}:Al_{14}:Cr_3:Ru_3 (at.%)) in the as-cast and heat treated conditions are given in Figure 2.71 (a,b) [2008Sho2], together with Pt_{80}:Al_{11}:Cr_4:Ru_5 (at.%) which showed some cracking (Figure 2.71 (c)) and Pt_{80}:Al_{11}:Cr_3:Ru_6 (at.%) which showed some pin-cushioning (Figure 2.71 (d)). Barrelling was observed in most of the samples, rather than pin-cushioning. Cracking around indentations is an indication of brittleness, while the slip mode around indentations shows whether the alloy has reasonable toughness by planar slip or wavy slip, indicating much better resistance. The hardness of the heat treated samples decreased with higher precipitate size and increased with increasing precipitate volume fraction. The hardness also showed a slight decrease with increasing platinum content.

Table 2.12. Summary of microstructure, hardness and slip modes for heat treated Pt-based alloys [2009Sho1].

Nominal alloy (at.%)	Microstructure	Hardness (HV_{10})	Slip mode
Pt_{78}:$Al_{15.5}$:$Cr_{4.5}$:Ru_2	Very fine ~Pt_3Al in (Pt) matrix	164 ± 5	Planar slip
Pt_{80}:Al_{14}:Cr_3:Ru_3	Very fine ~Pt_3Al in (Pt) matrix	361 ± 24	Wavy slip
Pt_{81}:$Al_{11.5}$:$Cr_{4.5}$:$Ru_{2.5}$	Fine ~Pt_3Al in (Pt) matrix	391 ± 24	Wavy slip
Pt_{82}:Al_{12}:Cr_4:Ru_2	Fine ~Pt_3Al in (Pt) matrix	378 ± 4	Wavy slip
Pt_{84}:Al_{11}:Cr_3:Ru_2	Fine ~Pt_3Al in (Pt) matrix	395 ± 27	Wavy slip
Pt_{85}:Al_7:Cr_5:Ru_3	Fine ~Pt_3Al in (Pt) matrix	380 ± 17	Planar slip
Pt_{80}:Al_{11}:Cr_4:Ru_5	Very fine ~Pt_3Al in (Pt) matrix	247 ± 13	Planar slip
Pt_{80}:Al_{11}:Cr_6:Ru_3	Fine ~Pt_3Al in (Pt) matrix	237 ± 22	Planar slip
Pt_{80}:Al_{11}:Cr_3:Ru_6	Fine ~Pt_3Al in (Pt) matrix	226 ± 9	Planar slip
Pt_{78}:Al_{11}:Cr_6:Ru_5	Fine ~Pt_3Al in (Pt) matrix	357 ± 4	Planar slip
Pt_{78}:Al_{11}:Cr_8:Ru_3	Fine ~Pt_3Al in (Pt) matrix	354 ± 26	Planar slip
Pt_{78}:Al_{11}:Cr_3:Ru_8	Fine ~Pt_3Al in (Pt) matrix	396 ± 17	Planar slip

The morphology of the majority of the precipitates was rounded, in agreement with Wenderoth *et al.* [2005Wen1, 2004Vor], although a few cubic precipitates were observed in some samples [2009Sho1]. Pt_{80}:Al_{11}:Cr_3:Ru_6 (at.%) had ogdoadically-diced precipitates [1958Wes], similar to the findings of Süss [2006Süs] and Cornish *et al.* [2006Cor]. Pt_{85}:Al_7:Cr_5:Ru_3 (Figure 2.72(a)) and Pt_{78}:Al_{11}:Cr_6:Ru_5 (at.%) (Figure 2.72(b) [2009Sho2]) had the highest volume fraction of ~Pt_3Al precipitates with 27 ± 6% and 24 ± 3% respectively.



a) Pt_{80}:Al_{14}:Cr_3:Ru_3 (at.%) in the as-cast condition showing wavy slip, cracking and barrelling.

b) Pt_{80}:Al_{14}:Cr_3:Ru_3 (at.%) in the heat treated condition, showing wavy slip, cracking and barrelling.

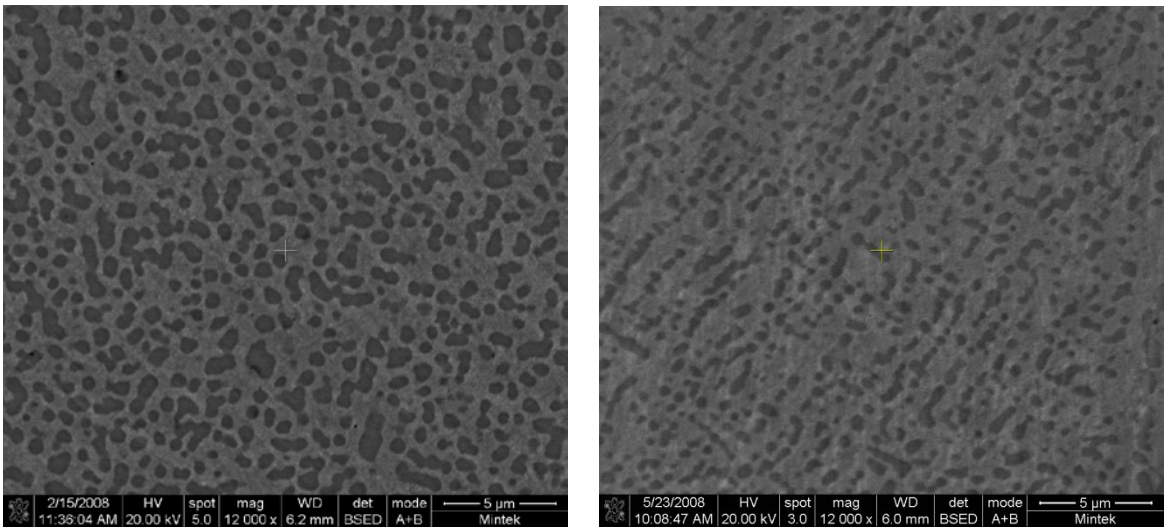
c) Pt_{80}:Al_{11}:Cr_4:Ru_5 (at.%) in the as-cast condition showing cracking, wavy slip and slight barrelling.

d) Pt_{80}:Al_{11}:Ru_6:Cr_3 (at.%) in the as-cast condition showing pin-cushioning.

Figure 2.71. Micrographs of hardness indentations of selected samples [2008Sho2].

Pt_{85}:Al_7:Cr_5:Ru_3 (at.%) appeared to be the optimum alloy, with a 41 ± 8% volume fraction of precipitates and reasonable hardness. However, the differences in hardnesses of Pt_{85}:Al_7:Cr_5:Ru_3 and Pt_{78}:Al_{11}:Cr_6:Ru_5 (at.%) was $23HV_{10}$ with errors of ±17 and ±14, together with a very small difference in volume fraction (~3%) and so these alloys had similar properties [2008Sho3, 2009Sho1]. Thus, both alloys can be said to be optimum in terms of the volume fraction and hardnesses compared to the rest of the samples. From an economic viewpoint, Pt_{85}:Al_7:Cr_5:Ru_3 (at.%) is unfavourable since it has a higher Pt content. Additionally, this alloy could suffer from oxidation because of low Al content, since according to Süss *et al.* [2001Süs2] and Hill *et al.* [2000Hil1] 11 at.% Al content is the minimum required to providing a protective adherent scale on the Pt-Al-based alloys, agreeing with Felten [1976Fel]. Thus, Pt_{78}:Al_{11}:Cr_6:Ru_5 was found to be the most promising

from both microstructure and economic perspectives [2008Sho1, 2008Sho2, 2008Sho3, 2009Sho1].



(a)Pt_{85}:Al_7:Cr_5:Ru_3 (at.%) **b) Pt_{78}:Al_{11}:Cr_6:Ru_5 (at.%)**

Figure 2.72. SEM-BSE images of heat treated samples showing ~Pt_3Al precipitates (dark) in a (Pt) matrix (light): a) random precipitates, and b) aligned precipitates [2009Sho1].

The effect of misfit on the microstructure was studied by Shongwe *et al*. [2009Sho2], deriving misfits from XRD measurements. The (220) peak was used to derive the (Pt) lattice parameters, (112) for tetragonal DO'_c ~Pt_3Al, and (211) for cubic $L1_2$ ~Pt_3Al, to be comparable with earlier work [2001Hil6]. These measurements were then used to derive the misfit ratios (δ) using the expression for nickel-based superalloys [1987Sim, 2006Ree], Equation 2.1. XRD showed that the precipitates were tetragonal DO'_c, rather than $L1_2$, thus only the DO'_c ~Pt_3Al misfit ratios were calculated.

The misfits were all negative, and fell within the range -0.0015 to -0.0102 [2009Sho2]. The different features in the microstructures were compared against the misfits. Samples with mostly rounded precipitates (Figure 2.73(a) [2009Sho2]) had misfits between -0.0067 and -0.0102. Irregular precipitates (Figure 2.73(b)) were associated with misfits between -0.0066 and -0.0089, and elongated precipitates (Figure 2.73(c)) had misfit values between -0.0044 and -0.0088. Although there were overlaps, the rounded precipitates had the highest misfits, followed by the irregular precipitates, and the elongated precipitates had the lowest misfits. This was expected, considering the relationship between surface energies and misfits [1979Jag]. Misfits of aligned and random microstructures gave no correlation, thus misfit was

not considered to be the driving force for alignment. There was also no correlation between the misfits and the hardnesses. It was not possible to deduce a relationship between mismatch and the Al, Cr or Ru contents [2009Sho2], although binary alloys [2001Hil6, 2004Dou, 2007Dou] had much lower misfits.

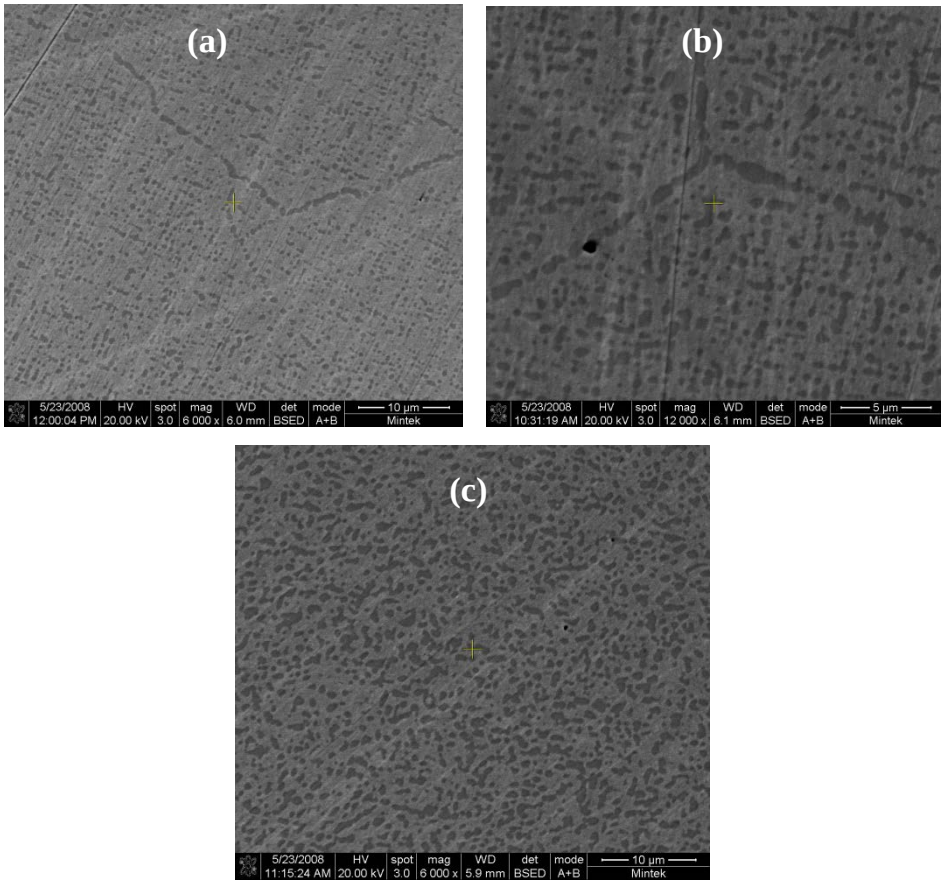


Figure 2.73. SEM-BSE images of heat treated Pt-based alloys, showing ~Pt_3Al precipitates (dark) in (Pt) matrices (light): (a) Pt_{78}:Al_{11}:Cr_3:Ru_8 (at.%) with rounded ~Pt_3Al, (b) Pt_{78}:Al_{11}:Cr_6:Ru_5 (at.%) with elongated ~Pt_3Al, and (c) Pt_{78}:Al_{11}:Cr_8:Ru_3 (at.%) with irregular ~Pt_3Al [2009Sho1].

Odusote *et al.* [2011Odu, 2012Odu1, 2012Odu2, 2013Odu, 2014Odu] studied the high temperature oxidation of Pt_{84}:Al_{11}:Cr_3:Ru_2 (at.%) in air between 1150°C-1350°C, for up to 500h. The heat treatment temperature was chosen to reflect the proposed operating temperature of the alloy [2000Wol, 2001Hil]. After the heat treatment, the samples were either air-cooled or water-quenched [2011Odu, 2012Odu1, 2012Odu2, 2013Odu, 2014Odu]. The water-quenched specimen exhibited the two-phase γ/γ′ mixture, while the microstructure of air-cooled specimen could not be resolved. More pores were observed on the water-quenched specimens than the air-cooled ones [2011Odu, 2013Odu].

The mass gain for each of the oxidized water-quenched and air-cooled specimens was measured and normalized per unit area to obtain the oxidation kinetics of the specimens at different exposure temperatures and times [2011Odu, 2012Odu1, 2012Odu2, 2013Odu, 2014Odu]. Figure 2.74 [2011Odu] compares the plots of specific mass gain as a function of oxidation time for both the water-quenched and air-cooled specimens after isothermal oxidation in air at 1150°C, 1250°C and 1350°C for up 100h. The curves showed that the parabolic mass increase law, $\Delta m = Kp.t^2 + C$ [1962Kub, 1975Sme, 2006Bir], was obeyed throughout the exposure times, and at all oxidation temperatures. This indicated that the oxidation kinetics were controlled by the diffusion of reactive species (anions and/or cations) through the external scale and/or in the substrate alloy [1962Kub, 1983Bir, 1988Kof], because diffusion-controlled high-temperature oxidation processes are governed by the parabolic rate law.

The scaling kinetics of both the water-quenched and air-cooled specimens were very close at 1150°C, and had started to level off at 100 hours exposure (Figure 2.74 [2011Odu]). At 1250°C, air-cooled specimens displayed faster growth kinetics than the water-quenched samples, and their curves were further away from levelling off after 100 hours exposure. This indicated that the steady-state kinetics were maintained for longer time at this temperature. The scale growth rates of both the water-quenched and air-cooled specimens were very close up to 10h at 1350°C [2011Odu].

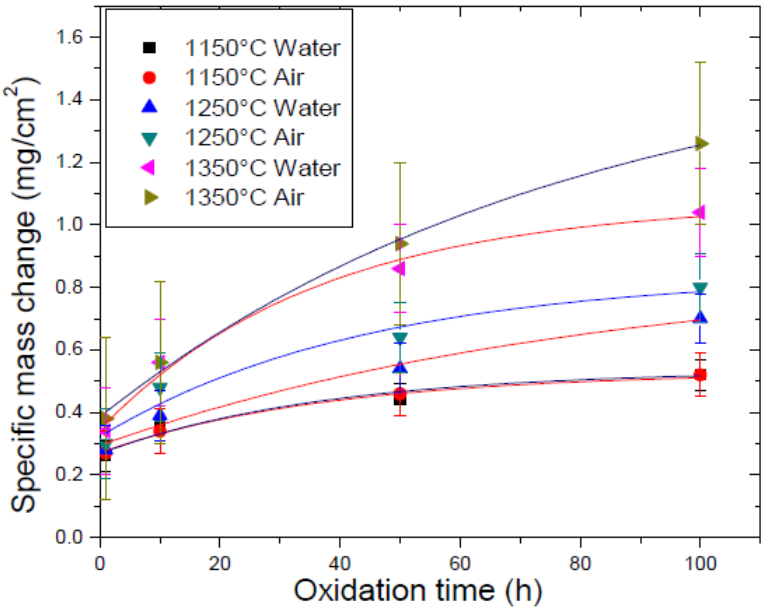
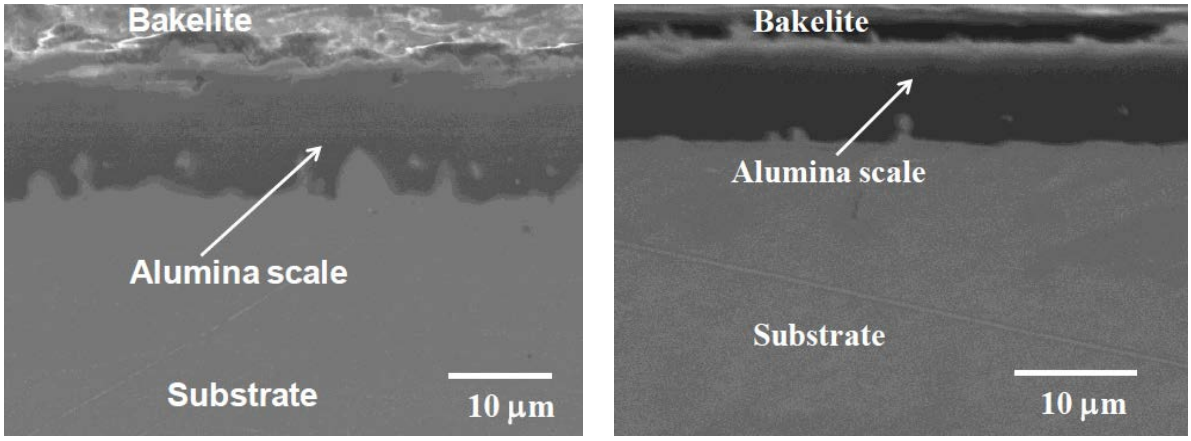


Figure 2.74. Specific mass change with time of water-quenched and air-cooled nominal Pt_{84}:Al_{11}:Cr_3:Ru_2 (at.%) specimens after isothermal oxidation in air at different temperatures (water-quenched curves in red; air-cooled curves in blue) [2011Odu].

SEM surface and cross-section examinations, as well as FIB-SEM cross-sectional observations, showed that the oxide scales that formed on the alloy specimens were continuous and adherent to the substrate (Figure 2.75 [2011Odu]). The scale layers were composed mainly of α-Al_2O_3, confirmed by XRD and Raman spectroscopy [2011Odu, 2013Odu]. The cross-sectional images revealed that the α-Al_2O_3 scales formed on the Pt_{84}:Al_{11}:Cr_3:Ru_2 (at.%) specimens were non-uniform in thickness, with localized oxide protrusions or ridges extending outward at the scale-gas interface, as well as intrusions of oxide or ridges at the scale-alloy interface (Figure 2.75 [2011Odu]).

High magnification SEM images revealed increased oxide grain sizes with increased exposure times at 1350°C [2011Odu]. In the early stages of oxidation, the scale appeared porous, but as more and larger flakes were formed on the external surface with increased exposure time, the porosity became less discernable. Instead of flakes, crystalline oxide grains of different sizes were observed after 50h exposure.



(a) **(b)**

Figure 2.75. SEM-SE images of cross-sections of oxide scales showing: (a) water-quenched Pt_{84}:Al_{11}:Cr_3:Ru_2 (at.%) after 100h oxidation in air at 1350°C, and (b) air-cooled Pt_{84}:Al_{11}:Cr_3:Ru_2 (at.%) after 100h oxidation in air at 1250°C [2011Odu].

Odusote *et al.* [2011Odu, 2012Odu1, 2012Odu2, 2013Odu, 2014Odu] concluded that the activation energies and the kinetics data supported the proposal that the growth of the α-Al_2O_3 scale was controlled by the diffusion of oxygen along grain boundaries in the oxide scale [1962Kub, 2006Bir]. The oxide protrusions suggested that counter-current diffusion of ions within the scale and substrate may be responsible for the growth of the α-Al_2O_3 scale

[1962Kub, 2006Bir].

The room temperature stresses in the scales of the alloy were found to be compressive [2011Odu] and lower than those of the Ni- and Fe-based superalloys oxidized at lower temperatures [1962Kub, 2006Bir], indicating that the alloy potentially possessed better oxidation resistance [2011Odu]. Residual stresses in the scales of water-quenched and air-cooled Pt_{84}:Al_{11}:Cr_3:Ru_2 (at.%) specimens oxidized in air at 1150ºC for up to 100h were measured using photostimulated Cr^{3+} luminescence piezospectroscopy [2013Odu]. One major advantage of this technique is that the luminescence signals are usually stronger and have a more direct relationship between the frequency shift and stress, than Raman spectroscopy [1996Lip]. During stress measurement, the α-Al_2O_3 scales fluoresced due to excitation of trace concentrations of Cr^{3+} in the scales, giving rise to characteristic strong R-line luminescence spectra, indicating the suitability of this non-destructive, non-contact technique.

The shifting of spectra for all the oxide scales to lower frequencies indicated that the scales were under uniform residual compressive stress [2013Odu], agreeing with results from other alumina-forming alloys and thermal-barrier coatings [1996Lip]. The average in-plane stresses were calculated assuming that the scales were under biaxial compression and Figure 2.76 [2013Odu] shows the room temperature residual stress in the scales as a function of oxidation time. The compressive stresses increased with oxidation time, reaching a constant value at 1.72 ± 0.16GPa for the water-quenched specimens and 1.66 ± 0.12GPa for the air-cooled specimens, both at 50h exposure (Figure 2.76 [2013Odu]) although the error bars showed that the difference might not be significant. Stress measurement results suggest that the scales on the air-cooled specimens possessed better adhesion than the water-quenched specimens [2013Odu], while both displayed lower stresses than scales on the Ni- and Fe-based superalloys [1996Lip]. Raman spectra confirmed corundum (α-Al_2O_3) on all the specimens, and the peak intensities increased with increased exposure time. At all exposure times, the peak at wavenumber 417.4 cm^{-1}, the strongest corundum peak, was also the strongest peak in the spectrum. No peaks matching other phases, such as PtO_2, CrO_3, RuO_3 and RuO_4, were observed [2013Odu].

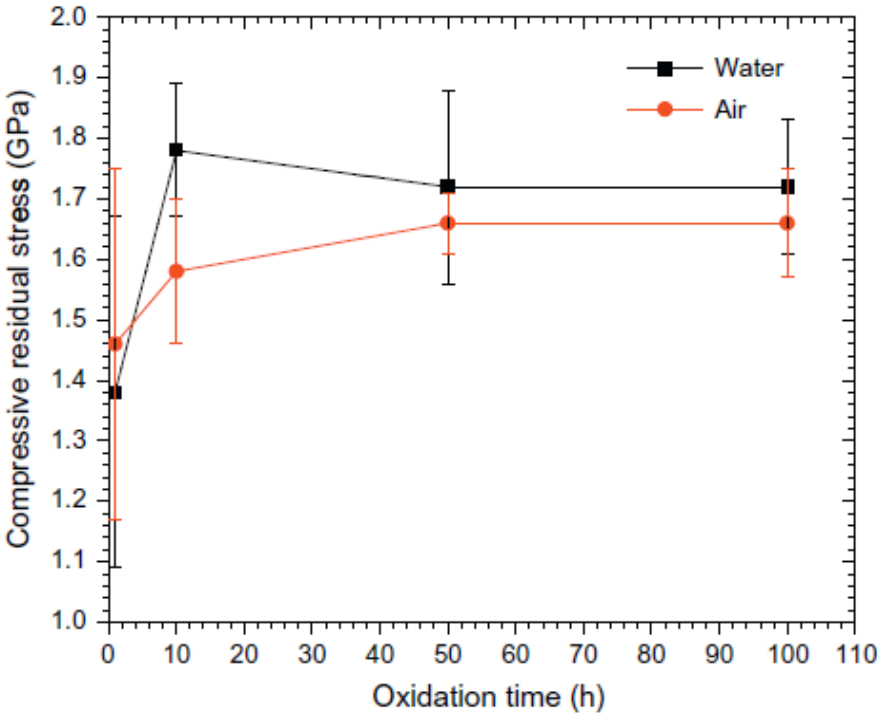


Figure 2.76. Mean stress in the scales of water-quenched and air-cooled $Pt_{84}:Al_{11}:Cr_3:Ru_2$ (at.%) calculated from the measured frequency shifts of the R2 luminescence line [2013Odu].

Recently, work has been done on the electrolytic etching of platinum-based alloys by Odera *et al.* [2012Ode]. Etching of Pt-based alloys has been problematic because most of the alloys are designed to withstand oxidation and corrosion. Previously in South Africa [2008Süs2, 2009Sho1, 2009Sho2, 2011Ode], microstructural imaging of Pt-Al based alloys was done using SEM in the backscattered electron mode. All the samples had been metallographically prepared by grinding using silicon carbide down to 1200 grit, followed by diamond polishing down to 1µm and final polishing with oxide polishing system (OP-S, Struers A/S, Denmark). In OP-S, polishing is achieved through a combination of chemical treatment (the solution has a pH of 8) and gentle abrasive action, allowing selective polishing of softer phases, thereby achieving a limited etching effect. Although some of the images derived from this method had reasonably good contrast, in some cases, the contrast was poor to the extent that analysis was rendered impossible [2009Sho2].

In Germany [2005Hül, 2007Wen], electrolytic etching of Pt-Al based alloys had been done in aqueous potassium cyanide (KCN) solution for microstructure investigation. The samples were electrolytically etched for 20 seconds with 5V direct current in 5% aqueous solution of potassium cyanide (KCN). The sample is nearly always the anode, although a few cathodic

etching solutions have been developed [2009Van]. Direct current (DC) is mostly used, although a few solutions require alternating current (AC). In electrolytic etching, the process is controlled by varying the voltage and time [2009Van]. Battaini [2011Bat1, 2011Bat2] obtained the best results for Pt alloys in saturated HCl/NaCl solution with an AC power supply when the voltage varied from 0.1V to 10V and the power supply provided a current of at least 10A. However, Odera *et al.* [2012Ode] has shown that it was possible to obtain good results using a DC power supply. Pt-based specimens were ground by silicon carbide down to 1200 grit and then diamond polished down to 1μm. The samples were then etched in a solution of 10g NaCl in 100 cm^3 HCl (32% concentration). Etching was done in a fume cupboard, a voltage in the range of 9V to 12V DC yielding good results [2012Ode]. The current density in the electrolyte was ~100$A.m^{-2}$, and the counter electrode was a stainless steel wire.

Figure 2.77 [2012Ode] shows images of Pt-Al based alloys taken using SEM in the backscattered electron mode and also the optical microscope. There was a large improvement in contrast when the SEM-BSE image of an $Pt_{64.7}$:$Al_{26.2}$:$V_{9.1}$ (at.%) alloy [2012Ode] in the unetched condition (Figure 2.77(a) [2012Ode]) was compared to the image of the same alloy (Figure 2.77(b) [2012Ode]) after being etched.

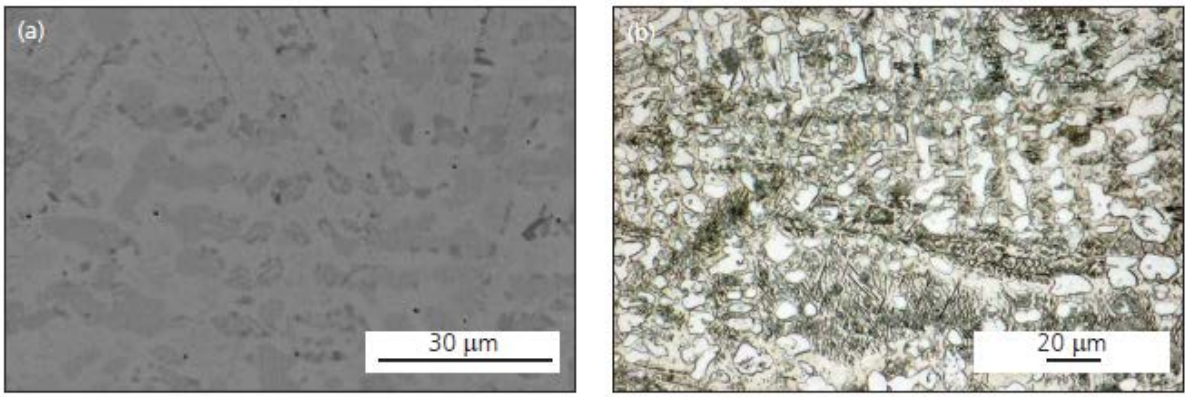


Figure 2.77. (a) SEM-BSE image of unetched, annealed $Pt_{64.7}$:$Al_{26.2}$:$V_{9.1}$ (at.%), showing medium contrast ~Pt_3Al, light ~Pt_5Al_3 and dark ~PtV [2011Ode], and (b) optical microscope image of etched, annealed $Pt_{64.7}$:$Al_{26.2}$:$V_{9.1}$ (at.%), showing light ~Pt_3Al, dark ~Pt_5Al_3 with needle-like precipitates [2012Ode].

Alloys of the quinary Pt-Al-Cr-Ru-V and Pt-Al-Cr-Ru-Nb system are being investigated as potential replacements of some NBSAs, even recognising their high density and expense [2011Ode, 2013Ode, 2014Ode]. Pt-Cr-V is one of the component ternary systems of the quinary and no data have been published, except by this research group. Thus, initial work by

Odera *et al.* [2013Ode, 2014Ode] focussed on the study of the microstructure of as-cast alloys of the Pt-Cr-V system to identify the phases and their distribution. Knowledge of the microstructure of these alloys will help in determining the optimum addition of vanadium to the Pt-based alloys and the phases which may exist therein. Usually, ternary and higher order phases tend to be brittle and need to be avoided [2014Ode]. Two ternary phases were found in the Pt-Al-V system and one in the Pt-Cr-V system. It was concluded that all the phase regions were identified correctly since the results were self-consistent. Four invariant reactions were identified in the Pt-Cr-V system [2013Ode, 2014Ode]. Four Pt-Al-Cr-Ru-V and two Pt-Al-Cr-Ru-Nb quinary alloys were also investigated. The compositions of the alloys were based on a quaternary alloy, Pt_{82}:Al_{12}:Cr_4:Ru_2 (at.%), which had been identified as one of the alloys having optimum properties in an earlier investigation [2011Cor]. Four of the as-cast alloys had a two-phase structure of ~Pt_3Al and (Pt), while two had single phase ~Pt_3Al. Vanadium partitioned more to ~Pt_3Al compared to (Pt). There was an improvement in hardness compared to the quaternary alloys which had been identified as having optimum properties [2013Ode, 2014Ode].

2.6 Rationale for Further Research in Pt-Based superalloys

The search for materials with improved properties for high-temperature applications is ongoing. Other lighter and cheaper materials are being researched, but all of these have disadvantages and most are very difficult to manufacture [2011Cor]. The Pt-based alloys show great promise for high-temperature applications, despite their high cost and density [2011Cor], as they have good mechanical properties, including formability and oxidation resistance. However, more research needs to be undertaken, as there is much potential for other alloying additions, especially those that could increase the melting temperature and decrease the density, e.g. niobium and vanadium. Further mechanical testing, especially long-term creep testing, should also be undertaken [2011Cor].

Recent ongoing work by Odera *et al.* [2014Ode] indicated that the addition of V and Nb to quaternary Pt-Al-Cr-Ru alloys has shown better hardness compared to the same alloy without V and Nb additions. These findings confirmed earlier suggestions by Cornish *et al.* [2011Cor] on the potential of other alloying additions.

CHAPTER THREE

3. EXPERIMENTAL PROCEDURE

3.1 Sample Manufacture

Alloy buttons of mass ~3.5g were prepared from pellets and chunks of the respective elements. The purity of the Pt, Al, Cr and Ru was at least 99.9 %. The combined elements were melted in a button arc furnace under argon and a Ti oxygen-getter, on a water-cooled copper hearth. The samples were turned at least three times and re-melted for improved homogeneity. The alloys were named according to their nominal compositions (Table 3.1).

Table 3.1. Pt-based samples manufactured in the current investigation.

Nominal Composition (at.%)
$Pt_{82}:Al_{12}:Cr_4:Ru_2$
$Pt_{85}:Al_7:Cr_5:Ru_3$
$Pt_{80}:Al_{11}:Cr_3:Ru_6$
$Pt_{80}:Al_{14}:Cr_3:Ru_3$
$Pt_{78}:Al_{11}:Cr_8:Ru_3$
$Pt_{78}:Al_{11}:Cr_6:Ru_5$

3.2 Sample Annealing

Arc-melted buttons were heat treated in air in a Lenton muffle furnace at 1500°C for 18 hours, followed by quenching in water, then annealed at 1100°C for 120 hours and air cooled. The buttons were not sealed off into ampoules.

3.3 Sample Preparation for SEM, AFM, TEM and Optical Microscopy (OM)

3.3.1 Sample Preparation for SEM, AFM and Optical Microscopy (OM)

3.3.1.1 Metallographic Sample Preparation

For each composition, a section of about 250µm thickness was cut from the centre of the button using an ISOMET^{TM} Buehler low speed saw. The 250µm thick sections were used to make TEM specimens, Section 3.3.2. The remaining two portions of the button were used for

SEM, optical microscopy and AFM investigations, and were mounted and ground to 1200 grit on SiC paper. The samples were then polished using diamond, 3µm down to 1µm, impregnated clothes followed by an oxide polishing (OP-S) system. (In the OP-S system, polishing was achieved through a combination of chemical treatment (the solution had a pH of 8) and gentle abrasive action, which allows selective polishing of the softer phases and often makes subsequent etching of the sample superfluous).

3.3.1.2 Electrolytic Etching of Samples

The samples were etched in a solution of 10g NaCl in 100cm^3 HCl (32% concentration). Etching was done in a fume cupboard using a DC power supply, and a voltage range of 9V to 12V gave good results. The current density in the electrolyte was ~100A.m^{-2}, and the counter electrode was a stainless steel wire suspended in the electrolyte solution [2012Ode].

3.3.2 Sample preparation for TEM

The main challenge of specimen preparation for TEM analysis techniques is the preparation of a very thin specimen with a smooth, flat surface. TEM samples must be thin enough to be electron transparent in order for electrons to pass through the sample and form an image on the viewing screen or CCD camera. For each specimen, a section of about 250µm in thickness was cut from the centre of an arc-melted button. The 250µm thick sections were ground down to 140µm and then a cylindrical disc of 3mm diameter was cut from the cores of the sections using either a Gatan 601 Ultrasonic Disc Cutter or a Gatan Disc Punch. The discs were then thermally bonded to a small steel holder using a melting wax at 130˚C and then mechanically ground down to a thickness of about 90µm. The surfaces of the samples were then polished using a 0.025µm alumina suspension. Final thinning of samples to perforation was carried out in a Gatan 691 Precision Ion Polishing System (PIPS) using argon gas (Figure 3.1 (a) [2007Rei]). This system bombards the specimen from both the top and bottom surfaces (Figure 3.1 (b) [2007Rei]). Ion milling was typically done at 5 kV, 5° angle of incidence for 3h, then at 4.5° for around 9h, after which final milling was carried out at 2.5 kV at 4.5° for about 4 minutes to reduce the amount of surface ion damage.

It was not initially possible to resolve the details of the sample microstructure due to the amount of remaining surface ion damage. To remove the ion damage, samples were electro-polished using a method developed by Witcomb [1992Wit, 2010Wit]. The samples were immersed in a solution made up of equal amounts of phosphoric, nitric and sulphuric acids at

20°C. The sample was positioned between two 3mm diameter Pt discs acting as the cathode. The polishing time was about 30s at 2.8V AC. Prior to insertion in the microscope, the microscope holder containing the sample was cleaned in a Fischone Plasma Cleaner for 30 minutes to remove surface carbon contamination.

a)



b)

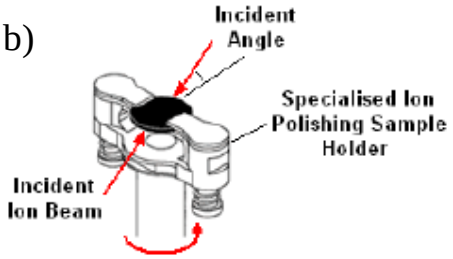


Figure 3.1. (a) Gatan Precision Ion Polishing System (PIPS) used for TEM sample preparation, and (b) schematic representation of the sample holder [2007Rei].

3.4 X–ray diffraction (XRD) instruments

A Philips PW 1710 was used for analysis of the earlier samples (before it broke down), and a D2 PHASER X-ray diffractometer was used afterwards. The latter was newer, with a lower noise background in the XRD spectrum than the Philips PW 1710. The samples were taken out of the resin mounts to prevent any extra peaks in the XRD spectrum from the resin, to ensure only the sample was analysed. A Cu–K_α source was used and the samples were rotated through a 2θ angular range from 10° to 100°. A step scan was used, with 0.02° step size and 1.0s scan step time. The generator settings were 40kV and 20mA. The peaks in the diffraction patterns were identified by matching with known standard patterns, using the X´pert Highscore basic evaluation search and match program [2003Xpe], and data from the International Crystallography Diffraction Database (ICDD). Some of the samples were put in both instruments and yielded similar phase identifications.

3.5 Optical Microscopy (OM) Instrument

An Olympus BX61 was used to examine the microstructure of the etched alloys. The BX61 is a fully automated microscope which is integrated with a motorized Z-focus with nm resolution (0.01µm) [2011Oly].

3.6 SEM Instrument

Both the unetched [2009Sho1] and etched samples from this study were observed in a FEI Nova Nano SEM 200 with an operating voltage of normally 20kV and a working distance (WD) of approximately 6mm for imaging. All micrographs were taken in the backscattered electron mode, so that phases with lower average atomic numbers could be identified by their darker contrasts. All the compositions were obtained by energy dispersive X-ray spectroscopy (EDX) using an EDAX detector with EDAX analysis software. The analyses quoted are the average of at least five determinations on different areas.

3.7 SEM and OM investigation of previous Pt-based superalloys

The original samples [2008Sho1, 2008Sho2, 2009Sho1] were re-prepared metallographically, in an attempt to remove scratches that were previously present. Electrolytic etching [2012Ode] of these samples [2008Sho1, 2008Sho2, 2009Sho1] revealed the true microstructures. Optical microscopy was carried out, which had not been possible before electrolytic etching.

The reported results were limited to features not seen before, and were compared to the previous images [2009Sho1]. Table 3.2 shows the samples studied previously and indicates samples for which different microstructural observations were made and which are consequently reported here.

3.8 Grid technique volume fraction measurements

The precipitate volume fraction measurements were done on the Pt-Al-Cr-Ru samples previously studied [2009Sho1] using the grid technique, since the contrast of the phases was not sufficient for conventional image analysis before etching was done. The precipitate volume fractions were derived from counting the precipitates that were on the nodes of 10

grid placements [1988Exn, 1999Rus]. There were 16 grids and 25 nodes in total. The grid technique was also used to estimate the volume fraction from TEM images.

Table 3.2. Pt-based samples previously studied [2009Sho1], indicating samples for which different microstructural observations were made after electrolytic etching.

Nominal Composition (at.%)	Different microstructural observations
Pt_{78}:$Al_{15.5}$:$Cr_{4.5}$:Ru_2	Yes
Pt_{80}:Al_{14}:Cr_3:Ru_3	Yes
$Pt_{81.5}$:$Al_{11.5}$:$Cr_{4.5}$:$Ru_{2.5}$	Yes
Pt_{82}:Al_{12}:Cr_4:Ru_2	Yes
Pt_{84}:Al_{11}:Cr_3:Ru_2	No
Pt_{85}:Al_7:Cr_5:Ru_3	No
Pt_{80}:Al_{11}:Cr_4:Ru_5	Yes
Pt_{80}:Al_{11}:Cr_6:Ru_3	Yes
Pt_{80}:Al_{11}:Cr_3:Ru_6	No
Pt_{78}:Al_{11}:Cr_6:Ru_5	No
Pt_{78}:Al_{11}:Cr_8:Ru_3	No
Pt_{78}:Al_{11}:Cr_3:Ru_8	Yes

3.9 Image analysis: Olympus stream software

Images for ~Pt_3Al volume fraction analysis from all the heat treated, newly-etched alloys from previous samples [2009Sho1], and the newly-manufactured etched samples were taken using an FEI Nova Nano SEM 200. The images from the SEM were saved in TIF (Tagged Image File) format, to allow for further processing using Olympus Stream image analysis software, version 1.3 [2011Oly]. At least five images with representative microstructures of each sample were selected for image analysis.

3.10 AFM and WSxM Software for volume fraction analysis

AFM observations were performed using a Veeco Dimension^{TM} 3100 Atomic Force Microscope (Digital Instruments, Veeco), (Section 3.13.2). Topographic images were obtained by scanning etched surfaces and controlling the z-displacement to hold the cantilever tip at a constant height. This instrument had a vertical resolution (z) of 0.05-1nm and lateral resolution (x/y) of 2-5nm and is generally limited by the tip geometry, not the

instrument. The sample preparation was the same as for SEM observation (metallographic preparation, including etching).

Images were analysed with the WSxM software [2007Hor], a freeware scanning probe microscopy software using MS-Windows. The software uses the "flooding" function [2007Hor], which converts the AFM image into a binary image and identifies the precipitates as "holes" and calculates the area fraction of the "holes", which are then translated as the precipitate volume fractions. Stereology and quantitative metallography showed that the area fraction is equal to volume fraction [1985Mil]. Earlier studies by Hilliard and Cahn [1961Hil] have also shown that the precipitate area fraction was in good agreement with their volume fraction. At least seven different regions of area 25µm x 25µm were randomly selected in each sample to determine the volume fraction.

3.11 TEM Instruments

The TEMs used in this investigation were a JEOL JEM-2100 TEM at the Nelson Mandela Metropolitan University (NMMU) and a CM200 at the University of the Witwatersrand. Both these TEMs had LaB_6 filaments and were operated at an accelerating voltage of 200kV and 197kV respectively. The phase compositional analyses were determined using the JEOL TEM 2100, with an Oxford INCA Energy Dispersive X-ray analysis system (EDX) and associated INCA analysis software. A low background beryllium analytical double tilt specimen holder was used for EDX analysis. The elemental composition was determined using the standardless software of the INCA system.

Representative regions on the different samples were imaged at different magnifications using both bright and dark field imaging conditions to capture the relevant primary, secondary and/or tertiary γ' precipitates, the γ/γ' interface and dislocations. Occasionally, under challenging conditions such as multi-grain images, multi-beam images were utilized. Particular attention was also given to the morphology and volume fraction of the γ' precipitates. Compositional analyses were done on both the γ and γ' phases. To determine the variation, the compositions were also measured from approximately the centre of the precipitates to the centre of the matrix channel over a distance of about 250nm in steps of about 20nm and repeated five times in different regions. TEM diffraction studies were also carried out using both selected area diffraction (SAD) and microdiffraction to determine the

orientation relationship between the γ and γ′ phases, and the structure of the γ′ precipitates. Electron diffraction patterns were taken in the microdiffraction mode using a small electron probe size, typically in the nanometer range.

3.12 Determination of the Structure of ~Pt_3Al and Orientation Relationship between the Matrix and Precipitates

Two different methods were used to identify the structure of ~Pt_3Al. The first involved manual measurements of the diffraction pattern interplanar spacings and angles [2001Cha], while the second involved the use of the Java Electron Microscope Simulator (JEMS) software. Diffraction patterns used in the manual method were obtained in the CM200 TEM, while those used in the JEMS software were from the JEOL TEM 2100. For the CM200 and JEOL 2100, both TEM selected area diffraction and microdiffraction were employed to determine which phase was present. Camera length calibrations were obtained using a thin aluminium foil after the analysis of each precipitate, the lens settings and location settings being stored immediately prior to sample removal. On insertion of the aluminium foil, lens and location settings were re-established and sample focus obtained using only the Z control.

3.12.1 Indexing of diffraction pattern using Java Electron Microscope Simulator (JEMS) software

The Java Electron Microscope Simulator (JEMS) (at NMMU) is a TEM image simulation package for both electron diffraction analysis and HREM image simulation [2004Sta]. Diffraction pattern indexing consists of determining the (*hkl*) indices of the reflections and calculating the zone axis [*uvw*] indices. The first step consisted of loading and displaying the diffraction pattern in the JEMS Window [2004Sta]. Digital Micrograph.dm3 images were used, and their format contained information about the accelerating voltage and camera length of the TEM used [2012Oli]. The second step was to select the possible crystal structures for indexing, then used the JEMS software to calculate the electron diffraction patterns for all orientations to be compared with the experimental diffraction pattern [2004Sta]. Two crystal structures, cubic and tetragonal were selected for indexing of the ~Pt_3Al diffraction patterns. The cubic ($L1_2$) Pt_3Al structure based on the $AuCu_3$ prototype

proposed by Bronger [1962Bro] was used, as used by Douglas [2004Dou2]. The tetragonal (DO'_c) Pt_3Al proposed by Chattopadhay *et al.* [1975Chat] was selected, also as used by Douglas [2004Dou2]. The selected (Pt) structure was fcc, as reported by McAlister and Kahan [1986McA]. The modified DO'_c structure reported by Douglas *et al.* [2007Dou] was not employed since there was no evidence of superlattice spots or twinning.

3.13 Nanoindentation

3.13.1 Nanoindentation Hardness Testing

Nanoindentation hardness measurements were performed using a CSM nanoindentation hardness tester at NMMU with the atomic force microscope and optical microscope shown in Figure 3.2. Figure 3.3 [2006CSM] is a schematic diagram of the nanoindenter head assembly. The diamond Berkovich indenter was pushed into the material through magnetic repulsion when a current was passed through the coil. The displacement of the indenter was measured with respect to the surface, through the reference ring and displacement sensor assembly. The area for nanoindentation was carefully selected using the AFM, and thereafter the indenter head would be shifted directly to the same place using the same coordinates given by the AFM. The residual indentation area was confirmed by observing the indented region using the AFM and automated optical microscope. Since the samples were etched, this made the contrast difference high and the precipitates could easily be seen on the optical microscope, making it easier to change the magnification from x200 to x4000 and ensure staying on the same area, thus ensuring reproducibility.

Due to alignment discrepancies, the AFM probe for topographic imaging would shift during the tapping mode. Normally about 5-10 minutes was necessary to obtain an area image when using the AFM [2006CSM], although the probe would only be stable for about 1½ minutes. Hence, it was not possible to take images of the residual indentions using the CSM AFM. However, reviewing the indentation area was still possible before and after the indentations. For this reason, topographic imaging of the residual Berkovich impressions was carried out in tapping mode using a Veeco Dimension^{TM} 3100 Atomic Force Microscope, Section 3.13.2.

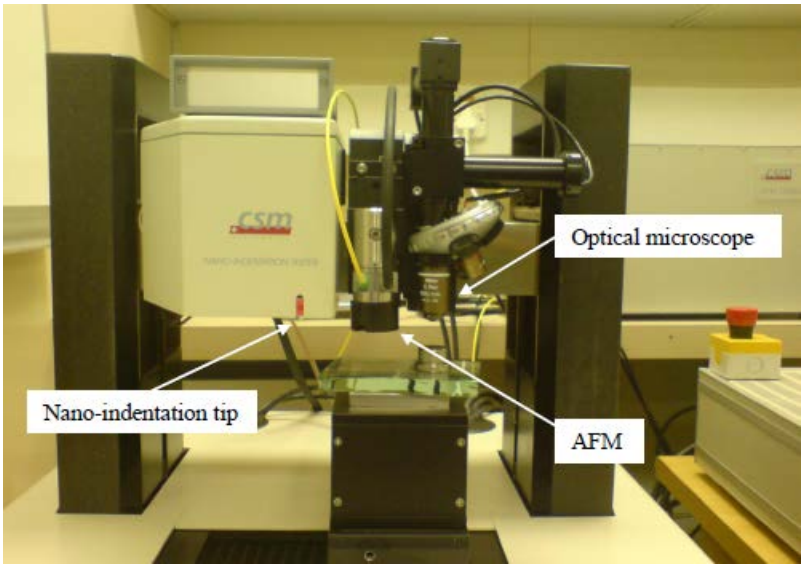


Figure 3.2. CSM nanoindentation tester with AFM and optical microscope at NMMU.

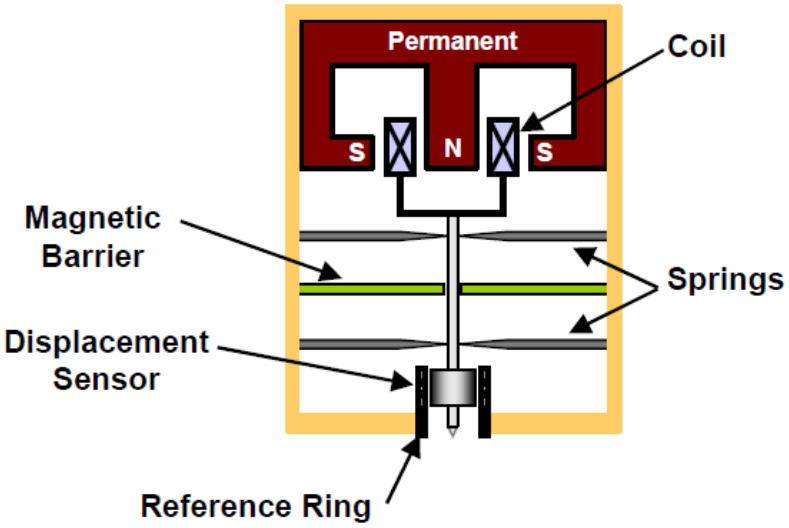


Figure 3.3. Schematic diagram of the nano indenter head assembly [2006CSM].

3.13.2 Atomic Force Microscopy Imaging

AFM topographic imaging of the residual Berkovich impressions was carried out in the tapping mode using a Veeco Dimension™ 3100 Atomic Force Microscope (Digital Instruments, Veeco) (Figure 3.4) and high resolution Si probe tips. The images were simultaneously recorded in height and amplitude contrasts. The former served to dimensionally quantify the topography, while the latter enabled resolution of the finer variations or features in topography. The surface roughness of the specimens was determined from the AFM images.

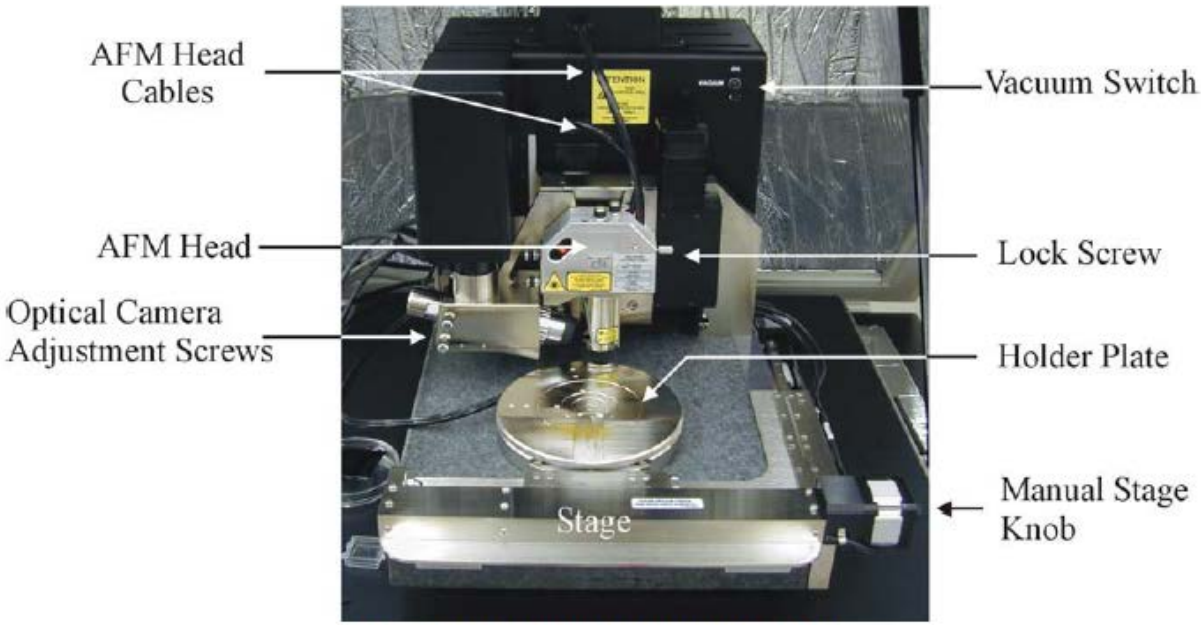


Figure 3.4. Overall view of the Veeco Dimension™ 3100 Atomic Force Microscope.

3.13.3 Calculation of Nanohardness and Elastic Modulus

The Oliver and Pharr method described in Appendix E was employed by the "Indentation 4.35 (2011), CSM Instruments™ (version 2011)" software to calculate the elastic modulus (E_s) and the nanohardness (H) by employing Equations E.6 and E.7. The indention software used was the most recent version at the time and took into account improvements that had been made to date [2010Jan].

3.13.4 Indentation Procedure

The mechanical properties (hardnesses and modulus of elasticity) of γ and γ′ for the six Pt-Al-Cr-Ru alloys were measured by nanoindentation, using a CSM nanoindentation hardness tester. Preliminary studies of the hardness and indentation depth were done first to ensure that at the maximum applied load, only the properties of a single phase are tested [1992Oli, 1999Gök, 2003Sch2]. For this purpose, indentations were performed at depths of ~40nm to ~150nm in steps of 1nm, in order to obtain a depth resolved hardness curve for the matrix and precipitates. The minimum indentation depth achievable was limited by the 2.5mN load, while for loads of 1mN, indentation depths of 20nm were achievable [1999Gök]. For each

indentation, the loading and unloading rates were kept constant at 50µN.s^{-1}. When the desired depth was achieved, the load was maintained for a further 20 seconds before unloading. Force and penetration depth were monitored throughout the indentation procedure at a sampling rate of 30Hz. Wherever feasible, the indentations were performed approximately in the centre of the precipitate, although this was not always possible.

During the preliminary indentation depth work, it was observed that at loads below 2.5mN, the pop-in effect occurred [1992Pag], and all load-displacement curves with the pop-in effect were fitted with the Hertzian contact model. (The method used for the Hertzian fit is described in Section 3.13.5 and related background is given in Appendix E.) No specific software could be found to do the fitting and the other researchers [2004Dur, 2004Gon1] did not divulge the software used, although its use was definitely mentioned. For reliability of the results, it was decided that 2.5mN would be used as the minimum possible load, since it could accurately indent the γ′ and γ phases separately within the acceptable error (<10%) [2006CSM], and with no sign of a pop-in effect. After the hardness and indentation depth preliminary work, the mechanical properties were then determined by performing ten indentations on each phase, and for the overall alloy. The indentations were performed at maximum load levels of 2.5mN, 5mN, 10.0mN, 20.0mN and 100mN.

The tip shape was calibrated according to the Oliver-Pharr method [1992Oli, 2004Oli], considering machine compliance. Quantitative nanohardness and elastic modulus values were determined from the load–displacement curves using the method of Oliver and Pharr [1992Oli, 2004Oli]. For indentation, a trapezoidal load profile with a holding time of 20s at a maximum load was used. The extended holding time ensured that most of the plastic deformation was completed. The smallest load (2.5mN) was used for indenting the individual phases, and larger loads (10mN and 100mN) were used for testing the nanomechanical properties of the alloy. Ten individual indentations were averaged for determining the hardness and modulus of elasticity of the matrix and precipitates.

3.13.5 Hertzian Fit Calculations

A discontinuity in the load-displacement curve during loading was observed when using loads lower than 2.5mN and this resulted in a high standard deviation. In this case, the reduced elastic modulus was calculated using Equation E.5 and since it is calculated from the

unloading part of the load displacement curve, it is assumed not to be affected by the pop-in effect [1985Jon, 1986Bin, 1987Kin]. The radius of curvature (R) for the Berkovich indenter was assumed to be 150nm [2006CSM], and h was increased in increments of 1nm until the maximum load P was reached, using Equation E.7. At the maximum indentation load, the new final contact depth (which subtracts the shift due to the pop-in effect) was calculated (Section 4.4.1). This new final indentation depth was used to re-calculate the hardness and elastic modulus using Equations E.6 and E.7.

CHAPTER FOUR

4. RESULTS

All error bars plotted on the figures in this thesis indicate ± 1 *sigma (standard deviation), i.e. 67% certainty.*

4.1 X-ray diffraction (XRD)

X-ray diffraction (XRD) was used to ascertain the presence of the (Pt) and ~Pt_3Al phases. Figures 4.1 to 4.6 show the XRD spectra, with the peaks labelled for their phases: (Pt), DO'_c - ~Pt_3Al and $L1_2$ - ~Pt_3Al. The XRD spectra of the heat treated samples were slightly different for the different compositions, due to the different solubilities of each element in the γ and γ′ phases, thus changing the peak positions slightly. Also, there were different proportions of the phases in the different alloys. The unmatched peaks (Figures 4.1 to 4.6) were probably due to noise during measurements and contributions from the plasticine holding the samples (Appendix D). The (Pt) and DO'_c - ~Pt_3Al peaks were found to be in better agreement with the XRD spectra than $L1_2$ - ~Pt_3Al. There were more smaller unidentified peaks in Pt_{78}:Al_{11}:Cr_8:Ru_3 (at.%) (Figure 4.6), which is thought to be background noise. The XRD spectra (Figures 4.1 to 4.6) had some broad peaks. The matches for all three phases were associated with minor shifts, which was expected since the phases were not pure and had varying amounts of Cr and Ru. The average lattice parameters deduced from the XRD results for ~Pt_3Al were a = 3.7084 Å ($L1_2$) and a = 5.4398 Å, c = 8.0247 Å (DO'_c).

As a check, because the (Pt), DO'_c - ~Pt_3Al and $L1_2$ - ~Pt_3Al structures were very similar, being based on the fcc Pt, the peaks of the pure phases from the ICDD database [2003Xpe] were compared against each other. The differences between them were then sought in the XRD pattern for each sample. The differences between the pure phases are shown in Table 4.1. A comparison of the Pt peaks with all the XRD spectra (Figures 4.1 to 4.6) identified Pt peaks as present, although with many other unidentified peaks. The $L1_2$ - ~Pt_3Al phase had three peaks which were found to be unique when compared with the (Pt) and DO'_c - ~Pt_3Al phases. The three peaks of the $L1_2$ - ~Pt_3Al phase could be matched, although very minor shifts were observed, which was expected. The DO'_c - ~Pt_3Al phase had several unique peaks (Table 4.1), more than the $L1_2$ - ~Pt_3Al phase. A comparison of the DO'_c - ~Pt_3Al with the XRD spectra (Figures 4.1 to 4.6) showed that some of the the peaks unique to DO'_c - ~Pt_3Al

could be matched (Table 4.1). The comparisons with the other samples, are shown in Table 4.1, where N means no match, while Y means a match was found. However, in the XRD spectra in the range of ~89˚ to ~90˚, the peak intensities were very low and were difficult to identify as a true peak or noise, especially in Figure 4.6. The unidentified peaks together with the noise in the XRD spectra made it necessary to further study the samples using TEM.

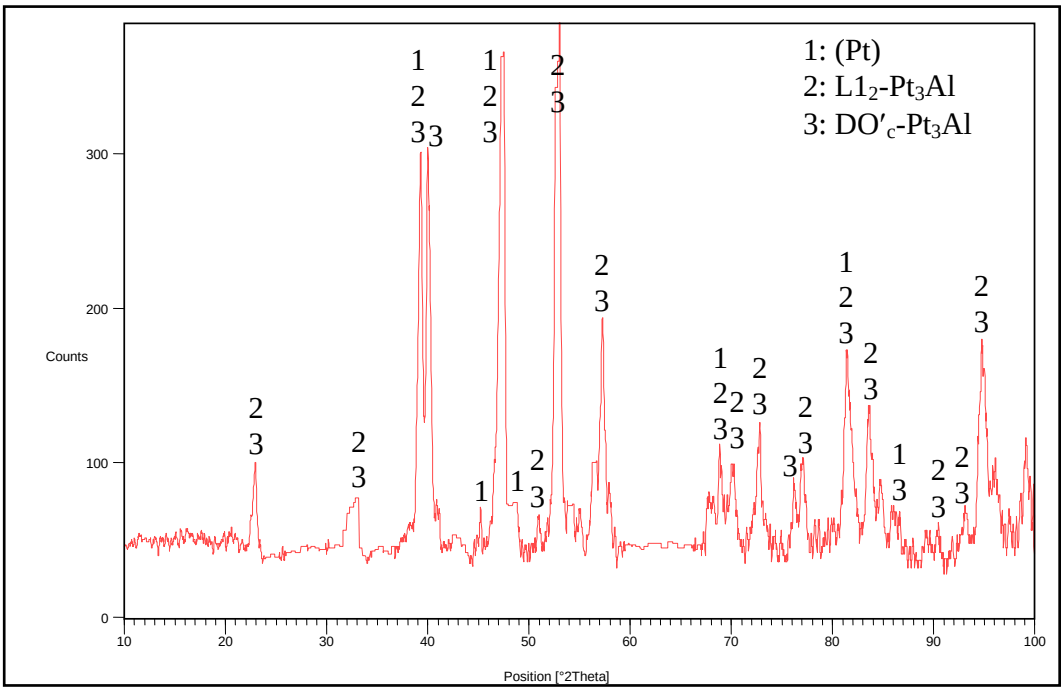


Figure 4.1. XRD pattern of nominal Pt_{82}:Al_{12}:Cr_4:Ru_2 (at.%) in the heat treated condition, showing all identified phases.

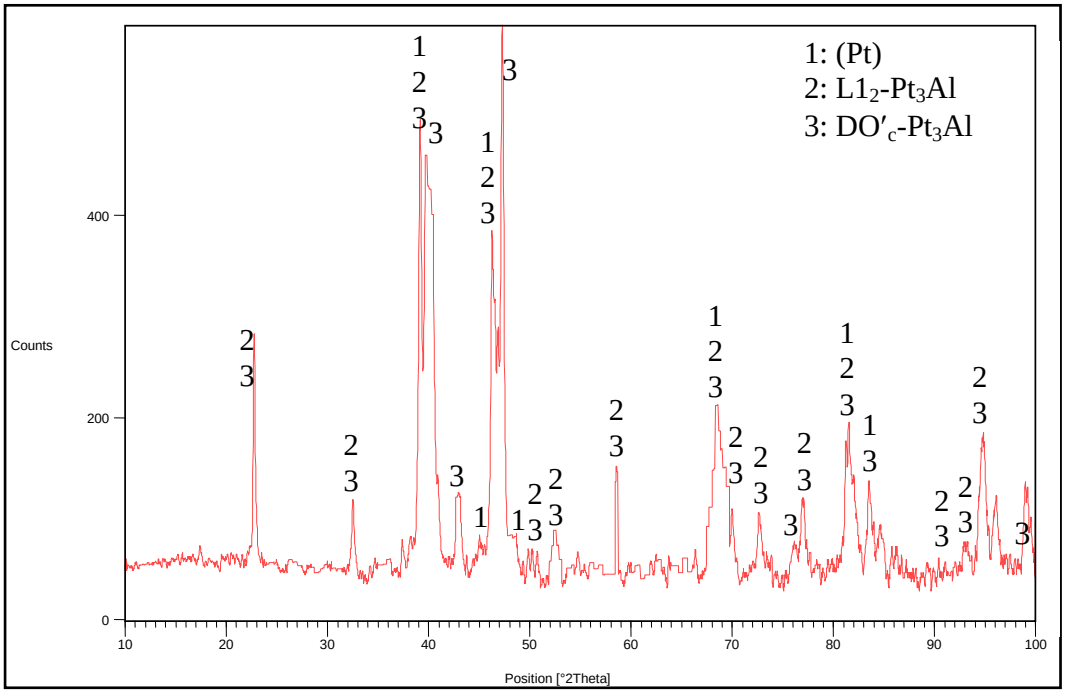


Figure 4.2. XRD pattern of nominal Pt_{85}:Al_7:Cr_5:Ru_3 (at.%) in the heat treated condition, showing all identified phases.

Table 4.1. Differences in the angular positions of the XRD peaks for pure DO'_c - Pt_3Al phase from the ICDD database [2003Xpe], where Y = match and N = no match.

Position 2 θ(°)	Match of DO'_c - Pt_3Al for Figures 4.1 to 4.6					
DO'_c - Pt_3Al	Fig. 4.1	Fig. 4.2	Fig. 4.3	Fig. 4.4	Fig. 4.5	Fig. 4.6
23.071	Y	Y	Y	Y	Y	Y
38.680	Y	Y	Y	Y	Y	Y
43.760	N	Y	N	N	N	Y
47.150	Y	Y	Y	Y	Y	Y
51.316	Y	N	N	Y	Y	Y
53.112	Y	Y	Y	Y	Y	Y
70.058	Y	Y	Y	Y	N	Y
71.340	N	N	N	Y	N	N
71.716	N	N	N	Y	Y	N
72.224	Y	N	Y	Y	Y	N
72.481	N	N	Y	Y	Y	Y
72.545	N	Y	Y	Y	Y	Y
73.595	N	Y	N	Y	N	Y
74.886	Y	N	N	N	Y	Y
75.941	Y	Y	Y	N	Y	N
77.251	Y	Y	Y	Y	N	Y
78.306	Y	N	N	Y	Y	Y
78.459	Y	N	N	N	Y	Y
79.315	N	N	N	Y	N	Y
79.551	Y	N	N	Y	N	Y
81.673	Y	Y	Y	Y	Y	Y
81.926	N	Y	Y	Y	Y	Y
82.957	N	Y	Y	Y	Y	Y
83.928	Y	N	Y	Y	Y	N
84.197	Y	Y	Y	Y	Y	Y
88.491	N	N	N	N	Y	Y
89.412	N	N	N	Y	Y	Y
89.934	N	N	N	Y	Y	Y
90.356	N	N	N	Y	N	Y
91.107	Y	Y	Y	Y	Y	Y
92.205	Y	Y	N	N	Y	Y
93.335	N	Y	Y	Y	Y	Y
94.381	Y	N	Y	Y	Y	Y
95.699	N	Y	Y	Y	Y	Y
96.313	Y	Y	Y	Y	Y	Y
96.686	Y	Y	N	Y	Y	Y
98.738	Y	Y	Y	Y	Y	Y
99.535	Y	Y	Y	Y	Y	Y

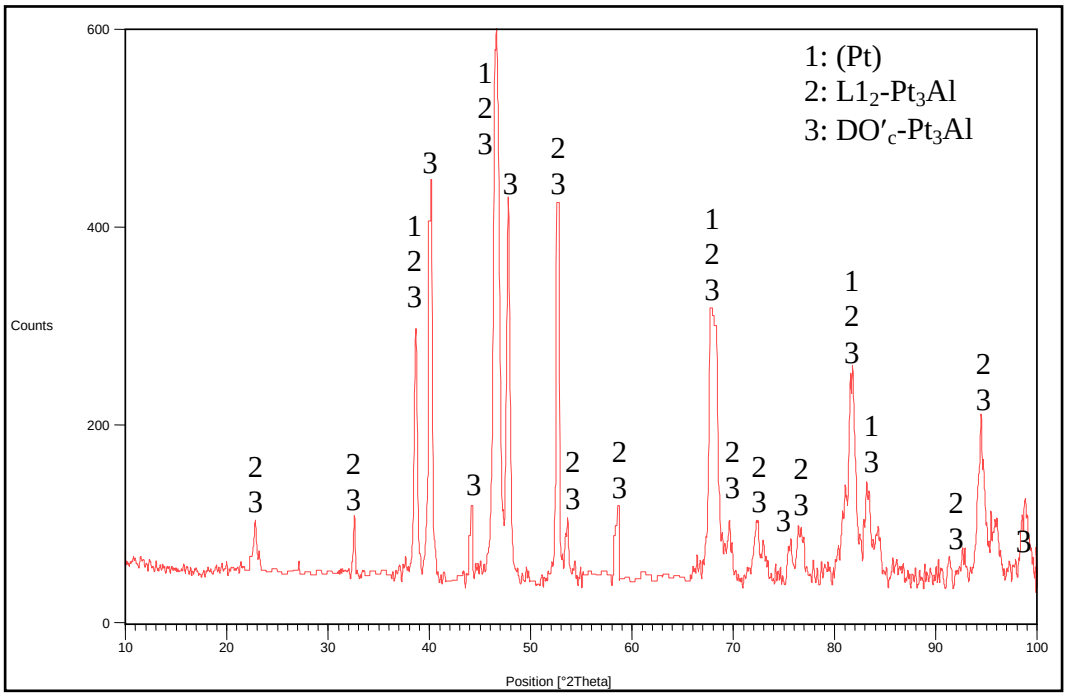


Figure 4.3. XRD pattern of nominal Pt_{80}:Al_{11}:Cr_3:Ru_6 (at.%) in the heat treated condition, showing all identified phases.

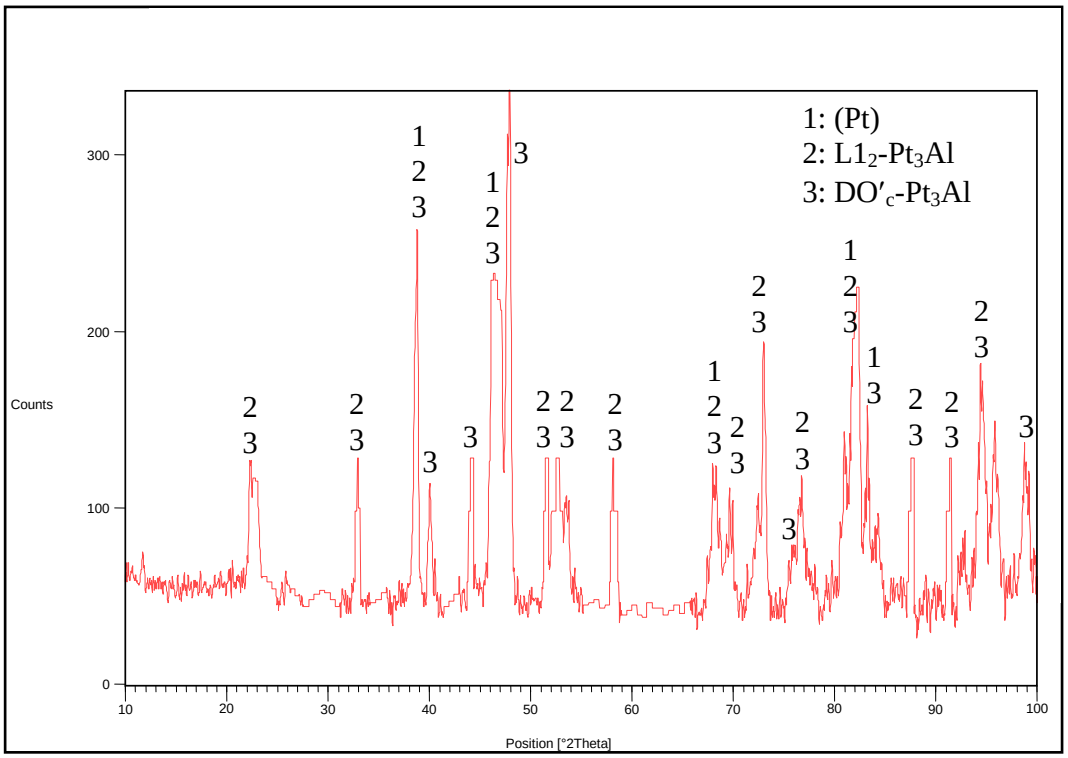


Figure 4.4. XRD pattern of nominal Pt_{80}:Al_{14}:Cr_3:Ru_3 (at.%) in the heat treated condition, showing all identified phases.

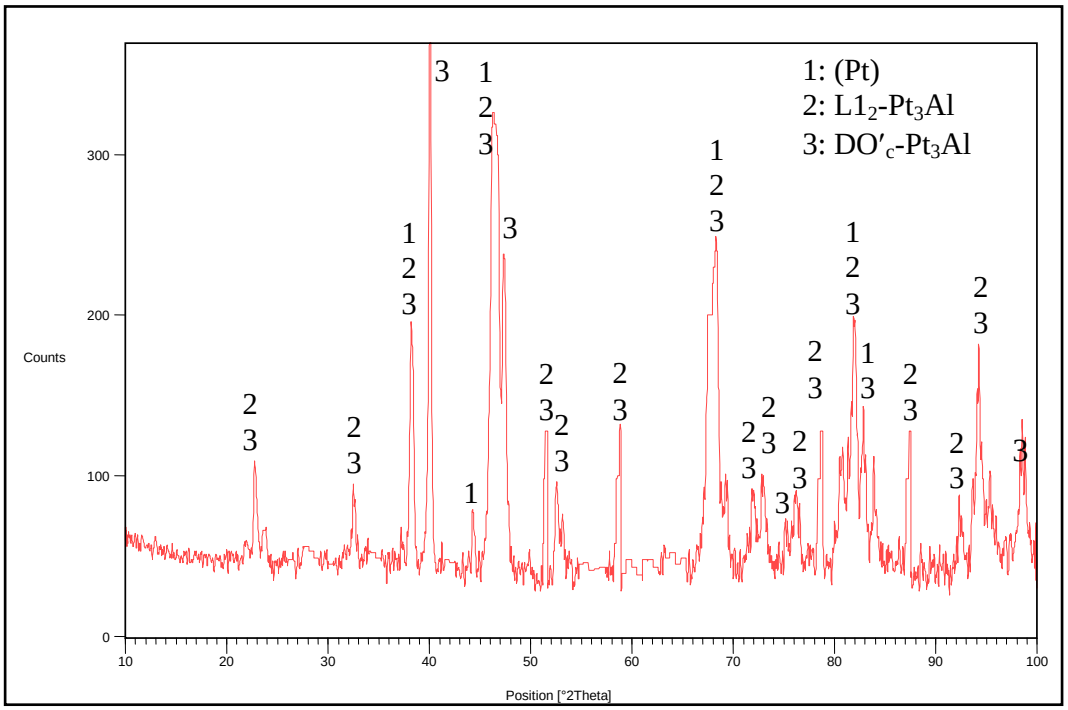


Figure 4.5. XRD pattern of nominal Pt_{78}:Al_{11}:Cr_8:Ru_3 (at.%) in the heat treated condition, showing all identified phases.

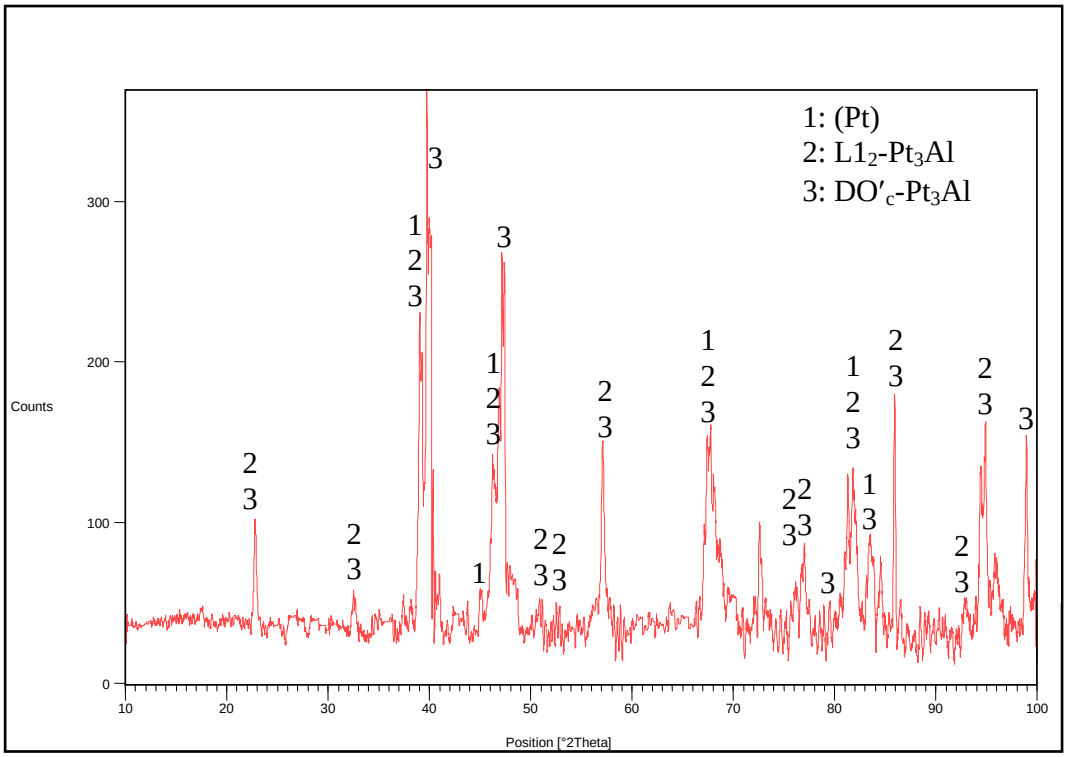


Figure 4.6. XRD pattern of nominal Pt_{78}:Al_{11}:Cr_6:Ru_5 (at.%) in the heat treated condition, showing all identified phases.

4.2 OM, SEM, AFM and Image Analysis Studies

4.2.1 New observations in some Pt-Based Superalloys after Etching

4.2.1.1 Nominal Pt_{82}:Al_{12}:Cr_4:Ru_2 (at.%)

Figure 4.7(a) is an SEM-BSE image of alloy Pt_{82}:Al_{12}:Cr_4:Ru_2 (at.%) after etching and shows an interdendritic region with lamellae between dendrites. EDX analyses indicated that the lamellae (actually a fine eutectoid) were rich in Pt, and confirmed the dendrites (surrounding region) were a two-phase mixture (Table 4.2). The optical microscope image of the etched sample (Figure 4.7(b)) showed a coarsened eutectic/eutectoid, as well as dark ~Pt_3Al precipitates in light (Pt) matrix. There was no discernable layer at the edges of the dendrites adjacent to the eutectic/eutectoid, although this was apparent in Figure 4.7(a). Figure 4.7(c) is an SEM-BSE image of another area of the eutectic/eutectoid observed in the optical image of Figure 4.7(b) and the area composition is shown in Table 4.2. The precipitates were very fine and mostly rounded in shape. The samples were analysed after etching because it was difficult to see the phases and some of the features observed before etching. It was difficult to distinguish between the eutectic and eutectoid because they are composed of the same phases, (Pt) and ~Pt_3Al, although the lamellar structure is more likely to be eutectoid (since it is finer and most eutectoids are lamellar [2013Van]), and the coarser structure is more likely to be eutectic (since it is formed at a higher temperature). Thus, the sample could be inhomogeneous.

Table 4.2. EDX analyses (at.%) of etched nominal Pt_{82}:Al_{12}:Cr_4:Ru_2 (at.%) in the heat treated condition (Figure 4.7(a) and (c)).

Phase description	**Pt**	**Al**	**Cr**	**Ru**	**Phase**
Two-phase mixture	89.9 ± 0.4	6.9 ± 0.4	2.1 ± 0.1	1.1 ± 0.2	(Pt) and Pt_3Al
Eutectoid (Figure 4.7(a))	86.4 ± 0.9	9.2 ± 0.2	2.3 ± 0.4	2.1 ± 0.1	(Pt) + ~Pt_3Al
Eutectic (Figure 4.7(c))	63.5 ± 1.8	33.8 ± 0.7	1.9 ± 0.5	0.8 ± 0.4	(Pt) + ~Pt_3Al

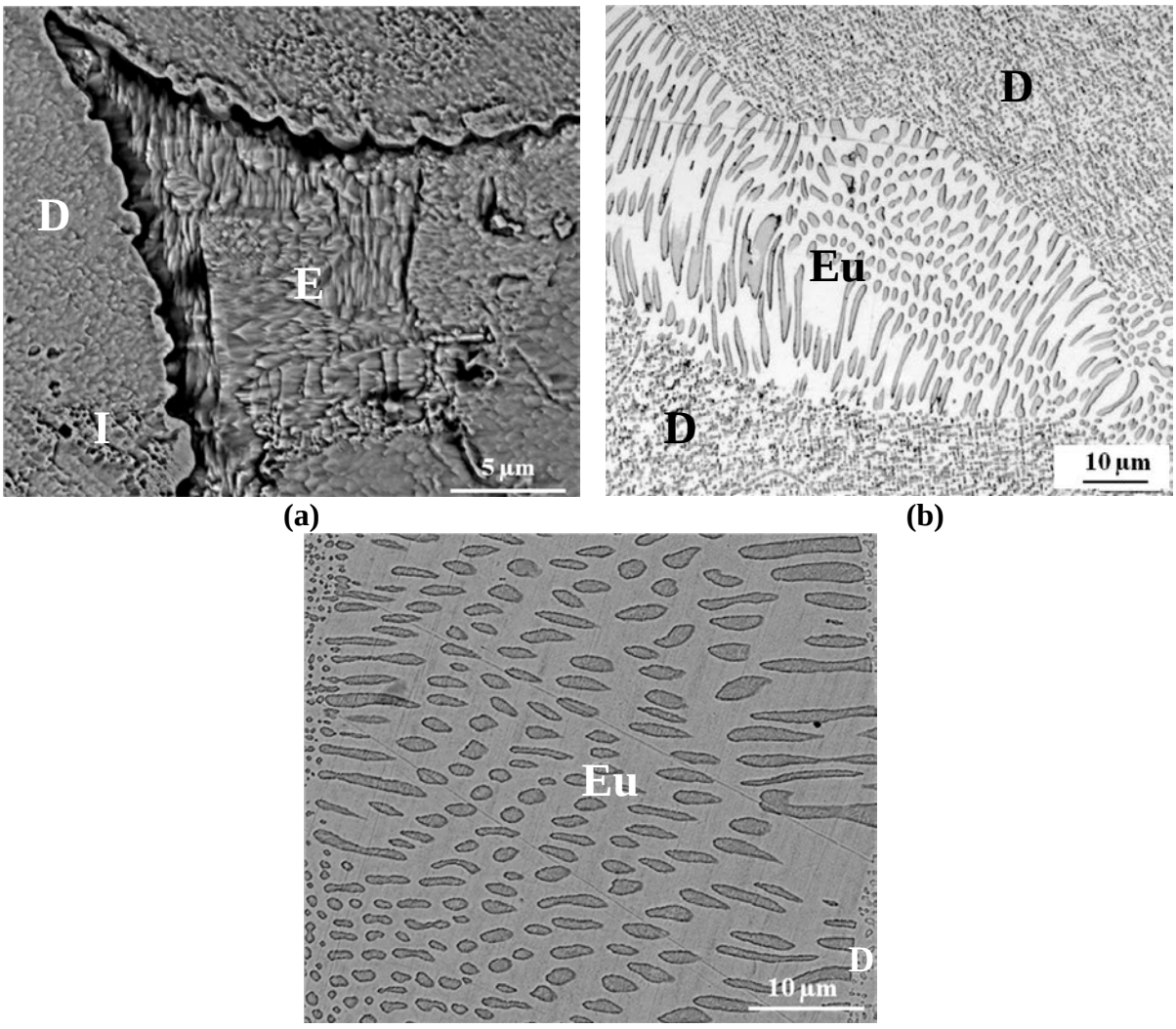


Figure 4.7. Annealed nominal Pt_{82}:Al_{12}:Cr_4:Ru_2 (at.%): (a) SEM-BSE image showing eutectoid (E) between dendrites (D), and irregular regions in the dendrites (I), (b) optical microscope image showing ~Pt_3Al precipitates in light (Pt) matrix in the dendrite (D), as well as a (Pt) + ~Pt_3Al eutectic (Eu), and (c) SEM-BSE image showing eutectic (Eu) between dendrites (D).

4.2.1.2 Nominal $Pt_{81.5}$:$Al_{11.5}$:$Cr_{4.5}$:$Ru_{2.5}$ (at.%)

The contrast after etching of the nominal $Pt_{81.5}$:$Al_{11.5}$:$Cr_{4.5}$:$Ru_{2.5}$ (at.%) sample was much improved from before [2009Sho1] and showed dark ~Pt_3Al precipitates in a light (Pt) matrix (Figure 4.8(a)), as well as the grain boundaries (Figure 4.8(b)). Figure 4.8(c) shows the eutectic/eutectoid at the grain boundaries. Figure 4.8(a) reveals features (Arrows A), which appeared fairly commonly and had not been observed before etching. EDX analysis confirmed that this feature had a higher Pt content than the surrounding region (Table 4.3). Since the dark precipitates were far too small to analyse accurately, the largest were selected for qualitative analysis, Table 4.3. The white irregular regions at the grain boundaries in

Figures 4.8(b) and 4.8(c) indicated by Arrow B are shown as SEM-BSE images in Figures 4.8(d) and 4.8(e). These features could have been a coarsened eutectoid. The compositions of the different regions are shown in Table 4.3 and were similar to the circular feature observed in Figure 4.8(a), within experimental error. In Figure 4.8(d) laths in area B can be seen, while some of the other lines are thought to be scratches from sample preparation.

Table 4.3. EDX analyses (at.%) of etched nominal $Pt_{81.5}$:$Al_{11.5}$:$Cr_{4.5}$:$Ru_{2.5}$ (at.%) in the heat treated condition for the different features in Figure 4.8.

Phase description	Pt	Al	Cr	Ru	Phase
Dark (Precipitates)	77.2 ± 0.8	20.1 ± 0.3	1.9 ± 0.2	0.8 ± 0.3	~Pt_3Al
Light (Matrix) (Figure 4.8(a))	85.2 ± 0.7	9.1 ± 0.3	4.0 ± 0.3	1.7 ± 0.1	(Pt)
Circular feature (A) (Figure 4.8(a))	90.6 ± 1.1	4.1 ± 0.5	2.9 ± 0.4	2.4 ± 0.3	(Pt)
Region B (Figure 4.8(d))	89.2 ± 1.9	5.9 ± 0.3	1.8 ± 0.7	3.1 ± 0.5	(Pt)
Region C (Figure 4.8(e))	90.0 ± 1.6	3.7 ± 0.8	2.1 ± 0.5	4.2 ± 0.4	(Pt)
Region D (Figure 4.8(e))	89.8 ± 1.4	2.9 ± 0.5	4.3 ± 0.6	3.0 ± 0.8	(Pt)

4.2.1.3 Nominal Pt_{78}:$Al_{15.5}$:$Cr_{4.5}$:Ru_2 (at.%)

After etching, the SEM revealed the presence of randomly aligned precipitates in some regions and some precipitate-decorated grain boundaries in the nominal Pt_{78}:$Al_{15.5}$:$Cr_{4.5}$:Ru_2 (at.%) sample, while other regions were free of precipitates (Figure 4.9(a)). The EDX phase analyses are recorded in Table 4.4, and as expected, the matrix had a higher Pt content than the precipitates. The optical microscope image after etching the specimen showed grains with differing contrasts due to their orientations, porosity (black spots), and a fine precipitation of ~Pt_3Al (Figure 4.9(b)). Most of the precipitates were too small for analyses and larger precipitates were targeted, although some were still smaller than 3µm. Thus, it is expected that the precipitates' EDX analyses have contributions from the surrounding matrix, so that the actual Pt content of the precipitates is lower than reported in Table 4.4.

Table 4.4. EDX analyses (at.%) of etched nominal Pt_{78}:$Al_{15.5}$:$Cr_{4.5}$:Ru_2 (at.%) in the heat treated condition.

Phase description	Pt	Al	Cr	Ru	Phase
Dark (Precipitates)	79.3 ± 1.4	18.2 ± 0.9	1.7 ± 0.3	0.8 ± 0.4	~Pt_3Al
Light (Matrix)	87.3 ± 1.2	7.1 ± 0.8	3.8 ± 0.8	1.8 ± 0.3	(Pt)

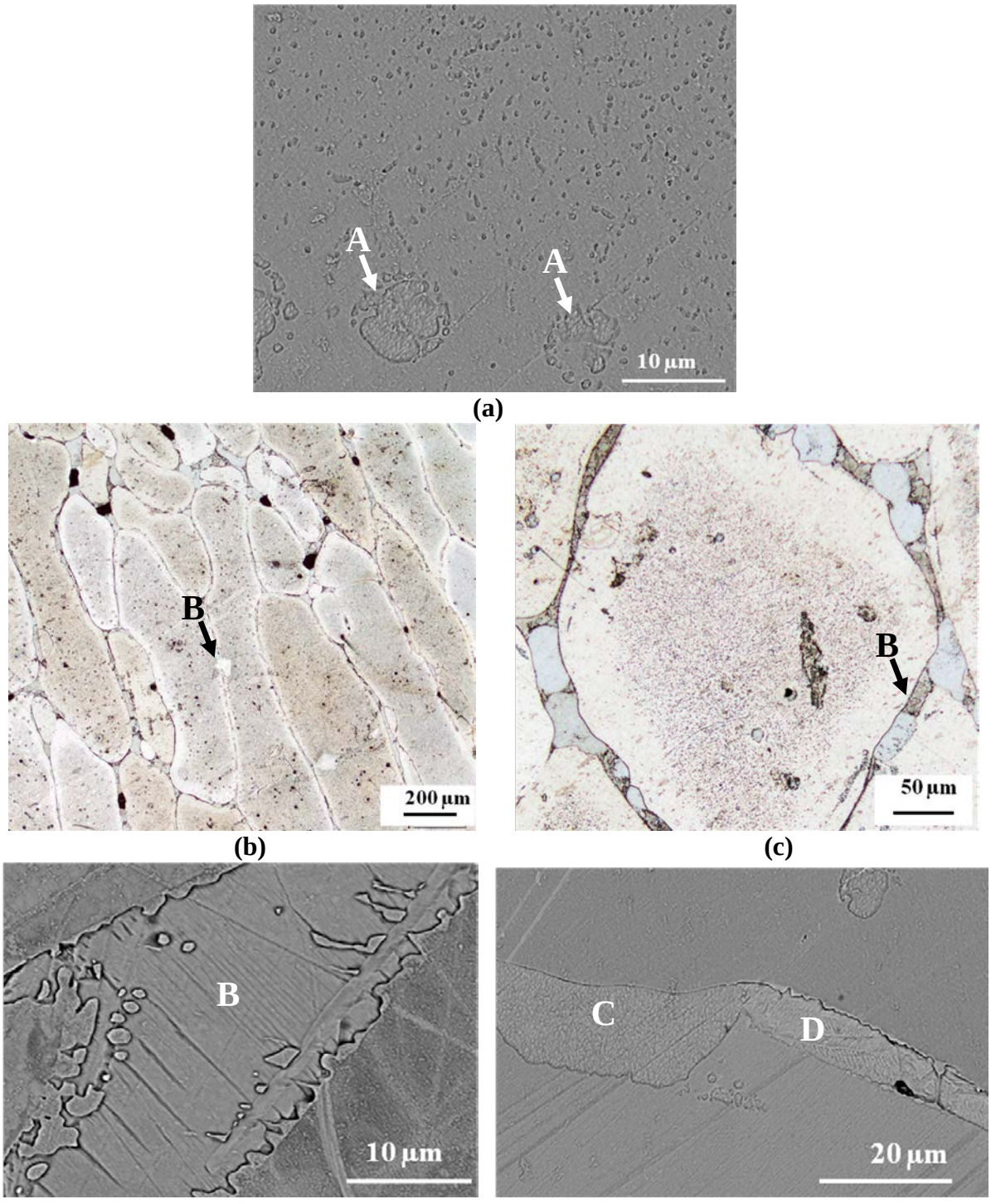
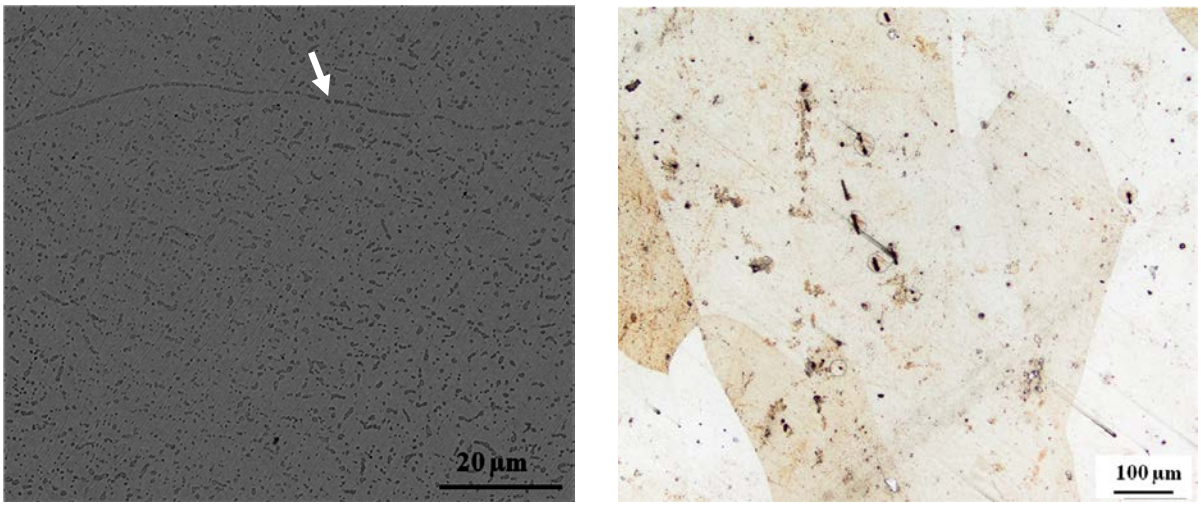


Figure 4.8. Annealed nominal $Pt_{81.5}$:$Al_{11.5}$:$Cr_{4.5}$:$Ru_{2.5}$ (at.%): (a) SEM-BSE image showing fine dark ~Pt_3Al precipitates in light (Pt) matrix and circular features (Arrows A), (b) optical microscope image showing fine dark ~Pt_3Al precipitates in light (Pt) matrix and grain boundaries, (c) coarsened eutectic/eutectoid ~Pt_3Al + (Pt) at the grain boundaries, and (d) and (e) SEM-BSE images of features indicated by Arrow B in (b) and (c), with laths (B) in (d), possibly a eutectoid (C) and (D) in (e).



(a) **(b)**

Figure 4.9. Annealed nominal Pt_{78}:$Al_{15.5}$:$Cr_{4.5}$:Ru_2 (at.%): (a) SEM-BSE image showing very fine dark ~Pt_3Al precipitates in light (Pt) matrix and precipitate-decorated grain boundary (indicated by arrow), and (b) optical microscope image showing different grains, and fine dark ~Pt_3Al precipitates in lighter (Pt) matrix.

4.2.1.4 Nominal Pt_{80}:Al_{14}:Cr_3:Ru_3 (at.%)

Figure 4.10 shows the microstructure of nominal Pt_{80}:Al_{14}:Cr_3:Ru_3 (at.%) after etching. Decorated subgrain boundaries were seen and the precipitates within the grains were not particularly aligned. Darker shades on the microstructure were thought to be sample preparation artifacts, since there were no composition differences. The phase analyses are given in Table 4.5 and larger precipitates were targeted, although they were still too small to analyse accurately.

Table 4.5. EDX analyses (at.%) of etched nominal Pt_{80}:Al_{14}:Cr_3:Ru_3 (at.%) in the heat treated condition.

Phase description	Pt	Al	Cr	Ru	Phase
Dark (Precipitates)	78.5 ± 1.1	19.4 ± 0.4	1.4 ± 0.4	0.7 ± 0.3	~Pt_3Al
Light (Matrix)	86.8 ± 0.9	7.5 ± 0.6	4.1 ± 0.5	1.6 ± 0.2	(Pt)

4.2.1.5 Nominal Pt_{80}:Al_{11}:Cr_4:Ru_5 (at.%)

The etched nominal Pt_{80}:Al_{11}:Cr_4:Ru_5 (at.%) sample showed ~Pt_3Al precipitates in a (Pt) matrix (Figure 4.11(a)). Some regions on the sample were free of precipitates, probably due to the low precipitate volume fraction and the inhomogeneity of the sample. The improved contrast after etching can been seen in Figure 4.11(b), showing grains with different contrast

due to differences in orientation, and porosity. The phase analyses are given in Table 4.6, and the largest precipitates were measured (although too small to analyse accurately).

Table 4.6. EDX analyses (at.%) of etched nominal Pt_{80}:Al_{11}:Cr_4:Ru_5 (at.%) in the heat treated condition.

Phase description	Pt	Al	Cr	Ru	Phase
Dark (Precipitates)	79.8 ± 1.2	18.1 ± 0.6	1.2 ± 0.3	0.9 ± 0.2	~Pt_3Al
Light (Matrix)	86.4 ± 0.9	8.1 ± 0.4	3.8 ± 0.7	1.7 ± 0.3	(Pt)

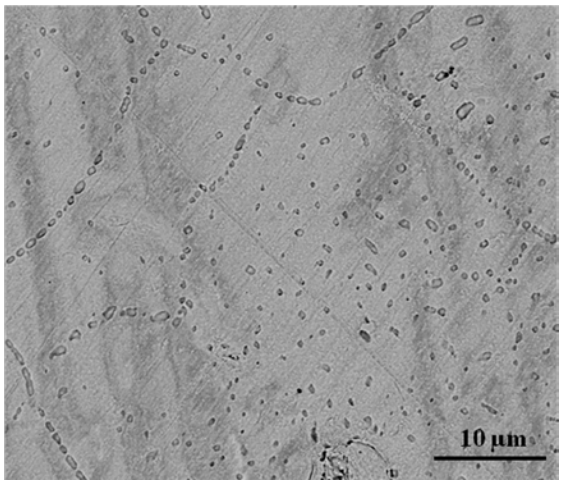
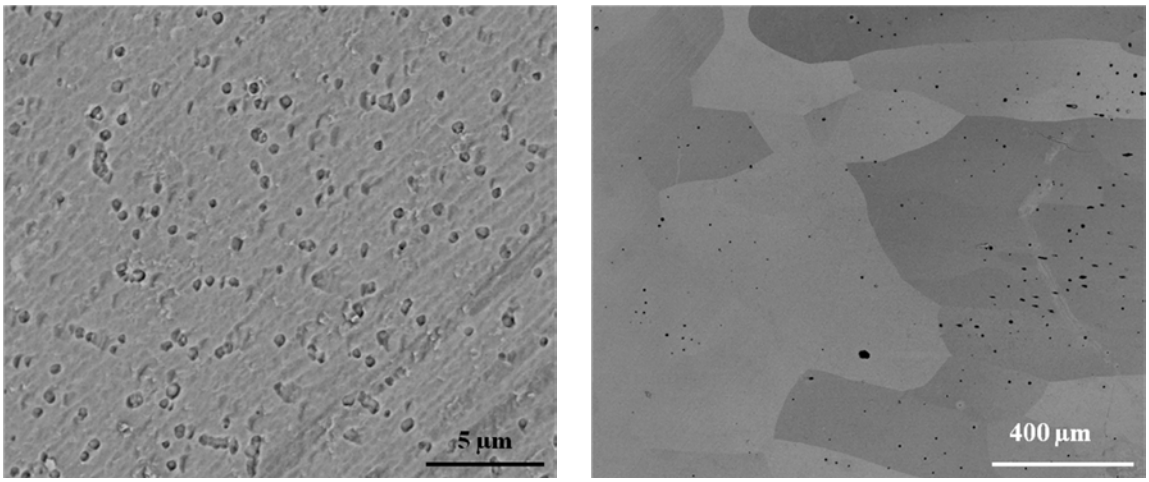


Figure 4.10. SEM-BSE image of heat treated nominal Pt_{78}:$Al_{15.5}$:$Cr_{4.5}$:Ru_2 (at.%), showing dark ~Pt_3Al precipitates in light (Pt) matrix and precipitates on sub-grain boundaries.



(a) **(b)**

Figure 4.11. SEM-BSE images of annealed nominal Pt_{80}:Al_{11}:Cr_4:Ru_5 (at.%) showing: (a) very fine dark ~Pt_3Al precipitates in light (Pt) matrix, and (b) optical microscope image showing differing contrasts due to different grain orientations, and porosity.

4.2.1.6 Nominal Pt_{78}:Al_{11}:Cr_3:Ru_8 (at.%)

After etching, the Pt_{78}:Al_{11}:Cr_3:Ru_8 (at.%) microstructure showed a coarsened eutectic (Figure 4.12), which indicated that the heat treatment did not fully eliminate the eutectic. The precipitates appear to have been over-etched. EDX analyses of the overall of the eutectic and the dendrites are recorded in Table 4.7.

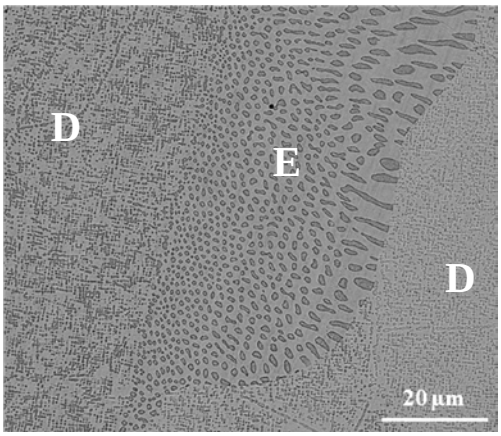


Figure 4.12. SEM-BSE image of heat treated nominal Pt_{78}:Al_{11}:Cr_3:Ru_8 (at.%) showing ~Pt_3Al precipitates in light (Pt) dendrite (D), and a coarsened (Pt) + ~Pt_3Al eutectic (E).

Table 4.7. EDX analyses (at.%) of etched nominal Pt_{78}:Al_{11}:Cr_3:Ru_8 (at.%) in the heat treated condition.

Phase description	Pt	Al	Cr	Ru	Phase
Dendrites (D)	84.1 ± 1.5	11.2 ± 0.7	2.9 ± 0.3	1.8 ± 0.2	(Pt)
Eutectic (E)	56.4 ± 1.3	41.6 ± 0.9	1.3 ± 0.6	0.7 ± 0.4	(Pt) + ~Pt_3Al

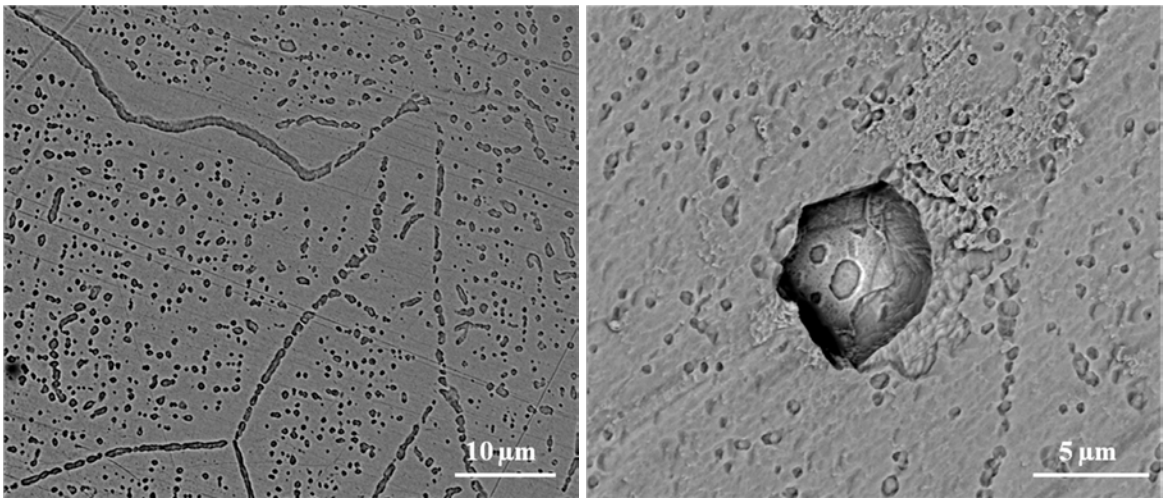
4.2.1.7 Nominal Pt_{80}:Al_{11}:Cr_6:Ru_3 (at.%)

The microstructure of Pt_{80}:Al_{11}:Cr_6:Ru_3 (at.%) had good contrast after etching, and is shown in Figure 4.13. Some of the grain boundaries were fully decorated with precipitates, with an adjacent precipitate-free zone in the grain. Figure 4.13(b) shows some porosity, and possible over-etching can be seen on the edges of the hole and surrounding regions.

4.2.1.8 Nominal Pt_{78}:Al_{11}:Cr_6:Ru_5 (at.%) and Pt_{85}:Al_7:Cr_5:Ru_3 (at.%)

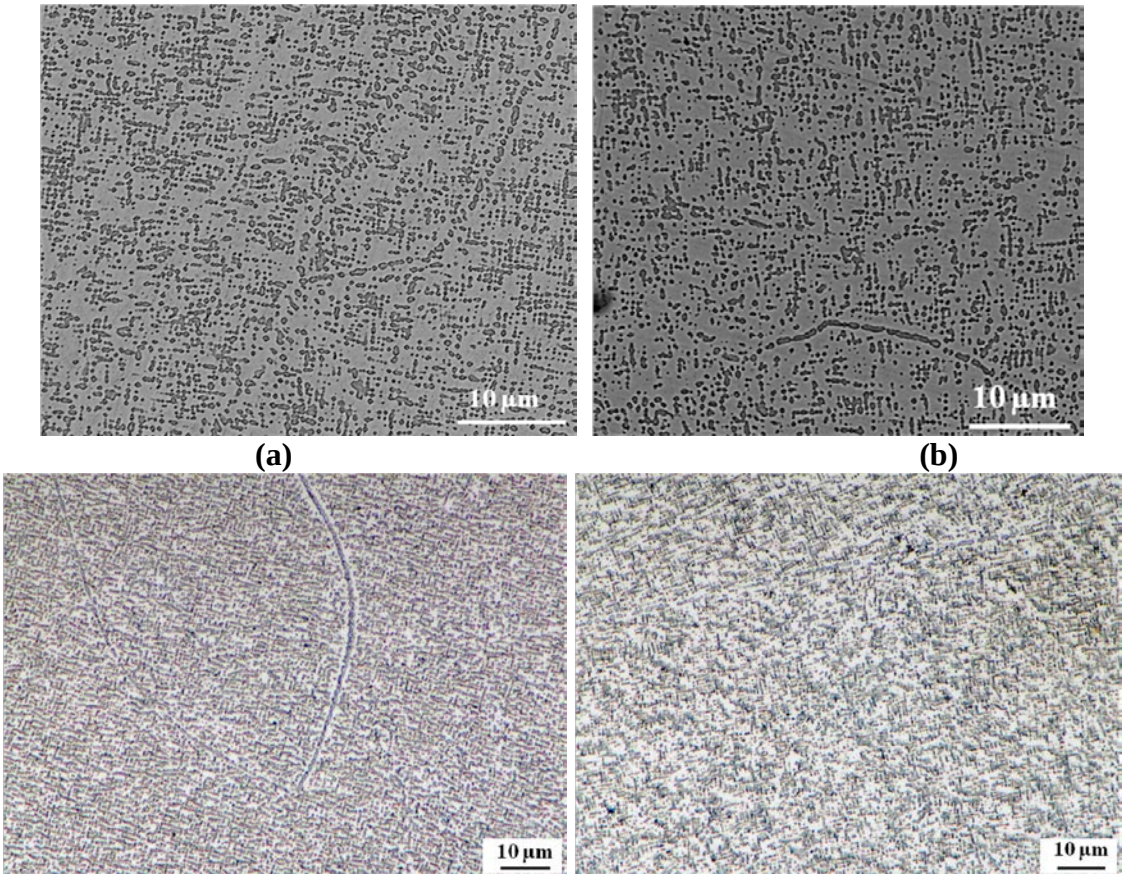
The SEM and optical microscope images of etched Pt_{78}:Al_{11}:Cr_6:Ru_5 and Pt_{85}:Al_7:Cr_5:Ru_3 (at.%), which had high ~Pt_3Al volume fractions (using the grid method [2009Sho1]) are shown in Figure 4.14. Compared to the unetched sample images [2009Sho1], the contrast was much improved and revealed aligned precipitates, indicating that etching was beneficial. Image analysis was only performed on the unprocessed SEM micrographs due to the too

small features of the optical images. Image analysis (Section 4.2.3) confirmed that these two samples had high volume fractions compared to the rest of the samples.



(a) **(b)**

Figure 4.13. SEM-BSE images of annealed nominal Pt_{80}:Al_{11}:Cr_4:Ru_5 (at.%) showing: (a) dark ~Pt_3Al precipitates in light (Pt) matrix, and (b) porosity (black spots) and a pit from possible over-etching.



(a) **(b)**

(c) **(d)**

Figure 4.14. Annealed nominal Pt_{78}:Al_{11}:Cr_6:Ru_5 (at.%) and Pt_{85}:Al_7:Cr_5:Ru_3 (at.%): (a,b) SEM-BSE images showing fine dark ~Pt_3Al precipitates in light (Pt) matrix and decorated grain boundaries, and (c,d) optical microscope images showing fine dark ~Pt_3Al precipitates in light (Pt) matrix and grain boundaries.

4.2.3 Image analysis

4.2.3.1 Olympus Software and Grid Method

The newly-prepared alloys had similar precipitate volume fractions, within experimental error, compared to the re-measured alloys, both measured using the Olympus stream image analysis software on SEM-BSE images (Table 4.8). Due to the low contrast between the phases on TEM images, it was not possible to perform image analyses on the TEM images, unlike the SEM images when the samples were etched. As a result, inorder to get an estimate of the precipitate volume fraction from the different samples analysed in TEM, the grid method was used on the TEM images and the results are given in Table 4.8.

4.2.3.2 AFM and WSxM

Figure 4.15 shows a typical window that was used for the calculation of the volume fraction for Pt_{80}:Al_{14}:Cr_3:Ru_3 (at.%) using the WSxM software, together with the AFM images. In Figure 4.15(a) the precipitates are dark and the matrix has a range of contrast, and in Figure 4.15(b) the matrix contrasts were light and medium, and the precipitates had the appearance of “holes”. The changes in the matrix contrast were due to changes in height, since in this AFM study, phases were identified by height. Results of all six alloys are given in Table 4.9. The Pt_{85}:Al_7:Cr_5:Ru_3 and Pt_{78}:Al_{11}:Cr_6:Ru_5 (at.%) alloys had the highest precipitate volume fractions, in agreement, within experimental error, with the Olympus stream image analysis software results for the newly-prepared alloys (Table 4.8).

Table 4.8. Approximate ~Pt_3Al volume fractions using the Olympus stream image analysis software on SEM-BSE images and grid method for TEM images

Nominal Composition (at.%)	Approximate ~Pt_3Al volume fraction		
	Olympus stream on SEM-BSE images		Grid method for TEM images
	Re-measured from previous alloys [2009Sho1]	Newly-prepared alloys	Newly-prepared alloys
$Pt_{78}:Al_{15.5}:Cr_{4.5}:Ru_2$	13 ± 4	Not analysed	Not analysed
$Pt_{80}:Al_{14}:Cr_3:Ru_3$	17 ± 3	13 ± 8	64 ± 9
$Pt_{81.5}:Al_{11.5}:Cr_{4.5}:Ru_{2.5}$	22 ± 6	Not analysed	Not analysed
$Pt_{82}:Al_{12}:Cr_4:Ru_2$	27 ± 7	26 ± 7	75 ± 6
$Pt_{84}:Al_{11}:Cr_3:Ru_2$	24 ± 4	Not analysed	Not analysed
$Pt_{85}:Al_7:Cr_5:Ru_3$	41 ± 8	45 ± 6	80 ± 6
$Pt_{80}:Al_{11}:Cr_4:Ru_5$	18 ± 4	Not analysed	Not analysed
$Pt_{80}:Al_{11}:Cr_6:Ru_3$	16 + 3	Not analysed	Not analysed
$Pt_{80}:Al_{11}:Cr_3:Ru_6$	21 ± 6	15 ± 4	61 ± 9
$Pt_{78}:Al_{11}:Cr_6:Ru_5$	40 ± 5	51 ± 6	83 ± 4
$Pt_{78}:Al_{11}:Cr_8:Ru_3$	31 ± 7	34 ± 9	67 ± 11
$Pt_{78}:Al_{11}:Cr_3:Ru_8$	28 ± 8	Not analysed	Not analysed

Table 4.9. Approximate ~Pt_3Al volume fractions analysed with WSxM software on AFM images.

Nominal composition (at.%)	Approximate ~Pt_3Al volume fraction (%)
$Pt_{80}:Al_{14}:Cr_3:Ru_3$	19 ± 4
$Pt_{82}:Al_{12}:Cr_4:Ru_2$	31 ± 7
$Pt_{85}:Al_7:Cr_5:Ru_3$	48 ± 8
$Pt_{80}:Al_{11}:Cr_3:Ru_6$	20 ± 5
$Pt_{78}:Al_{11}:Cr_6:Ru_5$	57 ± 9
$Pt_{78}:Al_{11}:Cr_8:Ru_3$	38 ± 6

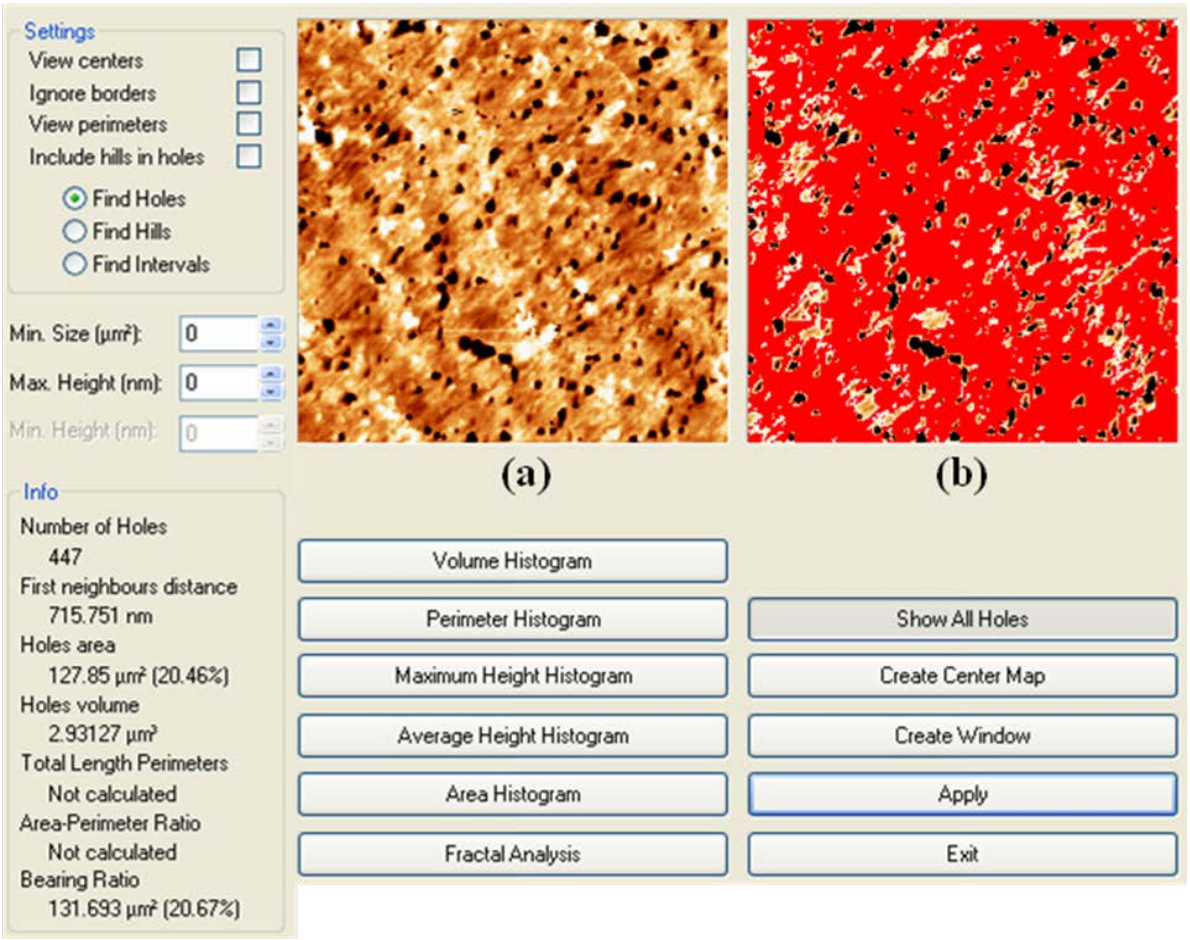


Figure 4.15. Window for ~Pt_3Al volume fraction calculation from AFM images for nominal Pt_{80}:Al_{14}:Cr_3:Ru_3 (at.%) using the WSxM software flooding function: (a) AFM topographic image, and (b) AFM topographic image after flooding and identification of precipitates as "holes".

4.3 Transmission Electron Microscopy Studies

4.3.1 TEM Microstructural Characterisation

In this section, the findings of the six alloys are reported in terms of their microstructure as determined by TEM. Particular attention was given to the study of the γ′ phase due to their associated precipitation hardening effects. The characterization was undertaken on a JEOL TEM 2100 (NMMU), unless otherwise stated. All error bars plotted on the Figures in this thesis indicate ± 1 sigma (standar deviation), i.e. 67% certainty.

4.3.1.1 Nominal Pt_{82}:Al_{12}:Cr_4:Ru_2 (at.%)

TEM images of nominal Pt_{82}:Al_{12}:Cr_4:Ru_2 (at.%) after being heat treated at 1500°C for 18

hours, followed by a water quench, then annealing at 1100°C for 120h and air cooling, are shown in Figures 4.16 to 4.18. The precipitate volume fraction was approximated to be 75 ± 6% (Table 4.8) by the grid method of Exner and Russ [1988Exn, 1999Rus] in this TEM localised area. Figure 4.16 shows a network of cubic, elongated and some "U" shaped precipitates indicated by symbol "A" on the image. The elongated precipitates were in the majority in the imaged area. Over the number of TEM samples of this alloy viewed, the precipitate distribution was found to vary, some areas had a high volume fraction of precipitates, while other regions had fewer precipitates. Figure 4.17 shows a different region in the thinned section where the γ′ precipitates had coarsened. The γ/γ′ interfaces showed dislocations. The size of the coarsened γ′ particles was ~250nm. The precipitates had an irregular shape, deviating greatly from cubic, showing a strong propensity for forming rounded precipitates. The coarsening of particles was noticed only once. At "Arrow B" (Figure 4.17), secondary particles are indicated, which were mostly rounded. "Arrow C" shows very fine tertiary γ′ precipitates. TEM EDX analyses were undertaken to measure the compositions of areas B, C and D in Figure 4.17 and the results are given in Table 4.10. These results reveal that the composition of area C was closer to D than E, supporting the view that there was precipitation of fine precipitates in C. However, small precipitates can be seen in the matrix in E, so the true matrix composition is actually higher in Pt than indicated in Table 4.10. The matrix protruded at the edges of the thinned section (Figures 4.16 and 4.17), showing that it was less affected by the ion milling.

A different section of the sample, an isolated region with fewer precipitates, Figure 4.18, shows the γ/γ′ interfaces with dislocation networks (Arrow A). Dislocations in the surrounding matrix were also seen (B). The presence of the interface dislocations indicates that the γ/γ′ interface was incoherent. Figures 4.16 to 4.18 show the inhomogeneous nature of the precipitate size and distribution in the alloy. Table 4.11 shows the composition of the matrix in Figure 4.18 next to the γ′ precipitate and also the γ′-free region, and differences being observed especially in the Al content. It is probable that there was some scattering of electrons into the neighbouring precipitates for matrix E (Figure 4.17, Table 4.10) and for the matrix next to the γ′ (γ′-rich region) (Figure 4.18, Table 4.11) due to the narrow width of the matrix between the precipitates.

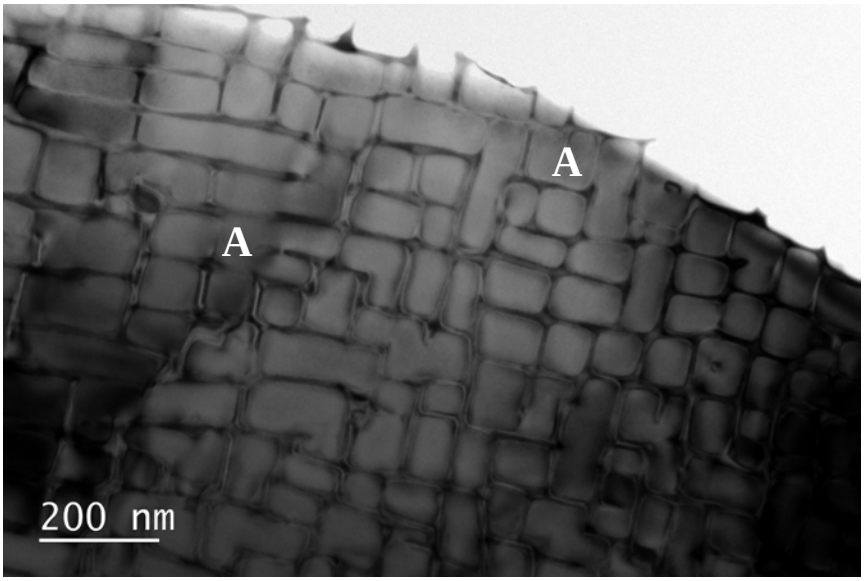


Figure 4.16. Bright field TEM image of nominal Pt_{82}:Al_{12}:Cr_4:Ru_2 (at.%) after heat treatment, showing a high volume fraction of γ′ precipitates, which had a cubic, elongated and (A) "U morphology" in a γ matrix.

Table 4.10. EDX analyses (at.%) of nominal Pt_{82}:Al_{12}:Cr_4:Ru_2 (at.%) in the heat treated condition for Figure 4.17.

Phase Description	Pt	Al	Cr	Ru	Phase
Matrix + Precipitates (C)	83.4 ± 0.2	14.1 ± 0.2	1.8 ± 0.1	0.7 ± 0.2	(Pt) + ~Pt_3Al
Precipitate (D)	80.8 ± 0.2	17.4 ± 0.1	1.3 ± 0.3	0.5 ± 0.2	~Pt_3Al
Matrix (E) (with small precipitates)	89.1 ± 0.4	5.3 ± 0.4	4.1 ± 0.1	1.5 ± 0.1	(Pt)

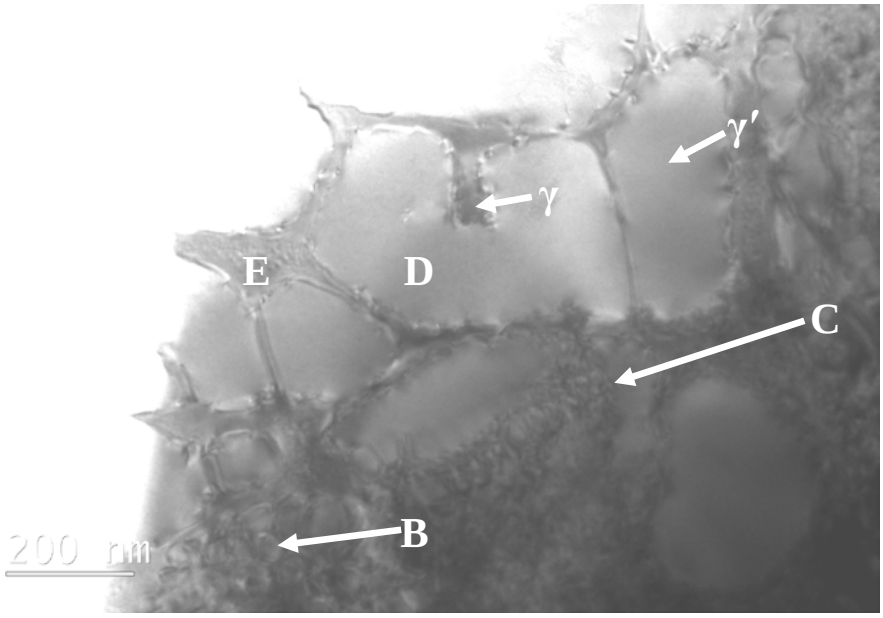


Figure 4.17. Bright field TEM image of nominal Pt_{82}:Al_{12}:Cr_4:Ru_2 (at.%) after heat treatment, showing coarsened γ′ precipitates and dislocations at the γ/γ′ interfaces, (B) isolated spherical γ′ precipitates, (C) tertiary γ′ precipitates, (D) irregular γ′ precipitates, and (E) γ matrix.

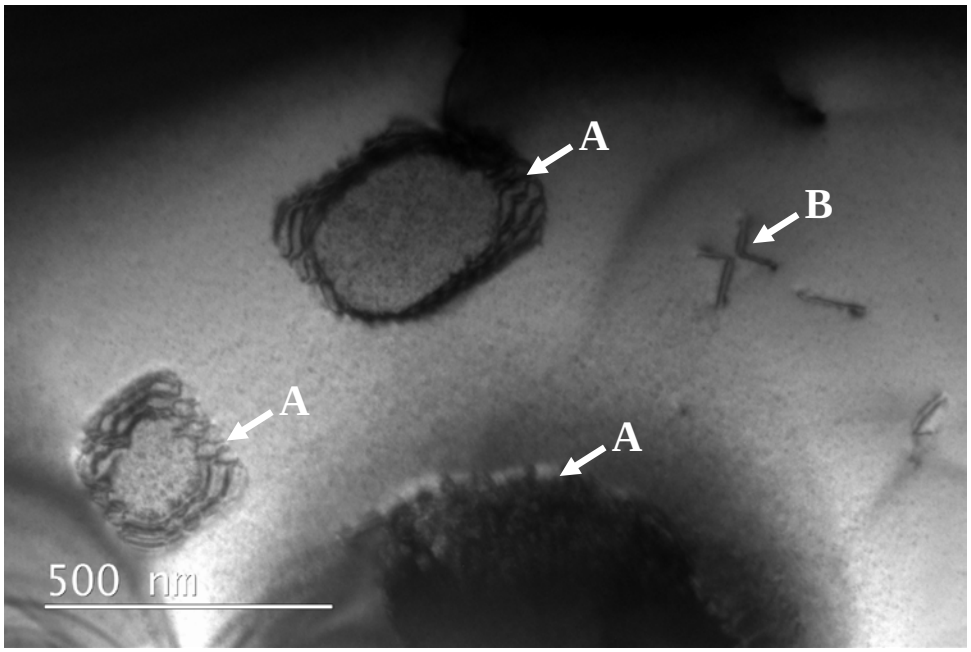


Figure 4.18. Bright field TEM image of nominal Pt_{82}:Al_{12}:Cr_4:Ru_2 (at.%) after heat treatment, showing (A) dislocations at the γ/ γ′ interface, and (B) dislocations in the γ matrix.

Table 4.11. EDX analyses (at.%) of nominal Pt_{85}:Al_7:Cr_5:Ru_3 (at.%) in the heat treated condition for Figure 4.18.

Phase Description	Pt	Al	Cr	Ru	Phase
Matrix next to γ′ (γ′-rich region)	84.7 ± 0.9	7.9 ± 0.3	4.6 ± 0.3	2.8 ± 0.4	(Pt)
Matrix with no γ′ (γ′-free region)	88.9 ± 0.7	1.1 ± 0.2	5.2 ± 0.4	4.8 ± 0.5	(Pt)

4.3.1.2 Nominal Pt_{85}:Al_7:Cr_5:Ru_3 (at.%)

Figure 4.19 shows a TEM image obtained from Pt_{85}:Al_7:Cr_5:Ru_3 (at.%). The microstructure consisted of a large volume fraction of γ′ precipitates separated by narrow γ channels. The precipitates were mainly cubic, with rounded edges and had an average edge length of ~50 - 100nm. Varying sizes of precipitates were observed along the thinned region (Figure 4.20): in A the precipitates were mainly coarse and cubic and in B, the precipitates were finer and rounded. Area B is thought to be a coarsened eutectic/eutectoid region. Figure 4.21 shows that some precipitates had coalesced and subsequently formed new and irregular shapes, although these were in limited isolated regions. The precipitates indicated by Arrows A suggest that they might have been initially cubic, and the shape change could have been due to some dissolution. A fine precipitation of secondary γ′ precipitates was observed, this was

confirmed by EDX analysis and also by electron diffraction. Isolated rounded γ′ precipitates were also observed (Arrows C). The γ′ precipitate volume fraction was estimated to be 80 ± 5% by the grid method of Exner and Russ [1988Exn, 1999Rus] for these localised regions.

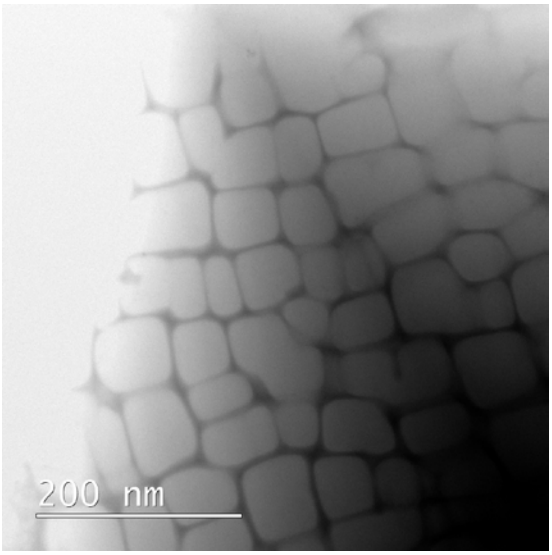


Figure 4.19. Bright field TEM image of nominal Pt_{85}:Al_7:Cr_5:Ru_3 (at.%) after heat treatment, showing homogenous distribution of mainly cubic shaped γ′ precipitates in a γ matrix.

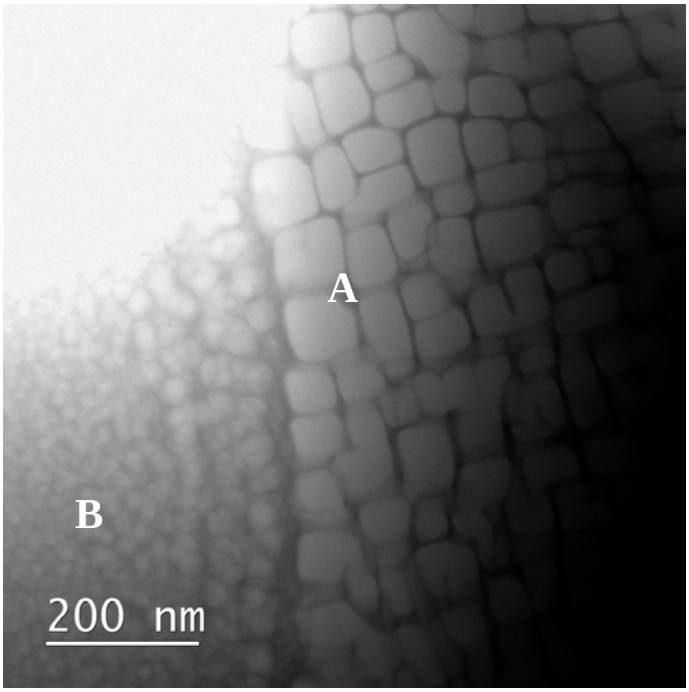


Figure 4.20. Bright field TEM image of nominal Pt_{85}:Al_7:Cr_5:Ru_3 (at.%) after heat treatment, showing areas of different γ′ precipitate shapes, with (A) cubic and (B) fine rounded morphology in a γ matrix.

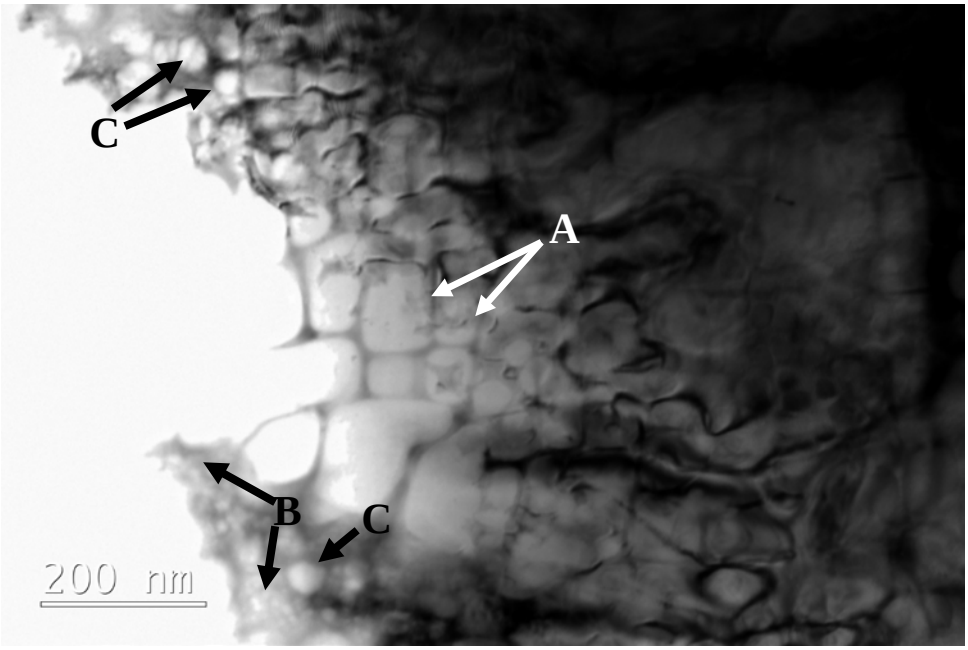


Figure 4.21. Bright field TEM image of nominal Pt_{85}:Al_7:Cr_5:Ru_3 (at.%) after heat treatment, showing (A) irregular, near-cubic shaped γ′ precipitates in a γ matrix, (B) tertiary precipitates, and (C) spherical γ′ precipitates.

4.3.1.3 Nominal Pt_{80}:Al_{11}:Cr_3:Ru_6 (at.%)

As observed in the other samples, the Pt_{80}:Al_{11}:Cr_3:Ru_6 (at.%) alloys had γ′ precipitates in a γ matrix (Figure 4.22). The γ′ volume fraction was measured to be, 61 ± 9%, using the grid technique [1988Exn, 1999Rus]. The precipitate morphology was mostly rounded and the size varied from ~100nm to 450nm. Smaller cubic γ′ precipitates with rounded edges (Figure 4.22, Arrows A) were observed. There was some short range alignment of the γ′ precipitates. A higher magnification image of the area of Figure 4.22 is given in Figure 4.23 and shows dislocations in the γ/γ′ interface (Arrows A). A different section of the thinned specimen showed a different microstructure which had many variations in the γ′ morphology (Figure 4.24). Coarsened primary and irregular γ′ particles were observed (Figure 4.24, Arrows A). A cluster of fine secondary particles was also seen (Figure 4.24, Arrow B). Some precipitates were observed with curved interfaces (Figure 4.24, Arrows C). A fine tertiary precipitation of γ′ precipitates was also seen at D, which was confirmed by microdiffraction having a diffraction pattern indicating the presence of both γ′ and γ. Table 4.12 shows EDX results of the smaller rounded γ′ precipitates and the primary γ′ precipitates, and differences in the composition for Cr and Pt were observed, with the primary γ′ having less Pt and more Cr.

The γ region near the γ′ in Figure 4.24 had a different composition from region D in Figure 4.24 (Table 4.12).

According to image analysis (Section 4.2.3), the alloy had a low volume fraction of γ′ precipitates, which was also seen in Figures 4.25 to 4.26 showing isolated precipitates. Each precipitate was surrounded by an interface dislocation network (Arrows A). Arrows B (Figure 4.25) show matrix dislocations, which were pinned by the precipitates. The compositions of the precipitates and matrix were measured across a precipitate/matrix interface (Table 4.13, Figure 4.23), and a compositional gradient of Cr was plotted (Figure 4.27). The error is not shown in Table 4.13 because the spot analyses were conducted once per spot only to approximate the composition along the γ/ γ′ interface due to focussed probe concerns.

Table 4.12. EDX analyses (at.%) of nominal Pt_{80}:Al_{11}:Cr_3:Ru_6 (at.%) in the heat treated condition for Figure 4.24.

Phase Description	Pt	Al	Cr	Ru	Phase
Primary γ′	77.3 ± 0.9	19.1 ± 0.4	2.9 ± 0.2	0.7 ± 0.2	~Pt_3Al
Secondary spherical γ′	79.9 ± 0.7	18.7 ± 0.4	0.5 ± 0.1	0.9 ± 0.3	~Pt_3Al
Matrix	84.7 ± 0.9	6.9 ± 0.4	5.2 ± 0.3	3.2 ± 0.3	(Pt)
Matrix + fine γ′ (D)	79.9 ± 0.8	14.6 ± 0.7	3.9 ± 0.3	1.6 ± 0.2	(Pt) + ~Pt_3Al

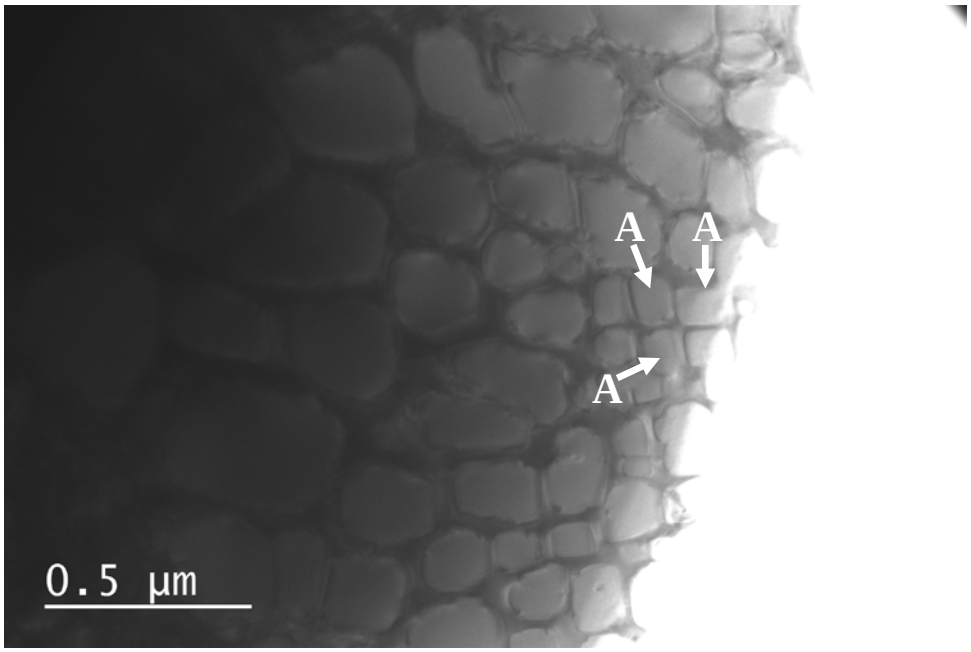


Figure 4.22. Bright field TEM image of nominal Pt_{80}:Al_{11}:Cr_3:Ru_6 (at.%) after heat treatment, showing different morphologies, sizes of spherical and cuboid-like γ′ precipitates (A) in γ matrix.

Table 4.13. EDX analyses (at.%) of nominal Pt_{80}:Al_{11}:Cr_3:Ru_6 (at.%) in the heat treated condition for Figure 4.23, measured across a precipitate/matrix interface.

Average distance (nm)	0*	40	60	70	85	95	110	125	135	150
Cr content (at.%)	5.1	4.8	4.5	4.2	4.3	4	3.8	3.7	3.8	2.4

***** *Approximate centre of γ matrix.*

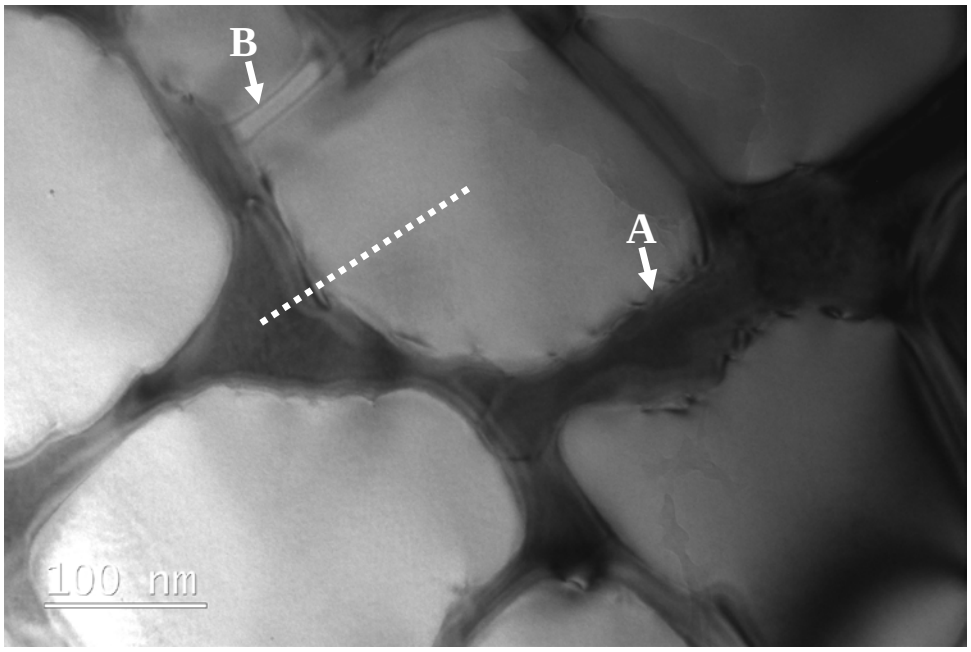


Figure 4.23. Bright field TEM image of nominal Pt_{80}:Al_{11}:Cr_3:Ru_6 (at.%) after heat treatment, showing (A) dislocations at the γ/γ′ interfaces, the dotted line shows the region used to study the composition gradient reported in Figure 4.27, and (B) is a clear view of the matrix material between two precipitates.

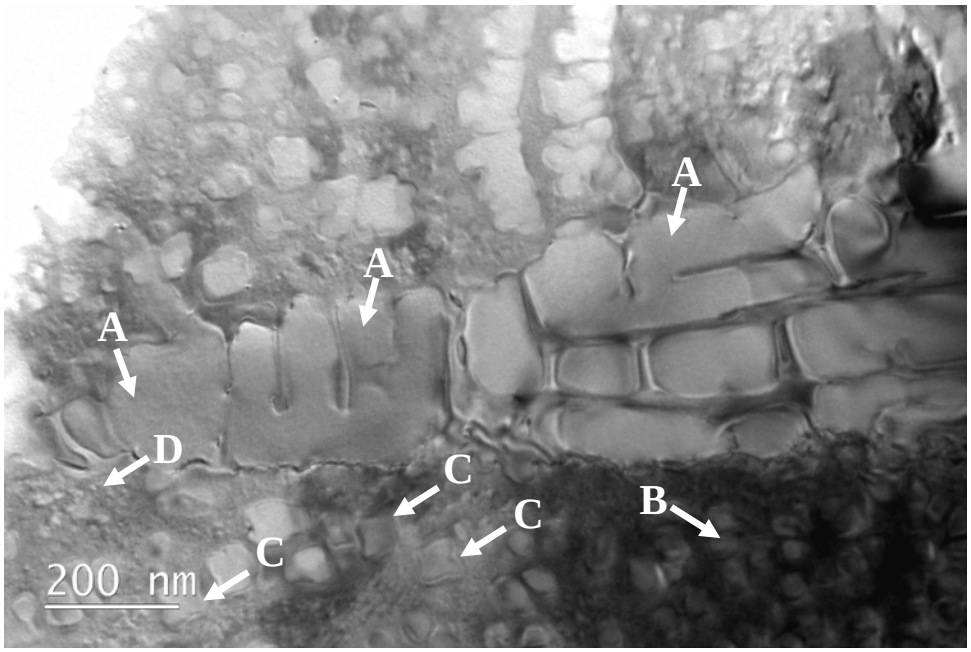


Figure 4.24. Bright field TEM image of nominal Pt_{80}:Al_{11}:Cr_3:Ru_6 (at.%) after heat treatment showing: (A) coalesced γ′ precipitates, (B) cluster of secondary γ′, (C) curving γ′ interfaces, and (D) a fine tertiary precipitation of γ′ in a γ matrix.

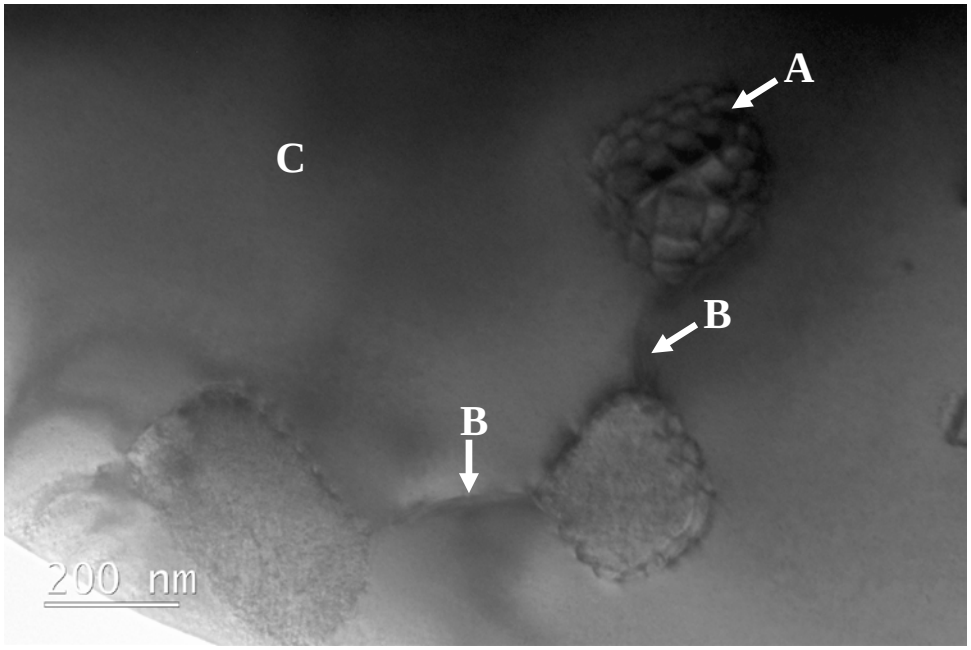


Figure 4.25. Bright field TEM image of nominal Pt_{80}:Al_{11}:Cr_3:Ru_6 (at.%) after heat treatment, showing (A) network of dislocations at the γ/γ′ interfaces, (B) matrix dislocations pinned by the precipitates, and (C) a precipitate-free area.

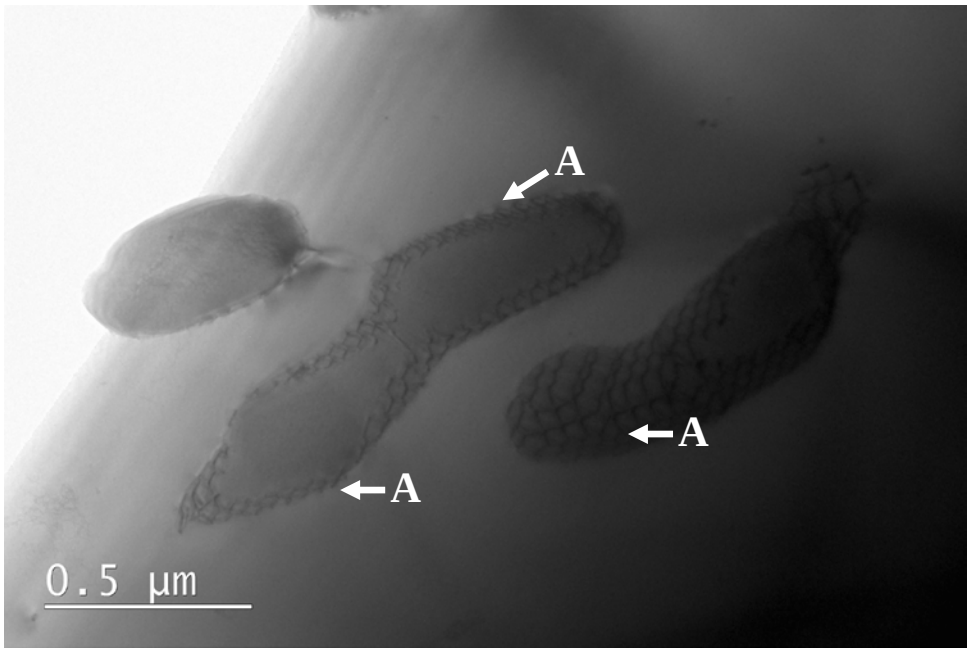


Figure 4.26. Bright field TEM image of nominal Pt_{80}:Al_{11}:Cr_3:Ru_6 (at.%) after heat treatment showing a network of dislocations (A) at the γ/γ′ interface.

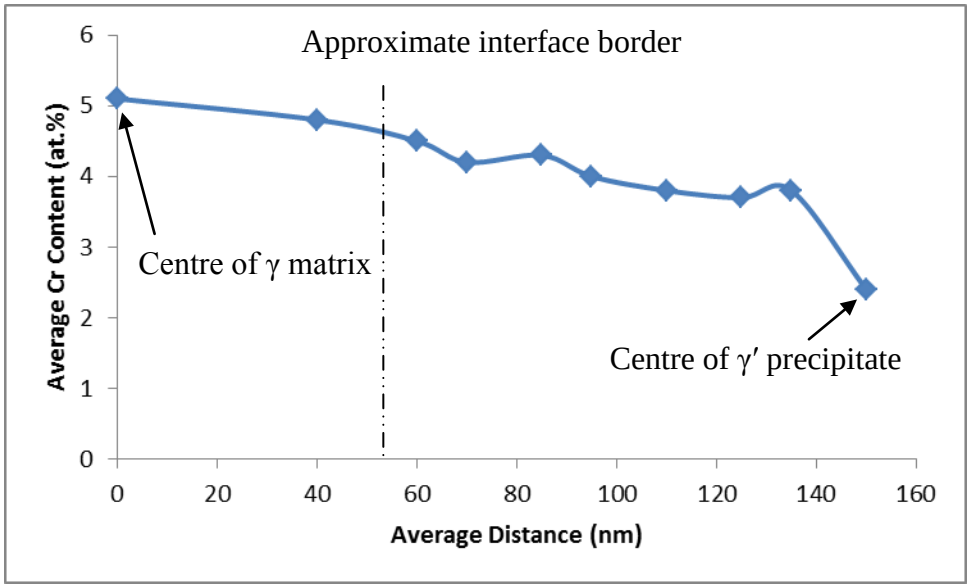


Figure 4.27. Composition gradient of Cr from centre of γ matrix to centre of γ′ precipitate in Pt_{80}:Al_{11}:Ru_6:Cr_3 (at.%), where the dotted line in Figure 4.23 is a typical region from the centre of the γ matrix channel to the centre of the γ′ precipitate.

4.3.1.4 Nominal Pt_{80}:Al_{14}:Cr_3:Ru_3 (at.%)

The microstructure of the Pt_{80}:Al_{14}:Cr_3:Ru_3 (at.%) alloy was inhomogeneous, as shown by Figures 4.28 to 4.32. The precipitates had different morphologies with varying sizes, from ~50nm to 450nm (along the longest side) (Figure 4.28), and the volume fraction was measured by the grid method to be 64 ± 9%. The largest precipitates (A) had irregular shapes, while medium-sized precipitates were more spherical (B), and the smallest precipitates were closer to being cubic with rounded edges (C) (Figure 4.28). Figure 4.28 shows cubic γ′ precipitates separated by varying width channels of γ matrix, giving the impression that the primary γ′ particles in some regions had coalesced to reduce surface energy. Figure 4.30 shows three different grains. "Area B" had varying shaped and sized γ′ precipitates separated by narrow γ matrix channels. "Area C" was a (Pt) single phase region (mainly composed of Pt (Table 4.14)), and the contrast variation was associated with minor changes in thickness. "Area D" was a mixture of fine γ′ precipitates in a γ matrix and the composition was different from that of "Area C", with a higher Al concentration, due the presence of the γ′ precipitates. Thus, the variation in alloy composition from one grain to the other provided a wide range of precipitate shapes, and different microstructures.

Figures 4.31 and 4.32, taken along the thinned section of a different region, using different contrast conditions, show isolated spherical precipitates bounded by a network array of interface dislocations (Arrow A), and also dislocations in the matrix (Arrows B).

Table 4.14. EDX analyses (at.%) of overall compositions of areas C and D in Figure 4.30 for nominal Pt_{80}:Al_{14}:Cr_3:Ru_3 (at.%) in the heat treated condition.

Phase Description	Pt	Al	Cr	Ru	Phase
Area C: Single phase	84.9 ± 1.1	7.9 ± 0.6	4.9 ± 0.4	2.3 ± 0.3	(Pt)
Area D: Matrix + precipitates	78.0 ± 0.9	17.8 ± 0.6	2.8 ± 0.2	1.4 ± 0.3	(Pt) + ~Pt_3Al

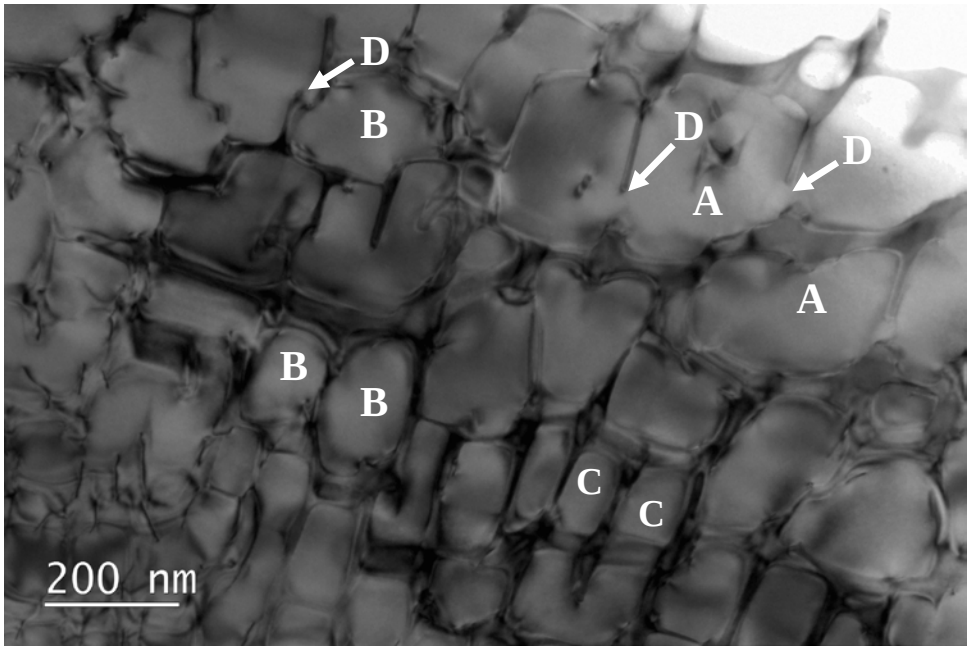


Figure 4.28. Bright field TEM image of nominal Pt_{80}:Al_{14}:Cr_3:Ru_3 (at.%) after heat treatment showing: (A) large irregular γ′ precipitates, (B) spherical γ′ precipitates, (C) cubic γ′ precipitates in a γ matrix, and (D) coalesced γ′ precipitates connected by necks.

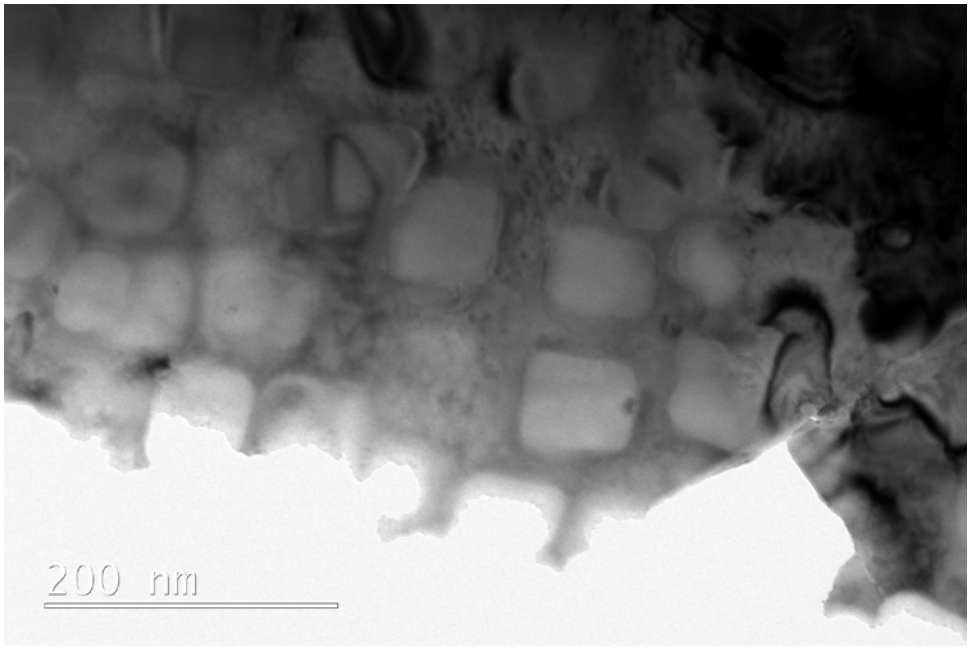


Figure 4.29. Bright field TEM image of nominal Pt_{80}:Al_{14}:Cr_3:Ru_3 (at.%) after heat treatment, showing cubic γ′ precipitates separated by varying widths of γ matrix.

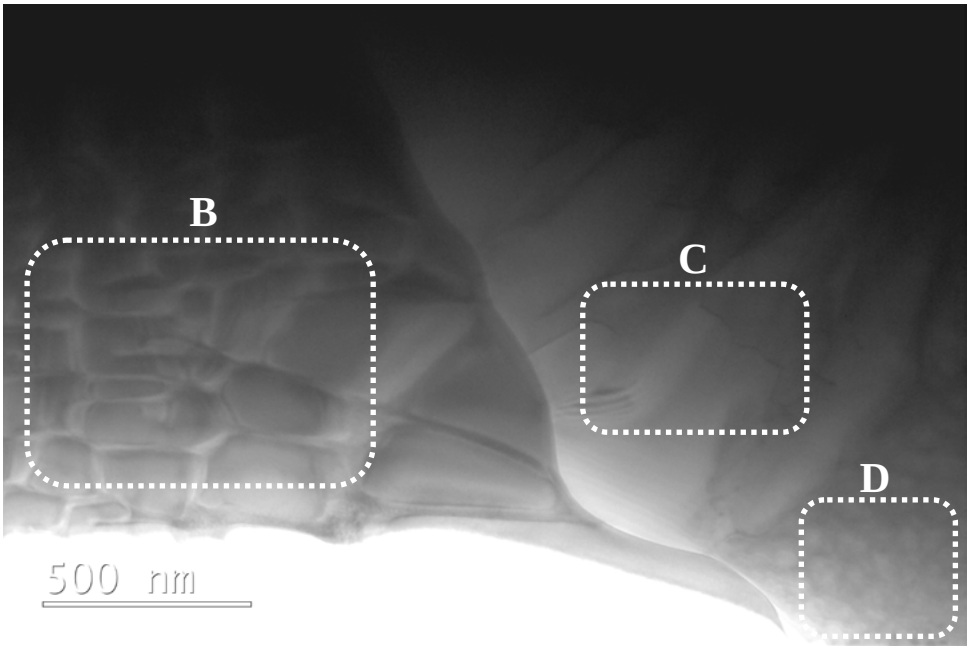


Figure 4.30. Bright field TEM image of nominal Pt_{80}:Al_{14}:Cr_3:Ru_3 (at.%) after heat treatment, showing three different grains with different microstructures (Areas B, C and D).

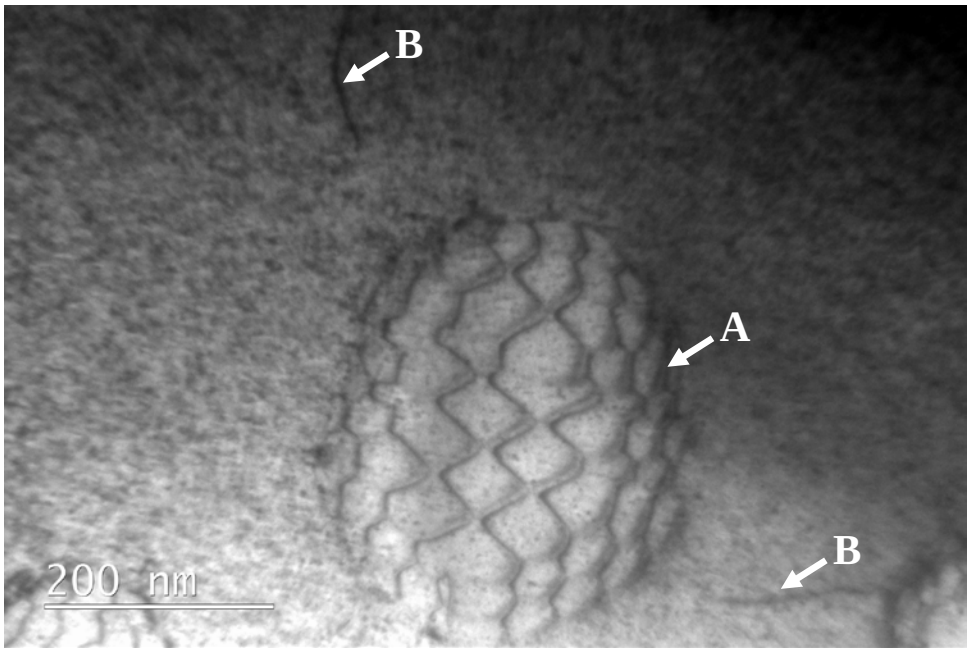


Figure 4.31. Bright field TEM image of nominal Pt_{80}:Al_{14}:Cr_3:Ru_3 (at.%) after heat treatment, showing an isolated, rounded precipitate with an interface network of dislocations (A), and dislocations in the matrix (B). General spotty background is damage resulting from ion milling.

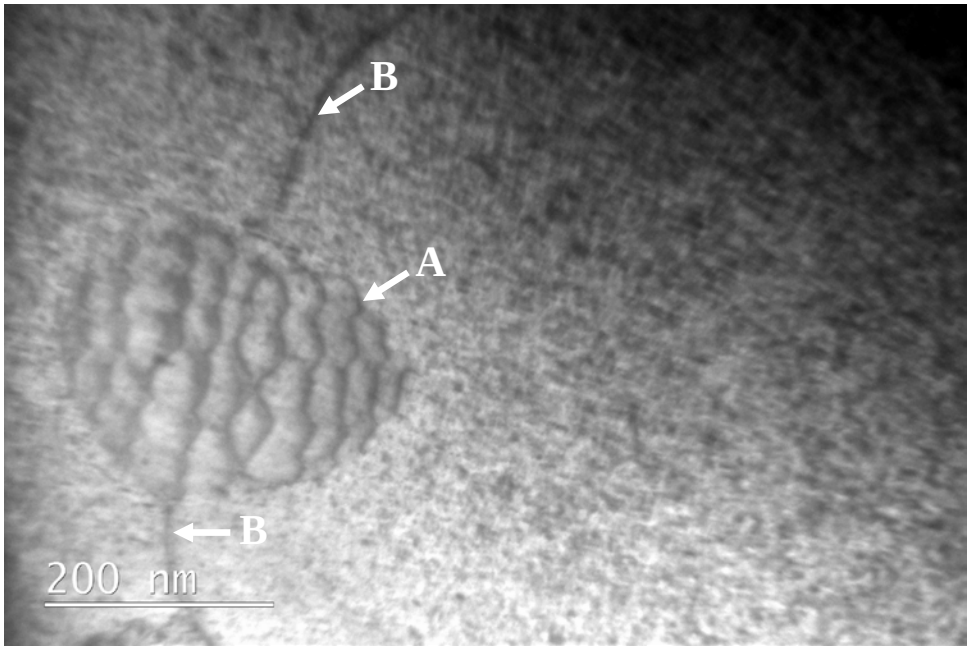


Figure 4.32. Bright field TEM image of nominal Pt_{80}:Al_{14}:Cr_3:Ru_3 (at.%) after heat treatment, showing an isolated, rounded precipitate with an interface network of dislocations (A), and dislocations in the matrix (B). General spotty background is damage resulting from ion milling.

4.3.1.5 Nominal Pt_{78}:Al_{11}:Cr_8:Ru_3 (at.%)

TEM revealed that different areas of the Pt_{78}:Al_{11}:Cr_8:Ru_3 (at.%) sample had γ′ precipitates of different shapes (Figures 4.33 and 4.34). A few rounded γ′ precipitates were observed, Figure 4.33 (A). Most of the precipitates in this region were mainly cubic with slightly rounded edges, although some cubic precipitates with straight edges were also observed (Figure 4.33, B). Figure 4.34 shows elongated γ′ precipitates. TEM EDX analyses were carried out on both the cubic (Figure 4.33) and the elongated γ′ precipitates (Figure 4.34). Within experimental error, the Al and Pt contents of the elongated γ′ precipitates were different from the cubic γ′ precipitates (Table 4.15). This suggests that higher Al content promoted larger and elongated γ′ particles, although more diffraction conditions would be necessary to prove this. No dislocations were observed in the matrix, precipitates or γ/γ′ interfaces under the 2-beam imaging conditions utilised. The γ′ precipitate volume fraction was estimated to be 67 ± 11% by the grid method.

Table 4.15. EDX analyses (at.%) of nominal Pt_{78}:Al_{11}:Cr_8:Ru_3 (at.%) in the heat treated condition.

Phase Description	Pt	Al	Cr	Ru	Phase
Figure 4.33, γ′	82.4 ± 0.5	16.4 ± 0.1	0.8 ± 0.3	0.4 ± 0.1	~Pt_3Al
Figure 4.34, γ′ (elongated)	76.7 ± 0.2	21.5 ± 0.1	1.3 ± 0.3	0.5 ± 0.2	~Pt_3Al

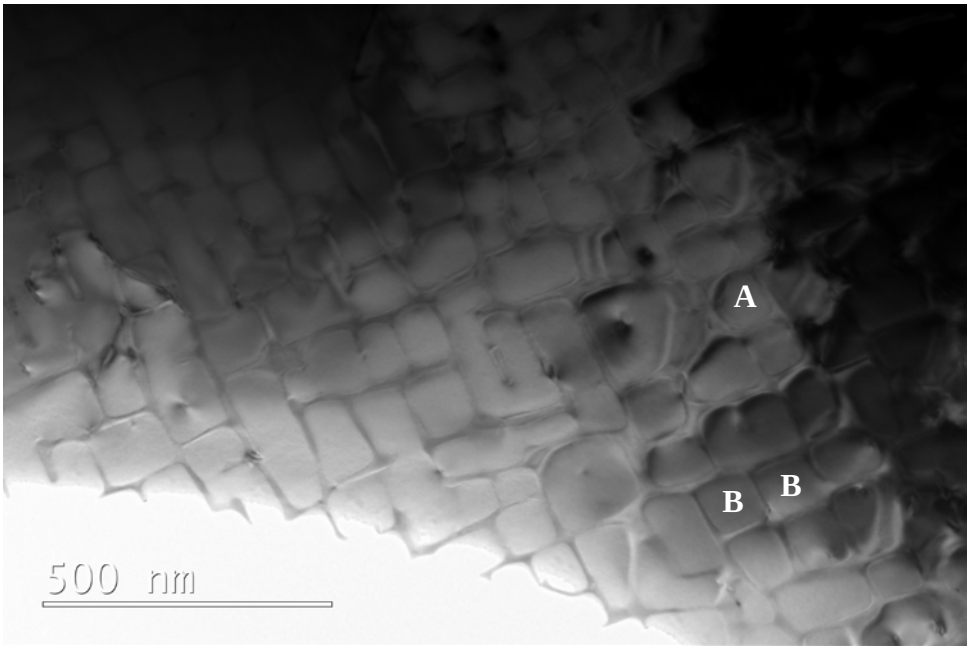


Figure 4.33. Bright field TEM image of nominal Pt_{78}:Al_{11}:Cr_8:Ru_3 (at.%) after heat treatment, showing γ′ precipitates in a γ matrix, (A) rounded and (B) cubic γ′ with straight edges.

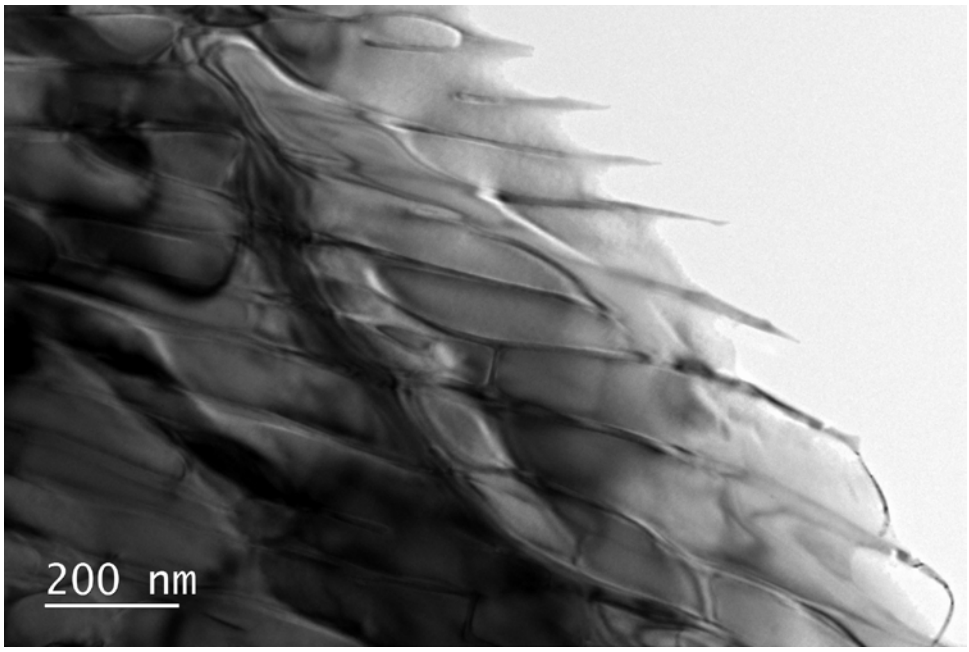


Figure 4.34. Bright field TEM image of nominal Pt_{78}:Al_{11}:Cr_8:Ru_3 (at.%) after heat treatment, showing an elongated morphology of γ′ precipitates in a γ matrix.

4.3.1.6 Nominal Pt_{78}:Al_{11}:Cr_6:Ru_5 (at.%)

TEM images of the nominal Pt_{78}:Al_{11}:Cr_6:Ru_5 (at.%) sample in the heat treated condition with various γ′ precipitate shapes are shown in Figures 4.35 to 4.37, and the sample had an approximate precipitate volume fraction of 83 ± 4% measured using the grid method. Figure 4.35, "Arrow A" shows γ′ precipitates that coalesced. This image shows a high γ′ precipitate density, with particle widths of 200-300nm. Figure 4.36 shows some alignment of cubic γ′ precipitates (dotted box). More irregular shaped precipitates were also seen. Finer rounded precipitates were observed (Figure 4.36, Arrows A). Figure 4.37 shows a wider area of the thinned sample, indicating a local, more homogenous distribution of the precipitates.

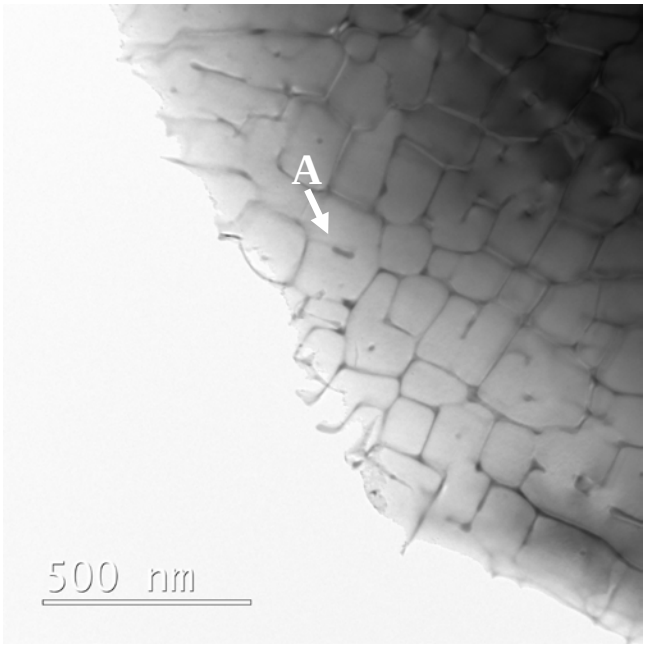


Figure 4.35. Bright field TEM image of nominal Pt_{78}:Al_{11}:Cr_6:Ru_5 (at.%) after heat treatment, showing cubic and (A) coalesced γ′ precipitates in a γ matrix.

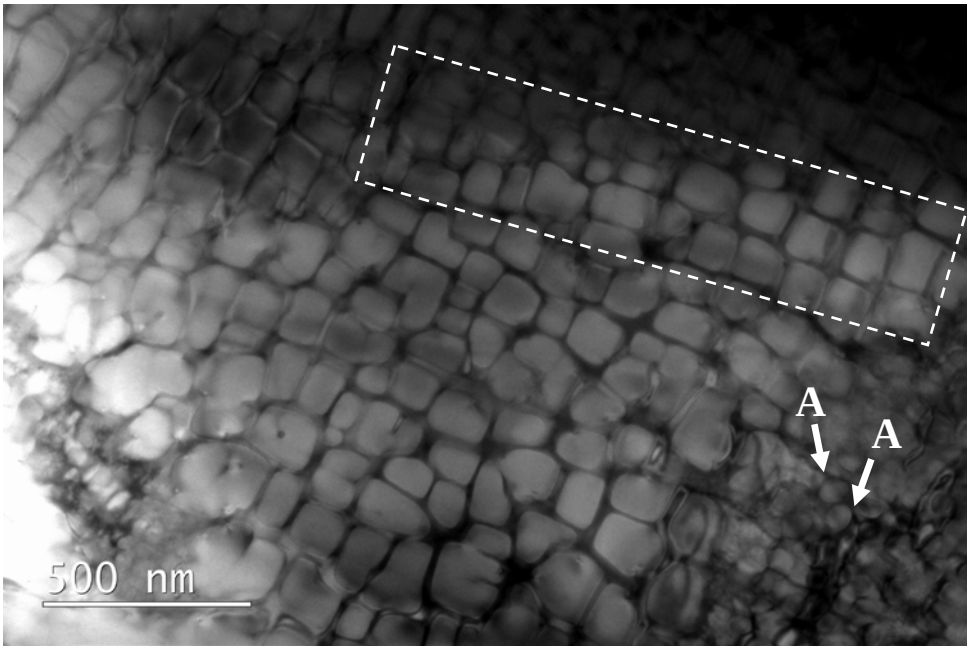


Figure 4.36. Bright field TEM image of nominal Pt_{78}:Al_{11}:Cr_6:Ru_5 (at.%) after heat treatment, showing mainly cubic and irregular morphology (A) of γ′ precipitates in a γ matrix, dotted box indicates alignment of γ′ precipitates.

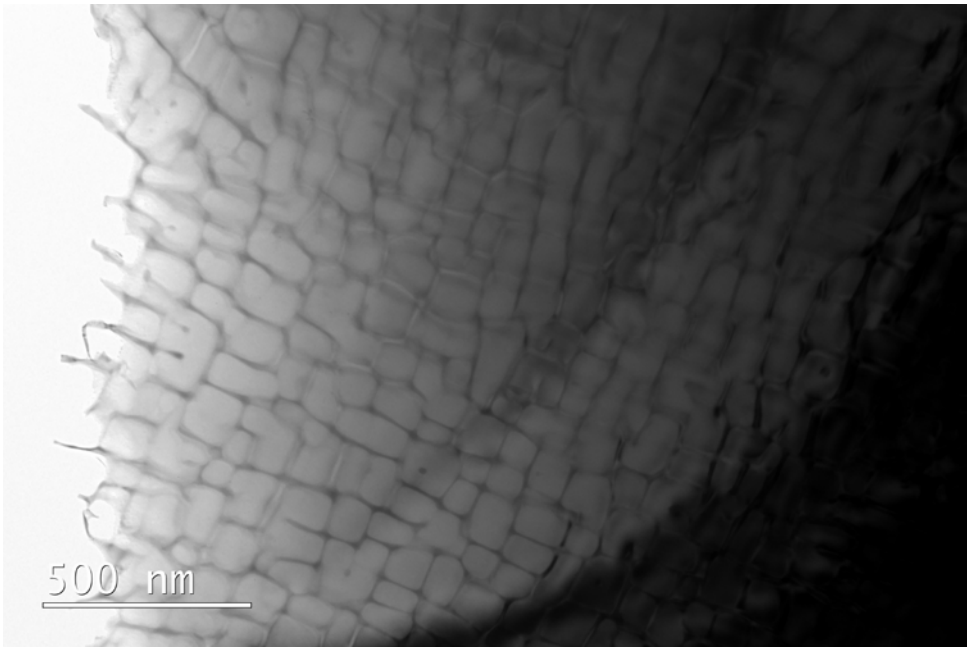
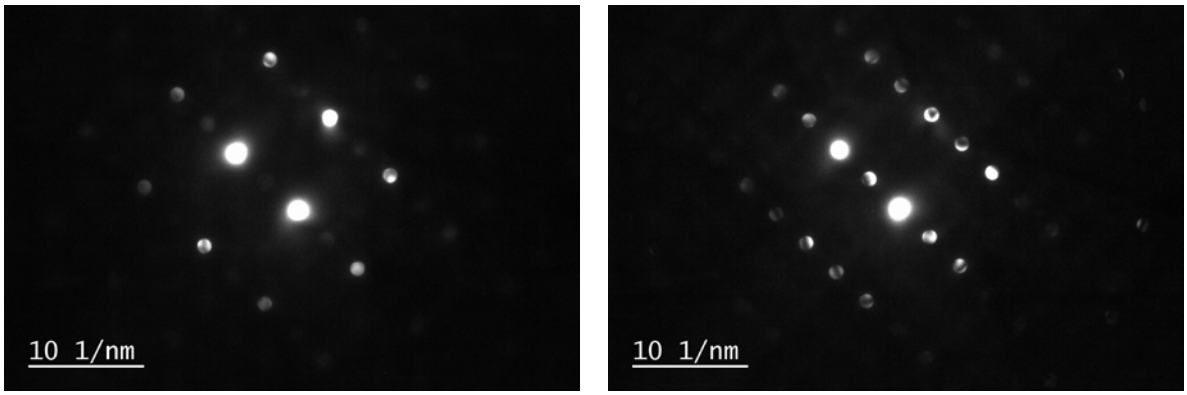


Figure 4.37. Bright field TEM image of nominal Pt_{78}:Al_{11}:Cr_6:Ru_5 (at.%) after heat treatment, showing a wider area of the thinned section, with a local homogenous distribution of γ′ precipitates in γ.

4.3.2 TEM diffraction patterns and orientation relationship between the Matrix and Precipitate

Manual measurements of diffraction patterns obtained from all γ′ precipitates analysed in the CM200 TEM all indexed as cubic $L1_2$ ~Pt_3Al rather than tetragonal DO'_c ~Pt_3Al or the modified DO'_c structure reported by Douglas *et al.* [2007Dou] because there were no superlattice diffraction spots seen at any zone axes sampled or during tilting to any zone axes, nor evidence of any twinning. Figures 4.38, 4.41 and 4.44 show three different experimental diffraction patterns for both the matrix and precipitates obtained from the JEOL 2100 TEM, these being representative of others taken. The precipitate and matrix diffraction pattern pairs shown in each case were obtained using the same beam conditions in order to determine the orientation relationship. The matrix diffraction patterns also revealed faint spots (Figures 4.38(a), 4.41(a) and 4.44(a)), which are attributed to the fact that the aperture would sample at least some of the precipitates. The matrix diffraction patterns were simulated with the JEMS software and were successfully indexed with the cubic Pt structure (Figures 4.39, 4.42, 4.45) reported by McAlister and Kahan [1986McA]. Simulations with the JEMS software package showed that it was not possible to index any of the experimental diffraction patterns of Pt_3Al given here (Figure 4.38(b), 4.41(b) and 4.44(b) and others not shown) using the tetragonal structure. Indexing was only possible with the cubic Pt_3Al phase (Figures 4.40, 4.43, 4.46 and others not shown). The orientation relationship between matrix (M) and precipitate (P) was for many precipitates: $[114]_M||[114]_P$; $[001]_M||[001]_P$; $[103]_M||[103]_P$.



(a) **(b)**

Figure 4.38. TEM diffraction pattern from nominal Pt_{78}:Al_{11}:Cr_6:Ru_5 (at.%) of: (a) γ matrix, and (b) γ′ precipitate.

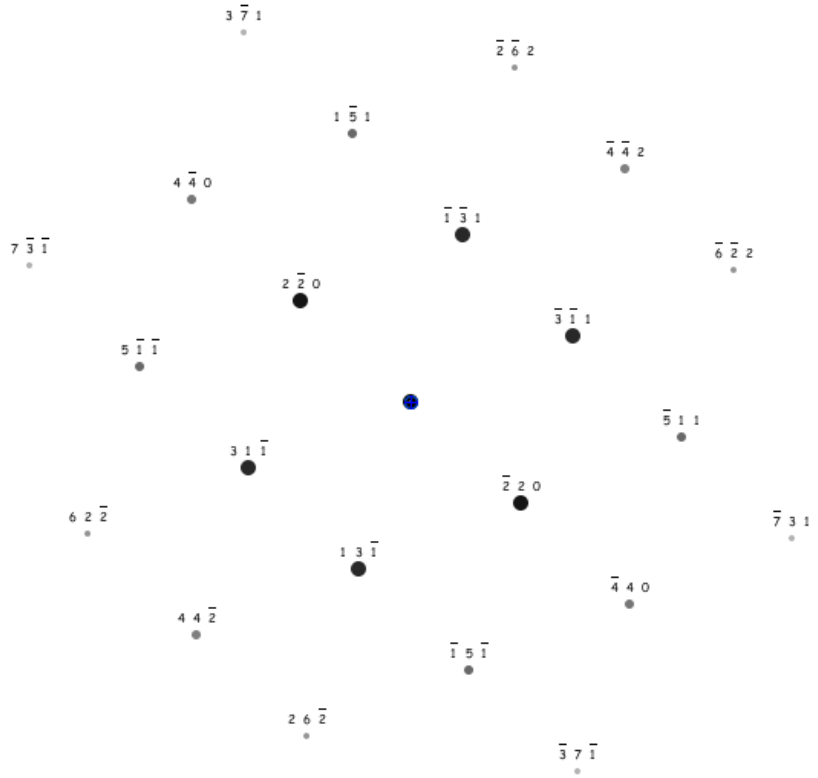


Figure 4.39. JEMS simulated diffraction of the γ matrix corresponding to experimental diffraction in Figure 4.38(a) on the [114] zone axis.

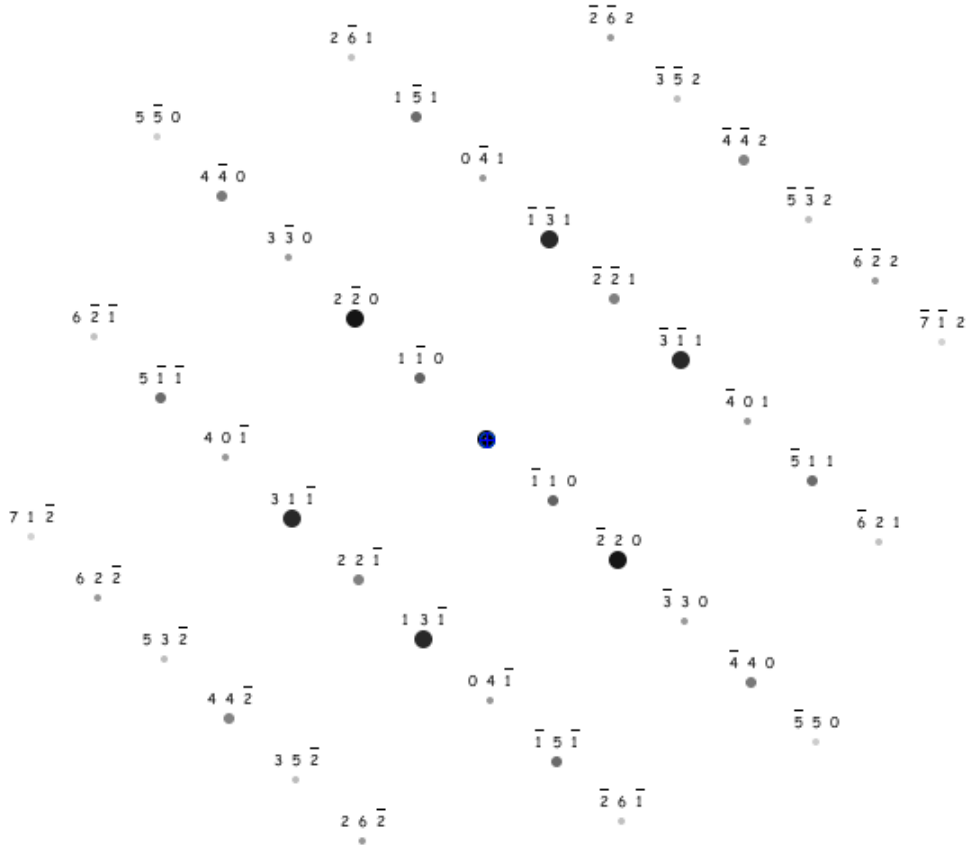
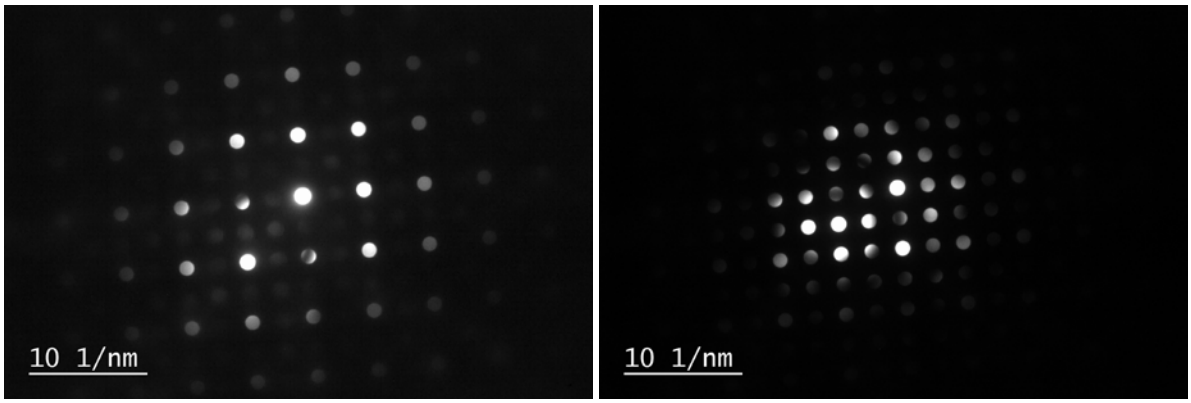


Figure 4.40. JEMS simulated diffraction of the γ′ precipitate corresponding to experimental diffraction in Figure 4.38(b) on the [114] zone axis.



(a) **(b)**

Figure 4.41. TEM diffraction patterns from nominal Pt_{78}:Al_{11}:Cr_6:Ru_5 (at.%) of: (a) γ matrix, and (b) γ′ precipitate.

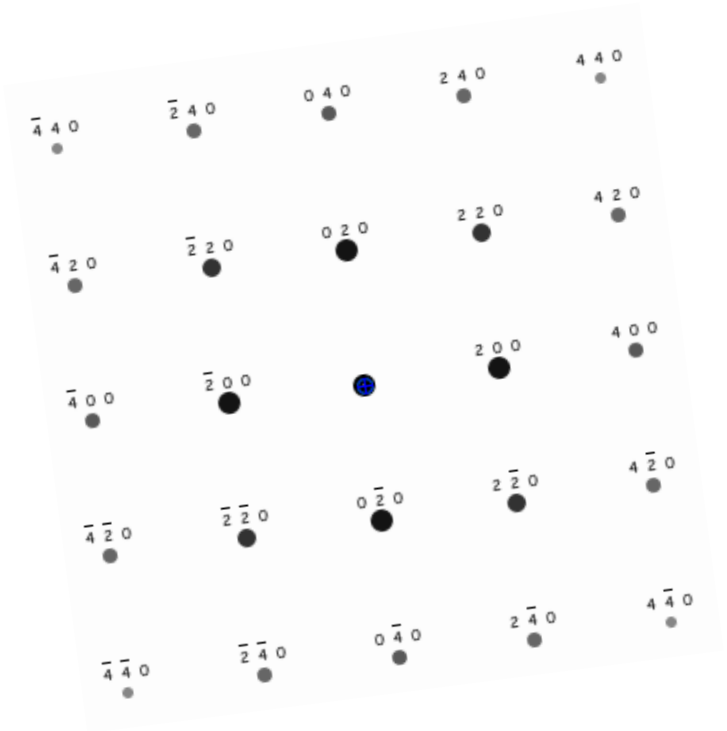


Figure 4.42. JEMS simulated diffraction of the γ matrix corresponding to experimental diffraction in Figure 4.41(a) on the [001] zone axis.

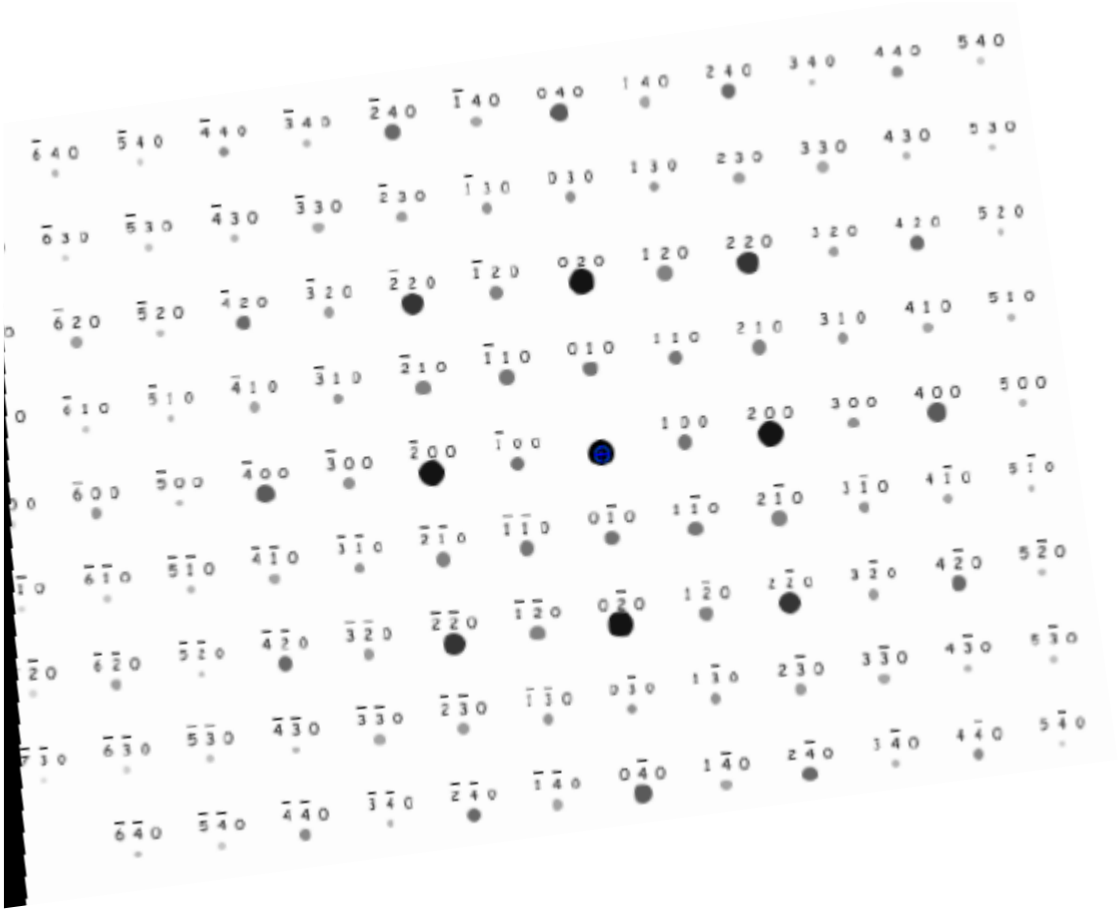
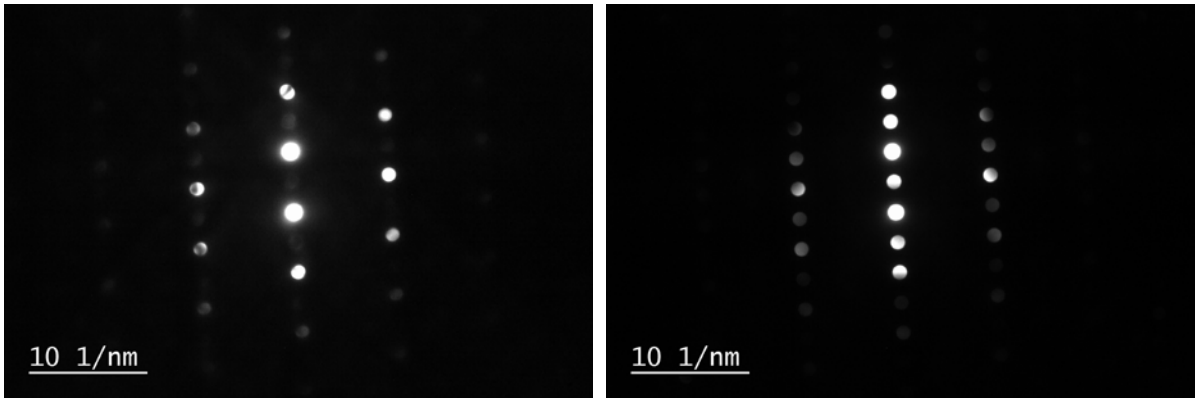


Figure 4.43. JEMS simulated diffraction of the γ′ precipitate corresponding to experimental diffraction in Figure 4.41(b) on the [001] zone axis.



(a) **(b)**

Figure 4.44. TEM diffraction patterns from nominal Pt_{78}:Al_{11}:Cr_6:Ru_5 (at.%) of: (a) γ matrix, and (b) γ′ precipitate.

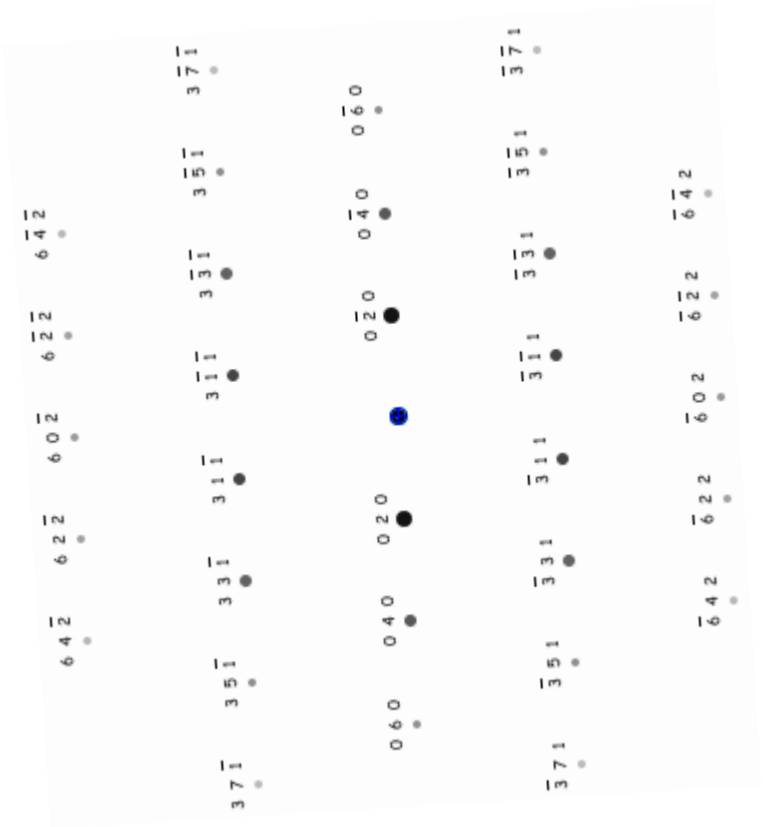


Figure 4.45. JEMS simulated diffraction of the γ matrix corresponding to experimental diffraction in Figure 4.44(a) on the [103] zone axis.

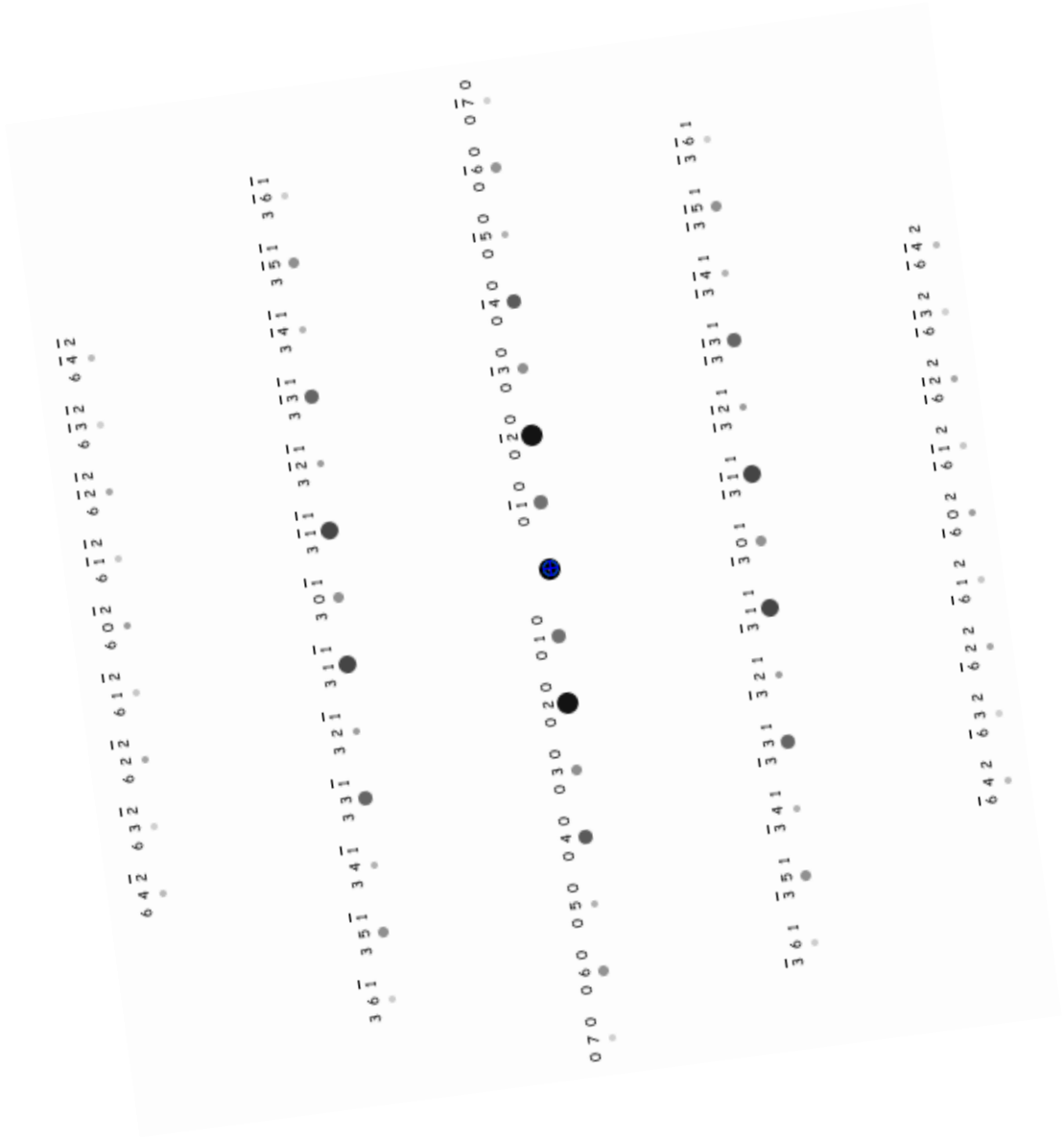


Figure 4.46. JEMS simulated diffraction of the γ′ precipitate corresponding to experimental diffraction in Figure 4.44(b) on the [103] zone axis.

4.4 Nanomechanical Properties Studies

4.4.1 Effect of Indentation Depth on Nanohardness and Elastic Modulus

Preliminary hardness and depth dependence studies were undertaken on two samples. To ensure that the testing conditions were suitable for the precipitate volume fraction range to be covered, the samples selected were for the two extreme ends of the range, that is, for the high and low γ′ volume fractions. Similar results were achieved for both extremes of the range, the results for Pt_{78}:Al_{11}:Cr_6:Ru_5 (at.%), high precipitate volume fraction, and for Pt_{80}:Al_{14}:Cr_3:Ru_3

(at.%), low precipitate volume fraction, are reported here. The reason for the indentation depth studies was to obtain an understanding of the depth dependence of the hardness, especially for very small phases (e.g. γ′). Preliminary studies of the hardness and indentation depth are important to ensure that at the maximum applied load, only the properties of a single phase are tested [1992Oli, 1999Gök, 2003Sch2].

Figure 4.47 shows a load displacement curve of the γ phase at a load of 2.5mN without any sign of the pop-in effect. However, it was observed that at loads lower than 2.5mN, the indentations were still visible, but the standard deviation was far more than 10%, being up to ~40% in more than half of the results. The high standard deviation was a result of the pop-in effect (Figure 4.48), which is a discontinuity found during loading in the load–displacement curve [1992Pag]. These sudden displacement jumps in the force (load)-displacement curve result from the transition from pure elastic to elastic-plastic deformation. All the Hertzian-fitted nanohardness and elastic modulus values were ~20% lower than the 2.5mN and 2.0mN curves that showed no pop-in effect. This probably meant that the fitting was not properly done, since it was done manually in Microsoft Excel using the raw data from nanoindentation measurements. Measurements were also done at 1mN, and also required a Hertzian fit of the loading parts, due to the pop-in effect, and similar results to the 2mN load were obtained. The results from the 1 and 2mN loads are reported separately in Appendix A, and compared with those from the 2.5mN load. The 2.5mN was the lowest load which showed no pop-in effect and the standard deviation was lower than the 10% acceptable error limit [2006CSM] when testing the individual phases. Thus, further hardness and depth dependence studies were carried out using the 2.5mN load, to ensure that only the properties of a single phase were tested.

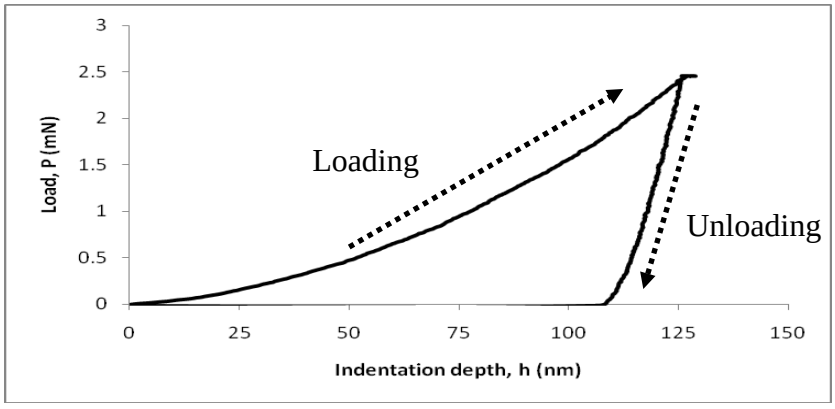


Figure 4.47. Example of a typical load-displacement curve (P-h curve) obtained during nanoindentation of Pt_{85}:Al_7:Ru_3:Cr_5 (at.%) in γ phase at 2.5mN load, showing no pop-in effect.

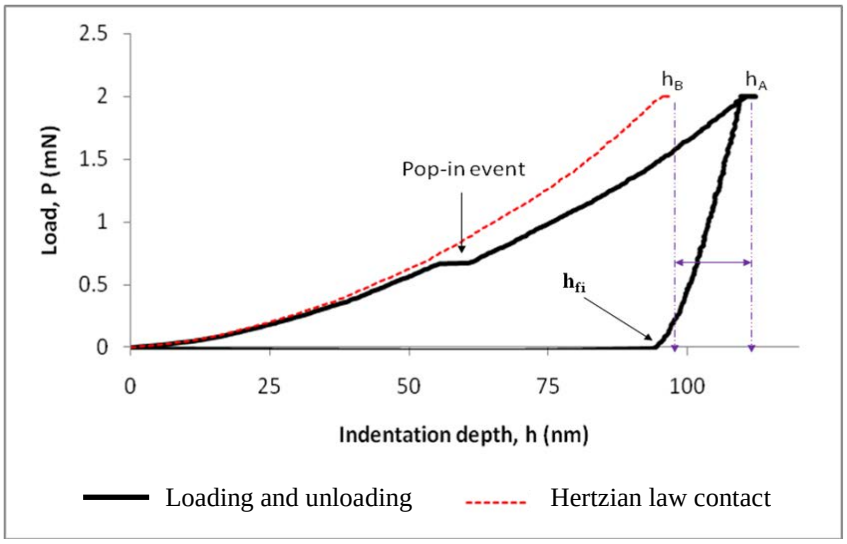


Figure 4.48. Example of a typical load-displacement curve (P-h curve) obtained during nanoindentation of Pt_{85}:Al_7:Cr_5:Ru_3 (at.%) in γ phase at 2.0mN load, showing a pop-in event and fitted Hertzian contact curve, with the final indentation depth re-defined, as h_{fi}.

The results for hardness against indentation depth for both Pt_{80}:Al_{14}:Cr_3:Ru_3 (at.%) and Pt_{80}:Al_{14}:Cr_3:Ru_3 (at.%) are shown in Figures 4.49 to 4.52 for the γ′ and γ phases. Each datum point represents the average value of indentation depth *h* and hardness *H* from 10 indentations with the same maximum load. The indentations were performed approximately in the centre of the precipitates, although this was not always possible. This was because the indenter tip would shift slightly to the surrounding regions. Indentations that fell outside the precipitate were not included in the calculations, and more indentations were performed that were approximately in the centre of the precipitate. For the matrix, it was easier to place the indentation in the centre, since the channels were much larger compared to the indentation size.

The γ′ phase hardness was up to around 50% higher (Figures 4.49 and 4.51) than for the γ matrix (Figures 4.50 and 4.52), and decreased with increasing indentation depth. Figure 4.53 shows typical load-displacement curves for the matrix and the precipitates at a maximum load of 2.5mN. Five indentations were taken to show the difference of the final contact depth between the precipitates and matrix. Each load-displacement curve represents a single indentation. At the same applied load, a smaller final contact depth was found for the γ′ precipitates, indicating a higher hardness compared to the matrix. This indicates that at the maximum applied load of 2.5mN with a maximum indentation depth of 75nm, the properties of the γ′ phase were mainly tested, beyond which there was a contribution of the γ phase to

the hardness of γ′. This observation is related to the γ′ precipitate sizes and the strain field around the indentations. In Figure 4.49, this was confirmed, since beyond 75nm, there was a sudden drop in the hardness of the γ′ phase. These results are important, since they indicated that the 2.5mN load could, within reasonable experimental error, indent the γ′ phase with only minor influence from the surrounding γ phase. The γ phase was not affected by an increase in the indentation depth (Figure 4.50).

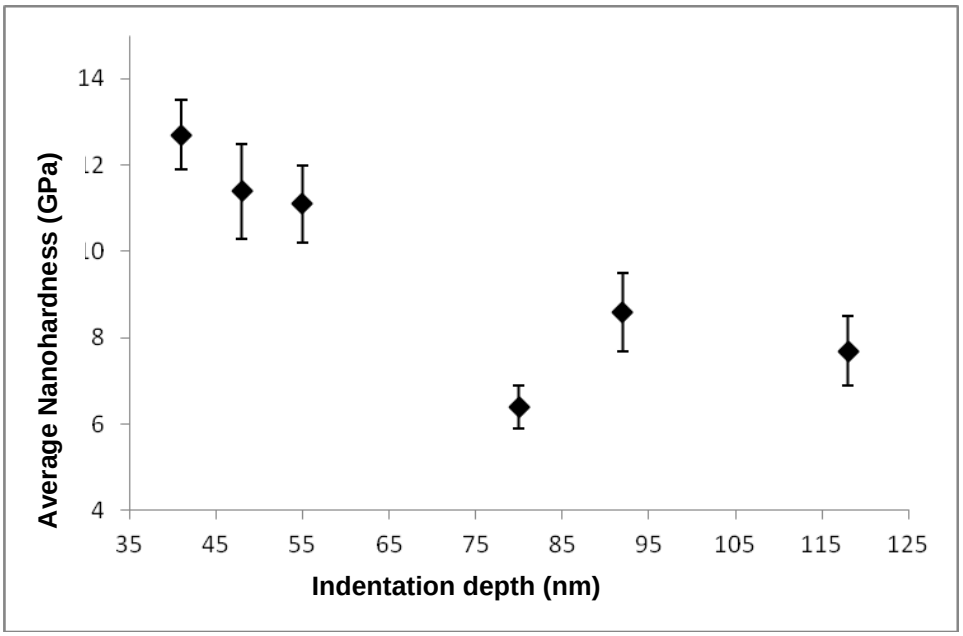


Figure 4.49. Nanohardness as a function of indentation depth for the γ′ precipitates in Pt_{78}:Al_{11}:Cr_6:Ru_5 (at.%).

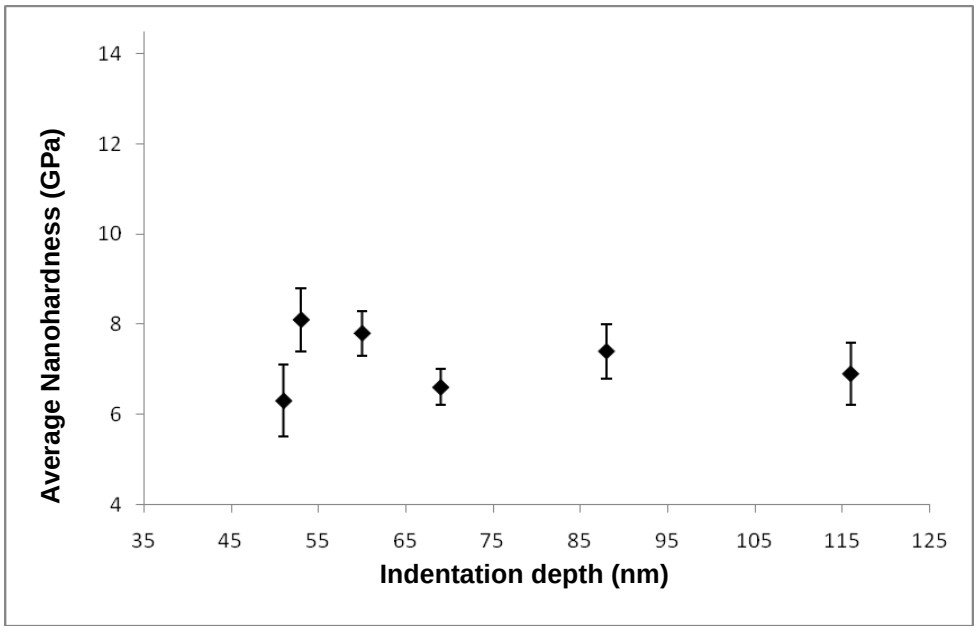


Figure 4.50. Nanohardness as a function of indentation depth for the γ matrix in Pt_{78}:Al_{11}:Cr_6:Ru_5 (at.%).

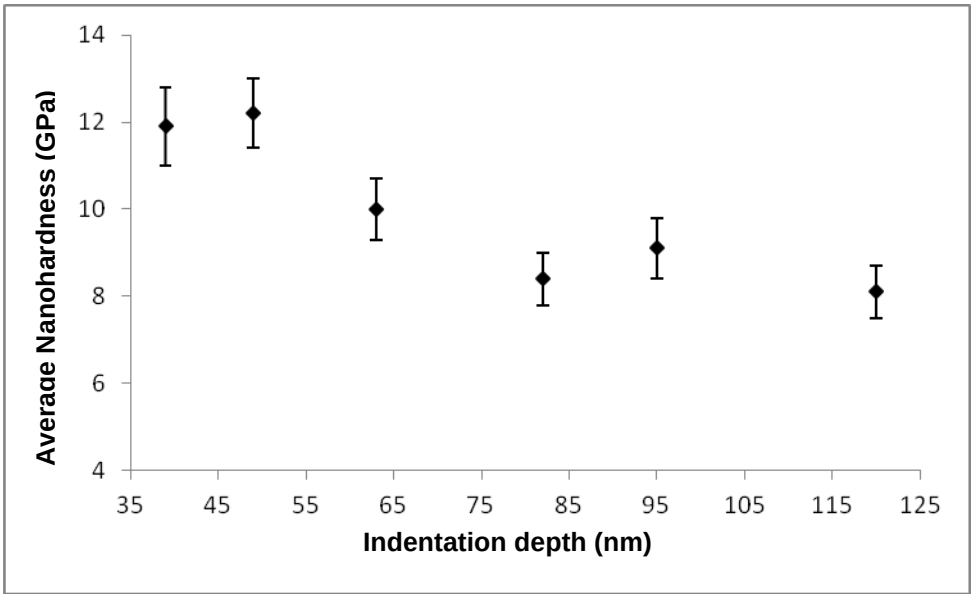


Figure 4.51. Nanohardness as a function of indentation depth for γ´ precipitates in Pt_{80}:Al_{14}:Cr_3:Ru_3 (at.%).

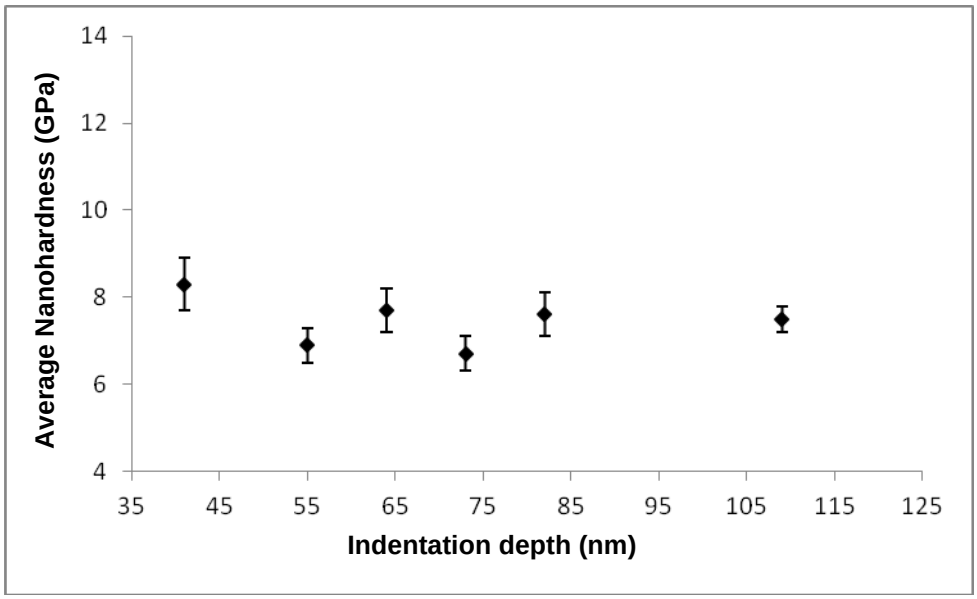


Figure 4.52. Nanohardness as a function of indentation depth for γ matrix in Pt_{80}:Al_{14}:Cr_3:Ru_3 (at.%).

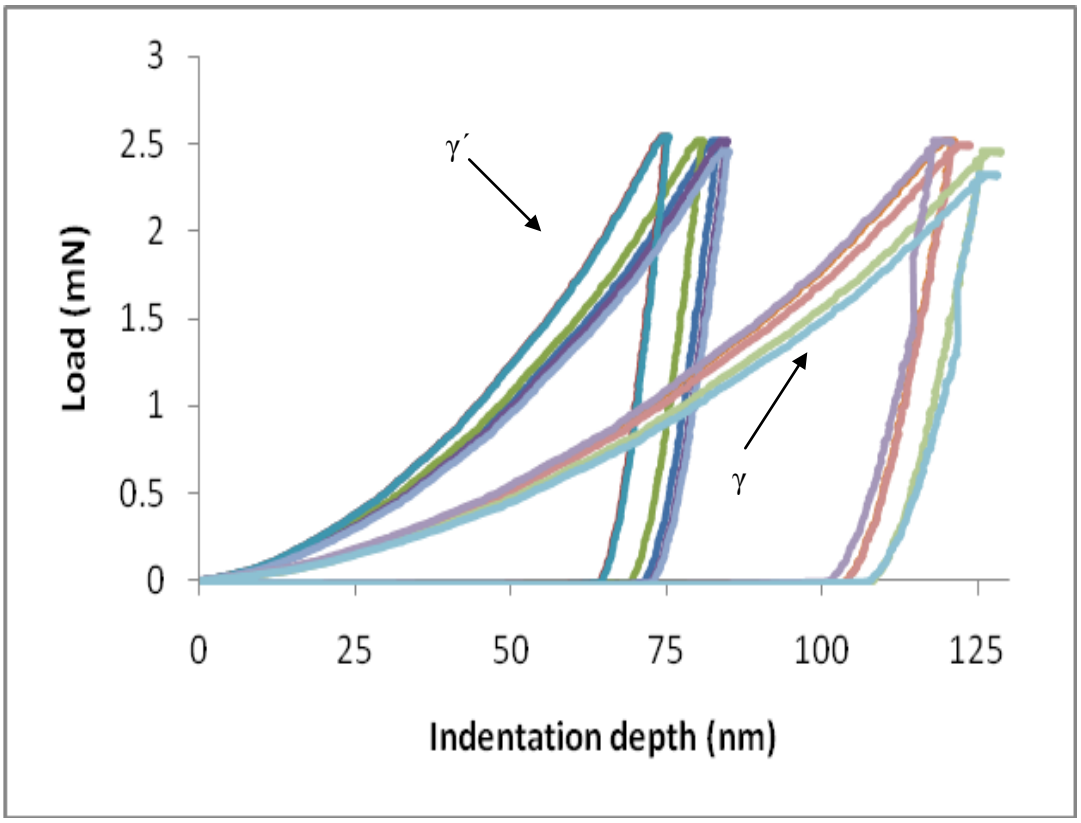


Figure 4.53. Load-displacement curves for the γ matrix and the γ´ precipitates in Pt_{78}:Al_{11}:Cr_6:Ru_5 (at.%) at a maximum applied load of 2.5mN, showing the final contact depth.

It should be noted that in this work, only very small differences of ~5% were observed between the reduced elastic modulus (E_r) and the true elastic modulus (E_s) in this work. In the following sections, the modulus of elasticity refers to the true modulus (E_s).

The elastic modulus of Pt_{78}:Al_{11}:Cr_6:Ru_5 (at.%) and Pt_{80}:Al_{14}:Cr_3:Ru_3 (at.%) was extracted from the same set of load-displacement curves (Section 3.13.3), and is shown in Figures 4.54 and 4.55. Within experimental error, the elastic modulus for γ´ was in the range 252 - 270GPa (Figures 4.54 and 4.55). The values for the matrix were slightly lower than for the precipitates, 233-246GPa. Neither the matrix nor the precipitates showed any trend as a function of the indentation depth.

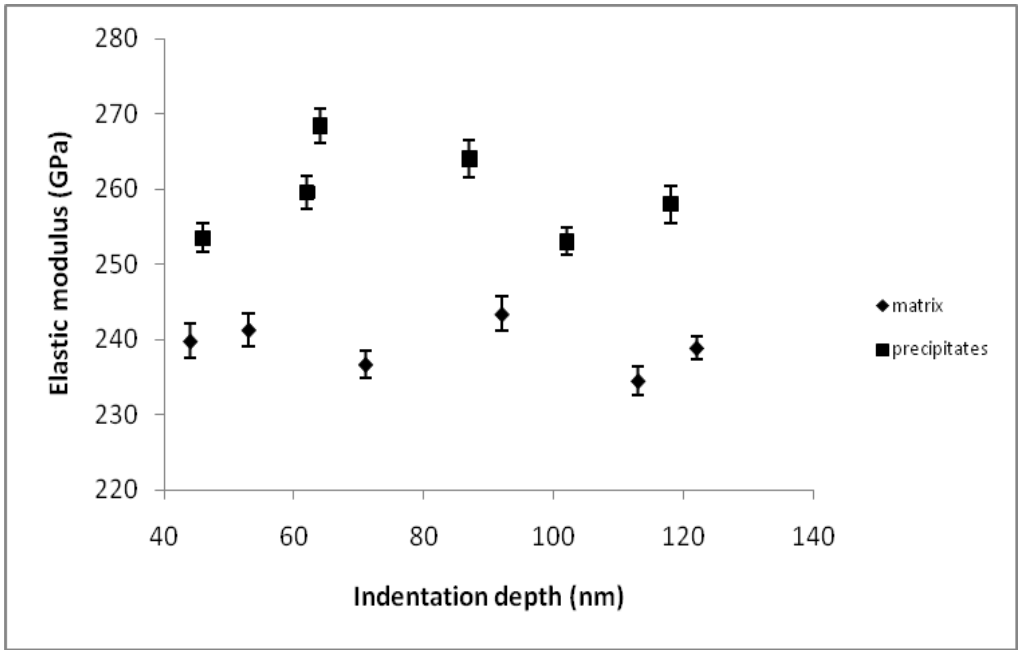


Figure 4.54. Elastic modulus as a function of indentation depth for Pt_{78}:Al_{11}:Cr_6:Ru_5 (at.%).

Figures 4.56 to 4.57 and Figures 4.58 to 4.59 show the nanohardness and elastic modulus of the alloys respectively as a function of indentation depth. In these cases, the indentations were performed at depths of ~80nm to 400nm in order to obtain a depth resolved nanohardness and elastic modulus of the alloy. Larger loads of ~150mN were used to give larger indentation depths. At indentation depths less than ~240nm, both the hardness and elastic modulus were not significantly affected by the indentation depth, but for indentation depths greater than ~240nm, the nanohardness and elastic modulus decreased.

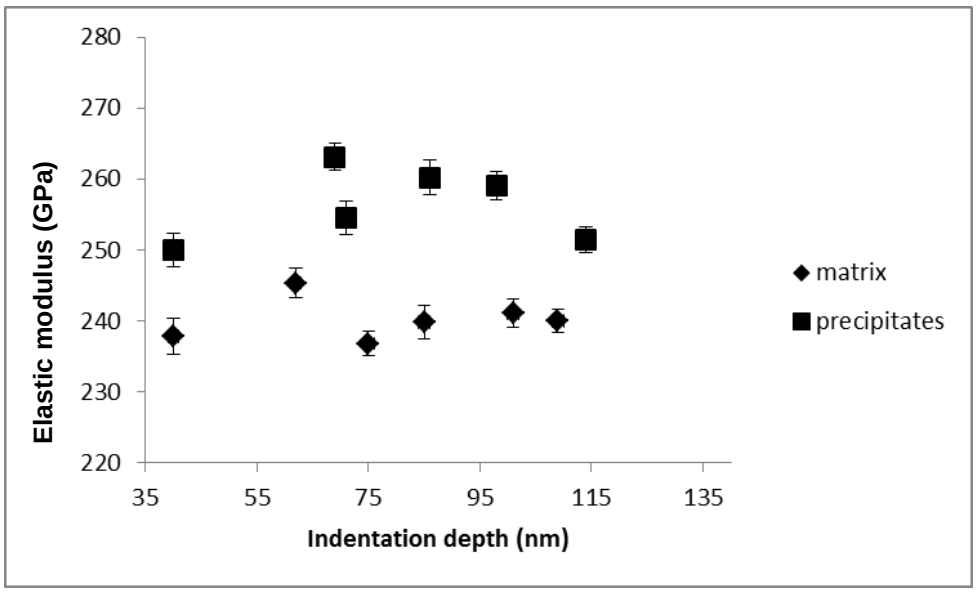


Figure 4.55. Elastic modulus as a function of indentation depth for Pt_{80}:Al_{14}:Cr_3:Ru_3 (at.%).

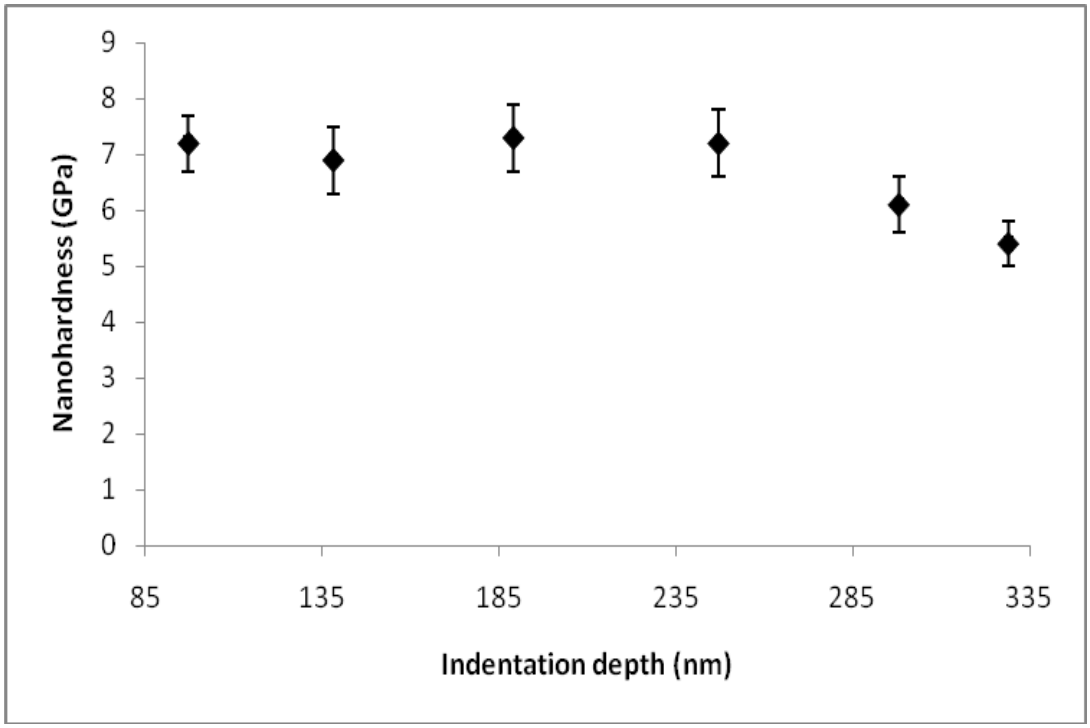


Figure 4.56. Alloy overall nanohardness as a function of the indentation depth for Pt_{78}:Al_{11}:Cr_6:Ru_5 (at.%).

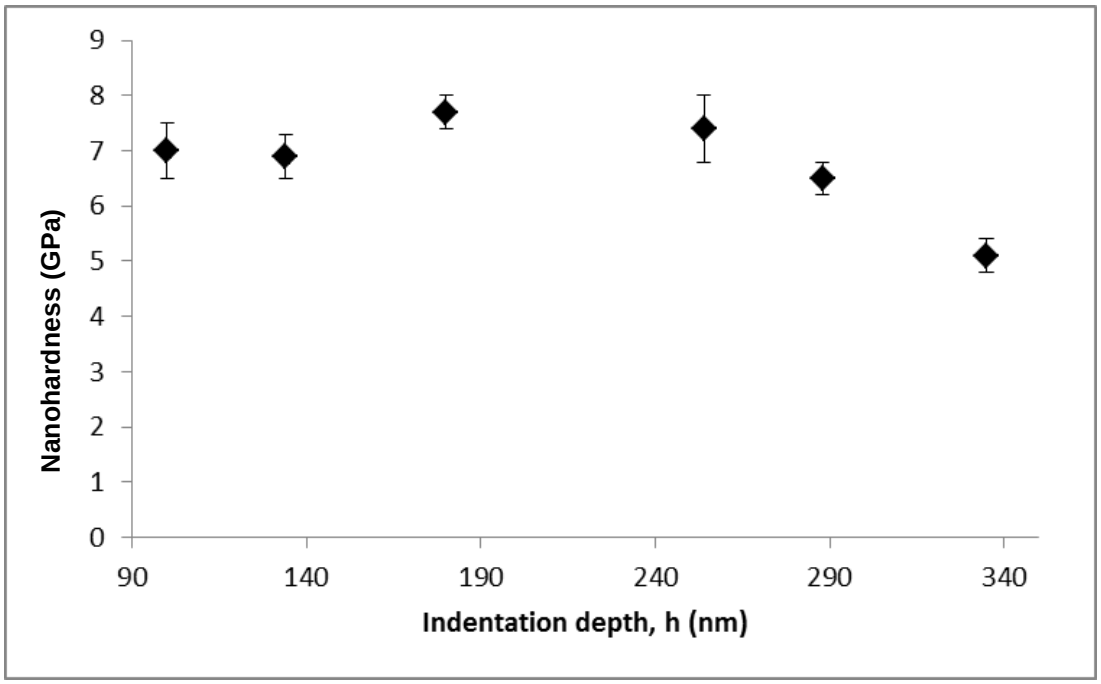


Figure 4.57. Alloy overall nanohardness as a function of the indentation depth for Pt_{80}:Al_{14}:Cr_3:Ru_3 (at.%).

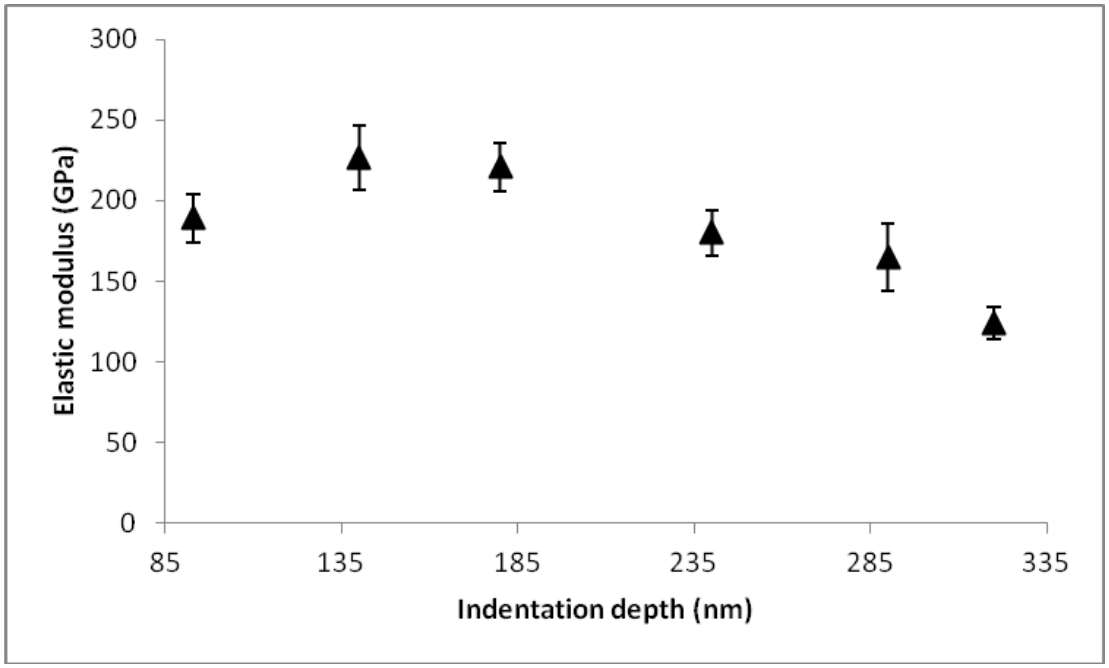


Figure 4.58. Alloy overall elastic modulus as a function of the indentation depth for Pt_{78}:Al_{11}:Cr_6:Ru_5 (at.%).

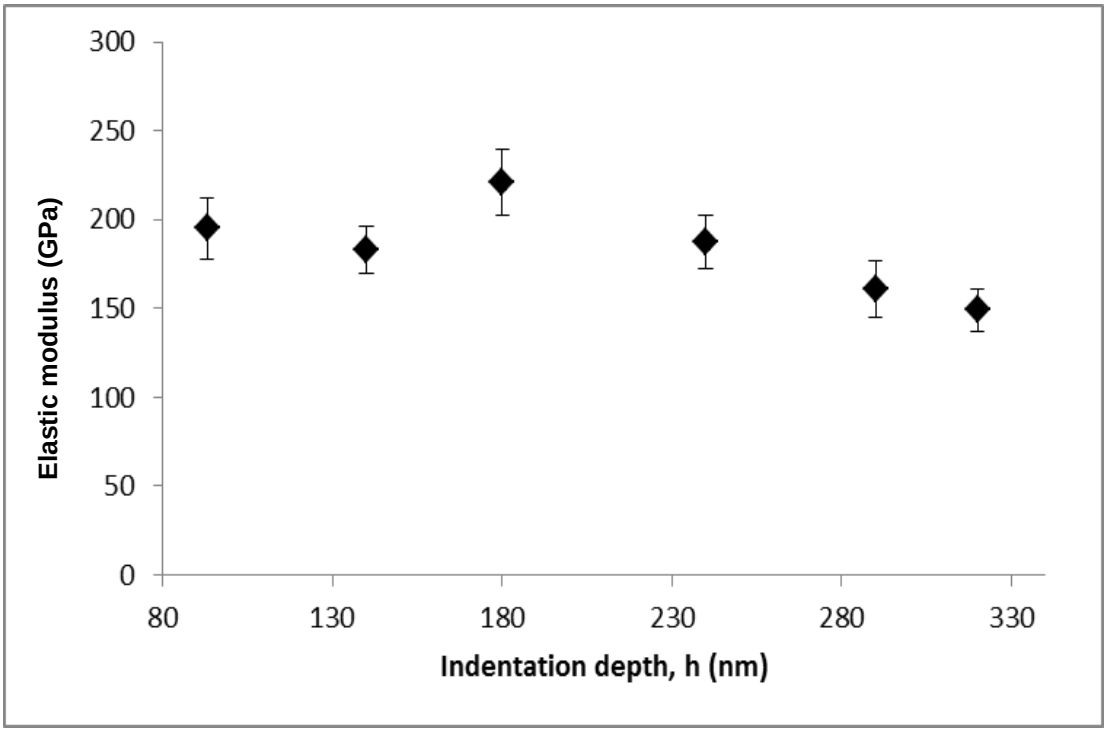
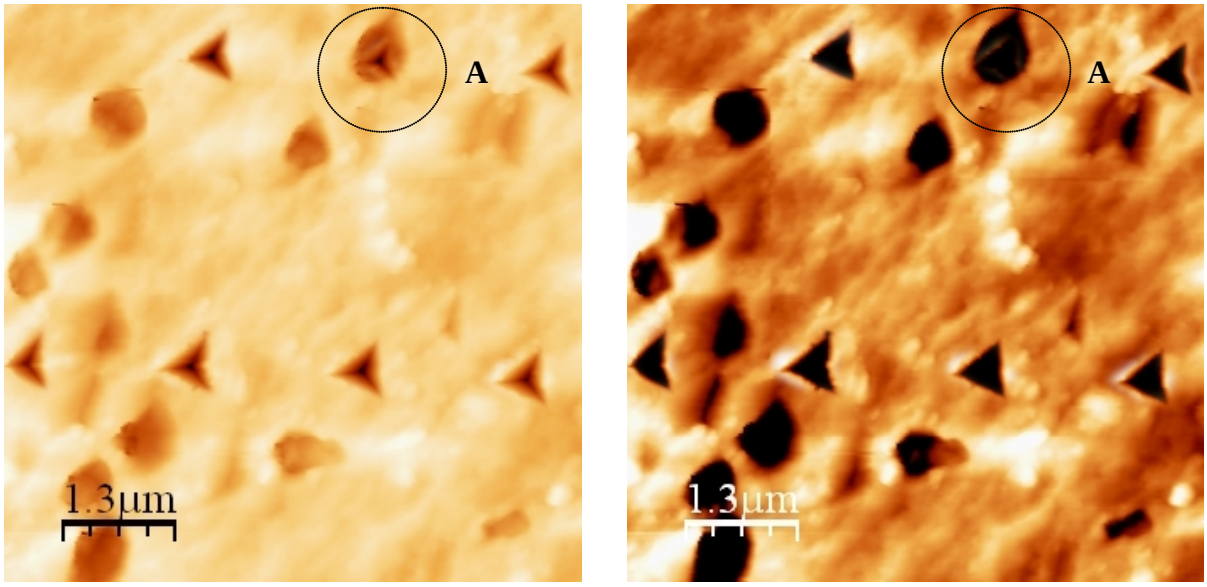


Figure 4.59. Alloy overall elastic modulus as a function of the indentation depth for Pt_{80}:Al_{14}:Cr_3:Ru_3 (at.%).

4.4.2 Nanohardness and Elastic Modulus: Matrix, Precipitates and Overall Alloy

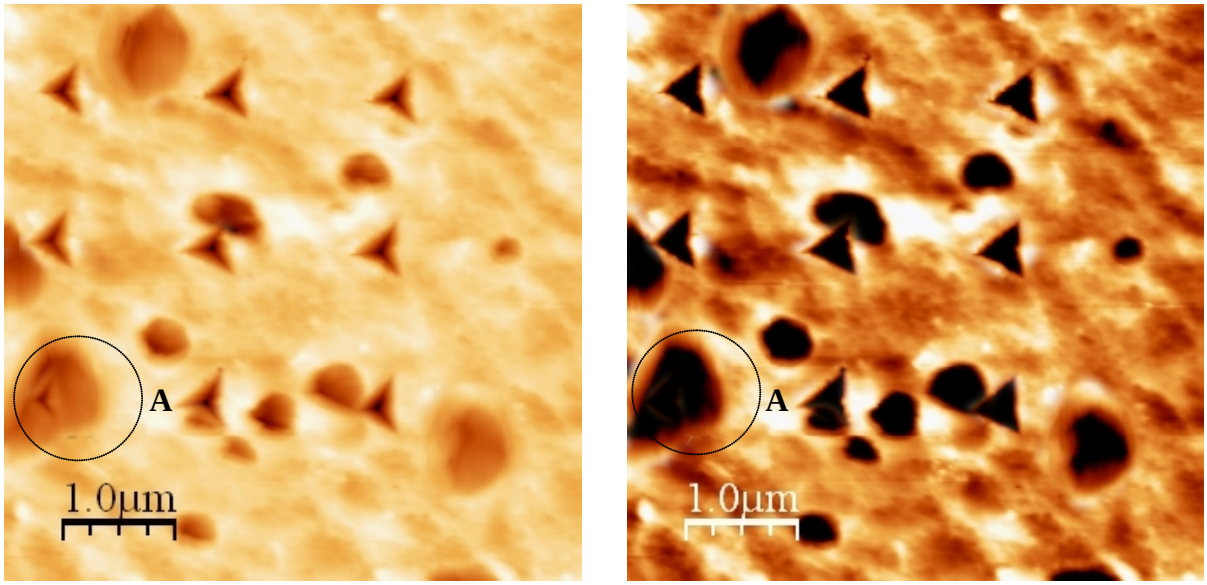
Figure 4.60 shows AFM images of the indentations in Pt_{80}:Al_{14}:Cr_3:Ru_3 (at.%) at a load of 2.5mN. In some cases, the precipitates were too small and part of the indentation (circle A in Figure 4.60) was outside the precipitate. Figure 4.61 shows residual indentations where the precipitate size was about twice the indentation size. Nanohardness measurements of the γ′ phase were taken on regions where the residual indentations were well within the precipitate (circle A in Figure 4.61).

Table 4.16 shows the nanohardness and elastic modulus results for the γ′ and γ phases. The standard deviation of the precipitate nanohardness was slightly larger than that of the matrix phase (possibly due to the surface roughness as standing proud of the surrounding matrix would induce rounding of the precipitate during polishing and result in an under-valued hardness) as the γ′ phase was normally higher than the γ phase [1999Gök, 1992Oli]. Comparison of the nanohardness values clearly shows that the γ′ phase had a higher nanohardness than the matrix, 21 to 68%, depending in the alloy composition (Table 4.16). In contrast, within experimental error, no difference was found between the elastic modulus of the matrix or γ′ precipitates (Table 4.16).



(a) **(b)**

Figure 4.60. AFM images of Pt_{80}:Al_{14}:Cr_3:Ru_3 (at.%), showing ~Pt_3Al precipitates (dark) in a (Pt) matrix (light) with indentations (black triangles) performed with a Berkovich tip at an applied load of 2.5mN, and an example of an indentation in ~Pt_3Al is marked A: (a) height difference, and (b) contrast difference.



(a) **(b)**

Figure 4.61. AFM images of Pt_{80}:Al_{11}:Cr_3:Ru_6 (at.%), showing ~Pt_3Al precipitates (dark) in a (Pt) matrix (light) with nanoindentations (black triangles) performed with a Berkovich tip at an applied load of 2.5mN, and an example of an indentation in ~Pt_3Al is marked A: (a) height difference, and (b) contrast difference.

Table 4.16. Nanohardnesses and elastic moduli calculated at final contact depth and maximum applied load 2.5mN for the different heat treated alloys.

Nominal composition (at.%)	Nanohardness (GPa)		Elastic Modulus (GPa)	
	γ´ phase	γ phase	γ´ phase	γ phase
Pt_{82}:Al_{12}:Cr_4:Ru_2	11.4 ± 0.9	7.3 ± 0.6	259.7 ± 23.7	233.3 ± 21.8
Pt_{85}:Al_7:Cr_5:Ru_3	12.1 ± 0.8	9.0 ± 0.7	271.8 ± 25.7	241.6 ± 18.4
Pt_{80}:Al_{11}:Cr_3:Ru_6	11.1 ± 0.9	8.3 ± 0.6	258.4 ± 19.8	238.7 ± 23.3
Pt_{80}:Al_{14}:Cr_3:Ru_3	12.6 ± 1.1	7.5 ± 0.4	273.9 ± 24.3	236.7 ± 21.6
Pt_{78}:Al_{11}:Cr_8:Ru_3	11.8 ± 0.7	8.1 ± 0.5	263.2 ± 24.4	237.2 ± 19.7
Pt_{78}:Al_{11}:Cr_6:Ru_5	11.0 ± 0.5	9.1 ± 0.7	269.4 ± 23.5	243.5 ± 16.4

Due to the relatively large channels of the γ phase in some areas of the microstructure, it was possible to measure the γ phase hardness at 5mN load, so that the indentation size was still small enough to measure the γ phase nanohardness without overlapping into the surrounding γ´ phase. TEM showed that, for Pt_{78}:Al_{11}:Cr_6:Ru_5 and Pt_{85}:Al_7:Cr_5:Ru_3 (at.%), the precipitates were closely spaced and in order to prevent errors in the measurement of the γ phase, regions with widely spaced precipitates were selected to be precipitate-free when observed under the AFM (Section 3.13.1). Table 4.17 gives a summary of the nanohardness and elastic modulus results calculated at a load of 5mN for the different alloys. The 2.5mN (Table 4.16) and 5mN

(Table 4.17) loads for the γ phase gave similar results. The combined results of the two loads (2.5mN and 5mN) for the γ phase are shown in Appendix B for ease of comparison.

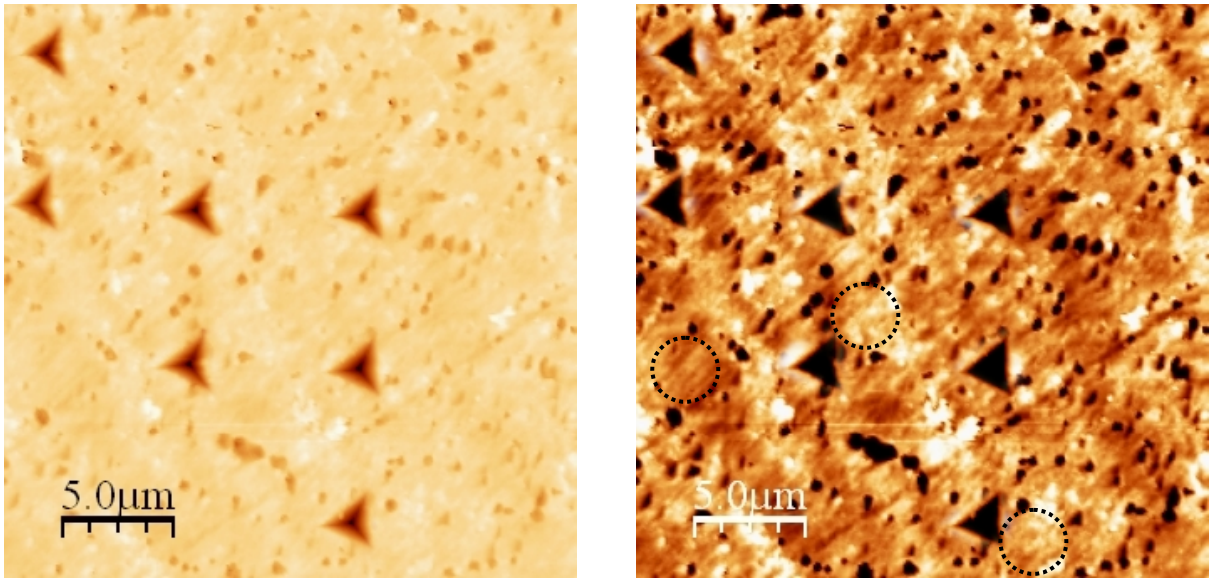
The overall alloy hardnesses and elastic modulus were measured at loads of 10mN and 20mN. A load of 10mN was chosen so that the properties could be compared directly with the Pt-Al-Cr-Ni-Re alloys by Nikulina *et al.* [2010Nik]. The areas where the indentations were placed were successfully selected to ensure that the areas looked similar to avoid discrepancies.

Table 4.17. Nanohardnesses and elastic moduli for the γ phase calculated at final contact depth and maximum applied load of 5mN for the different heat treated alloys.

Nominal composition (at.%)	Nanohardness (GPa)	Elastic Modulus (GPa)
Pt_{82}:Al_{12}:Cr_4:Ru_2	7.9 ± 0.6	238.6 ± 23.1
Pt_{85}:Al_7:Cr_5:Ru_3	8.8 ± 0.7	239.7 ± 21.8
Pt_{80}:Al_{11}:Cr_3:Ru_6	8.5 ± 0.8	239.6 ± 20.9
Pt_{80}:Al_{14}:Cr_3:Ru_3	7.5 ± 0.7	236.5 ± 22.4
Pt_{78}:Al_{11}:Cr_8:Ru_3	7.8 ± 0.9	237.3 ± 21.6
Pt_{78}:Al_{11}:Cr_6:Ru_5	9.3 ± 0.4	241.9 ± 22.4

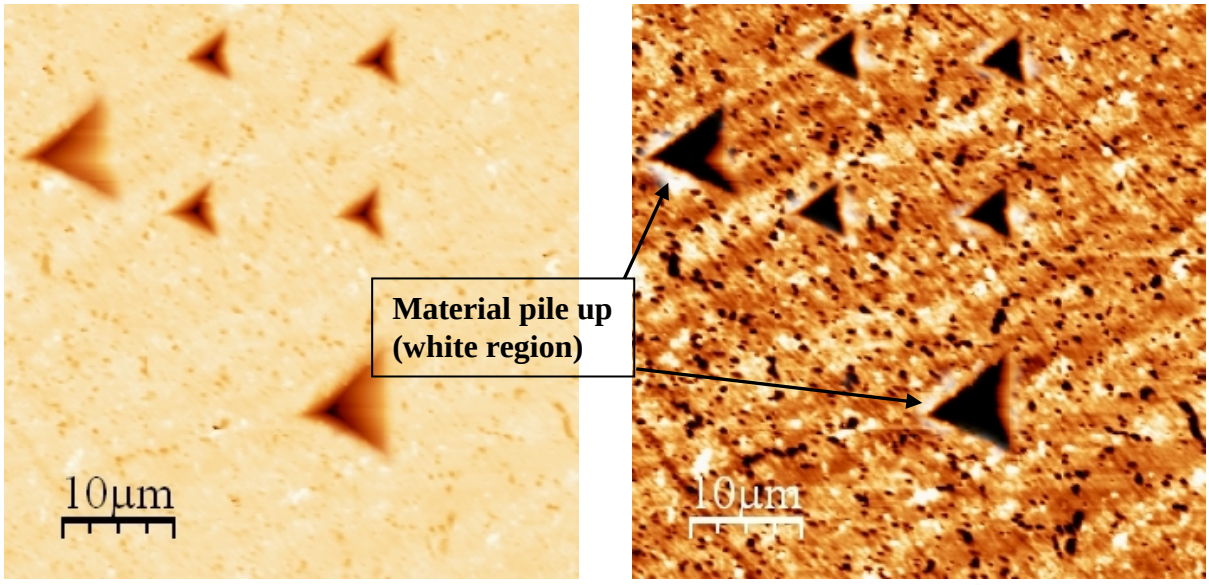
Figures 4.62 and 4.63 show AFM images of the indentations at loads of 10 and 20mN, with larger indentations at 20mN. Figure 4.62 also shows how at a load of 10mN the alloy's overall nanohardness can be misinterpreted if the precipitate volume fraction is too small, because the indenter could be on a region that is almost free of precipitates as shown in the dotted circles. Thus, care was taken to ensure the indented area had precipitates, especially for alloys with smaller precipitate volume fractions.

The nanohardness results for both the 10mN and 20mN loads are given in Table 4.18, showing indentical alloy hardnesses within experimental error. The standard deviation of the 20mN hardness was smaller than for 10mN. The elastic moduli (Table 4.19) were identical within experimental error for 10mN, 20mN and 100mN loads and no major differences between the standard deviations were observed.



(a) (b)

Figure 4.62. AFM images of Pt_{80}:Al_{14}:Cr_3:Ru_3 (at.%), showing ~Pt_3Al precipitates (dark) in a (Pt) matrix (light) with nanoindentations for the alloy hardness, performed with a Berkovich tip at an applied load of 10mN: (a) height difference, and (b) contrast difference, where circles (similar in size to the indentations) indicate regions that are almost precipitate-free.



(a) (b)

Figure 4.63. AFM images of Pt_{82}:Al_{12}:Cr_4:Ru_2 (at.%), showing ~Pt_3Al precipitates (dark) in a (Pt) matrix (light) with nanoindentations for the alloy hardness, performed with a Berkovich tip at applied loads of 10 and 20mN, revealing material pile-up: (a) height difference, and (b) contrast difference.

Table 4.18. Nanohardnesses for heat treated Pt-based samples at maximum loads of 10mN, 20mN and 100mN.

Nominal composition (at.%)	Nanohardness (GPa) at maximum loads (mN)			Approximate γ´ volume fraction (%)
	10	20	100	
$Pt_{82}:Al_{12}:Cr_4:Ru_2$	7.3 ± 0.7	7.4 ± 0.3	7.4 ± 0.2	26 ± 7
$Pt_{85}:Al_7:Cr_5:Ru_3$	8.8 ± 0.8	9.1 ± 0.5	9.0 ± 0.3	45 ± 6
$Pt_{80}:Al_{11}:Cr_3:Ru_6$	7.5 ± 0.6	7.4 ± 0.4	7.5 ± 0.4	15 ± 4
$Pt_{80}:Al_{14}:Cr_3:Ru_3$	7.2 ± 0.6	7.1 ± 0.4	7.1 ± 0.2	13 ± 8
$Pt_{78}:Al_{11}:Cr_8:Ru_3$	7.1 ± 0.5	7.4 ± 0.3	7.4 ± 0.3	34 ± 9
$Pt_{78}:Al_{11}:Cr_6:Ru_5$	9.0 ± 0.7	8.8 ± 0.2	9.2 ± 0.3	51 ± 6

Table 4.19. Alloy elastic moduli for heat treated Pt-based samples at maximum loads of 10mN, 20mN and 100mN.

Nominal composition (at.%)	Elastic Modulus (GPa) at maximum loads (mN)			Approximate γ´ volume fraction (%)
	10	20	100	
$Pt_{82}:Al_{12}:Cr_4:Ru_2$	180.5 ± 16.2	177.1 ± 15.3	184.3 ± 12.8	26 ± 7
$Pt_{85}:Al_7:Cr_5:Ru_3$	196.2 ± 17.8	193.7 ± 14.2	195.7 ± 13.4	45 ± 6
$Pt_{80}:Al_{11}:Cr_3:Ru_6$	168.4 ± 12.1	177.5 ± 13.7	174.4 ± 10.2	15 ± 4
$Pt_{80}:Al_{14}:Cr_3:Ru_3$	195.2 ± 14.7	197.3 ± 17.6	192.8 ± 11.6	13 ± 8
$Pt_{78}:Al_{11}:Cr_8:Ru_3$	185.1 ± 17.4	191.7 ± 14.7	189.1 ± 13.3	34 ± 9
$Pt_{78}:Al_{11}:Cr_6:Ru_5$	208.7 ± 19.1	210.9 ± 16.1	209.7 ± 15.5	51 ± 6

In order to give a good approximation of the nanohardness as a function of the γ´ volume fraction, the maximum load was increased to 100mN, in 5mN stages, after which there were no noticeable changes in the nanohardness and elastic modulus compared to the 10 and 20mN loadings (Figure 4.64(a)). Figure 4.64(b) shows declustered points at a load of 10mN and 100mN and suggests that generally the nanohardness measurement error decreased with increasing load.

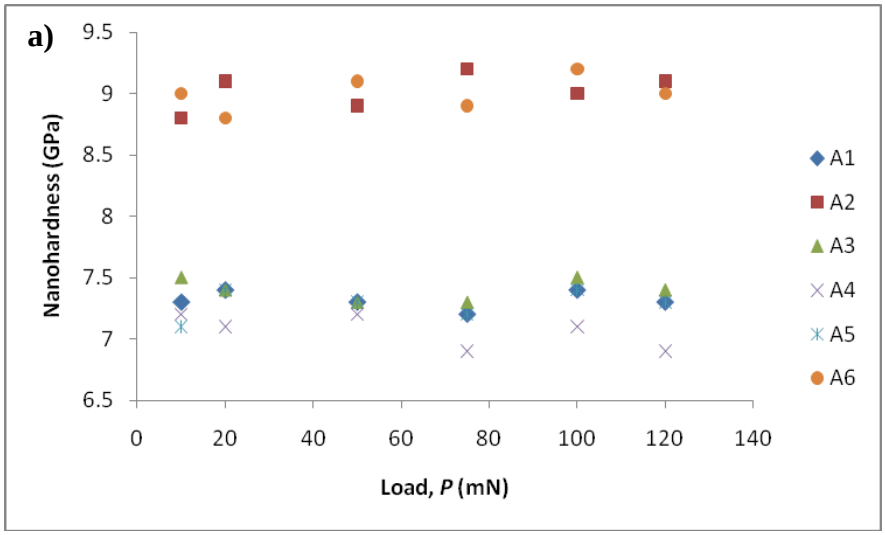
A plot of the nanohardness and γ´ volume fraction (from image analysis) shows that $Pt_{78}:Al_{11}:Cr_6:Ru_5$ and $Pt_{85}:Al_7:Cr_5:Ru_3$ (at.%) had the highest nanohardness, which corresponded to the higher γ´ volume fractions (Figure 4.65), and the curve had a sigmoidal shape. According to Joslin and Oliver *et al.* [1990Jos, 1992Oli, 2004Oli] for an alloy with two phases, and where the second phase average diameter was ~1μm, a nanohardness measured at 100mN gave a good approximate of the alloy's nanohardness. At this load, the indentations were larger and the probability of not having precipitates included was minimised. However, the results might not be valid because of the size of the precipitates.

Thus, it was assumed that at a maximum load of 100mN, the nanohardness of the alloy, as function of the γ′ phase volume fraction, gave a good approximation of the alloys' nanohardness. In the present work, some of the precipitates were smaller than 1μm, while in some cases the γ′ precipitates were ~1μm and slightly larger, thus for measuring the elastic modulus using the different loads (10, 20 and 100mN) larger γ′ precipitates were carefully selected. The elastic modulus did not show any major dependence on the γ′ volume fraction (Figure 4.66). The highest elastic modulus was observed at the highest γ′ volume fraction, although the values were very similar.

In an attempt to study the effect of subgrain boundaries on the nanohardness, a load of 20mN was used to measure the nanohardness at subgrain boundaries by indenting the subgrain boundary (Table 4.20). Figure 4.67 shows an AFM image of the indentation on a sub-grain boundary. The nanohardness along the subgrain boundary was similar to the surrounding regions (Table 4.18).

Table 4.20. Nanohardnesses and elastic moduli of Pt-based alloys at subgrain boundaries for a maximum applied load of 20mN.

Nominal composition (at.%)	Nanohardness (GPa)	Elastic Modulus (GPa)
Pt_{82}:Al_{12}:Cr_4:Ru_2	7.7 ± 0.4	179.4 ± 14.2
Pt_{85}:Al_7:Cr_5:Ru_3	8.9 ± 0.5	191.9 ± 18.2
Pt_{80}:Al_{11}:Cr_3:Ru_6	7.5 ± 0.3	180.1 ± 17.1
Pt_{80}:Al_{14}:Cr_3:Ru_3	6.9 ± 0.4	196.8 ± 16.9
Pt_{78}:Al_{11}:Cr_8:Ru_3	7.3 ± 0.7	190.1 ± 14.7
Pt_{78}:Al_{11}:Cr_6:Ru_5	9.1 ± 0.4	212.2 ± 20.8



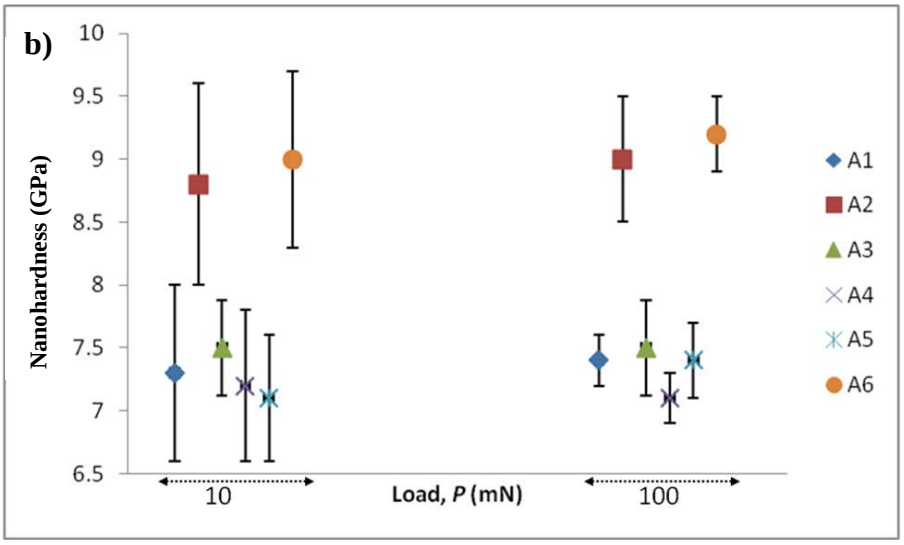


Figure 4.64. (a) Nanohardness of Pt-based alloys at different loads, and (b) Nanohardness of Pt-based alloys at loads of 10 and 100mN to show clearly the error bars, where A1 = Pt_{82}:Al_{12}:Cr_4:Ru_2, A2 = Pt_{85}:Al_7:Cr_5:Ru_3, A3 = Pt_{80}:Al_{11}:Cr_3:Ru_6, A4 = Pt_{80}:Al_{14}:Cr_3:Ru_3, A5 = Pt_{78}:Al_{11}:Cr_8:Ru_3, and A6 = Pt_{78}:Al_{11}:Cr_6:Ru_5 (at.%).

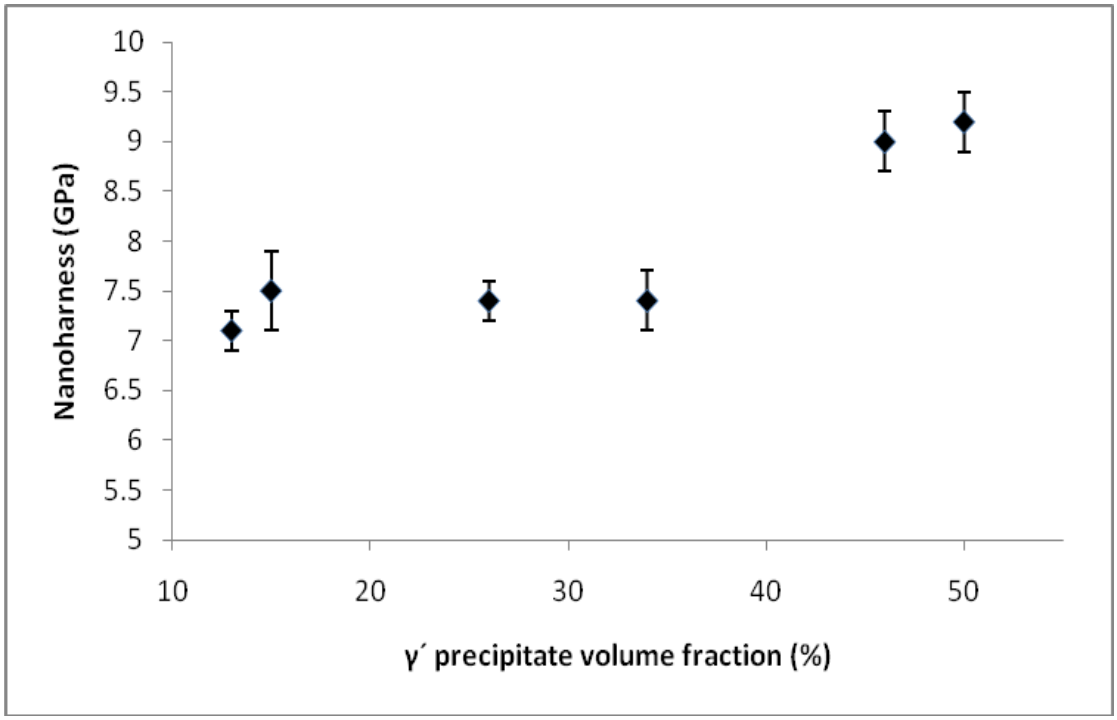


Figure 4.65. Effect of γ´ volume fraction (from SEM) on nanohardness of Pt-based alloys at a maximum load of 100mN.

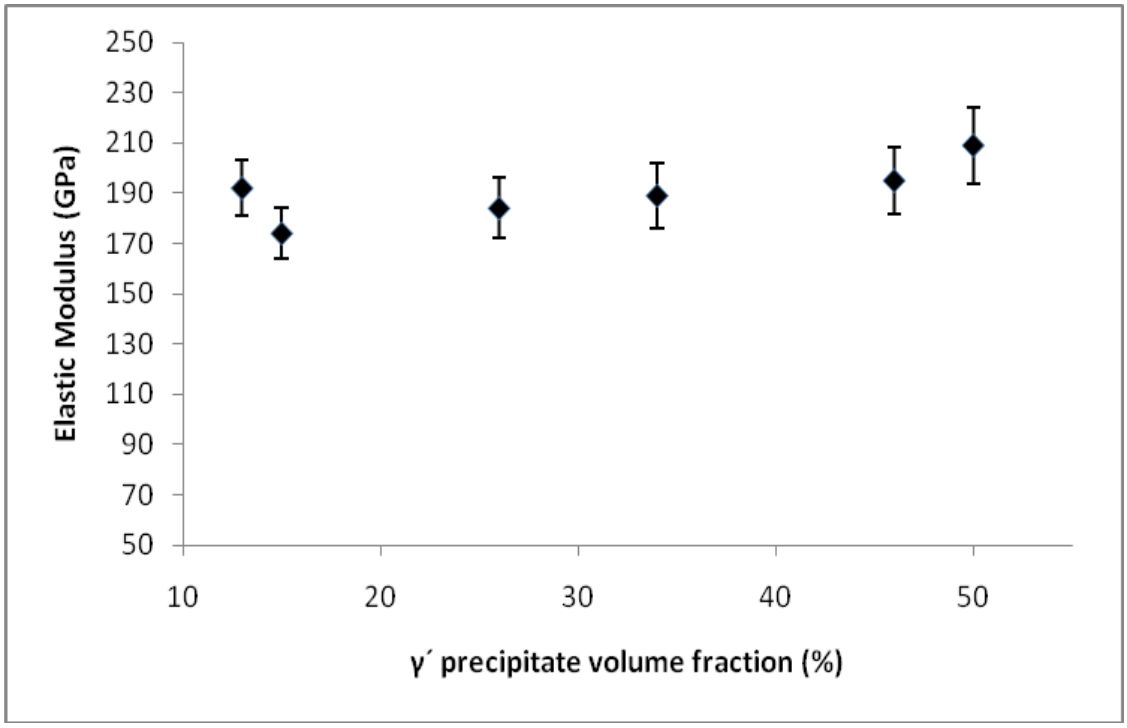
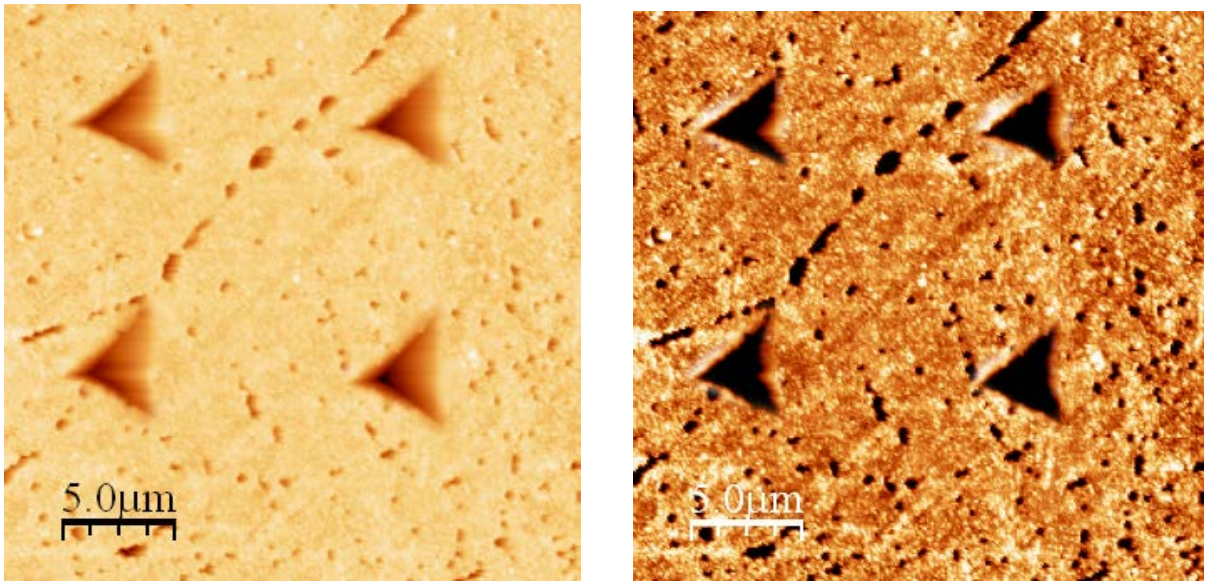


Figure 4.66. Effect of γ´ volume fraction (from SEM) on elastic moduli at a maximum load of 100mN for Pt-based alloys.



(a) (b)

Figure 4.67. AFM images of Pt_{80}:Al_{11}:Cr_3:Ru_6 (at.%), showing ~Pt_3Al precipitates (dark) in a (Pt) matrix (light) with nanoindentations for the alloy hardness, performed with a Berkovich tip at an applied load of 20mN: (a) height difference, and (b) contrast difference.

Tables 4.21 to 4.23 show a summary of the EDX compositions and nanohardness of the γ′, γ and overall alloy compositions. The analyses of Pt, Al, Cr and Ru quoted in Tables 4.21 to 4.23 are the average of five determinations on different areas. Within experimental error, the measured nanohardness of the γ′ precipitates was the same in all six alloys, the nanohardness of the γ matrix for the alloys was smaller, while the alloy nanohardness was highest for Pt_{85}:Al_7:Cr_5:Ru_3 and Pt_{78}:Al_{11}:Cr_6:Ru_5 (at.%), measuring at least 10% higher than the other alloys.

Table 4.21. EDX analyses (at.%) and nanohardnesses of γ′ measured at 2.5mN on heat treated samples.

Nominal composition (at.%)	γ′ compositions (at.%)				γ′ nanohardness (GPa)
	Pt	Al	Cr	Ru	
Pt_{82}:Al_{12}:Cr_4:Ru_2	78.3 ± 0.5	18.7 ± 0.5	2.5 ± 0.3	0.5 ± 0.2	11.4 ± 0.9
Pt_{85}:Al_7:Cr_5:Ru_3	76.1 ± 0.2	20.6 ± 0.4	2.2 ± 0.3	1.1 ± 0.4	12.1 ± 0.8
Pt_{80}:Al_{11}:Cr_3:Ru_6	78.4 ± 0.4	17.5 ± 0.3	2.7 ± 0.4	1.4 ± 0.1	11.1 ± 0.9
Pt_{80}:Al_{14}:Cr_3:Ru_3	78.2 ± 0.2	18.3 ± 0.2	2.5 ± 0.1	1.0 ± 0.2	12.6 ± 1.1
Pt_{78}:Al_{11}:Cr_8:Ru_3	76.9 ± 0.6	20.0 ± 0.6	2.2 ± 0.1	0.9 ± 0.3	11.8 ± 0.7
Pt_{78}:Al_{11}:Cr_6:Ru_5	80.4 ± 0.7	16.4 ± 0.7	2.3 ± 0.3	0.9 ± 0.4	10.9 ± 0.5

Table 4.24 shows measurements obtained from larger (>0.5μm) and smaller (≤0.5μm) γ′ precipitates and Table 4.25 shows nanoindentation measurements performed on regions of narrow (≤1μm) and broad (>1μm) matrix channels. Within experimental error, the larger and smaller γ′ precipitates yielded the same nanohardness for a given alloy as did the broad and narrow γ channels. The nanohardness of the larger γ′ precipitates was greater than that of the broad γ channels in all six alloys.

Table 4.22. EDX analyses (at.%) and nanohardnesses of γ matrix measured at 2.5mN on heat treated samples.

Nominal composition (at.%)	γ compositions (at.%)				γ nanohardness (GPa)
	Pt	Al	Cr	Ru	
$Pt_{82}:Al_{12}:Cr_4:Ru_2$	86.5 ± 0.8	6.7 ± 0.4	4.6 ± 0.5	2.2 ± 0.3	7.3 ± 0.6
$Pt_{85}:Al_7:Cr_5:Ru_3$	84.3 ± 0.6	7.4 ± 0.6	5.6 ± 0.3	2.7 ± 0.4	9.0 ± 0.7
$Pt_{80}:Al_{11}:Cr_3:Ru_6$	84.9 ± 0.7	8.3 ± 0.3	5.1 ± 0.3	1.7 ± 0.2	8.3 ± 0.6
$Pt_{80}:Al_{14}:Cr_3:Ru_3$	86.2 ± 0.9	9.0 ± 0.4	3.6 ± 0.4	1.2 ± 0.3	7.5 ± 0.4
$Pt_{78}:Al_{11}:Cr_8:Ru_3$	84.2 ± 0.8	7.6 ± 0.6	6.1 ± 0.5	2.1 ± 0.6	8.1 ± 0.5
$Pt_{78}:Al_{11}:Cr_6:Ru_5$	83.6 ± 0.6	9.0 ± 0.8	5.1 ± 0.4	2.3 ± 0.3	9.1 ± 0.7

Table 4.23. EDX analyses (at.%) and nanohardnesses of heat treated alloys measured at 100.0mN.

Nominal composition (at.%)	Heat treated alloy compositions (at.%)				Alloy nanohardness (GPa)
	Pt	Al	Cr	Ru	
$Pt_{82}:Al_{12}:Cr_4:Ru_2$	83.4 ± 0.6	8.7 ± 0.4	5.0 ± 0.3	2.9 ± 0.3	7.4 ± 0.2
$Pt_{85}:Al_7:Cr_5:Ru_3$	83.0 ± 0.7	9.2 ± 0.7	4.7 ± 0.2	3.1 ± 0.4	9.0 ± 0.3
$Pt_{80}:Al_{11}:Cr_3:Ru_6$	83.8 ± 0.8	8.5 ± 0.5	3.5 ± 0.5	4.2 ± 0.4	7.5 ± 0.4
$Pt_{80}:Al_{14}:Cr_3:Ru_3$	84.2 ± 0.9	8.2 ± 0.4	4.3 ± 0.2	3.3 ± 0.3	7.1 ± 0.2
$Pt_{78}:Al_{11}:Cr_8:Ru_3$	82.9 ± 0.6	7.8 ± 0.6	7.1 ± 0.6	2.2 ± 0.5	7.4 ± 0.3
$Pt_{78}:Al_{11}:Cr_6:Ru_5$	82.0 ± 0.4	9.9 ± 0.3	5.4 ± 0.3	2.7 ± 0.2	9.2 ± 0.3

Table 4.24. Nanohardnesses of larger (>0.5μm) **and smaller** (≤0.5μm) **γ′ precipitates measured at 2.5mN on heat treated samples.**

Nominal composition (at.%)	Nanohardness (GPa)	
	Larger γ′	Smaller γ′
$Pt_{82}:Al_{12}:Cr_4:Ru_2$	11.4 ± 0.9	10.7 ± 3.9
$Pt_{85}:Al_7:Cr_5:Ru_3$	12.1 ± 0.8	10.9 ± 4.1
$Pt_{80}:Al_{11}:Cr_3:Ru_6$	11.1 ± 0.9	9.4 ± 4.9
$Pt_{80}:Al_{14}:Cr_3:Ru_3$	12.6 ± 1.1	9.9 ± 3.6
$Pt_{78}:Al_{11}:Cr_8:Ru_3$	11.8 ± 0.7	9.1 ± 5.1
$Pt_{78}:Al_{11}:Cr_6:Ru_5$	11.0 ± 0.5	9.6 ± 4.7

Table 4.25. Nanohardnesses of narrow (≤1μm) and broad (>1μm) γ matrix channels measured at 2.5mN on heat treated samples.

Nominal composition (at.%)	Nanohardness (GPa)	
	Broad γ channels	Narrow γ channels
Pt_{82}:Al_{12}:Cr_4:Ru_2	7.4 ± 0.5	7.2 ± 0.7
Pt_{85}:Al_7:Cr_5:Ru_3	9.0 ± 0.8	9.2 ± 0.3
Pt_{80}:Al_{11}:Cr_3:Ru_6	8.3 ± 0.5	8.0 ± 0.8
Pt_{80}:Al_{14}:Cr_3:Ru_3	7.5 ± 0.6	7.7 ± 0.6
Pt_{78}:Al_{11}:Cr_8:Ru_3	8.1 ± 0.7	8.3 ± 0.5
Pt_{78}:Al_{11}:Cr_6:Ru_5	9.1 ± 0.6	8.8 ± 0.4

CHAPTER FIVE

5. DISCUSSION

5.1 XRD, OM, SEM, AFM and IMAGE ANALYSIS STUDIES

5.1.1 OM and SEM Microstructures and XRD

XRD showed the presence of (Pt) and both cubic and tetragonal ~Pt_3Al and agreed with previous work for the quaternary alloys [2008Sho1, 2008Sho2, 2009Sho1, 2009Sho2]. The peaks of the pure phases from the ICDD database [2003Xpe] were compared against each other. This showed that all the peaks unique to (Pt) and $L1_2$ - ~Pt_3Al phase could be matched by the XRD spectra for all six samples (Tables 4.1(a) and (b)). For the DO'_c - ~Pt_3Al phase, some of its unique peaks could not be found in the XRD spectra (Table 4.1(c)). Thus, TEM work was therefore considered necessary to ascertain which ~Pt_3Al phase was present. TEM found evidence only of the cubic phase in the alloys. While some of the peaks unique to DO'_c - ~Pt_3Al could not be found in the XRD spectra, XRD also identified peaks that were unique to DO'_c - ~Pt_3Al. Thus, XRD identified the structure as DO'_c - ~Pt_3Al, similar to previous findings of Shongwe [2009Sho1]. However, this conclusion is subject to uncertainties, because, according to Biggs [2001Big2], it is possible to pick up peaks in XRD that belong only to the $L1_2$ - ~Pt_3Al phase, only if very extended time scans with very small steps size are employed, although this is difficult. This raises the question whether there are potentially further X-ray peaks possible from the current alloys that belong only to the $L1_2$ - ~Pt_3Al. While TEM found evidence only of the cubic phase, TEM only samples thin, relatively small areas of the material. In constrast, XRD collects from much larger and thicker regions of the material. This leaves uncertainties regarding the crystallographic structure of the precipitates and recommendations are suggested in Section 6 to investigate this further, such as increasing the scanning time and using Reitveld refinement.

In an additional attempt to determine whether the $L1_2$ - ~Pt_3Al or DO'_c - ~Pt_3Al was present in the Pt-Al-Cr-Ru alloys, the method used by Biggs [2001Big2] was employed, and is shown in Appendix D. Biggs [2001Big2] identified several potential regions on the XRD spectra where possible distinctions could be made between the $L1_2$ - ~Pt_3Al and DO'_c - ~Pt_3Al phases. Experimental XRD spectra were collected over a range of samples with different

compositions to test the reliability of the technique. A correlation between the method and experimental data was seen by Biggs [2001Big2]. Steps 1 to 4 were used in the current work (adopted from Biggs [2001Big2]) to distinguish between the two forms of Pt_3Al. Each of the Pt-Al-Cr-Ru alloys XRD spectra was checked against Steps 1 to 4 (Table 5.1). A "Y" indicates that the DO'_c - ~Pt_3Al is possibly in the alloys, while a "N" indicates the possible presence of the $L1_2$ - ~Pt_3Al. Not all the peaks identified by Biggs [2001Big2] were present in the XRD spectra, particularly all of the peaks of Steps 1 and 2, and some of Step 3. This makes the results inconclusive, since the absence of the peaks in Steps 1 and 2 implies the presence of the $L1_2$ Pt_3Al phase, while Step 4 implies the opposite, as some splitting was observed. Although the results are inconclusive, they could imply the presence of both the $L1_2$ - and DO'_c - ~Pt_3Al phases in the Pt-Al-Cr-Ru alloys. However, it must be remembered that Biggs [2001Big2] used this technique on binary and ternary alloys, whereas these are quaternary alloys.

Table 5.1. Examination of Pt-Al-Cr-Ru alloys XRD spectra using the methodology of Biggs [2004Big2].

Steps	Figure 4.1	Figure 4.2	Figure 4.3	Figure 4.4	Figure 4.5	Figure 4.6
Step 1	N	N	N	N	N	N
Step 2	N	N	N	N	N	N
Step 3	N	N	N	N	N	N
Step 4	N	Y	Y	Y	N	N

Step 1: Edge of peaks at 2θ = 21°, 30° and 35° shows DO'_c - ~Pt_3Al

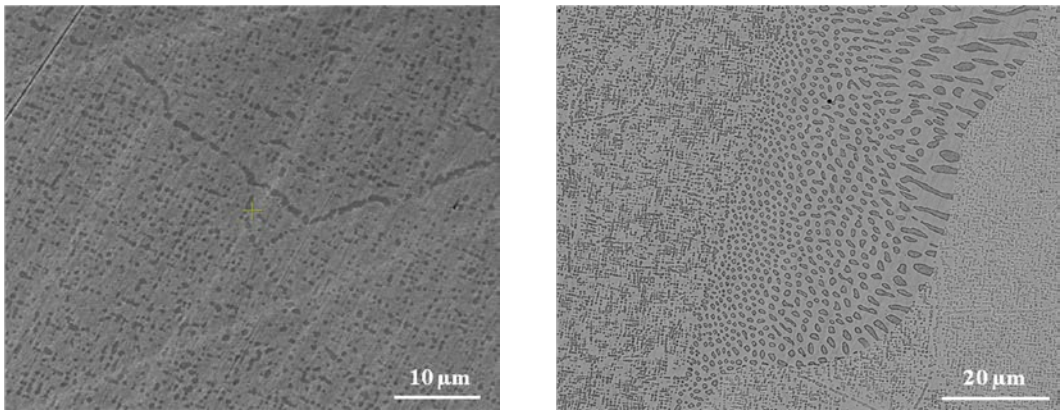
Step 2: Examine 2θ = 21° to 31°, peaks at 2θ = 24°, 26° and 28°, splitting or doublets shows DO'_c - ~Pt_3Al

Step 3: Examine 2θ = 39° to 45°, peaks at 2θ = 40°, 43° and 44°, splitting or doublets shows DO'_c - ~Pt_3Al

Step 4: Examine 2θ = 46° to 54°, peaks at 2θ = 47°, 49° and 53°, splitting or doublets shows DO'_c - ~Pt_3Al

Before etching, the precipitates in alloys Pt_{78}:$Al_{15.5}$:$Cr_{4.5}$:Ru_2, Pt_{80}:Al_{14}:Cr_3:Ru_3 and Pt_{80}:Al_{11}:Cr_4:Ru_5 (at.%) were not discernable by both OM and SEM, although XRD did confirm the presence of ~Pt_3Al precipitates [2009Sho1]. Etching resulted in a large improvement in contrast, allowing visualization of the precipitates and general microstructure as well as revealing a eutectic in Pt_{82}:Al_{12}:Cr_4:Ru_2 (at.%). In Pt_{78}:Al_{11}:Ru_8:Cr_3 (at.%) after etching (Figure 5.1(b)), a eutectic and a higher precipitate volume fraction and precipitate

alignment was observed, whereas no eutectic was observed before etching (Figure 5.1(a)). However, the identification of the eutectic after etching could have also been due to the samples being inhomogeneous, which has already been seen in the TEM studies. In Figure 4.8(a), the circular feature is similar to that observed in Figure 4.13(b). It is thought that the formation of the hole is related to the eutectoid, since the eutectoid originated from the eutectic which should have been the last to solidify and separation of the eutectic from the surrounding region could have been caused by shrinkage.



(a) **(b)**

Figure 5.1. SEM-BSE images of annealed nominal Pt_{78}:Al_{11}:Cr_3:Ru_8 (at.%) showing ~Pt_3Al precipitates in light (Pt) matrix [2008Sho1, 2009Sho1]: (a) before etching, and (b) after etching, now showing a eutectic as well.

Thus, successful etching of the alloys for the current work using the etching method of Odera *et al*. [2012Ode] enabled the microstructure to be seen clearly for the first time in these alloys. This is important because now the quaternary alloys could be safely etched to achieve good constrast in both OM and SEM. The electrolytic etching of Pt-Al based alloys carried out in an aqueous KCN solution had serious health and safety concerns which has been eliminated by using the method of Odera *et al*. [2012Ode].

The observation of both the eutectoid (Figure 4.7(a)) and the coarsened eutectic (Figure 4.7(b) and (c)) was unexpected in the same annealed sample. This must mean that the eutectoid was stabilized (thus, not coarsening perceptibly), whereas the eutectic was not stabilized. This also demonstrates that these regions in the nominal Pt_{82}:Al_{12}:Cr_4:Ru_2 (at.%) alloy had different compositions (Table 4.2) (i.e. the sample was still inhomogeneous, despite annealing) and reacted differently. It also demonstrates that the eutectoid temperature for the alloy was lower than the last annealing temperature of 1100°C. Any alloy which has eutectic/eutectoid areas must have had these regions after the solution treatment, suggesting that the composition was not ideal, as the microstructure should have all been (Pt) after the

solution treatment. Thus, the alloys probably had too much aluminium for the solution treatment to be successful. Considering that the eutectic of the Pt-Al binary is at 1507°C [1986McA, 1987Oya] (although the temperature will be different for these alloys with more components), a better solution treatment temperature might be ~1450°C to ensure that there was no local melting, which appeared to have occurred in at least some of the samples of this study (e.g. Pt_{82}:Al_{12}:Cr_4:Ru_2 (at.%)). Using differential scanning calorimetry (DSC) was considered in order to determine the Pt-Al eutectic temperature which could assist in choosing the correct heat treatment temperature, but none were available during the course of the study. For a similar composition, $Pt_{81.5}$:$Al_{11.5}$:$Cr_{4.5}$:$Ru_{2.5}$ (at.%) (Figure 4.8 (d) and (e)), there were larger precipitates at the grain boundaries, which did not appear to be either eutectic or eutectoid, suggesting a different reaction, or possible melting, or coarsening.

Larger precipitates were found to form by coarsening or coalescing, such as in $Pt_{81.5}$:$Al_{11.5}$:$Cr_{4.5}$:$Ru_{2.5}$ and Pt_{80}:Al_{11}:Cr_4:Ru_5 (at.%). Durand-Charre [1997Dur] made a similar observation for heat treated NBSA AM1, where the close cuboid precipitates subsequently coalesced (Figure 5.2). However, when the homogenizing treatment was prolonged to 50 hours and more, this phenomenon completely disappeared. Thus, in the current work, it is thought that the possible coarsening or coalescing of the precipitates could have been an issue of the heat treatment not being the right temperature rather than having the heat treatment for a prolonged time. The combined effects of an inappropriate temperature and heat treating the sample at that temperature would have worsened the situation. Vorberg *et al.* [2004Vor] reported that for $Pt_{78.5}$:$Al_{12.5}$:Cr_3:Ni_6 (at.%) after air cooling, there was a fine distribution of precipitates, while after furnace cooling, there was a mixture of very fine and large precipitates. The large particles formed by coarsening of the small ones. This further suggests that the larger precipitates observed in the current work could be by coarsening of the small precipitates that took place during heat treatment, even though the samples were not furnace cooled. Similar observations have been made in nickel-based superalloy GH742 by Hongyu *et al.* [2010Hon] for furnace cooled samples from 1050°C.

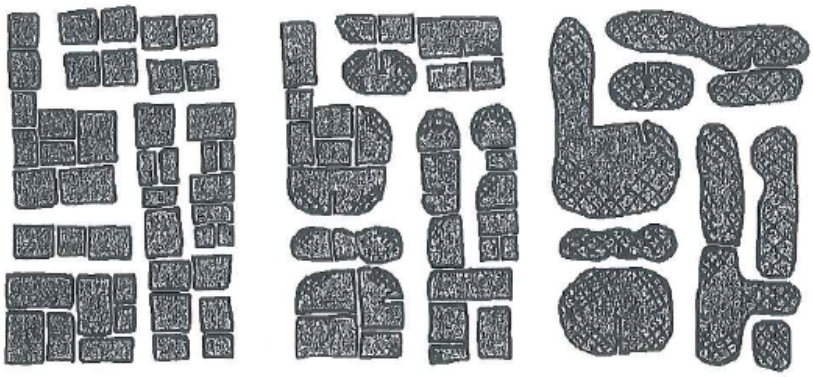


Figure 5.2. Schematic illustration of the formation of γ′ platelets: (a) alignment of γ′ particles to minimise misfit stresses, followed by coalescence to reduce interface area, widening some matrix corridors, facilitating dislocation movement, (b) continued coalescence and formation of dislocation networks, and (c) final coalescence and complete loss of coherence [1997Dur].

5.1.2 SEM and AFM Image Analysis

Table 5.2 shows the image analysis results of all the alloys. Previously and before etching [2009Sho1], some alloys had ~Pt_3Al which was indiscernible and hence the volume fractions could not be determined. The volume fractions found by image analysis on etched samples were higher than those of the grid placement method [2009Sho1]. This was expected, since the contrast before etching between the (Pt) and ~Pt_3Al phases was poor, and secondly, the grid method is very simplistic [2009Sho1]. Wenderoth *et al*. [2005Wen1] did image analysis on Pt-based superalloys with Ni additions (Pt_{79}:Al_{14}:Cr_3:Ni_4, Pt_{77}:Al_{14}:Cr_3:Ni_6 and Pt_{75}:Al_{14}:Cr_3:Ni_8 (at.%)), and the ~Pt_3Al volume fraction was found to be in the range 23 to 30%. For determination of the ~Pt_3Al volume fractions in the Pt-Al-Cr-Ni alloys, the ~Pt_3Al particles were marked manually in several digital SEM micrographs for each alloy [2005Wen1]. The digital SEM micrographs were successively converted into binary images by means of standard Photoshop software. The ~Pt_3Al area fraction was given by the number of pixels belonging to ~Pt_3Al divided by the number of pixels in the entire micrograph [2005Wen1]. The major difference between the method used by Wenderoth *et al.* [2005Wen1] and the one used in the current work is the manual marking of precipitates in the method used by Wenderoth *et al.* [2005Wen1], while identification of phases was part of the package in the Olympus stream image analysis software, version 1.3 [2011Oly]. Manual marking of precipitates could introduce human error, resulting in over and/or under estimation of the ~Pt_3Al volume fraction. Later work on the Pt-Al-Cr-Ni system by

Wenderoth *et al.* [2006Wen2] and Völkl *et al*. [2006Völ] gave a volume fraction of 51% for both Pt_{77}:Al_{12}:Cr_6:Ni_5 and Pt_{76}:Al_{12}:Cr_6:Ni_6 (at.%). The ~Pt_3Al volume fraction of the etched sample Pt_{78}:Al_{11}:Cr_6:Ru_5 (at.%) was, within experimental error, similar to the highest volume fraction found in the Pt-Al-Cr-Ni [2006Wen1, 2006Völ]. Another study of the Pt-Al-Cr-Ni system with Re additions [2007Wen] gave a volume fraction of 57% for Pt_{75}:Al_{12}:Cr_6:Ni_5:Re_2 (at.%), which, within experimental error, was similar to Pt_{78}:Al_{11}:Cr_6:Ru_5 (at.%).

Table 5.2. Approximate ~Pt_3Al volume fractions from previous work [2009Sho1], compared to re-measured previous samples (after repolishing and etching) and newly-prepared etched alloys.

Nominal composition (at.%)	Approximate ~Pt_3Al volume fraction (%)			
	Grid placements [2009Sho1]	Previous samples after etching, re-measured by Olympus	Newly prepared, Olympus	Newly prepared, WSxM-AFM
Pt_{78}:$Al_{15.5}$:$Cr_{4.5}$:Ru_2	~Pt_3Al indiscernible	13 ± 4	-	-
Pt_{80}:Al_{14}:Cr_3:Ru_3	~Pt_3Al indiscernible	17 ± 3	13 ± 8	19 ± 4
$Pt_{81.5}$:$Al_{11.5}$:$Cr_{4.5}$:$Ru_{2.5}$	12 ± 6	22 ± 6	-	-
Pt_{82}:Al_{12}:Cr_4:Ru_2	10 ± 5	27 ± 7	26 ± 7	31 ± 7
Pt_{84}:Al_{11}:Cr_3:Ru_2	12 ± 5	24 ± 4	-	-
Pt_{85}:Al_7:Cr_5:Ru_3	27 ± 6	41 ± 8	45 ± 6	48 ± 8
Pt_{80}:Al_{11}:Cr_4:Ru_5	~Pt_3Al indiscernible	18 ± 4	-	-
Pt_{80}:Al_{11}:Cr_6:Ru_3	10 ± 5	16 + 3	-	-
Pt_{80}:Al_{11}:Cr_3:Ru_6	6 ± 4	21 ± 6	15 ± 4	20 ± 5
Pt_{78}:Al_{11}:Cr_6:Ru_5	24 ± 3	40 ± 5	51 ± 6	57 ± 9
Pt_{78}:Al_{11}:Cr_8:Ru_3	20 ± 3	31 ± 7	34 ± 9	38 ± 6
Pt_{78}:Al_{11}:Cr_3:Ru_8	10 ± 5	28 ± 8	-	-

The WSxM (AFM) and Olympus software (SEM) for the etched newly-prepared samples results agreed well (Table 5.2), indicating that the WSxM 4.0 software can be used to estimate the ~Pt_3Al volume fraction from AFM images. Sobchenko *et al*. [2007Sob] have also estimated the volume fraction of second phase particles using the WSxM 4.0 software from AFM images.

Figure 5.3 shows a strong correlation for the relationship of the precipitate volume fraction decreasing with increasing Pt content. The error bars for data points A, B and C overlap, thus it cannot be said that A is better than B in terms of volume fraction. Similarly, it cannot be said that A and B are better than C in terms of platinum contents. Thus, the error bars indicate

that the uncertainty in the data means these three points cannot be distinguished. Pt-Al-Cr-Ni alloys were reported to have γ′ volume fractions of 51-57% [2006Völ, 2007Wen] (indicated by dotted lines on Figure 5.3) and only one alloy in the current study falls within this range: A = Pt_{78}:Al_{11}:Cr_6:Ru_5 (at.%). Even for Alloy B (Pt_{85}:Al_7:Cr_5:Ru_3 (at.%)), only the extreme top part of the error bar falls within the 51-57% γ′ volume fraction range, and so it cannot qualify.

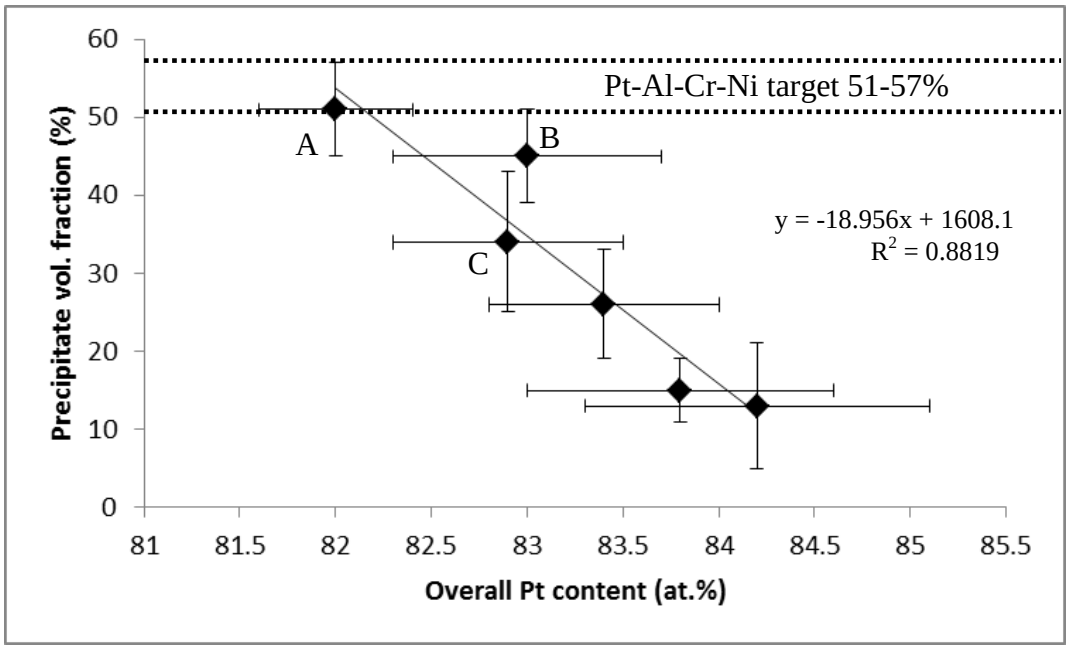


Figure 5.3. Relationship between overall Pt content (at.%) and precipitate volume fraction (measured from SEM images), showing a strong correlation with the γ′ volume fraction decreasing with increasing Pt content.

5.2 Transmission Electron Microscopy Studies

5.2.1 TEM Microstructural Characterisation

The precipitates of the six Pt-based superalloys were evaluated by TEM to primarily determine the precipitate structure, morphology and to give an indication of their distribution. A large range of precipitate morphologies and sizes was found in the different alloys.

5.2.1.1 Nominal Pt_{82}:Al_{12}:Cr_4:Ru_2 (at.%)

Figure 4.16 of Pt_{82}:Al_{12}:Cr_4:Ru_2 (at.%) is representative of some areas of the sample, while other regions were found to have an entirely different microstructure and precipitate volume

fraction (Figures 4.17 and 4.18). The precipitate volume fraction was estimated to be 75 ± 6% by the grid method [1988Exn, 1999Rus] in this TEM somewhat localised area. The TEM volume fraction results compared to those of SEM and AFM are much higher, and are believed to be an over-estimate, because TEM only reveals the microstructure in relatively small regions. Counter to this argument however, these findings confirm the suggestion of Süss *et al.* [2008Süs1], that some precipitates were too small to be observed in SEM, but possible in the TEM, thus the higher volume fraction observed in TEM. Figure 4.18 exhibits γ′-free zones, and similar findings had been reported previously for some Ni-based superalloys [2000Bla, 2001Mil, 2008Sud]. According to Zhang *et al*. [200Zha], Sudbrack *et al*. [2000Bla, 2008Sud] and Miller [2001Mil], lower diffusivity at higher undercooling rates was responsible for the formation of these γ′-free zones, since there is limited long-range equilibration of the γ matrix composition, and it was observed that the current alloys were inhomogeneous.

Secondary and tertiary precipitates were observed, meaning that a second and third nucleation burst took place after the primary precipitates formed. The secondary particles were generally spherical and located between the large coarsened γ′ precipitates (Figure 4.17). Figure 4.16 shows that the smaller γ′ precipitates were mainly cubic with rounded edges, while larger γ′ precipitates were elongated and/or irregular. Similar changes in morphology were observed in some NBSAs [2001Mil, 2008Sud]. According to Hill *et al.* [1982Hil] and Wenderoth *et al.* [1983Wen], the morphology of the γ′ precipitates during the early stages of growth is a function of both the misfit and particle size, since the transition from spheres to cubes (or any shape) depends on the total matrix/precipitate strain which is due to the lattice mismatch. This suggests that the shape of the precipitates in the Pt_{82}:Al_{12}:Cr_4:Ru_2 (at.%) alloy was a function of both particle size and the γ/γ′ misfit [2004Dou2]. It is likely that some of the γ′ precipitates might have been initially cubic, but during growth, the corners became blunt, changing the morphology from cuboid to oval, spheroid, or to other irregular shapes; this was probably due to large strains between the γ′ precipitates and surrounding γ matrix [1982Hil, 1983Wen]. Alternatively, this could have been to reduce the surface energy.

The γ′-free region was enriched in Ru, and depleted in Al compared to the region surrounding the γ′ precipitate-rich area, which suggested that those regions did not have enough Al for the formation of the γ′ precipitates (Table 4.11). This agrees with the work of Douglas

[2004Dou2] where the γ′ precipitates were rich in Al, and the matrix was rich in Ru which provided solid-solution strengthening to the matrix (Table 2.6 [2004Dou2]). In Pt_{82}:Al_{12}:Cr_4:Ru_2 (at.%), Cr partitions preferentially to the matrix phase, with some minor solubility in the precipitates (Tables 4.10 and 4.11), similar to the findings of Douglas [2004Dou2], shown in Table 2.5. According to Douglas [2004Dou2], the partitioning behaviour influences the precipitate crystal structure. Although Cr partitions preferentially to the matrix, there is some solubility in the precipitate, which stabilised the $L1_2$ structure in the Pt_{86}:Al_{10}:Cr_4 (at.%) alloy. In Pt_{86}:Al_{10}:Ru_4 (at.%), Douglas [2004Dou2] found that Ru did not stabilise the $L1_2$ structure, since the precipitates exhibited the modified DO'_c structure [2004Dou2]. Pt_{86}:Al_{10}:Ru_4 (at.%) exhibited plates in the precipitates (Figure 2.40 [2004Dou2]) that were not seen in Pt_{86}:Al_{10}:Cr_4 (at.%) [2004Dou2], nor in the present work for the Pt-Al-Cr-Ru alloys, indicating that the Cr contents were sufficient to stabilise $L1_2$ (else the plates would have been seen).

5.2.1.2 Nominal Pt_{85}:Al_7:Cr_5:Ru_3 (at.%)

Figure 4.19 shows the microstructure of Pt_{85}:Al_7:Cr_5:Ru_3 (at.%) which was the same in most regions after heat treatment, and this microstructure was similar to those observed for NBSAs [1998Gro, 1999Car1] and rapidly quenched NBSAs with a high volume fraction of the γ′ phase [1982Rit, 1986Bow]. The morphology of the precipitates was mainly cubic, with some regions having finer rounded precipitates (Figure 4.20). It is thought that the region of fine and rounded precipitates was a coarsened eutectic/eutectoid (Figure 4.20, area B). Figure 4.21, taken from a different region of the sample, showed a totally different microstructure which had very irregular precipitates. It is believed that this microstructure was a result of precipitates that coalesced to reduce the surface energy, similar to Figure 5.2. This difference emphasises the importance of viewing many different regions to obtain a balanced view by TEM of the overall, and often inhomogeneous nature of the microstructure.

5.2.1.3 Nominal Pt_{80}:Al_{11}:Cr_3:Ru_6 (at.%)

Figure 4.22 shows precipitates which were formed in Pt_{80}:Al_{11}:Cr_3:Ru_6 (at.%) after heat treatment. The γ′ precipitate shapes were mainly spherical, or at least nearly spherical. The morphology of the rest of the precipitates gradually changed to increasingly irregular shapes

due to the increasing misfit strain between particle and matrix with increasing precipitate size [1998Gro]. The more irregular morphology could also be due to either coarsening or coalescence of neighbouring γ′ precipitates, again similar to Figure 5.2.

Only in a few areas were smaller secondary γ′ precipitates observed (Figure 4.24, Arrow B). Investigations by Grosdidier *et al.* [1998Gro] of NBSAs have shown that the secondary spherical γ′ population nucleates at a lower temperature, due to very high undercoolings and grows at much lower rates, due to limited diffusivity. Due to the limited growth, these secondary γ′ precipitates exhibit near to spherical morphology, with sizes ranging from 10-50nm diameter. At this size scale of the smaller γ′ spherical precipitates, accurate EDX analysis was difficult, since even for spot analysis, the beam can scatter onto the surrounding regions, especially if contamination builds up on the analysed region during analysis. To eliminate contamination, prior plasma cleaning of the sample was undertaken. EDX performed on these smaller spherical γ′ precipitates indicated that they were depleted in Cr compared to the primary γ′ precipitates, while Al and Ru contents were similar (Table 4.12).

The higher Pt content in the secondary precipitates is thought to be from contributions from the surrounding γ matrix. According to Ricks *et al.* [1983Ric] in NBSAs, the large difference in sizes is related to the temperatures at which primary and secondary γ′ precipitates are formed, and means that they have different compositions. Even though there was a variation in the size of primary γ′ precipitates in the current work, TEM EDX phase analyses showed little variability in primary γ′ precipitate compositions, even taking into account the small areas analysed. The γ region near the γ′ in Figure 4.23 had a different composition from region D in Figure 4.24, indicating the possible presence of tertiary γ′ precipitates in region D, Figure 4.24 (Table 4.12). If so, these tertiary γ′ precipitates regions were richer in Al and depleted in Cr compared to the γ region near the γ′ in Figure 4.23.

The secondary γ′ precipitates were restricted to the regions away from the primary γ′ precipitates (Figure 4.24), which agrees with Hill [2001Hil5] and Douglas [2004Dou2]. The primary γ′ precipitates that were close to each other did not contain any secondary γ′ precipitates between them (Figures 4.24 and 4.25). According to Ricks *et al*. [1983Ric], this suggests that the γ region becomes severely depleted in γ′-forming elements, resulting in no precipitation of γ′ at lower temperatures. The tertiary γ′ precipitates were smaller than the secondary γ′ precipitates (Figure 4.24, Arrow D), and originated from a third burst of precipitate nucleation at lower temperatures. A nucleation burst in this context is the

formation of a large number of nuclei in a short space of time [1950LaM, 1952LaM, 1983Wen]. Due to the small size of the γ′ precipitates and limitations in the viewable TEM area of the samples, it was difficult to ascertain the true size and distribution of these precipitates.

A compositional gradient was observed from approximately the centre of the matrix channel to the centre of the precipitate (Figure 4.27). This compositional gradient is a function of two factors: contributions from the surrounding phase due to electron and X-ray scattering, and the edges of the phases being depleted of certain elements. There was a steep drop of the Cr content near the centre of the γ′ precipitates. Several investigators of NBSAs observed changes in image contrast towards the centre of the γ′ precipitates, due to depletion of certain elements [1986Joy, 1998Gro, 2002Zha]. Even though the compositional data are associated with measurement errors, these results indicated that the primary γ′ precipitates may have internal compositional variations (Table 4.13).

5.2.1.4 Nominal Pt_{80}:Al_{14}:Cr_3:Ru_3 (at.%)

Figure 4.28 shows coarsened primary γ′ precipitates, and most were irregularly shaped. Many precipitates were close to each other, coalescing to form larger irregular shaped precipitates, similar to Figure 5.2. This microstructure was observed in a few regions of the sample. The γ′ precipitates were interconnected by visible necks (Figure 4.28, Arrow D). In a study of precipitates in NBSAs, Balikci [1993Bal], Roy [2005Roy] and Dwarapureddy *et al.* [2008Dwa] postulated that the adjacent precipitates coalesced by the attractive force between them, due to the elastic strain field, by the migration of atoms in the matrix. Such experimental observations on the γ′ coarsening were consistent with the prediction of Ricks *et al.* [1983Ric], who reasoned that the process is controlled by atomic diffusion, with the operating coarsening mechanism mainly dependent on vacancy-solute interactions. Here, it is thought that the interaction between adjacent precipitates dominated the agglomeration process, forming the so-called “diffuse neck” via the overlap of the associated diffusion fields around the γ′ precipitates [2007Mao]. During the water quenching stage in the present study, it is thought that many γ′ nuclei formed rapidly (i.e. a nucleation “burst” occurred) at high temperatures, since the diffusion rate decreased during cooling and the initial density of cooling γ′ was high enough to cause the overlap of the diffusion fields [2007Mao].

Compared to other samples for this alloy composition, the smaller precipitates appeared to have decreased in number. In addition, there were fewer precipitates having a cuboid morphology. Spherical precipitates were the most prominent, although a smaller number of cubic γ′ precipitates were visible in different regions (Figure 4.29). The inhomogeneous nature of this alloy could be seen in Figure 4.30, although it was a multi-beam image, where the microstructure varied between grains. Fine tertiary precipitates could just be seen in Figure 4.30 (area D). The true morphology and size of such small precipitates was difficult to determine, although 3D atom probe analysis could give the true size and morphology of these precipitates [1999Fur]. Since tertiary precipitates were observed in only a few regions, this confirmed that there was a nucleation after the primary and secondary precipitates formed.

Dislocations in the matrix (Figures 4.31 and 4.32, Arrows B) ended around the precipitates, suggesting that the precipitates reduced the mobility of the dislocations. This would give some strengthening, assuming there were enough precipitates.

5.2.1.5 Nominal Pt_{78}:Al_{11}:Cr_8:Ru_3 (at.%)

Figures 4.33 to 4.34 show the different microstructures of the Pt_{78}:Al_{11}:Cr_8:Ru_3 (at.%) alloy after heat treatment. Some regions were found to be free of precipitates, which explains the low volume fraction observed. An inhomogeneous overall composition, probably due to poor mixing in the melting stage, is thought to be the major contributing factor to the observed inhomogeneous microstructure. The reasons for the formation of the different shapes of precipitates have been covered in the discussion of other samples. The elongated γ′ precipitates in Figure 4.34 were rich in Al compared to those in Figure 4.33 (Table 4.15). It is therefore thought that formation of these large and elongated precipitates was the result of a higher Al content in these regions.

5.2.1.6 Nominal Pt_{78}:Al_{11}:Cr_6:Ru_5 (at.%)

Figure 4.35 shows γ′ precipitates distributed in the γ matrix, and this microstructure was representative for most of the thinned sections. There was a shape variation between different γ′ particles. From Figures 4.35 and 4.36, the smaller precipitates exhibited a more spheroidal morphology, the medium size γ′ precipitates having a cubic morphology, while larger

precipitates had irregular shapes (possible as result of smaller precipitates coalescing). According to Maheshwari *et al.* [1992Mah] for NBSAs, the growth of the large and irregular precipitates is along the elastically soft direction of the γ phase which is <001>, and because of these higher growth rates, the precipitates attain a non-cubic morphology. At solidification, these γ′ precipitates are still in the growth regime and restricted in their further evolution, due to fast cooling rates and limited diffusion. During solidification, there is also an increase in strain energy with increased precipitate size, resulting in changed morphology of γ′ precipitates [1974Lau, 1975Lau, 1988Zha]. In Figure 4.36, where the sizes of γ′ precipitates were very similar, all the precipitates formed during a single nucleation event. Smaller secondary γ′ precipitates were seen in Figure 4.36 (Arrows A), and Zhao *et al.* [1988Zha] proposed that these precipitates retained a nearly spherical morphology, due to diffusion-limited growth of precipitates at lower temperatures. Due to random distribution of γ′ precipitates inside the matrix, during growth, some of the precipitates developed a non-spherical morphology, since there was no particular alignment of the precipitates. Where there are many precipitates, it is less likely that there will be any further precipitation, because the microstructure has no room, e.g. Figure 4.37. This would also be beneficial for the properties, because the structure is more homogeneous. In Figure 4.36 (Arrows A) the matrix was not homogeneous and according to Grosdidier *et al.* [1998Gro], this is because during cooling, the matrix does not have enough time to reach equilibrium.

5.2.1.7 Dislocations

Comparison with NBSAs

Some dislocations were observed at some of the γ/γ′ interfaces after heat treatment (Figures 4.18, 4.25, 4.26, 4.31 and 4.32), but most of the precipitates were still coherent after heat treatment, and so had no interface dislocations. Such dislocation networks have been previously observed in NBSAs [1975Las, 1987Lin]. The nature of the dislocations, shown in Figures 4.18 and 4.32 for the current work are similar to those shown in Figure 2.7 [1986Ric], and the comparison of these TEM images is shown in Figure 5.4. Drawing from the work of Ricks *et al*. [1986Ric], it is thought the dislocations observed here (Figures 5.4(a) (4.18) and 5.4(b) (4.32)) are a function of misfit and heat treatment temperature. The heat treatment would have encouraged the creation and mobility of dislocations, since the loss of coherency requires these, and this preferentially happens at high temperatures and/or for

fairly long ageing treatments [1987Nat, 1996Ver]. Similar findings were observed by Grosdidier *et al.* [1998Gro]. The lattice mismatches and heat treatment are thought to be the major two factors that contributed to the observed dislocations, since there was no applied stress [1986Fer, 1989Gab]. The nominal Pt_{80}:Al_{11}:Cr_3:Ru_6 (at.%) sample after heat treatment also showed a network of dislocations at the γ/γ′ interfaces and matrix dislocations pinned by the precipitates (Figure 4.25), and once again this was similar to NBSA Nimonic 80A. The precipitates with dislocations were surrounded by a matrix region free of precipitates (Figures 4.25 and 4.26). A possible reason for this could be that that during heating to high temperatures, the primary γ′ particles dissolved [2004Bar]. Barabash *et al.* [2004Bar] also suggested that the dissolution of γ′ leads to an increased activity of dislocations and these mobile dislocations interact with each other to form a stack of dislocations (Figure 5.4(b)). Ference *et al*. [1986Fer] found that for deformed specimens the slip bands acted as preferred coarsening sites for the γ′ particles by relieving coherency strains.

Comparison with other Pt-based superalloys

According to Douglas [2004Dou2], the dislocations observed in Figures 4.18, 4.25, 4.26, 4.31 and 4.32 would be due to misfit between the phases that led to internal coherency stresses. After long annealing times or deformation at elevated temperatures, coherency is partly lost and interfacial dislocation networks are formed. This explanation is similar to that of Ricks *et al*. [1986Ric], but different from Ference *et al.* [1986Fer]. Similar networks were formed in creep-deformed NBSAs [1996Gab, 2000Sug]. The networks can be classified into mismatch networks built up during annealing experiments [1975Las, 1989Fel]. The γ/γ′ interfaces with dislocations in the current work were curved (Figures 4.25 and 4.26), similar to those of Douglas [2004Dou2] (Figure 2.44), as a result of misfit coherency stress. Dislocations were observed to bow out between precipitates (Figure 4.25), similar to the observations made by Douglas [2004Dou2] (Figure 2.45). The dislocations observed in this work were mostly confined to the precipitates/matrix interface resulting from misfit. The few other dislocations seen were unlikely to penetrate through the interface region (Figure 4.18), being effectively pinned. Since it would have meant many dislocation interactions. According to Benyoucef *et al.* [1995Ben] and Douglas [2004Dou2], this restriction of the motion of dislocations reduces the amount of plastic deformation and is a strengthening mechanism in the alloy.

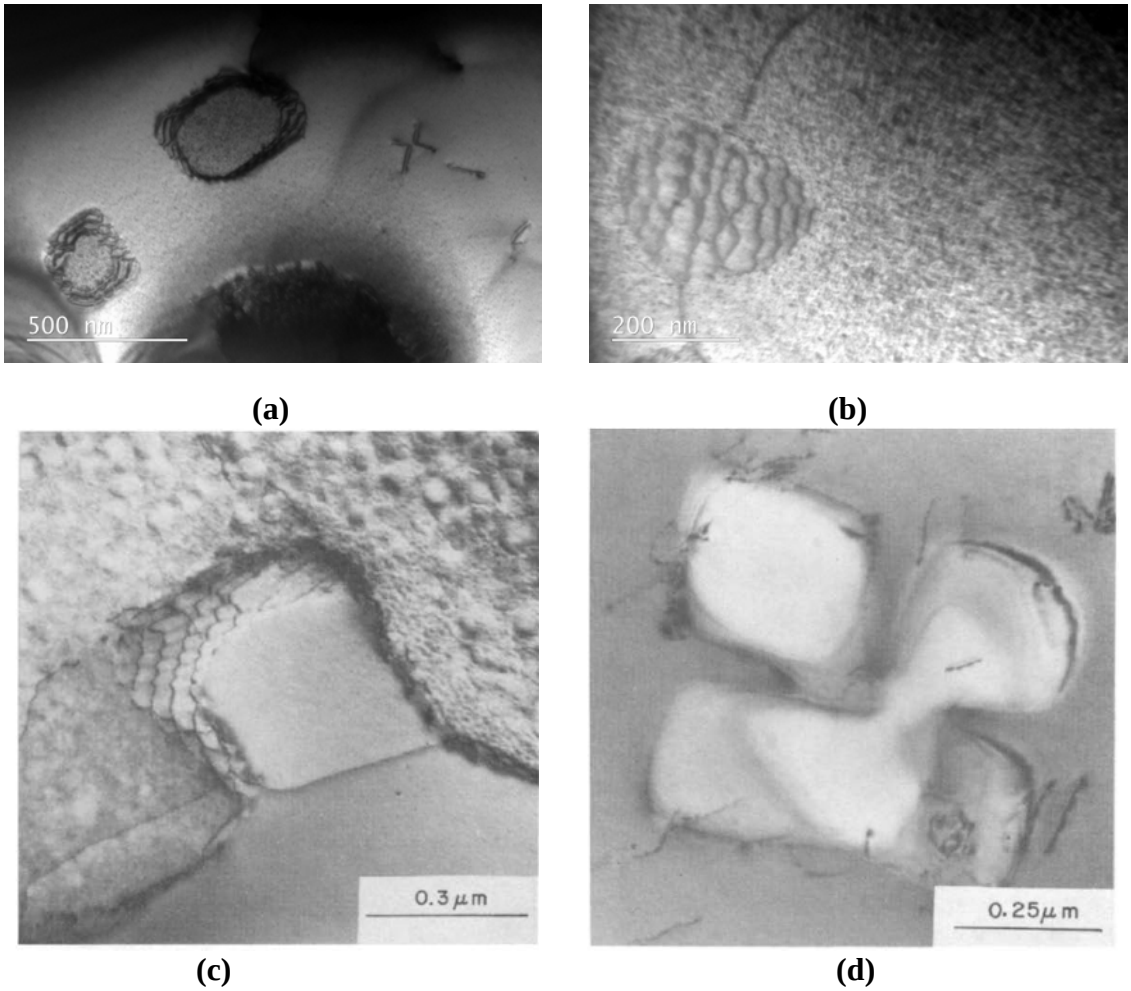


Figure 5.4. Bright field TEM images showing similar misfit dislocations in the γ/γ′ interfaces of Pt-Al-Cr-Ru and NBSAs: (a) Pt_{82}:Al_{12}:Cr_4:Ru_2 (at.%), (b) Pt_{80}:Al_{14}:Cr_3:Ru_3 (at.%), (c) Nimonic 115 [1983Ric], and (d) Nimonic 80A [1983Ric].

Dislocations were observed between larger γ′ precipitates (e.g. Figures 4.23 and 4.26) and this could be because firstly, it was easier for dislocations to nucleate at the relatively larger γ′ precipitates/matrix interface than in the matrix with the high density of small precipitates with thin matrix channels, and secondly, since the mobility of dislocations was relatively difficult in this region, thus encouraging nucleation [2004Dou2]. This is different from the earlier reason given by Barabash *et al.* [2004Bar] that during heating to high temperatures, the primary γ′ particles dissolved. Douglas [2004Dou2] also suggested that some of the dislocations nucleated where stress was present, although the current alloys were not deformed. Possible sources of stress could have been during cutting of the samples and metallographic preparation, but this was unlikely due to the extreme care taken in the whole

sample preparation. Nominal Pt_{80}:Al_{11}:Cr_3:Ru_6 (at.%) (Figure 4.23) showed distorted γ/γ′ interface dislocations similar to those observed in $Pt_{86}Al_{10}Ta_4$ (at.%) deformed at 800˚C (Figure 2.43 [2004Dou2]). For alloys showing a high dislocation density, Douglas [2004Dou2] suggested that these alloys underwent more plastic deformation at higher temperatures. It is therefore thought that the alloys in the present work that exhibited high dislocation density networks were mostly affected by the heat treatment. In Pt_{82}:Al_{12}:Cr_4:Ru_2 (at.%) (Figure 4.18), the γ/γ′ interfaces most likely acted as barriers to dislocation motion by preventing dislocations from entering the precipitates because many interactions would have been neccessary, and a similar observation was made by Douglas [2004Dou2] in Pt_{86}:Al_{10}:Ti_4 (at.%) deformed at 1100˚C (Figures 2.44 and 2.45). In addition, it should be remembered that the ordering of the precipitates provides a better strengthening mechanism of the precipitates than the matrix. EDX data from the current work showed that Ru partitions preferentially to the matrix, similar to the findings of Hill *et al.* [2001Hil2] and Douglas [2004Dou2]. In nominal Pt_{80}:Al_{11}:Cr_3:Ru_6 (at.%) (Figure 4.25) dislocations were mobile in the matrix and found a barrier at the γ/γ′ interfaces, so adding to the network of dislocations at the γ/γ′ interfaces. According to Benyoucef *et al.* [1995Ben], this is one of the strengthening mechanisms in NBSAs.

The precipitates in Pt_{80}:Al_{11}:Cr_3:Ru_6 (Figure 4.24) and Pt_{80}:Al_{14}:Cr_3:Ru_3 (at.%) (Figure 4.29) had coalesced to form larger precipitates and a similar observation was made by Douglas [2004Dou2] in Pt_{86}:Al_{10}:Ti_4 (at.%) where the $L1_2$ precipitates also coalesced to reduce surface energy, similar to Figure 5.2. Plates with different orientations were observed for the modified DO'_c precipitate structure for Pt_{86}:Al_{10}:Ru_4 (Figure 2.40, 2004Dou2]) and Pt_{86}:Al_{10}:Ir_4 (at.%) (Figure 2.50, [2004Dou2]), and this were not observed for the Pt-Al-Cr-Ru alloys in the current work. According to Douglas [2004Dou2], these platelets are indicative of a modification of the DO'_c crystal structure, and since such platelets were not observed in the current work, it is therefore deduced that the modified DO'_c precipitate structure could not have been present. In Figure 4.23 (Arrow B), the two beam bright field TEM image of Pt_{80}:Al_{11}:Cr_3:Ru_6 (at.%) shows a clear view of the matrix material between two precipitates, and is different from the platelets observed in Pt_{86}:Al_{10}:Ru_4 (at.%) (Figure 2.40 [2004Dou2]) and Pt_{86}:Al_{10}:Ir_4 (at.%) (Figure 2.50 [2004Dou2]). The absence of the DO'_c phase was confirmed by the absence of superlattice spots in the electron diffraction patterns, and the absence of twinning. The γ/γ′ interface dislocations in Pt_{80}:Al_{11}:Cr_3:Ru_6 (at.%) (Figure 4.26) are similar to those observed in Pt_{86}:Al_{10}:Ti_4 (at.%) with the $L1_2$ γ′ phase

structure. In Pt_{80}:Al_{14}:Cr_3:Ru_3 (at.%) (Figures 4.31 and 4.32), the dislocations appeared to be mostly confined at the larger precipitates interface.

Figure 5.5 shows misfit dislocations observed in the Pt-based ternary alloys Pt_{86}:Al_{10}:Ti_4 (Figure 5.5(a)) and Pt_{86}:Al_{10}:Cr_4 (at.%) (Figure 5.5(b)) by Hill [2001Hil5]. The misfit strains were observed in the interfaces between the precipitates and the matrix (Figure 5.5(a)), indicating a semi-coherent structure similar to those in Pt_{80}:Al_{11}:Cr_3:Ru_6 (at.%) (Figure 5.5(c)). The dislocations in Pt_{86}:Al_{10}:Cr_4 (at.%) [2001Hil5] interfaces appeared to have formed a hexagonal network-like structure, resembling a honeycomb [2001Hil5] (Figure 5.5(b)) similar to those seen in Pt_{80}:Al_{14}:Cr_3:Ru_3 (at.%) (Figure 5.5(d)).

Vorberg *et al.* [2005Vor] undertook a TEM investigation of dislocations in the γ/γ′ phase boundaries for some Pt-based superalloys with Ni additions. They concluded that the γ/γ′ interface dislocations were due to misfit stresses between the two phases. A high lattice misfit resulted in a loss of coherency, the semi-coherent relationship between precipitate and matrix material explaining the irregular-shaped γ′ particles with dense dislocation networks at the γ/γ′ interface boundaries [2005Vor].

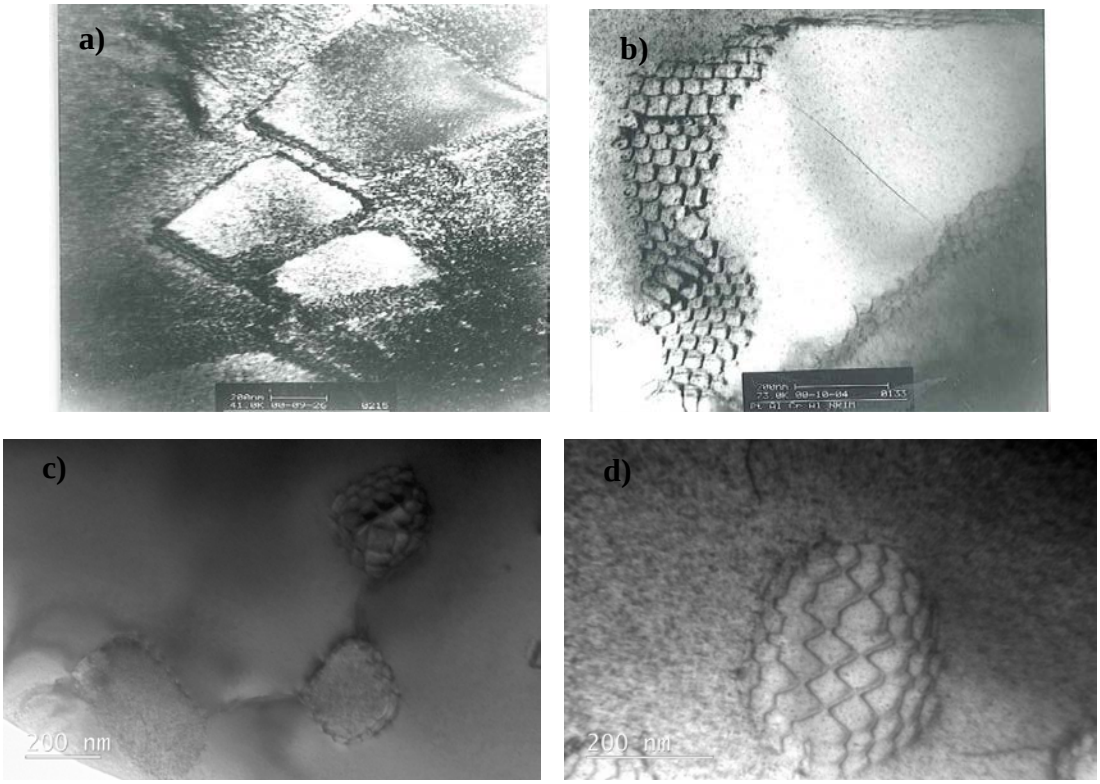


Figure 5.5. Bright field TEM images showing similar misfit dislocations in the γ/γ′ interfaces of Pt-Al-Cr-Ru and some ternary alloys: nominal (a) Pt_{86}:Al_{10}:Ti_4 (at.%) [2001Hil5], (b) Pt_{86}:Al_{10}:Cr_4 (at.%) [2001Hil5], (c) Pt_{80}:Al_{11}:Cr_3:Ru_6 (at.%) and (d) Pt_{80}:Al_{14}:Cr_3:Ru_3 (at.%).

5.2.2 TEM Diffraction Pattern and Orientation Relationship between Matrix and Precipitate

Manual calculations of electron diffraction patterns from numerous of ~Pt_3Al precipitates at different major zone axis orientations, as well as computer simulated diffraction patterns, revealed the precipitate structure to be the high temperature $L1_2$ cubic phase. Only five major zone axes could be indexed by the cubic structure due to sample holder tilt limitations, while only for one precipitate, within experimental error, could it be indexed by both the cubic and tetragonal structure. XRD measurements determined the lattice parameter to be a = 3.7084 Å for Pt_{82}:Al_{12}:Cr_4:Ru_2 (at.%). This compares with a = 3.876 Å ($L1_2$) for $Pt_{72.8}$:$Al_{27.2}$ (at.%) determined by Bronger *et al*. [1962Bro], and a = 3.85 – 3.91 Å ($L1_2$) for Pt_{86}:Al_{10}:X_4 where X was Ti, Cr, Ru, Ta and Ir by Hill *et al.* [2001Hil6]. The orientation relationship between the γ matrix (M) and γ′ precipitates (P) was: $[114]_M||[114]_P$; $[001]_M||[001]_P$; $[103]_M||[103]_P$, indicating that a matrix and a precipitate have the same orientation for the same alloy [1984Sim, 1983Ric, 2009Xin]. A TEM analysis on NBSA CMSX-4 [2009Vat] was undertaken and once again confirmed that a matrix and a precipitate have the same orientation for the same alloy ($[100]_M||[100]_P$; $[010]_M||[010]_P$). The precipitate and matrix orientation relationship in Pt_{86}:Al_{10}:Z_4 (Z = Cr, Ta, Ti, Ir and Ru) (at.%) alloys are listed in Table 5.3. Compared to the Pt-Al-Cr-Ru alloys, the orientation relationship between the matrix and precipitate for the Pt_{86}:Al_{10}:Z_4 (Z = Cr, Ta, Ti, Ir and Ru) (at.%) alloys are complex, and were different to those of Pt-Al-Cr-Ru samples. The orientation relationship between the matrix and precipitate for Pt_{86}:Al_{10}:Z_4 (Z = Cr, Ta and Ti) (at.%) alloys were the same (Table 5.3). For Pt_{86}:Al_{10}:Z_4 (Ir and Ru) (at.%) (both with precipitates platelets indicative of a modification of the DO'_c crystal structure [2004Dou2]), the matrix and precipitate orientation relationship were not all the same (Table 5.3). According to Verhoeven [1975Ver], the “cube-cube” orientation relationship optimizes the atomic matching across the interface, thereby lowering the interfacial energy.

Table 5.3. Matrix and precipitates' orientation relationship in $Pt_{86}:Al_{10}:Z_4$ (Z = Cr, Ta, Ti, Ir and Ru) (at.%) alloys [2004Dou2] and Pt-Al-Cr-Ru alloys.

Alloy (at.%)	Matrix and precipitate orientation relationship
$Pt_{86}:Al_{10}:Cr_4$	$(110)_M \parallel (110)_P$; $<002>_M \parallel <002>_P$; $<\bar{2}\,20>_M \parallel <\bar{2}\,20>_P$
$Pt_{86}:Al_{10}:Ta_4$	$<11\bar{1}>_M \parallel <11\bar{1}>_P$; $<2\,\bar{2}\,0>_M \parallel <2\,\bar{2}\,0>_P$; $(112)_M \parallel (112)_P$
$Pt_{86}:Al_{10}:Ti_4$	$<101>_M \parallel <101>_P$; $<111>_M \parallel <111>_P$; $(001)_M \parallel (001)_P$
$Pt_{86}:Al_{10}:Ir_4$	$(001)_M \parallel (100)_P$; $[110]_M \parallel [100]_P$
$Pt_{86}:Al_{10}:Ru_4$	$(001)_M \parallel (100)_P$; $[110]_M \parallel [100]_P$
Pt-Al-Cr-Ru	$[114]_M \parallel [114]_P$; $[001]_M \parallel [001]_P$; $[103]_M \parallel [103]_P$

5.3 Comparison of γ´ Precipitate Volume Fraction by SEM, TEM, AFM and Commercial NBSAs

This section gives a discussion summary on the precipitate volume fractions found using the different methods.

TEM studies of the six samples showed that the size, morphology and density of the γ´ precipitates varied with the composition of the samples, and there was also variation within each sample. The objectives set out in Section 1.2 were achieved and more detailed discussions are given in the preceeding sections for each of the samples (Sections 5.2.1.1 to 5.2.1.6). It was not possible to perform image analyses on the TEM images because the contrast between the phases was lower, unlike the SEM images when the samples were etched. Thus, for the purpose of obtaining a rough comparison of the precipitate volume fraction from the different samples, the grid method was used on the TEM images and the results are given in Figure 5.6. Although the TEM volume fraction results did not represent large regions, samples were taken at the core of each specimen and TEM transparent regions were limited. The TEM volume fraction estimates were considerably higher compared to those found by SEM (Figure 5.6). This is probably due to, firstly, the fact that TEM focuses on relatively small localised regions (which would make it very difficult for inhomogeneous samples), and secondly, the resolution is higher and can easily resolve secondary and tertiary γ′ precipitates which are difficult or impossible to observe in the SEM. SEM allowed a wider section of the samples to be studied easily and to observe high and low precipitate density areas. Even though the TEM results were not, in some ways, an accurate presentation of the overall precipitate volume fractions of the alloys compared to SEM, it should be noted that

the reliability of the TEM results was improved somewhat by performing analyses on areas of two, and in some cases, three discs per alloy (more would have been preferred).

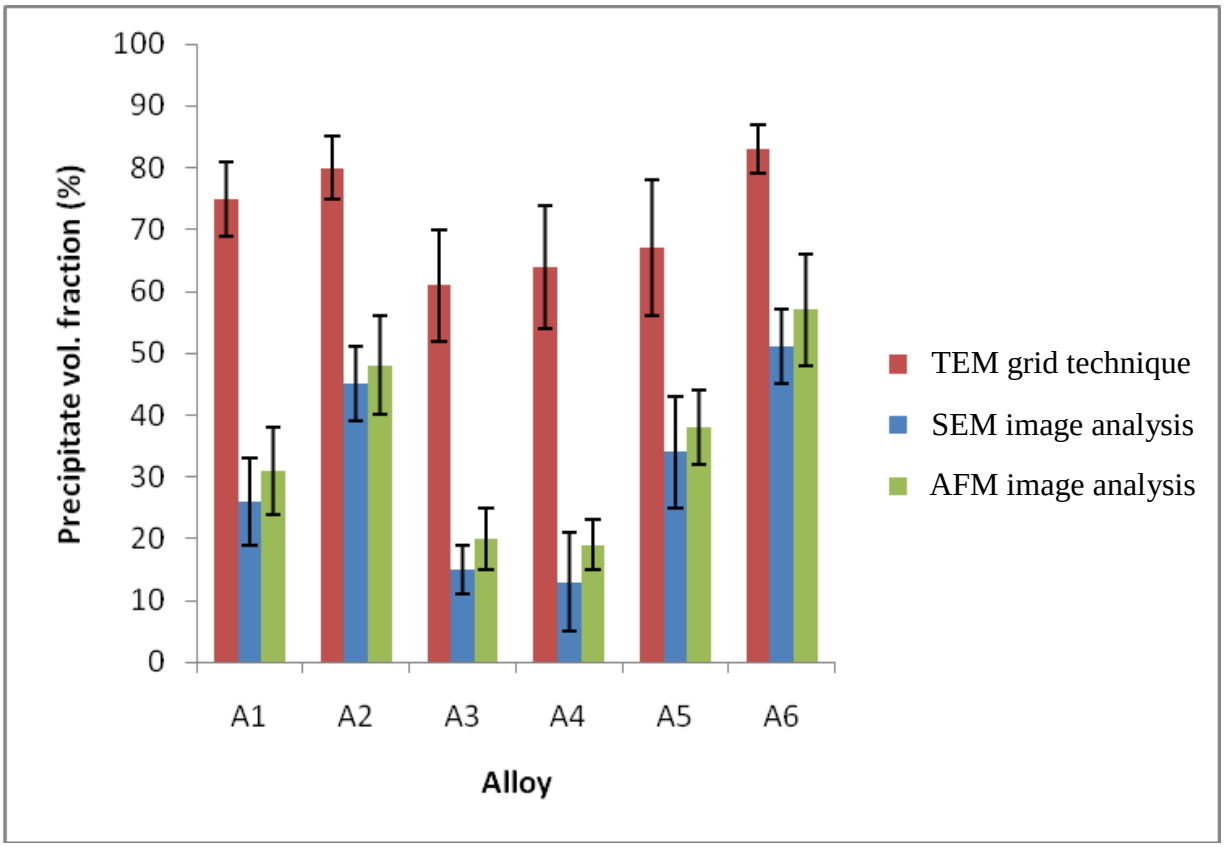


Figure 5.6. Comparison of precipitate volume fractions from TEM, SEM and AFM, showing consistently higher TEM γ′ volume fractions, with similar fractions for SEM and AFM: A1 = Pt_{82}:Al_{12}:Cr_4:Ru_2, A2 = Pt_{85}:Al_7:Cr_5:Ru_3, A3 = Pt_{80}:Al_{11}:Cr_3:Ru_6, A4 = Pt_{80}:Al_{14}:Cr_3:Ru_3, A5 = Pt_{78}:Al_{11}:Cr_8:Ru_3 and A6 = Pt_{78}:Al_{11}:Cr_6:Ru_5 (at.%).

The previously-used grid method [2009Sho1] gave results which were an under-estimate of the precipitate volume fraction since the samples were not etched and so the precipitates were not clearly revealed, and the method itself was simplistic. The SEM and AFM results have been discussed in Section 5.1.2. Comparison of SEM and AFM results showed that AFM gave precipitate volume fractions that were slightly higher than SEM. This due to the fact that in AFM, real holes were measured as precipitates (Figure 4.15), coupled with the fact that the samples were etched; this becomes another main source of measurement bias, possibly because the edges of the precipitates become much darker and hence larger areas are measured. Another disadvantage of the AFM method is that a smaller area (25μm x 25μm) was used for volume fraction measurement compared to SEM, even though this was done five times at different areas, and this was exacerbated due to the inhomogeneous samples.

The 25µm x 25µm area size limitation resulted from the AFM scan limitations. Thus, the major advantage of the SEM images analysis is that a large area could be selected, enabling viewing of both high and low density precipitate regions. While it is believed that SEM gave a more accurate analysis of the volume fraction compared to AFM and TEM, it could miss smaller precipitates [2008Süs2]. Although there were differences between the SEM and TEM volume fraction measurements, both methods agreed that, on average, an increase in SEM γ′ volume fraction corresponded to an increase in TEM γ′ volume fraction (Figure 5.7). Thus, the increase in TEM γ′ volume fraction can be explained in 79% (from $R^2 = 0.7915$) of the instances by an increase in SEM γ′ volume fraction. Due to the high errors associated with all volume fraction measurements, the two apparently highest values, datapoints A and B, are not significantly different from or higher than the adjacent datapoints C for SEM, and C and D for TEM, since their error bars overlap. Thus, within these large errors, the A, B and C alloys have the highest γ′ volume fractions for SEM measurements, whereas A, B, C and D alloys have the highest γ′ volume fractions for TEM measurements, which agrees with the observation for Figure 5.3

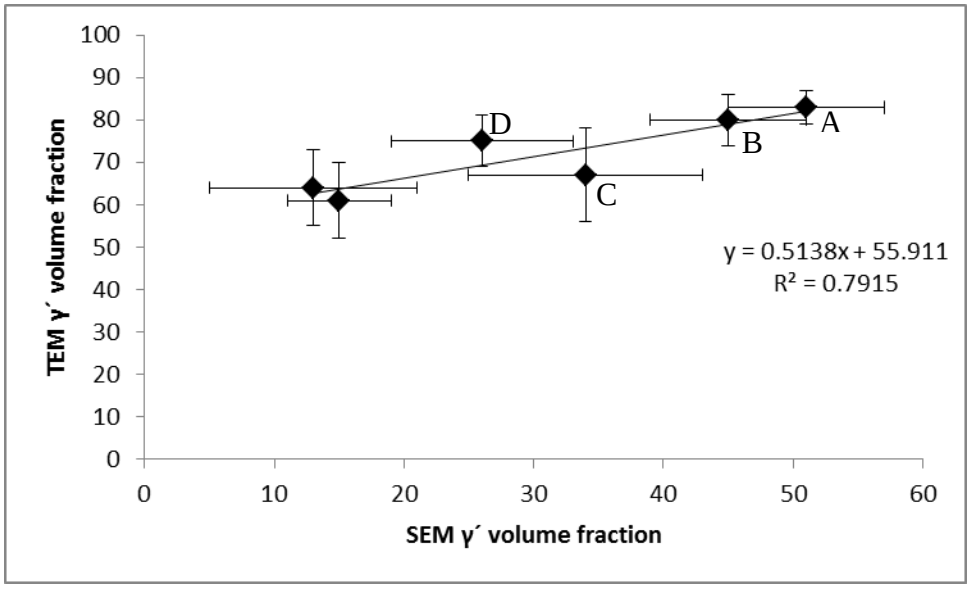


Figure 5.7. Comparison of γ′ volume fractions as measured by SEM and TEM, showing that SEM γ′ volume fraction is proportional to TEM γ′ volume fraction.

The γ′ precipitate volume fractions of the nominal $Pt_{78}:Al_{11}:Cr_6:Ru_5$ (51 ± 6% (SEM)) and $Pt_{85}:Al_7:Cr_5:Ru_3$ (at.%) (45 ± 6 (SEM)) were found to be comparable with commercial NBSAs within experimental error, Table 5.4. The volume fractions of the rest of the samples ($Pt_{82}:Al_{12}:Cr_4:Ru_2$, $Pt_{80}:Al_{11}:Cr_3:Ru_6$, $Pt_{80}:Al_{14}:Cr_3:Ru_3$ and $Pt_{78}:Al_{11}:Cr_8:Ru_3$ (at.%)) were lower than commercial NBSAs. Similar findings were observed for the AFM volume fraction

measurements. A comparison of the TEM volume fraction estimates (from the grid method, Figure 5.6) with the commercial NBSAs (Table 5.4) showed that for Pt_{78}:Al_{11}:Cr_6:Ru_5 and Pt_{85}:Al_7:Cr_5:Ru_3 (at.%) the volume fraction was about 25% higher and these results are not believed to be correct, since the TEM volume fraction estimate is thought to be in considerable error, due to reasons highlighted earlier. The best creep resistance is obtained when the volume fraction of γ′ precipitates is around 65% [1997Ro, 2004Mur], and from the Pt-Al-Cr-Ru alloys studied in this work, Pt_{78}:Al_{11}:Cr_6:Ru_5 (at.%), had the closest γ′ volume fractions to this value. Ignoring other factors, it can be expected that they could show good creep resistance in high temperature applications.

Table 5.4. Summary of γ′ volume fractions of commercial NBSAs.

Alloy Name	Vol. fraction measuring technique and reliability	γ′ vol. fraction (%)	Description	Reference
René 88 DT	Fovea Pro [2003Fov] and Photoshop, good reliability with ±2% error	41-43	Commercial NBSA used in the high-temperature section of aerospace propulsion systems, with about 13% wt% Co	[2009Til]
UM-F9	Grid method, poor reliability, errors not specified	48	Commercial nickel-based single superalloy with 5.7 - 9.7 wt% Ru additions, refractory elements and up to 6.7 wt% Cr	[2004Row]
UM-F11	Grid method, poor reliability, errors not specified	50	Commercial nickel-based single crystal superalloy with varying Ru and Cr additions (different from UM-F9), and refractory elements	[2004Row]
TMS-196	Details not given on technique	64	5th generation (SC) superalloy with improved microstructural stability and environmental properties	[2008Sat]
Supercast 247A	Details not given on technique	56	Commercial NBSA with high mechanical strength and corrosion resistance at elevated temperatures, and used in turbine blades and automotive turbo charger rotors	[2013Lav]

The γ′ volume fraction measurements for René 88 DT [2009Til] were conducted on SEM-BSE images captured at different magnifications to identify the primary and/or secondary

precipitates and processed using Fovea Pro [2003Fov] and Adobe Photoshop to isolate each precipitate. The area fraction was then determined from the image pixels. The René 88 DT samples were etched and the precipitates were clearly visible, as in the current work. While the method used to measure the volume fraction in René 88 DT did not involve manual measurements, as here, it is felt that the techniques could have similar accuracy. The volume fractions of the precipitates in UM-F9 and UM-F11 [2004Row] were determined from SEM-BSE images using etched samples and the manual point count method (grid method) [1999AST, 1999Rus]. The grid method has been used in the current work and was simplistic, and believed to yield an under-estimate of the volume fraction of the precipitates. Thus, it is thought that the grid method used to measure the precipitate volume fraction for UM-F9 and UM-F11 could be less reliable compared to the Olympus stream method used in the current work. The techniques used to measure the volume fractions of TMS-196 [2008Sat] and Supercast 247A [2013Lav] were not stated, and literature searches on same alloys failed to mention the type of method used to measure the volume fraction. However, the TMS-196 [2008Sat] and Supercast 247A [2013Lav] NBSAs were etched and the precipitates were clearly visible for image analysis.

5.4 Summary of γ´ Precipitate Formation Mechanisms

In Sections 5.2.1.1 to 5.2.1.6, the reasons responsible for the formation of different γ′ precipitates observed in the various alloys are discussed. In this section, a summary of how the different precipitates were formed is considered, drawing from the work on NBSAs. The morphology of the γ′ precipitates in the present work varied from spheres, cubes, rod-like and irregular. The different precipitate morphologies formed are associated with the lattice mismatch between the γ matrix and the γ′ precipitates [1984Doi, 1996Haz]. In nominal Pt_{78}:Al_{11}:Cr_8:Ru_3 (at.%) (Figure 4.34), elongated γ′ precipitates were observed and they had increased Al content. According to Doi *et al.* [1984Doi], partitioning of solute atoms takes place between the γ′ precipitates and γ matrix. This results in a change in the equilibrium mean composition of the phases, and has been identified by different authors after ageing treatments [1988Sin, 1993Rac]. This mechanism is likely to be effective in the current work, and thus would explain the different morphologies observed.

Different γ′ morphologies surrounded by dislocations were observed in the different specimens: Pt_{82}:Al_{12}:Cr_4:Ru_2 (at.%) with near-spherical precipitates (Figure 4.18), Pt_{80}:Al_{11}:Cr_3:Ru_6 (at.%) with irregular precipitates and near-cuboid (Figures 4.23, 4.25 and 4.26) and Pt_{80}:Al_{14}:Cr_3:Ru_3 (at.%) with irregular and rod-like precipitates (Figures 4.31 and 4.32). The shape of the precipitates in these alloys is thought to be strongly a function of both particle size and the γ/γ′ misfit [1982Hil, 1983Wen, 2004Dou2], while the heat treatment and lattice mismatches are thought to be the two major factors that contributed to the observed dislocations, since there was no applied stress or load [1986Fer, 1989Gab]. Details on the mechanisms responsible for the formation of the dislocations have already been covered in Section 5.2.1. According to Ricks *et al.* [1983Ric], precipitate growth will follow the shape changes: sphere > cube > octocube > octodendrite > dendrite (Figure 5.8). The irregular γ′ morphologies formed in the current work can be associated with a loss of coherency that took place during heat treatment which is associated with long distance diffusion of solute [1987Nat, 1996Ver] (Figure 5.8). In nominal Pt_{82}:Al_{12}:Cr_4:Ru_2 (at.%), the small precipitates were spherical (Figure 4.17, Arrow B), and some of the larger precipitates had irregular shapes (Figure 4.17), following the sequence in Figure 5.8. Rastogi *et al.* [1971Ras] and Cho *et al.* [1997Cho] observed similar shape changes in NBSAs, and attributed them to the fact that as precipitates grow, the elastic contribution increases and irregular shapes are favoured. In Pt_{78}:Al_{11}:Cr_8:Ru_3 (at.%) (Figure 4.34), the rod-like precipitate formation is thought to be driven by the reduction of interface area, as observed by Rastogi *et al*. [1971Ras] in nickel-silicon alloys. The alignment of the precipitates in Pt_{78}:Al_{11}:Cr_6:Ru_5 (at.%) (Figure 4.36) is believed to have taken place during cooling, which encourages interactions between the precipitates and rearrangement of precipitate locations. According to Yang *et al.* [1999Yan], cooling promotes the altering of precipitates size and the misfit the between the γ and γ′ phases, and the changes in precipitates size and misfit cause different γ′ precipitates to change size and shape and during this time interaction of different precipitates takes place.

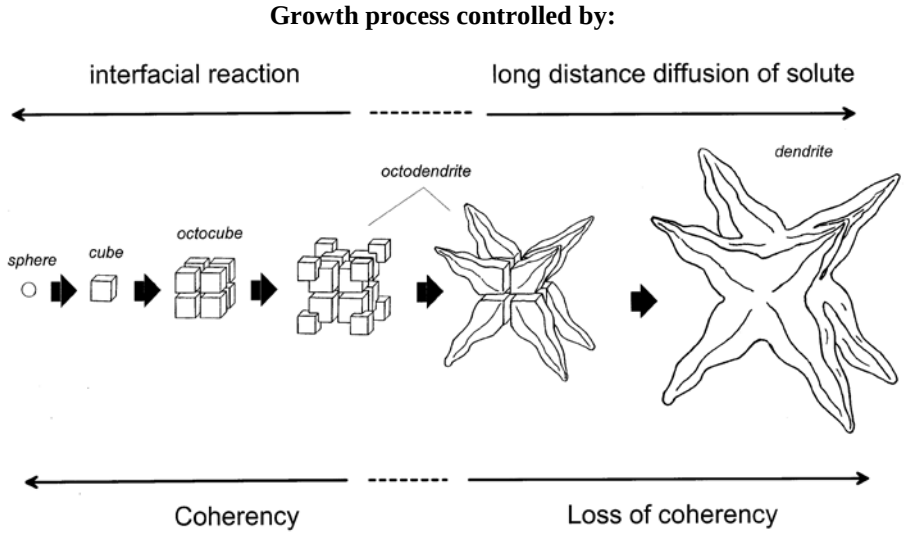


Figure 5.8. Schematic diagram of the successive shape changes encountered during the structural evolution of a freely growing precipitate [1997Dur].

This section and Section 5.2.1 have highlighted several factors which are responsible for the formation of the different γ′ precipitate morphologies. The most important factors noted in this work, with comparison to NBSAs, are as follows:

1) The mismatch associated with the γ and γ′ phases has a strong influence on the formation of different γ′ morphologies. The shape of the γ′ precipitates depends not only on their size, but also on their volume fraction, which encourages interactions of the different precipitate and impingment of precipitates.

2) The schematic diagram shown in Figure 5.8 indicates that in situations where the γ′ precipitates remain coherent, they keep a cubic shape, and in cases where coherency is lost, an irregular shape occurs.

3) The shape changes observed here can be understood by also considering a precipitate which grows firstly in a γ′ matrix and then grows further under an increasing amount of elastic interaction due to its neighbours, resulting in different morphologies because of their interactions.

4) When the precipitate loses coherency, dislocations are formed to take up the misfit, and the precipitate then tends to take on a more rounded shape. The arrangement of the dislocations is a function of the misfit and heat treatment.

5.5 Nanomechanical Properties Studies

5.5.1 Effect of Indentation Depth on Nanohardness and Elastic Modulus

It is important to realise that the nanohardness results could be affected by the sample preparation, since there could still be a surface deformation layer, even after polishing. Thus, there would be a systematic error at the very least, even though the precipitates were always harder than the matrix. However, since the samples were etched, this might have removed some, or all, of the damage, and would make the results more representative.

The difference in hardness between the γ′ and γ phases at all load levels in all the alloys was clearly evident (Figures 4.49 and 4.50). Glas *et al.* [1996Glas] reported data on the hardness of ~Ni_3Al and (Ni), and the ~Ni_3Al nanohardness was found to be ~33% higher than the (Ni), which is comparable to the 25% difference in nanohardness which was found in this investigation.

Figure 4.49 indicates that the measured γ′ nanohardness of Pt_{78}:Al_{11}:Cr_6:Ru_5 decreases with indentation depth, with the exception of one point. The indentation depth was related to the applied load. One explanation of this nanohardness decrease is the proportion of γ′ phase that the indenter deforms; this effect is dominant in superalloys [1956Mot, 1985Jon]. Figure 5.9 [1956Mot] shows different conditions that can exist under different indentation depths for different γ′ morphologies. Thus, for the current investigation, this means that as the indentation depth was increased (the indentor went deeper into the sample) the contribution from more than one phase might be measured, such that if the γ′ phase was being measured, there would be a contribution from the surrounding γ phase, thus reducing the apparent nanohardness of the γ′ phase. The different conditions illustrated in Figure 5.9 demonstrate the varying precipitate morphologies observed in the alloys for the current investigation. Figure 5.9(a) shows a situation where the hardness of the precipitate would be lower because the precipitate is too narrow and the indentor interacts with the surrounding matrix. Figure 5.9(b) shows a case where the measured precipitate is broad but shallow, and the indentor interacts with the matrix below the precipitate. Figure 5.9(c) indicates a more extreme situation which could have been experienced in this work, where the precipitate is much too shallow, and the reported precipitate hardness has a much higher contribution from the matrix. Nix and Gao [1998Nix] suggested that the main part of the hardness increase is caused by the geometric size effect of indentations. Similar observations were made by Vlaak *et al.* [1994Vla]. There was no discernable trend in the depth dependence and elastic

modulus, and thus nanohardness for the γ phase (Figure 4.54). However, Schöberl *et al.* [2003Sch2] recorded that although the matrix nanohardness decreased with increasing indentation depth, the effect was less pronounced than for the ~Ni_3Al phase, which was also found in the current work.

The precipitate elastic modulus was clearly larger than for the matrix at similar indentation depths (Figure 4.54). No systematic change in elastic modulus was observed with indentation depth for either the matrix or precipitates (Figure 4.54). Göken *et al.* [1996Gök] reported similar results. In order to demonstrate the effect of small precipitates and narrow matrix channels on the elastic modulus, the indentations were intentionally performed on these features. This meant that the indentations were not on a single phase, and the proportions of the different phases affected the hardnesses. Thus, some of the γ´ values were closer to the γ values (than in Figure 4.54 which were measured on coarser γ´ features), because the indentation involved both phases (Figure 5.10). The matrix elastic modulus was not affected and was similar to the results in Figure 4.54, although the lowest precipitate moduli were closer to the highest matrix moduli for the small precipitates. This was expected, since the narrow matrix channels were still large enough for larger indentation depths without being too influenced by the surrounding γ´ precipitates.

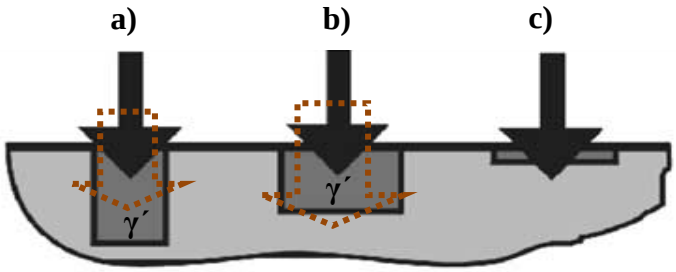


Figure 5.9. Schematic diagram showing possible positions of the final indentation and effect of the precipitate size on the hardness: (a) precipitate too narrow for indentor and load, (b) precipitate is too shallow for indentor and load, and (c) precipitate much too shallow for indentor and load [1956Mot].

The alloys' overall nanohardness as a function of indentation depth (load) (Figure 4.56) showed a decrease after a 235nm indentation depth. Apart from the data points at the two lowest indentation depths (Figure 4.56), the elastic modulus decreased with increasing indentation depth. Glass *et al.* [1996Glas] also observed a similar decrease in the nanohardness and elastic modulus at high indentation depth, due to sample preparation, since surface material had been work hardened on a nanoscale during metallographic preparation.

Vlassak and Nix [1994Vla] also observed decreasing overall nanohardness and elastic modulus with increasing indentation depth for NBSAs. Nanoindentation studies of the hardness as a function of the indentation depth had not been undertaken before on Pt-based superalloys, and the only results for Pt-based superalloys, by Nikulina *et al*. [2010Nik], showed the final depth at maximum loads. Thus, no comparison for the alloys could be done for indentation depth studies with other Pt-based superalloys.

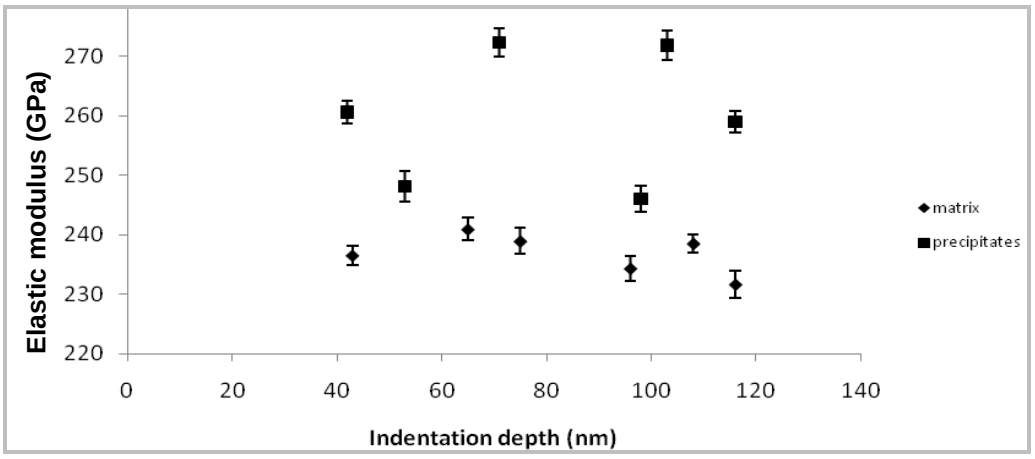


Figure 5.10. Elastic modulus as a function of indentation depth for fine γ′ precipitates and narrow regions of the γ matrix of Pt-based alloys, showing no effect of indentation depth on the matrix, and for precipitates, a slight decrease with increasing elastic modulus.

5.5.2 Hardness and Elastic Modulus: Matrix, Precipitates and Overall Alloy

To account for the influence of indentation size effects and tip shape, all measurements were performed with the same load of 2.5mN and same Berkovich tip with an average opening angle of 140.6° when measuring the mechanical properties of γ′ and γ. Material pile-ups at the indentation edges were observed (Figure 4.63), suggesting plastic deformation [2010Jan]. Table 4.16 and Figure 5.11 show the nanohardnesses of γ′ and γ for the six investigated alloys, and the hardnesses of the γ′ phase were higher than the matrix for all alloys. The standard deviation of the 20mN hardness was smaller than for 10mN (Table 4.18). This is expected, since as the load increases, the surface roughness, indentation depth and indentation size has less effect on the nanohardness [1990Jos, 1992Oli]. Due to the closeness of the elastic modulus of the different alloys and the size of the experimental error involved in those determinations (Table 4.19), no relationship could be obtained between the elastic modulus and the γ′ volume fraction at different maximum loads in the range 10-100mN.

Durst *et al.* [2001Dur] found differences in the nanohardness of the (Ni) matrix in NBSAs CMSX-6, CMSX-4 and CMSX-10, these being attributed to the variations in matrix composition. Variations in both nanohardness and compositions for the alloys in the present work were also observed. The measured compositions of the γ′, γ and alloy overalls were plotted against the nanohardness in order to determine any possible relationships. The nanohardness was found to decrease with increasing Pt content for the individual phases, but with large scatter (Figure 5.12 and 5.13). The hardness was higher at lower Pt overall alloy contents (<~83 at.%) and became lower above ~83 at.% Pt with a slight decrease at the highest Pt content (Figure 5.14). This is due to the precipitate proportion and morphology, since the ~Pt_3Al had a higher hardness than (Pt). The nanohardness of the individual phases increased with increasing Al content, but with large errors (Figures 5.15 and 5.16). For the overall alloy compositions, low Al content yielded low hardnesses, and there was a sudden increase above ~9 at.% Al (Figure 5.17). Figures 5.14 and 5.17 are complimentary since the hardness depends on the proportion of the γ′ ~Pt_3Al : γ (Pt). Thus, the hardness of γ′, γ and the overall alloy were a function of the Pt and Al content, which is due to Al being a precipitate component, whereas Pt was present in both.

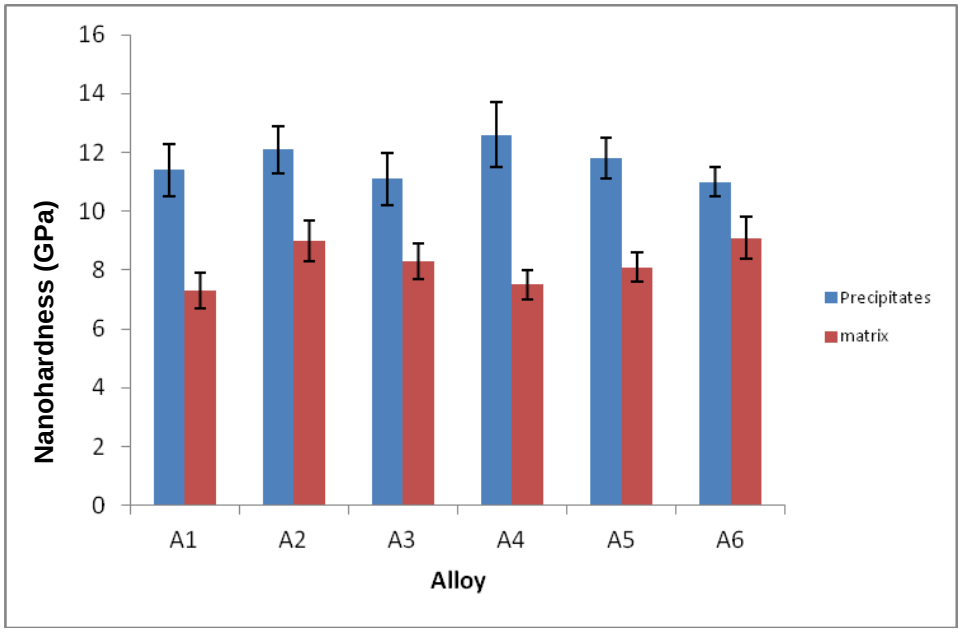


Figure 5.11. Comparison of nanohardnesses of γ′ precipitates and γ matrix at maximum load of 2.5mN and final indentation depth, showing a higher γ′ phase hardness than the matrix for all six alloys: A1 = Pt_{82}:Al_{12}:Cr_4:Ru_2, A2 = Pt_{85}:Al_7:Cr_5:Ru_3, A3 = Pt_{80}:Al_{11}:Cr_3:Ru_6, A4 = Pt_{80}:Al_{14}:Cr_3:Ru_3, A5 = Pt_{78}:Al_{11}:Cr_8:Ru_3, and A6 = Pt_{78}:Al_{11}:Cr_6:Ru_5 (at.%).

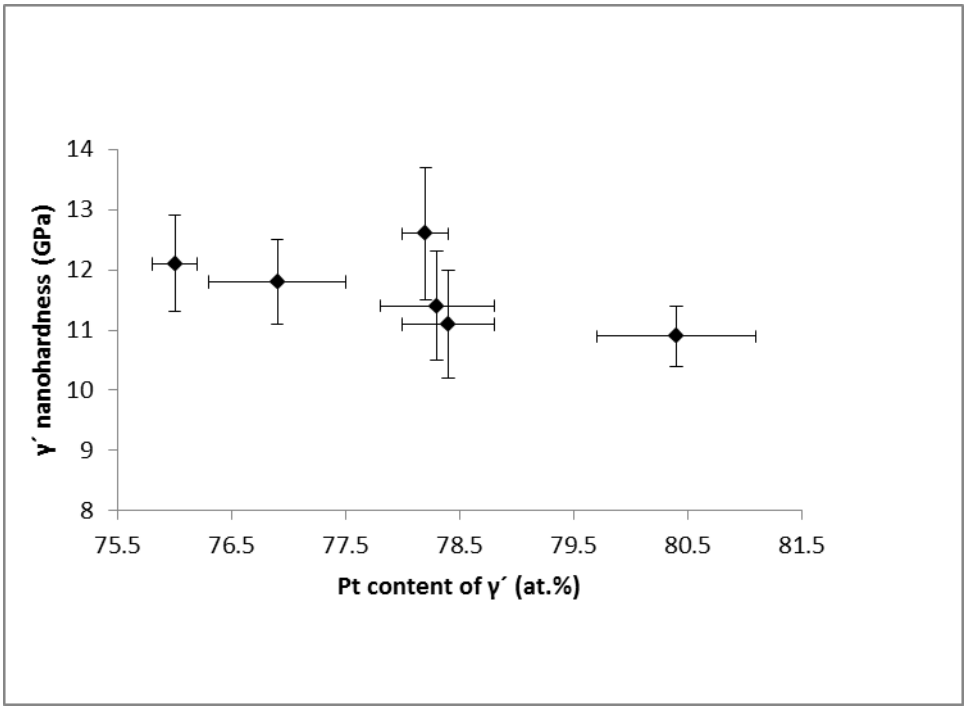


Figure 5.12. Relationship between nanohardness and measured Pt content for γ´, where each datum point represents the average Pt composition for each sample, showing a decrease in nanohardness with increasing Pt content γ´, but with large scatter.

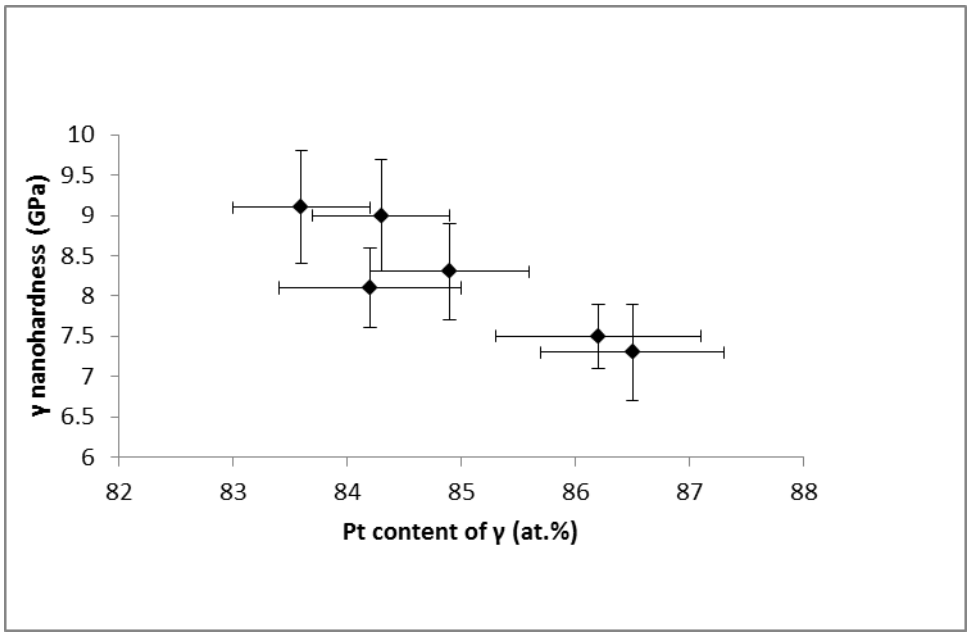


Figure 5.13. Relationship between nanohardness and measured Pt content for γ, where each datum point represents the average Pt composition for each sample, showing a decrease in nanohardness with increasing Pt content for γ, but with large scatter.

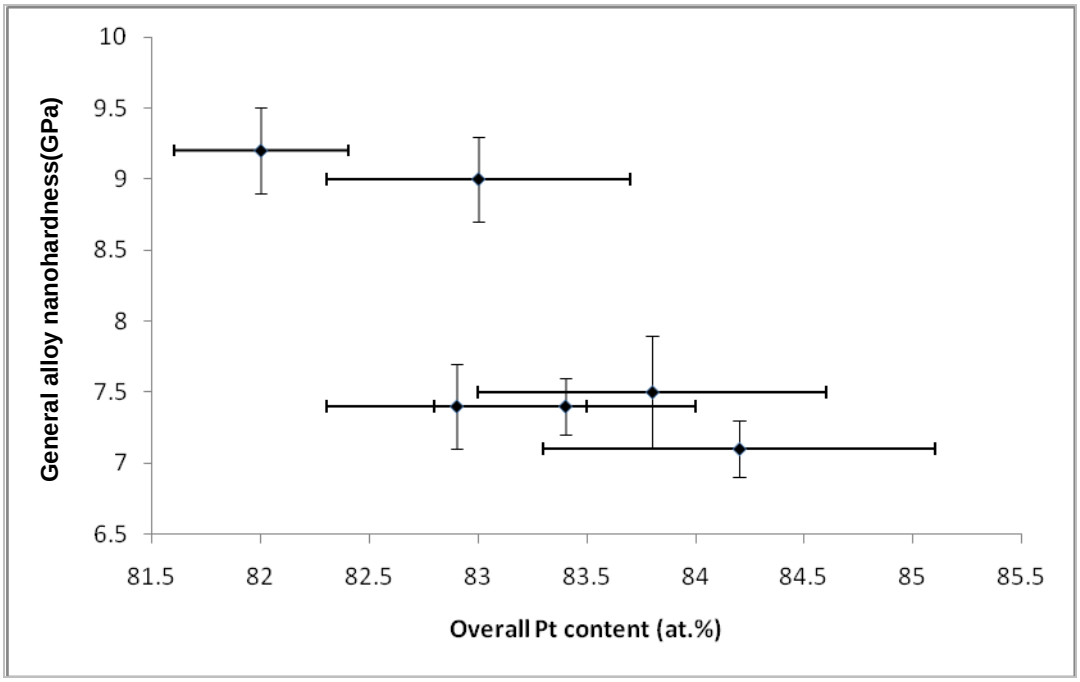


Figure 5.14. Relationship between alloy overall nanohardness and overall measured Pt content, where each datum point represents the average Pt composition for each sample, showing a high hardness at lower Pt contents (<~83 at.%) and lower hardness above ~83 at.% with a slight decrease at the highest Pt content.

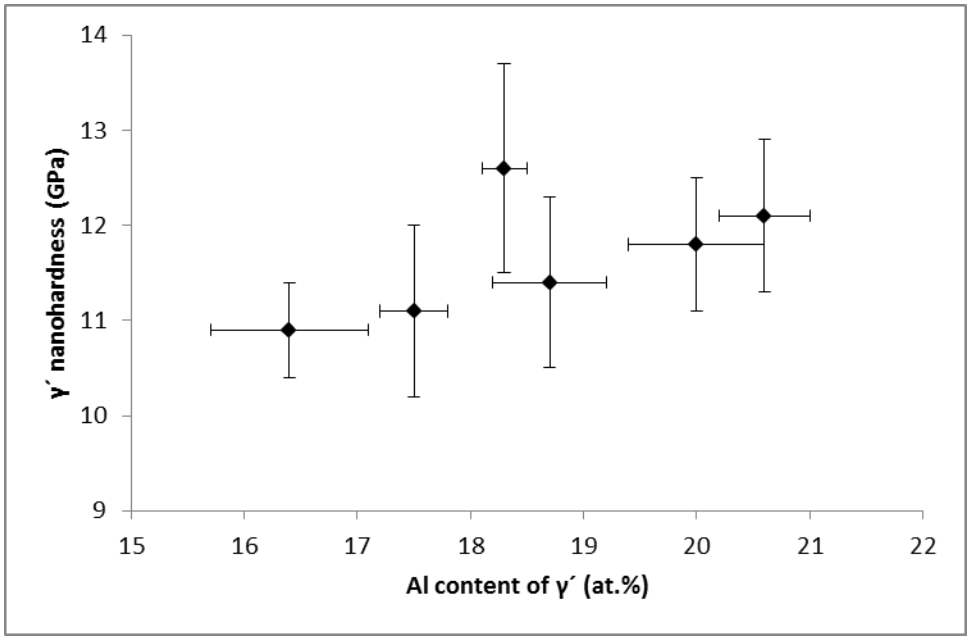


Figure 5.15. Relationship between nanohardness and measured Al content for γ´, where each datum point represents the average Al composition for each sample.

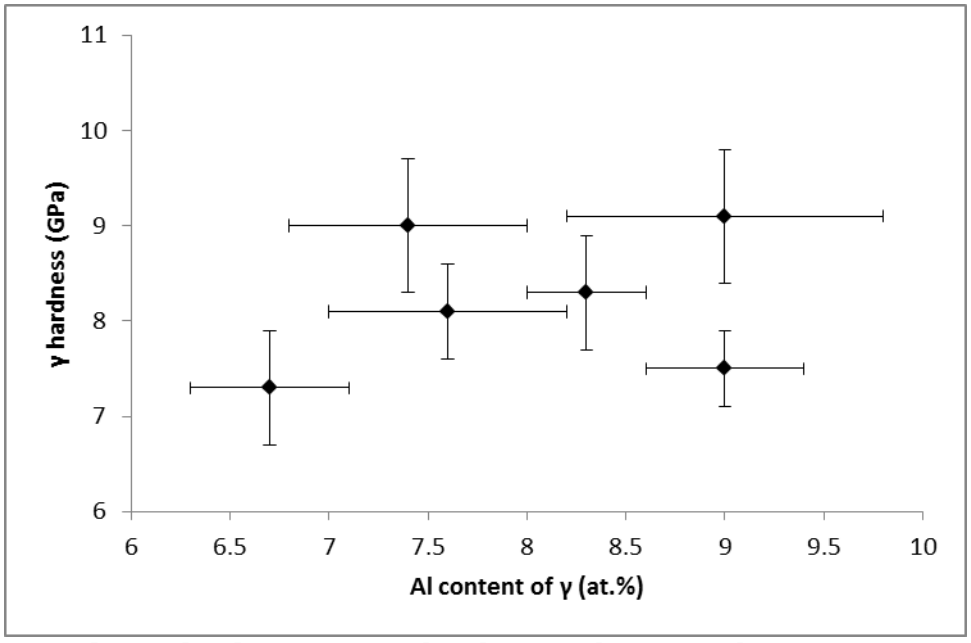


Figure 5.16. Relationship between nanohardness and measured Al content for γ, where each datum point represents the average Al composition for each sample.

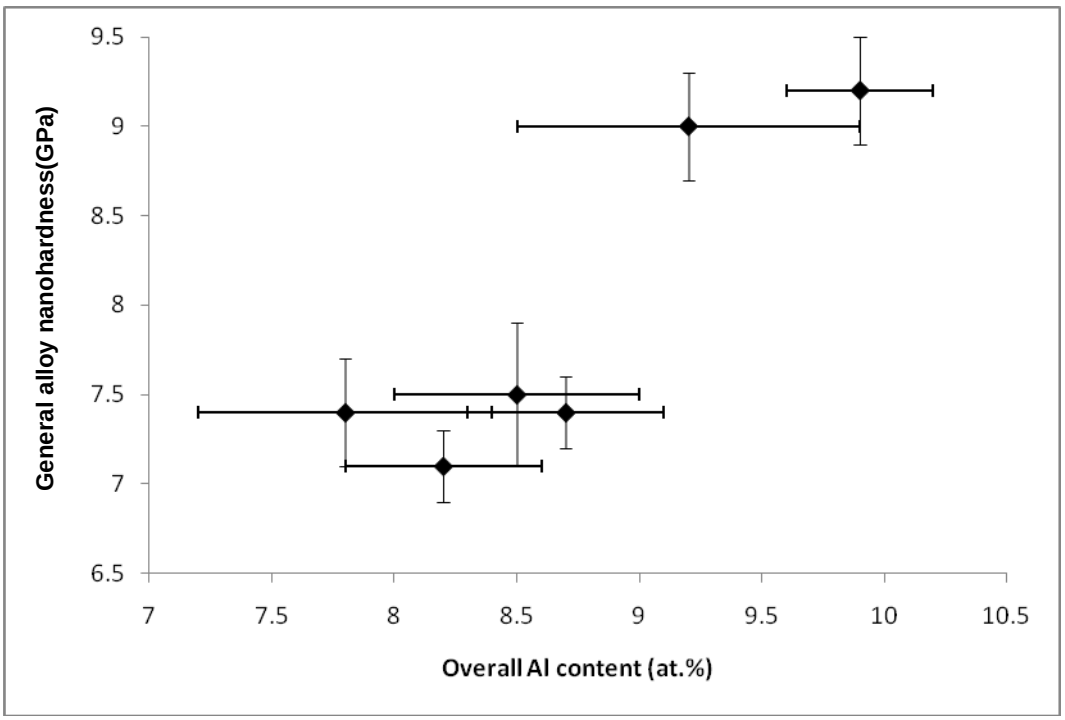


Figure 5.17. Relationship between alloy overall nanohardness and measured Al content, where each datum point represents the average Al composition for each sample, showing a low hardness at lower Al contents (<~9 at.%) and higher hardness above ~9 at.% Al content.

It has been established that the composition of the γ′, γ and the overall alloy affected the nanohardness. More factors were evaluated in order to verify which factor contributed mostly to the nanohardness results. The thickness of the matrix-channels was sufficient for

nanoindentation for all the samples (assuming the structure remains the same beneath the surface), thus the influence of the surrounding particles on the matrix hardness had little effect on the hardness, although the small influence of the channel width on the nanoindentation measurements cannot be excluded. The effects of surface roughness were excluded since the average surface roughness was 1/20 of the magnitude of the indentation size [2006CSM], and so should have had little effect. All the alloys were prepared the same way and were similar in composition, with the same phases, so the roughness would be a systematic error. In order to minimize indentation size effects on the γ′ phase, indentations were performed on larger γ′ regions in order to remain within only that region.

To illustrate the influence of small precipitates (≤0.5μm) on the nanohardness, indentations were intentionally performed on smaller precipitates (Table 4.24). Figure 5.18 shows a plot of the nanohardness for large (≥0.5μm) and small precipitates. No difference between the two sized precipitates could be determined due to the large standard deviations associated with the smaller precipitates (Figure 5.18), resulting from their indentations including a contribution from the surrounding γ phase. For better reliability, indentations on the γ′ phase were performed on larger γ′ precipitates.

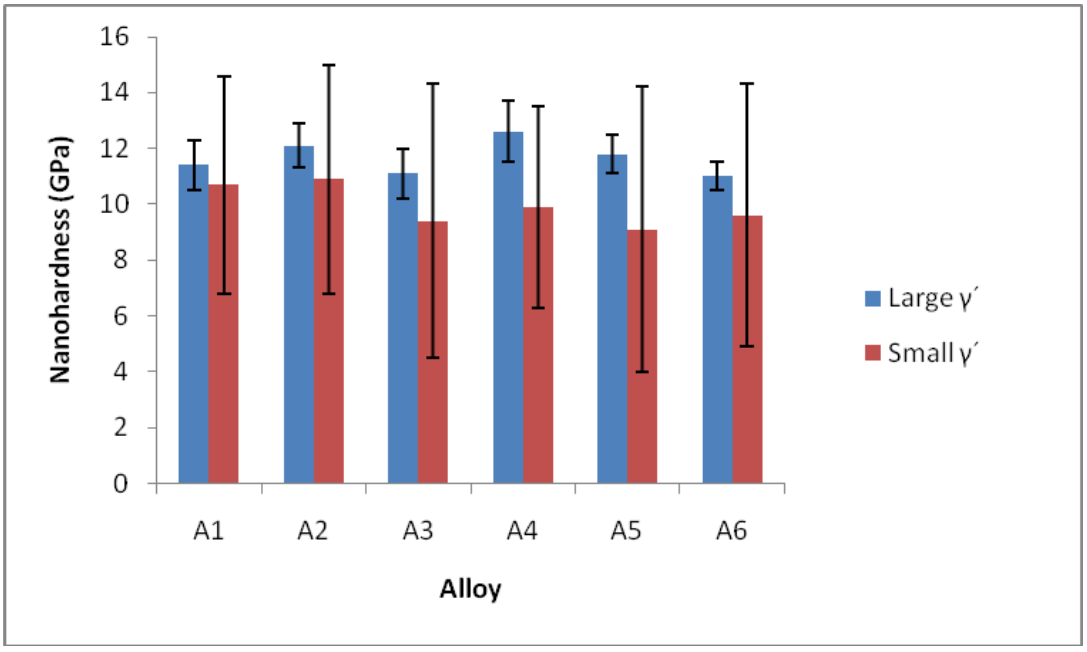


Figure 5.18. Nanohardness of coarse and fine γ′, showing smaller precipitates with lower nanohardnesses and large standard deviations compared to the larger precipitates, where A1 = Pt_{82}:Al_{12}:Cr_4:Ru_2, A2 = Pt_{85}:Al_7:Cr_5:Ru_3, A3 = Pt_{80}:Al_{11}:Cr_3:Ru_6, A4 = Pt_{80}:Al_{14}:Cr_3:Ru_3, A5 = Pt_{78}:Al_{11}:Cr_8:Ru_3, and A6 = Pt_{78}:Al_{11}:Cr_6:Ru_5 (at.%).

In order to study the effect of the matrix channel width on the hardness, nanoindentation measurements were performed on regions where the matrix channels were much narrower (Table 4.25). Figure 5.19 shows the nanohardness from both narrow and broader γ matrix regions. The hardness of the γ phase was similar in both cases taking the errors into account. Additionally, there can be changes in tip geometry due to wear [2004Dur] or small variations in surface roughness, which compromises accuracy. These results ruled out the width of the matrix channel as a major effect on the matrix hardness determined, because the narrow region was still large enough for indentation, and left the matrix composition as the major contributing factor to the differences in the matrix nanohardness. This means that for the six different samples, the differences observed in the matrix hardness are mainly due to the differences in the matrix composition for the different samples.

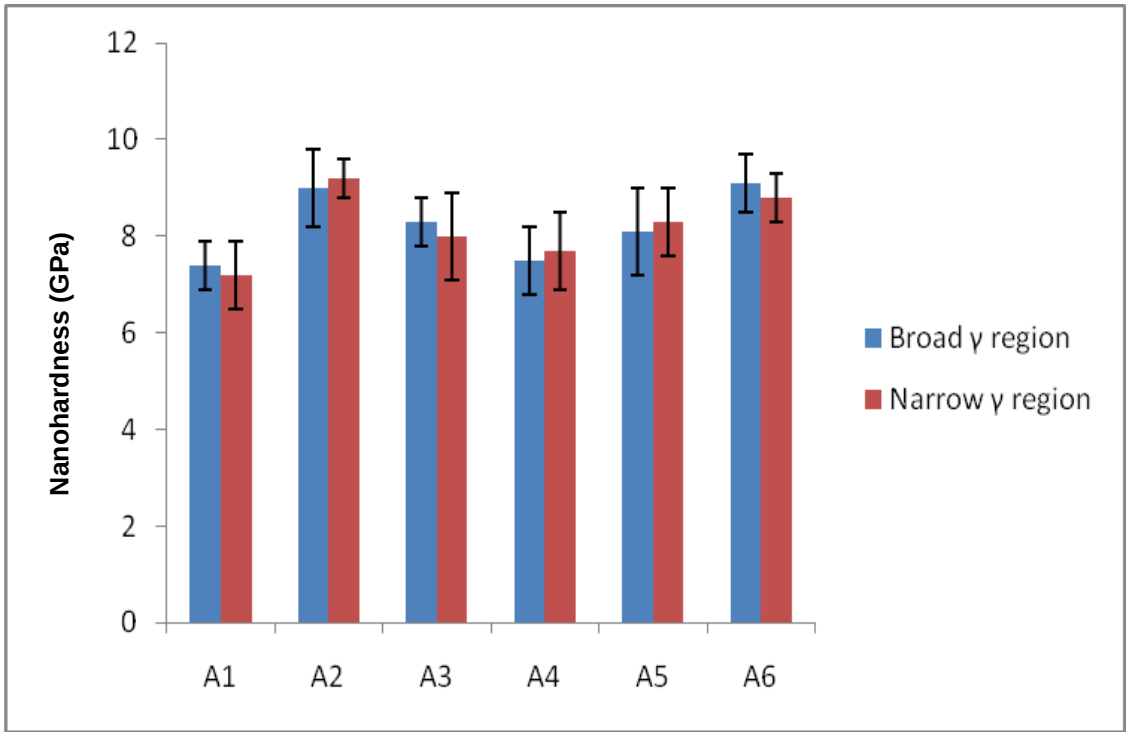


Figure 5.19. Nanohardness of broad and narrow γ channels, showing similar hardness of the γ phase for broad and narrow γ regions, where A1 = Pt_{82}:Al_{12}:Cr_4:Ru_2, A2 = Pt_{85}:Al_7:Cr_5:Ru_3, A3 = Pt_{80}:Al_{11}:Cr_3:Ru_6, A4 = Pt_{80}:Al_{14}:Cr_3:Ru_3, A5 = Pt_{78}:Al_{11}:Cr_8:Ru_3, and A6 = Pt_{78}:Al_{11}:Cr_6:Ru_5 (at.%).

Figure 5.20 shows a comparison of nanohardnesses of γ′ and γ for some alloys in this investigation compared with some NBSAs [2003Wöl, 2004Dur] and Pt_{75}:Al_{12}:Cr_6:Ni_5:Re_2 (at.%) [2010Nik], although they quoted no errors. The γ′ precipitate hardness for PWA1484 was similar to those recorded for Pt-Al-Cr-Ru alloys, whereas the matrix hardness of

PWA1484 was slightly higher. For PWA1484, the matrix was harder than, but comparable to, Pt_{78}:Al_{11}:Cr_6:Ru_5 (at.%) (which had the highest γ′ volume fraction), whereas the γ′ hardnesses were similar. CMSX-6, with no rhenium, had the lowest γ and γ′ nanohardnesses [2004Dur]. CMSX-4 had 3 wt% Re, and CMSX-10 had 6 wt% Re, and the nanohardness of both phases increased with Re content. All the Pt-Al-Cr-Ru alloys had higher nanohardnesses than the CMSX alloys, showing good potential, and were comparable with Pt_{75}:Al_{12}:Cr_6:Ni_5:Re_2 (at.%).

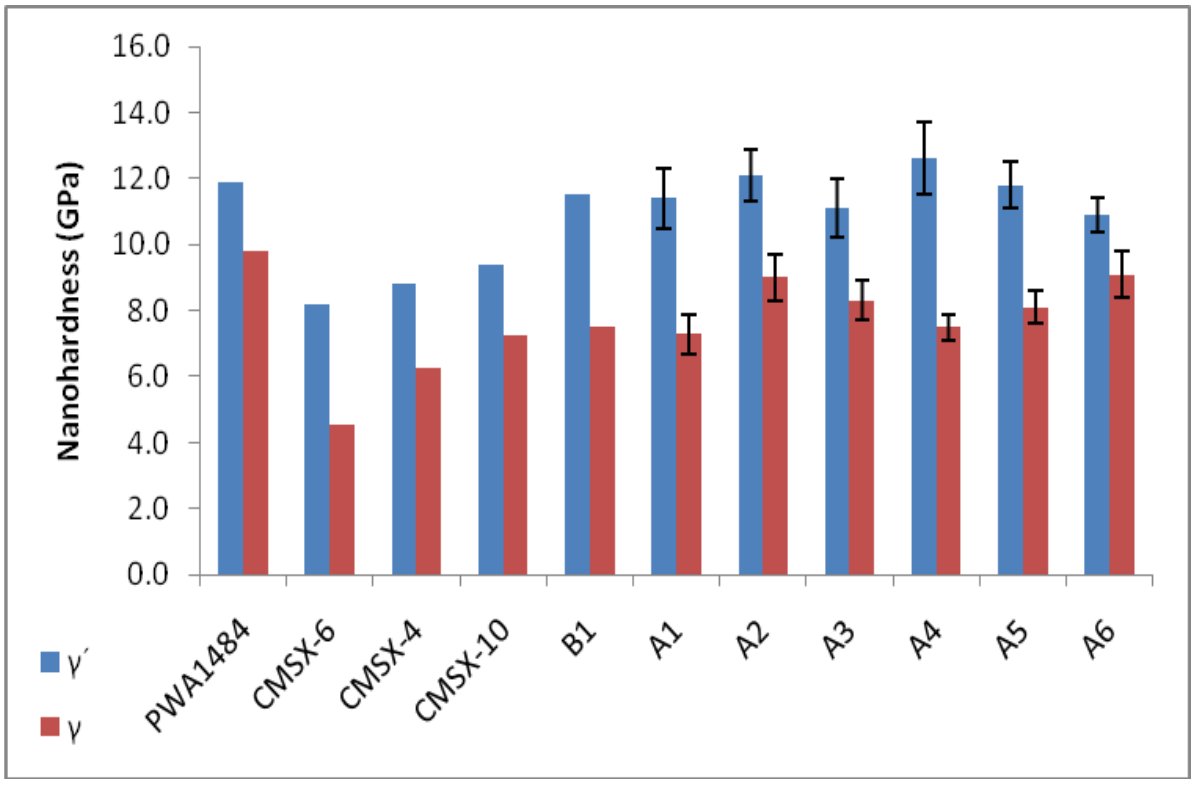


Figure 5.20. Nanohardnesses of γ′ and γ for different alloys [2003Wöl, 2004Dur], showing higher nanohardnesses for Pt-Al-Cr-Ru alloys than the CMSX alloys and comparable hardnesses to B1, where B1 = Pt_{75}:Al_{12}:Cr_6:Ni_5:Re_2 [2010Nik], A1 = Pt_{82}:Al_{12}:Cr_4:Ru_2, A2 = Pt_{85}:Al_7:Cr_5:Ru_3, A3 = Pt_{80}:Al_{11}:Cr_3:Ru_6, A4 = Pt_{80}:Al_{14}:Cr_3:Ru_3, A5 = Pt_{78}:Al_{11}:Cr_8:Ru_3, and A6 = Pt_{78}:Al_{11}:Cr_6:Ru_5 (at.%).

Figure 5.21 shows a summary of the nanohardness results for selected Pt-Al-Cr-Ru alloys (selected for large, medium and small differences between γ and γ′ hardnesses) compared with other alloys [2003Wöl, 2010Nik] for different loading levels and final indentation depth, although no standard deviations were available from the literature. The γ′ precipitate nanohardnesses were close to each other for all alloys, while the γ matrix hardness had a spread in values. This spread is thought to be due to the large differences in loading levels. Similar results were observed by Nikulina *et al.* [2010Nik], where the γ hardness was lower

than for PWA1484 when measured at two different loads (1mN and 0.5mN). When measured at 0.5mN, the hardnesses of γ´ were close to each other. For the overall alloy nanohardnesses, there was a smaller spread of results than for γ, which would be expected taking the effect of γ´ into account.

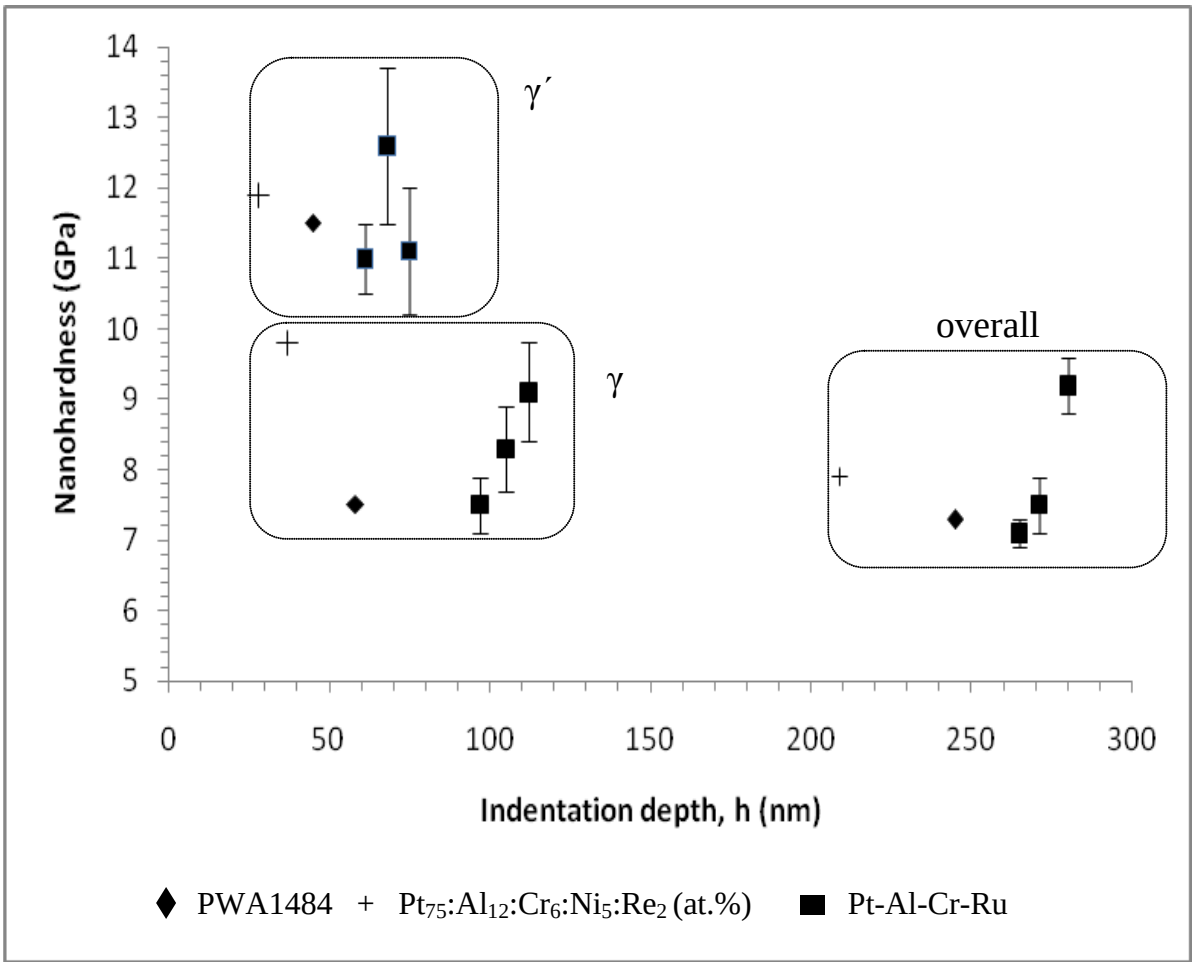


Figure 5.21. Nanohardness of Pt-Al-Cr-Ru alloys compared with Pt_{75}:Al_{12}:Cr_6:Ni_5:Re_2 (at.%) [2010Nik] and PWA1484 [2003Wöl] for different loading levels, showing similar γ´ precipitate nanohardnesses for all alloys, and a spread in γ matrix and overall alloy nanohardnesses.

No significant difference in the modulus of elasticity was observed between precipitates in the different Pt-Al-Cr-Ru alloys (Figure 5.22), and nor, within experimental error, between the γ and γ´. Figure 5.23 is a comparison of selected Pt-Al-Cr-Ru elastic moduli (selected for a large, medium and small differences between γ and γ´ hardnesses) with those of Pt_{75}:Al_{12}:Cr_6:Ni_5:Re_2 [2010Nik] and the Ni-based superalloys [2004Dur]. Even without error bars for the latter alloys, all the moduli were similar.

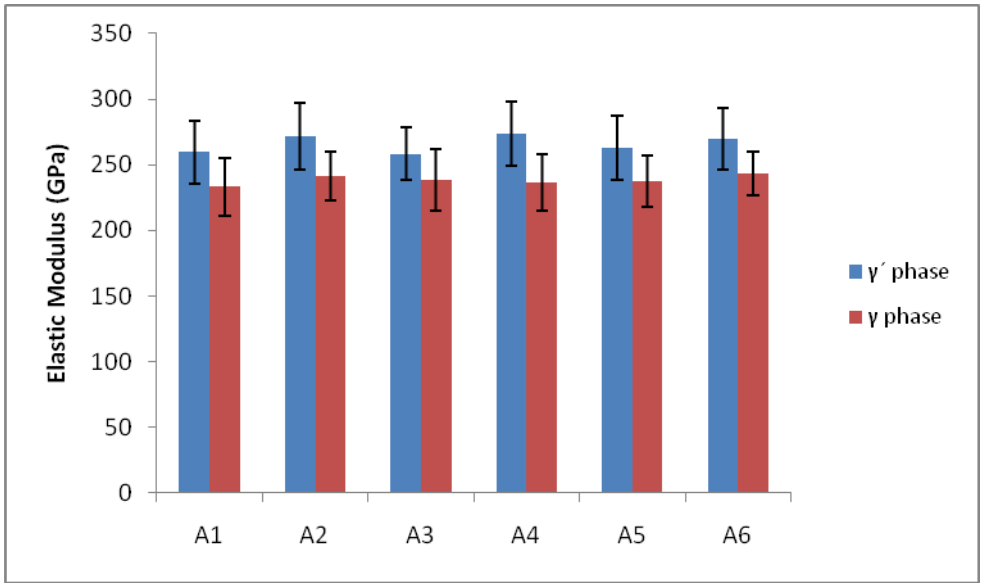


Figure 5.22. Comparison of elastic modulus for γ´ and γ at maximum load of 2.5mN and final indentation depth, showing no significant difference in the modulus of elasticity between precipitates in the different Pt-Al-Cr-Ru alloys, and ~10% higher γ´ modulus than γ, where A1 = Pt_{82}:Al_{12}:Cr_4:Ru_2, A2 = Pt_{85}:Al_7:Cr_5:Ru_3, A3 = Pt_{80}:Al_{11}:Cr_3:Ru_6, A4 = Pt_{80}:Al_{14}:Cr_3:Ru_3, A5 = Pt_{78}:Al_{11}:Cr_8:Ru_3, and A6 = Pt_{78}:Al_{11}:Cr_6:Ru_5 (at.%).

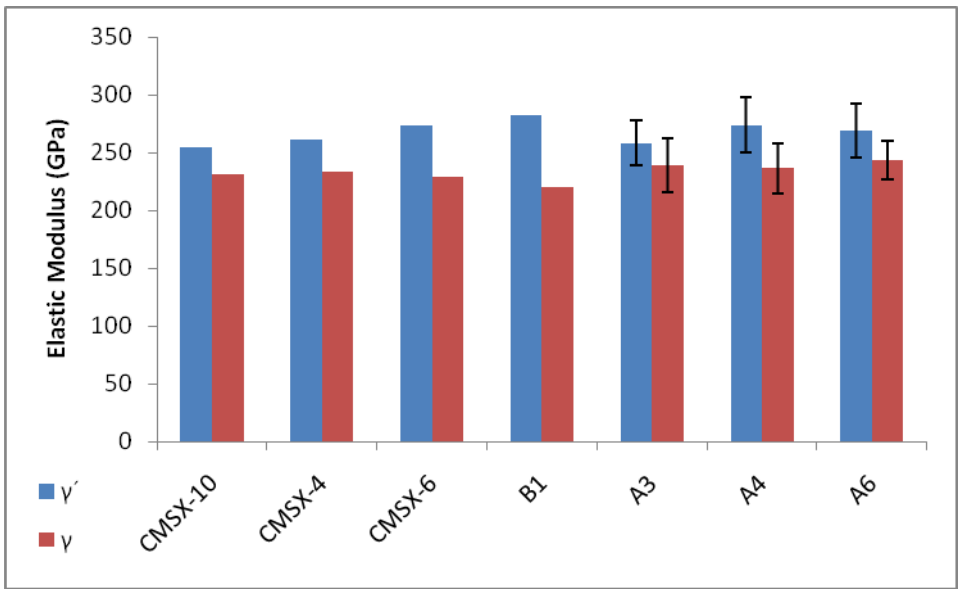


Figure 5.23. Elastic modulus of γ´ and γ for different alloys [2004Dur], showing similar moduli, except for B1 and CMSX-6, with a lower γ elastic modulus and slightly higher γ´ elastic moduli than for the other alloys, where B1 = Pt_{75}:Al_{12}:Cr_6:Ni_5:Re_2 [2010Nik], A3 = Pt_{80}:Al_{11}:Cr_3:Ru_6, A4 = Pt_{80}:Al_{14}:Cr_3:Ru_3, and A6 = Pt_{78}:Al_{11}:Cr_6:Ru_5 (at.%).

The overall alloy moduli of elasticity for Pt_{85}:Al_7:Cr_5:Ru_3 and Pt_{78}:Al_{11}:Cr_6:Ru_5 (at.%) are plotted in Figure 5.24 together with values from PWA1484 [2003Wöl], (CMSX-4, René 95) [2008Saw], IN 100 [2010Kob] and Pt_{75}:Al_{12}:Cr_6:Ni_5:Re_2 (at.%) [2010Nik]. These Pt-Al-Cr-Ru alloys were selected because they had the highest absolute γ′ volume fractions with SEM

and TEM measurements, although their error bars overlapped with Pt_{78}:Al_{11}:Cr_8:Ru_3 (at.%) for SEM, and Pt_{78}:Al_{11}:Cr_8:Ru_3 and Pt_{82}:Al_{12}:Cr_4:Ru_2 (at.%) for TEM, and so were not the highest. However, the moduli of elasticity of Pt_{85}:Al_7:Cr_5:Ru_3 and Pt_{78}:Al_{11}:Cr_6:Ru_5 (at.%) were similar to the other Pt-Al-Cr-Ru alloys in the current work, and were also similar to those of Pt_{75}:Al_{12}:Cr_6:Ni_5:Re_2 (at.%) [2010Nik] and CMSX-4, PWA 1484, IN100 and René 95 NBSAs [2003Wöl, 2008Saw, 2010Kob], although the experimental errors were not quoted for the latter five alloys. Nikulina *et al.* [2010Nik] did not provide the γ′ volume fraction for Pt_{75}:Al_{12}:Cr_6:Ni_5:Re_2, although the same alloy studied by Wenderoth *et al*. [2007Wen] had 57% γ′ for the same heat treatment conditions. The Pt_{75}:Al_{12}:Cr_6:Ni_5:Re_2 (at.%) and Ni-based superalloys contained Re, which strengthens the matrix by forming Re clusters, which act as obstacles to dislocation movements [1984Bla, 1995Wan, 1998War]. The Pt_{85}:Al_7:Cr_5:Ru_3 and Pt_{78}:Al_{11}:Cr_6:Ru_5 (at.%) alloys had no Re, and yet their moduli of elasticity were similar to the (CMSX-4 [2003Wöl], PWA 1484 [2008Saw], IN100 and René 95 [2010Kob]) NBSAs and Pt_{75}:Al_{12}:Cr_6:Ni_5:Re_2 (at.%) [2010Nik]. These findings suggest that there is no potential for improvement of Pt_{85}:Al_7:Cr_5:Ru_3 and Pt_{78}:Al_{11}:Cr_6:Ru_5 (at.%) by the addition of Re.

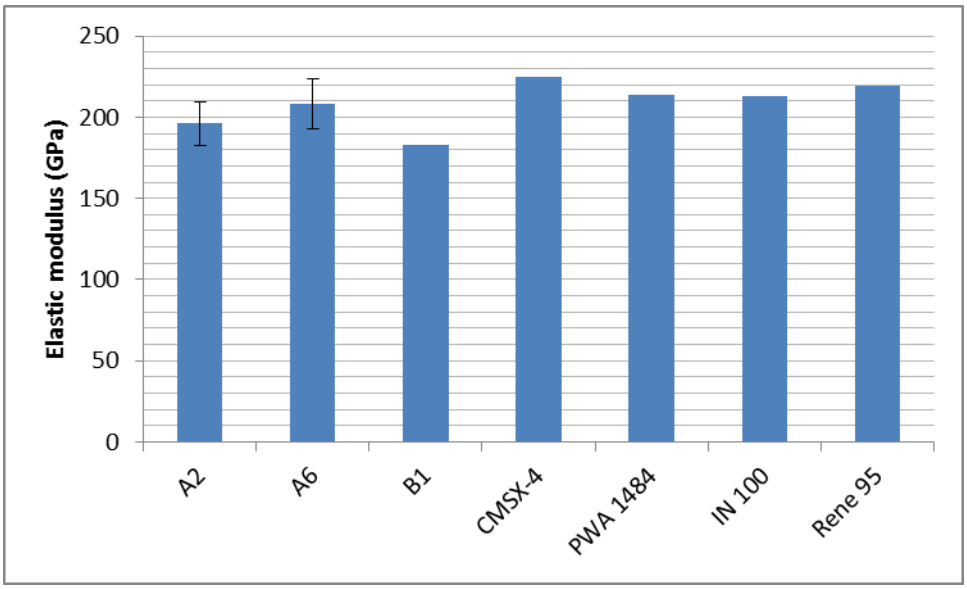


Figure 5.24. Comparison of the overall elastic modulus of Pt-Al-Cr-Ru alloys (A2 = Pt_{85}:Al_7:Cr_5:Ru_3, A6 = Pt_{78}:Al_{11}:Cr_6:Ru_5 (at.%)) with Ni-based superalloys [2003Wöl, 2008Saw, 2010Kob] and B1 = Pt_{75}:Al_{12}:Cr_6:Ni_5:Re_2 (at.%) [2010Nik], showing that within experimental error, the modulus of elasticity of A2 and A6 were equivalent to the NBSAs and Pt_{75}:Al_{12}:Cr_6:Ni_5:Re_2 (at.%) [2010Nik].

The γ′ volume fraction decreased with increasing differences between γ and γ′ nanohardnesses, with the exception of one point (indicated by an arrow in Figure 5.25). There

was no clear trend between the overall alloy hardness and differences in hardness of the γ and γ′ (Figure 5.25), although a higher overall alloy hardness was noticed at lower differences between the γ and γ′ hardness, while a lower overall alloy hardness with a slight decrease was seen at high differences in hardness between the γ and γ′ hardness. It is thought that the overall alloy nanohardness is a function of other factors, such as the size of the precipitates, thus making it difficult to measure it as a function of the differences in nanohardness alone. A plot of the overall alloy nanohardness against the precipitate volume fraction (Figure 5.26) showed that the nanohardness was lower at low precipitate volume fraction (<~35%) and became higher above ~44% precipitate volume fraction with a slight increase at the highest precipitate volume (Figure 5.26). This is due to the fact that as the precipitate volume fraction increases, the overall alloy nanohardness would also increase because the precipitate phase is the hardest, while below a precipitate volume fraction of ~35% the nanohardness of the matrix is more prominent.

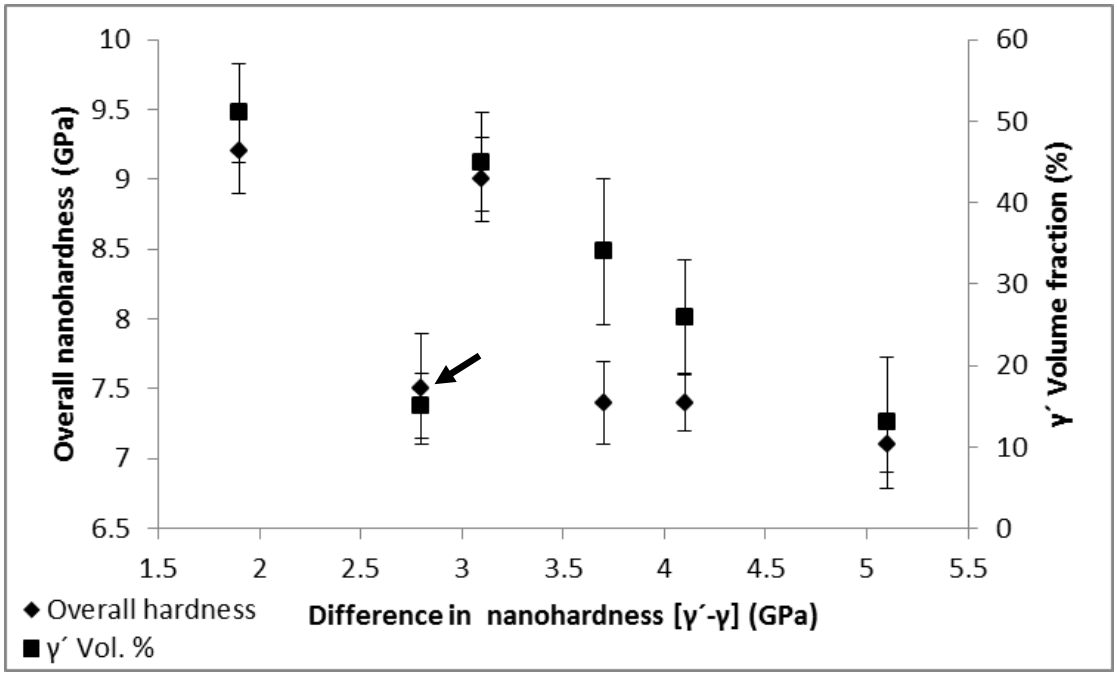


Figure 5.25. Overall alloy nanohardnesses and γ′ volume fractions as a function of the differences between γ and γ′ nanohardnesses, showing the γ′ volume fraction decreasing with increasing differences between γ and γ′ nanohardnesses, with the exception of one point (Arrow), and no clear trend between the overall alloy nanohardness and differences in hardness of the γ and γ′.

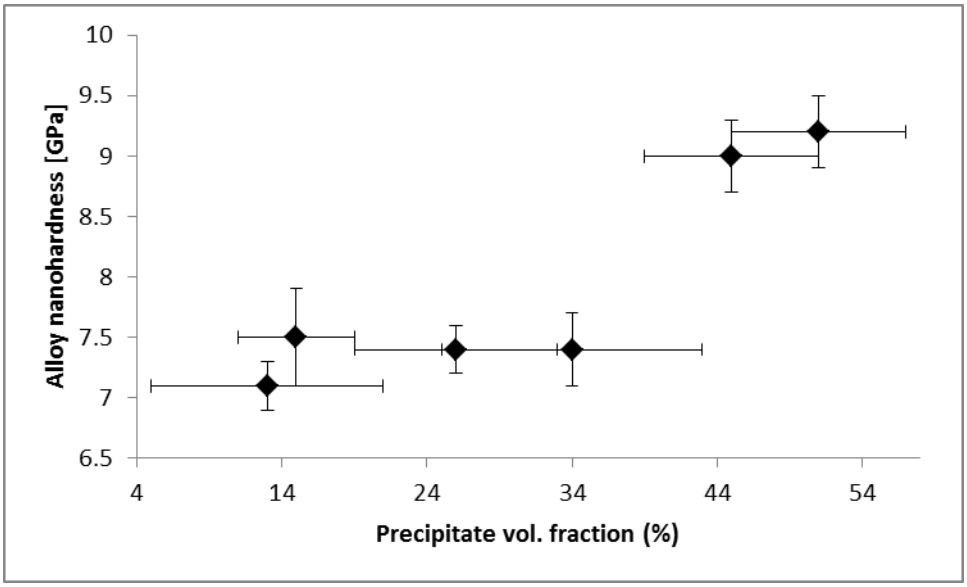


Figure 5.26. Overall alloy nanohardnesses as a function of the γ´ volume fractions, showing lower overall alloy nanohardness at low precipitate volume fractions (< ~35%) and higher above ~44% precipitate volume fraction.

Summaries of the comparison of the two alloys (with the highest volume fractions) in the current work, together with commercial NBSAs are shown in Figures 5.27 and 5.28. For the different alloys, the nanohardness increased with increasing γ´ volume fraction, as expected (Figure 5.27), except for one datum point for Pt_{75}:Al_{12}:Cr_6:Ni_5:Re_2 (at.%) [2010Nik]. The latter result could be below the threshold for having sufficient γ´ precipitates to contribute fully to the hardness. Within experimental error, the nanohardness of Pt_{78}:Al_{11}:Cr_6:Ru_5 (at.%) was close to that of PWA1484 [2003Wöl], although the volume fraction of Pt_{78}:Al_{11}:Cr_6:Ru_5 (at.%) was lower. No trend could be seen between the elastic modulus and the volume fraction (Figure 5.28), because of the lack of error bars on previous values [2003Wöl, 2008Saw, 2010Kob, 2010Nik].

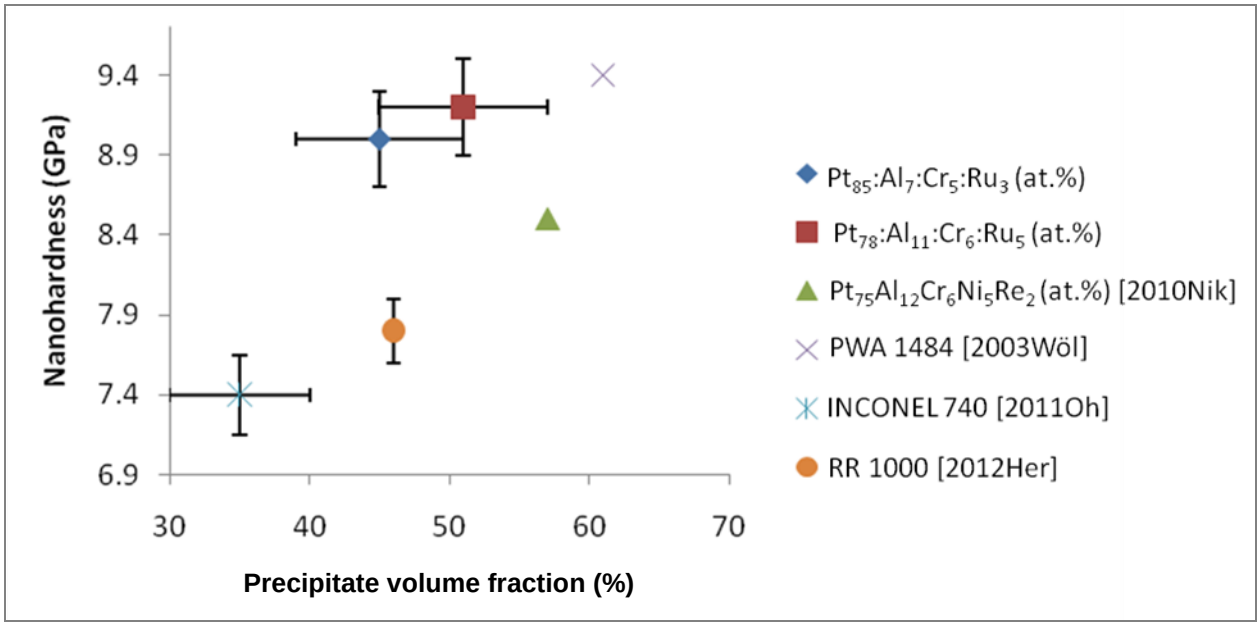


Figure 5.27. Comparison of Pt-Al-Cr-Ru overall alloy nanohardnesses with commercial alloys [2003Wöl, 2011Oh, 2012Her] and Pt_{75}:Al_{12}:Cr_6:Ni_5:Re_2 (at.%) [2010Nik], showing the nanohardness increasing with increasing volume fraction for the different alloys.

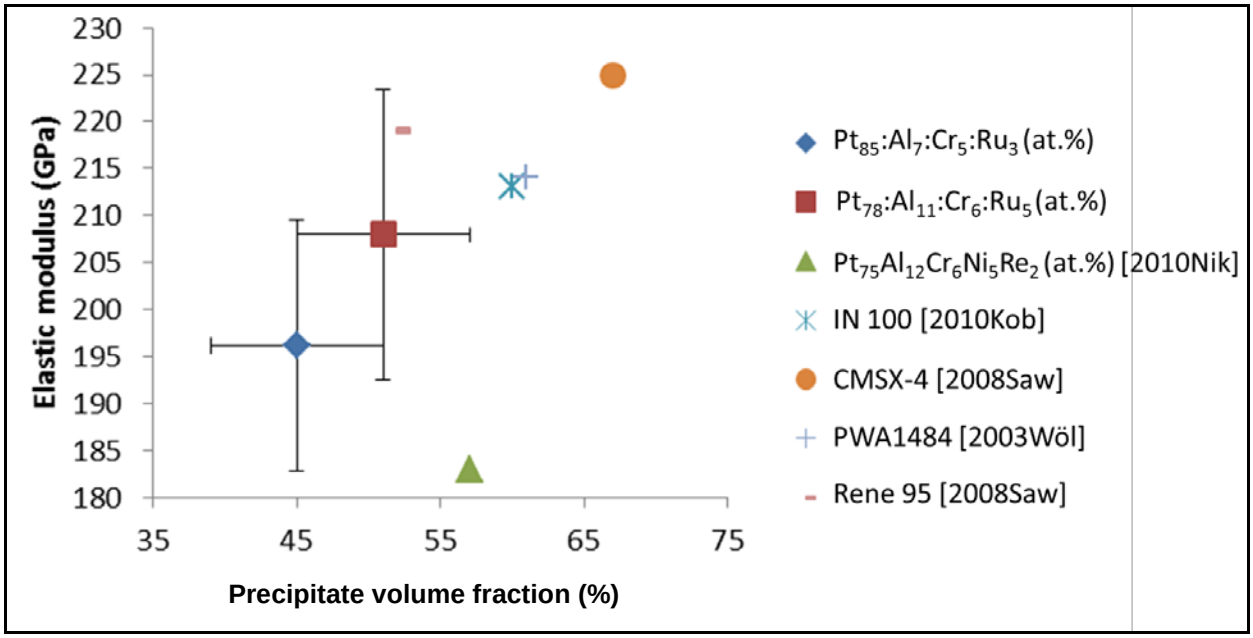


Figure 5.28. Comparison of Pt-Al-Cr-Ru overall alloy elastic modulus with commercial alloys [2003Wöl, 2008Saw, 2010Kob] and Pt_{75}:Al_{12}:Cr_6:Ni_5:Re_2 (at.%) [2010Nik], showing that within experimental error, the elastic modulus of Pt_{85}:Al_7:Cr_5:Ru_3 and Pt_{78}:Al_{11}:Cr_6:Ru_5 (at.%) were similar to the other alloys.

The comparison of the current alloys with other commercial alloys has already been discussed. The Ru contents for the alloy overalls (Table 4.23), for nominal Pt_{82}:Al_{12}:Cr_4:Ru_2, Pt_{80}:Al_{11}:Cr_3:Ru_6 and Pt_{78}:Al_{11}:Cr_6:Ru_5 (at.%) were significantly higher than for the precipitates (Table 4.21) and matrix (Table 4.22). A similar observation was noticed for the

Cr values in nominal Pt_{80}:Al_{14}:Cr_3:Ru_3 and Pt_{78}:Al_{11}:Cr_8:Ru_3 (at.%). This indicates that there was a non-systematic error in the Cr and Ru measurements. Since these elements were present in small amounts, any error would probably be reflected as a large percentage. Thus, the values of Cr and Ru were not used to try to correlate to any of the alloys' properties or precipitate volume fractions. As a final check, it was considered necessary to evaluate the effect of the interaction of the different variables (Al content and Pt content) on the nanohardness and volume fraction of the alloys in the present work. A multiple regression analysis was therefore performed in order to better understand which of the variables (Al content, Pt content) had a stronger effect on the γ′ precipitate volume fraction and nanohardness of the alloys, and the effect of the volume fraction on the nanohardness.

It was thought that using the raw data would increase the reliability of the results, although this would create complications in interpreting the results, because, for nanoindentations, ten regions were averaged to acquire the nanohardness for each alloy [2006CSM]. In contrast, the EDX composition was an average of about five measurements which gave a reasonable statistical error (less than 2%), as normally carried out in measuring the compositions for the Pt-based alloys [2004Süs2, 2008Süs2, 2009Mul]. As a result, the points would not correlate, because for nanohardness there were ten points, while for EDX compositions, there would be about five points for each sample. Even so, assuming that 10 points were collected per sample for the overall EDX compositions, there would be more uncertainties because for each datum point for EDX the corresponding nanoindentation for that point would need to be known. Thus, to remove all these uncertainties, the averaged data points were used to do the multiple regression analysis and included the effect on interactions within the variables Al content, Pt content and γ′ precipitate volume fractions on the nanohardness. (This should be valid because the averaged values were deemed to be statistically valid, even though different numbers of results were averaged). Including the interactions was important because the dependent variable (nanohardness) could depend not only on the independent variables (Al content, Pt content and γ′ precipitate volume fractions) but also on the interaction between the variables.

The γ′ precipitate volume fraction is thought to affect the nanohardness, although the γ′ precipitate volume fraction itself is affected by the Al and Pt content. Thus, to begin with, multiple regression analysis was done on the volume fraction as a dependent variable and the Al and Pt contents as independent variables and not including the interactions between the

two independent variables. The results from Excel are reported in Table 5.5, and the important values are the predictor variable (p-value) and the regression coefficients [URLQua]. The p-value for each term tests the null hypothesis that the coefficient is equal to zero (no effect). A low p-value (< 0.05) indicates that a null hypothesis can be rejected. The null hypothesis refers to a default position that there is no relationship between two measured variables [URLSta], for example the null hypothesis suggests that there will be no relationship between the γ′ precipitate volume fraction and Al content, although if the p-value is less than 0.05, the null hypothesis is rejected meaning that a relationship exists between the γ′ precipitate volume fraction and Al content. In other words, a predictor that has a low p-value is likely to be a meaningful addition to the model, because changes in the predictor's value are related to changes in the response variable. The p-values were used to determine which term(s) to keep in the regression model [URLQua]. Regression coefficients represent the mean change in the response variable for one unit of change in the predictor variable, while holding other predictors in the model constant. Another important value from the regression output summary is the significance F, which shows the overall significance of the model, but this is not as important as the p-value and regression coefficients [URLQua]. The other regression analysis outputs, namely: degrees of freedom (df), sum of squares (SS), mean square (MS) and F-ratio (F) are calculated from the regression analysis input data of the dependant and independent variable. There is low relevance of the outputs df, SS, MS and F to determine the relationship between the dependent and independent variable compared to the more important p-value and regression coefficients [URLQua, URLSta].

In the output in Table 5.5, the p-value of the Pt content was 0.043, i.e. less than 0.05, which means that the Pt content is statistically significant; it affects the volume fraction and should be kept in the regression model. The Al content p-value was 0.610, i.e. greater than 0.05 and does not affect the volume fraction (not significant). The term that remains is the Pt content in the regression model. The coefficient of the Pt content was -17.073. This means that for every 1 at.% increase in Pt content, the volume fraction is predicted to fall by ~17% [URLQua], although this would only work over a certain region of composition, i.e. where the precipitate phase is present, in the two-phase region. It should be remembered that the results used here already have a standard error associated with them. The regression coefficients are often called slope coefficients, and from the current output results, the slope was -17.073, meaning that for an increase in Pt content there was a drop in the volume fraction (already indicated in Figure 5.3). This confirmed the strong correlation shown in

Figure 5.17. Another important observation from the output was the overall significance of the model [URLQua], which at 0.035, i.e. less than 0.05, meant that the model was significant.

Table 5.5. Regression output for dependant variable (γ´ volume fraction), and independent variables (Al and Pt contents), with no interaction term.

SUMMARY OUTPUT								
Regression Statistics								
Multiple R	0.945							
R Square	0.893							
Adjusted R Square	0.822							
Standard Error	6.556							
Observations	6							
ANOVA								
	df	*SS*	*MS*	*F*	*Significance F*			
Regression	2	1080.382	540.191	12.567	0.035			
Residual	3	128.951	42.984					
Total	5	1209.333						
	Coefficients	*Standard Error*	*t Stat*	*P-value*	*Lower 95%*	*Upper 95%*	*Lower 95.0%*	*Upper 95.0%*
Intercept	1425.686	451.479	3.158	0.051	-11.122	2862.495	-11.122	2862.495
Overall Al	2.954	5.211	0.567	0.610	-13.630	19.538	-13.630	19.538
Overall Pt	-17.073	5.051	-3.380	0.043	-33.147	-0.999	-33.147	-0.999

The second step was to gauge the interaction between the Al and Pt content and observe their effect on the volume fraction. The model to use in this case is [URLQua, URLRea]:

$$y = \beta_0 + \beta_1 x_1 + \beta_2 x_2 + \beta_3 x_1 x_2 + \varepsilon$$ Equation 5.1

where $x_3 = x_1 x_2$ is the interaction term between Al content and Pt content and is given by multiplying the two variables [URLQua, URLRea]. (Background details are given in "A Primer on Interaction Effects in Multiple Linear Regression" [URLQua].) The output results (Table 5.6) indicate that "the interaction between Al and Pt contents" was not significant, since the significance F value was far greater than the p-value (0.05) [URLQua]. Furthermore, the individual p-values were also larger than 0.05. Thus, the model with the interaction cannot be used to explain the γ´ volume fraction changes, and no further plots were undertaken. Similar results were observed with the nanohardness (Table 5.7), where the interaction between Al content and Pt content was included. It is thought that interaction between the Al and Pt did affect the nanohardness, although due to the errors already associated with the results, it was not possible for the model to accurately explain the combined effect of Al and Pt content on the nanohardness.

Table 5.6. Regression output for dependant variable (γ´ volume fraction), and independent variables (Al and Pt contents), with an interaction term.

SUMMARY OUTPUT								
Regression Statistics								
Multiple R	0.960							
R Square	0.922							
Adjusted R Square	0.806							
Standard Error	6.848							
Observations	6							
ANOVA								
	df	*SS*	*MS*	*F*	*Significance F*			
Regression	3	1115.538	371.846	7.929	0.114			
Residual	2	93.795	46.898					
Total	5	1209.333						
	Coefficients	*Standard Error*	*t Stat*	*P-value*	*Lower 95%*	*Upper 95%*	*Lower 95.0%*	*Upper 95.0%*
Intercept	6271.486	5616.676	1.117	0.380	-17895.120	30438.093	-17895.120	30438.093
Overall Al	-555.231	644.720	-0.861	0.480	-3329.236	2218.775	-3329.236	2218.775
Overall Pt	-75.737	67.961	-1.114	0.381	-368.149	216.675	-368.149	216.675
inter. Al.Pt	6.760	7.808	0.866	0.478	-26.835	40.355	-26.835	40.355

Table 5.7. Regression output for dependant variable (alloy nanohardness), and independent variables (Al and Pt contents), with an interaction term.

SUMMARY OUTPUT								
Regression Statistics								
Multiple R	0.976							
R Square	0.953							
Adjusted R Square	0.767							
Standard Error	0.442							
Observations	6							
ANOVA								
	df	*SS*	*MS*	*F*	*Significance F*			
Regression	4	3.998	0.999	5.106	0.319			
Residual	1	0.196	0.196					
Total	5	4.193						
	Coefficients	*Standard Error*	*t Stat*	*P-value*	*Lower 95%*	*Upper 95%*	*Lower 95.0%*	*Upper 95.0%*
Intercept	-36.761	64.950	-0.566	0.672	-862.028	788.506	-862.028	788.506
Overall Al	0.135	1.910	0.071	0.955	-24.131	24.402	-24.131	24.402
Overall Pt	0.501	0.748	0.670	0.624	-8.998	10.000	-8.998	10.000
Vol fraction	-0.051	0.390	-0.131	0.917	-5.003	4.901	-5.003	4.901
interaction	0.000	0.001	0.271	0.832	-0.007	0.007	-0.007	0.007

In Table 5.6 the Al content was not apparently significant in affecting the gamma prime fraction, although Al is linked to Pt (hence is not independent) because of the Pt_3Al formula. Considering that Al and Pt are linked, a different approach would be to make Pt, Al and γ´ volume fraction all as non-independent x variables, and nanohardness as the y-value. Alloy Pt_{78}:Al_{11}:Cr_8:Ru_3 (at.%) can be considered an outlier since the Cr content was higher than the

others and can be ignored, and the number of datapoints would now be five (n = 5). Thus, Pt and Al are completely dependent (and Ru and Cr are considered constants). In order to undertake the regression analysis of the overall alloy nanohardness with overall (Al, Pt and γ′ volume fraction), the interaction between the three x variables was considered and the regression analysis used was Equation 5.2 since there are multiple variables.

$$y = \beta_0 + \beta_1 x_1 + \beta_2 x_2 + \beta_3 x_1 x_2 + \beta_4 x_1 x_2 x_3 + \varepsilon$$ Equation 5.2

Figure 5.29 shows the regression analysis plot of the alloys nanohardness as a function of all three x-variables. The results show a strong dependence of the overall alloy nanohardness on the x-variables, with R^2 = 0.88, indicating that the regression analysis is reliable. This result indicates that all three factors (Al, Pt and γ′ volume fraction) affect the alloy nanohardness, but to different degrees. The overall p-value of the model is 0.033, i.e. less than 0.05, which means that the overall model is statistically significant, meaning the interaction of the three variables affects the nanohardness and explains 88% of the increase in the volume fraction (R^2 = 0.88). The individual x-variables' p-values indicate that the volume fraction has the most effect on the nanohardness with a p-value of 0.021, followed by Al content (p-value = 0.038) and lastly, Pt-content (p-value = 0.059). The p-value of the Pt-content is 0.059, which is greater than 0.05, meaning that the Pt-content is not statistically significant in explaining the increase of the alloy nanohardness. This was expected, since a plot of the overall alloy nanohardness and overall Pt content (Figure 5.14) showed a decrease in nanohardness with increasing Pt content. However, the volume fraction is dependent on the Pt content and regression analysis on the γ′ volume fraction (y-value) and overall Pt-content (x-value) in Figure 5.30 shows the strong dependence of the γ′ volume fraction on the Pt content with a p-value of 0.034 (less than 0.05), meaning the relationship is statistically significant. The γ′ volume fraction is related to the Pt content by the linear equation: -19.312 (γ′ volume fraction) + 1638.3. The data are also more evenly distributed along the Pt axis (Figure 5.30) than for the relationship between alloy nanohardness and interaction of Pt, Al and γ′ volume fraction (Figure 5.29), and consequently the linear regression is more reliable.

Regression analysis on the nanohardness with γ′ volume fraction also shows a strong correlation, with a p-value = 0.023 (less than 0.05, so the relationship is significant) (Figure 5.31). The alloy nanohardness is related to the γ′ volume as: alloy nanohardness = 0.054 (γ′ volume fraction) + 6.3995. Pt-Al-Cr-Ni alloys were reported to have γ′ volume fractions of

51-57% [2006Völ, 2007Wen], and a γ′ volume fraction of 51% correlates with a hardness of ~9GPa in Figure 5.31 and matches the γ′ hardness plateau for Waspalloy (Figure 2.12(b)) and the maximum for CMSX-10 (Figure 2.17).

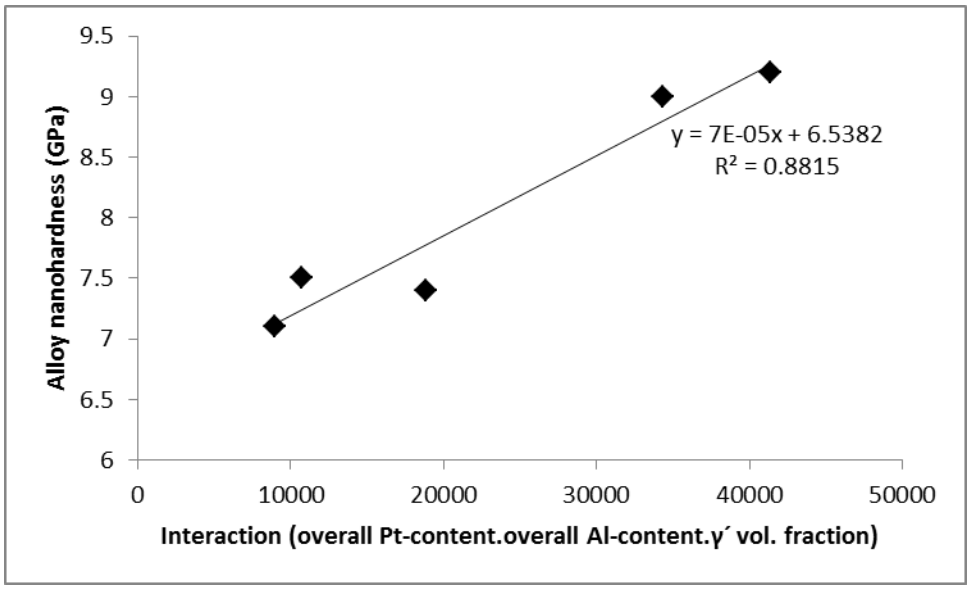


Figure 5.29. Relationship between alloy nanohardness and interaction of overall Pt content, overall Al content and γ′ volume fraction, showing a strong correlation with the alloys' nanohardnesses increasing with increasing x variables.

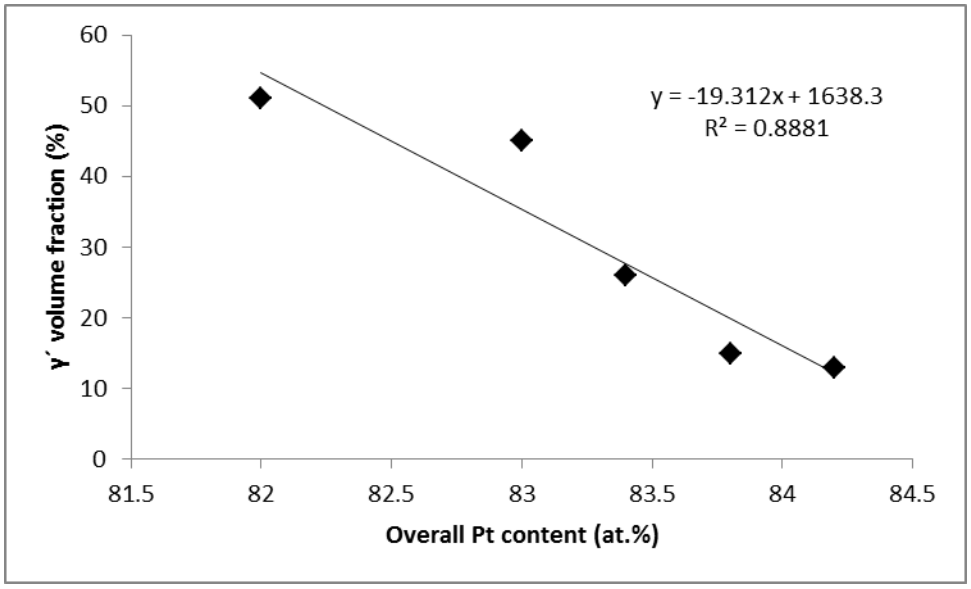


Figure 5.30. Relationship between γ′ volume fraction and overall Pt content, showing a strong correlation with the γ′ volume fraction decreasing with increasing overall Pt content.

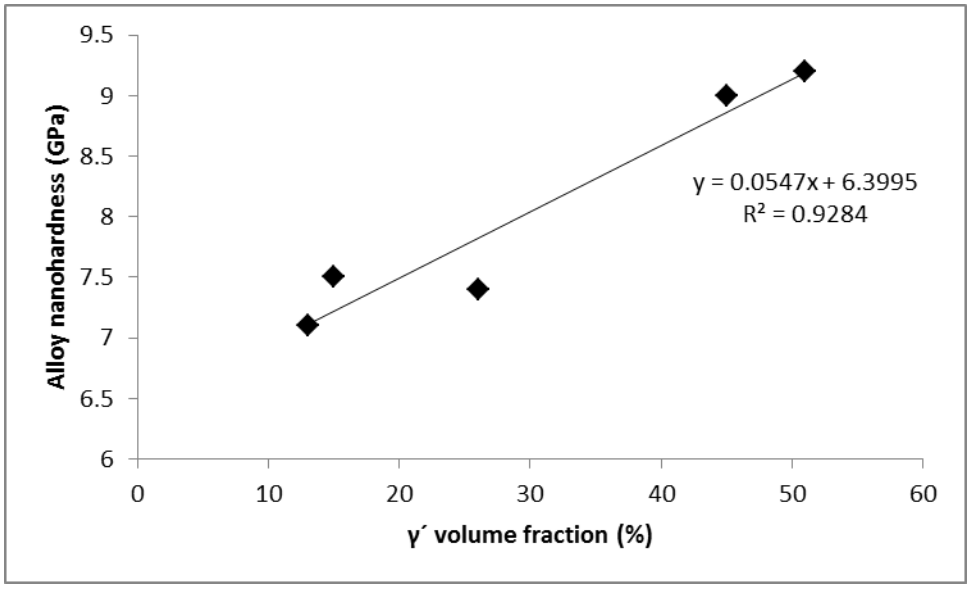


Figure 5.31. Relationship between alloy nanohardness and γ´ volume fraction, showing a strong correlation with the alloys' nanohardnesses increasing with increasing γ´ volume fraction.

The same procedure used in Figure 5.29 for regression analysis on the alloys' nanohardnesses was used for γ´ nanohardnesses. Figure 5.32 shows the plot of the regression analysis results with γ´ nanohardness as the y-value and (Al, Pt and γ´ volume fraction) as the x-value. The p-value of the regression analysis was 0.98, which is much larger than 0.05. Thus, the relationship with the three variables Al, Pt and γ´ volume fraction cannot be used to explain the change in the γ´ nanohardness. However, a relationship which did not include the γ´ volume fraction, and only the Al and Pt contents as the x variables showed a better correlation (Figure 5.33) than in Figure 5.32. The p-value for the regression analysis was 0.047, which was less than 0.05, therefore the relationship is statistically significant. The individual p-values of Al and Pt are 0.040 and 0.098 and this means that Al explains better the increase in the γ´ nanohardness and is statistically valid (p-value <0.05), while the individual effect of the Pt content is not statistically valid (p-value >0.05). Figures 5.12 and 5.15 confirm this, where the γ´ nanohardness decreased with increasing Pt content (Figure 5.12) and increased with increasing Al content (Figure 5.15). The correlation between the γ´ volume fraction and γ´ Pt content has already been shown in Figure 5.3 with a p-value of 0.043, i.e. less than 0.05, which means that the Pt content is statistically significant; it affects the volume fraction and should be retained in the regression equation.

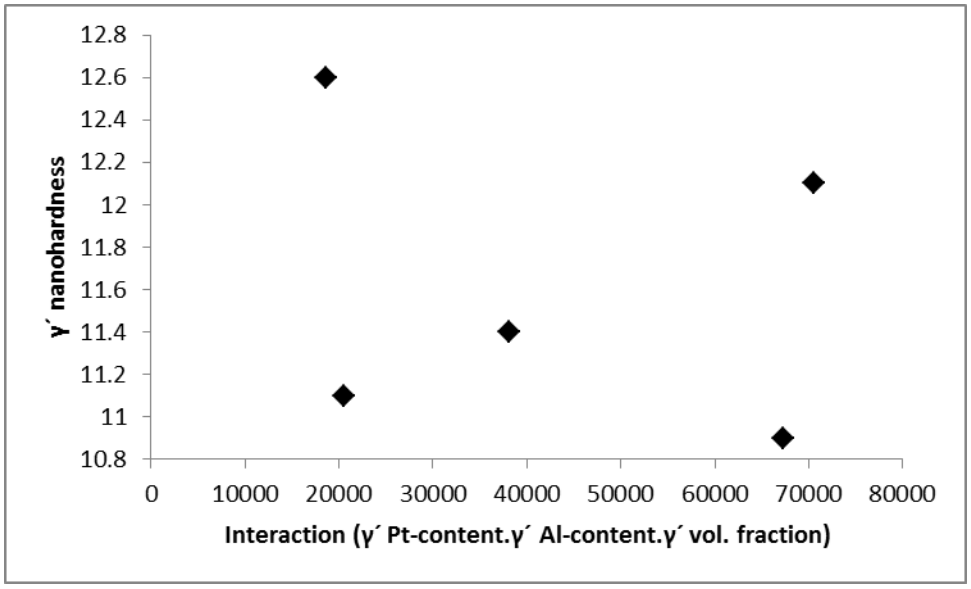


Figure 5.32. Relationship between γ´ nanohardness and interaction of γ´ Pt content, γ´ Al content and γ´ volume fraction, showing no correlation of the y value and x variables.

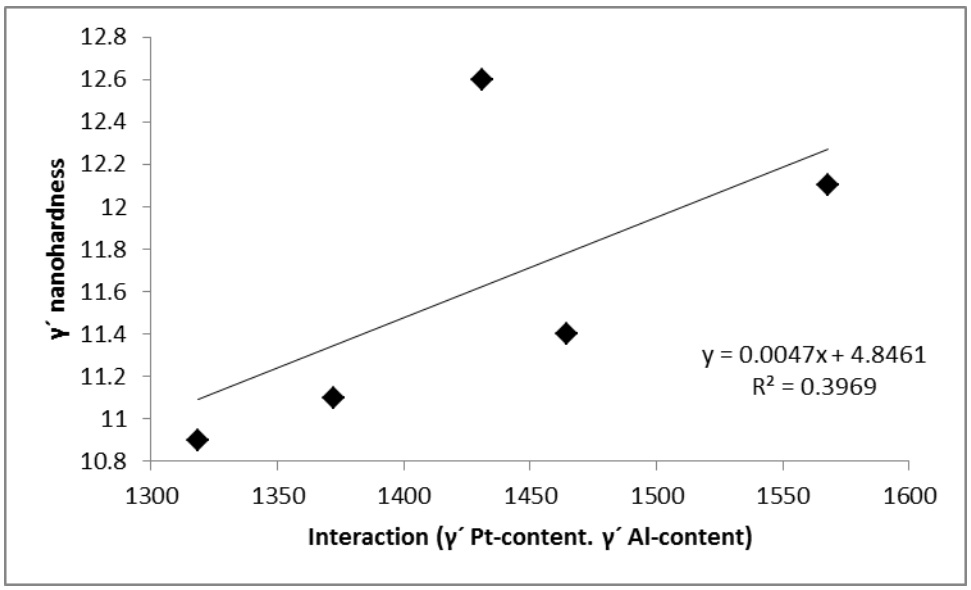


Figure 5.33. Relationship between γ´ nanohardness and interaction of γ´ Pt content and γ´ Al content, showing a weak correlation with the γ´ nanohardness increasing with increasing γ´ Pt content and γ´ Al content.

The regression analysis on the γ nanohardness (y-value) and γ Al content, γ Pt content and γ´ volume fraction as the x variables is shown in Figure 5.34. The γ nanohardness increased with increasing γ Al content, γ Pt content and γ´ volume fraction. The overall p-value of regression analysis was 0.037, while the individual p-values for γ Al content, γ Pt content and γ´ volume fraction were 0.031, 0.14 and 0.039 respectively. This means that γ Al content and γ´ volume fraction are statistically valid (p-values <0.05) and explains the increase in γ nanohardness, while the γ Pt content p-value was 0.14, i.e. greater than 0.05 and does not

explain the increase in γ nanohardness (not significant). This was expected, since Figure 5.13 shows a decrease in γ nanohardness with increasing γ Pt content, but with large scatter. The increase in γ nanohardness with increasing γ′ volume fraction is thought to be due to narrower matrix channels being affected by the precipitates.

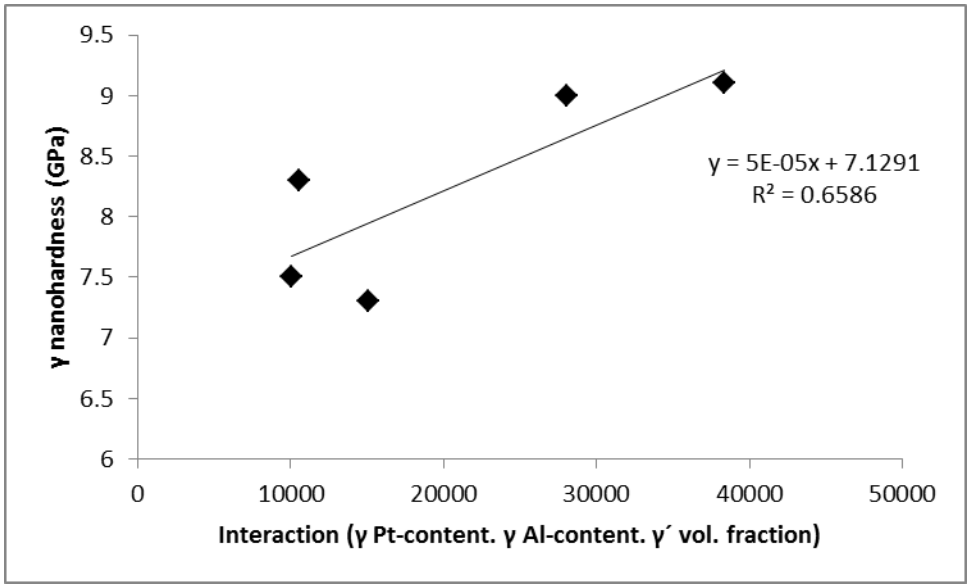


Figure 5.34. Relationship between γ nanohardness and interaction of γ Pt content, γ Al content and γ′ volume fraction showing a medium correlation with the γ nanohardness increasing with increasing γ Pt content, γ Al content and γ′ volume fraction.

CHAPTER SIX

6. CONCLUSIONS AND RECOMMENDATIONS

6.1 Conclusions

Electrolytic etching was applied to the Pt-Al-Cr-Ru alloys, and, as a result, both optical microscopy and SEM analysis gave much clearer microstructures than previously achieved, such that more reliable image analyses could be undertaken. Although XRD did confirm the presence of ~Pt_3Al precipitates, previously in OM and SEM the precipitates were not discernable in Pt_{78}:$Al_{15.5}$:$Cr_{4.5}$:Ru_2, Pt_{80}:Al_{14}:Cr_3:Ru_3 and Pt_{80}:Al_{11}:Cr_4:Ru_5 (at.%) alloys. Not only that, a previously unseen eutectic was observed in Pt_{82}:Al_{12}:Cr_4:Ru_2 (at.%).

The γ′ volume fractions found by image analysis on the etched samples were higher than obtained by the grid placement method. This was expected, since before etching, the contrast between the (Pt) and ~Pt_3Al phases was poor, and secondly, the grid method was very simplistic. The quantitative analysis of atomic force microscopy images using the WSxM software proved to be a useful method for measuring the γ′ volume fraction in Pt-based superalloys. The standard deviations were similar to results from the Olympus microscope, indicating that results can be obtained with a similar accuracy. The TEM volume fraction estimates were very high compared to those measured by SEM and AFM. This discrepancy is believed to be due to the fact that TEM focuses on relatively small localised regions and may not see inhomogeneities while the resolution is much higher and thus can easily resolve secondary and especially tertiary γ′ precipitates which are difficult to observe in SEM. The γ′ volume fractions of Pt_{78}:Al_{11}:Cr_6:Ru_5 (at.%) (Section 4.2.3) were equivalent to the best obtained for Pt-Al-Cr-Ni alloys, and similar to commercial Ni-based superalloys (Section 5.3), as was the precipitate morphology. Due to TEM only revealing the microstructure in relatively small regions, the γ′ volume fractions obtained are believed to be non–representative.

TEM work implied that there may be some influence of the heat treatment, including the cooling rate, on the formation of different generations of γ′ precipitates, their size and morphology, along with the partitioning of elements across the γ/γ′ interface. A coarsened eutectic/eutectoid was observed. Formation of large irregular shaped γ′ precipitates was mainly attributed to diffuse necks that interconnected γ′ precipitates, while the misfit between

the matrix and the precipitates also played a major role in the final precipitate shape. The lattice misfit between the matrix and the precipitate led to γ/γ′ interface dislocations.

The structure of ~Pt_3Al was deduced to be cubic by TEM studies. The orientation relationship between the γ matrix and γ′ precipitates were: $[114]_M||[114]_P$; $[001]_M||[001]_P$; $[103]_M||[103]_P$. The morphology of the γ′ precipitates was found to vary from near-spheres, cuboids, rod-like and irregular. The different precipitate morphologies formed were believed to be associated with the lattice mismatch and loss of coherency between the γ matrix and the γ′ precipitates. The shape of the γ′ precipitates depends not only on their size, but also on their volume fraction, which encourages interactions of the different precipitates and impingment of precipitates. The shape changes observed here can be understood by also considering a precipitate which grows firstly in a γ matrix and then grows further under an increasing amount of elastic interaction due to its neighbours, resulting in different morphologies through their interactions.

Nanoindentation was used for the first time to characterize the mechanical properties of γ´, γ and the alloys themselves in the Pt-Al-Cr-Ru superalloys. The following were found:

- The elastic moduli and nanohardnesses of γ and γ′ were measured separately and repeatably at a load of 2.5mN. The γ´ phase in all six alloys was harder at room temperature, with a difference of ~25% between the γ´ and γ phases.

- Nanohardnesses of both γ and γ′ phases showed a decrease with increasing indentation depth, which is widely known for nearly all micro- and nano-hardness testing in metals and alloys as the indentation size effect. For the precipitates, this decrease appeared more clearly, whereas for the matrix, the hardness decrease was less pronounced.

- The hardness of γ´, γ and the overall alloy was a function of the Pt content, and the hardness of the overall alloy was also a function of the Al content. The composition affects the volume fraction of ~Pt_3Al which in turn affects the hardness. The overall nanohardness of the Pt-Al-Cr-Ru alloys increased with increasing precipitate volume fraction and a similar trend has been reported with commercial NBSAs.

- The Pt-Al-Cr-Ru nanohardnesses of γ and γ´ were similar to Pt_{75}:Al_{12}:Cr_6:Ni_5:Re_2 (at.%) and PWA1484, and higher than all the CMSX alloys.

- The elastic modulus showed no significant difference between the two phases within experimental error.

- The elastic modulus of γ and γ′ in Pt-Al-Cr-Ru alloys appeared to be similar to Pt_{75}:Al_{12}:Cr_6:Ni_5:Re_2 (at.%) and similar to CMSX-4, CMSX-6 and CMSX-10 NBSAs.

- The Pt-Al-Cr-Ru overall alloy nanohardness was lower at low γ′ precipitate volume fraction (< ~35%) and became higher above ~44% γ′ precipitate volume fraction. This is due to the fact that as the precipitate volume fraction increases, the overall alloy nanohardness would also increase because the precipitate phase is the hardest, while below a precipitate volume fraction of ~35%, the nanohardness of the matrix is more prominent. Comparison of the Pt-Al-Cr-Ru alloys and commercial NBSAs hardnesses showed that the nanohardness increased with increasing γ′ volume fraction.

- Regression analysis indicated that the Pt content affects the γ′ volume fraction significantly; an increase in Pt content causes a decrease in the γ′ volume fraction. The overall alloy nanohardness had a strong correlation with the combined Al, Pt and γ′ volume fraction, and were directly proportional. The γ′ volume fraction had the most effect, followed by Al content, and the Pt content (0.059 p-value being >0.05) was not statistically significant. The correlation between the γ′ nanohardness with γ′ Pt content and γ′ Al content was weaker than for the overall alloy nanohardness, but stronger than for all three x variables (γ′ volume fraction, γ′ Pt content and γ′ Al content). The relationship between γ nanohardness and γ Pt content, γ Al content and γ′ volume fraction showed a medium correlation with the γ nanohardness, increasing with increasing γ Pt content, γ Al content and γ′ volume fraction.

6.2 Recommendations for Future Work:

- Sample preparation is known to affect the nanohardness results [2004Dur], so the use of the electropolishing method developed by Witcomb [1992Wit] should be considered.

- Re-do nanohardness on a much lower scale force of 1mN and take AFM images instantaneously with nanohardness and elastic modulus measurements, to be able to

correspond specific values and positions, which could not be done having to take images of indentations on a different systems.

- Study the effect of heat treatment on nanohardness by using different heat treatments.
- It is suggested that differential scanning calorimetry (DSC) or differential thermal analysis (DTA) be used to determine the Pt-Al eutectic temperatures, which could assist in choosing the correct heat treatment temperatures.
- While TEM found evidence only of the cubic phase in the alloys, TEM only samples thin, relatively small areas of the material. In contrast, XRD collects from much larger and thicker regions of the material. Thus, it is suggested that to reasonably eliminate any possible uncertainty regarding the crystallographic nature of all the precipitates, the XRD analysis procedure be altered. The scan step size should be reduced to at least 0.010° and the scan step size be increased to at least 10s, thus increasing collection time 20-fold or more over that of the presently collected spectra. The sample should be rotated to eliminate any possible textural differences. In addition, Reitveld refinement should be applied and/or equivalent crystallographic software be employed to model the lattices and predict their X-ray spectra and peak shapes, in addition, the 2θ angular range to be scanned be increased to try to unambiguously confirm the precipitate structure(s) present.
- Analyse the composition of Pt_{85}:Al_7:Cr_5:Ru_3, Pt_{78}:Al_{11}:Cr_6:Ru_5 and Pt_{78}:Al_{11}:Cr_8:Ru_3 more accurately than by EDS using WDS. Thus, these data could be used for further statistical analyses, such as either a t-test or anova.

REFERENCES

[1950LaM] V.K. LaMer and R.J. Dinegar, Theory, Production and Mechanism of Formation of Monodispersed Hydrosols, *J. Am. Chem. Soc*., 72 (1950) 4847-4854.

[1952LaM] V.K. LaMer, Nucleation in Phase Transitions, *Ind. Eng. Chem*., 44 (1952) 1270-1277.

[1956Mot] B. Mott, Microindentation Hardness Testing, Butterworths, London (1956).

[1957Yos] H. Yoshioka, Effect of Inelastic Waves on Electron Diffraction, *J. Phys. Soc*., 12 (1957) 618-628.

[1958Wes] J.H. Westbrook, Precipitation of Ni_3Al from Nickel Solid Solution as Ogdoadically Diced Cubes, *Z. Kristallogr*., 110 (1958) 21-29.

[1961Hil] J.E. Hilliard and J.W. Cahn, An Evaluation of Procedures in Quantitative Metallography for Volume-Fraction Analysis, *TMS*, 221 (1961) 344-352.

[1961Sta] H.H. Stadelmeir and W.K. Hardy, Ternäre Kohlenstofflegierungen von Palladium und Platin mit Magnesium, Aluminium, Zink, Gallium, Germanium, Kadmium, Indium, Zinn, Quecksilber, Thallium und Blei, *Z. Metallkd*., 52 (1961) 391-396.

[1962Bro] W. Bronger and W. Klemm, Darstellung von Legierungen des Platins mit unedlen Metallen, *Z. Anorg. Chemie*, 319 (1962) 58-81.

[1962Gue] P. Guex and S. Feshotted, Les Systèmes Binaires Platine-Aluminium, Platine-Gallium et Platine-Indium, *J. Less-Common Metals*, 45 (1962) 101-116.

[1964Huc] R. Huch and W. Klemm, Das System Platin-Aluminium, *Z. Anorg. Chemie*, 329 (1964) 123-135.

[1962Kub] O. Kubaschewski and B.E. Hopkins, Oxidation of Metals and Alloys, 2nd edition, Butterworths, London (1962).

[1968Wea] G.C. Weatherly and R.B. Nicholson, An Electron Microscope Investigation of the Interfacial Structure of Semi-coherent Precipitates, *Phil. Mag.*, 17 (1968) 801-831.

[1969Kha] A.G. Khachaturyan and G.A. Shatalov, Theory of Macroscopic Periodicity for a Phase Transition in the Solid State, *J. Exp. Theor. Phys*., 29 (1969) 557-561.

[1970Dar] A.S. Darling, G.L. Selman and R. Rushforth, Platinum and the Refractory Oxides, *Plat. Met. Rev*., 14 (1970) 124-130.

[1970Mur] L.E. Murr, Electron Optical Applications in Materials Science, McGraw-Hill, New York (1970).

[1970Pie] B.J. Piercey, Shell Mold Construction with Chill Plate having Uniform Roughness, U.S. Patent 3, 519, 063 (1970).

[1970Ver] F.L. Ver Snyder and M.E. Shank, The Development of Columnar Grain and Single Crystal High Temperature Materials through Directional Solidification, *Mat. Sci. Eng*., 6 (1970) 213-247.

[1971Ras] P.K. Rastogi and A.J. Ardell, The Coarsening Behavior of the γ′ Precipitate in Nickel-Silicon Alloys, *Acta Metall.*, 19 (1971) 321-330.

[1972Sim] C.T. Sims and W.C. Hagel, The Superalloys, John Wiley & Sons, New York (1972).

[1973Hur] D.T.J. Hurle, Melt Growth, Crystal Growth: An Introduction, North-Holland Pub. Co., New York (1973) 210-233.

[1973Sel] G.L. Selman and A.S. Darling, Dispersion Strengthening of Platinum Group Metals Based Alloys and Gold Based Alloys, Johnson Matthey Co. Ltd, British Patent, 1,340,076 (1973).

[1974Avn] S.H. Avner, Introduction to Physical Metallurgy, McGraw-Hill, Singapore (1974).

[1975Car] C. Carry and J.L. Strudel, Direct Observation of 110 {110} Slip in FCC Single Crystals of a Nickel Base Superalloy, *Scripta Metall.*, 9 (1975) 731-736.

[1975Cha] T. Chattopadhyay and K. Schubert, Kristallstruktur von $Pt_3Ga(r)$ und Einigen Phasen der Mischung Pt_3Al, *J. Less-Common Metals*, 41 (1975) 19-32.

[1975Edi] J.W. Edington, Electron Diffraction in the Electron Microscope, Macmillan Press Ltd., London (1975).

[1975Las] A. Lasalmonie and J.L. Strudel, Interfacial Dislocation Networks around γ′ Precipitates in Nickel-base Alloys, *Phil. Mag*., 32 (1975) 937-949.

[1975Lau] D.E. Laughlin and J.W. Cahn, Spinodal Decomposition in Age Hardening Copper-Titanium Alloys, *Acta Metall*., 23 (1975) 329-339.

[1975Lor] M.H. Loretto and R.E. Smallman, Defect Analysis in Electron Microscopy, T. & A. Constable, Edinburgh (1975).

[1975Sme] W.W. Smeltzer and D.J. Young, Oxidation Properties of Transition Metals, *Prog. Solid-State Chem.*, 10 (1975) 17-54.

[1975Ver] J.D. Verhoeven, Fundamentals of Physical Metallurgy, John Wiley & Sons, New York (1975).

[1976Fel] E.J. Felten and F.S. Pettit, Development, Growth, and Adhesion of Al_2O_3 on Platinum-Aluminium Alloys, *Oxid. Met.*, 10 (1976) 189-223.

[1976Gue] P. Guex and P. Feschotte, Les Systemes Binaires Platine-Aluminium, Platine-Gallium et Platine-Indium, *J. Less-Common Metals*, 46 (1976) 101-116.

[1977Car] C. Carry and J.L. Strudel, Apparent and Effective Creep Parameters in Single Crystals of a Nickel Base Superalloy - I Incubation Period, *Acta Metall.*, 25 (1977) 767-777.

[1977Hir] P. Hirsch, A. Howie, R. Nicholson, D.W. Pashley and M.J. Whelan, Electron Microscopy of Thin Crystals, R.E. Krieger Publishing Co., Malabar, Florida (1977).

[1977Kog] E. Kogiso, Group-Theoretical Method in the Many-Beam Theory of Electron Diffraction, *J. Phys. Soc.*, 42 (1977) 223-229.

[1978Car] C. Carry and J.L. Strudel, Apparent and Effective Creep Parameters in Single Crystals of a Nickel Base Superalloy - II. Secondary Creep, *Acta Metall.*, 26 (1978) 859-870.

[1978Ree] M. Reed and B. Simon, Methods of Modern Mathematical Physics, Vol IV, Analysis of Operators, Academic Press, New York (1978).

[1978Sch] K. Schubert, On the Binding of Mixtures, *Z. Kristallogr.*, 148 (1978) 193-206.

[1979Jag] K. Jagannadham and M.J. Marcinkowski, Relationship between Surface Tension and Energy, Interfacial Energy and Lattice Friction, *J. Mater. Sci.*, 14 (1979) 1717-1732.

[1979Sch] M.J. Schaller, Constitution of Palladium-Boron Alloys, *Z. Metallkd.*, 70 (1979) 313-321.

[1979Nor] J.E. Northword, Improving Turbine Blade Performance by Solidification Control, *Metall. Met. Form.*, 46 (1979) 437-442.

[1980Pea] D.D. Pearson, F.D. Lemkey and B.H. Kear, in J.K. Tien, S.T. Wlodek, H. Morrow III, M. Gell and G.E. Maurer (Eds.), Superalloys 1980, Proc. 4th Int. Symp. on Superalloys, Seven Springs, PA, American Society for Metals, Metals Park, Ohio, $21^{th} – 25^{th}$ September 1980, 513-520.

[1981Gan] C. Gandhi and R. Raj, An Upper Bound in Strain Rate for Wedge-Type Intergranular Fracture in Nickel during Creep, *Metall. Mater. Trans. A*, 12A (1981) 515-520.

[1981Liu] C.T. Liu, H. Inouye and A.C. Schaffhauser, Effect of Thorium Additions on Metallurgical and Mechanical Properties of Ir-0.3 pct W Alloys, *Metall. Mater. Trans. A*, 12A (1981) 993-1002.

[1981Oto] M. Otto, Trends in Refractory Metals, Hard Metals and Special Metals and their Technology, Metallwerk Plansee, Reutte, Austria (1981).

[1981Roe] F.K. Roehrig, Process for Producing Dispersion Strengthened Precious Metal Alloys, Owens-Corning Fiberglass Corp, World Patent Application, 81/00,977 (1981).

[1981Tou] S.M. Tuominen, Cyclic Oxidation Testing of Molybdenum Protected by Silicide Coatings, *J. Less-Common Met.*, 81 (1981) 249–260.

[1982Ham] G. Hammer and D. Kaufmann and A.G. Degussa, Method for the Production of Semi-finished Products made of Platinum Dispersion, German Patent Application, DE3030751 A1 (1982).

[1982Hil] S.A. Hill and B. Ralph, Continuous Phase Separation in a Nickel-Aluminium Alloy, *Acta Metall*., 30 (1982) 2219-2225.

[1982Miy] T. Miyazaki, M. Imamura and T. Kozaki, The Formation of 'γ′ Precipitate Doublets' in Ni-Al Alloys and their Energetic Stability, *Mater. Sci. Eng*., 54 (1982) 9-15.

[1982Rit] M.A. Ritter and M.F. Henry, Precipitation in an As-atomized Nickel-based Superalloy Powder, *J. Mat. Sci*., 17 (1982) 73-80.

[1983Bir] N. Birks and G.H. Meier, Introduction to High-temperature Oxidation of Metals, Edward Arnold (Publishers) Ltd, London (1983) p. 198.

[1983Ric] R.A. Ricks, A.J. Porter and R.C. Ecob, The Growth of γ′ Precipitates in Nickel-Base Superalloys, *Acta Metall*., 31 (1983) 43-53.

[1983Wen] H. Wenderoth and P. Haasen, Nucleation and Growth of γ′-precipitates in Ni-14 at.% Al, *Acta Metall*., 31 (1983) 1649-1659.

[1984Bla] D. Blavette and A. Bostel, Phase Composition and Long Range Order in γ′ Phase of a Nickel Base Single Crystal Superalloy CMSX2: An Atom Probe Study, *Acta Metall.*, 32 (1984) 811-816.

[1984Doi] M. Doi, T. Miyazaki and T. Wakatsuki., The Effect of Elastic Interaction Energy on the Morphology of γ′ Precipitates in Nickel-based Alloys, *Mater. Sci. Eng. A*, 67A (1984) 247-253.

[1984Fre] A. Fredholm and J.L. Strudel, in M. Gell, C.S. Kortovich, R.H. Bricknell, W.B. Kent and J.F. Radavich (Eds.), Superalloys 1984, *Proc. 5th Int. Symp. on*

Superalloys, Seven Springs, PA, The Metallurgical Society of AIME, Warrendale, PA, 7^{th} – 11^{th} October 1984, 211-220.

[1984Mir] D.B. Miracle, V. Srinivasan and H.A. Lipsitt, Nickel-Aluminum-Molybdenum Phase Equilibria, *Metall. Mater. Trans. A*, 15A (1984) 481-486.

[1985Jon] K.L. Johnson, Contact Mechanics, Cambridge University Press, Cambridge (1985).

[1985Mil] K. Mills, J.R. Davis, J.D. Destefani, D.A. Dietrich, G.M. Crankovic, J. Frissel, D.M. Jenkins, W.H. Cubberly and R.L. Stedfeld, Eds., Metals Handbook, 9th Edition, ASM, Metals Park, Ohio (1985) p. 9.

[1986Bin] G. Binning, C.F. Quate and C. Gerber, Atomic Force Microscope, *Phys. Rev. Lett.*, 56 (1986) 930-943.

[1986Bow] R.R. Bowmen and S.D. Antolovich, Microstructure and Stability of Melt Spun INCONEL 713 LC, *Metall. Trans. A*, 17 (1986) 173-180.

[1986Doe] M.F. Doerner and W.D. Nix, A Method for Interpreting the Data from Depth-sensing Indentation Instruments, *J. Mater. Res.*, 1 (1986) 601-609.

[1986Fer] T.G. Ference and S.M. Allen, Dislocation/Precipitate Interactions during Coarsening of a Plastically Strained High-misfit Nickel-Base Superalloy, *Metall. Trans. A*, A17 (1986) 2239-2247

[1986Gia] A.F. Giamei, D.D. Pearson and D.L. Anton, High-temperature Ordered Intermetallic Alloys, *MRS Symp. Proc.*, Pittsburg, Vol. 39 (1986) 293-300.

[1986Hil] B. Hillig, Prospects for Ultrahigh Temperature Ceramic Composite, in Tailoring Multiphase and Composite Ceramics. Eds. R.E. Tressler, G.L. Messing, C.G. Pantano and R.E. Newnham, Plenum Press, New York (1986) 697-712.

[1986Joy] D.C. Joy, A.D. Romig Jr. and J.I. Goldstein, Principles of Analytical Electron Microscopy, Plenum Press, New York (1986).

[1986McA] A.J. McAlister and D.J. Kahan, The Al-Pt (Aluminium-Platinum) System, *Bull. Alloy Phase Diagrams*, 7 (1986) 47-51.

[1986Mis] Y. Mishima, Y. Oya and T. Suzuki, $L1_2 \leftrightarrow$ DO'C Martensitic Transformation in Pt_3Al and Pt_3Ga, Proceedings of International Conference on Martensitic Transformations, *Japan Inst. Met.*, (1986) 1009-1014.

[1987Kin] R.B. King, Elastic Analysis of Some Punch Problems for a Layered Medium, *Int. J. Solids Struct*., 23 (1987) 1657–1664.

[1987Lin] T. Link and M. Feller-Kniepmeier, Electron Microscopic Study of Single-Crystal Nickel-based Alloy SRR99 Treated Tempering of γ/γ' Phase Boundary, *Z. Metallkd.*, 78 (1987) 617–621.

[1987Nat] M.V. Nathal, R.A. Mackay, The Stability of Lamellar γ-γ′ Structures, *Mat. Sci. Eng.*, 85 (1987) 127-138.

[1987Oya] Y. Oya, U. Mishima and T. Suzuki, Pt-Al and Pt-Ga Phase Diagram with Emphasis on the Polymorphism of Pt_3Al and Pt_3Ga, *Z. Metallkd.*, 78 (1987) 485-490.

[1987Sim] C.T. Sims, N.S. Stoloff and W.C Hagel, Superalloys II: High Temperature Materials for Aerospace and Industrial Power, Wiley Interscience, New York (1987).

[1987Woo] G.C. Wood and F.H. Stott, Oxidation of Alloys, *Mater. Sci. Technol.*, 3 (1987) 519-530.

[1988Exn] H.E. Exner and H.P. Hougardy, Quantitative Image Analysis of Microstructures, DCM Informationsgesellschaft Verlag, Germany (1988).

[1988Kac] A.G. Kachaturyan, S.V. Semenovskaya and J.W. Morris, Theoretical Analysis of Strain-induced Shape Changes in Cubic Precipitates During Coarsening, *Acta Metall.*, 36 (1988) 1563-1572.

[1988Kof] P. Kofstad, High Temperature Corrosion, Elsevier Applied Science, New York (1988).

[1988Lah] D.F. Lahrman, R.D. Field, R. Darolia and H.L. Fraser, Investigation of Techniques for Measuring Lattice Mismatch in a Rhenium Containing Nickel Base Superalloy, *Acta Metall.*, 36 (1988) 1309-1320.

[1988Mac] R.A. MacKay and M.V. Nathal. In: B.L. Bramfit, R.C. Benn, C.R. Brinkman and G.F. Vander Voort, Eds. MICON86: Optimization of Processing, Properties, and Service Performance Through Microstructure Control (ASTM STP 979 7th edition), American Society for Testing and Materials, Philadelphia (1988) p. 202.

[1988Sin] A.K. Singh, N. Louat and K. Sadanaka, Dislocation Network Formation and Coherency Loss Around Gamma-prime Precipitates in a Nickel-Base Superalloy, *Met. Trans. A*, A19 (1988) 2965-2973.

[1988Spe] J. Spence, Experimental High-Resolution Electron Microscopy, 2nd Edition, Oxford University Press, Oxford (1988).

[1988Wha] M.V. Whalen, The Compatibility of Dispersion-strengthened Platinum with Candidate Propellants, *Plat. Met. Rev*., 32 (1988) 2-10.

[1988Zha] J.C. Zhao and M.R. Notis, Spinodal Decomposition, Ordering Transformation, and Discontinuous Precipitation in a Cu–15Ni–8Sn Alloy, *Acta Mater.*, 46 (1988) 4203-4218.

[1989Fel] M. Feller-Kniepmeier and T. Link, Dislocation Structures in γ-γ′ Interfaces of the Single-crystal Superalloy SRR 99 after Annealing and High Temperature Creep, *Mat. Sci. Eng. A*, A113 (1989) 191-195.

[1989Gab] T.R Gabb, S.L. Draper, D.R. Hull, R.A. Mackay and M.V. Nathal, The Role of Interfacial Dislocation Networks in High Temperature Creep of Superalloys, *Mater. Sci. Eng. A*, A118 (1989) 59-69.

[1989Haz] A. Hazotte and J. Lacaze, Chemically Oriented γ′ Plate Development in a Nickel Base Superalloy, *Scripta Metall.*, 23 (1989) 1877-1882.

[1990Fle] R.L. Fleischer and R.J. Zabala, Mechanical Properties of Diverse Binary High-temperature Intermetallic Compounds, *Metall. Mater. Trans. A*, 21 (1990) 2709-2802.

[1990Jos] D.L. Joslin and W.C. Oliver, New Method for Analyzing Data from Continuous Depth-sensing Microindentation Tests, *J. Mater. Res.*, 5 (1990) 123-126.

[1990Lee] H.T. Lee and S.W. Lee, The Morphology and Formation of Gamma Prime in Nickel-base Superalloy, *J. Mat. Sci. Lett*., 9 (1990) 516-517.

[1990Lup] D. Lupton, Noble and Refractory Metals for High Temperature Space Applications, *Adv. Mater.*, 5 (1990) 29-30.

[1990Mas] T.B. Massalski, Binary Alloy Phase Diagrams, ASM International, Ohio (1990).

[1990Tho] F.A. Thompson, The Use of Platinum and its Alloys in the Glass Industry, *Glass*, 7 (1990) 279-280.

[1991Fle] R.L. Fleischer, R.D. Field and C.L. Briant, Mechanical Properties of High-Temperature Alloys of AlRu, *Metall. Mater. Trans. A*, 22 (1991) 403-414.

[1992Bro] W.F. Brown Jr., H. Mindin and C.Y. Ho, Aerospace Structural Metals Handbook, Cindas/Purdue University, Lafayette, Indiana (1992) 4218-4229.

[1992Cow] J.M. Cowley, Electron Diffraction Techniques, International Union of Crystallography, Oxford University Press, Oxford (1992).

[1992Doi] M. Doi, Coarsening Behaviour of Coherent Precipitates in Elastically Constrained Systems - with Particular Emphasis on Gamma-Prime Precipitates in Nickel-base Alloys, *Mater. Trans. JIM*, 33 (1992) 637-649.

[1992Flo] N. Floquet, O. Bertrand, J.J. Heizmann, Structural and Morphological Studies of the Growth of MoO_3 Scales during High-temperature Oxidation of Molybdenum, *Oxid. Met.*, 37 (1992) 253–280.

[1992Gol] J.I. Goldstein, D.E. Newbury, P. Echlin, D.C. Joy, A.D. Romig Jr., C.E. Lyman, C. Fiori and E. Lifshin, Scanning Electron Microscopy and X-Ray Microanalysis, 2nd Edition, Plenum Press, New York (1992).

[1992Mah] A. Maheshwari and A.J. Ardell, Anomalous Coarsening Behavior of Small Volume Fractions of Ni_3Al Precipitates in Binary Ni-Al Alloys, *Acta Metall. Mater*., 40 (1992) 2661-2667.

[1992Oli] W.C. Oliver and G.M. Pharr, An Improved Technique for Determining Hardness and Elastic Modulus Using Load and Displacement Sensing Indentation Experiments, *J. Mater. Res.*, 7 (1992) 1564-1583.

[1992Pag] T.F. Page, W.C. Oliver and C.J. McHargue, The Deformation Behavior of Ceramic Crystals Subjected to Very Low Load (Nano)Indentations, *J. Mater. Res*., 7 (1992) 450-473.

[1992Wit] M.J. Witcomb, Preparation of Pt and Pt-C Foils for Conventional and Atomic Resolution TEM, *Proc. 31st Ann. Conf. EMSSA*, 22, 39-40, Pietermaritzburg, 2nd-4th December 1992.

[1993Bal] E. Balikci, A. Raman and R.A. Mirshams, Influence of Various Heat Treatments on the Microstructure of Polycrystalline IN738LC, *Metall. Mater. Trans. A*, A28 (1993) 1993-2003.

[1993Fle] R.L. Fleischer and D.W. McKee, Mechanical and Oxidation Properties of AlRu-Based High-temperature Alloys, *Metall. Mater. Trans. A*, A24 (1993) 759-763.

[1993Gyu] A.M. Gyurko and J.M. Sanches, Characterization of Mechanical Properties in the Ir-Nb-Zr Intermetallic System, *Mat. Sci. Eng. A*, A170 (1993) 169-175.

[1993Har] K. Harris, G.L. Erickson, S.L. Sikkenga, W.D. Brentnall, J.M. Aurrecoechea and K.G. Kubarych, Development of Two Rhenium Containing Superalloys for Single Crystal Blade and Directionally Solidified Vane Application in Advanced Turbine Engines, *JMEP*, 2 (1993) 481-487.

[1993Raj] R. Raj, Fundamental Research in Structural Ceramics for Service near 2000°C, *J. Am. Ceram. Soc.*, 76 (1993) 2147-2174.

[1993Rac] A. Racine and A. Hazotte, Chemical-Composition around Gamma Gamma Interface in Single-crystal Nickel-Based Superalloys in the Early-stage of Creep, *J. Phys. III*, (1993) 355-358.

[1993Yos] M. Yoshiba, Effect of Hot Corrosion on the Mechanical Performances of Superalloys and Coating Systems, *Corros. Sci*., 35 (1993) 1115-1124.

[1994Bar] J. Bard, G.L. Selman, J. Day, A.A. Bourne, A.E. Heywood and R.A. Benedek, Dispersion Strengthened Materials Platinum-Based Alloys, Mechanical Properties of Metallic Composites, Ed. Shojiro Ochiai, Marcel Dekker Inc., New York (1994) pp. 341-371.

[1994Gla] U. Glatzel, Microstructure and Internal Strains of Undeformed and Creep Deformed Samples of a Nickel-Base Superalloy, Habilitationsschrift, Technische Universität Berlin (1994), Verlag Dr. Köster, Berlin, ISBN 3-929937-91-3 (1994).

[1994Gro] T. Grosdidier, A. Hazotte and A. Simon, On the Dissolution Mechanisms of γ′ Precipitates in Nickel-based Superalloys, *Scripta Mater*., 30 (1994) 1257-1262.

[1994Har] D.E. Harasyn, R.L. Heest and C.T. Liu, Deep Drawing of Ir-0.3%W Alloys, *Mat. Sci. Eng. A*, A187 (l994) 155-160.

[1994Vla] J.J. Vlassak and W.D. Nix, Measuring the Elastic Properties of Anisotropic Materials by Means of Indentation Experiments, *J. Mech. Phys. Solids*, 42 (1994) 1223-1245.

[1994Zha] Y.H. Zhang and E.L. Lyndon, On the Blocking Effect of Grain Boundaries on Small Crystallographic Fatigue Crack Growth, *Mater. Sci. Eng. A*, A188 (1994) 121-132.

[1995Ben] M. Benyoucef, N. Clement and A. Coujou, TEM In Situ Straining of the MC2 Superalloy at Room Temperature, *Phil. Mag. A*, A72 (1995) 1043-1056.

[1995Eri] G.L. Erikson, A New Third Generation, Single Crystal, Casting Superalloy, *JOM*, 47 (1995) 36-39.

[1995Esm] S. Esmaeili, C.C. Engler-Pinto Jr, B. Ilschner and F. Rezai-Aria, Interaction Between Oxidation and Thermo-Mechanical Fatigue in IN738LC Superalloy - I, *Scripta Metall. et Mater*., 32 (1995) 1777-1781.

[1995Wan] N. Wanderka and U. Glatzel, Chemical Composition Measurements of a Nickel-base Superalloy by Atom Probe Field Ion Microscopy, *Mater. Sci. Eng. A*, A203 (1995) 69-74.

[1995Wes] J.H. Westbrook and R.L. Fleisher, Intermetallic Compounds – Principles and Practice, John Wiley and Sons, Chichester (1995).

[1995Yoo] M.H. Yoo and C.L. Fu, Mechanistic Modelling of High-Temperature Ordered Intermetallics, *Proc. 2nd Pacific Rim International Conference on Advanced Materials and Processing*, Eds. K.S. Shin, J.K. Yoon and S.J. Kim, *The Korean Institute of Metals and Materials* (1995) 2389-2390.

[1996Doi] M. Doi, Elasticity Effects on the Microstructure of Alloys Containing Coherent Precipitates, *Prog. Mater. Sci*., 40 (1996) 79-180.

[1996Eri] G.L. Erikson, Nickel-base Superalloy for High Temperature, High Strain Application, *Superalloys 1996* (1996) pp. 35-44.

[1996Gab] H. Gabrisch, D. Mukherji and R. P. Wahi, Deformation-induced Dislocation Networks at the γ-γ′ Interfaces in the Single-crystal Superalloy SC16: a Mechanism-based Analysis, *Phil. Mag.*, 74 (1996) 229-249.

[1996Ger] W.W. Gerberich, J.C. Nelson, E.T. Lilleodden, P. Anderson and J.T. Wyrobek, Indentation Induced Dislocation Nucleation: The Initial Yield Point, *Acta Mater.*, 44 (1996) 3585-3598.

[1996Gla] R. Glas, M. Jouiad, P. Caron, N. Clement and H.O.K. Kirchner, Order and Mechanical Properties of the γ Matrix of Superalloys, *Acta Mater.*, 44 (1996) 4917-4926.

[1996Gök] M. Göken and H. Vehoff, Quantitative Metallography of Structural Materials with the Atomic Force Microscope, *Scripta Mater.*, 35 (1996) 983-989.

[1996Haz] A. Hazotte, T. Grosdidier and S. Denis, γ′ Precipitate Splitting in Nickel-based Superalloys: a 3-D Finite Element Analysis, *Scripta Mater.*, 34 (1996) 601-608.

[1996Lip] D.M. Lipkin, D.R. Clarke, Measurement of the Stress in Oxide Scales formed by Oxidation of Aluminum-containing Alloys, *Oxid. Met.*, 45 (1996) 267-280.

[1996Mey1] M.K. Meyer, M.J. Kramer and M. Akinc, Compressive Creep Behavior of Mo_5Si_3 with the Addition of Boron, *Intermetallics*, 4 (1996) 273-281.

[1996Mey2] M.K. Meyer and M.J. Akinc, Isothermal Oxidation Behavior of Mo-Si-B Intermetallics at 1450°C, *J. Am. Ceram. Soc.*, 79 (1996) 2763-2766.

[1996Wil] D.B. Williams and C.B. Carter, Transmission Electron Microscopy: A Textbook for Materials Science, Plenum Press, New York (1996).

[1996Wol] I.M Wolff and G. Sauthoff, High-temperature Behavior of Precious Metal Base Composites, *Metall. Mater. Trans. A*, A27 (1996) 2642-2652.

[1996Ver] M. Veron, Y. Brechet, F. Louchet, Strain Induced Directional Coarsening in Ni Based Superalloys, *Scripta Mater.*, 34 (1996) 1883-1886.

[1996Yam] Y. Yamabe-Mitarai, Y. Koizumi, H. Murakami, Y. Ro, T. Maruko and H. Harada, Development of Ir-base Refractory Superalloys, *Scripta Mater.*, 35 (1996) 211-215.

[1997Ben] L.A. Bendersky and F.W. Gayle, Electron Diffraction Using Transmission Electron Microscopy, *J. Res. Nat. Inst. Stand. Techn.*, 106 (2001) 997-1012.

[1997Ber1] D.M. Berczik, Method for Enhancing the Oxidation Resistance of a Molybdenum Alloy, and a Method of Making a Molybdenum Alloy, U.S. Patent 5,595,616 (1997).

[1997Ber2] D.M. Berczik, Oxidation Resistant Molybdenum Alloys, U.S. Patent 5,693,156 (1997).

[1997Bro] W. Bronger, K. Wrzesien and P. Müller, High Temperature Phase Transitions in $Al_{1+x}Pt_{3-x}$, *Solid State Ionics*, 101-103 (1997) 633-640.

[1997Cho] J.H. Cho and A.J. Ardell, Coarsening of Ni_3Si Precipitates in Binary Ni-Si Alloys at Intermediate to Large Volume Fractions, *Acta Mater.*, 45 (1997) 1393-1400.

[1997Dur] M. Durand-Charre, The Microstructure of Superalloys, CRC Press, New York (1997).

[1997Nab] F.R.N. Nabarro, The Chemical Driving Force for Rafting in Superalloys, *Scripta Mater.*, 37 (1997) 497-501.

[1997Ro] Y. Ro, Y. Koizumi and H. Harada, High Temperature Tensile Properties of a Series of Nickel-base Superalloys on a γ/γ' Tie Line, *Mater. Sci. Eng. A*, 223 (1997) 59-63.

[1997Tor] F. Torster, G. Baumeister, J. Albrecht, G. Lutjering, D. Helm and M.A. Daeubler, Influence of Grain Size and Heat Treatment on the Microstructure and Mechanical Properties of the Nickel-base Superalloy U 720 LI, *Mater. Sci. Eng. A*, A234-236 (1997) 189-192.

[1997Sha] R.E. Shalin, I.L. Svetlov, E.B. Kachanov, V.N. Toloranya and O.S. Gavrilin, Single Crystals of Nickel Based Superalloys, Russian Metallurgy, Moscow (1997) 336-341.

[1997Wil] J.C. Williams, Intermetallics for Structural Applications: Potential, Reality and the Road Ahead, Structural Intermetallics, *Proc. 2nd Int. Symp. Structural Intermetallics*, 21st-26th Sept. 1997, Seven Springs, Champion, USA. Eds. M.V. Nathal, R. Darolia, C.T. Liu, P.L. Martin, D.B. Miracle, R. Wagner and M. Yamaguchi, *Miner. Met. Mater. Soc.*, (1997) 3-8.

[1997Yam1] Y. Yamabe-Mitarai, Y. Ro, T. Maruko, T. Yokokawa and H. Harada, PGM-Based Refractory Superalloys for Ultra-High Temperature Use, Structural Intermetallics, *Proc. 2nd Int. Symp. Structural Intermetallics*, 21st-26th Sept. 1997, Seven Springs, Champion, USA., Eds. M.V. Nathal, R. Darolia, C.T. Liu, P.L. Martin, D.B. Miracle, R. Wagner and M. Yamaguchi, *Miner. Met. Mater. Soc.*, (1997) 805-814.

[1997Yam2] Y. Yamabe-Mitarai, Y. Koizumi, H. Murakami, Y. Ro, T. Maruko and H. Harada, Rh-base Refractory Superalloys for Ultra-high Temperature Use, *Scripta Mater.*, 36 (1997) 393-398.

[1997Yam3] Y. Yamabe-Mitarai, Y. Koizumi, H. Murakami, Y. Ro, T. Maruko and H. Harada, Platinum Group Metals Base Refractory Superalloys, in High-temperature Ordered Intermetallic Alloys VII. Eds. C.C. Koch, C.T. Liu, N.S. Stoloff and A. Wanner, *Mater. Res. Soc. Symp. Proc. 460*, pp. 701-710, Warrendale, PA, (1996-1997) MRS Fall Meeting 1997, 2nd-6th Dec. 1997.

[1998Bah] D.F. Bahr, D.E. Kramer and W.W. Gerberich, Non-Linear Deformation Mechanisms during Nanoindentation, *Acta Mater.*, 46 (1998) 3605-3617.

[1998Gro] T. Grosdidier, A. Hazotte and A. Simon, Precipitation and Dissolution Processes in γ/γ′ Single Crystal Nickel-based Superalloys, *Mater. Sci. Eng.* A, A256 (1998) 183-196.

[1998Kie] J.D. Kiely and J.E. Houston, Nanomechanical Properties of Au (111), (001), and (110) Surfaces**,** *Phys. Rev. B*, B57 (1998) 12588-12594.

[1998Mic] T.A. Michalske and J.E. Houston, Dislocation Nucleation at Nano-scale Mechanical Contacts, *Acta Mater.*, 46 (1998) 391-396.

[1998Nix] W.D. Nix and H. Gao, Indentation Size Effects in Crystalline Materials: A Law for Strain Gradient Plasticity, *J. Mech. Phys. Solids*, 46 (1998) 411-425.

[1998War] P.J. Warren, A. Cerezo and G.D.W. Smith, An Atom Probe Study of the Distribution of Rhenium in a Nickel-based Superalloy, *Mater. Sci. Eng. A*, A250 (1998) 88-92.

[1998Yam] Y. Yamabe-Mitarai, H. Murakami, Y. Ro, T. Maruko and H. Harada, Ir-base Refractory Superalloys for Ultra-high Temperatures, *Metall. Mater. Trans. A*, A29 (1998) 537-549.

[1999Akin] M. Akinc, M.K. Meyer, M.J. Kramer, A.J. Thom, J.J. Heubsch and B. Cook, Boron-doped Molybdenum Silicides for Structural Applications, *Mater. Sci. Eng. A*, A261 (1999) 16-23.

[1999AST] ASTM E562, Standard Test Method for Determining Volume Fraction by Systematic Manual Point Count.

[1999Boy] A.D. Boyd-Lee, Fatigue Crack Growth Resistant Microstructures in Polycrystalline Ni-base Superalloys for Aeroengines, *Int. J. Fatigue*, 21 (1999) 393-405.

[1999Car1] P. Caron and T. Khan, Evolution of Ni-based Superalloys for Single Crystal Gas Turbine Blade Applications, *Aerosp. Sci. Technol.*, 3 (1999) 513-523.

[1999Car2] P. Caron and T. Khan, High Temperature Alloys for Gas Turbines and other Applications, Materials Make the Difference Conference, Winchester, UK, 12 (1999) 1-10.

[1999Cle] W.J. Clegg, A. Kelly and J.E. Pitchford, Composites for Use at High Temperatures, *Key Eng. Mat.*, 161-163 (1999) 315-320.

[1999Fur] D.U. Furrer and H.J. Fecht, γ′ Formation in Superalloy U720Li, *Scripta Mater.*, 40 (1999) 1215-1220.

[1999Fis] B. Fischer, A. Behrends, D. Freund, F. Lupton and J. Merker, High Temperature Mechanical Properties of the Platinum Group Metals, *Plat. Met. Rev.*, 43 (1999) 18-28.

[1999Gök] M. Göken and M. Kempf, Microstructural Properties of Superalloys Investigated by Nanoindentations in an Atomic Force Microscope, *Acta Mater.*, 47 (1999) 1043-1052.

[1999Gur] I. Gurrappa, Hot Corrosion Behavior of CM 247 LC Alloy in Na_2SO_4 and NaCl Environments, *Oxid. Met.*, 51 (1999) 353-382.

[1999Hil] P.J. Hill, L.A. Cornish and M.J. Witcomb, Constitution of the Al–Ir–Ru System, *J. Alloys Compds.*, 291 (1999) 130-144.

[1999Jac] M.P. Jackson, M.J. Starnik and R.C. Reed, Determination of the Precipitation Kinetics of Ni_3Al in the Ni–Al System Using Differential Scanning Calorimetry, *Mater. Sci. Eng. A*, 264 (1999) 26-38.

[1999Mey] M.K. Meyer, A.J. Thom and M. Akinc, Oxide Scale Formation and Isothermal Oxidation Behavior of Mo‑Si‑B Intermetallics at 600‑1000˚C, *Intermetallics*, 7 (1999) 153-161.

[1999Ngw] K.P. Ngwenya and I.M. Wolff, Precipitation Strengthening in Ferritic Fe-Cr-Al-Ru Alloys, *Proc. Microsc. Soc. south. Afr.*, Bloemfontein, 29 (1999) p. 19, 1st–3rd December 1999.

[1999Rus] J.C. Russ and R.T. Dehoff, Practical Stereology, Plenum Press, New York (1999).

[1999Sur] S. Suresh, T.G. Nieh and B.W. Choi, Nano-Indentation of Copper Thin Films on Silicon Substrates, *Scripta Mater.*, 41 (1999) 951-957.

[1999Yan] A. Yang, Y. Xiong and L. Liu, Effect of Cooling Rate on the Morphology of γ′ Precipitates in a Nickel-base Superalloy Under Direction Solidification, *Sci. Technol. Adv. Mater.*, 2 (2001) 105-107.

[2000Bla] D. Blavette, E. Cadel and B. Deconihout, The Role of the Atom Probe in the Study of Nickel-based Superalloys, *Mater. Char.*, 44 (2000) 133-157.

[2000Fai1] G. Fairbank, C. Humphreys, A. Kelly and C.N Jones, Ultra-high Temperature Intermetallics for the Third Millennium, *Intermetallics*, 8 (2000) 1091-1100.

[2000Fai2] G. Fairbank, C. Humphreys, A. Kelly and C.N Jones, New Platinum Alloys for Ultra High Temperature Applications, presented at *Fifth Charles Parsons Turbine Conference*, Cambridge, UK, 3rd-7th July (2000).

[2000Gou] A. Gouldstone, H.J. Koh, K.Y. Zeng, A.E. Giannakopoulos and S. Suresh, Discrete and Continuous Deformation During Nanoindentation of Thin Films, *Acta Mater.*, 48 (2000) 2277-2295.

[2000He] D. He, H. Guan, X. Sun and X. Jiang, Manufacturing, Structure and High Temperature Corrosion of Palladium-modified Aluminide Coatings on Nickel-base Superalloy M38, *Thin Solid Films*, 376 (2000) 144-151.

[2000Hil1] P.J. Hill, P. Ellis, L.A. Cornish, M.J. Witcomb and I.M. Wolff, The Oxidation Behaviour of Pt-Al-X Alloys at Temperatures Between 1200 and 1350°C, *Proc. High-Temperature Corrosion and Protection 2000*, pp. 185-190, Sappora, Japan, 17th-22nd Sept. 2000.

[2000Hil2] P. Hill, L.A. Cornish, M.J. Witcomb and P. Ellis, The (Pt)/Pt_3Al Relationship in the Pt-Al-Cr and Pt-Al-Ti Systems, *Proc. Microsc. Soc. south. Afr.*, 30 (2000) p. 13, Grahamstown, 6th-8th Dec. 2000.

[2000Lup] D.F. Lupton, J. Merker, B. Fischer and R. Völkl, Platinum Materials for the Glass Industry, *24th Int. Precious Metals Conf. 2000*, Williamsburg, Virginia, USA, 11th-14th June 2000.

[2000Sug] T. Sugui, Z. Huihua, Z. Jinghua, Y. Hongcai, X. Yongbo and H. Zhuangqi, Formation and Role of Dislocation Networks During High Temperature Creep of a Single Crystal Nickel–base Superalloy, *Mat. Sci. Eng. A*, A279 (2000) 160-165.

[2000Tan] R. Tanaka, Research and Development of Ultra-high Temperature Materials in Japan, *Materials at High Temperatures*, 17 (2000) 457-464.

[2000Wol] I.M. Wolff and P.J. Hill, Platinum Metals-based Intermetallics for High-temperature Service. *Plat. Met. Rev.*, 44 (2000) 158-166.

[2000Zha] Y. Zhang, N. Wanderka, G. Schumacher, R. Schneider and W. Neumann, Phase Chemistry of the Superalloy SC16 after Creep Deformation, *Acta Mate*r., 48 (2000) 2787-2793.

[2001Bab] S.S. Babu, M.K. Miller, J.M. Vitek and S.A. David, Characterization of the Microstructure Evolution in a Nickel Base Superalloy During Continuous Cooling Conditions, *Acta Mater*., 49 (2001) 4149-4160.

[2001Big1] T. Biggs, P.J. Hill, L.A Cornish and M.J. Witcomb, An Investigation of the Pt-Al-Ru Diagram to Facilitate Alloy Development, *J. Phase Equil*., 22 (2001) 214-218.

[2001Big2] T. Biggs, An Investigation into Displacive Phase Transformations in Platinum Alloys, Ph.D. Thesis, University of the Witwatersrand, Johannesburg, South Africa (2001).

[2001Cha] P.E. Champness, Electron Diffraction in the Transmission Electron Microscope, BIOS Scientific Publisher Ltd., Oxford, UK, (2001).

[2001Dur] K. Durst and M. Göken, Quantitative Microstructural Characterisation by Atomic Force Microscopy and Electron Microscopy - A Comparative Study on the Superalloy Waspaloy, *Prakt. Metallogr.*, 38 (2001) 197-215.

[2001Fis1] B. Fischer, New Platinum Materials for High Temperature Applications, *Adv. Eng. Mater*., 3 (2001) 811-820.

[2001Fis2] B. Fischer, D. Freund, J. Merker, R. Völkl and D.F. Lupton, A Novel Class of Dispersion Hardened Platinum Materials Produced by a New Manufacturing Route, in *Proc. 8th Int. Conf. Composites Engineering*, Ed. D. Hui, University of New Orleans, New Orleans (2001) 249-250.

[2001Goo] P.J. Goodhew, J. Humphreys and R. Beanland, Electron Microscopy and Analysis, 3rd edition, Taylor & Francis, London (2001).

[2001Hil1] P.J. Hill, T. Biggs, P. Ellis, J. Hohls, S. Taylor and I.M. Wolff, An Assessment of Ternary Precipitation-strengthened Pt Alloys for Ultra-high Temperature Applications, *Mater. Sci. Eng., A*, A301 (2001) 167-179.

[2001Hil2] P.J. Hill, L.A. Cornish, P. Ellis and M.J. Witcomb, The Effects of Ti and Cr Additions on the Phase Equilibria and Properties of (Pt)/Pt_3Al Alloys, *J. Alloys Compds*., 322 (2001) 166-175.

[2001Hil3] P.J. Hill, Y. Yamabe-Mitarai and I.M. Wolff, High-temperature Compression Strengths of Precipitation-Strengthened Ternary Pt-Al-X Alloys, *Scripta. Mater*., 44 (2001) 43-48.

[2001Hil4] P.J. Hill, L.A. Cornish and M.J. Witcomb, Microstructural Investigation of the Pt-based Superalloy Pt_{80}:Al_{14}:Cr_3:Ru_3, *Proc. Microsc. Soc. South. Afr.*, 31 (2001) p. 22, Johannesburg, 5th-7th Dec. 2001.

[2001Hil5] P.J. Hill, Superalloy Analogues Based on Platinum for Ultra–high Temperature Applications, PhD Thesis, University of Witwatersrand, Johannesburg, South Africa (2001).

[2001Hil6] P.J. Hill, Y. Yamabe-Mitarai, H. Murakami, L.A. Cornish, M.J. Witcomb, I.M. Wolff and H. Harada, The Precipitate Morphology and Lattice Mismatch of Ternary (Pt)/Pt_3Al Alloys, *3rd Inter. Symp. Structural Intermetallics*, pp. 527-533, Snow King Resort, Jackson Hole, Wyoming, USA, Eds. K.J. Demker, D.M. Dimiduk, H. Clemens, R. Darobia, H. Inui, J.M. Larsen, V.K. Sukka, M. Thomas and J.D. Whitten Berger, 23rd–27th September 2001, TMS (The Minerals, Metals & Materials Society) (2001). (Rescheduled to 28th April – 1st May 2002)

[2001Mac] D.W. MacLachlan and D.M. Knowles, Modelling and Prediction of the Stress Rupture Behaviour of Single Crystal Superalloys, *Mater. Sci. Eng. A*, A302 (2001) 275-285.

[2001Mer] J. Merker, D. Lupton, M. Töfer and Knake, High Temperature Mechanical Properties of the Platinum Group Metals: Elastic Properties of Platinum,

Rhodium and Iridium and their Alloys at High Temperatures, *Plat. Met. Rev.*, 45 (2001) 74-82.

[2001Mil] M.K. Miller, Contributions of Atom Probe Tomography to the Understanding of Nickel-based Superalloys, *Micron*, 32 (2001) 757-764.

[2001Pur] A.L. Purvis and B.M. Warnes, The Effects of Platinum Concentration on the Oxidation Resistance of Superalloys Coated with Single-phase Platinum Aluminide, *Surf. Coat. Technol.*, 146–147 (2001) 1-6.

[2001Süs1] R. Süss, P.J. Hill, P. Ellis and I.M. Wolff, The Oxidation Resistance of Pt-Base γ/γ' Analogues to Ni-Base Superalloys, *7th Eur. Conf. Advanced Materials and Processes*, Paper No. 287, CD-ROM, Rimini, Italy, 10th–14th June 2001.

[2001Süs2] R. Süss, P.J. Hill, P. Ellis and L.A. Cornish, The Oxidation Resistance of Pt-base Superalloy Pt_{80}:Al_{14}:Cr_3:Ru_3 compared to that of Pt_{86}:Al_{10}:Cr_4, *Proc. Microsc. Soc. South. Afr.*, 31 (2001) p. 21, Johannesburg, 5th-7th Dec. 2001.

[2002Chi1] Y.L. Chiu and A.H.W. Ngan, Time-Dependent Characteristics of Incipient Plasticity in Nanoindentation of a Ni_3Al Single Crystal, *Acta Mater.*, 50 (2002) 1599-1611.

[2002Chi2] Y.L. Chiu and A.H.W. Ngan, A TEM Investigation on Indentation Plastic Zones in Ni_3Al(Cr,B) Single Crystals, *Acta Mater.*, 50 (2002) 2677-2691.

[2002Cor] L.A. Cornish, J. Hohls, P.J. Hill, S. Prins, R. Süss and D.N. Compton, The Development of Platinum-Based Alloys and their Thermodynamic Database, *J. Min. Metall. B*, 38 (2002) 197-204.

[2002Gla] U. Glatzel, T. Mack, J. Wortmann, S. Wöllmer, Nickel-Based Alloy for Producing Structural Member Solidified as Single Crystal by Casting Method, Japanisches Patent JP 2002302724 (2002).

[2002Hil] P.J. Hill, N. Adams, T. Biggs, P. Ellis, J. Hohls, S.S. Taylor and I.M. Wolff, Platinum Alloys Based on Pt–Pt_3Al for Ultra-High Temperature Use, *Mater. Sci. Eng. A*, A329–331 (2002) 295-304.

[2002Par] T.A. Parthasarathy, M.G. Mendiratta and D.M. Dimiduk, Oxidation Mechanisms in Mo-reinforced Mo_5SiB_2(T2)–Mo_3Si alloys, *Acta Mater.*, 50 (2002) 1857-1868.

[2002Pat] R. Pather, W.A. Mitten, P. Holdway, H.S. Ubhi and A. Wisbey, Effect of High Temperature Environment on High Strength Titanium Aluminide Alloy, *Advanced Materials and Processes for Gas Turbines*, pp. 309-316, Eds. G.E.

Fuchs, A.W. James, T. Gabb, M. McLean and H. Harada, TMS, Copper Mountain, Colorado, 22nd-26th September 2002.

[2002Pha] G.M. Pharr and A. Bolshakov, Understanding Nanoindentation Unloading Curves, *J. Mater. Res*., 17 (2002) 2660-2671.

[2002Pra] G.S. Prakash and S. Singh, Effects of MgO and CaO on Hot Corrosion of Fe Base Superalloy Superfer 800H in Na_2SO_4-60%V_2O_5 Environment, *Brit. Corros. J*., 37 (1) (2002) 56-62.

[2002Sch] J.H. Schneibel, M.J. Kramer and D.S. Easton, A Mo–Si–B Intermetallic Alloy with a Continuous α-Mo Matrix, *Scripta Mater*., 46 (2002) 217-221.

[2002Süs1] R. Süss, D. Freund, R Völkl, B. Fischer, P.J. Hill, P. Ellis and I.M. Wolff, The Creep Behaviour of Platinum-based γ/γ′ Analogues of Nickel-based Superalloys at 1300°C, *Mater. Sci. Eng. A*, 338 (2002) 133-141.

[2002Süs2] R. Süss, L.A. Cornish, P.J. Hill, J. Hohls and D.N. Compton, Properties of a New Series of Superalloys Based on Pt_{80}:Al_{14}:Cr_3:Ru_3, Advanced Materials and Processes for Gas Turbines, Eds. G. Fuchs, A. James, T. Gabb, M. McLean and H. Harada, TMS, pp. 301-307, Copper Mountain, Colorado, USA, 22nd-26th Sep. 2002.

[2002Zha1] J. Zhang and R.F. Singer, Hot Tearing of Nickel-based Superalloys during Directional Solidification, *Acta Mater*., 50 (2002) 1869-1879.

[2002Zha2] J.C. Zhao, M.R. Jackson, L.A. Peluso and L.N. Brewer, A Diffusion Multiple Approach for the Accelerated Design of Structural Materials, *MRS Bulletin* (2002) 324-329.

[2002Zha3] T. Zhang and W. Xu, Surface Effects on Nanoindentation, *J. Mater. Res*., 17 (2002) 1715-1720.

[2003Big] T. Biggs, M.B. Cortie, M.J. Witcomb and L.A. Cornish, Platinum Alloys for Shape Memory Applications. *Plat. Met. Rev*., 47 (2003) 142-156.

[2003Cor] L.A. Cornish, B. Fischer and R. Völkl, Development of PGM Superalloys for High-Temperature use, *MRS Bulletin* (2003) 632-638.

[2003Fov] Fovea Pro Software, Reindeer Graphics, Asheville, North Carolina (2003).

[2003Gon] J. Gong, H. Miao and Z. Peng, A New Function for the Description of the Nanoindentation Unloading Data, *Scripta Mater*., 49 (2003) 93-97.

[2003Ker1] T. Keraan and C.I. Lang, High Temperature Investigation into Platinum-Base Superalloys, *Proc. Microsc. Soc. South. Afr*., 32 p. 14, Cape Town, 3rd–5th Dec. 2003.

[2003Ker2] T. Keraan and C.I. Lang, High Temperature Mechanical Properties and Behaviour of Platinum-base Superalloys for Ultra-High Temperature Use, *African Materials Research Society Conference*, pp. 154-155, University of the Witwatersrand, Johannesburg, South Africa, 8th–11th Dec. 2003.

[2003Ker3] T. Keraan, High Temperature Mechanical Properties and Behaviour of Platinum-base Alloys, MSc Dissertation, University of Cape Town, South Africa (2004).

[2003Kob] D. Kobayashi, A.T. Yokobori Jr., R. Sugiura and A. Fuji, Crack Growth Behavior of IN100 Alloy Using In-situ Observational Methods under High Temperature Creep and Fatigue Conditions, *Mater. Trans.*, 51 (2010) 2201-2207.

[2003Pro] Prospectus, Dispersion-Strengthened High-temperature Materials, Plansee GmbH, Reutte, Austria (2003).

[2003Sch1] U. Schultz, C. Leyens, K. Fritscher, M. Peters, B. Saruhan-Brings, O. Lavinge, J. Dorvaux, M. Poulain, R. Mevrel and M. Caliez, Some Recent Trends in Research and Technology of Advanced Thermal Barrier Coatings, *Aero. Sci. Techn.*, 7 (2003) 73-80.

[2003Sch2] T. Schöberl, H.S. Gupta and P. Fratzl, Measurements of Mechanical Properties in Ni-base Superalloys Using Nanoindentation and Atomic Force Microscopy, *Mater. Sci. Eng. A*, A363 (2003) 211–220.

[2003Sub] C.K. Sudbrack, K.E. Yoon, Z. Mao, R.D. Noebe, D. Isheim and D.N. Seidman, Electron Microscopy: Its Role in Materials Science, *Proc. Mike Meshii Symp.*, (2003) p. 43.

[2003Sup] V. Supatarawanich and D.R. Johnson and C.T. Liu, Effects of Microstructure on the Oxidation Behavior of Multiphase Mo-Si-B Alloys, *Mater. Sci. Eng. A*, A344 (2003) 328-339.

[2003Wan] W. Wang, C.B. Jiang and K. Lu, Deformation Behavior of Ni_3Al Single Crystals During Nanoindentation, *Acta Mater.*, 51 (2003) 6169-6180.

[2003Wen] Y.H. Wen, J.P. Simmons, C. Shen, C. Woodword and Y. Wang, Phase-field Modeling of Bimodal Particle Size Distributions During Continuous Cooling, *Acta Mater*., 51 (2003) 1123-1132.

[2003Wöl] S. Wöllmer, S. Zaefferer, M. Göken, T. Mack and U. Glatzel, Characterization of Phases of Aluminized Nickel Base Superalloys, *Surf. Coat. Technol.*, 167 (2003) 83-96.

[2003Xpe] X´pert Highscore, (PW3209), 1.0d, PANalytical B.V., Almelo, The Netherlands, 31st March 2003.

[2003Yok] T. Yokokawa, M. Osawa, K. Nishida, T. Kobayashi, Y. Koizumi and H. Harada, Partitioning Behaviour of Platinum Group Metals on the γ and γ′ Phases of Ni Base Superalloys at High Temperatures, *Scripta Mater.*, 49 (2003) 1041-1046.

[2003Zha] J.C. Zhao and J.H. Westbrook, Ultrahigh-temperature Materials for Jet Engines, *MRS Bulletin* (2003) 622-630.

[2004Bar] O.M. Barabash, J.A. Horton, S.S. Babu, J.M. Vitek, S.A. David, J.W. Park, G.E. Ice and R.I. Barabash, Evolution of Dislocation Structure in the Heat Affected Zone of a Nickel-based Single Crystal, *J. Appl. Phys*., 96 (2004) 3673-3679.

[2004Cor] L.A. Cornish, R. Süss, L.H. Chown, S. Taylor, L. Glaner, A. Douglas and S.N. Prins, Platinum-based alloys for high temperature and special applications, *International Platinum Conference 'Platinum Adding Value'*, South African Institute of Mining and Metallurgy Symposium Series S38, pp. 329–336, Sun City, South Africa, 3rd-7th October 2004.

[2004Dou1] A. Douglas, J.H. Neethling and L.A. Cornish, Dislocation Distribution in a Pt-based Analogue of Ni-Based Superalloys, *Proc. Microsc. Soc. South. Afr.*, 34, p. 12, Pretoria, 30th November-3rd December 2004.

[2004Dou2] A. Douglas, Microstructure and Deformation of Ternary Platinum Alloys as Superalloy Analogues, PhD Thesis, University of Port Elizabeth, Port Elizabeth, South Africa (2004).

[2004Dur] K. Durst and M. Göken, Micromechanical Characterisation of the Influence of Rhenium on the Mechanical Properties in Nickel-base Superalloys, *Mater. Sci. Eng. A*, A387–389 (2004) 312–316.

[2004Fis] A. Fischer-Cripps, Nanoindentation, Springer, New York (2004).

[2004Gon1] J. Gong, H. Miao and Z. Peng, Analysis of the Nanoindentation Data Measured with a Berkovich Indenter for Brittle Materials: Effect of the Residual Contact Stress, *Acta Mater.*, 52 (2004) 785-793.

[2004Gon2] J. Gong, H. Miao and Z. Peng, On the Contact Area for Nanoindentation Tests with Berkovich Indenter: Case Study on Soda-lime Glass, *Mater. Lett.*, 58 (2004) 1349-1353.

[2004Kru] J.J. Kruzic, J.H. Schneibel and R.O. Ritchie, Fracture and Fatigue Resistance of Mo-Si-B Alloys for Ultrahigh-temperature Structural Applications, *Scripta Mater.*, 50 (2004) 459-464.

[2004Mur] T. Murakumo, T. Kobayashi, Y. Koizumi and H. Harada, Creep Behaviour of Ni-base Single-crystal Superalloys with Various γ′ Volume Fraction, *Acta Mater.*, 12 (2004) 3737-3744.

[2004Oli] W.C. Oliver and G.M. Pharr, Measurement of Hardness and Elastic modulus by Instrumented Indentation: Advances in Understanding and Refinements to Methodology, *J. Mater. Res.*, 19 (2004) 3-20.

[2004Row] L.J. Rowland, Q. Feng and T.M. Pollock, Microstructural Stability and Creep of Ru-containing Nickel-base Superalloys, *Superalloys 2004*, pp. 697-706, Eds. K.A. Green, T.M. Pollock, H. Harada, T.E. Howson, R.C. Reed, J.J. Schirra and S, Walston, Champion, Pennsylvania, USA, 19th-23rd September (2004).

[2004Sch] C.A. Schuh and A.C. Lund, Application of Nucleation Theory to the Rate Dependence of Incipient Plasticity During Nanoindentation, *J. Mater. Res.*, 19 (2004) 2152-2158.

[2004Sta] P. Stadelmann, JEMS Electron Microscopy Software Java Version, Users Guide (2004).

[2004Süs1] R. Süss, L.A. Cornish, L.H. Chown and L. Glaner, Tensile Properties of Pt-Based Superalloys, Beyond Nickel-Base Superalloys, *TMS 2004, 133rd Annual Meeting and Exhibition of The Minerals, Metals and Materials Society*, Charlotte, North Carolina, U.S.A., 14th-18th March 2004.

[2004Süs2] R. Süss, A. Douglas, L.A. Cornish and B. Joja, An Electron Microscope Investigation of Tensile Samples of Pt-based Superalloys, *Proc. Microsc. Soc. South. Afr.*, 34, p. 10, Pretoria, 30th November–3rd December 2004.

[2004Wal] W.S. Walston, A. Cetel, R. MacKay, K. O'Hara, D. Duhl and R. Dreshfield, Joint Development of a Fourth Generation Single Crystal Superalloy, *Superalloys 2004*, pp. 15-24, TMS, Warrendale, PA, 19th-23rd September 2004.

[2004Vor] S. Vorberg, M. Wenderoth, B. Fischer, U. Glatzel and R. Völkl, Pt-Al-Cr-Ni Superalloys: Heat Treatment and Microstructure, *JOM*, 56 (2004) 40-43.

[2004Völ] R. Völkl and B. Fischer, Mechanical Testing of Ultra-high Temperature Alloys, *Exp. Mech.*, 44 (2) (2004) 121-127.

[2005Bah] D.F. Bahr and G. Vasquez, Effect of Solid Solution Impurities on Dislocation Nucleation during Nanoindentation, *J. Mater. Res*., 20 (2005) 1947-1951.

[2005Hül] M. Hüller, M. Wenderoth, S. Vorberg, B. Fischer, U. Glatzel and R. Völkl. Optimization of Composition and Heat Treatment of Age-hardened Pt-Al-Cr-Ni Alloys. *Metall. Mater. Trans. A*, A36 (2005) 681-689.

[2005Kru] J.J. Kruzic, J.H. Schneibel and R.O. Ritchie, Ambient- to Elevated-temperature Fracture and Fatigue Properties of Mo-Si-B alloys: Role of Microstructure, Metall. *Mater. Trans. A*, A36 (2005) 2393-2402.

[2005Pri] S.N. Prins, L.A. Cornish and P.S. Boucher, Derivation of the Liquidus Surface Projection for the Al–Pt–Ru System from As-cast Samples, *J. Alloys Compds*., 403 (2005) 245-257.

[2005Roy] I. Roy, E. Balikci, S. Ibekwe and A. Raman, Precipitate Growth Activation Energy Requirements in the Duplex Size γ′ Distribution in the Superalloy IN738LC, *J. Mater. Sci*., 40 (2005) 6207-6215.

[2005Sar] P.M. Sarosi, G.B. Vishwanathan, D.D. Whitis and M.J. Mills, Imaging and Characterization of Fine Gamma-Prime Precipitates in Commercial Nickel-based Superalloys, *Ultramicroscopy*, 103 (2005) 83-93.

[2005Wen1] M. Wenderoth, L.A. Cornish, R. Süss, S. Vorberg, B. Fischer and U. Glatzel, On the Development and Investigation of Quaternary Pt-based Superalloys with Ni Additions. *Metall. Mat. Trans. A*, A36 (2005) 567-575.

[2005Wen2] M. Wenderoth, R. Völkl, T. Yokokawa, Y. Yamabe-Mitarai and H. Harada, High Temperature Strength of Pt-base Superalloys with Different γ′ Volume Fractions, *Scripta Mater*., 54 (2005) 275-279.

[2005Vis] G.B. Vishwanathan, P.M. Sarosi, M.F. Henry, D.D. Whitis, W.W. Milligan and M.J. Mills, Investigation of Creep Deformation Mechanisms at Intermediate Temperatures in René 88 DT, *Acta Mater*., 53 (2005) 3041-3057.

[2005Vor] S. Vorberg, M. Wenderoth, U. Glatzel, B. Fischer and R. Völkl, A TEM Investigation of the γ/γ′ Phase Boundary in Pt-based Superalloys, *JOM*, 57 (2005) 49-51.

[2006Bir] N. Birks, G.H. Meier and F.S. Pettit, Introduction to the High-temperature Oxidation of Metals, 2nd edition, Cambridge University Press, Cambridge (2006) p. 338.

[2006Bou] K.D. Bouzakis and N. Michailidis, Indenter Surface Area and Hardness Determination by Means of a FEM-supported Simulation of Nanoindentation, *Thin Solid Films*, 494 (2006) 155–160.

[2006Cor] L.A. Cornish, R. Süss, L.H. Chown, A. Douglas, M. Matema, L. Glaner and G. Williams, New Pt-based Alloys for High Temperature Application in Aggressive Environments: *The Next Stage, Second International Platinum Conference:'Platinum Surges Ahead'*, South African Institute of Mining and Metallurgy Symposium Series S45, pp. 57-66, Sun City, 8th–12th October 2006.

[2006CSM] CSM Instruments Indentation Software User's Guide, Version: R0.0.5, Rue de la Gare, Switzerland (2006).

[2006Kaw] K. Kawagishi, H. Harada, A. Sato and H. Kobayashi, The Oxidation Properties of Fourth Generation Single-crystal Nickel-based Superalloys, *JOM*, 30 (2006) 43-46.

[2006Mal] N.B. Maledi, J.H. Potgieter, M. Sephton, L.A. Cornish, L. Chown and R. Süss, Hot Corrosion Behaviour of Pt-Alloys for Application in the Next Generation of Gas Turbines: *The Next Stage, Second International Platinum Conference:'Platinum Surges Ahead'*, South African Institute of Mining and Metallurgy Symposium Series S45, pp. 81-90, Sun City, 8th-12th October 2006.

[2006NIM] NIMS and IHI, Fifth Generation Nickel Base Single Crystal Superalloy TMS-196, Tokyo, Japan, July 2006.

[2006Ree] R.C. Reed, The Superalloys: Fundamental and Applications, Cambridge University Press, Cambridge (2006).

[2006Saf] J. Safari, S. Nategh and M. McLean, Evolution of Microstructure of Nickel Base Superalloy at High Temperatures, *J. Mater. Sci. Technol.*, 22 (2006) 888-898.

[2006Süs] R. Süss, L.A. Cornish, A. Douglas, A. Mwamba, L. Glaner, L. H. Chown and G. Williams, External Report 4466, Experimental and Thermo-Calc^{TM} Work on the Development of Pt based Superalloys: 13th Report, Mintek, 22 November 2006.

[2006Tsh] W. Tshawe, A. Douglas, B. Joja and L.A. Cornish, A Study of the Pt_3Al, Pt_2Al and β Phases in the Pt-Al System, *Proc. Microsc. Soc. South. Afr.*, 36, p. 15, Port Elizabeth, 28th Nov. - 1st Dec. 2006.

[2006Vor] S. Vorberg, Entwicklung von Platinbasis-Superlegierungen, PhD thesis, Universität Bayreuth, Germany (2006).

[2006Völ] R. Völkl, M. Wenderoth, J. Preussner, S. Vorberg, B. Fischer and U. Glatzel, A Review on the Progress towards Pt-base Superalloys for Ultra High Temperature Applications, *Southern African Institute of Mining and Metallurgy Conference 'Platinum Surges Ahead'*, Symposium series S45, pp. 67-71, Sun City, 8th-12th October 2006.

[2006Wen1] Y.H. Wen, B. Wang, J.P. Simmons and Y. Wang, A Phase-Field Model for Heat Treatment Applications in Ni-based Alloys, *Acta Mater*., 54 (2006) 2087-2099.

[2006Wen2] M. Wenderoth, R. Völkl, T. Yokokawa, Y. Yamabe-Mitarai and H. Harada, High Temperature Strength of Pt-base Superalloys with Different γ′ Volume Fractions, *Scripta Mater*., 54 (2006) 275-279.

[2006Zho] X.Y. Zhou, Z.D. Jiang, H.R. Wang and Q. Zhu, A Method to Extract the Intrinsic Mechanical Properties of Soft Metallic Thin Films Based on Nanoindentation Continuous Stiffness Measurement Technique, *J. Phys.*, 48 (2006) 1096-1101.

[2007Cor] L.A. Cornish, R. Süss, R. Völkl, M. Wenderoth, S. Vorberg, B. Fischer, U. Glatzel, A. Douglas, L.H. Chown, T. Murakumo, J. Preussner, D. Lupton, L. Glaner, N.B. Maledi, J.H. Potgieter, M. Sephton and G. Williams, Overview of the Development of New Pt-based alloys for High Temperature Application in Aggressive Environments. *J. South. Afr. Inst. Min. Met.*, 107 (2007) 697-711.

[2007Dou] A. Douglas, J.H. Neethling, R. Santamarta, D. Schryvers and L.A. Cornish, Unexpected Ordering Behaviour of Intermetallic Precipitates, *J. Alloys Compds.*, 432 (2007) 96-102.

[2007Hor] I. Horcas, R. Fernández, J.M. Gómez-Rodríguez, J. Colchero, J. Gómez-Herrero and A.M. Baro, WSxM: A Software for Scanning Probe Microscopy and a Tool for Nanotechnology, *Rev. Sci. Instrum*., 78 (2007) 1-8.

[2007Mao] Z. Mao, C.K. Sudbrack, Y.K. Yoon, G. Martin and D.N. Seidman, The Mechanism of Morphogenesis in a Phase-separating Concentrated Multicomponent Alloy, *Nature Mater.*, 6 (2007) 210-216.

[2007Rei] L. Reimer and H. Kohl, Transmission Electron Microscopy: Physics of Image Formation, Springer, New York (2007).

[2007Sar] P.M. Sarosi, B. Wang, J.P. Simmons, Y. Wang and M.J. Mills, Formation of Multimodal Size Distributions of γ′ in a Nickel-base Superalloy during Interrupted Continuous Cooling, *Scripta Mater*., 57 (2007) 767-770.

[2007Sei1] D.N. Seidman, K.E. Yoon and R.D. Noebe, Effects of Rhenium Addition on the Temporal Evolution of the Nanostructure and Chemistry of a Model Ni-Cr-Al Superalloy. I: Experimental Observations, *Acta Mater*., 55 (2007) 1145-1157.

[2007Sei2] D.N. Seidman, K.E. Yoon and R.D. Noebe, Effects of Rhenium Addition on the Temporal Evolution of the Nanostructure and Chemistry of a Model Ni–Cr–Al Superalloy. II: Analysis of the Coarsening Behavior, *Acta Mater*., 55 (2007) 1159-1169.

[2007Sob] I. Sobchenko, J. Pesicka, D. Baither, W. Stracke, T. Pretorius, L. Chi, R. Reichelt and E. Nembach, Atomic Force Microscopy (AFM), Transmission Electron Microscopy (TEM) and Scanning Electron Microscopy (SEM) of Nanoscale Plate-shaped Second Phase Particles, *Phil. Mag*., 87 (2007) 2427-2460.

[2007Wen] M. Wenderoth, R. Völkl, S. Vorberg, Y. Yamabe-Mitarai, H. Harada and U. Glatzel. Microstructure, Oxidation Resistance and High-Temperature Strength of γ′ Hardened Pt-base Alloys, *Intermetallics*, 15 (2007) 539-549.

[2008Cor] L.A. Cornish, M.J. Witcomb, S.H. Coetzee, W. Tshawe and S.N. Prins, Anomalies and Pitfalls in Phase Analyses using BSE, *Proc. Microsc. Soc. South. Afr*., 38, p. 9, Gabarone, Botswana, 23rd–25th July 2008.

[2008Dwa] A. Dwarapureddy, E. Balikci, S. Ibekwe and A. Raman, Activation Energy for Growth in Single Size Distribution and the Dissolution Features of γ′ Precipitates in the Superalloy IN738LC, *J. Mater. Sci*., 43 (2008) 1802-1810.

[2008ElB] N. El-Bagour, M. Walya and A. Nofala, Effect of Various Heat Treatment Conditions on Microstructure of Cast Polycrystalline IN738LC Alloy, *Mater. Sci. Eng. A*, 487 (2008) 152-161.

[2008Sat] A. Sato, H. Harada, An-C. Yeh and K. Kawagishi, A 5th Generation SC Superalloy with Balanced High Temperature Properties and Processability, *Superalloys 2008*, pp. 131-138, Seven Springs, Pennsylvania, 14th-18th September 2008.

[2008Saw] A. Sawant, S. Tin and J.C. Zhao, High Temperature Nanoindentation of Ni-base Superalloys, *Superalloys 2008*, pp. 863-871, Eds. R.C. Reed, K.A. Green, P. Caron, T.P. Timothy, M.G. Fahrmann, E.S. Huron and S.A. Woodard, Champion, Pennsylvania, 14th-18th September 2008.

[2008Sho1] M.B. Shongwe, LA. Cornish and R. Süss, *Proc. Microsc. Soc. south. Afr.*, 38, p. 27, Gaborone, Botswana, 23rd–25th July 2008.

[2008Sho2] M.B. Shongwe, LA. Cornish and R. Süss, Improvement of ~Pt_3Al Volume Fraction and Hardness in a Pt-Al-Ru-Cr Pt-based Superalloy, *Advanced Metals Initiative Conference*, CD-ROM, Johannesburg, 18th-19th November 2008.

[2008Sud] C.K. Sudbrack, T.D. Ziebell, R.D. Noebe and D.N. Seidman, Effects of a Tungsten Addition on the Morphological Evolution, Spatial Correlations and Temporal Evolution of a Model Ni-Al-Cr Superalloy, *Acta Materialia*, 58 (2008) 448-463.

[2008Süs1] R. Süss, Private Communication, Advanced Materials Division, Mintek (2008).

[2008Süs2] R. Süss, Investigation of the Pt-Al-Cr System as Part of the Development of the Pt-Al-Cr-Ru Thermodynamic Database, PhD Thesis, University of the Witwatersrand, Johannesburg, South Africa (2008).

[2008Tia] G. Tian, C. Tia, Y. Wen, G. Liu and B. Fu, Cooling γ′ Precipitation Behavior and Strengthening in Powder Metallurgy Superalloy FGH4096, *Rare Metals*, 27 (2008) 410-417.

[2008Tsh] W. Tshawe, Behaviour of Platinum Based Alloys at High Temperatures, MSc Dissertation, University of the Witwatersrand, Johannesburg, South Africa (2008).

[2008Wu] R.T. Wu and R.C. Reed, The Compatibility of Single Crystal Superalloys with a Thermal Barrier Coating, *Acta Mater.*, 56 (2008) 313-323.

[2008Yeh] A. Yeh, A. Sato, T. Kobayashi and H. Harada, On the Creep and Phase Stability of Advanced Ni-base Single Crystal Superalloys, *Mater. Sci. Eng. A*, A490 (2008) 445-451.

[2009Bou] G. Boussinot, A. Finel and Y. Le Bouar, Phase-field Modeling of Bimodal Microstructures in Nickel-based Superalloys, *Acta Mater.*, 57 (2009) 921-931.

[2009Cor1] L.A. Cornish, R. Süss, A. Douglas, L.H. Chown and L. Glaner, The Platinum Development Initiative: Platinum-based Alloys for High Temperature and Special Applications: Part I, *Plat. Met. Rev.*, 53 (2009) 2-10.

[2009Cor2] L.A. Cornish, R. Süss, L.H. Chown and L. Glaner, The Platinum Development Initiative: Platinum-based Alloys for High Temperature and Special Applications: Part III, *Plat. Met. Rev.*, 53 (2009) 155-163.

[2009Dou] A. Douglas, P.J. Hill, T. Murakumo, L.A. Cornish and R. Süss, The Platinum Development Initiative: Platinum-based Alloys for High Temperature and Special Applications: Part II, *Plat. Met. Rev.*, 53 (2009) 69-77.

[2009Hwa] J.Y. Hwang, R. Banerjee, J. Tiley, R. Srinivasan, G.B. Viswanathan and H.L. Fraser, Nanoscale Characterization of Elemental Partitioning between Gamma and Gamma Prime Phases in René 88 DT Nickel-Base Superalloy, *Metall. Mater. Trans. A*, A40 (2009) 24-35.

[2009Mul] F.M.L. Mulaudzi, Constitution of the Pt-Cr-Nb System, MSc Dissertation, University of the Witwatersrand, Johannesburg, South Africa (2009).

[2009Rio] F.A. Rioult, S.D. Imhoff, R. Sakidja and J.H. Perepezko, Transient Oxidation of Mo-Si-B Alloys: Effect of the Microstructure Size Scale, *Acta Mater.*, 57 (2009) 4600-4613.

[2009Sho1] M.B. Shongwe, Optimisation of Compositions and Heat Treatments of Pt-Based Superalloys, MSc Dissertation, University of the Witwatersrand, Johannesburg, South Africa (2009).

[2009Sho2] M.B. Shongwe, L.A. Cornish and R. Süss, Effect of Misfit on the Microstructure of Pt Based Superalloys, *Proc. Microsc. Soc. south. Afr.*, 39, p. 59, Durban, 8th-11th December 2009.

[2009Til] J. Tiley, G.B. Viswanathan, R. Srinivasan, R. Banerjee, D.M. Dimiduk and H.L. Fraser, Coarsening Kinetics of γ′ Precipitates in the Commercial Nickel Base Superalloy René 88 DT, *Acta Mater*., 57 (2009) 2538–2549.

[2009Van] G.F. Vander Voort, Metallography: Principles and Practice, Material Science and Engineering Series, ASM International, Materials Park, Ohio, 1999.

[2010Bur] S. Burk, B. Gorr, V.B. Trindade and H.-J. Christ, Effect of Zr Addition on the High-Temperature Oxidation Behaviour of Mo-Si-B Alloys, *Oxid. Met.*, 73 (2010) 163-181.

[2010Jan] N. Janakiraman and F. Aldinger, Indentation Analysis of Elastic and Plastic Deformation of Precursor-derived Si-C-N Ceramics, *J. Eur. Ceram. Soc*., 30 (2010) 775-785.

[2010ElB] N. El-Bagour and A. Nofala, Microstructure of a Experimental Ni Base Superalloy under Various Casting Conditions, *Mater. Sci. Eng. A*, A527 (2010) 7793-7800.

[2010Hon] L. Hongyu, S. Xiping, W. Yanli and C. Guoliang, Characterization of γ′ Precipitates in a Nickel Base Superalloy Quenching from Ageing Temperature at Different Rates, *Rare Metals*, 29 (2010) 204-208.

[2010Kam] S. Kamal, R. Jayaganthan and S. Prakash, High Temperature Cyclic Oxidation and Hot Corrosion Behaviours of Superalloys at 900°C, *Bull. Mater. Sci.*, 33 (2010) 299-306.

[2010Nik] E. Nikulina, K. Durst, M. Göken, R. Völkl and U. Glatzel, Microstructural and Micromechanical Characterisation of a Pt-Al-Cr-Ni-Re Alloy, *Int. J. Mat. Res.*, 101 (2010) 585-588.

[2010Pot] J.H. Potgieter, N.B. Maledi, M. Sephton and L.A. Cornish, Platinum-based Alloys for High Temperature and Special Applications: Part IV, *Plat. Met. Rev.*, 54 (2010) 112–119.

[2010Tsu] Y. Tsukada, Y. Murata, T. Koyama and M. Morinaga, Phase-field Simulation on Coarsening of the γ′ Phase Particles in Ni-based Superalloys considering Elastic Inhomogeneity, *Defect and Diffusion Forum*, 297-301 (2010) 376-383.

[2010Sho] M.B. Shongwe, B. Odera, S. Samal, A.M. Ukpong, A. Watson, R. Süss, L.H. Chown, G.O. Rading and L.A. Cornish, Assessment of Microstructures in the Development of Pt-based Superalloys, Light Metals Conference, SAIMM, Paper 184-202 Shongwe on CD, Muldersdrift, South Africa, 27th-29th Oct. 2010.

[2010Wit] M.J. Witcomb, Private Communication, University of the Witwatersrand, Johannesburg, South Africa (2010).

[2011Bat1] P. Battaini, Final Analysis: Electrolytic Etching for Microstructure Detection in Platinum Alloys, *Plat. Met. Rev*., 55 (2011) 71-72.

[2011Bat2] P. Battaini, Microstructure Analysis of Selected Platinum Alloys**,** *Plat. Met. Rev*., 55 (2011) 74-83.

[2011Cor] L.A. Cornish and L.H. Chown, Platinum-based Alloys and Coatings: Materials for the Future? Advances in Gas Turbine Technology (2011) pp. 337-370.

[2011Ode] B.O. Odera, L.A. Cornish, M.B. Shongwe, G.O. Rading and M.J. Papo, A Study of some As-cast and Heat Treated Alloys of the Pt-Al-V System at the Pt-Rich Corner, in ZrTa2011: New Metals Development Network Conference, on CD, Magaliesburg, South Africa, 12th-14th October 2011.

[2011Odu] J.K. Odusote, High Temperature Oxidation of Pt-based Alloys, PhD Thesis, University of the Witwatersrand, Johannesburg, South Africa (2011).

[2011Oh] J. Oh, I. Choi, Y. Kim, B. Yoo and J. Jang, Variations in Overall- and Phase-hardness of a New Ni-based Superalloy during Isothermal Aging, *Mater. Sci. Eng. A*, A528 (2011) 6121–6127.

[2011Oly] Olympus Corporation, BX61 Microscope System User's Guide, Version:11 (2011).

[2011Sho] M.B. Shongwe, M.J. Witcomb, L.A. Cornish and M.J. Papo, TEM Investigation of ~Pt_3Al Precipitate Morphology and Volume Fraction of Pt_{82}:Al_{12}:Ru_2:Cr_4, *Proc. Microsc. Soc. South. Afr.*, 41, p. 81, Pretoria, 6th-9th Dec. 2011.

[2012Her] C. Herbert, D. Axinte, M. Hardy and P.D. Brown, Investigation into the Characteristics of White Layers Produced in a Nickel Based Superalloy from Drilling Operations, *Mach. Sci. Techn.*, 16 (2012) 40-52.

[2012Ode] B.O. Odera, L.A. Cornish, M.J. Papo and G.O. Rading, Electrolytic Etching of Platinum-Aluminium Based Alloys, *Plat. Met. Rev.*, 56 (2012) 256-261.

[2012Odu1] J.K. Odusote, L.A. Cornish and M.J. Papo, High Temperature Oxidation of Pt-Al-Cr-Ru alloy: Scale Morphology and Adherence, *Metallography, Microstructure and Analysis*, 1 (2012) 142-149.

[2012Odu2] J.K. Odusote, L.A. Cornish and L.H. Chown, Oxidation Kinetics and Mechanisms of Growth of Alumina Scale on Precipitation-hardened Pt-Al-Cr-Ru Alloys, *Corr. Sci.*, 63 (2012) 119-128.

[2012Oli] J. Olivier, Private Communication, Nelson Mandela Metropolitan University (NMMU), Department of Physics and Centre for HRTEM, Port Elizabeth, South Africa (2012).

[2013Lav] A. Lavakumar, P.K. Singh, S. Srivastava, S. Kori and L.A. Kumar, Gamma Prime Coarsening Behavior of Nickel Super Alloy Super Cast 247A after Prolonged Thermal Exposures, *J. Mech. Civ. Eng.*, 334 (2013) 37-42.

[2013Ode] B.O. Odera, PhD Thesis, Addition of Vanadium and Niobium to Platinum-based Alloys, University of the Witwatersrand, Johannesburg, South Africa (2011).

[2013Odu] J.K. Odusote, L.A. Cornish, L.H. Chown and R.M. Erasmus, Determination of Residual Stress in Alumina Scale by Photostimulated Cr^{3+} Luminescence Piezospectroscopy, *Corr. Sci.*, 70 (2013) 276–284.

[2013Van] G.F Vander Voort, Private communication to L.A. Cornish.

[2014Hwa] S.H. Hwang, J.M. Byun, S. Lee, M-J. Yung, S.-T. Oh, Y.D. Kim, Fabrication of Mo-Si-B Intermetallic Powder by Mechano-chemical Process, *J. Alloys Compds*., 585 (2014) 418–422.

[2014Ode] B.O. Odera, M.J. Papo, G.O. Rading and L.A. Cornish, Experimental Solidification Projection, Liquidus Surface Projection and Isothermal Section at 1000°C for the Pt-Cr-V System, *J. Phase Equilib. Diff.*, 35 (2014) 476–489.

[2014Odu] J.K. Odusote, L.A. Cornish, L.H. Chown and R.M. Erasmus, Measurement of the Stress in Oxide Scales Developed upon Oxidation of a Pt-based Alloy in air at 1250°C, *Int. J. Appl. Cer. Tech.*, 11 (2014) 602-610.

[URLPGM] The PGM Database, Platinum: http://www.platinummetalsreview.com/jmpgm/index.jsp., date accessed: 4 May 2012.

[URLQua] A Primer on Interaction Effects in Multiple Linear Regression: http://www.quantpsy.org/interact/interactions.htm., date accessed: 5 December 2013.

[URLRea] http://www.real-statistics.com/multiple-regression/interaction/., date accessed: 5 December 2013.

[URLSta] http://www.statsdirect.com/help/default.htm#basics/p_values.htm., date accessed: 29 May 2014.

APPENDIX A

Hertzian fitted results at loads of 2mN and 1mN compared with results at a load of 2.5mN

Tables A.1 and A.2 show nanoindentation results at loads of 2.0 and 1.0mN. The Hertzian-fitted nanohardness and elastic modulus were ~20% lower than the 2.5mN results (Table 4.17). Similar to the 2.5mN results, the standard deviations of the Hertzian-fitted results were also slightly less than 10%. Pt_{80}:Al_{14}:Cr_3:Ru_3 (at.%) had the highest precipitate hardness for loadings of 2.0mN and 2.5mN, and for the 1.0mN, it had the second highest precipitate hardness.

Table A.1. Nanohardness and elastic moduli calculated at final contact depth and maximum applied load 2.0mN, using the Hertzian fit.

Nominal composition (at.%)	Nanohardness (GPa)		Elastic Modulus (GPa)	
	γ´ Phase	γ Phase	γ´ Phase	γ Phase
Pt_{82}:Al_{12}:Cr_4:Ru_2	8.8 ± 0.7	5.9 ± 0.4	192.2 ± 18.1	203.0 ± 19.3
Pt_{85}:Al_7:Cr_5:Ru_3	9.8 ± 0.9	7.6 ± 0.7	239.2 ± 21.9	205.4 ± 18.8
Pt_{80}:Al_{11}:Cr_3:Ru_6	9.8 ± 0.8	6.1 ± 0.4	209.3 ± 24.5	193.3 ± 8.3
Pt_{80}:Al_{14}:Cr_3:Ru_3	10.3 ± 0.9	5.4 ± 0.4	210.9 ± 19.8	182.3 ± 17.2
Pt_{78}:Al_{11}:Cr_8:Ru_3	8.4 ± 0.6	6.8 ± 0.5	213.2 ± 20.1	168.4 ± 15.9
Pt_{78}:Al_{11}:Cr_6:Ru_5	8.3 ± 0.5	7.6 ± 0.5	204.7 ± 19.1	214.3 ± 20.7

Table A.2. Nanohardness and elastic moduli calculated at final contact depth and maximum applied load 1.0mN, using the Hertzian fit.

Nominal composition (at.%)	Nanohardness (GPa)		Elastic Modulus (GPa)	
	γ´ Phase	γ Phase	γ´ Phase	γ Phase
Pt_{82}:Al_{12}:Cr_4:Ru_2	8.2 ± 0.7	6.2 ± 0.5	200.0 ± 18.2	177.3 ± 16.2
Pt_{85}:Al_7:Cr_5:Ru_3	9.8 ± 0.8	6.9 ± 0.4	222.9 ± 21.9	178.8 ± 16.9
Pt_{80}:Al_{11}:Cr_3:Ru_6	8.5 ± 0.6	6.7 ± 0.4	214.5 ± 20.9	191.0 ±18.3
Pt_{80}:Al_{14}:Cr_3:Ru_3	9.1 ± 0.8	6.3 ± 0.5	238.3 ± 22.1	184.6 ± 16.2
Pt_{78}:Al_{11}:Cr_8:Ru_3	8.9 ± 0.7	6.2 ± 0.5	213.2 ± 20.9	182.6 ± 15.6
Pt_{78}:Al_{11}:Cr_6:Ru_5	8.7 ± 0.6	7.3 ± 0.6	234.4 ± 22.8	189.9 ± 17.3

APPENDIX B

Nanohardnesses and elastic moduli for the γ phase calculated at final contact depth and maximum applied load of 5mN

Table B.1. Nanohardnesses and elastic moduli for the γ phase calculated at final contact depth and maximum applied load of 5mN.

Nominal composition (at.%)	Nanohardness (GPa)		Elastic Modulus (GPa)	
	2.5mN	5mN	2.5mN	5mN
$Pt_{82}:Al_{12}:Cr_4:Ru_2$	7.3 ± 0.6	7.9 ± 0.6	233.3 ± 21.8	238.6 ± 23.1
$Pt_{85}:Al_7:Cr_5:Ru_3$	9.0 ± 0.7	8.8 ± 0.7	241.6 ± 18.4	239.7 ± 21.8
$Pt_{80}:Al_{11}:Cr_3:Ru_6$	8.3 ± 0.6	8.5 ± 0.8	238.7 ± 23.3	239.6 ± 20.9
$Pt_{80}:Al_{14}:Cr_3:Ru_3$	7.5 ± 0.4	7.5 ± 0.7	236.7 ± 21.6	236.5 ± 22.4
$Pt_{78}:Al_{11}:Cr_8:Ru_3$	8.1 ± 0.5	7.8 ± 0.9	237.2 ± 19.7	237.3 ± 21.6
$Pt_{78}:Al_{11}:Cr_6:Ru_5$	9.1 ± 0.7	9.3 ± 0.4	243.5 ± 16.4	241.9 ± 22.4

APPENDIX C

ATTEMPT TO CAST SINGLE CRYSTALS

CHAPTER ONE

1. LITERATURE REVIEW

1.1 Manufacture of Single Crystals

Single crystal (SC) castings were a further development on the technological advances made in the directionally solidified (DS) casting processes. SC castings are produced in a similar fashion to DS by selecting a single grain, via a grain selector [1970Ver, 1979Nor]. During solidification, this single grain grows to fill the entire part. Single crystals obtain their outstanding strength by not having the grain boundaries that are present in both equiaxed and directionally solidified materials. Single crystal superalloys also have the <001> low modulus orientation in the plane normal to the solidification direction and a random secondary orientation in the plane normal to the direction of solidification. Other specific primary or secondary orientations are possible with the use of seed crystals. The seed crystal should be of the desired alloy, or with an equivalent or higher melting temperature. It is positioned so that its orientation will be repeated in the alloy that fills the mould cavity [1970Ver, 1979Nor].

1.2 Single Crystal Growth using the Bridgman Method

The Bridgman method was developed for growing single crystals. It was integrated with investment casting and used to produce superalloy single-crystal airfoils for the aerospace industry in the 1970s [1974Sal, 1987Sim]. The process essentially involves a furnace set up with a region of high temperature which is above the melting temperature of the Ni-based alloy, controlled by heaters, and a lower temperature melting zone, with a gradient zone where the solid-liquid interface occurs (Figure C.1) [1994Lud]. The superalloy is initially entirely within the high temperature zone in molten form, and then the alloy is lowered extremely slowly in the furnace, corresponding to a rate of about 0.1mm/minute, so that the solid liquid interface rises slowly up the mould [1994Lud]. The superalloy solidifies from the base upwards. The slow rate of solidification causes grains to grow as dendrites in the

direction in which the mould is pulled from the furnace. To ensure no grain boundaries form, a grain selector is attached to the bottom of the mould [1987Sim]. As the vertical dendrites grow at the base of the mould, only one dendrite is able to grow through the grain selector and eventually into the mould. Thus, once the solidification is complete, the NBSA is created entirely from one grain and is a single crystal NBSA [1974Sal, 1987Sim, 1994Lud, 2009Ony].

There are multiple parameters in the Bridgman crystal growth which can be varied to achieve optimal crystal growth conditions [1989Fav], including the crucible material, crucible diameter and translation speed. Each material has a critical growth velocity: below this critical value, a single crystal can be grown, whereas above this velocity, a polycrystalline material will form [1986Bri, 1989Fav].

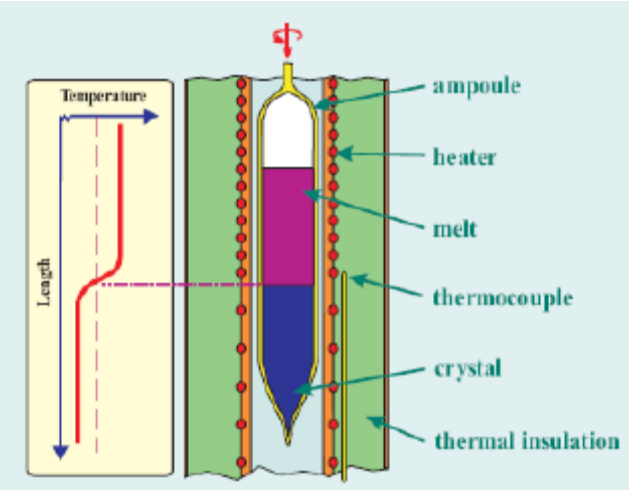


Figure C.1. Simplified diagram illustrating the Bridgman method [1994Lud].

1.3 Single Crystal Growth using the Czochralski Method

In the Czochralski method, a single crystal is pulled from the melt, whereas in the Bridgman method, the central chamber is pushed down from the high temperature region towards the low temperature region [1957Pfa, 1972Sim]. A schematic diagram of the Czochralski method is illustrated in Figure C.2 [1994Lud]. The Czochralski process is a method of crystal growth used to obtain single crystals for semiconductors (e.g. silicon, germanium and gallium arsenide), metals (e.g. palladium, platinum, silver, gold), salts, and synthetic gemstones. The most important application may be the growth of large cylindrical ingots of single crystal

silicon. An obvious advantage of the Bridgman method over the Czochralski method is the lower defect densities of the single crystal [1957Pfa, 1987Sim].

The Czochralski method has also been employed for the production of large single crystal nickel alloys, since the late 1950s [1957Pfa, 1987Sim]. However, the crystals had a high density of defects until in the late 1970s, when Kuriyama *et al*. [1978Kur] varied the melt temperature and fluid velocity to control the density of defects. Since the 1970s, large nickel single crystals have been grown by the Czochralski technique with a low concentration of defects [1987Sim]. Subsequently, more improvements have been made with the Czochralski method by changing the interface shape, interface velocity, pulling speed and fluid velocity near the interface [2009Ony].

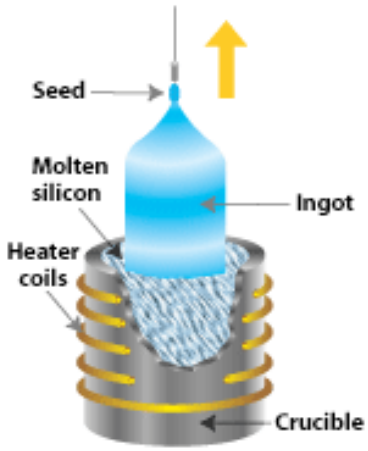


Figure C.2. Simplified diagram illustrating the Czochralski method [1994Lud].

CHAPTER TWO

2. EXPERIMENTAL PROCEDURE

2.1 Single Crystal Attempt: Sample Manufacture

The apparatus used in the attempt to grow single crystals was a vertical Bridgman system made by Crystalox, Ltd [1982Cry]. The alumina crucible containing the solid Pt-based alloy was lowered out of the furnace at a constant rate between 0.08 and 0.30mm/min, within the vacuum chamber. Figure C.3 shows the Crystalox system used, and the induction furnace. Problems were experienced in reaching the melting point of the Pt-Al-Cr-Ru alloys, which

was expected to be about 1800°C (whereas 1769°C is the melting point of pure Pt). The highest possible temperature that could be reached was 1570°C, above which vacuum was lost and the power supply would trip. This meant that it was not possible to melt the alloy button. It was then decided to use the crystal grower system as a high temperature furnace to heat treat the sample. Thus, the next step was to heat the alloy to 1565°C and hold it at this temperature for 20 minutes, and then lower it within the chamber to the lower temperature zone at about 0.30mm/minute and the furnace was switched off, allowing the alloy to cool down to room temperature overnight.

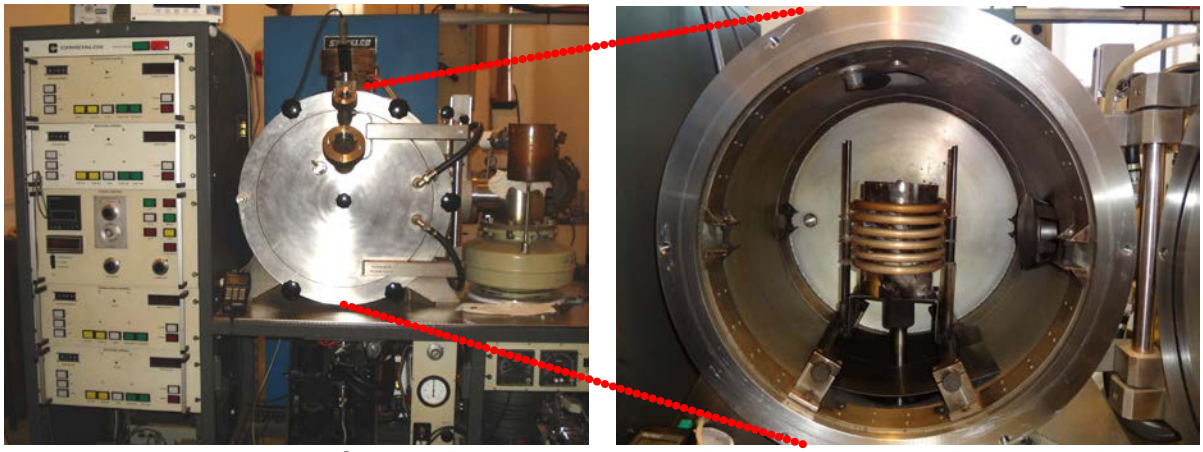


Figure C.3. Front view of Crystal Grower System, showing (a) Crystalox control unit and vacuum chamber, and (b) vacuum chamber and induction furnace unit.

CHAPTER THREE

3. RESULTS

Figure C.4 shows an SEM image of as-cast Pt_{85}:Al_7:Cr_5:Ru_3 (at.%) before being placed into the Crystalox system. The alloy consisted of mainly cored (Pt) dendrites with a (Pt) + ~Pt_3Al eutectic. The eutectic/matrix interface was darker, possibly due to shrinkage on solidification.

The microstructure of Pt_{85}:Al_7:Cr_5:Ru_3 (at.%) after being heat treated to 1565°C and furnace cooled to room temperature in the Bridgman Crystalox system is shown in Figure C.5. A fine homogenous distribution of ~Pt_3Al precipitates was seen, with subgrain boundaries. This microstructure confirmed that the required melting point and single crystal growth were not achieved. However, remnants of the eutectic were found, which were areas with higher concentrations of the ~Pt_3Al precipitates (Arrow, Figure C.5), which could have been the

edges of the dendrites near the eutectic/eutectoid areas. Some of the precipitates looked like "Maltese crosses" [1958Wes] (Figure C.5). SEM image analysis of the single crystal attempt alloy (nominal Pt_{85}:Al_7:Cr_5:Ru_3 (at.%)) had a ~Pt_3Al volume fraction of ~43 ± 5%.

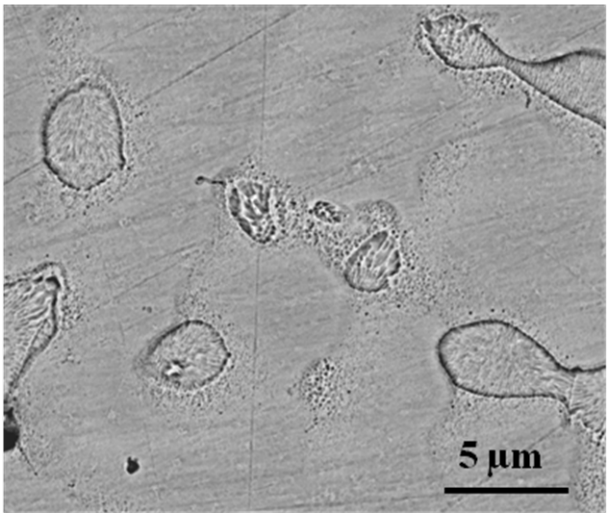


Figure C.4. SEM-BSE image of as-cast and unetched nominal Pt_{85}:Al_7:Cr_5:Ru_3 (at.%), showing (Pt) dendrites (light) with ~Pt_3Al precipitates and a eutectic of (Pt) + ~Pt_3Al.

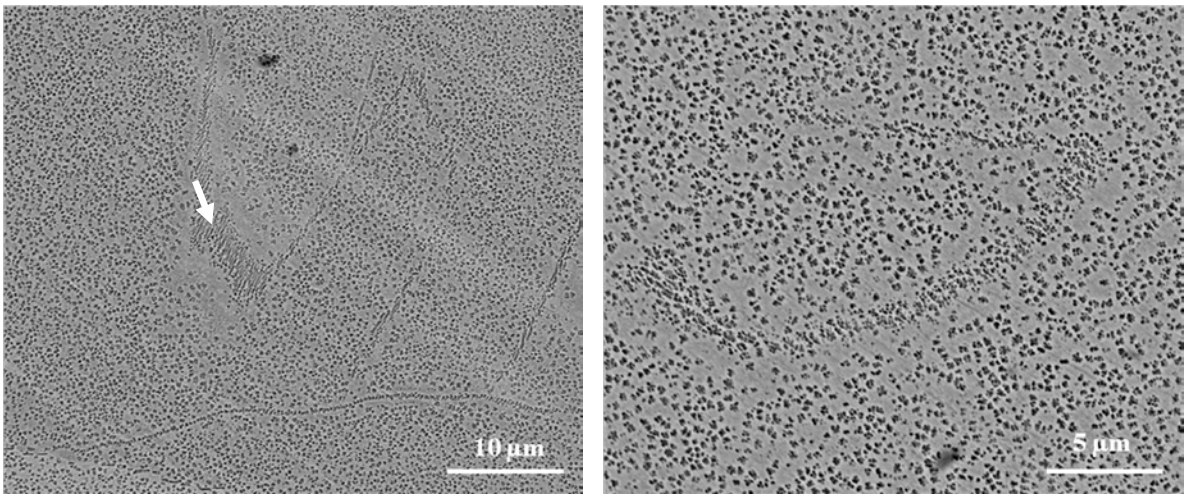


Figure C.5. SEM-BSE images of nominal Pt_{85}:Al_7:Cr_5:Ru_3 (at.%) after annealing in the crystal grower, furnace cooled and electrolytically etched in HCl/NaCl solution, showing very fine dark ~Pt_3Al precipitates in light (Pt) matrix, with grain boundaries and regions of higher ~Pt_3Al concentration.

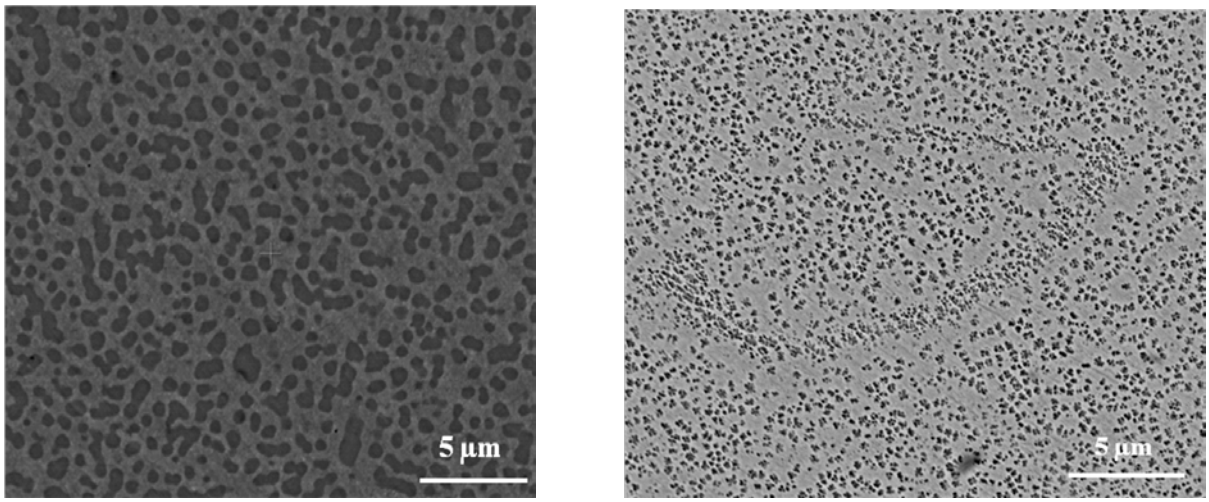
CHAPTER FOUR

4. DISCUSSION

Comparison of the furnace-cooled sample from the Crystalox system (Figure C.6(b)) to the sample with the same nominal composition previously studied (Figure C.6(a)) [2009Sho1],

showed a finer distribution of precipitates, with a similar ~Pt_3Al volume fraction. The precipitate morphology was also different, and the furnace-cooled alloy had precipitates that were quadri- or ogdoadically diced [1958Wes]. Similar precipitate morphologies have also been observed in Pt_{86}:Al_{10}:Ir_4 [2004Dou2] and Pt_{86}:Al_{10}:Ru_4 (at.%) [2001Hil5]. Durand-Charre [1997Dur] observed that during heat treatment of NBSA AM1, the cuboid precipitates tended to group together in blocks, which subsequently coalesced (Figure 5.2). However, when the homogenizing treatment was prolonged to 50 hours and more, this phenomenon completely disappeared. It is therefore thought the Pt_{85}:Al_7:Cr_5:Ru_3 (at.%) microstructure in Figure C.6(b) developed because the heat treatment was not optimal, since the sample was only at the highest temperature of 1565°C for 20 minutes. A longer heat treatment time at this temperature might have produced a different microstructure, similar to the observations by Durand-Charre [1997Dur], although when the heat treatment time was increased from 20 minutes to 40 minutes, no ogdoadically diced precipitates were observed. Coring was observed in the sample before annealing in the crystal grower (Figure C.4), although after heat treatment at 1565°C for 20 minutes and furnace cooling to room temperature overnight, no coring was observed (Figure C.5). NBSA René 77 had ogdoadically diced precipitates when it was heat treated at 1160°C for 2h then furnace cooled [1997Dur]. Heat treatment at the same temperature for 4h followed by air cooling gave a fine distribution of precipitates without the ogdoadically shaped precipitates [1987Sim], showing that the ogdoadically shaped precipitates formed when the heat treatment was not optimal.

Vorberg *et al.* [2004Vor] reported that for $Pt_{78.5}$:$Al_{12.5}$:Cr_3:Ni_6 (at.%) after air cooling, there was a fine distribution of precipitates, while after furnace cooling, there was a mixture of very fine and large precipitates. The large particles formed by coarsening of the small ones. Similar observations have been made in nickel-based superalloy GH742 by Hongyu *et al.* [2010Hon] for furnace cooled samples from 1050°C. In the present work, no coarsening of the finer precipitates was observed, even though the sample was furnace cooled from a temperature of 1565°C, close to the 1500°C of Vorberg *et al*. [2004Vor]. It should be noted that in the present work, the sample heat treatment was different, since the cooling was done under vacuum in an induction furnace (Appendix C) and the sample was transferred from the high temperature zone to the lower temperature zone of the furnace. Thus, obtaining similar results to other workers was unlikely.



(a) **(b)**

Figure C.6. SEM-BSE images of nominal Pt_{85}:Al_7:Cr_5:Ru_3 (at.%): (a) after annealing at 1500°C for 18 hours, then water quenching, and annealed at 1100°C for 120 hours and air cooled, showing ~Pt_3Al precipitates (dark) in a (Pt) matrix (light) [2008Sho1, 2009Sho1], and (b) after annealing in crystal grower at 1565°C for 20 minutes and furnace cooled overnight and electrolytic etching in HCl/NaCl solution, showing very fine dark ~Pt_3Al precipitates in light (Pt) matrix.

CHAPTER FIVE

5. CONCLUSION

Attempts to produce a single crystal alloy were made, but the furnace could not reach a high enough temperature to melt the alloy, and so the furnace was used for a high temperature heat treatment instead. Heat treating a sample under the vacuum environment gave a fine distribution of ~Pt_3Al precipitates in a (Pt) matrix, and removed coring. Thus, heat treatment at 1500°C followed by furnace cooling might produce a fine distribution of precipitates.

CHAPTER SIX

6. REFERENCES

[1957Pfa] W.G. Pfann, Techniques of Zone Melting and Crystal Growing, *Solid State Physics*, 4 (1957) 423-521.

[1958Wes] J.H. Westbrook, Precipitation of Ni_3Al from Nickel Solid Solution as Ogdoadically Diced Cubes, *Z. Kristallogr*., 110 (1958) 21-29.

[1970Ver] F.L. Ver Snyder and M.E. Shank, The Development of Columnar Grain and Single Crystal High Temperature Materials through Directional Solidification, *Mat. Sci. Eng*., 6 (1970) 213-247.

[1972Sim] C.T. Sims and W.C. Hagel, The Superalloys, John Wiley & Sons, New York (1972).

[1974Sal] K.Z. Saleeb and S. Kadečková, Some Observations on Twin Grains in As-Grown Iron Single Crystals, *J. Cryst. Growth*, 26 (1974) 303-310.

[1978Kur] M. Kuriyama, W.J. Boettinger and H.E. Burdette, Crystal Perfection in Czochralski Grown Nickel Single Crystals, *J. Cryst. Growth*, 43 (1978) 287-300.

[1979Nor] J.E. Northword, Improving Turbine Blade Performance by Solidification Control, *Metall. Met. Form.*, 46 (1979) 437-442.

[1982Cry] Crystalox Ltd, CGS, Czochralski Growth System, Abingdon, UK (1982).

[1986Bri] J.C. Brice, Crystal Growth Processes, Thomson Science and Professional, Blackie, Glasgow, UK (1986).

[1987Sim] C.T. Sims, N.S. Stoloff and W.C Hagel, Superalloys II: High Temperature Materials for Aerospace and Industrial Power, Wiley Interscience, New York, USA (1987).

[1989Fav] J.J. Favier and D. Camel, Fundamentals of Melt Growth, Crystal Growth in Science and Technology, Plenum Press, New York, USA (1989) pp. 69-83.

[1994Lud] A. Ludwig, I. Wagner, J. Laakmann and P.R. Sahm, Undercooling of Superalloy Melts: Basis of a New Manufacturing Technique for Single-crystal Turbine Blades, *Mater. Sci. Eng. A*, A17 (1994) 299-303.

[1997Dur] M. Durand-Charre, The Microstructure of Superalloys, CRC Press, New York, USA (1997).

[2001Hil5] P.J. Hill, Superalloy Analogues Based on Platinum for Ultra-high Temperature Applications, PhD Thesis, University of Witwatersrand, Johannesburg, South Africa (2001).

[2004Vor] S. Vorberg, M. Wenderoth, B. Fischer, U. Glatzel and R. Völkl, Pt-Al-Cr-Ni Superalloys: Heat Treatment and Microstructure, *JOM*, 56 (2004) 40-43.

[2008Sho1] M.B. Shongwe, LA. Cornish and R. Süss, *Proc. Microsc. Soc. south. Afr.*, 38, p. 27, Gaborone, Botswana, 23rd–25th July 2008.

[2009Ony] A. Onyszko, K. Kubiak and J. Sieniawski, Turbine Blades of the Single Crystal Nickel Based CMSX-6 Superalloy, *Journal of Achievements in Materials and Manufacturing Engineering*, 32 (2009) 66-69.

[2009Sho1] M.B. Shongwe, Optimisation of Compositions and Heat Treatments of Pt-Based Superalloys, MSc Dissertation, University of the Witwatersrand, Johannesburg, South Africa (2009).

[2010Hon] L. Hongyu, S. Xiping, W. Yanli, and C. Guoliang, Characterization of γ′ Precipitates in a Nickel Base Superalloy Quenching from Ageing Temperature at Different Rates, *Rare Metals*, 29 (2010) 204-208.

APPENDIX D

XRD Pattern of the Plasticine and the Methodology for Distinguishing between the two Forms of Pt_3Al and the Platinum-rich Solid Solution Phase

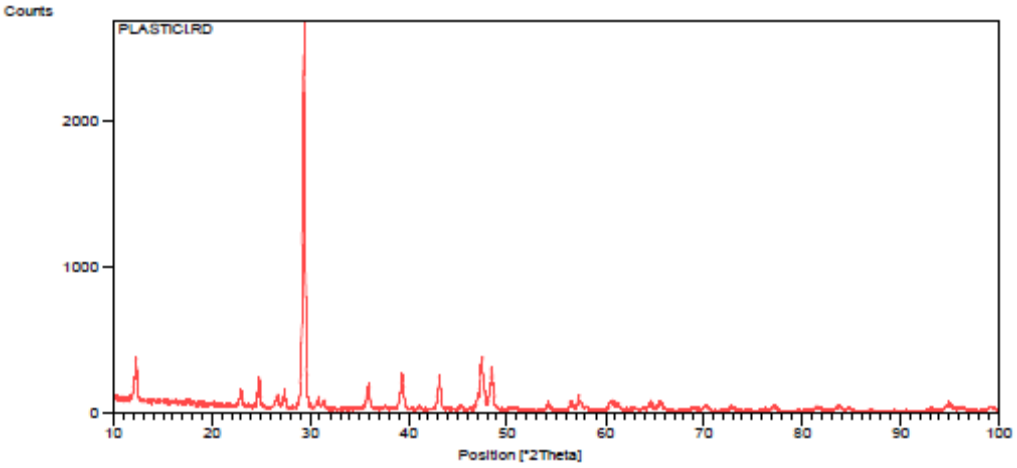


Figure D.1. XRD pattern of plasticine.

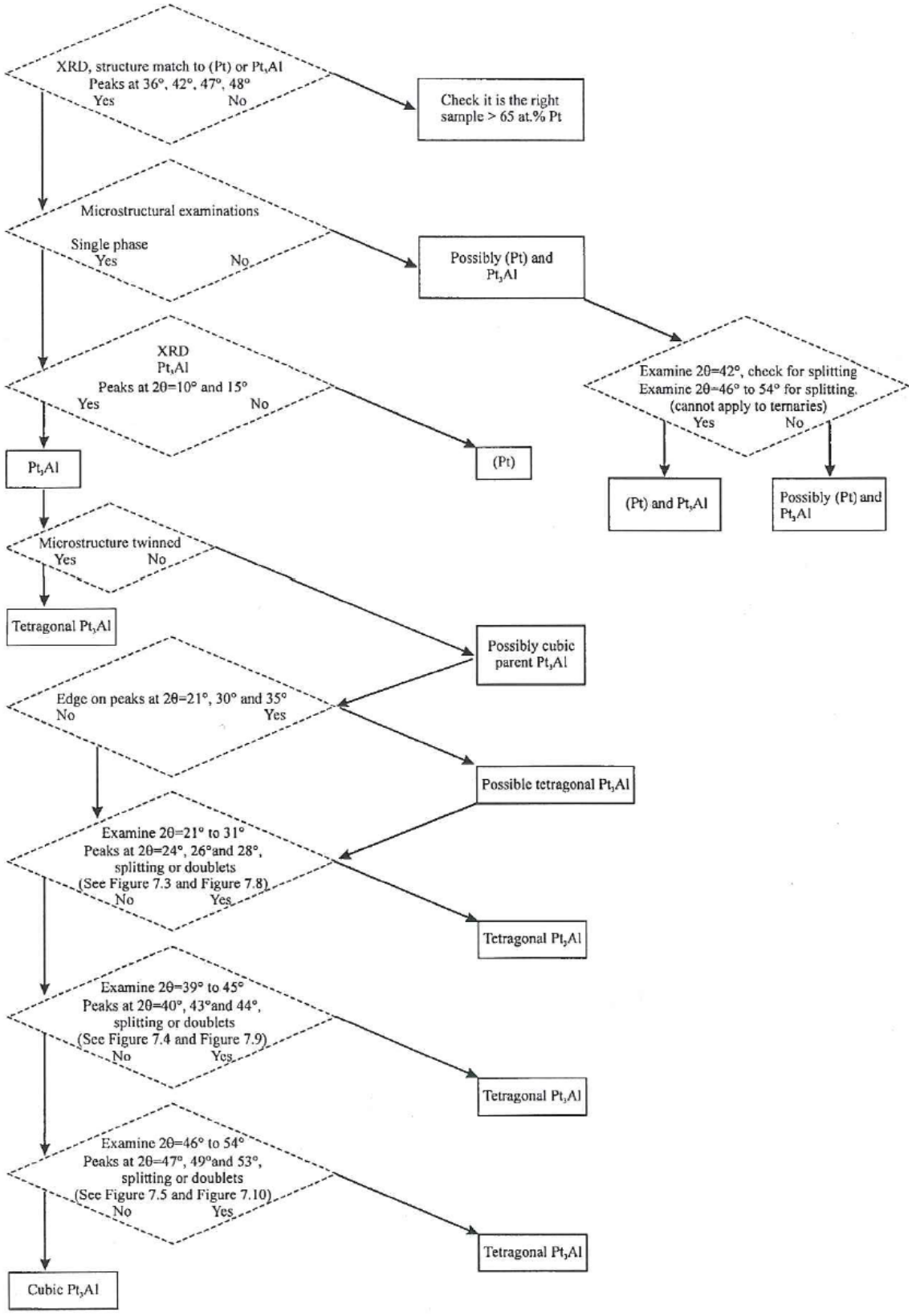


Figure D.2. Methodology for distinguishing between the two forms of Pt_3Al and the platinum-rich solid solution phase using a Mo Radiation [2001Big].

APPENDIX E

Hardness Testing and the Oliver-Pharr Approach

This section gives a summary of the Oliver-Pharr method used in this work, explains the phenomenon of the pop-in event as well as the method of calculations.

Hardness, the resistance of a material to plastic deformation, is measured on a variety of different scales such as Vickers, Rockwell and Martens, which differ in measurement procedure and method of calculation. These methods typically consist of indenting the surface of the specimen with a hard (e.g. diamond for Vickers hardness) indenter and measuring the residual imprint left in the material after removal of the indenter. On the other hand, instrumented hardness testing relies on indenting the material surface with an indenter of which the geometry is known to a high precision, while monitoring the applied load and penetration depth throughout the insertion and removal of the indenter [1986Doe]. Having the applied load and penetration depth data enables estimation of properties such as material hardness, elastic modulus and fracture toughness [1986Doe, 1992Oli]. The indentation analysis procedure developed by Oliver and Pharr [1992Oli, 2002Pha, 2004Fis, 2004Oli] has been widely used for hard materials such as metals and ceramics. Preliminary studies of the hardness and indentation depth are done first to ensure that at the maximum applied load, only the properties of a single phase are tested [1992Oli, 1999Gök, 2003Sch2].

The nanoindentation technique has been established as a powerful means of characterising the near-surface mechanical properties of materials [2004Fis, 1992Oli]. This technique relies on high-resolution instruments that simultaneously measure the load, P, and indenter displacement, h, during the loading and unloading indentation steps. The important parameters obtained from the resultant P-h curve, schematically illustrated in Figure E.1 [1992Oli], are:

P_{max} = peak load,

h_{max} = maximum penetration depth reached while the maximum load is applied,

h_f = final penetration depth obtained when the load is removed and the material is relaxed,

S = the contact stiffness.

Figure E.2 [1992Oli] shows a schematic cross-section of an indentation and identifies the various parameters.

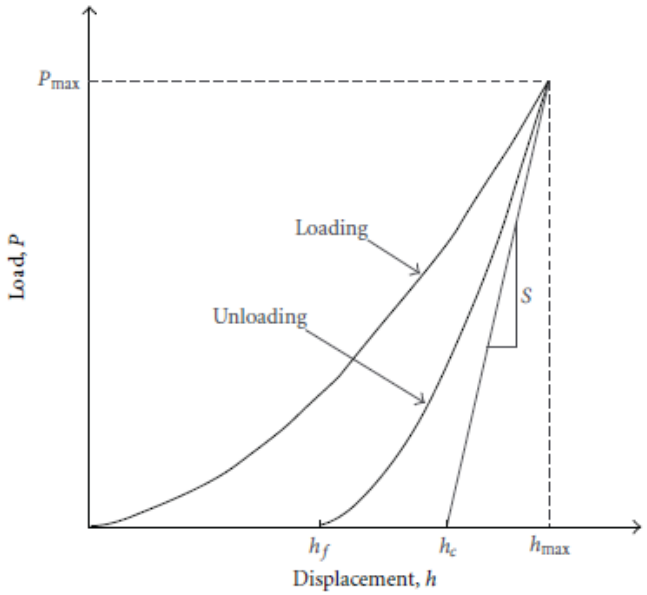


Figure E.1. Typical load-displacement curve during a loading-unloading cycle where h_{max} = maximum indenter displacement at peak indentation load P_{max}, S = initial unloading slope of the load-displacement curve, and h_c = contact depth [1992Oli].

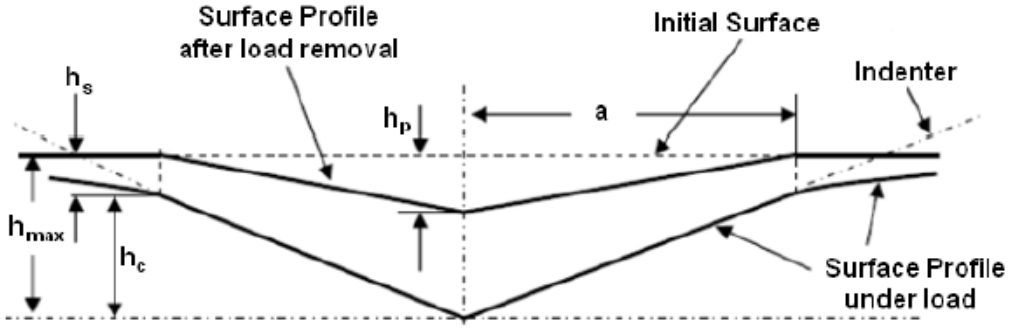


Figure E.2. Schematic representation of a section through an indentation, defining: h_c = vertical contact depth, h_s = displacement of the surface at the perimeter of the contact, h_{max} = maximum penetration depth at maximum load, a = radius of the contact, and h_p (≈h_f) = final depth penetration depth when the indenter is fully withdrawn [1992Oli].

The Oliver and Pharr method [1992Oli, 2004Oli] makes use of the data taken from the upper portion of the unloading curve fitted to the power-law relation given as:

$$P = \alpha\left(h - h_f\right)^m \qquad \text{Equation E.1}$$

where m is the displacement exponent in the load displacement relation, and α is an unloading fitting parameter dependent on the elastic response of the material. Both m and α are empirical constants determined using the power fitting of unloading data [2003Gon]. The

derivative of P (Equation E.1) with respect to h yields the contact stiffness S, which is the initial unloading slope of the P-h curve [1992Oli]:

$$S = \left(\frac{dP}{dh}\right)_{unloading} = m\alpha\left(h - h_f\right)^{m-1} \qquad \text{Equation E.2}$$

The contact depth of the indent impression h_c can either be derived by extrapolating the initial slope of the unloading P-h curve to P = 0, or otherwise determined using an empirical formula defined by Oliver and Pharr [1992Oli, 2002Pha, 2004Oli] given by:

$$h_c = h_{\max} - \in \frac{P_{\max}}{S} \qquad \text{Equation E.3}$$

where, for the Berkovich indenter geometry, $\in$ = 0.75 [2004Oli].

The contact area, A_c, is the cross-sectional area at h_c [2004Gon1, 2004Gon2]. Experimental and numerical studies have established that, for the Berkovich indenter geometry, the projected A_c can be approximated by the empirical formula [1992Oli, 2000Gon2, 2006Bou]:

$$A_c\left(h_c\right) = \left(24.56h_c^2 + C_1h_c^{1/2} + C_2h_c^{1/4} + C_3h_c^{1/8} + ...\right) \qquad \text{Equation E.4}$$

where C_1,C_2, . . . ,C_n are constants determined by curve fitting procedures [1992Oli, 2004Gon1, 2004Gon2] and are defined based on the indenter tip radius [2003Gon]. However, for the Berkovich indenter geometry, the projected area can be reduced to $A_c\left(h_c\right) \approx 24.56h_c^2$ without compromising the accuracy of the results [2004Fis, 2004Gon1, 2010Jan].

When S and A_c have been determined, the specimen's reduced elastic modulus E_r can be evaluated using:

$$E_r = \left(\frac{\sqrt{\pi}}{2\beta}\right)\left(\frac{S}{\sqrt{A_c}}\right) \qquad \text{Equation E.5}$$

where β is a correctional factor introduced by King [1987Kin] to address the lack of indenter symmetry. For the Berkovich indenter β = 1.034 [2010Jan].

The reduced modulus, E_r, is a direct result of the Oliver-Pharr method [1992Oli], and is slightly lower than the true modulus of the sample. It takes into account contributions of the diamond indenter to the measurements.

The modulus of elasticity, E_s (or $E_{specimen}$) the true modulus of the specimen, is calculated from the reduced elastic modulus, E_r, by [1992Oli]:

$$\frac{1}{E_r} = \frac{1-\nu_{specimen}^2}{E_{specimen}} + \frac{1-\nu_{indenter}^2}{E_{indenter}} \qquad \text{Equation E.6}$$

where $\nu_{specimen}$ and $\nu_{indenter}$ are the specimen and indenter Poisson's ratios, and $E_{indenter}$ is the indenter elastic modulus [1992Oli, 2004Fis, 2010Jan]. A Poisson's ratio of 0.1 and a modulus of elasticity of 1140GPa were used for diamond [1992Oli] and for the CMSX-6 superalloy phases (γ and γ'), a constant Poisson's ratio of 0.3 was assumed [1995Yoo, 1999Gök, 2001Mer, 2012Pop].

The indentation hardness H, has long been defined as the test force P_{max} divided by the projected area of contact A_c [1956Mot]:

$$H = \frac{P_{max}}{A_c} \qquad \text{Equation E.7}$$

A discontinuity in the load-displacement curve during loading, widely known as the pop-in event [1992Pag], is found on most crystalline materials, and is related to the nucleation of dislocations on carefully prepared smooth sample surfaces. The pop-in event has been recorded in metals [1998Kie, 1998Mic, 1999Sur, 2000Gou], alloys [1996Ger, 1998Bar] and intermetallic compounds [2002Chi1, 2002Chi2, 2003Wan]. During pop-in, the indenter travels without a measured increase of applied load (for a load-controlled experiment), or the load is rapidly released at a constant displacement. The loading part for all load-displacement curves with the pop-in effect has been fitted to a Hertzian model [1985Jon, 1986Bin, 1987Kin]. A similar procedure has also been utilized by Durst *et al.* [2004Dur] on NBSAs. The Hertzian fit expression (Equation E.8) has been found accurate for ceramics, titanium alloys and NBSAs when fitted to the loading parts of *P*-*h* curves [1996Ger, 1998Bar, 1998Kie, 1998Mic, 1999Sur, 2000Gou, 2004Sch, 2005Bah]:

$$P = \frac{4}{3} E_r R^{1/2} h^{3/2} \qquad \text{Equation E.8}$$

where P is the load, h the indentation depth and R is the radius of curvature of an assumed spherical indenter.

APPENDIX F

Conference Presentations

Presentations

1. A.M. Ukpong, **M.B. Shongwe**, L.A. Cornish, R. Süss and A. Watson, Comparison of Experimental and Calculated ~Pt_3Al Volume Fractions in Selected Pt-Al-Cr-Ru Superalloys, 5th International Conference of the African Materials Research Society, Book of Abstracts, Abuja, Nigeria, 14-18 Dec. 2009.

Published Conference Abstracts and Papers

1. **M.B. Shongwe**, L.A. Cornish and R. Süss, Effect of Misfit on the Microstructure of Pt Based Superalloys, Proceedings of the Microscopy Society of Southern Africa Conference, vol. 39, p. 59, Durban, South Africa, 8-11 Dec. 2009.

2. **M.B. Shongwe**, M.J. Witcomb, L.A. Cornish and M.J. Papo, TEM Investigation of ~Pt_3Al Precipitate Morphology and Volume Fraction of Pt_{82}:Al_{12}:Ru_2:Cr_4, Proceedings of the Microscopy Society of Southern Africa Conference, vol. 41, p. 81, Pretoria, South Africa, 6-9 Dec. 2011.

3. **M.B. Shongwe**, L.A. Cornish, and M.J. Witcomb, Microstructural Study of Pt-based Superalloys in the Heat Treated Condition, *Microscopy and Microanalysis*, 18 (2) 1686-1687, Phoenix, Arizona, USA, 29 July-2 August 2012.

4. L.A. Cornish, **M.B. Shongwe**, B. Odera, J.K. Odusote, M.J. Witcomb, L.H. Chown, G.O. Rading and M.J. Papo, Update on the Development of Platinum-Based Alloys for Potential High-Temperature Applications, The Southern African Institute of Mining and Metallurgy, *5th International Platinum Conference 2012*, pp. 905-924, Sun City, South Africa, 18th-20th September 2012.

5. **M.B. Shongwe**, L.A. Cornish, M.J. Witcomb and M.J. Papo, Micromechanical Characterisation of Pt-Al-Cr-Ru Alloys, Procedings of

Development Network, pp. 277-289, SAIMM, Magaliesburg, Johannesburg, 15-17 Oct. (2012).